Keck Observatory Report No. 90

The Design of the Keck Observatory and Telescope

(Ten Meter Telescope)

January 1985

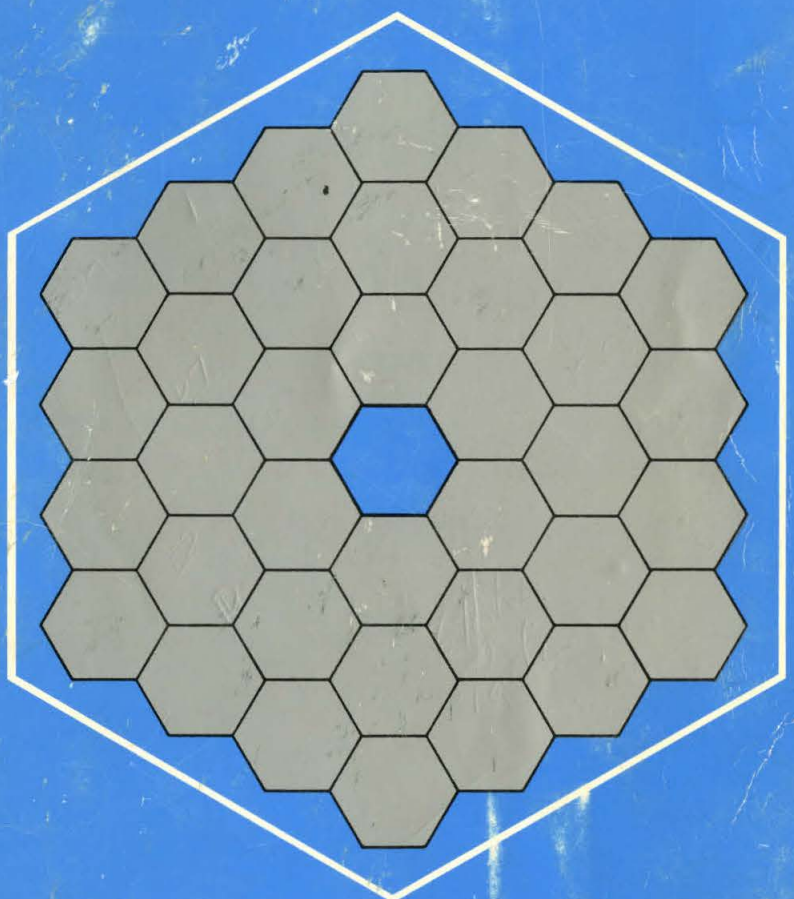

THE UNIVERSITY OF CALIFORNIA
Lick Observatory • Berkeley • Los Angeles • San Diego • Santa Cruz
Lawrence Berkeley Laboratory

CALIFORNIA INSTITUTE OF TECHNOLOGY

Keck Observatory Report No. 90

The Design of the Keck Observatory and Telescope

(Ten Meter Telescope)

January 1985

Editors

Jerry E. Nelson
Astronomy Department, University of California, Berkeley
and Lawrence Berkeley Laboratory

Terry S. Mast
Lawrence Berkeley Laboratory and Space Sciences Laboratory

Sandra M. Faber
Lick Observatory, University of California, Santa Cruz

Copies of this report may be obtained from the editors, from the Keck Observatory Science Office, Bldg 50, Room 351, Lawrence Berkeley Laboratory, Berkeley, CA 94720, or from the Keck Observatory Project Office, 535 S. Wilson Ave., Pasadena, CA 91106.

Preface

This report describes the design of the Ten Meter Telescope and Observatory. Since 1977 the University of California has been actively designing a ten meter telescope for visible and infrared ground-based astronomy. The University of California and the California Institute of Technology have now joined in a collaboration to construct and operate this telescope and observatory. A generous gift of seventy million dollars to Caltech from the W. M. Keck Foundation, announced in January 1985, will provide funds for the construction of the facility. In recognition the facility will be named the W. M. Keck Telescope and Observatory. The University of California will provide funds for its operation. We expect construction to be completed by 1990.

The design of the telescope and observatory continues to be improved as the detailed design progresses. The description given here is current as of January 1985. Although many design details will change before construction, this description is accurate in the general concept and in many particulars. The details of the design are described in an ongoing series of Reports and Technical Notes. An index to this series is given in the Reference Section of this report.

Acknowledgments

The design of the Ten Meter Telescope has captured the imagination of many people over the past seven years. Many have contributed their ideas, their critical judgment, their time, and their labor. This report describes the design they have created. The design of the telescope, building, and dome is now well defined. A great many details remain to be added and many aspects of the present design will be modified. However, the design as it now stands is a great and essential step toward creating an innovative and unique instrument for extending the frontiers of astronomy.

The existence of the project was made possible by the generous financial and political support and personal interest of David Saxon, William Fretter, William Frazer, David Gardner, Jim Albertson, Eugene Trefethen, Andrew Sessler, Dave Shirley, Robert Birge, Robert Kraft, and Don Osterbrock.

The administration of the statewide effort has been a difficult task and the efforts of the Executive Management Committee made this possible. The committee has been under the direction of Harold Ticho and its membership included Robert Kraft, Len Kuhi, Raymond Orbach, Roderic Park, Manuel Rotenberg, David Shirley, and Robert Sinsheimer.

The administration of the project required a great deal more than policy committees. The day to day work was accomplished by the heroics of Joe Calmes, Marlene Couture, Barbara Schaefer, Nancy Sherwin, and Teresa Yuen.

The crucial and active contributions from astronomers to the design have been largely through the efforts of an Astronomy Advisory Committee under the chairmanship of Harding E. Smith. Members of the committee included Marc Davis, Sandra Faber, Holland Ford, Barbara Jones, Ivan King, Lloyd Robinson, Roger Ulrich, Steve White, and Edward Wright. In addition valuable guidance from other members of the astronomical community came from Larry Barr, David Cudaback, Harland Epps, Keith Matthews, Aden and Marjorie Meinel, Larry Randall, Dave Rank, Maarten Schmidt, Charles Townes, Steve Vogt, Merle Walker, Joseph Wampler.

The design of the observatory building and dome has passed through several concepts and several architectural firms in the last six years. Beginning with John Wells of Hunt and Company the design now also includes the work of Richard Rose and Robert Hoggan, and from the current architectural firm of MBT; Lee Van de Kerchove, Peter Hockaday, and Ethan Clifton. Thermal analyses of the dome and telescope have been made by Bill Carroll and Craig Conners.

The optical design of the telescope has been primarily made by Harland Epps, Sandra Faber and Jerry Nelson.

The design of the telescope structure, created by Stefan Medwadowski and Jacob Lubliner is unique in telescope history. They were assisted by Jose Sandoval and David McCormack.

The mechanical design of the telescope system was created by Jack Osborne, Fred Hendy, Hans Boesgaard, and Robert Weitzmann.

The segmented primary mirror is the most innovative aspect of the telescope. Most of the technical effort since 1977 has been directed toward the development and testing of the support and control system. The analysis of the design has been made by Jerry Nelson, Terry Mast, Michael Budiansky, Barney Oliver, and William J. Welch. A major portion of the ideas, design, and testing was provided by George Gabor and Bob Weitzmann. They were supported in their efforts with the skilled work of Bob Minor, Al Biocca, Tom Merrick, and Dan Meier. The finite element analysis and optimization of the segment passive support system has been accomplished through the efforts of Alex Asfura, Michael Budiansky, Bijan Iraninejad, and Robert Taylor. The complexity of the mirror support system required the ideas and hard work of a great many people. The Lawrence Berkeley Laboratory and the Space Sciences Laboratory have been ideal facilities for this development. Members of these laboratories who have made significant and continuing contributions to the project include Steve Abbott, Al Arthur, John

Bercowitz, Jack Borde, Mike Breen, Larry Brown, John Carrieri, Andy Dubois, Jack Franck, Leif Hansen, Dick Jared, Ken Lou, Duane Norgren, and Ted Scalise. The hardware needed for the tests were built by the LBL and SSL shops, with particular help from Mike Long and Hudson Winslow.

The fabrication of the segments is one of the greatest challenges of the design. Beginning with the ideas and suggestions of Luis Alvarez and Jacob Lubliner, the method of stressed mirror polishing was developed by Lubiner and Nelson. A great many people then contributed to the demonstrations showing the method could be used to fabricate the TMT segments. These included the special contributions from Julius Meckel and Roland Wolf at Tinsley Laboratories and the work of Terry Mast, Jerry Nelson, Deborah Haber, Leslie Hunt, Barbara Schaefer, Nancy Sherwin, and Robin Lieberthal at Lawrence Berkeley Laboratory. At Kitt Peak National Observatory the efforts of Larry Barr, Lew Golden, John Richardson, Gary Poczulp, Ker-li Shu, and Joe Magner demonstrated the method on a full-sized mirror.

Students at the University have also made contributions to the design and testing of components. These include David Blakely, Eva Chow, Jim Kaufman, David Nelson, Susan Ottke, Arvin Park, Jim Patterson, Mark Temple-Raston, Don Terndrup, Maurizio Vecchione, and Richard Yang.

For the final stages of the design phase and now as we move into the construction phase the project is under the able direction of the Project Manager Gerald M. Smith.

Many of those named above also have contributed to this report. The bulk of the writing and the final editing of the report were the work of Jerry Nelson, Terry Mast, and Sandra Faber.

List of Participants in the Design of the Ten Meter Telescope

James Albertson
Luis Alvarez
Al Arthur
Larry Barr
Robert Birge
David Blakely
Hans Boesgaard
Jack Borde
Mike Breen
Larry Brown
Bill Brown
Michael Budiansky
Joseph Calmes
John Carrieri
Bill Carroll
Eva Chow
Ethan Cliffton
Marlene Couture
David Cudaback
Marc Davis
Andy Dubois
Harland Epps
Sandra Faber
Holland Ford
Jack Franck
William Frazer
William Fretter
George Gabor
David Gardner
Lewis Golden
Nancy Gusack
John Gustafson
Deborah Haber
Leif Hansen
Nancy Hanson
Fred Hendy
Bob Huestis
Peter Hockaday
Robert Hoggan
Jerry Hudson
Leslie Hunt
Bijan Iraninejad
Neal Jern
Barbara Jones
Jim Kaufman
Leonard Kuhi
Ivan King
Robert Kraft
Ron Laub
Robin Lieberthal
Michael Long
Ken Lou
Jacob Lubliner
Joseph Magner
Terry Mast
Keith Matthews
Julius Meckel
Stefan Medwadowski
Eden Meinel
Marjorie Meinel
Dan Meier
Tom Merrick
Bob Minor
Faye Mitschang
David Nelson
Jerry Nelson
Steve Nelson
Duane Norgren
Bernard Oliver
Raymond Orbach
Jack Osborne
Donald Osterbrock
Susan Ottke
Arvin Park
Roderic Park
Jim Patterson
Gary Poczulp
Kathy Poliakof
Larry Randall
David Rank
John Richardson
Lloyd Robinson
Richard Rose
Manuel Rotenberg
David Saxon
Jose Sandoval
Ted Scalise
Barbara Schaefer
Jan Schafer
Maarten Schmidt
Andrew Sessler
David Shirley
Gerry M. Smith
Harding E. Smith
Robert Sinsheimer
Nancy Sherwin
Ker-li Shu
Tom Soifer
Don Terndrup
Harold Ticho
Charles Townes
Eugene Trefethen
Roger Ulrich
Lee Van de Kerchove
Maurizio Vecchione
Steven Vogt
Joseph Wampler
Robert Weitzmann
William J. Welch
John Wells
Stephen White
Hudson Winslow
Roland Wolf
Edward Wright
Richard Yang
Teresa Yuen

Table of Contents

Key Issues Index

Some design issues are treated in more than one section of this report. We provide here a cross reference index for important subjects discussed in several different sections. In addition, Section 11 summarizes in tabular form information about many of these subjects.

1. Introduction and Summary

Contents

1.1 The Ten Meter Telescope Project Background

Our knowledge of most of the universe beyond the earth comes from observations made with telescopes. Since the time of Galileo (1564-1642) the power of telescopes has steadily improved. These improvements fall into three general categories; spectrum, sensitivity, and size. For centuries the spectral range of astronomical observations was limited to that seen by the human eye. The spectrum detected by Galileo's eye ranged from 0.4 μm to 0.6 μm. The spectrum of today's astronomy ranges from the short wavelengths of energetic gamma rays (10^{-8} μm) to the long wavelengths of radio waves (10^{+7} μm). The sensitivity of detectors has also improved, from that of Galileo's eye to the near perfect quantum efficiency of today's solid state detector arrays. And finally, the size of telescopes has grown from Galileo's .03m diameter lens to the 10m diameter aperture proposed here.

The wavelength spectrum used for astronomical observations has enormously widened in this century. In the 1930's radio telescopes first came into use, and in the 50's and 60's infrared astronomy became important. A huge step was taken in the 60's with the introduction of telescopes in space, above the absorption of the earth's atmosphere. This opened up the available spectral range to include wavelengths below .3μm and between 30 μm and $10^3\mu$m. Orbiting γ-ray, x-ray, ultraviolet, and infrared telescopes have dramatically extended our knowledge of the universe. The last two decades have shown that for each new object we detect with these instruments, we are always drawn back, both intuitively and scientifically, to ask " What does it look like? " It is a fundamental fact that most of the electromagnetic radiation in the universe is in the visible and infrared regions, accessible with ground based telescopes. This, and the richness of atomic phenomena in this wavelength region, inevitably draw us to make observations in the visual range of the spectrum. These visible light observations often provide additional data needed to understand new objects discovered in the other ranges of the spectrum.

To see dim and distant objects requires a telescope with a large aperture and a sensitive light detector. Detectors have been greatly improved in this century, providing us more quantitative information, as well as making more efficient use of the available light. The introduction

of photographic emulsions as detectors was of enormous importance. Today the introduction of CCD (charge coupled devices) detectors and related solid state detectors with their high quantum efficiency and excellent linearity is providing the next advance in sensitivity. These new devices detect nearly all the light impinging on them. Therefore, our ability to observe dim and distant objects can now only be improved by increasing the total amount of light collected, that is, by increasing the size of the telescope.

Presently the largest optical telescope in the world is the 6m BTA in the Soviet Union. The largest telescope in the United States is the 5m Hale telescope on Mt. Palomar, conceived in 1928 and finished in 1949. Table 1-1 shows the world's largest telescopes and their completion dates.

Table 1-1 Major Telescopes

	Location	Dia.(m)	f-ratio	Completion Date
1. Soviet Large Altazimuth	Caucasus	6.0	4.0	1976
2. Hale 200-inch	California	5.0	3.3	1949
3. Multiple Mirror Telescope	Arizona	4.5	2.7	1979
4. Cerro Tololo Interamerican Obs.	Chile	4.0	2.8	1976
5. Anglo-Australian Telescope	Australia	3.9	3.3	1975
6. Kitt Peak National Observatory	Arizona	3.8	2.8	1973
7. United Kingdon Infrared	Hawaii	3.8	2.5	1979
8. Canada-France-Hawaii	Hawaii	3.6	3.8	1979
9. European Southern Observatory	Chile	3.6	3.0	1976
10. Lick Obs. Shane Telescope	California	3.0	5.0	1959
11. NASA Infrared Telescope	Hawaii	3.0	2.5	1979

The University of California has had a strong committment to optical astronomy for the past 100 years. With the completion of the Shane 3m telescope at Lick Observatory in 1959, the University owned and operated the second largest telescope in the world. In 1974 the 3m became the third largest; it is currently about 13th in size. Along with this decrease in relative collecting area it now also suffers from increased light pollution from cities close to Lick Observatory. These have eroded the scientific power of the 3m. This and the general scientific need for larger telescopes led University of California astronomers to explore ideas for a new facility. In 1977 they began to study ways in which a very large telescope could be built. After extensive study, they concluded that an aperture of 10 meters, more than four times the collecting area of the Hale 200-inch (5m) was practical. A detailed study of the potential scientific uses of such a telescope was made by Sandra Faber.

Two alternate designs for the key element, the primary mirror, were pursued; a thin monolithic mirror design and a segmented mirror design were both studied. In late 1979, after two years of engineering studies, the segmented approach was selected for the new telescope. This design approach had been developed by the team of Nelson, Mast, Gabor, and Welch. The design achieves the required high optical quality at an acceptable cost and technological risk. A description of this design and its integration into a full observatory forms the technological heart of this Design Report.

Since 1979, the design of the Ten Meter Telescope has been developed in increasing detail and prototypes of the innovative components of the primary mirror have been built and tested. The key ideas and engineering tests are described in a series of Reports and Technical Notes. These are listed at the end of this Design Report. The early work on the primary mirror and the telescope configuration was done by Nelson. The conceptual work on the active control system needed to maintain the alignment of the primary mirror segments was developed by

Mast and Nelson. The critical hardware, the sensing system and the actuating system for the primary mirror control system has been developed largely by Gabor. A special technique for polishing the off-axis paraboloidal mirror segments (Stressed Mirror Polishing) was developed by Lubliner and Nelson. It is based on historical ideas demonstrated by Schmidt; work by a group at Kitt Peak National Observatory under the direction of Barr; and the ideas and experiences of Alvarez with similar techniques. The telescope structure is extremely efficient and lightweight in its design. Many of its key elements were originally conceived by Lubliner, and the complete development of the telescope structural design has been by Medwadowski. The segments require a passive support in addition to the active support system and the design of that system has been developed by Weitzmann. The bearing and drive system for moving and pointing the telescope were developed by Osborne.

1.2 Science with a Ten Meter Telescope: The Origin of Structure in the Universe

The past two decades have witnessed an explosive growth in astronomical science. A flood of new observations, many made with satellites above the earth's atmosphere, has dramatically altered and enlarged our view of the Universe. The list of discoveries is impressive--quasars, pulsars, gravitational lenses, stars that swallow their neighbors, colliding galaxies, and great clouds of mysterious dark matter that outweigh visible stars by ten to one--to name just a few.

These new finds have dazzled astronomers and instilled in all of us a sense of awe and wonder at the infinite variety of our Universe. On a deeper level, however, the fundamental questions that form the core of the astronomy still remain. Basically, astronomy focuses on origins: How do stars form? Where did the Sun and planets come from? What made galaxies? And even, what made the Universe? Progress on these deeper questions comes in a series of small steps, many of which are highly technical. It is much harder than just discovering new objects.

From the popular press one might not know that such progress is occurring. And yet, over the same two decades that have seen so many astronomical discoveries, critical steps have been taken to answer some of the fundamental questions. There are now specific theories that make testable predictions. If not final answers, we have a clearer view of where final answers might come from and what form they might take.

The Ten-Meter Telescope (TMT) will play a vital role in answering the fundamental questions of astronomy. Astronomers in the University of California believe that the TMT is the most critical, most essential instrument to be constructed for this purpose. To understand this, one must appreciate how optical astronomy relates to the other wavelengths that astronomers work with, such as X-rays, microwaves, and radio waves.

Optical astronomy always has been and remains today pre-eminent. Most objects in the universe shine brightest at visual wavelengths, or are closely paired with objects that do. The visual, along with its sister region, the infrared, is thickly populated with thousands of spectral lines arising from virtually all atomic elements and molecules in the Universe. Studying these lines yields basic measurements of compositions, physical conditions, and radial velocities (through the Doppler effect) of an enormous array of celestial objects.

New discoveries from X-ray satellites and radio telescopes, far from diminishing interest in optical-infrared telescopes, have in fact greatly increased their popularity. In nearly all cases, follow-up optical or infrared measurements are required to find out what kind of object has been seen and to determine its distance, basic properties, and so on.

We now consider some of the fundamental questions mentioned above, and discuss how the TMT will help answer them.

How Do Stars and Planets Form?

Star formation remains one of the most important questions of modern astronomy. How, when, and where stars form is a key to understanding galaxy evolution, the formation of the elements, and even the origin of life. Young stars are born deep within dense, dusty clouds of gas--so-called "stellar nurseries". These clouds are opaque to visual light, but fortunately can be mapped in infrared light, which penetrates the clouds. At the critical infrared wavelengths of 10μm and 20μm, the ability of existing telescopes to resolve sharp images increases directly with the size of their aperture. With its 10m aperture, the TMT will make infrared images that are two to three times sharper than any we now have. The TMT will also be 25-40 times "faster" at infrared wavelengths (just as there are "fast" and "slow" camera lenses), which will allow it to penetrate to much deeper levels of sensitivity.

This combination of higher speed and resolution will yield images of star-forming regions with unprecedented clarity. With the TMT, we will be able to pick out individual protostars to very faint levels, distinguish these from dust clouds, and measure the streams of gas flowing in the condensing protostellar envelopes. Theory suggests that leftover gas in the late stages of a stellar collapse can settle into a disk girdling the equatorial regions of the star. This disk is widely believed to be the first stage in planetary formation. The TMT will be able to detect such disks in infrared light, and thus directly address the question of where and how planets form.

How do Galaxies Form and Evolve?

Many important events in the Universe took place billions of years ago, long before humans evolved to study them. Remarkably, a great telescope like the TMT has the ability--unique in any science--to carry us far back in time as well as far out into space. Because of the finite velocity of light, looking out to larger distances means longer light-travel times, so we see emission from earlier epochs. With the greatest of effort, present telescopes can image distant galaxies that carry us back in time two-thirds of the way to the Big Bang. These distant pictures show us what the Universe was like more than 10 billion years ago. This is a magnificent achievement, but unfortunately it is not enough: the pictures by themselves are ambiguous. They cannot tell us how far away a given galaxy is, and therefore cannot tell us the age of the Universe when the galaxy emitted the light we now image.

The solution to this problem is spectra. Spectra tell us how fast a galaxy is receding, which in turn lets us infer its distance and age. Spectra also tell us what kinds of stars galaxies contain and how the stellar makeup changes with time. With spectra taken with the TMT, we will be able to make a map of the youthful Universe, follow the evolution of galaxies and galaxy clustering, and directly test modern notions asserting that galaxies and clusters are natural outgrowths of the Big Bang.

The Birth of the Milky Way Galaxy

Another way to travel back in time is to study objects that are very old. Our Galaxy contains many stars whose ages approach 20 billion years, dating from nearly the time of the Big Bang itself. The distribution and motions of these stars carry a ghostly image of the size and structure of the Milky Way when it first formed. Further, these stars provide a remarkable picture of the gradual buildup of heavy elements in the Galaxy, letting us calculate the masses of the first generations of stars and how matter flowed within the developing system. We have a crude picture of these stars, but we need to know a lot more--especially about their ages, motions, and compositions.

Unfortunately, the most interesting of these oldest stars are far from the Solar System, many tens of thousands of light years away in the Galactic Center or on the distant outer fringes of the Galaxy. Present telescopes are simply not large enough for studies at these large distances. Only the TMT can show the composition and dynamics of these stars with the required level of accuracy.

What is the Universe Made of?

As a last example, we consider the basis question: what is the nature of matter in the Universe? Until recently, the answer seemed obvious: electrons, neutrons and protons--the same "baryonic" matter that comprises the earth, sun, and stars. As has happened so many times during the past two decades, observations have revealed a totally unexpected surprise: some ninety percent of the total mass of the universe seems to be invisible, and its nature is a complete mystery. We can detect this component, called "dark matter" only via the large gravitational effect it exerts on the baryonic matter we can see. Because of its large mass contribution, the physics of dark matter dominates the universe, and hence cosmology. Although the idea is still uncertain, many scientists believe that dark matter consists of some as-yet-undiscovered elementary particle. This possibility has inspired an exciting new marriage between particle physicists and astronomers to unravel the mystery of the new component. The challenge, in effect, is to use the Big Bang as the ultimate high-energy particle accelerator to study the physics of elementary particles. Out of this collaboration is emerging a new consensus, mentioned above, that the origin of structure in the universe--galaxies and clusters included--can be explained as a natural consequence of the basic properties of matter itself!

How will the TMT help in this quest? The new telescope is essential as the premier instrument for studying the distribution and dynamics of dark matter. Various theories predict that dark matter should be parceled out among different-sized structures in different ways -- found only in the largest clusters and superclusters, for example, or spread equally among galaxies and clusters of all masses. The unparalleled power of the TMT for spectroscopic observations will let us measure the orbital velocities of stars and thus trace out the dark matter distribution around galaxies of all types, particularly the smallest ones. From these observations, a much clearer picture of the nature and distribution of dark matter should emerge.

This introduction has mentioned just a few highlights of the science that can be accomplished with the TMT. Like any optical-infrared telescope, the hallmark of the TMT is its versatility. In Section 2, 33 projects are described that illustrate a wide variety of observational techniques in every wavelength region from 0.33μm to 20μm. The scientific problems in the optical-infrared region are so numerous that telescopes built even a century ago are still active and productively used. As the world's largest such telescope, the TMT will lead astronomical science for many decades, and carry humankind's astronomical voyage of discovery to greater depths in the Universe than ever before.

1.3 A Summary of the Design

The Choice of Primary Mirror

The first decision to be made in the design of a large telescope is on the form of the aperture. The choice is between one telescope or an array of telescopes. This has a fundamental impact on the design, capability, and cost of the entire observatory. Our scientific motivation for a large telescope places strong emphasis on both infrared and high angular resolution observations. Thus the aperture that gives the best diffraction limited image quality is desired. A single, filled aperture gives the sharpest most centrally concentrated diffraction-limited images, hence this configuration was selected. This is the same optical configuration used in virtually all existing optical telescopes. Where the scientific emphasis is different, particularly in radio astronomy, arrays of telescopes are used successfully.

Three configurations for the primary were considered: a segmented primary, a monolithic primary, and a multiple aperture primary. The multiple aperture concept is best represented by the Multiple Mirror Telescope (MMT) in Arizona. This consists of six telescopes on a common mount with additional elements to optically combine the six beams at a single focus. The difficulty of phasing these mirrors for diffraction-limited performance, and the difficulty of obtaining a large field of view led us to reject this option. The monolithic primary concept has the

enormous size of the mirror as its major difficulty. First, the ability to fabricate a ten meter blank is unknown. If a blank could be formed, it would be quite expensive. Second, polishing such a mirror would require large and expensive equipment. In addition, transporting and handling such a mirror would be expensive and risky. The fundamental optical concern with a large mirror is its deformation under gravity. This deformation scales as the diameter to the fourth power and as the inverse of the thickness squared. Thus for a ten meter aperture the deformation is 16 times worse than for a five meter given the same mirror thickness and form of support. Furthermore, to limit the costs of the blank, the handling equipment, and the telescope structure that supports the mirror, its mass must be greatly restricted, hence thinner mirrors are much more desirable. This further increases the problems of controlling the gravitational deformation. The technical challenge of adequately supporting a thin monolith to avoid optically excessive deformations is formidable. An additional financial consequence of a large monolith arises from the need to put a reflective layer on the surface. Mirrors must be periodically recoated in a vacuum chamber to retain their high reflectivity, and such a chamber for a ten meter mirror is expensive. Finally, there are real concerns over the long term safety of a ten meter thin glass mirror that must be handled repeatedly. All of these concerns led us to consider and finally select the option of segmenting the primary.

A segmented mirror with relatively small segments avoids the problems of scale associated with a monolith, but it requires an active control system to maintain the segments in proper alignment. Selecting appropriate segment size requires balancing several elements. Dividing the mirror into more segments reduces the segment fabrication costs and the complexity of their individual support, but increases the complexity of the active control system. In balancing these engineering and cost issues, we selected the segmented design with 36 hexagonal segments shown in Figure 1-1 . Each segment is 1.8m across, and is 0.075m thick.

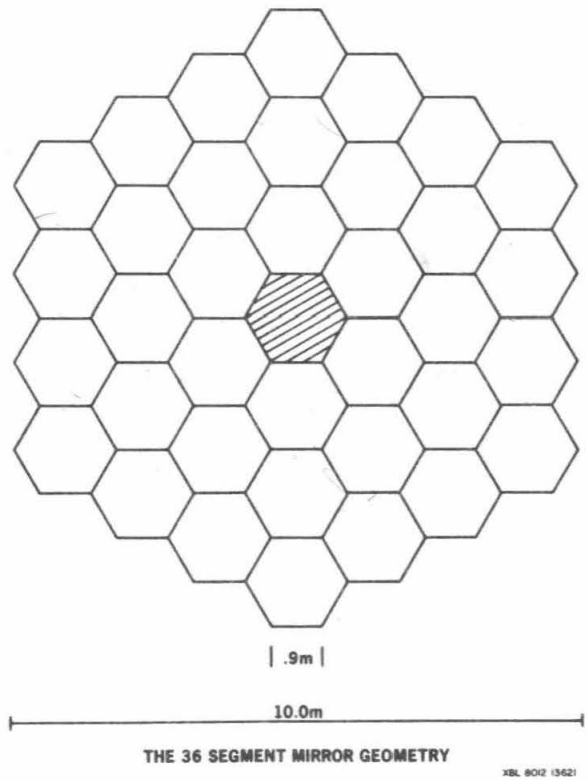

Figure 1-1 The segmentation geometry for the primary mirror is shown.

The cost of an observatory is traditionally divided about equally between the telescope and the building and dome. The major cost driver for the enclosure is the length of the telescope, so making the focal length of the primary mirror as short as practical is desirable. Investigations revealed that reducing the focal length increased the difficulty in fabricating the segments, increased the complexity of the active control system, and reduced the available field of view of the telescope. Balancing these technical and financial issues led to the decision to make the primary mirror an f/1.75 hyperbola with a 17.5m focal length.

Support of the Primary

The passive support of an individual segment must limit the deformations of the segment caused by gravitational and thermal perturbations to acceptable optical levels. Smaller, thicker segments suffer less deformation and a simpler support system will be adequate. Thinner segments reduce the mirror mass and hence the telescope weight. We selected 0.075m thick segments as a compromise that allows a lightweight mirror and telescope as well as a passive support with acceptable complexity.

The passive support system is composed of two orthogonal supports; an axial support to carry all loads that are normal to the segment surface and a radial support to carry all loads in the plane of the segment. The axial support system consists of three 12-point whiffletrees that are each attached to a displacement actuator. Thus each segment is axially supported on a bed of 36 points which provides an adequate approximation to the ideal of a uniform support. When the telescope points towards the zenith essentially the entire weight of the segment is carried by these whiffletrees. The radial support is provided at the segment center of gravity in a hole bored into the back of the segment. A thin diaphragm whose plane contains the center of gravity is bonded into the glass segment and attached to a support post. When the telescope points to the horizon essentially the entire weight of a segment is carried in tension through this diaphragm.

The individual segments are supported by a mirror cell roughly ten meters in diameter. Although quite deep and stiff, this structure will deform about 1mm under gravitational loads. Since this is extremely large compared to the optical surface tolerances of 50nm, we require an active system to maintain the segments in their desired locations in the face of these deformations. This system consists of three basic parts; sensors to detect changes in the segment pistons and tilts, a control algorithm to interpret the sensor readings to determine where the segments are and where they should be, and actuators to move the segments to their correct or desired positions.

Among a wide range of possible sensing philosophies, we have selected a system of sensors that mount on the backs of the segments and do not interfere with the front optical surface. By design they measure relative motion between adjacent segments only in the direction normal to the optical surface. We have selected a capacitive sensor that uses the difference between two capacitances as a linear measure of the relative heights of adjacent segments. There are two sensors along every intersegment edge, for a total of 168 sensors.

The control algorithm uses the 168 sensor readings to determine the desired 108 actuator motion update commands. The sensor readings are linearly related to the actuator motions, so 168 linear equations relating the 108 actuator lengths to the 168 sensor readings can be established. These can be solved and the result has the convenient form of a matrix (dependent solely on the geometry of the system) that multiplies the vector of sensor readings to yield the desired actuator motions. This algorithm calculates the desired positions in an exact manner, hence iteration is not needed, and the corrections made are globally correct. We expect to update the segment positions in this fashion several times a second.

The actuators must move the segments smoothly at a level of 50nm over a range of about 1mm. A variety of actuators may perform this task. We have selected a mechanical, motor-driven screw for the actuator. Because friction and stiction are important parameters in such an actuator, we have selected a roller screw for the screw. This device employs rolling friction instead of sliding friction in its basic mechanism.

Segment Fabrication

The surface shape of the primary is a hyperboloid of revolution and is quite close to a paraboloid. This surface must be smooth and accurate on the scale of a small fraction of the wavelength of light, roughly 50nm, to make the desired high quality images. Such surfaces are most readily obtained by grinding and polishing glass or glasslike materials. Conventional optical polishing procedures readily make spherical surfaces by rubbing a large abrasive tool against a rotating mirror blank. By experience and art opticians also make non-spherical surfaces of revolution.

The segment fabrication faces an unusual complexity in that the individual segments are not figures of revolution about their own local centers. This lack of rotational symmetry greatly complicates the task of polishing the segments. This complication is so great that we chose to develop a new approach to polishing the segments rather than accept the high cost and long time needed if they were to be polished by conventional techniques.

We found that by elastically warping the mirror blanks with externally applied loads we could warp the desired surface shape into a spherical shape. The technique of Stressed Mirror Polishing thus consists of applying suitable forces to the mirror blank and polishing a spherical surface into it. After polishing, the forces are removed and the spherical surface elastically relaxes into the desired off-axis segment surface. This technique reduces the polishing problem to that of polishing spheres. As theoretical work and experimental tests have shown that this technique is quite practical, we will use it to fabricate the mirror segments.

Thermal perturbations are an inevitable experience for a telescope exposed to the night air. It is vital that this varying thermal environment not objectionably perturb the optical surface of the segments. To achieve this we require a mirror material with an extremely low coefficient of thermal expansion and have selected a glass-ceramic with an expansion coefficient $< 1\times10^{-7}/°C$.

The Telescope Structure

The telescope structure must maintain the optical elements and scientific instruments in proper alignment and point the system with high accuracy in the desired direction. It must do this in the face of gravitational, thermal, and wind perturbations. We selected an altitude-azimuth motion mount for its engineering simplicity. Space frames are used throughout the structure to maximize the stiffness while minimizing the total telescope weight. Figure 1-2 shows a model of the telescope. Both analytic and computer optimizations of the distribution of the steel have been carried out to provide maximum stiffness. The optimization was made to minimize the deformations and pointing errors due to wind loads on the telescope and to maximize the lowest resonant frequency in the telescope. Figure 1-3 shows the weight of the TMT in comparison to other large optical telescopes. As the figure shows, the TMT mass of 150 tons is extremely low for its size, being about the same mass as 3-4m telescopes. In addition, the lowest resonant frequency is roughly 5Hz, a value at or above that of most other large telescopes. This shows clearly the virtues of reducing the weight of the primary, and of optimizing the steel distribution.

The Dome and Support Facility

The dome provides protection for the telescope against wind buffeting during observations, and against the effects of storms and sunlight when the dome is closed. The building and dome provide necessary support facilities for the telescope. This includes such tasks as normal telescope observing procedures, instrument handling, telescope maintenance, segment aluminizing, preliminary scientific data reduction, etc. As explained earlier, the cost of these facilities can be large, and tend to scale as the size of the telescope. Hence, it is particularly important to keep the dome size to a minimum, and to avoid unnecessary functions in the support building. Figure 1-4 shows the planned building and dome. Figure 1-5 shows the relative size of the TMT facility to that of other large telescopes. The small circle in each observatory shows to scale the size of the primary mirror. The figure clearly illustrates the efficiency of the TMT dome.

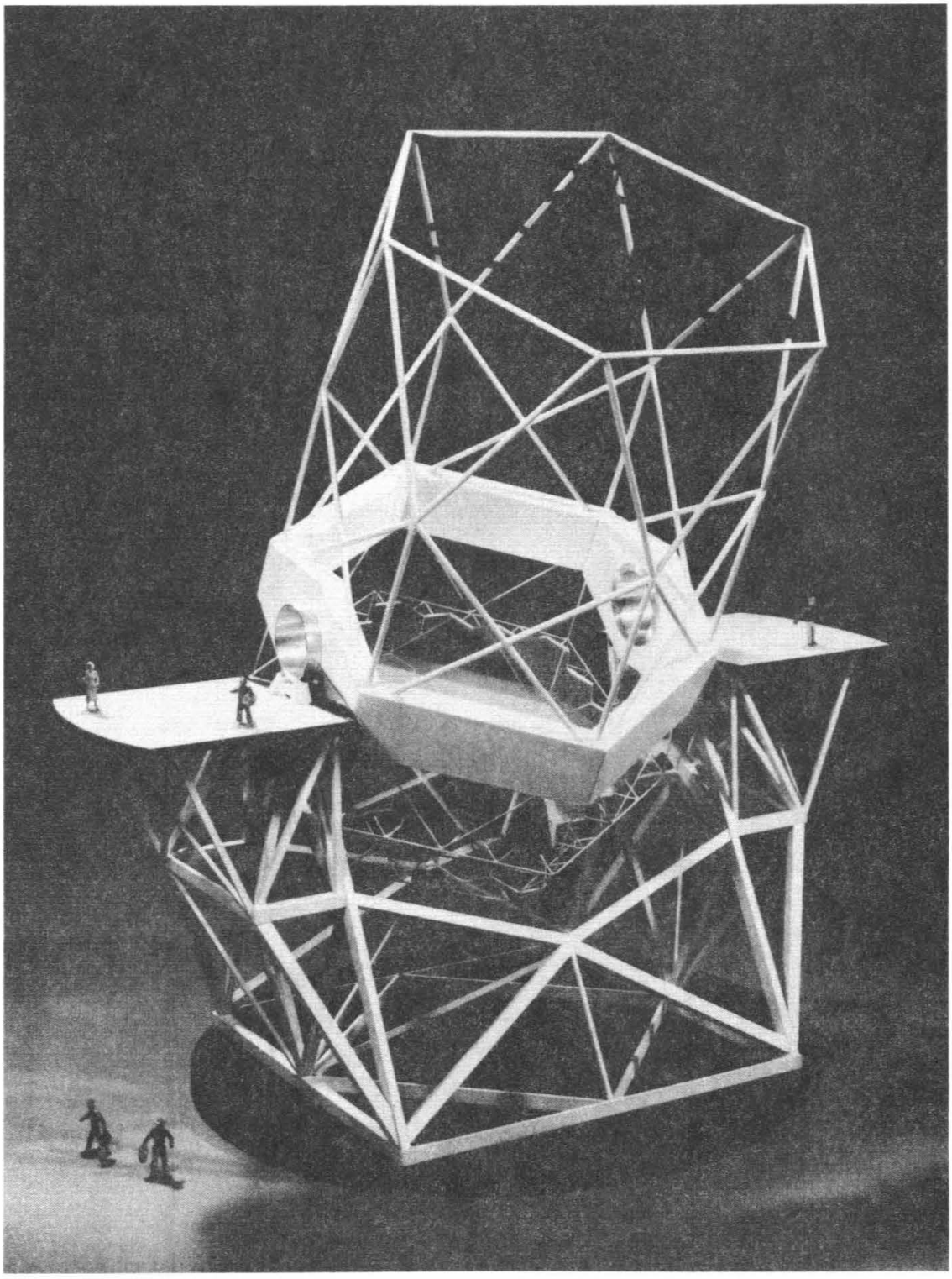

Figure 1-2 Conceptual model showing the optical arrangement of the primary mirror as well as the telescope tube and yoke.

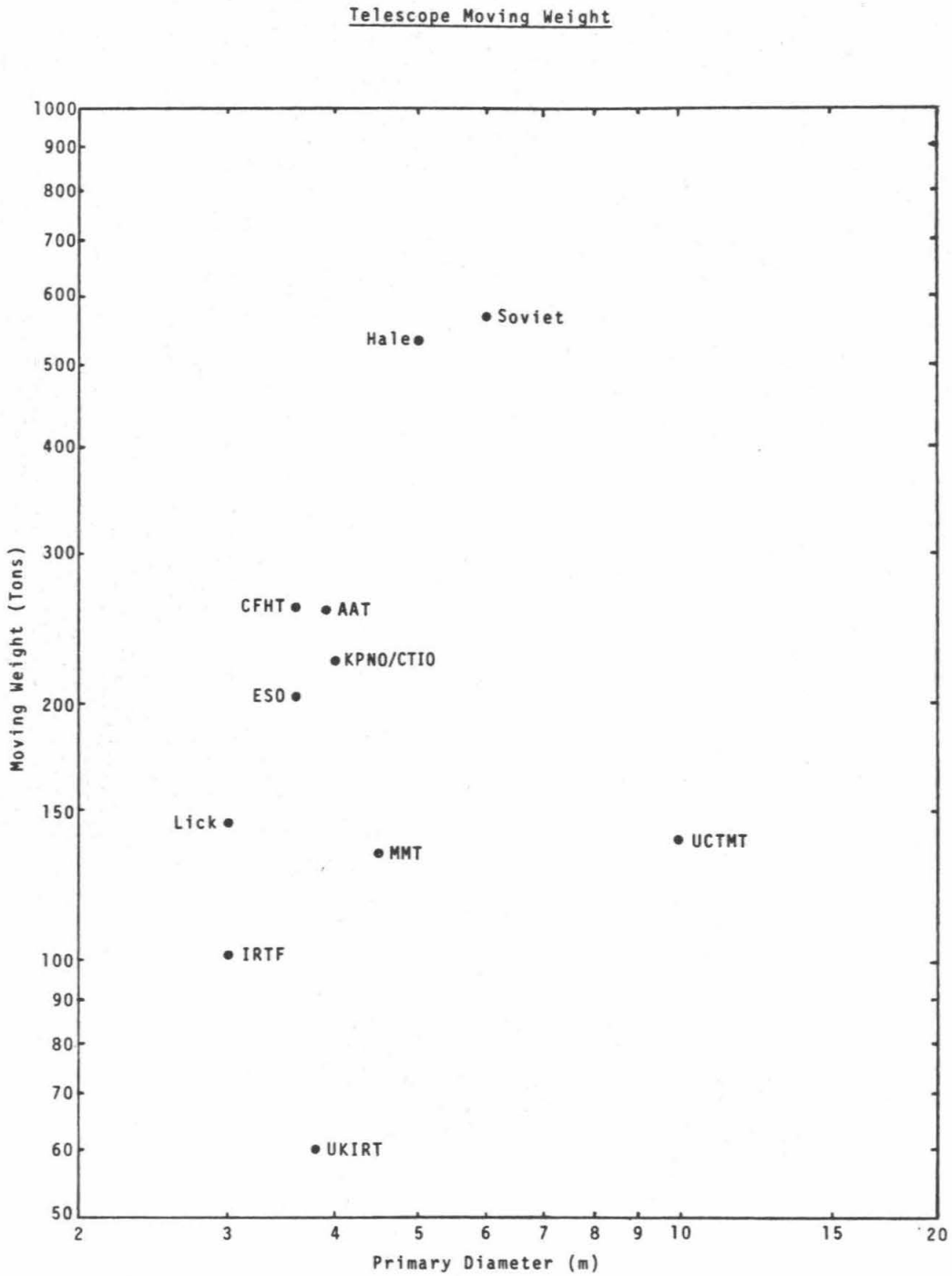

Figure 1-3 The total moving telescope weight plotted against telescope aperture for several large telescopes, including the currently anticipated Ten Meter Telescope weight.

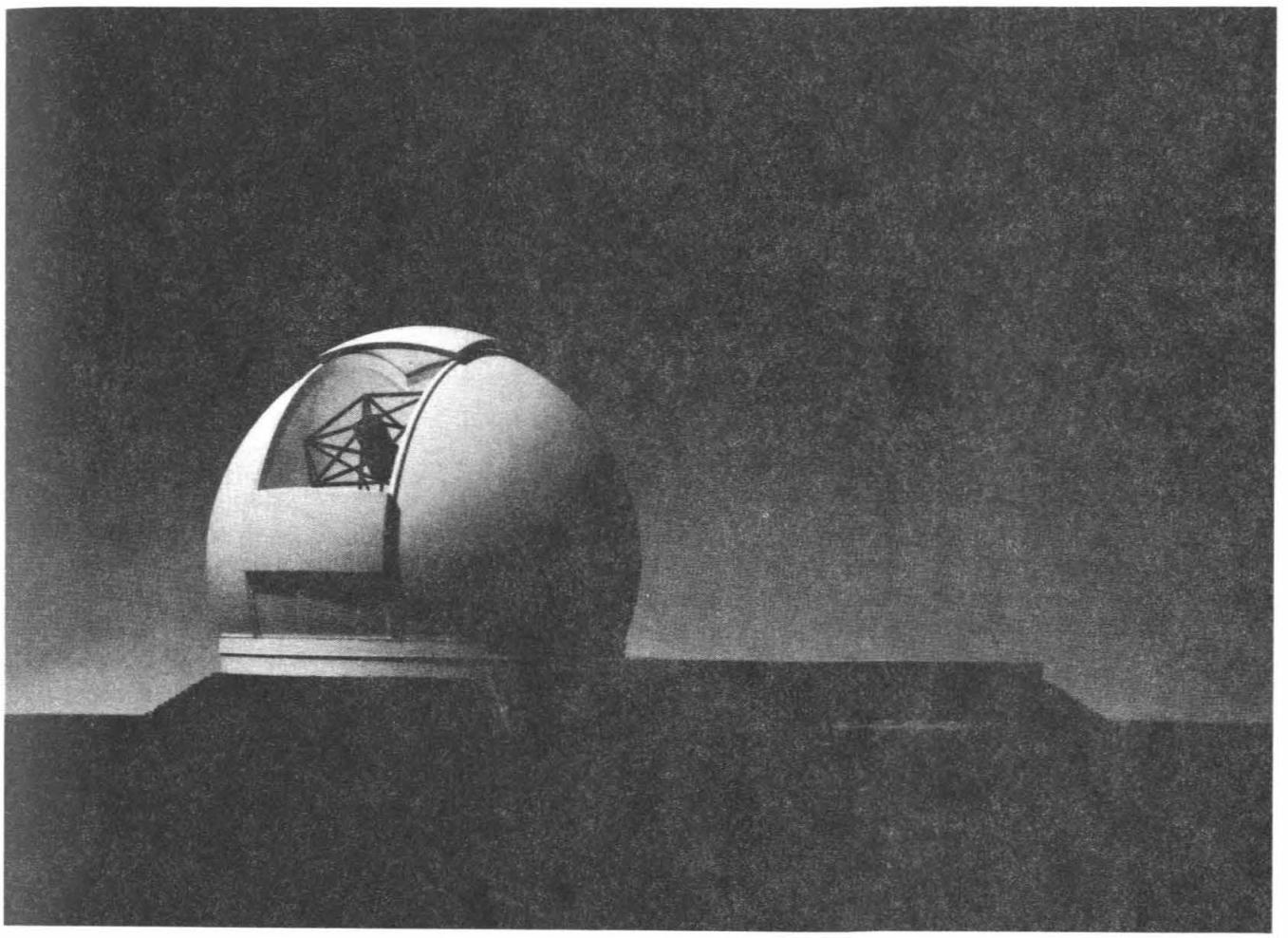

Figure 1-4 Model of the telescope, dome, and support building pictured on the mountain.

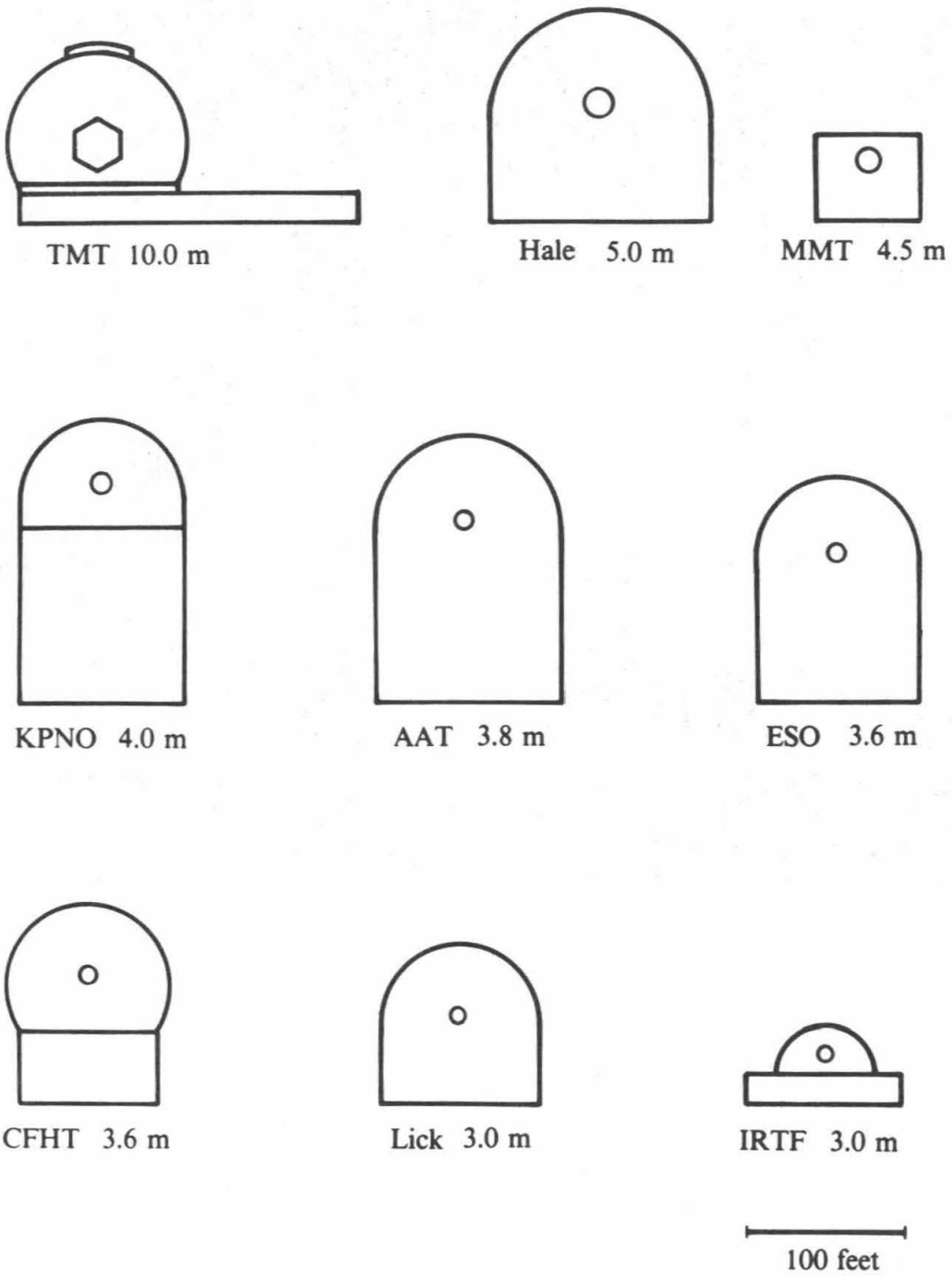

Figure 1-5 A comparison of features of existing telescopes with the Ten Meter Telescope. All are drawn to the same scale. The telescope aperture is given beneath each building.

It is critical that the air around the telescope be as close as possible to the ambient outside air temperature when observing. Air temperature variations cause locally induced "seeing" which degrades the image quality that is so important to most scientific programs. To maintain a thermally benign environment, we have housed all heat producing activities and sources in the building adjacent to the dome. All inside surfaces of the dome are heavily insulated to greatly reduce any conductive heat transfer into the dome volume from the outer dome wall, the building, or the ground. These surfaces are also designed to have low thermal mass to allow the interior surfaces to track the changing ambient air temperature as closely as possible.

The adjacent building contains the telescope control room, computing facilities, an aluminizing facility for the segments, an instrument assembly room, an electronics shop, and other related support facilities. Because of the high elevation of the site, we will provide an oxygen enriched environment in those areas frequently occupied.

The Site

Many characteristics are desired in a good observing site. The most important is good seeing. Ideally the telescope should be above the blurring effects of the earth's atmosphere, to ensure the sharpest possible image quality. The selected site of Mauna Kea, Hawaii, is as good as any known site in the world in this regard. Even with this excellent site, visual observations will still be limited in quality by the atmosphere. However, at infrared wavelengths beyond 10μm, the site is good enough that the telescope should be diffraction limited. Dark skies, a high incidence of clear weather, low water vapor, good access to the galactic center, and access to a site are other important factors in selecting the site. The Mauna Kea site is superb in all of these.

1.4 A Summary of the Technology Development Program

From the inception of the project in 1977 to the present, the vast majority of effort was spent on the development of the technology for the segmented primary mirror. The program addressed both the challenge of segment manufacture and segment support. We briefly summarize here the programs, the results, and the conclusions.

Segment Manufacture

The technology development program for segment fabrication began in 1979 with a survey of possible techniques. The concept of Stressed Mirror Polishing (SMP) appeared feasible and economical and the theoretical basis for the method was developed by Lubliner and Nelson. A particular non-axisymmetric optical surface is required for each segment. The surface is achieved by applying a set of forces to the blank to warp it in a controlled and predictable fashion. Then a sphere is ground and polished into the blank, the forces are removed, and the polished spherical surface deforms elastically into the desired non-axisymmetric surface.

The demonstration of the method began with the fabrication of a quarter-scale (360mm diameter) mirror in 1979. The target surface was a section of a paraboloid with a radius of curvature of 388.80mm and off-axis distance of 350.0mm. The achieved surface had a radius of curvature of 388.83mm, an off-axis distance of 350.7mm, and an rms surface error of 0.03μm. Thus the surface quality was excellent and the radius error was 1 in 10^4. This successful test established the viability of SMP and motivated full scale testing.

The demonstration then moved to two full-scale mirror projects in the years 1981 to 1984. Starting in 1980, in collaboration with Kitt Peak National Observatory, we began a program to demonstrate the method on a full-sized 2.0m mirror. That program at KPNO is concluding as this report is being written. The target mirror was a section of a paraboloid with a radius of curvature of 40.5m and an off-axis distance of 4.3m. This mirror is comparable to the most aspheric of the TMT segments. The program did not include an effort to precisely control the radius of curvature. The radius achieved was within about 1mm of the desired 40.5m. As of this writing only a single iteration of Stressed Mirror Polishing was completed.

The blank was stressed in a fixture, a spherical surface was ground and polished (about 150 machine hours), and releasing the forces and moments yielded a surface that differed from the target surface by only 0.187μm.

In 1981 a 1.9m-diameter blank was purchased by the University of California to make the segment and reference mirror for the active control system prototype. The polishing and testing of this mirror was carried out by a collaboration of the TMT Science Office and Tinsley Laboratories, Inc. The target surface was spherical and not an off-axis parabola. Thus, the Stressed Mirror Polishing technique was not used. However, other aspects of the required segment fabrication technology were demonstrated in the making of this mirror. These included accurate measurement and control of the radius of curvature, polishing to the surface quality required for the TMT, cutting the mirror into a hexagon, and boring the radial support-post hole. The target surface for the mirror was a spherical surface with a radius of curvature of 10000mm and a surface quality better than 42nm rms surface error. This allowed surface error includes the focus or radius of curvature contribution. A precise and accurate method of measuring the radius of curvature was developed and used to control the radius during polishing. The goal for the radius of curvature was thus 10000.000 $\pm$ 0.032mm. Supports for the mirror to be used during polishing and testing were developed. The final surface achieved was 45nm from the target surface and the radius was 10000.009 $\pm$ 0.014mm. Thus this aspect of segment fabrication was successfully demonstrated.

The next step was to evaluate the effect of cutting the hexagonal segment from the circular mirror. Unfortunately, the cutting caused a substantial change in the figure, 538nm rms surface error. This distortion was dominated by focus, but also contained 86nm rms of astigmatism and coma. The cause of the warping and possible options for removing it during the segment manufacture are being studied. Most of the effect is now believed to be a consequence of hoop stresses in the circular mirror. Their effect is expected to be some 3 times smaller for the geometry of the TMT segments. The central hole for the radial support post was successfully bored and the mirror is presently in use in the active control system.

A critical aspect of the segment fabrication is the optical testing of the surfaces. Measurement of the off-axis surfaces, including the focus or radius-of-curvature term, is unusual in conventional mirror fabrication.

The development of adequate interferometric testing environments and procedures was a substantial effort both at Tinsley and KPNO. Adequate thermal control was finally achieved and methods of removing the effects of the test optics and support were successfully applied. The equipment, environment, and procedures then allowed measurements of the surface that were reproducible at the 20nm rms level. This was at great cost of calendar time, human effort, and dollars. The processing time for the data analysis was typically a few days. We conclude from this experience that the test method, test environment, and analysis methods will need to be substantially improved to be used for the fabrication of the TMT segments. At KPNO the the Hartmann test was successfully developed and showed excellent repeatability at the 10nm level. At Tinsley we developed a method to measure precisely and accurately the radius of curvature. The method uses a fringe counting laser interferometer to measure a distance related to the radius of curvature. A "single" measurement of the surface typically included seven measurements of the radius of curvature. The rms spread in these measurements was about 0.030mm. On the basis of the experience gained at KPNO and at the University of California, we now believe that the mass production of segments for the TMT is both feasible and economical.

Segment Support

Segment support is a critical aspect of any telescope design and for a segmented mirror the active control is an additional critical technology. Each segment in the primary is assumed to behave as a rigid body and therefore has six degrees of freedom. Three of these are passively controlled and three are actively controlled. The passive degrees of freedom are constrained by

the radial post and diaphragm which is bonded into a hole in the back of the segment. These structures were built, installed, and used to support the full-sized segment in the active control prototype.

Each actuator of the active support system carries the load of the mirror through a whiffletree. This spreads the actuator force to 12 contact points on the mirror providing a more uniform support. The whiffletrees that have been built and tested as of this writing are shown to be inadequate in two respects. They introduce about 19nm rms surface deformation in the segment which gives an image blur of $\theta(80\%) = 0.106$arcseconds. This is a factor of 2 larger than the budgeted 0.05 arcseconds. The resonant frequency under piston is about 20Hz and this is about a factor of 2 lower than desired. A new whiffletree is being designed and the design is addressing both of these deficiencies. Design calculations show the new design to be substantially stiffer and significantly more tolerant of fabrication errors. Three whiffletrees of the new design will be built and tested in the coming months.

An assembly to test the proposed active control system was designed, built, and operated. The assembly contains a single full-sized hexagonal segment supported by whiffletrees and a radial support post and controlled by three actuators. The piston and tilts of the segment are measured with respect to a portion of a neighboring segment using four displacement sensors.

The goals for these tests were set by the performance requirements for the TMT active control system. These goals include limits on sensor noise levels, sensor stability, system stability, and active control reduction of external perturbations.

Measurements of the prototype assembly show that sensor noise levels are about 1nm, i.e., negligibly small. Sensor thermal dependence is about 2nm/^{o}C. This is marginally at a level needing correction, and thus only a rough temperature correction lookup table will suffice. The long term sensor stability tests (over a month) show variations of about 3nm per day, suggesting calibration using a star would be required about every three days. The sensitivity to transverse motions of the segments is also at a small enough level to allow for elevation angle correction using a lookup table.

The response of the active control system to piston forces applied to the mirror has been measured under a variety of conditions using control sampling frequencies up to 38Hz. The resonance characteristics of the whiffletree and flexibility of the reference mirror support structure limit the performance of the system. In the process of reducing the amplitude of the driven frequency the system excites the structural resonances that leak into the control via a hinging motion of the reference mirror. The structural elements oscillate at frequencies in the 20 to 30 Hz range. With these limitations the control system reduced the rms amplitude of perturbations at 0.2Hz by a factor of 3.

The structural resonances in the prototype are different from those expected in the TMT. Additional tests of the system were made with the structure stiffened and some of the resonances damped. Under these conditions the rms sensor reading was reduced by a factor of 3 at 1Hz. These results were then limited by delay in the control response from a phase shift induced by a notch filter used to remove a remaining resonance and by delay induced by the control calculation time. The measured results agree with a mathematical model of the system.

From the measurements with the active control assembly we draw the following conclusions.

1. The active control components, algorithm, and system perform as designed.

2. The performance of the control system in the present prototype configuration is limited by the presence of resonances in the segment support structure. The greater symmetry of the TMT mirror cell will eliminate some of the problems observed with the prototype in which the reference mirror and segment are supported on different structures. The stiffness of the support elements now being designed for the TMT segments must be emphasized in that design.

3. If the prototype structure is made stiffer, then the performance is limited by computation delay time and phase delays introduced by filters to remove remaining resonances. The computing hardware designed for the TMT will reduce the computation time to a level, at which it will introduce negligible delay (100μs). If resonances in the support structure are moved to higher frequencies, then control can be achieved without filters and their associated delays.

2. The Scientific Motivation for a Ten Meter Telescope

Contents **Page**

Summary

This section calculates the expected angular resolution and limiting magnitude of the TMT for various observations and compares the TMT to existing ground-based telescopes, the Space Telescope, and the SIRTF. There are many types of observations for which the TMT will be by far the world's most powerful telescope, especially for spectroscopic applications. The 1.0-2.0 magnitude gain of the TMT and its speed gain of 6.25-42.0 open up a large array of fundamental problems. These are illustrated by comprehensive descriptions of 33 observing projects in a variety of wavelength regions and spectral resolutions. Highlights include the formation and evolution of distant galaxies and clusters, fundamental composition studies of stars in our own and other galaxies, the dynamical state of a wide variety of stellar systems, and the structure and physics of star-forming regions in the Milky Way.

These descriptions are used to develop a body of goals for image quality, angular scale, field of view, and other parameters that the telescope should satisfy.

2.1 Theoretical Performance Limits

The performance of the TMT is determined by its collecting area, the geometrical shape of the primary mirror, the quality of images produced by the atmosphere and the optics, the thermal emissivity of the telescope (for infrared observations), the darkness of the sky, and the nature and efficiency of the instruments used to detect the signal. These factors are discussed below, and estimates are provided of the expected performance of the telescope for a variety of observations.

Angular Resolution

Factors that determine the angular resolution are summarized in Figure 2-1. The upward-sloping curve labeled "TMT: Diffraction Limit" is the FWHM of the Airy diffraction disk for a circular 10m aperture. The theoretical diffraction size of the hexagonal segmented TMT primary is close to this value (Mast, Nelson and Welch, 1982, TMT Report No. 68). Faber and Nelson (1981, TMT Report No. 57) have shown that the angular resolution of the actual TMT (excluding the atmosphere) should closely approach the theoretical limit at wavelengths longward of approximately 4μm, for fabrication and alignment errors as given in Tables 4-2 to 4-5. This is shown as the portion of the lower heavy curve at right. At visual wavelengths, the image size can be calculated by geometric optics and depends on the slope errors on the mirrors, fabrication and alignment errors of the secondary optics, and the defocus error. The above error budgets indicate a net FWHM of 0.24 arcseconds in the geometric-optics regime, a result that is fairly independent of focal position (Tables 4-2 - 4-5). For the purposes of this section, this error has been assumed to be independent of wavelength and is shown as the horizontal portion of the heavy curve at left. In the intermediate regime (roughly 2 to 6μm), detailed diffraction calculations are needed to determine the precise image size. These studies are underway, but for now, this gap is schematically bridged by the dashed line. A more complete discussion of expected image quality is given in Section 3.3.

Also shown is the FWHM of the image size produced by the atmosphere. This corresponds to a FWHM of 0.5 arcseconds at 0.55μm (midpoint of the V band). This value is approximately the 10th percentile for the seeing histogram at the CFHT telescope on Mauna Kea (Figure 3-3) and is taken as nominal in this report for observations requiring excellent angular resolution. The curve is scaled to other wavelengths as $\theta(\lambda) \approx \lambda^{-0.2}$ (Fried, 1966). Also shown is the net image size for the telescope and atmosphere in combination (upper heavy curve), the two assumed to add in quadrature. The projected image quality of the telescope is good enough that the net image closely approximates the theoretical limit produced by the atmosphere at all wavelengths shortward of the diffraction-limited regime.

Diffraction-limited performance is possible at short wavelengths using special techniques that circumvent atmospheric blurring (e.g., speckle interferometry). The lower left portion of the diffraction-limited curve is applicable to such observations. Also shown for comparison is

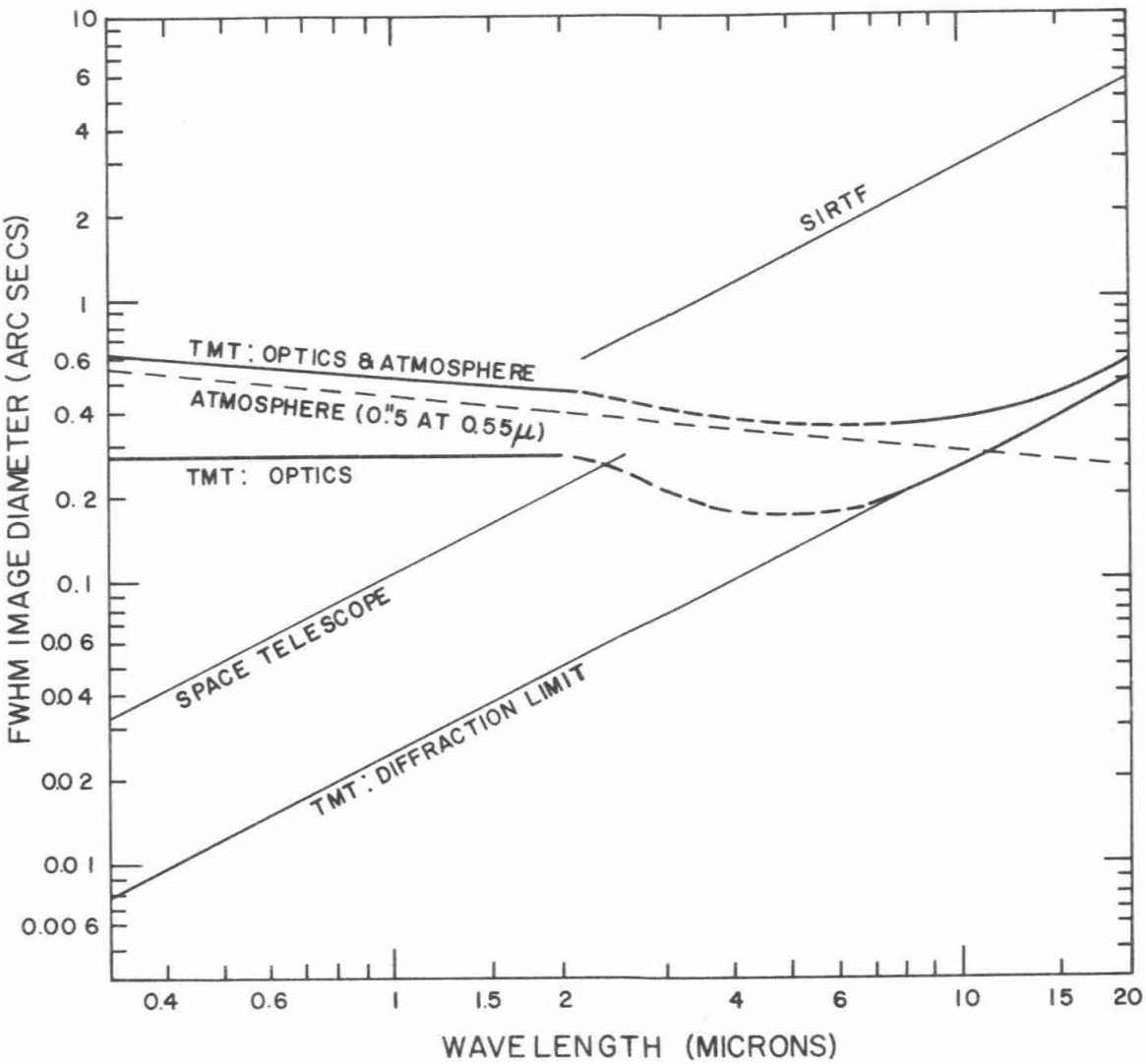

Figure 2-1: Image diameter (FWHM) for the TMT, compared to image diameters of Space Telescope (ST) and SIRTF versus wavelength. The latter are diffraction limited, with Θ(FWHM) = 1.0 λ/D. Three curves are shown for the TMT. The upward sloping line is the diffraction limit, which governs the image size at longer wavelengths ($\lambda \geq 4\mu$m; heavy line). At short wavelengths, the image size is governed by slope errors on the primary mirror, which are assumed to yield a constant image size independent of wavelength (see error budgets, Section 4.1). The gap between these two regimes is bridged schematically by the dashed interval. Diffraction calculations are now being carried out to estimate image sizes more accurately between 1μm and 6μm. Also shown is the atmospheric seeing FWHM, corresponding to the 10th percentile seeing at Mauna Kea, and the net telescope image size with the telescope and atmosphere added in quadrature.

the expected angular resolution for two planned space-borne telescopes, the 2.4m Space Telescope (ST), which will operate to 1.1μm initially but can operate to longer IR wavelengths with refurbished detectors, and the 0.9m Satellite Infrared Telescope Facility (SIRTF), which will operate in the thermal infrared beyond 2.5μm. Both of these telescopes should be essentially diffraction limited. They are discussed further in Section 2.2.

Atmospheric Transmission

Atmospheric transmission between 0.30μm and 0.80μm is controlled mainly by scattering by air molecules and by absorption and scattering by dust and aerosols (Allen, 1973). Absorption by ozone makes the atmosphere opaque below 0.3μm. The typical visual extinction coefficient at Kitt Peak is 0.18 mag per airmass, but at Mauna Kea the value is only 0.09 mag per airmass (Morrison et al., 1973). This lower value is due about equally to the smaller column of air (approximately 60% of that from sea level) and to a reduced dust and aerosol content. The net result is exceptionally high atmospheric transmission in the visual region, with over 90% at 0.55μm.

Beyond 0.80μm, transmission is controlled by various molecular absorptions, principally H_2O. The amount of water vapor over Mauna Kea is low, typically $\leqslant$2mm of precipitable H_2O. This compares to $\approx$10mm at typical inland sites at lower altitudes. The lower H_2O content greatly increases atmospheric transmission in the infrared windows. This can be seen in Figure 2-2, which shows transmission curves from 1μm to 10mm for three values of H_2O. These were calculated for various conditions as explained in the caption, with the minimum curve (highest line) similar to good conditions at Mauna Kea. The mean average transmission is greater than 95% through the 10μm window and 80% through the 5μm window. Figure 2-2 shows an expanded portion of a region near 1.4μm, illustrating the complex nature of the absorption at high spectral resolution.

Sensitivity and Signal-to-Noise Ratios

For planning purposes, it is useful to have estimates of exposure times for different types of observations at various wavelengths. For simplicity, we consider direct imaging on the V (0.55μm), I (0.9μm), H (1.6μm), K (2.2μm), and N (10.2μm) photometric system of Johnson (1966), plus moderate ($R = 10^3$) and high ($R = 10^5$) resolution spectroscopy at the same wavelengths. Where appropriate, similar observations with a 4m ground-based telescope, the Space Telescope, and the SIRTF are shown for comparison.

At visual wavelengths, the detector of choice is most often some type of low-noise photosensitive silicon array. The quantum efficiency of such arrays is roughly twice that of photosensitive cathodes, and the dark current and readout noise are low enough for most applications. Their small physical size is often a drawback compared to other detectors but may well increase in the future. Similar arrays are under development for the 1-2μm region, although the dark current due to impurities is likely to remain higher than the dark current of visual devices for some time (Rank, Capps, and Low, 1984). The use of silicon arrays is more problematical in the thermal infrared because of the high readout rates required by the thermal background of warm telescopes. Typically 10^4 reads/s for broad-band imaging are needed at 10μm. Readout rates are presently still a factor of 100 below this level, but can feasibly be increased (Rank, 1984). We have assumed such an array detector rather than the more conventional bolometer because of the larger number of pixels available in the array. The readout noise of the many rapid reads is treated in the equations as an effective dark current. The use of array detectors in the infrared on the SIRTF poses fewer problems because the telescope is cryogenically cooled and has negligible thermal background.

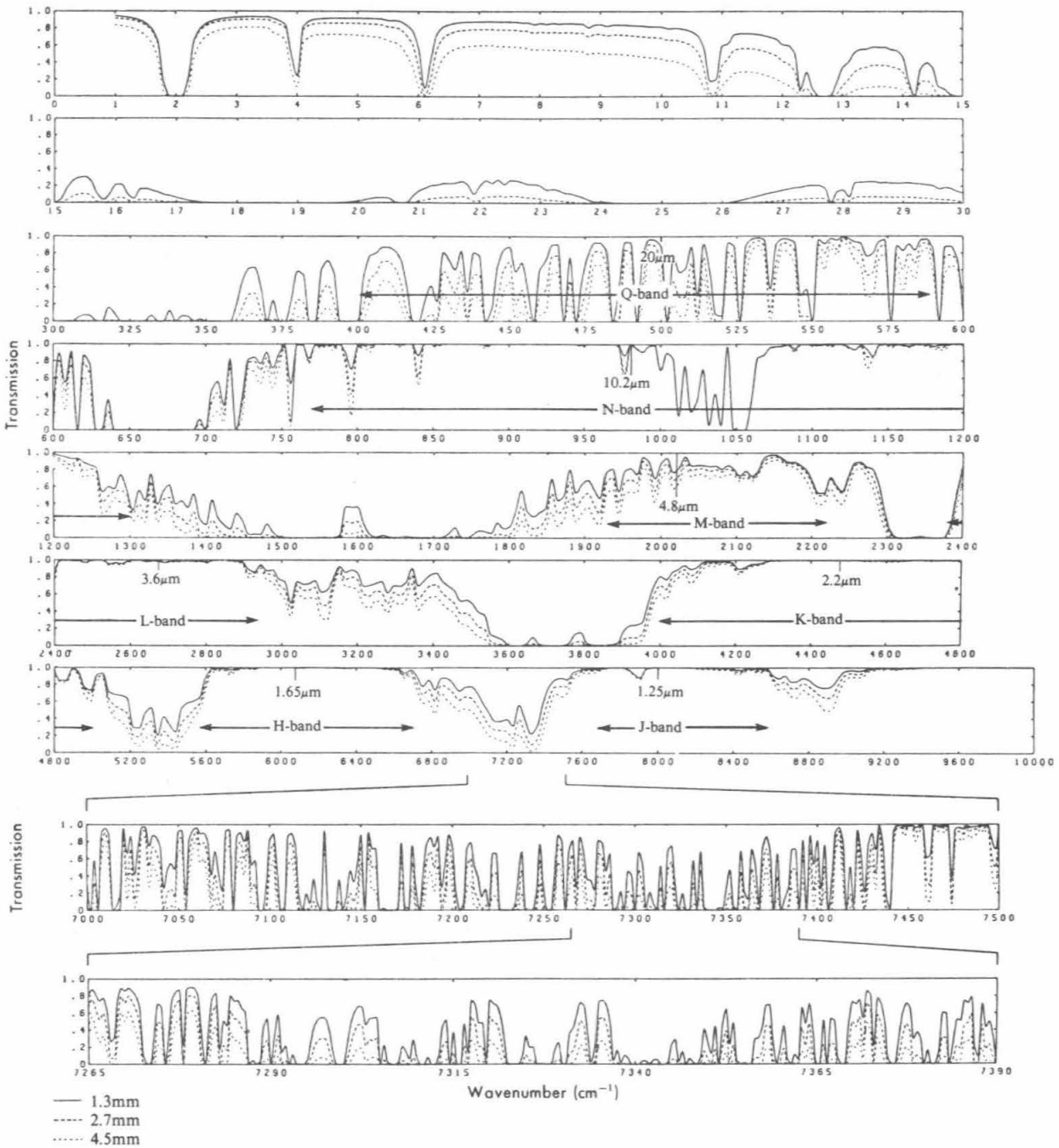

XBL 852-1412

Figure 2-2: Atmospheric transmission curves from 1μm to 10mm by Cudaback. The upper curve is for 1.3mm precipitable H_2O and the middle curve is 2.7mm at 4000m altitude. The lower curve is for 4.5mm at a more typical observatory altitude of 2000m. Although the pressure broadening is different because of the different altitude of the sites, the curves illustrate reasonably well the effects on transmission of varying amounts of H_2O. The upper curve is the best match to good conditions at Mauna Kea. The bottom two bars show the structure of H_2O absorption at 1.4μm under very high spectral resolution for 1.33mm H_2O at 4000m altitude. For convenience, the conventional IR photometric wavelength regions are indicated.

The signal-to-noise ratio, S/N, for point sources is given by

$$S/N = \frac{S}{\sqrt{S + B + T + D + RO}} \tag{2-1}$$

where S is the number of signal counts, B is the sky-background counts over the image, T is the thermal counts (in the infrared), D is the dark current, and RO is the readout noise of the array.

Define:

λ_μ = wavelength in microns

D_m = diameter of primary mirror in m (assumed circular)

t = integration time in seconds

$\delta\lambda/\lambda \equiv R^{-1}$ = fractional bandwidth

η_T = transmission of the atmosphere and optics

η_D = quantum efficiency of the detector

f_J^O = source flux, in Janskys

f_J^S = background flux from the sky, in Jy/arcsecond^2, including OH emission

f_J^T = thermal background in Jy/arcsecond^2

d = dark current in counts/pixel/sec

ϵ = effective thermal emissivity of the telescope

θ = FWHM of the image diameter for a point source, in arcseconds

r = readout signal per pixel, in electrons

n = number of pixels per image or spectroscopic resolution element

A major problem in computing S/N from Equation 2-1 is the effective area of the array that contributes to sky, thermal, dark, and readout noises. King (1983) has shown that, for direct imaging, the optimum method for flux measurement of sources fainter than the background involves the fit of a known profile to the data, with vertical normalization as a free parameter. This is superior to the usual "diaphragm" technique for sources whose profile form is known *a priori*. For a two-dimensional Gaussian point spread function (PSF), the effective noise area in the detector, A, is found to be $2.28\theta^2$ in the limit of infinitely small pixels (King, 1983), where θ is the Gaussian FWHM. The multiplicative constant is close to 2.28 as long as pixel sizes are less than $\theta/2$ (Faber, 1981, TMT Report No. 61). This is satisfied for most cases below and has been assumed uniformly throughout. Let σ be the one-dimensional Gaussian rms half-width. Using an ideal sampling criterion of 1.1 pixel/σ for a Gaussian PSF (Faber, 1981, TMT Report No. 61), one finds a total of 15.2 pixels per image. This optimum number was reduced in certain cases where it was found that readout noise or dark current was the limiting noise for faint observations. In such cases, the number of pixels was assumed rather arbitrarily to be 4.6, a value consistent with the sampling rate in the diffraction core of the images produced by the Wide Field/Planetary Camera of the Space Telescope in f/30 mode (Westphal, 1982).

For spectroscopic observations of point sources, the image area sampled per resolution element on the detector was assumed to be rectangular, with width $\Delta\lambda$ and height proportional to θ. The number of pixels depends on the desired spatial information perpendicular to the dispersion but must be at least 2 (Nyquist criterion of 2 samples per spectral resolution element). We have assumed that A is always $2\theta^2$ for spectroscopy but that the number of pixels depends on R. This is reasonable because, at moderate values of R, observers often want to study extended objects, for which better spatial information and more pixels/arcsecond are required. At high R the major targets are often point sources, for which the minimum number of 2 pixels is adequate. These conventions are summarized in Table 2-1.

Table 2-1

Parameters for S/N Calculations

Telescope	D_m	Mode	Band	λ_μ	R^{-1}	η_D	η_T	f_J^S(Jy/□")	T(^oK)	f_J^T(Jy/□")	Θ(FWHM;0.55μ) Atmosphere 0".5	1".00	A/θ^2	n(px)	$d(s^{-1})$	r	Major noise source(s) at t = 3600 sec
TMT	10 m	Direct	V	.55[b]	.162[b]	.30	.30	$1.25X10^{-5}$[d]	--	--	.57[a]	1".04[a]	2.28[k]	15.2[k]	.002[l]	7	Sky
and	and	Imaging	I	.90[b]	.267[b]	.30	.30	$8.24X10^{-5}$[e]	--	--	.53[a]	.94[a]	2.28	15.2	.002	7	Sky
4 m	4 m	S/N=10	H	1.6[b]	.2[b]	.50	.40	$2.0\ X10^{-3}$[f]	--	--	.48[a]	.84[a]	2.28	15.2	1[m]	20	Sky
			K	2.2[b]	.218[b]	.50	.40	$2.4\ X10^{-3}$[g]	275[h]	$4.1X10^{-4}$[i]	.47[a]	.81[a]	2.28	15.2	1	20	Sky
			N	10.2[b]	.2[b]	.50	.16[c]	--	275	$5.0X10^{2}$[i]	.38	.61 (10 m)[j]	2.28	15.2	$4X10^{6}$[n]	--	Thermal
											.69	.84 (4 m)[j]					
		Spectrosc.	V	.55	10^{-3}	.30	.25	$1.25X10^{-5}$	--	--	--	1.03	2.0[k]	9[k]	.002	7	Sky
		S/N=30	I	.90	10^{-3}	.30	.25	$8.24X10^{-5}$	--	--	--	.93	2.0	9	.002	7	Sky
			H	1.6	10^{-3}	.50	.35	$2.0\ X10^{-3}$	--	--	--	.84	2.0	9	1	20	Sky
			K	2.2	10^{-3}	.50	.35	$2.4\ X10^{-3}$	275	$4.1X10^{-4}$	--	.81	2.0	9	1	20	Sky
			N	10.2	10^{-3}	.50	.20[c]	--	275	$5.0X10^{2}$	.38	-- (10 m)	2.0	9	$4X10^{4}$[n]	--	Thermal
											.69	-- (4 m)					
		Spectrosc.	V	.55	10^{-5}	.30	.12	$1.25X10^{-5}$	--	--	--	1.03	2.0[k]	2[k]	.002	7	Signal
		S/N=60	I	.90	10^{-5}	.30	.12	$8.24X10^{-5}$	--	--	--	.93	2.0	2	.002	7	Signal
			H	1.6	10^{-5}	.50	.18	$2.0\ X10^{-3}$	--	--	--	.84	2.0	2	1	20	Signal, sky, dark
			K	2.2	10^{-5}	.50	.18	$2.4\ X10^{-3}$	275	$4.1X10^{-4}$	--	.81	2.0	2	1	20	Signal, sky, dark
			N	10.2	10^{-5}	.50	.10[c]	--	275	$5.0X10^{2}$	.38	-- (10 m)	2.0	2	$4X10^{2}$[n]	--	Thermal
											.69	-- (4 m)					
SIRTF	0.9	Direct	K	2.2	.218	.50[o]	.40[o]	$4.8X10^{-6}$[o]	7[o]	--	.61[p]		2.28[k]	4.62[w]	1[q]	20[q]	Dark
		S/N=10	N	10.2	.2	.50	.40	$4.8X10^{-4}$[o]	7	--	2.75[p]		2.28	15.2[k]	1	20	Sky
		Spectrosc.	K	2.2	10^{-3}	.50[o]	.35[o]	$4.8X10^{-6}$	7	--	.61		2.0[k]	2[k]	1[q]	20[q]	Signal, dark
		S/N=30	N	10.2	10^{-3}	.50	.50	$4.8X10^{-4}$	7	--	2.75		2.0	2	1	20	Sky
		Spectrosc.[r]	K	2.2	10^{-5}	.50[o]	.18[o]	$4.8X10^{-6}$	7	--	.61		2.0[k]	2[k]	1[q]	20[q]	Signal, dark
		S/N=60	N	10.2	10^{-5}	.50	.25	$4.8X10^{-4}$	7	--	2.75		2.0	2	1	20	Signal
Space Telescope	2.4 m	Direct	V	.55	.162	.25[s]	.30[s]	$6.5X10^{-6}$[t]	--	--	.061[s]		2.28[k]	4.62[s]	.002[s]	13[s]	Signal, sky
		S/N=10	I	.90	.267	.16[s]	.30[s]	$8.9X10^{-6}$[u]	--	--	.10		2.28	12.36[s]	.002[s]	13[s]	Signal, sky
			H[v]	1.6	.20	.50	.30	$8.7X10^{-6}$[u]	--	--	.18		2.28	4.62[w]	1	20	Dark
			K[v]	2.2	.218	.50	.30	$4.8X10^{-6}$[u]	294[x]	$9.5X10^{-4}$[x]	.24		2.28	4.62[w]	1	20	Thermal
		Spectrosc.	V	.55	10^{-3}	.25[s]	.30[s]	$6.5X10^{-6}$	--	--	.061[s]		2.0[k]	2.0[s]	.002[s]	0[s]	Signal
		S/N=30	I	.90	10^{-3}	.16[s]	.30[s]	$8.9X10^{-6}$	--	--	.10		2.0	2.0[s]	.002[s]	0[s]	Signal
			H[v]	1.6	10^{-3}	.50	.35	$8.7X10^{-6}$	--	--	.18		2.0	2.0[k]	1	20	Dark
			K[v]	2.2	10^{-3}	.50	.35	$4.8X10^{-6}$	294	$9.5X10^{-4}$	.24		2.0	2.0[k]	1	20	Signal, thermal, dark
		Spectrosc.	I	.90	10^{-5}	.16	.15	$8.9X10^{-6}$	--	--	.10[s]		2.0[k]	2.0[k]	.002	7	Signal
		S/N=60	H[v]	1.6	10^{-5}	.50	.18	$8.7X10^{-6}$	--	--	.18		2.0	2.0	1	20	Signal, dark
			K[v]	2.2	10^{-5}	.50	.18	$4.8X10^{-6}$	294	$9.5X10^{-4}$	.24		2.0	2.0	1	20	Signal, dark

Notes to Table 2-1:

[a] Based on image FWHM from error budgets of Section 4.1, convolved with the atmosphere in quadrature.

[b] Johnson (1966), Allen (1973).

[c] Reduced by 0.40 to allow for chop duty cycle. An array based on a photoconductive silicon material is assumed. $\sqrt{2}$ has not been added to the noise, as is usual for photoconductive detectors, since, when operated as an array, there is no generation-recombination noise (D. Rank, private communication).

[d] Corresponds to V = 21.25 magnitude/arcsecond^2. Source is Strittmatter (1980) and is evidently an all-sky average. At Galactic pole and away from zenith, the dark night sky is typically 22.0 V magnitude/arcsecond^2 (Walker 1970, TMT Report No. 49). This case is also shown in Figure 2-3a for 0.5 arcsecond seeing on the TMT.

[e] Turnrose (1974). The value of Strittmatter (1980) is known to be too high (J. Noxon, private communication).

[f] From nighttime OH measurements by Stair et al. (1971). Value fluctuates by at least a factor of 2 about this mean.

[g] Based on a private communication from R. Capps (1984), comparing sky backgrounds at Mauna Kea in H and K bands.

[h] Mean nighttime temperature at Mauna Kea is approximately $+2^{o}$C.

[i] An emissivity of $\epsilon = 0.1$ is assumed.

[j] TMT and 4m assumed to be intrinsically diffraction-limited, convolved with the atmospheric seeing in quadrature.

[k] For discussion, see text.

[l] Dark current of a typical CCD at visual and near IR wavelengths.

[m] An optimistically low value projected for future arrays in this wavelength range. Present-day detectors have dark currents 10^5 times higher. No obstacles *in principle* prevent reduction to 1cps, which would involve better removal of impurities (F. Low, private communication). Same for K band.

[n] Intrinsic dark current is very low (<1cps). See text.

[o] Basic performance and backgrounds for SIRTF were taken from the *SIRTF Interim Report,* (1978).

[p] SIRTF will be diffraction limited at all wavelengths.

[q] Dark current and readout noise for SIRTF detectors provided by D. Rank (private communication).

[r] No R = 10^5 spectrograph is currently planned for SIRTF. The comparison is therefore with a hypothetical satellite based instrument.

[s] Performance of currently planned instruments on ST is generally taken from *The Space Telescope Observatory,* Special Session of IAU Commission 44, Patras, Greece, 1982.

[t] Corresponds to V = 22.0 magnitude/arcsecond^2 or B $\approx$ 22.7 magnitude arcsecond^2. This is the currently adopted value at Space Telescope Science Institute (R. Griffiths, private communication). The darkest part of the sky at the Galactic poles and away from the ecliptic may be 0.4 magnitude fainter, based on data in Allen (1973). This would make only small change in Figure 2.3a.

[u] Scaled from V value, assuming that the background light has a spectral-energy distribution like a black body with T_{eff} = 5770K (solar T_{eff}).

[v] No instrumentation at H and K is included in the first-generation complement for ST. Performance estimate is based on hypothetical, future instruments.

[w] Noise is strongly dark-current-limited so number of pixels have been minimized. On ST, same instrumentation is assumed for K-band observations.

[x] ST mirror held at 294 $\pm$ 1 K; thermal emissivity ϵ = 0.05 (Pipher et al. 1984).

With these definitions, Equation 2-1 can be written as

$$S/N = \frac{1.18\times10^{7}D_m^2 tR^{-1}\eta_D\eta_T f_J^O}{[1.18\times10^{7}D_m^2 tR^{-1}\eta_D(\eta_T f_J^O + A\eta_T f_J^S + Af_J^T) + dtn + r^2n]^{1/2}} \quad (2\text{-}2)$$

The thermal background in Janskys/arcsecond^2 is

$$f_J^T = \epsilon\left[\frac{9.33\times10^{8}\lambda_\mu^{-3}}{exp(1.44\times10^{4}/\lambda_\mu T) - 1}\right], \quad (2\text{-}3)$$

where T is the temperature of the telescope.

The values of the parameters used to calculate S/N are summarized in Table 2-1, with explanatory notes. Figure 2-3 plots the resultant times to observe in different wavelength bands as a function of magnitude. A threshold signal-to-noise of 10 was adopted for all direct imaging, 30 for moderate-resolution spectroscopy ($R = 10^3$), and 60 for high-resolution spectroscopy ($R = 10^5$). This reflects the fact that better data are usually required when higher spectral resolution is employed. The graphs generally show similar behavior: a moderate slope for bright sources, where t varies as $(f_J^O)^{-1}$, and a steeper portion at faint levels, where $t \approx (f_J^O)^{-2}$. In the former regime, the major noise source is either signal shot noise or detector readout noise. In the steeper region, the major noise is sky background, thermal background, or detector dark current.

The calculations in Figure 2-3 are illustrative only. They are based on many uncertain assumptions concerning throughput and detector performance. The results do have comparative value, however, since an effort has been made to assume a consistent set of data for one telescope versus another. Comparison between the TMT and other telescopes based on these values is discussed in the next section, where additional considerations such as total field of view and suitability for multi-object spectroscopy are also taken into account.

A final word should be said about detector calibrations. Implicit in Equation 2-1 is the assumption that the detector response can be calibrated to better than $C^{-1/2}$, where C is the total background count (sky, thermal, and readout noise). In certain cases, this may require an extremely accurate calibration. For example, typical sky counts on the TMT over long, broadband, direct exposures in the I, H, and K bands can amount to 10^8 electrons per point-source image. Calibration accuracies of better than one part in 10^4 per image are therefore required. Great strides have been made on this problem at visual wavelengths using techniques that scan the image over many pixels while simultaneously reading out one row of the array at a time (McKay, 1982). The ability to calibrate to one part in 10^3 is now demonstrated, and there seems to be no known obstacle in pressing a decade further. Less is known about the even greater stability required of arrays in the thermal IR, where total thermal counts on long exposures can be of order 10^{13} electrons, and stabilities of $\approx 10^{-6.5}$ are required if no chopping secondary is used. With a chopping secondary, however, the required stability is greatly reduced, and calibration should not be a problem.

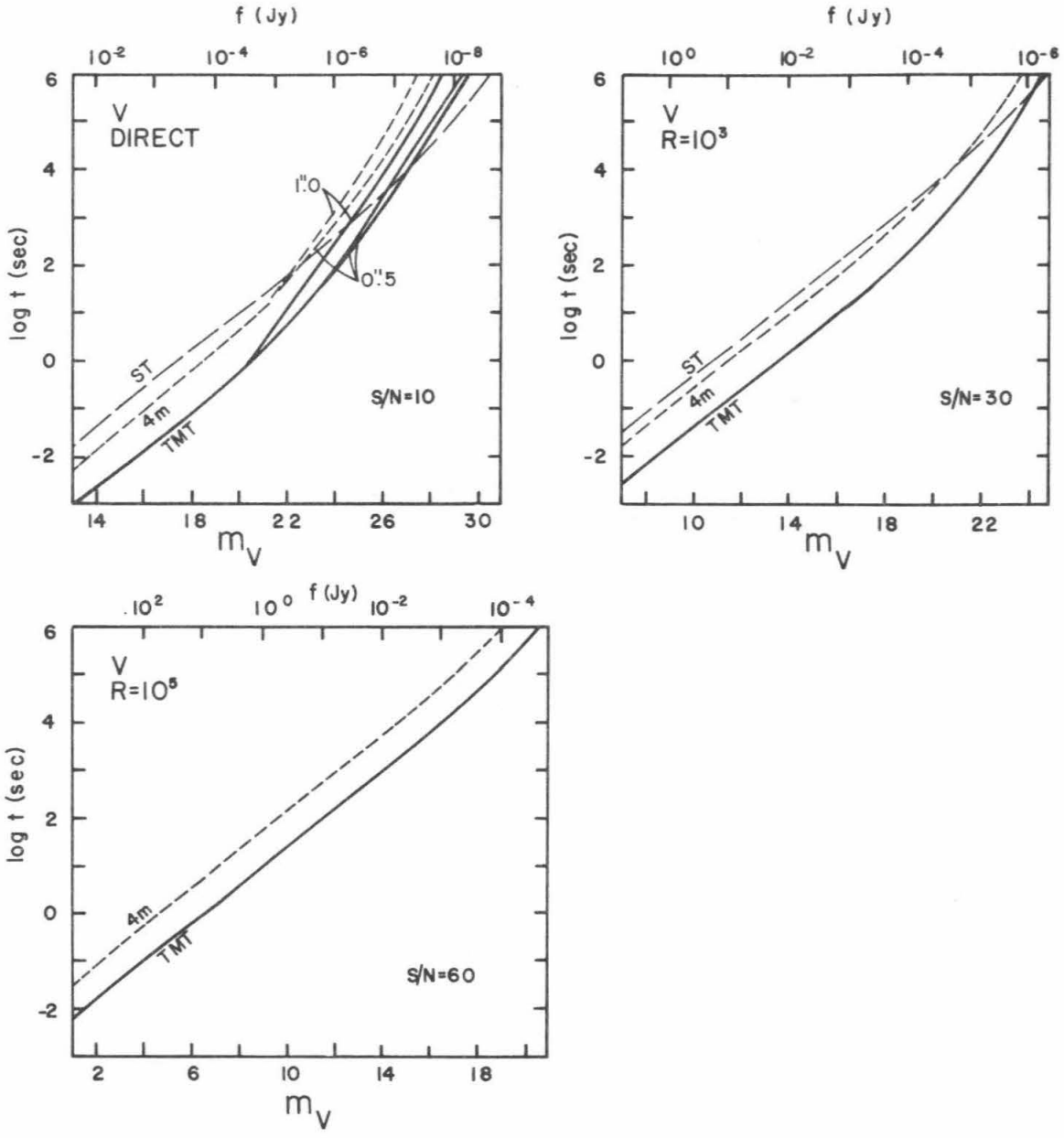

Figure 2-3a: The time required to reach the indicated S/N for direct imaging, moderate-resolution, and high-resolution spectroscopy for various telescopes in the V band (0.55μm). The parameters used to generate the curves are given in Table 2-1 and the associated notes. For direct imaging, the ground-based telescopes are shown for two different values of the seeing FWHM. The assumed sky brightness is 21.25 V magnitude per square arcsecond. In addition, the TMT is also shown for 22.0 V magnitude per square arcsecond, a value more typical of the darkest sky at the Galactic Poles and away from the zodiacal light. A seeing FWHM of 1.0 arcseconds at 0.55μm is assumed for all spectroscopy.

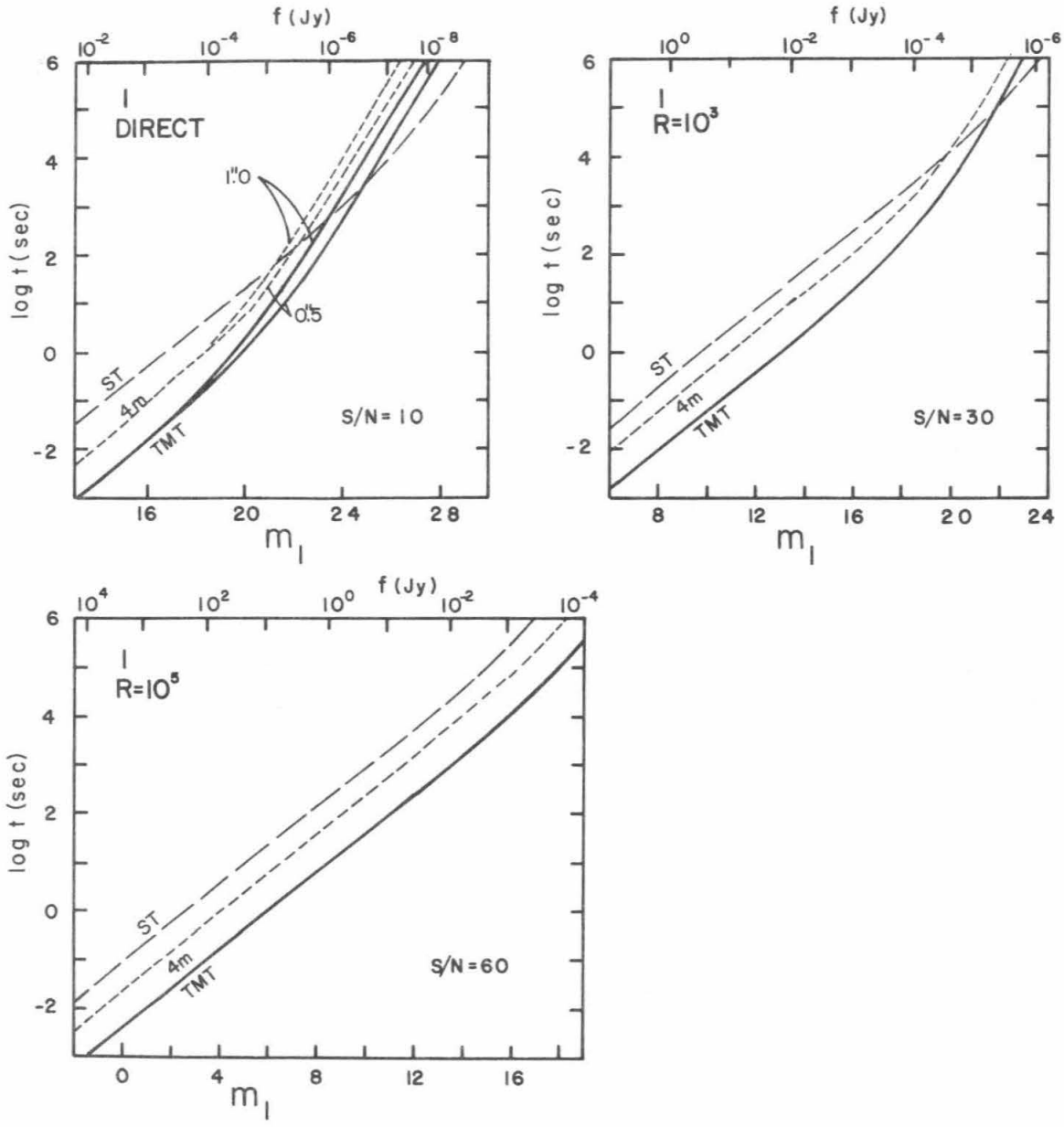

Figure 2-3b: Same as Figure 2-3a, for the I band (0.9μm).

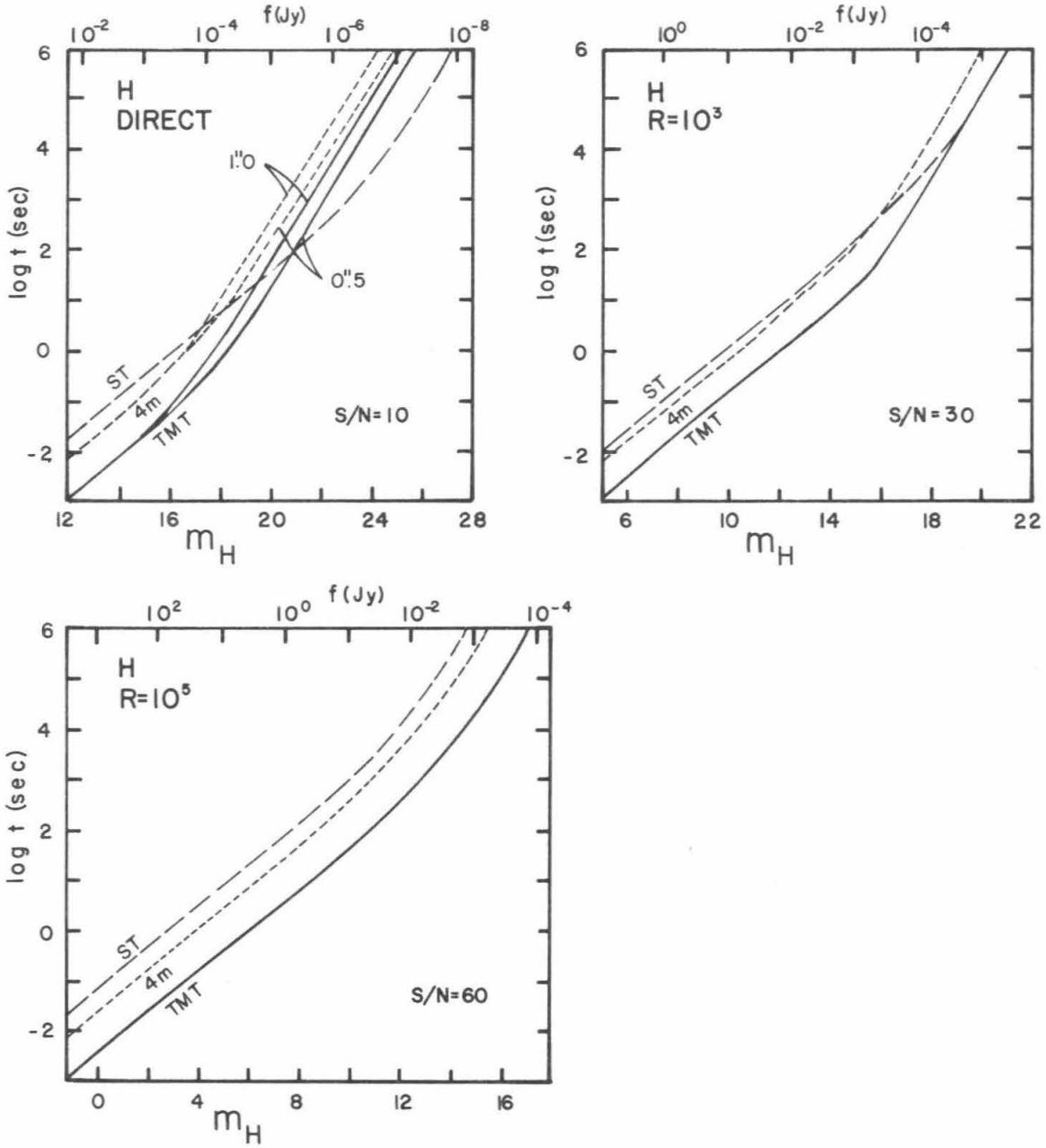

Figure 2-3c: Same as Figure 2-3a, for the H band (1.6μm).

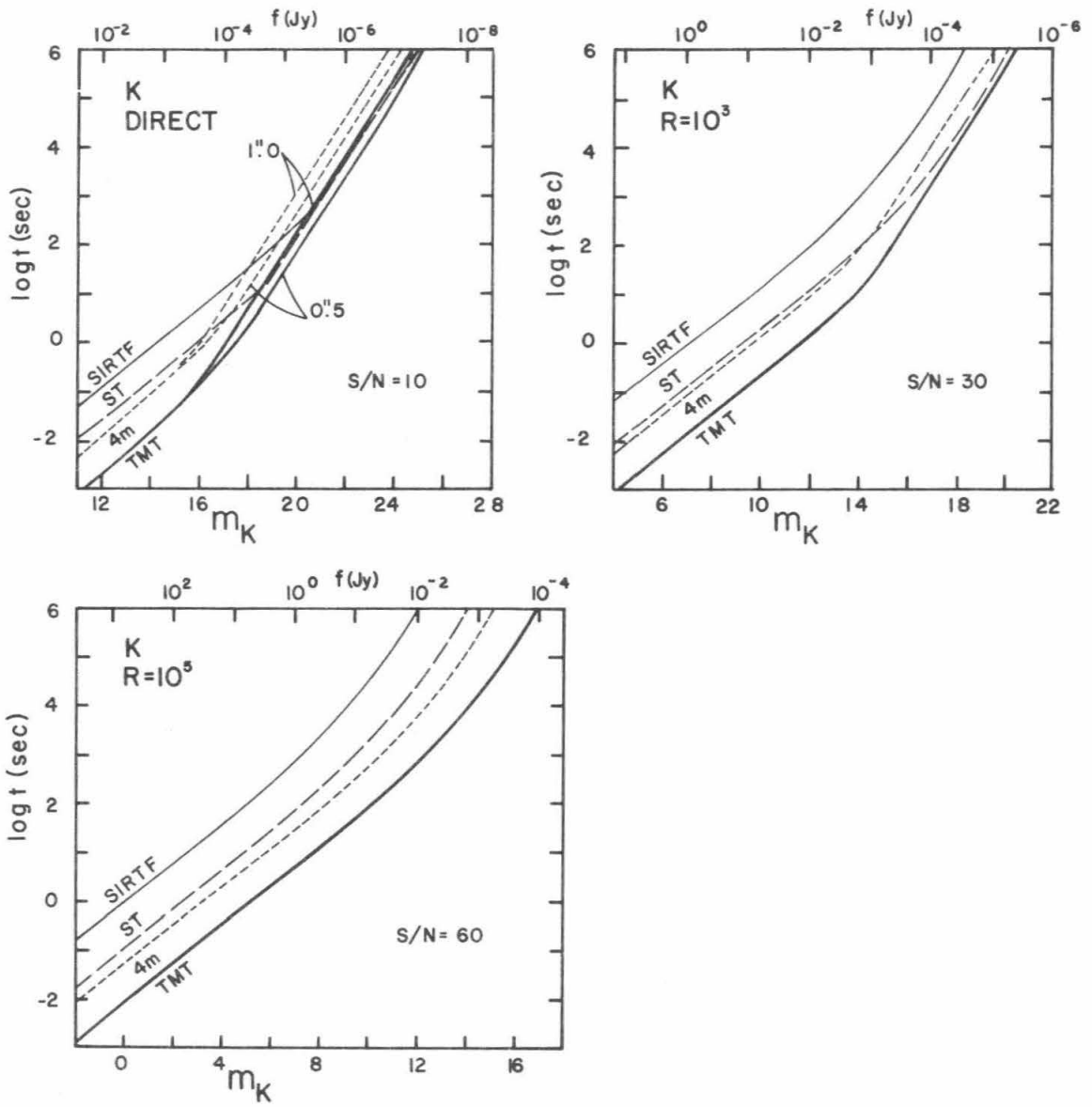

Figure 2-3d: Same as Figure 2-3a, for the K band (2.2μm).

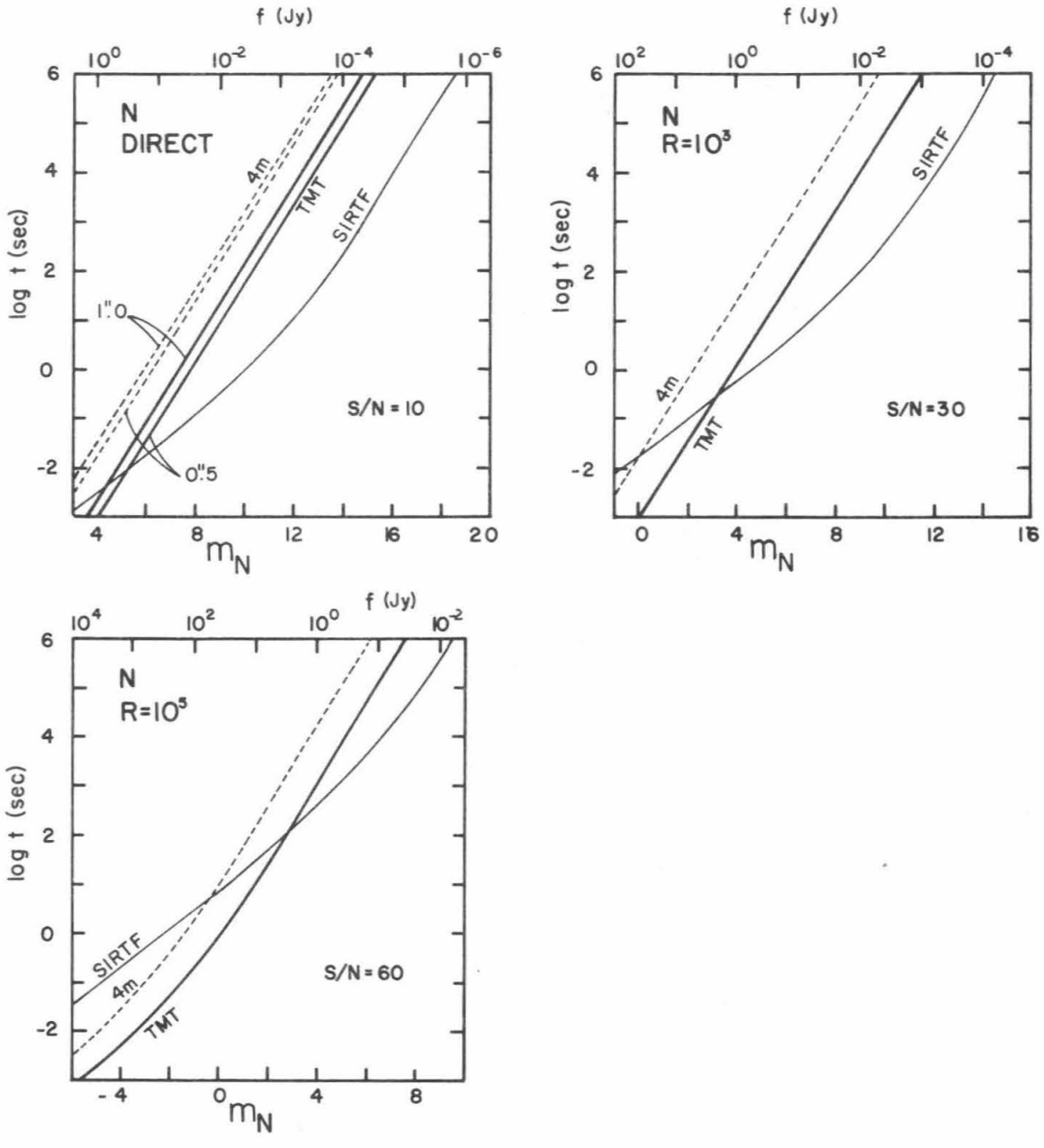

Figure 2-3e: Same as Figure 2-3a, for the N band (10.2μm).

2.2 Comparison with Other Facilities

This section compares the TMT with existing 4m-class ground-based telescopes, the ST, and the SIRTF. These are the TMT's three major competitors in the wavelength range 0.3μm to 20μm.

2.2.1 Four-Meter-Class Ground-Based Telescopes

The principle gain of the TMT over existing telescopes is its significantly larger aperture. This gain can be expressed in several ways. For any given observation, it means that the TMT will be significantly faster than a 4m telescope. This speed gain will make feasible many types of observations that would now take excessively long with present telescopes. Alternatively, in a given integration time, the TMT will be able to go fainter. How much fainter depends on the major noise sources, the relative size of the seeing disk, and the darkness of the night sky.

Direct Imaging: 0.33μm to 2.5μm

For limiting direct exposures at 2.5μm and shorter wavelengths, the major noise source for ground-based telescopes is sky background. Under these conditions, the flux limit in a given exposure time, f_{lim}, varies as D_m^{-1}, where D_m is the primary mirror diameter. (Figure 2-3 shows the effect of seeing and sky brightness on limiting magnitude in this regime.) The TMT will thus reach 2.5 times fainter than a comparable 4m at the same site, a gain of 1.0 magnitude. However, there are additional gains to be expected from the better seeing and dark sky at Mauna Kea. With the possible exception of the 4m at Cerro Tololo, no other 4m telescope in the world enjoys such an excellent site. When diameter and site differences are taken into account, we estimate the following speed and magnitude gains in the V band over existing telescopes: Cerro Tololo 4m - $\times$6.25 and 1.0 magnitude; CFHT 3.6m (on Mauna Kea) - $\times$7.6 and 1.1 magnitude; Palomar 5m - $\times$10 and 1.2 magnitude; Anglo-Australian 4m - $\times$25 and 1.75 magnitude; Kitt Peak 4m - $\times$28 and 1.8 magnitude. (No comparison is attempted with the 4.4m MMT on Mt. Hopkins, since this telescope has not generally been used for long-exposure direct imaging, or with the Soviet 6m telescope, for which information on image quality and atmospheric seeing are lacking.) These numbers illustrate the great importance of seeing and sky brightness when coupled with primary mirror diameter. Altogether, the gains of 6.25-28 in speed and 1.0-1.8 magnitude in flux limit for direct imaging are one of the major scientific opportunities afforded by the TMT.

Spectroscopy: 0.33μm to 2.5μm

The major noise sources for spectroscopy shortward of 2.5μm vary with wavelength and spectral resolution. Longward of 0.70μm (in the I, H and K bands), the major noise is always sky background from OH airglow emission. Expected gains in speed and limiting magnitude are therefore comparable to those for direct imaging above. Shortward of 0.70μm, sky background becomes progressively less important relative to the signal shot noise. For moderate-resolution spectroscopy, the TMT is in the transition region between the regime where observing time scales as (source brightness)$^{-1}$ and where it scales as (source brightness)$^{-2}$ (Figure 2-3). The gains in limiting magnitude here are larger, amounting to 1.5 to 2.0 magnitudes, with speed gains in the range 6.25-16.

For the highest spectroscopic resolutions, noise is dominated completely by signal at V and I and, on existing telescopes, by dark current at H and K. The net result is a gain of 6.25 to 10 in speed and a full 2 magnitude gain in limiting magnitude over existing telescopes, independent of site or seeing. This large gain in limiting magnitude opens up a wide range of high-resolution spectroscopic studies with the TMT. These numerical results are summarized in Table 2-2.

Table 2-2
Gains in Speed and Limiting Magnitude Over Existing 4m-Class Telescopes at Wavelengths $\leq 2.2\mu m$[a]

Type of Observation	Speed Gain	Limiting Magnitude
Direct Imaging	6.25-28	1.0-1.8
Mod. res. spectroscopy		
$\lambda < 700nm$	6.25-16	1.5-2.0
$\lambda > 700nm$	6.25-28	1.0-1.8
High res. spectroscopy	6.25-10	2.0

[a]All comparisons made at a level corresponding to a 3600 second integration time on the TMT.

Thermal Infrared Observations

Beyond 2.5μm, the background flux is dominated by thermal emission from the telescope and the atmosphere. This spectral region is therefore termed the "thermal infrared". For point sources, better rejection of the thermal background is obtained for the sharpest possible images, but at long wavelengths image size increases because of diffraction. Note that atmospheric seeing improves with increasing wavelength, varying as $\lambda^{-1/5}$. The crossover point for the TMT between diffraction and atmospheric seeing is near 6μm (Figure 2-1). In the limit of pure diffraction, the image size varies as D_m^{-1}, and image area as D_m^{-2}. The limiting flux in a given integration time then varies as $f_{lim} \approx D_m^{-2}$, and the time needed to reach a given flux level varies as $t \approx D_m^{-4}$. The comparable relations in the non-diffraction-limited regime are $f_{lim} \approx D_m^{-1}$ and $t \approx D_m^{-2}$, showing a much weaker dependence on D_m. An increase in primary diameter in the diffraction-limited regime thus offers very substantial gains in both limiting magnitude and speed, as well as angular resolving power.

The actual gain of the TMT over a 4m is slightly less than the theoretical limit because the telescope is never completely diffraction limited, the atmosphere having some influence even at 20μm and under excellent seeing (Figure 2-1). Table 2-3 illustrates the real effects with seeing taken into account. The first entry compares the TMT to a 4m telescope at an identical site. This case is only of academic interest, since there exists no 4m infrared-optimized telescope at a site as well suited to the IR as Mauna Kea. The second example takes into account the generally better seeing at Mauna Kea compared to most sites. This causes a significant improvement at the shorter IR wavelengths but only a small difference at 10μm and beyond. The third and most realistic entry compares the TMT to 3.5m class IR telescopes now on Mauna Kea. Based on these values, we expect speed gains in the IR between 15 and 40 and magnitude gains of 1.5 to 2.0 mag, with generally larger gains at longer wavelengths.

The final entry shows the effect of seeing changes at the TMT itself, and shows that better seeing on point sources yields a big gain, especially at the shorter IR wavelengths. Limiting thermal IR measurements on the TMT are therefore heavily dependent on excellent seeing, even at the highest spectral resolutions. The thermal IR thus differs from shorter wavelengths, where high-resolution observations are independent of sky brightness, since they involve sources much brighter than the sky. In the thermal IR, all sources are faint compared to the thermal background, at even the highest spectroscopic resolutions.

The final advantage of the TMT over existing telescopes is its factor of 2-3 higher diffraction-limited resolution owing to the larger primary mirror diameter. This capability is important for infrared imaging at longer wavelengths and for interferometric imaging at shorter wavelengths, as discussed in Section 2.3.

Table 2-3
Gains in Speed and Limiting Magnitude for Point Sources at Diffraction-Limited Infrared Wavelengths[a]

Comparison[b]	$\lambda_{\mu m}$	Speed Gain	Lim. Mag.
TMT vs. 4m at same	5	12.3	1.36
site; 0.5 arcseconds	10	20.7	1.65
seeing for both	20	32.7	1.89
TMT vs. 4m, with	5	27.6	1.80
1.0 arcsecond	10	31.2	1.87
seeing for 4m	20	36.3	1.95
TMT vs. 3.5m at same	5	14.7	1.46
site; 0.5 arcseconds	10	26.1	1.77
seeing for both	20	42.2	2.03
TMT only:	5	3.44	0.67
0.5 arcseconds vs.	10	2.68	0.54
1.0 arcsecond seeing	20	1.58	0.25

[a]Speed comparisons are made at a level corresponding to a 3600 second integration time on the TMT.
[b]Atmospheric seeing is characterized by the FWHM at 0.55μm. Seeing size at $\lambda_{\mu m}$ is assumed to vary as $\lambda^{-0.2}$.

2.2.2 Space Telescope

The Space Telescope is a 2.4m, UV-optical satellite telescope presently scheduled for launch in August 1986. It will be the first large high-quality imaging telescope placed in orbit. Its location above the atmosphere frees it from the effects of atmospheric seeing, and it will be close to diffraction-limited at all wavelengths from the far ultraviolet to the near IR (Figure 2-1). In the V band, this means a gain in angular resolution of about a factor of 10 over the best available on the ground, including Mauna Kea. This yields a tremendous increase in the quality of images, which will be invaluable in resolving structure in crowded star fields, distant galaxies, galactic nuclei, and other regions where a wealth of fine detail is blurred out by the atmosphere. For bright objects, however, speckle imaging on the TMT will have resolution four times better than the ST.

The second major advantage of the ST is its ability to make spectroscopic observations at wavelengths where the atmosphere is opaque. These include the entire region below 0.32μm, obscured by ozone, plus certain windows in the near-infrared that are partially obscured by H_2O (1.4μm and 1.9μm; Figure 2-2). (There are no instruments for the near-infrared region in the first instrument complement, however.)

A major disadvantage of the ST is its relatively small aperture. By the standards of ground-based telescopes, the ST's aperture is not large. For applications where photon flux is important, the TMT wins handsomely with its 17.4 times larger collecting area. Spectroscopic observations generally require larger photon fluxes, since more signal is needed to resolve fine details in a spectrum than is needed to detect an object. For point sources, the two instruments therefore tend to be complementary, with the ST generally superior for most imaging problems and the TMT generally superior for spectroscopy.

This simple summary is amplified somewhat in the following sections. For completeness, performance estimates are given for hypothetical near-infrared instruments on the ST, even though none are contained in the initial instrument complement.

Point Source Sensitivity

For imaging and detection of point sources in the V, I, and K bands, Figure 2-3 shows that the ST and TMT actually have about equal sensitivity in a 3600 second exposure, both yielding limiting magnitudes of 26.5 in V, 25 in I, and 22 in K for S/N = 10. The poorer background rejection of the TMT (due to its fuzzier images) is compensated for by its much larger photon flux. Which telescope is better at any given task thus involves additional considerations. For example, the TMT has a well corrected field of view (FOV) of 30 arcminutes at prime focus, whereas the maximum FOV of the Wide Field Camera on the ST in the f/12.9 mode is only 2.7 arcminutes. The TMT thus offers a potential advantage in total areal throughput of a factor of about 100. In crowded star fields, however, the TMT will not be able to resolve individual stars owing to its poorer angular resolution, and the ST will clearly be preferred.

In the H band, the equation shifts to favor the ST. The sky background on the ground is bright at these wavelengths from OH atmospheric airglow (see Table 2-1). The much lower sky background from space gives the ST an advantage of about 1.5 mag in limiting magnitude for a direct 3600s exposure at this wavelength.

Extended Source (Galaxy) Sensitivity

As an example of detecting and imaging extended sources, photometry of distant galaxies is considered at a redshift $z \approx 1$. Two types of objects are examined: a highly concentrated, first-brightest cluster elliptical galaxy ($M_V = -23$ magnitude) and a luminous but lower-surface-brightness Sc spiral ($M_V = -22$ magnitude). A major question is again how to calculate the effective area of the array that contributes to background, dark current, and readout noise. As before, if the galaxy profile form is known *a priori,* the most efficient method of flux measurement involves fitting the known profile function to the data with a few free parameters, including the normalization for total brightness. The results of this calculation have not yet been published for galaxy profiles, so the area equivalent to King's effective area for Gaussian profiles is lacking. An alternative, simpler method that yields a lower limit to the S/N is the "diaphragm" technique, in which one simply adds up the total counts from the object and background within a specified aperture. This method has been optimized by Phillipps (1984) for galaxies in first order, who derives the diaphragm size that maximizes S/N for galaxy profiles of different functional forms.

We have applied Phillipps' results to the two types of galaxy as imaged by each telescope. For galaxy parameters as described in the notes to Table 2-4, the optimum diameter for the elliptical at z = 1 is 0.30 arcseconds, and is 2.26 arcseconds for the spiral (H = 50km/s Mpc and $q_o = 1/2$). The angular resolution of the ST is sufficiently high to allow aperture photometry on these scales. The optimum diameters were therefore adopted as calculated. The ground-based TMT can resolve the spiral (2.26 arcseconds) but not the elliptical (0.30 arcseconds). A diameter for the E of 1.00 arcseconds was therefore adopted, which degrades the maximum S/N slightly. Object fluxes for a 3600 second exposure were calculated within these diameters, based on growth curves and K-corrections as described in the notes.

For the ST, pixel size proved to be important owing to dark current and readout noise. A pixel size of 0.043 arcseconds was adopted at V and I, equivalent to the WF/PC in f/30 mode (used above for point sources). A comparable pixel size scaled to the diffraction limit was adopted for H and K. To reduce readout noise, schemes were also explored that binned pixels on readout (see notes). These are generally equivalent to the alternative of using the WF/PC in f/12.9 mode, which is probably what most imaging of distant galaxies will employ.

Table 2-4 S/N on Galaxies at z=1 with the TMT and the Space Telescope[a]

Band	Optimum Diam.[c] (arcseconds)	f_J^{gal}(Jy)[d]	f_J^{bgrd}(Jy)[e]	n	Sig. Counts	Bkgd. Counts	Readout Counts	Dark Counts	S/N
a) First-Brightest Cluster Elliptical[b]									
TMT: direct imaging									
V	1.0	1.14(-7)	1.25(-5)	20.5[f]	7.06(3)	6.08(5)	1005	1.45(2)	9.0
I	1.0	4.03(-6)	5.5 (-4)	20.5	4.11(5)	4.41(7)	1005	1.45(2)	62
H	1.0	1.53(-5)	2.0 (-3)	20.5	2.60(6)	2.67(8)	8200	7.38(4)	158
K	1.0	2.91(-5)	2.8 (-3)	20.5	5.39(6)	4.07(8)	8200	7.38(4)	265
Space Telescope: direct imaging									
V	0.30	5.16(-8)	6.5 (-6)	38.2[g]	1.53(2)	1.37(3)	6.46(3)	2.75(2)	1.7(3.0)[g]
I	0.30	1.82(-6)	8.9 (-6)	38.2[h]	5.71(3)	1.97(3)	6.46(3)	2.75(2)	48(61)[h]
H[i]	0.30	6.92(-6)	8.7 (-6)	4.24[i]	5.08(4)	4.51(3)	1.70(3)	1.53(4)	189[i]
K[i]	0.30	1.31(-5)	9.5 (-4)	4.24[i]	1.05(5)	5.37(5)	1.70(3)	1.53(4)	129[i]
Spectroscopy: time to reach S/N = 20 at I with R = 250:							TMT: 66 minutes ST[p]: 10 orbits (90 minutes/orbit)		
b) Luminous Sc Spiral[j]									
TMT: direct imaging									
V	2.26	1.70(-7)	1.25(-5)	105[k]	4.20(4)	3.11(6)	5.14(3)	7.56(2)	24
I	2.26	1.44(-6)	5.5 (-4)	105	3.67(5)	3.37(7)	5.14(3)	7.56(2)	64
H	2.26	4.54(-6)	2.0 (-3)	105	1.94(6)	1.36(9)	4.20(4)	3.78(5)	53
K	2.26	8.64(-6)	2.8 (-3)	105	4.03(6)	2.08(9)	4.20(4)	3.78(5)	89
Space Telescope: direct imaging									
V	2.26	1.70(-7)	6.5 (-6)	2170[l]	2.02(3)	7.75(4)	3.67(5)	1.56(4)	3.0(5.5)[l]
I	2.26	1.44(-6)	8.9 (-6)	2170[l]	1.14(4)	1.12(5)	3.67(5)	1.56(4)	16(26.9)[l]
H[m]	2.26	4.54(-6)	8.7 (-6)	241[m]	8.39(4)	2.56(5)	9.64(4)	8.68(5)	68[n]
K[m]	2.26	8.64(-6)	9.5 (-4)	241[m]	1.74(5)	3.05(7)	9.64(4)	8.68(5)	31[o]
Spectroscopy: time to reach S/N = 20 at I with R = 250:							TMT: 395 minutes ST[p]: 20 orbits (90 minutes/orbit)		

Notes to Table 2-4:

a. The integration time for all direct images is 3600 seconds. These are lower limits to the actual achievable S/N, as described in the text. The underestimate is likely to penalize the ST more than the TMT because it neglects the superior resolving power of the ST. H = 50km /s Mpc and $q_o = ½$ assumed throughout. Detector and telescope parameters not specified here were taken from Table 2-1.

b. $M^V = -23$ mag; Sandage's (1972) $D_{metric} = 85.5$kpc; de Vaucouleurs' $D_{eff} = 14.9$kpc, based on comparison of Sandage's growth curve with the growth curve in the *Second Reference Catalogue* (de Vaucouleurs et al., 1976); D_{opt} (Phillipps, 1984) = 2.52kpc. K corrections from spectrum of NGC 4472, by Oke et al. (1981).

c. For discussion, see text.

d. Galaxy flux within the specified aperture, based on the RC2 growth curve for E's, and on information given by Phillipps (1984).

e. $f_J^S + f_J^T$ from Table 2-1.

f. This choice is essentially arbitrary. For reasonable pixel sizes, dark and readout do not affect the results.

g. Number of pixels per image, assuming the WF/PC pixel size of 0.043 arcseconds (f/30 mode). The major noise source is readout noise. Binning 3X3 pixels on readout raises S/N to 3.0. This is given in parentheses under S/N.

h. Same pixel size as for the V band. Since the signal is now high, there is not much advantage in binning on readout. Binning 3X3 increases S/N to 61 (parentheses).

i. A hypothetical near-IR camera on the ST is assumed. The maximum pixel size is constrained by the need to resolve stellar images. The pixel size can be scaled from the present WF/PC pixel size from 0.55μm to 1.6μm, based on the change in size of the diffraction-limited image. The pixels should therefore be roughly three times larger, or ~ 0.12 arcseconds. At this size, they do not seriously affect the resultant S/N.

j. $M_V = -22$ mag; assumed exponential scale-length = 5.4kpc plus discussion in Phillipps (1984) yield $D_{opt} = 19.3$kpc. K corrections from Aaronson (1978) and unpublished IUE data of Wu, Gallagher, and Faber.

k. Consistent with pixel size assumed above for E galaxy. Has no effect on S/N.

l. WF/PC pixel = 0.043 arcseconds assumed. Binning 3X3 on readout raises S/N to 5.5 in V and 26.9 for I (parentheses).

m. Hypothetical near-IR camera, as described in Note i.

n. Major noise source is dark current, which cannot be reduced by binning on readout. It *could* be reduced, however, by a focal-ratio change to f/12.9

o. Major noise source is thermal background, not helped by binning or focal-ratio change.

p. Hypothetical spectrograph assumed at I. Maximum time for single exposure is 2500 seconds (dark time during one orbit) owing to background particle flux. Calculate S/N for one orbit as $(S/N)_{orb}$. Number of orbits to reach S/N = 20 is then $(20/(S/N)_{orb})^2$.

Table 2-4 indicates that, for a 3600 second exposure, the two telescopes are of roughly comparable overall sensitivity in the detection and photometry of large ellipticals near z = 1, with the TMT somewhat superior to the ST at V and K. The TMT is also better at all wavelengths for the spiral. The overall advantage of the TMT, coupled with its much wider field of view, makes it the better telescope for general surveys, counts, and colors of distant large galaxies. However, ST is still vitally needed for sharp images of distant galaxies to study their morphological evolution with time. ST will also be more sensitive to small galaxies below the angular resolution of the TMT.

Spectroscopy

Since spectroscopy often involves sources brighter than the sky, the superior sky rejection of the ST is not of much value here, and the TMT is expected to be more efficient at all wavelengths that are accessible from the ground. This reasoning is borne out by Figure 2-3. The TMT also lends itself readily to multi-object spectroscopy (Section 2.3), which allows observation of as many as 100 objects simultaneously in the same FOV. This technique has the potential to increase throughput greatly, but is probably too complex to be attempted on a satellite experiment in the foreseeable future. It gives the TMT a further edge over the ST in many spectroscopic applications. Spectroscopy on the ST is of course uniquely valuable at wavelengths not accessible from the ground, and also for a range of problems for which high angular resolution is essential (e.g., the structure of galactic nuclei).

A particular spectroscopic application where the TMT is pre-eminent involves redshift measurements of distant galaxies. This is demonstrated by the bottom entries in Table 2-4, based on hypothetical spectra of the elliptical and spiral galaxies considered above (see notes to Table 2-4). The TMT is able to take useful spectra of both galaxies in a reasonable amount of time (1 to 6 hours), whereas the ST would require a very large number of orbits. The study of the clustering and evolution of distant galaxies is highly dependent on such redshifts, as they provide the necessary redshift indicator for distance. The essential role of the TMT as a survey instrument for distant redshifts is discussed more fully in Section 2.3 on scientific opportunities.

This comparison between the TMT and the ST is best summarized by saying that they are complementary instruments, each with its own unique capabilities. The high-resolution imaging of the ST and high-quality spectroscopic data of the TMT will together provide a much more comprehensive picture of many important objects in the universe than we now have.

2.2.3 Space Infrared Telescope Facility (SIRTF)

The SIRTF is an infrared satellite telescope now under study by NASA. Current plans call for a 0.9m primary mirror diffraction-limited at all IR wavelengths. Despite its small primary, it achieves a major gain because the entire facility is to be cryogenically cooled to a temperature of 7K, and it will be above the atmosphere, thus eliminating the thermal emission that limits the sensitivity of warm, ground-based telescopes (see Table 2-1).

The superiority of the SIRTF on point sources is illustrated in Figure 2-3, which indicates that the SIRTF has an edge at 10μm (N) of about 3.5 magnitude for direct imaging, 3.0 magnitude for moderate resolution spectroscopy, and 0.7 magnitude for high resolution spectroscopy. It can also look in many wavelength bands (2.7μm, 6μm, 15μm, and beyond 30μm) where the atmosphere is completely opaque. Its main drawback is its comparatively poor angular resolution--only 2.75 arcseconds at 10.2μm versus 0.38 arcseconds for the TMT in good seeing. This is comparable to the difference in angular resolving power between Space Telescope and ground-based telescopes, but in this case the advantage lies with the TMT. A major use of the TMT will involve very high angular resolution imaging at infrared wavelengths.

A further advantage of the TMT is its ability to carry very high resolution spectrographs. Although Figure 2-3 suggests that the SIRTF should in principle have a slight sensitivity advantage at R = 10^5, this advantage is in fact moot because no instruments of such high resolution are being planned for the SIRTF. Large and complex devices of this type will likely be con-

fined to the ground for the foreseeable future.

As with the ST, the uses of the satellite-based telescope the SIRTF and the ground-based TMT are seen to be complementary.

The general conclusions of this section are summarized for reference in Table 2-5, which illustrates schematically the comparisons between the TMT, the ST, and the SIRTF. The major strengths of the TMT are its high photon throughput, its wide field of view, and its high angular resolution in the thermal infrared. As a ground-based telescope, the TMT is also able to carry more complex, state-of-the-art instrumentation than is possible on space-borne telescopes. Examples of scientific programs that utilize these capabilities are described in the next section.

Table 2-5
A Comparison of the TMT, Space Telescope, and the SIRTF: Areas of Superiority †

	Point Sources			Distant Galaxy: z = 1††	
Wavelength Band	Direct Imaging	Mod. Res. Spectroscopy	High Res. Spectroscopy	First-Ranked Cluster E	Large Sc Spiral
V	TMT (large FOV) ST (crowded fields)	TMT	TMT	TMT	TMT
I	TMT (large FOV) ST (crowded fields)	TMT	TMT	TMT ≈ ST	TMT
H	ST (future instrum.)	TMT	TMT	TMT ≈ ST	TMT ≈ ST
K	TMT (large FOV) ST (crowded fields) (future instrum.)	TMT	TMT	TMT	TMT
N	SIRTF TMT (crowded fields)	SIRTF	SIRTF (in principle)†† TMT (in practice)†††		

† Comparison includes only common wavelength regions. Both ST and SIRTF can observe in wavelength regions that cannot be seen from the ground.

†† Comparison is for integrated photometry only. ST is better for luminosity profiles, morphology, and other studies requiring high angular resolution.

††† See text.

2.3 Scientific Opportunities

The unique capabilities of the TMT will allow a wide variety of important new scientific programs. Careful consideration of programs is useful now because it helps to refine important requirements for the design and operation of the telescope and observatory. This section describes many projects that astronomers in the University of California and throughout the world consider outstanding research programs for large optical telescopes. Information in this section has been borrowed freely from several previously published studies (TMT Report No. 43; Strittmatter, 1980; Swings and Kjar, 1983; Gehrz, 1984). Contributions from a large number of University of California and Caltech astronomers are also acknowledged.

The present section is arranged in six parts, with projects grouped according to wavelength range and observational technique. At the end of each part is a summary of the major constraints on telescope performance imposed by projects in that section.

2.3.1 Multiple Object Spectroscopy

Multiple object spectroscopy (MOS) is a new technique which is not yet in common use but which promises to increase greatly the total efficiency of telescopes in the near future. MOS is the process of obtaining simultaneously the spectra of many objects in a single field of view. There are presently two methods to accomplish MOS: the use of optical fiber feeds, each one coupled to a spectrograph slit, and the use of short, multiple slits on a single spectrograph. Each of these techniques will have important applications. The fiber technique has the advantage of extreme flexibility in aperture placement and allows the arrangement of spectra on the detector with maximum efficiency. On the other hand, it is likely that multiple slits will be needed when highly accurate sky subtraction is required, i.e., when the objects to be observed are faint compared to the sky. Many important projects are of this type, especially those involving spectroscopy of faint, extended sources such as distant galaxies.

The number of objects that can be handled with MOS is limited by their distribution over the sky, by the spectroscopic resolution desired, and by the number of detector pixels and spectrograph technology available. Sky spectra must also be taken, so the total number of spectra is two to four times greater than the actual number of objects. Present day fiber-fed MOS can handle roughly 50 fibers for low-resolution observations. Multi-slit spectroscopy is more limited, with numbers presently equivalent to about 30 fibers. In what follows, we have assumed 100 objects, or 200 to 400 spectra in total, which appears to be a reasonable extrapolation over today's techniques.

Since MOS increases the number of spectra taken per unit time, one of its major advantages is a lengthening of the maximum tolerable exposure. An astronomer may be willing to invest 10 or even 20 hours in a single exposure if 100 good-quality spectra result. Limiting magnitudes with MOS may thus be 1 to 3 magnitudes fainter than for a nominal one hour exposure (see Table 2-6). Another way of stating it is that MOS coupled with the larger light-gathering power of the TMT gives a roughly 600-fold increase in total throughput over that in common use today. This is a power quite extraordinary by today's standards, one that opens up a number of important new areas that have remained out of reach until now.

Table 2-6 Limiting Magnitude for V-Band Spectroscopy

Resolution (R)	Regular Exposure (1 hr)	MOS (10 hr)
10^3	21.2	22.7
10^4	18.0[a]	20.2[a]
10^5	15.3	17.8

[a]Obtained by interpolation

Because of the limited number of pixels on present detectors, the major application of MOS today is to low-to-moderate resolution spectroscopy, because the required number of pixels per spectrum is smaller. Important applications at very high resolution can already be identified, however, and will increase as detector sizes increase.

The Universe as It Was Ten Billion Years Ago (Part I)

Observations of galaxies show them to be clustered on many scales, from small groups less than a million light years across to giant superclusters spanning nearly a billion light years. It is believed that these structures grew via gravitational instability from small density irregularities in the Big Bang. The amplitude and sizes of these irregularities are a powerful clue to processes in the Big Bang, and the distributions and motions of galaxies on all scales constitute vital cosmological data.

The origin of small and medium-sized clusters of galaxies is not difficult to explain theoretically, but the existence of the largest-scale inhomogeneities so far remains a puzzle. Paradoxically, these largest structures may owe their existence to one or more as-yet-

unidentified elementary particles--a miraculous coupling of the infinitely large with the infinitesimally small. Adding to the mystery is the fact that the largest structures seem to be arranged in enormous "filaments" or chains. This peculiar morphology appears to be a powerful clue to their origin.

Recent computer simulations indicate that the clustering process is still continuing. Conversely, by looking back in time--that is, out in space--to large distances, we can trace the clustering development to the present. Evolutionary effects are evident only by looking back an appreciable fraction of the age of the universe; very large distances are thus involved, and the sources are very faint. The large light gathering power of the TMT is essential to this task.

Distant galaxies at redshift z = 1 (whose light was emitted when the universe was only 1/3 its present age) can be detected with existing telescopes, and their colors and luminosities can be roughly measured. However, a major datum still lacking is a true distance measurement. This comes from an accurate knowledge of the redshift, but for this a spectrum is required. Spectra require much greater light-gathering power, as is shown in Table 2-4, where spectra and photometry in the I band are compared. Both the spiral and elliptical are easily detected in broad-band photometry in a one-hour exposure, but a good spectrum of the spiral is predicted to take over 6 hours, even with the TMT. (Note that distant galaxies may actually be somewhat brighter owing to younger, brighter stellar populations in the past, but this effect, which would shorten the exposure, has not been included.) Even with the added capability of MOS, spectroscopic redshift surveys of galaxies near z = 1 clearly require the largest possible telescope. This will be a major area of research for the TMT.

The average density of galaxies on the sky at 24.0 V magnitude is roughly 3 galaxies/arcminute^2. To observe 100 galaxies simultaneously thus requires a field of view of 7 arcminutes in diameter. Since exposures will be long, it is important to be able to observe to large hour angles and air masses; an atmospheric-dispersion compensator (ADC) is therefore required to null out the dispersive effects of atmospheric refraction.

The Formation and Evolution of Galaxies

The same spectra taken for redshifts contain important information about the colors and ages of stars in distant galaxies, and therefore about how stellar populations age with time. By extrapolating backwards, it is believed that stringent limits can be set on the time of formation of elliptical galaxies and hence on the epoch of galaxy formation and the age of the Universe.

The few spectra of distant galaxies we now have already indicate an anomalous component of bright, blue galaxies in clusters at redshifts near z=0.5. Counts of faint galaxies versus magnitude also indicate that galaxies must have been brighter in the past. Altogether, both theory and observation suggest strongly that galaxies have evolved substantially over observable times. Reaching out to z = 1 with the TMT will double or triple the effects that can be seen at z = 0.5 in the present data.

Spectroscopic surveys will also permit dynamical studies of galaxies in clusters. These help trace the evolution of clustering and provide information on cluster evolutionary processes, such as ram-pressure stripping of gas from galaxies and the formation of dominant central galaxies via merging and galactic cannibalism.

For galaxies in the range z = 0.5 to 1.0, the most useful wavelength range for spectra is 0.40μm to 1μm. Table 2-5 indicates that the TMT is considerably superior to the Space Telescope in this region. Longer-wavelength observations are also useful to survey for Hα emission, which is redshifted beyond 1μ for z $>$ 0.5, and to search for galaxies at even higher redshifts. The table suggests that the S/N ratio on a single galaxy would be similar beyond 1μm for the TMT and ST, but in practice the TMT would have an advantage because of its MOS capability. As noted above, a FOV of order 7 arcminutes is needed for surveys of field galaxies. Typical large clusters of galaxies are roughly 4 $\times$ (50/H_o)Mpc across and would subtend about 8 arcminutes at z = 1, comparable in size to the FOV needed for field surveys. Nearer clusters could benefit from fields twice as large.

The Internal Structure and Composition of Globular Clusters

Globular star clusters in the Milky Way are among the oldest objects in the Universe and provide powerful clues to the formation of the Galaxy and the buildup of heavy elements via nucleosynthesis. The TMT opens up important new vistas in the study of these objects. A primary problem is the precise chemical composition of old clusters. There is controversy on even the most basic level concerning the mean abundance of heavy elements in metal-rich clusters. Detailed information on the abundance of one element relative to another is also very sparse. Many giant-branch stars in clusters are contaminated at their surfaces by the products of nuclear burning in their interiors. This contamination can tell us much about stellar evolution, but it confuses attempts to measure the primordial composition of clusters. For this, it is necessary to observe unevolved main-sequence stars, which are very faint. In a few nearby clusters, main-sequence stars appear at +18 V mag, but in most they are one to two magnitudes fainter.

Table 2-6 shows limiting magnitudes for V band spectroscopy at three spectral resolutions, as inferred from Figure 2-3. Values are given for a one hour exposure and a 10 hour exposure, as would be suitable with MOS. The table shows that it will be possible with MOS to reach a few cluster main-sequence stars at the highest resolution. These high-quality measurements will provide a firm foundation for the chemical abundances of spheroid stars. It should also be possible to reach many more cluster stars at slightly lower resolution. These will provide somewhat coarser but nevertheless extremely valuable abundance information, and will also allow a wide variety of fundamental dynamical studies of clusters with radial velocity measurements. Estimates suggest that a S/N ratio of 30 and a resolution R = 10^4 together yield a velocity accuracy of $\approx$1km /sec. At this level, it will be possible to study the dynamics of stars of different masses, the dynamical structure of the outer envelopes of clusters, and the incidence of binary stars, which are fundamental to the dynamical evolution of clusters.

Globular clusters are ideal for MOS because the areal density of stars in a small field is high. For many purposes, a radius of 10 core radii (10 - 20 arcminute diameter) is adequate, a region that contains many thousands of stars of all types. At the cluster periphery, the star density is typically $\approx$0.3 stars/ arcminute^2 to 20th magnitude, most of which are main-sequence dwarfs. A 20 arcminute field is therefore needed to fill the MOS capability of 100 objects. Studies of the rarer K giants at the periphery would benefit from a larger FOV. The nearest clusters also tend to have somewhat larger radii than these values. In summary, for globulars a minimum FOV is required with full ADC over 10 arcminutes, with a maximum field of 60 arcminutes of value for the largest objects.

The Chemical Composition, Membership, and Dynamics of Main Sequence Stars in Open Clusters

The study of the lower main sequence stars in open clusters is presently hampered by uncertain membership criteria, owing to contamination of cluster color-magnitude diagrams by field stars at apparent magnitude V $\approx$ +15. Proper motion studies are limited and are often also affected by field contamination. MOS allows the TMT to act as its own survey instrument for faint cluster members, using radial velocities as a sensitive membership criterion. Stars as faint as M_V = +9 magnitude on the main sequence can be studied in clusters to a distance of 1kpc, based on Table 2-6. High-resolution abundance studies will be possible for somewhat brighter stars, including accurate abundance ratios of rare elements.

These data will permit examination of a number of important evolutionary processes. Uniformity in composition will indicate how efficiently gas is mixed in the interstellar medium. The incidence of binary stars can be determined in detail. The structure and dissolution of open clusters due to stellar evaporation can also be studied, providing crucial data on how the field-star population is built up by the evaporation of disk clusters. An important byproduct will be a clearer picture of chemical composition versus radius in the disk and how abundances scatter about the mean at each radius.

Typical FOVs required for open clusters are 10 arcminutes in diameter, with some as large as 20 arcminutes.

The Composition and Dynamics of Globular Cluster Systems in External Galaxies

Globular cluster systems in nearby galaxies are believed to be similar in age and origin to the globular clusters of the Milky Way. As such, they are a window on the early stages of formation of galaxies other than our own. They are also a useful dynamical tracer of the mass distribution outside the visible envelopes of elliptical galaxies, which are difficult to study since they lack the gaseous disks of spirals in circular motion.

Magnitudes of typical external globulars range from +19 to +23 V mag. A spectral resolution R = 10^3 will provide accurate radial velocities ($\pm$ 10 km/s) and integrated chemical compositions. Throughput over present telescopes will be aided greatly by the better seeing at Mauna Kea and by the atmospheric dispersion compensator (ADC), which will allow efficient long exposures. Most globular cluster systems in the Virgo cluster subtend 15 arcminutes, but the two largest extend to 30 arcminutes. A minimum ADC field of 15 arcminutes is therefore required, and there would be some additional benefit in extending this to 30 arcminutes.

The Nuclear Bulge and Halo of the Galaxy

The Galactic nuclear bulge is important as the only example of an elliptical-type stellar population that is near enough to be studied star by star. As such, it an important key to understanding the integrated light of elliptical galaxies. It also offers an extreme comparison to the properties of the spheroid stellar population in the vicinity of the sun, thus affording a maximal view of composition gradients among spheroid stars in the Milky Way.

The giant stars in the nuclear bulge have V magnitudes +16 to +18, whereas the brightest unevolved main sequence stars are +19 to +21. Table 2-6 suggests that very high-resolution spectroscopic observations should be possible on the giants, and moderate-resolution observations on many dwarfs. The accompanying radial velocities will allow us to detect binary stars and test whether the well-known correlation between abundance and kinematics that is seen in the solar neighborhood also extends to the central core of the Galaxy.

The density of stars in the direction of the Galactic nuclear bulge is high. At galactic latitude +12.6°, the number of main sequence dwarfs in the magnitude interval +19 to +21 is 12 stars/arcminute^2 (Terndrup, 1984), and the FOV needed to obtain 100 objects is 3.3 arcminutes in diameter. The ratio of giants to dwarfs is about 1:10, so the necessary field to find 100 giants is $\approx$10 arcminutes. Closer to the center, the required fields are even smaller.

Studies farther out in the Galactic halo will allow us to study the kinematics and composition of the most distant, metal-poor stars in the Galaxy. The Bahcall-Soneira model of the Galaxy (Bahcall and Soneira, 1981) predicts a total of 646 main-sequence dwarfs/deg^2 between M_V = +19 and +21 towards the Galactic poles. This requires a FOV 27 arcminutes in diameter to obtain 100 objects. Somewhat larger fields would be needed in the Galactic anticenter region. The number of faint giants in the same magnitude interval is only six. The giants are therefore not the best candidates for MOS, as they are rather sparsely distributed.

In addition to the above programs, several other MOS projects may be mentioned more briefly:

Surveys of Candidate QSOs and Active Galactic Nuclei

The Very Large Array (VLA) radio telescope and the future AXAF x-ray satellite will discover large numbers of previously unidentified radio and x-ray sources. Many of these sources are distant quasistellar objects (QSOs), radio galaxies, and active galactic nuclei (AGNs). Optical spectra and redshifts are needed to type these sources and to cull out interesting objects for further study. MOS is an excellent way to survey these objects efficiently. The VLA can map a 30 arcminute field, and AXAF has a planned field of 20 arcminutes. A few hundred sources

per field are expected, indicating that a FOV of ≈15 arcminutes on the TMT is adequate for an initial survey. Follow-up studies may key on subsets of objects with specific properties, however, at which time the largest possible FOV would be desirable.

The Environment of QSOs

Although evidence is now virtually conclusive that QSOs are an active stage in the life of galactic nuclei, there is as yet little understanding of the QSO mechanism and why it turns on in some galaxies but not in others. Environmental conditions around galaxies may play an important role. Studies of nearby QSOs and their relation to neighboring galaxies are therefore interesting. Moreover, since neighboring galaxy types tend to correlate strongly, the spectra and morphology of neighbor galaxies tell us something in a statistical sense about what kinds of galaxies give rise to QSOs. Morphological types are best measured using the high spatial resolution data of the ST, but spatial proximity can only be established using redshifts from the TMT. The angular FOV required at z = 1 will be a few arcminutes.

Masses of Nearby Dwarf Galaxies

If the Universe contains large amounts of matter in the form of weakly interacting elementary particles, their nature is tightly constrained by whether or not they cluster strongly in dwarf galaxies. This matter ought to be detectable via dynamical mass estimates of these systems, based on radial velocity measurements of individual stars. Such observations are presently strongly flux-limited. The brightest stars in dwarf galaxies are 18-20 mag, and 1km/s accuracy is required ($R = 10^4$). MOS on the TMT is thus ideal (Table 2-6). The nearest dwarf galaxies subtend up to 40 arcminutes, but their inner regions contain more than enough candidate stars. A FOV of 20 arcminutes diameter is adequate.

Stellar Populations in Nearby Galaxies

With MOS, extensive spectroscopy at moderate resolution ($R = 10^3$) of the brighter stars in nearby galaxies could be carried out. The apparent magnitude limit of V = 22.7 in Table 2-6 corresponds to $M_V \leqslant -1$ for several local group dwarf irregulars; $M_V \leqslant -2$ for M31, M32, M33, and NGC 205; and $M_V < -5$ for galaxies in the M81 group. Spectroscopic analysis would provide important information on dynamics, galaxy masses, the chemical composition of young stars and the interstellar medium, the distribution of metal-poor versus metal-rich stars, and the physics of the late stages of stellar evolution as a function of age and chemical composition. The necessary FOV is hard to estimate. Nearby large galaxies like M31 subtend a few degrees, but since the areal density of most types of objects is very high, not much field is needed to fill the MOS capacity. More distant galaxies subtend a smaller solid angle. If we take the apparent visual diameter of M81 as a reasonable goal, a FOV of 25 arcminutes is adequate.

The Chemical Composition of H II Regions in Nearby Galaxies

Composition estimates of H II regions are sensitively dependent on accurate gas temperatures, which in turn depend on the strengths of very weak emission lines, notably λ4363 of [O III]. Present H II surveys are strongly biased to brighter H II regions because of flux limitations. Our picture of the chemical composition of the interstellar medium in nearby galaxies would benefit greatly from a more thorough survey of H II regions to fainter magnitudes. The problem is ideally suited to MOS. This work can be extended to larger distances than the faint-star studies mentioned above. Typical galaxy diameters are thus slightly smaller, of order 10 to 20 arcminutes.

Summary of Requirements for Multiple Object Spectroscopy

MOS can profitably be used at all spectroscopic resolutions. The prime requirements are on field of view and image size, which must be such that all light falls within a 1 arcsecond aperture. (This value is chosen because of the perceived difficulty of maintaining alignment of

apertures to much better than this tolerance over a wide FOV (Boesgaard, 1984).) One arcsecond image quality must be achieved over a bandwidth 0.33μm-1.1μm, without refocus.

Of the 11 listed programs (12 separate field requirements), seven have maximum FOV less than or equal to 20 arcminutes, two are in the range 20-30 arcminutes, one extends to one degree, and two can utilize an essentially unlimited FOV. This suggests that a 20-arcminute FOV for MOS is an absolute minimum. There would clearly also be considerable value in extending this to 30 arcminutes, but gains beyond this value would be smaller. Fields of view approaching one degree are important to only a few programs or a few specific objects of large angular size.

MOS becomes of greatest value with increased exposure times (Table 2-6). For maximum exposures, ADC compensation is needed to keep the image size within 1 arcsecond down to elevation angles of 30° (2 airmasses). The above programs suggest that it would be highly desirable to have a basic wide-field ADC that can correct all wavelengths from 0.33μm to 1.1μm simultaneously. Atmospheric dispersion effects beyond 1.1μm are small enough that no ADC is needed there.

Stellar abundance and QSO absorption-line studies require high throughput down to 0.33μm.

Because various techniques are available to mate incoming and outgoing beams to fibers (Powell, 1983, Hill et al., 1983), there is no requirement on f-ratio at the MOS focus.

2.3.2 Direct Imaging in the Thermal Infrared

Imaging in the thermal infrared includes direct imaging and polarization studies from 2.5μm to 20μm. Image size for point sources is set by the atmosphere shortward of 6μm and by the atmosphere and diffraction longward of 6μm (Figure 2-1). Interferometric techniques in the IR are discussed in Section 2.3.6. The principal gain of the TMT over other telescopes for thermal IR imaging comes from its higher angular resolution and better thermal background rejection for point sources (Table 2-5).

The Structure of Star Forming Regions

Why, where, and how stars form are among the major unsolved problems in astronomy. Star formation is critical to our understanding of star clusters, galaxy evolution, planetary formation, and even the origin of life. Star forming regions are difficult to study because they are embedded in obscuring dust clouds that shroud young stars from view at optical wavelengths. This dust is more transparent to infrared radiation, so that infrared images give us a better view of star-formation processes deep within the cores of these clouds.

Study of these processes has so far been hampered by lack of adequate angular resolution. Typical star densities in a forming cluster are $\approx$100 objects/arcminute^2, requiring an angular resolution of 1 arcsecond or better for confusion-free images. Without a clearer view, we cannot tell how many stars there are in a young cluster, or determine basic characteristics such as temperature and luminosity. The higher angular resolution of the TMT, three times higher than that of the best existing infrared telescopes, will provide essential improvement.

As young stars contract, their surfaces increase in temperature. In the initial, coolest stages, they shine primarily at millimeter wavelengths and are best studied by millimeter radio telescopes. As they heat up, their characteristic wavelength of emission shortens. The longest wavelengths to which the TMT has high sensitivity are 10μm and 20μm, set by the atmospheric transmission windows (Figure 2-2). By the time young stars emit at these wavelengths, they are relatively hot (100-300K) and are nearing the end of the collapse process. Their angular sizes and shapes in this stage may reflect the presence of circumstellar nebular disks, the analogues of the proto-solar nebula that gave rise to our local planetary system (see Section 2.3.6). Stellar collapse models suggest disk sizes of 10-1000 a.u., structures that should be resolvable by the TMT out to distances of 1kpc. Such a disk has recently been discovered around the young T Tauri star HL Tau. It subtends about 1 arcsecond and would be easily resolvable by the TMT.

An important and specific problem in star formation is the process that determines the mass distribution of young stars. This function is a key unknown in the evolutionary history of galaxies. Mysteriously, there are many small stars known in the general solar neighborhood, yet they seem to be lacking in young clusters. Is there a separate star-forming mechanism for small stars that operates outside of clusters? With its gain of 1.8 mag over existing telescopes, the TMT will be able to probe the initial mass function for objects with $T \geqslant 280K$ down to bolometric magnitude $M_{bol} = +11$ in typical starforming regions. This is equivalent to a typical M6V dwarf on the main sequence. The origin of low-mass stars should thus become much better understood.

In the highly confused regions where stars form, it is often difficult to tell what is a star and what is not. Dust clumps can scatter stellar radiation and mimic real stars. The higher angular resolution of the TMT will help to cull out such sources. An even more efficient discriminator is polarization, because scattered starlight is highly polarized. Modeling the relative amounts of thermal and polarized radiation is a powerful clue to the complex geometry of star forming regions. Polarization can also give valuable information on the shapes and sizes of circumstellar disks and, via the grain alignment mechanism, on the intensity and direction of magnetic fields.

Altogether, high-resolution imaging and polarization studies of star-forming regions will be a major task for the TMT. The main requirements are excellent IR performance and excellent image quality over a FOV that ideally could subtend up to several tens of arcminutes in diameter.

Star Formation in Nearby Galaxies

A complementary view to the close-up picture we have of star-forming regions in our own galaxy is provided by our more global view of external galaxies. The presence of hot, young stars and regions of ionized gas shows clearly that many nearby galaxies are active star-formers. Unfortunately, it has been impossible to quantify the amount of star formation accurately up to now because it is probable that many young stars live out their lives hidden entirely within dense dust clouds. Counting these objects, estimating the rate of at which they enrich the interstellar medium with metals and otherwise contribute to galactic evolution is possible only with infrared images at extremely high angular resolution. The first such studies, albeit at very crude resolution, have shown that some spiral galaxies are indeed very luminous at 10μm, radiating as much energy there as at all other wavelengths combined. The TMT's angular resolution of 0.38 arcseconds at 10μm (Table 2-1) corresponds to a linear size of 9pc at 5Mpc, comparable to or smaller than the major star forming complexes in our own galaxy. Fields of view of up to 20 arcminutes would match nicely to the angular diameters of nearby galaxies, but a few arcminutes would also give very useful results.

The Center of the Galaxy

The Galactic center can be seen directly only at infrared and radio wavelengths, owing to approximately 25 magnitudes of dust extinction that obscures the view in visible light. IR and radio studies have revealed a very peculiar region, with chaotically moving clouds of ionized gas, supernovae remnants, and rapid gas motions very close to the center that are believed by some to be the gravitational trace of a central black hole. There is also a compact radio source directly at the center that is weak in strength but otherwise resembles the strong, nonthermal sources that power radio galaxies and QSOs. The Galaxy source is of interest as an analogue to these much more powerful objects. The evidence for a black hole is especially relevant because this is now the most popular model for the energy source of radio galaxies, QSOs, and active galactic nuclei.

Because the Galactic center is fairly near, we get a much more detailed view of it than we do external sources. Even so, the limited angular resolution of existing IR telescopes has not been adequate. With the TMT under good seeing, an angular resolution of 0.38 arcseconds should reveal the high velocity region ($\approx$ 750km/sec) of a central black hole, if one exists,

and should clearly distinguish such a hole from a compact star cluster, the second most likely candidate for the central mass. Proper motions of Galactic center sources should amount to ≈ 0.005 arcseconds/year and should be detectable in just a few years. Imaging in conjunction with spectroscopy (Section 2.3.4) will produce a complete picture of the distribution of sources at the Galactic center and their motions.

A field of view of 2 arcminutes corresponds to 5pc at the center of the Galaxy.

Two other IR imaging programs may be mentioned more briefly:

Bursts of Star Formation in Galactic Nuclei, and the Properties of Extragalactic IRAS Sources

A substantial fraction of galaxies seems to be experiencing prodigious abnormal bursts of star formation in their nuclei (starburst galaxies). This process is obscured by dense dust clouds and can be studied only in the infrared, where the nuclei emit most of their energy. Imaging studies will emphasize high spatial resolution and comparison with maps of thermal and nonthermal radio emission and ionized gas.

Starburst galaxies and other powerful IR sources have recently been discovered with the all-sky IRAS satellite survey. Many of these objects are quite distant and have small apparent angular size. IRAS was a low-resolution discovery instrument. High resolution imaging at 10μm and 20μm with the TMT is now needed to investigate the detailed structure of these sources.

Fields of view of ≈3 arcminutes are adequate for these observations.

Monochromatic IR Images of Emission Line Regions in Our Galaxy

Several important emission lines of ionized gas are visible through the infrared atmospheric transmission windows. These lines are important diagnostics of density, temperature, and abundance in obscured regions (see Section 2.3.3). In addition, the vibration-rotation bands of molecular H_2 at 2.2μm are often seen in emission, indicating shocked gas heated to a temperature of ≈1000°K. Such shocks may provide an important trigger to the star-formation process and provide a mechanism whereby the energy from one newly-formed star precipitates the collapse of nearby stars. Molecular H_2 has also been detected in Seyfert galaxies, planetary nebulae, and Herbig-Haro objects. High-resolution monochromatic imaging with the TMT in ionic and molecular emission lines will provide an important probe of conditions in all of these regions.

Fields of view of a few arcminutes are required.

Summary of Requirements for Thermal IR Imaging

Thermal infrared imaging requires low telescope emissivity (low thermal background), excellent image quality, maximum sensitivity to point sources, and low and predictable instrumental polarization for both transmitted light and telescope thermal emission. The optical quality shown in Figure 2-1 is adequate to match the expected atmospheric and diffraction limits. The above projects suggest that fields of view of up to several tens of arcminutes would be useful, but, in practice, the technological limitations of IR instrumentation will probably allow fields of only a few arcminutes for the foreseeable future. Even at these field sizes, very useful information will be obtained.

Standard IR techniques call for chopping rates up to 30Hz. For studying extended objects such as galaxies, chop angles up to several arcminutes are desirable. In practice, the maximum rate will probably not be attainable for maximum chop angles, but a reasonable goal is to chop at 30Hz up to half-angles of ±30 arcseconds with a duty cycle of 80%. The secondary mirror should also be undersized so that the geometric projection of the secondary lies completely in the primary even at maximum chop. The shape of the secondary should be tailored to minimize light losses.

Many IR observations can be made during the day, especially in the early morning when

the seeing is still good. Flexibility in IR operation is needed to take advantage of the morning hours, and also to respond to changes in seeing and atmospheric H_2O content at night. Quick changeover capability is therefore required between the IR focus and other foci. Changeover will entail removal of all optical baffles and installation of the IR instrument and chopping secondary on a time scale of 20 minutes or less, and similarly for the reverse procedure.

2.3.3. Thermal Infrared Spectroscopy

Thermal infrared spectroscopy is defined as spectroscopy in the atmospheric windows between 2.5μm and 20μm under conditions such that thermal noise dominates. The S/N calculations of Figure 2-3 indicate that thermal noise dominates at 20μm even for R = 10^5. At 3μm, low-to-moderate resolution spectroscopy will be thermal-noise limited, and high-resolution spectroscopy will be photon- or detector-noise limited.

The IR region of the spectrum involves a variety of emission mechanisms and spectral features that yield information on density, temperature, composition, dust, molecules, and the dynamics of optically obscured regions. Useful emission lines include Brackett α and γ at 4.0μm and 2.2μm from ionized hydrogen, and fine structure lines of Ar III (9.0μm), S IV (10.5μm), and Ne II (12.8μm). Molecular features are produced by H_2, CO, H_2O, OH, and other molecules. Thermal dust emission from silicate grains peaks near 10μm, and several as yet unidentified dust features are seen at other wavelengths. Many extragalactic sources also emit strong synchrotron radiation in this region. The energy spectrum of the electrons and the magnetic field intensity can be inferred from the shape and variability of the observed spectral-energy distribution.

Star Forming Regions in Our Galaxy

High-angular-resolution spectroscopy will provide important information that is complementary to the direct imaging of star forming regions described above. Dynamical studies of ionized gas and shock-heated H_2 will probe the gaseous inflows and outflows associated with star formation, already known from existing studies to be surprisingly large--several tens or hundreds of km/s. Particularly interesting young stellar objects are the "cometary," or bi-polar, nebulae--fan-shaped reflection nebulae in which rapid mass-loss is occurring from an embedded protostar near the apex of the fan. These oppositely directed, conical mass-loss flows are thought to be constrained by the presence of a close-in circumstellar torus of material girdling the equatorial regions of the star. Simple estimates indicate sizes of these tori in the range 0.1 arcsecond to 1 arcsecond, which might be resolvable with the TMT. As noted above, such disks may be the precursors of planetary systems. Dynamical measurements of rotation speeds and gas motions in and around these disks would provide important data. A technique that promises even higher angular resolution is speckle spectroscopy (Section 2.3.6).

Star Forming Regions in Other Galaxies

Infrared spectroscopy can provide important windows on star forming regions in other galaxies. The spectra of starburst nuclei have recently been shown to resemble the integrated spectrum of the Orion nebula. This confirms their nature as star forming regions, a conclusion which had previously been in doubt. High-resolution dynamical studies near the nuclei will probe the central mass distributions and discover large mass concentrations, such as black holes. These data could also establish a connection, if any, between starburst nuclei and the active nuclear sources of QSOs, AGNs, and radio galaxies.

Also of interest would be an IR spectroscopic survey of normal H II regions in spirals. The total IR flux versus ionized gas is sensitive to the number of very massive stars present. Correlations between line width and IR flux could also probe the dynamical state of the regions and test a controversial relation between velocity dispersion and H II region size recently inferred from visual data. Spectroscopic surveys of H II regions in different Hubble-type galaxies would examine how the star formation proceeds in different environments.

In addition, several other IR programs can be mentioned more briefly:

Stellar Magnetic Fields

Chromospheric emission lines at 12μm have recently been discovered in the solar spectrum arising from high-level recombinations of MgI and other abundant neutral atoms. The lines are strongly split and broadened in sunspot spectra by the Zeeman effect. Because Zeeman splitting varies with wavelength as λ^2, the lines are 25 times more sensitive than lines conventionally used in the visual portion of the spectrum. Measurements in stars with active chromospheres could thus trace the relationship between stellar rotation, chromospheric activity, and magnetic fields down to much lower field strengths than are now possible. These measurements are currently just beyond the sensitivity limit with present telescopes.

Mass Loss from Evolved Stars

Mass loss in the form of outflowing winds from evolved cool giants is an important phenomenon for stellar evolution and the resupply of gas and dust back to the interstellar medium. The structure of these flows is complex, but models have become highly sophisticated, including hydrodynamic effects, shocks, molecular line opacity, and dust shielding. IR observations at high spectral resolution show a wide variety of molecules in emission and absorption, including CO, SiO, and CN. Comparison with models yields the structure of the outflow region, the mass-loss rate, the composition of the outflow, and the nature of the mechanism during the flow. With present telescopes, only 5-10 stars can be observed with adequate spectral resolution. The TMT would increase this by over tenfold, which is needed to study the phenomenon as a function of stellar mass and composition.

Solar System Objects

These observations would utilize the high angular resolution and large light gathering power of the TMT to study solar system objects. High spectral-resolution studies of IR molecular bands would yield information about gas flows and weather patterns on the outer planets. Low-resolution IR spectroscopy of small bodies in the outer solar system would be a sensitive test of surface composition and the amount of volatile gases that remains frozen on their surfaces. These in turn would tell us about the chemical environment in which these bodies formed and their subsequent thermal histories.

Galactic Center Sources

The most important application here would use the higher angular resolution of the TMT to probe the velocity field of the Ne II (12.8μm) ionized gas as near as possible to the Galactic center. This observation is a sensitive test for a central black hole. Also interesting is a lower-resolution spectral survey of individual IR sources near the center, which could identify stars and yield their ages, masses, and compositions.

Stellar Spectroscopy from 2.5μm to 5μm

Molecular bands of H_2O, CO, CN, C_2, CH, OH, HCl, HF, and SiO are visible in cool stars in this spectral region. At high spectral resolutions, one may measure isotope ratios and abundances of C and O, a sensitive barometer of nuclear processes within stars. The 1.8 mag gain of the TMT over present telescopes is needed to reach stars below the horizontal branch in globular clusters and K giants in the Galactic center. The abundances of cool main sequence dwarfs are also virtually unstudied. These stars are faint and hard to read with present telescopes and require the TMT.

Summary of Requirements for Thermal IR Spectroscopy

Requirements in this area are similar to those of thermal IR imaging above. Starburst nuclei and star forming regions in nearby galaxies subtend $\leqslant$10 arcminutes, individual protos-

tellar objects in our galaxy a few arcseconds, and solar system objects ≤25 arcseconds. On the other hand, the introduction of fiber-fed multiple-object spectroscopy could increase desired field sizes considerably. Star-forming regions in our own galaxy and other galaxies could use fields of up to a degree with this technique. Infrared fibers are not now in common use but are under development. In summary, it seems safe to say that, for future IR spectroscopy, there is strong pressure to maintain the IR FOV as large as possible.

2.3.4 Wide-Field Imaging at Visual and Near Infrared Wavelengths

Direct imaging in this wavelength range includes two-dimensional imaging and slitless spectroscopy from 0.32μm to approximately 2.5μm. Over this range, the background is principally sky noise. Detectors are only now becoming available beyond 1.1μm. The present list of projects emphasizes the region shortward of 1.1μm, about which more is presently known.

As illustrated in Figure 2-3, the S/N ratio on individual point sources with the ST and the TMT is about the same at V, I, and K. However, the ST is strongly preferred for the H band, for crowded fields, and for objects where high angular resolution is important. The TMT has an advantage for wide fields of view and for integrated luminosities and colors of distant galaxies.

The Universe as It Was Ten Billion Years Ago (Part II)

Under multi-object spectroscopy in Section 2.3.1, a research program was outlined involving redshifts and spectral energy distributions of distant galaxies as a window on galactic and cosmological evolution 10 billion years ago. A wide-field imaging program to deep magnitudes would provide essential complementary information. Direct images must precede any redshift program in order to locate candidate galaxies. The distribution of these galaxies on the sky provides a measure of galaxy clustering, which can be compared in angular and redshift coordinates. Cluster radii and densities can be measured from the distribution of members, and galaxy environments quantified as to number, density, and sizes of neighbors. Direct images through narrow bandpasses can provide crude spectrophotometry, allowing us to study the stellar populations of many galaxies in a short time. Direct images also reach roughly 2.5 magnitudes fainter than spectra. The most distant objects we see in the Universe (save for QSOs) are likely to come from these deep surveys.

As noted in Section 2.3.1, there are roughly three galaxies/arcminute^2 at V = 24 mag. A 30 arcminute FOV therefore contains over 2000 objects and subtends 15Mpc at z = 1, adequate to survey a volume comparable in angular size to a cluster or supercluster. As suitable detectors become available, such studies will increasingly utilize wavelengths near 2μm, where S/N is highest (Table 2-4).

Surveys for Quasars and Active Galaxies Using Slitless Spectroscopy

With slitless spectroscopy, one places a prism or a grating in front of the detector, dispersing the light of the source into a small spectrum. The method allows spectroscopic surveys of many sources at one time. The drawback is that the net contrast of the source against the sky background is reduced, with consequent loss in limiting magnitude. The loss compared to broad-band imaging is approximately $\Delta m = -2.5 \log (5/R)$ where R is the spectral resolution ($\lambda/\delta\lambda$). In QSO surveys, an R of 50 is typical, and the magnitude loss is about 2.5 mag. In all other respects, slitless spectroscopy resembles ordinary imaging, and the relative performance of two telescopes can be compared in Figure 2-3 by shifting both instruments by an amount Δm.

Slitless surveys for QSOs and other emission-line objects using the dark sky and good seeing of Mauna Kea will penetrate 1 to 2 magnitudes beyond present instruments. If emission-line galaxies are an adequate tracer of the overall galaxy distribution, they could show the onset of clustering at early epochs. The relative distribution of QSOs and galaxies could likewise clarify the order of galaxy formation and clustering. A final possibility is that the luminosity function of QSOs evolves strongly with redshift, with QSOs intrinsically brighter at early epochs. Surveys to deeper levels are needed to test this result conclusively.

QSOs have no natural scale on the sky, and surveys can benefit in principle from an arbitrarily large FOV.

The Stellar Population of the Galactic Spheroid

On theoretical grounds, the spheroidal population of our galaxy is thought to extend to very large distances of order 100kpc. Virtually no stars have been identified at these distances, however, because they are faint and the stellar density is low. Stars on the periphery of the Galaxy are of extreme interest. Their radial velocities can be used to place a lower limit on the total mass of the Galaxy, and their compositions according to conventional theory are likely to approach the pristine, metal-free state of gas emerging from the Big Bang.

A slitless spectroscopic survey of the halo with R = 100 could locate main sequence dwarfs at +23 V mag out to 60kpc and giants throughout the halo. The density of spheroid dwarfs at 23 mag is about 300 stars/deg^2 on the Bahcall-Soneira model (Bahcall and Soneira 1981), so a FOV of 40 arcminutes is required to discover 100 stars. Giants at 60kpc and beyond have apparent V magnitude +18 and fainter, and a density on the sky of about 30/deg^2, necessitating a much larger FOV. Although stars are point sources, the TMT is clearly preferred over the ST because the stars are uncrowded and the field required is large. An important by-product of these observations will be a measurement of the spheroidal stellar luminosity function to faint magnitudes, a quantity that is essential to nucleosynthesis models of the collapsing protogalaxy.

Faint Radio Galaxies and QSOs

Instruments like the VLA and x-ray telescopes have revealed many sources with no optical counterparts on existing images. These sources are probably far away and are thus a good way of probing the distant universe, but the discoveries are of little value until a distance (i.e., a redshift) for each source is known. The large light-gathering power and wide field of the TMT make it a good instrument to survey these faint sources for optical counterparts and measure their redshifts.

Summary of Requirements for Wide-Field Imaging

Only one of the above projects has any natural field size, and this is set by the fields of other instruments--the VLA and x-ray satellites. A second project--distant galaxies--is such that rather small fields of 10 arcminutes will suffice. For the remaining two, the objects are so widely scattered that there would be a benefit in making the field very large. We conclude that the field for wide-field imaging should be as large as possible consistent with other requirements, with 30 arcminutes in diameter as a lower limit. The image quality over this field should be sufficient to avoid significant degradation of 0.5 arcsecond images produced by the atmosphere.

A further requirement is placed upon camera f-ratio and image scale to match properly to the pixel sizes of existing detectors. This requirement is flexible, but appears to lead to camera f-ratios in the neighborhood of f/2.0 (see discussion, Section 3.1). Atmospheric dispersion compensation is also required to maintain small images up to large airmasses over the whole FOV.

In the immediate future, most imaging will emphasize the wavelength range 0.33μm to 1.1μm. For optimum anti-reflection coatings, it is desirable to cover this range with two separate cameras, each operating over less than one octave in wavelength. Both focal planes should be flat, with extra glass allowed for a dewar window and filter. For calibration purposes, each camera should be capable of taking high-quality images in the V passband. Because the index of refraction of glass varies rapidly at short wavelengths, the blue camera is the more difficult of the two. This camera should be able to take excellent exposures over the whole field in passbands that are equivalent in range of refractive index to the photographic J band. This is a very wide band that extends from 0.39μm to 0.54μm. Practically speaking, this means that the blue camera should be able to image in a single exposure over bands that cover 0.33μm-0.40μm, 0.39μm-0.54μm and 0.44μm-0.60μm. For the red camera, a minimum bandwidth of $\delta\lambda$

= 0.3μm should be achievable anywhere in the range 0.5μm to 1.1μm in a single exposure without refocus. These bandwidths also apply to the ADC.

Both cameras should contain, or be able to accept, dispersing elements capable of yielding slitless spectra with a spectral resolution R = 50-100, based on a final image size of 0.55 arcseconds. A device to compensate for field rotation is also required.

2.3.5 Spectroscopy and Polarimetry of Single Objects in the Visual and Near Infrared

Observations in this category include spectroscopy and spectropolarimetry of single objects at resolutions R = 10^3 to 10^5. The wavelength range is 0.32μm to 2.5μm, beyond which thermal emission begins to dominate the noise.

Most projects emphasize high spectral resolution, which in turn requires many photons. The present list of problems cannot be dealt with using existing telescopes because the photon collection rate is too small.

Absorption Features in QSOs

There exists a dense network of absorption lines to the blue of the Ly α emission in the spectra of high-redshift QSOs. Dubbed the "Ly α forest," this network arises from absorption by neutral H I clouds along the line of sight to the QSO. The nature of the clouds producing these features is hotly debated. Some believe that they represent the extended gaseous halos or disks of very distant galaxies, and others that they are independent intergalactic gas clouds. Some of the broader lines certainly represent outflow from the QSOs themselves. In addition to the Ly α clouds, resonance absorption lines of metal atoms are also seen, including C, Mg, and Ca. These are almost certainly the gaseous disks of intervening galaxies. Considered collectively, QSO absorption features represent a rare opportunity to study non-stellar gaseous matter early in the Universe, at an epoch much earlier than we can see directly by the light of galaxies.

Major questions involve the clumping of matter along the line of sight and the relation that this might have to the clustering of galaxies. The metal content of the Ly α clouds is also of interest--do these clouds consist of primordial, metal-poor gas, or are they metal-enriched? How does the abundance of the observed metal species change with lookback time? Answers to all of these questions depend on higher spectral resolution and larger samples than we now have. Because of the present flux limit, existing observations are strongly biased toward brighter QSOs, with possible systematic errors. Resolutions of $\approx 10^{4.5}$ on objects with V = +19 mag are needed, which require multiple-hour exposures on even the TMT (Table 2-6).

Stellar Seismology, Precision Line Profiles, and Radial Velocities

The observed radial velocity of the Sun shows a rich spectrum of oscillatory modes with periods from 5 to 160 minutes and amplitudes 1m/s or less. The modes should be observable in the spectra of other stars if they oscillate similarly. The modes in the Sun provide information on its interior density and temperature structure that cannot be obtained in any other way. The spectrum of the solar modes is still not fully understood and may point to the existence of fundamental flaws in existing solar models.

Observations of modes in stars similar to the Sun but differing in age, composition, and rotation speed would be of great interest. Unfortunately, the number of stars that can be observed with existing telescopes is limited to a handful because the exposure times must be kept short and the required S/N ratio is extremely high. The 2.0 mag gain of the TMT for high resolution spectroscopy will enlarge the available sample pool by a factor of more than 10.

A related question concerns turbulent motions on the surfaces of stars with convective atmospheres. The temperature structure differs in upward and downward moving elements, yielding distinctive absorption-line spectra, radial velocities, and absorption-line profiles. In cool stars, it should be possible to map convective motions as a function of height using the radial velocities of lines formed at different depths. As above, the TMT will extend studies such as these to an adequate sample of stars.

Line Profiles and Polarization in Seyfert Galaxies and QSOs

Seyfert galaxies and QSOs are objects in which the nucleus of a galaxy generates abnormally high luminosity by means of synchrotron radiation. Seyferts and QSOs form a continuum with overlapping properties, the nuclei of Seyferts being generally fainter and less prominent relative to the surrounding galaxy than in QSOs. The favored model for these sources is presently a central mass, perhaps a black hole, surrounded by a disk or cloud of diffuse gas. Accretion and infall from this gas provide the energy to power the source via the release of gravitational potential energy.

Models for the central source typically invoke disks of order 10^{16}m in radius (0.1pc). For even the nearest Seyfert galaxies (10Mpc), the predicted angular size of such structures is only of order 0.1 milliarcsecond, ten times smaller than the resolution limit of any foreseeable ground-based telescope. Direct viewing of the central source structure will thus likely remain out of reach for some time.

Spectropolarimetry offers a unique tool for deducing source structure in a different way. By comparing the polarization of the nonthermal continuum, broad emission lines, and narrow emission lines, active nuclei can be divided empirically into two classes in which the optical polarization is perpendicular and parallel to the poles of the ejected radio emission, respectively. This division in turn suggests two families of source models involving dense and highly flattened disks for the perpendicular class, and diffuse, puffed-up disks for the parallel class.

Polarization observations of these objects are at present severely flux limited. The polarization is generally rather weak (1-10%), and extremely high quality data are required. Fairly high wavelength resolution ($\leqslant 0.002\mu$m) is also required. Observable candidates now number only a handful but would increase roughly tenfold with the TMT. These new observations could provide unique information on an enigmatic class of objects that has puzzled astronomers for years and that cannot be studied directly in any other way.

Very High Resolution Abundance Studies of Stars

Nissen (1983) has recently emphasized the importance of extremely high spectral resolution ($R = 10^5$) in fundamental abundance determinations of rare elements, and for cool stars with very crowded spectra. High dispersion is needed to isolate weak lines, which are the most reliable abundance indicators. At any given magnitude, the TMT yields a resolution gain of a factor of 6.25, a major advantage for fundamental abundance calibrations.

Related high-resolution studies would examine lithium abundances in a wide variety of old stars. A recent program has measured a constant, low value of Li in a handful of spheroid stars. Lithium is an element synthesized in the Big Bang, and this low value sets a stringent upper limit to the allowed density of baryonic matter in the Universe. Before adoption, this limit must be tested on a wide sample of distant, metal-poor halo stars, for which the large light-gathering capacity of the TMT is essential.

Detector-Limited Spectroscopy from 1.25μm to 2.5μm

Figure 2-3 shows a factor of 6.25 gain in speed between the TMT and 4m telescopes for moderate- and high-resolution spectroscopy between 1.25μm and 2.5μm (J, H, and K bands). This differential actually understates the present advantage of the TMT because it assumes hypothetical detectors with low dark current that presently do not exist. State-of-the-art detectors in this regime now have dark currents of 10^5counts/s, with the result that moderate- and high-resolution spectroscopy are both strongly detector-noise-limited. As long as this situation persists, the speed gain of the TMT over existing 4m telescopes is actually 40, and the limiting magnitude gain is 2.0 mag.

Under these circumstances, there are a number of important spectroscopy projects at 2μm that can only be carried out with the TMT. One involves QSOs at moderate and high redshift. To obtain a complete picture of physical conditions in the emission-line regions of QSOs requires observations of diagnostic emission lines of several elements widely spaced over the

spectrum. For QSOs at appreciable redshift, these lines are shifted into the near IR, where they are now unobservable because the objects are too faint for present equipment. The present picture of QSO emission-line spectra thus relies on a composite of different objects compiled at different redshifts, based on the unproven assumption that low- and high-redshift QSOs are similar. With increased 2μm capability, we could obtain complete data on individual QSOs from the far UV (using the Space Telescope) to the near IR (with TMT). Such observations would also include polarization measurements.

In another area, it has been suggested (Strittmatter, 1980) that it might be possible to classify cool stars based on moderate-resolution spectra between 1.5μm and 2.5μm. If such a scheme could be perfected, we would have a powerful tool for studying the stellar content of obscured regions, including the galactic-center and star-forming regions containing young stellar objects.

There are also several important spectroscopy problems on galaxies in the 2μm region. The 2μm light of galaxies is dominated by highly evolved M giant and supergiant stars. Many uncertainties remain in their evolutionary histories: their luminosity functions, distribution with effective temperature, maximum luminosities, and the dependence of these quantities on population age and composition. A start on these questions has been made with present telescopes, but the number of observable galaxies is only a handful. A larger sample would allow us to compare and contrast different objects, which is essential in studying stellar populations.

Distant elliptical galaxies emit most of their light in the 2μm region, owing to their large redshifts. As with QSOs, spectral-energy distributions are needed over the whole spectral region from 0.5μm to 2μm. These can then be compared with spectra from 0.25μm to 1μm for local galaxies, giving a complete picture of how the stellar populations have evolved over the last several billion years. Such studies could provide key input on the time of formation of elliptical galaxies and their change in luminosity with time, which are important data for cosmology and the Hubble diagram. These studies are currently severely flux-limited.

Summary of Requirements for High-Resolution Spectroscopy

For high-resolution observations of single objects, the TMT is required only to form high-quality images over a small FOV. In contrast to virtually all other high-priority projects discussed in this report, high-resolution observations are not inherently seeing-limited. They are therefore logical candidates when the seeing is less than excellent. High-resolution spectrographs must thus be able to operate efficiently under typical or worse-than-typical seeing conditions. Based on the seeing data in Figure 3-3, TMT high-resolution spectrographs should be able to operate with slit widths of up to 1.5 arcseconds and still achieve high resolution and throughput. An image slicer may be needed to ensure this performance. A strawman high-resolution spectrograph design is outlined in Section 6.4.

The telescope must be equipped with stable rigid platforms on which large spectrographs can be located. These platforms must be such that they can be fully enclosed if necessary to keep out stray light and provide a thermally controlled environment. To adjust to changes in seeing, it must be possible to switch quickly back and forth between high-resolution spectrographs and other instruments. A scheme is also needed for rapid interchange of instrumentation on the Nasmyth platforms.

For moderate-resolution polarization measurements, the polarization introduced by the telescope must be $\leq$0.3% and stable in amplitude and position angle to a level of 0.1% within a single observing session.

2.3.6 Interferometry and High-Resolution Spatial Imaging

Several specialized techniques allow diffraction-limited resolution via removal of atmospheric seeing. A fundamental distinction is whether signals are combined from separate telescopes in an array, or a single filled aperture is used. Arrays offer high angular resolution, but image reconstruction can be difficult owing to incomplete Fourier (u,v) coverage, and combin-

ing the beams is technically difficult. Filled apertures like the TMT offer a more modest baseline but complete coverage in the Fourier (u,v) plane.

For the TMT, the main interferometric techniques that we foresee are speckle interferometry, based on the morphology of high-frequency speckles within the atmospheric seeing disk, and Michelson interferometry, in which beams from opposing hexagonal segments would be constructively interfered. Speckle interferometry is the more commonly employed and will be focused on here. The diffraction-limited resolution of a circular filled aperture is roughly one-half the Airy disk, or 1.0 λ/D. For the TMT, this amounts to 0.012 arcseconds at 0.55μm and 0.09 arcseconds at 4μm, a factor of 2-3 higher than existing telescopes. These gains come at a level where significant scientific rewards are expected, as shown below.

Speckle at Visual Wavelengths

The most successful application of speckle interferometry at visual wavelengths has been the measurement of radial separations in over 600 close binary stars. The results give fundamental data on orbits, stellar masses, and the mass-to-light relation. The present sample is heavily biased to large separations, however, and hence to giant stars. Typical main-sequence pairs have separations of only $\approx$0.1 a.u. (Allen, 1973), and virtually all are located beyond 10pc, just out of reach of present telescopes. The TMT would bring many within view. Higher angular resolution would also allow study of several important eclipsing systems that are now also just beyond reach.

Infrared Speckle

For two reasons, the near infrared from 1μm to 4μm is even more attractive for speckle interferometry than visible light. For faint sources, the S/N ratio at high angular frequencies (above $D/2\lambda$) scales as n_s^{-2}, where n_s is the number of speckles per image. This in turn is inversely proportional to $(\theta/\lambda)^2$, θ the atmospheric FWHM. The speckle lifetime also scales as $\lambda^{6/5}$, allowing longer integration times and more photons per speckle. Combining these factors, one finds that the S/N ratio in a single speckle exposure scales as $\lambda^{4.6}$, which strongly favors longer wavelengths. The maximum usable wavelength is 4μm, since direct imaging becomes more appropriate at longer wavelengths, where the telescope is diffraction limited.

Various types of speckle observations would benefit from the increased angular resolution of the TMT. Several apparently single protostars have been shown to consist of multiple components, a discovery that has had a significant impact on models of their structure and evolution. The existence of a low-mass companion near T Tauri has called isolated collapse models for star formation into question. Circumstellar shells of outflowing dust and gas from hot OB stars, cool Mira variables, and carbon stars have also been studied. By imaging in the continuum and in strong absorption features such as CO, it is possible to compare the diameter of a star at different wavelengths and explore the absorption-line structure of its atmosphere and the velocity structure of any outflowing wind (see Speckle Spectroscopy below).

A third application involves the speckle IR detection of cool, low-mass companions near normal stars, many of which have been confirmed by astrometric methods. Owing to the very long cooling time of "brown dwarfs" (stars too small to burn hydrogen), this technique is an excellent way to explore the lower end of the initial mass function and search for objects at the upper range of planetary masses. The discovery of an object small enough to be termed a true planet has just been announced with this technique.

All these problems are currently limited by the angular resolution of present telescopes. The number of candidates for observation would increase approximately ten-fold with the TMT.

A future use of IR speckle involves the imaging of material distributed anisotropically around protostellar objects. Many such objects are shedding mass in the form of a rapidly flowing, bipolar stellar wind. Evidence is accumulating that the bipolar nature of these winds is caused by a dense torus or disk of gas that girdles the equatorial regions of the protostar. Such

disks are seen far out in radio CO emission, but higher angular resolution is needed to trace them closer to the star. Disks are interesting as possible precursors to proto-solar nebulae. Theoretical models of such disks indicate temperatures of a few hundred degrees and sizes from a few to 1000 a.u., yielding typical IR diameters of 0.1 to 1 arcsecond for sources out to 1kpc. Similar size estimates for many IR sources are obtained under the simple assumption that the observed flux is black-body radiation. Both arguments suggest that there are many IR sources in the size range that might be resolved by the TMT.

Speckle Spectroscopy

An additional technique is speckle spectroscopy, involving the comparison of speckle images at two or more wavelengths. One application utilizes a self-calibrating procedure in which a source at one wavelength can be assumed to be point-like, thus giving the instantaneous modulation transfer function for the atmosphere plus telescope. An example is Beckers' (Beckers, Hege, and Murphy, 1983) observations of the extended Hα envelope around Betelguese, which used the continuum image of Betelgeuse as an unresolved calibration source. Future speckle spectroscopy may utilize various overtones of near-IR CO bands to probe the velocity structure of outflowing stellar winds as a function of radius, leading to a more accurate estimate of the mass-loss rate. Another possibility would be to observe in opposite sides of a stellar absorption line broadened by rotation. Small shifts in the center of gravity of the image would be detectable down to 0.002 arcseconds (Roddier, 1983). Studies could be made on A-type stars brighter than M_V = +1.0, K-type stars brighter than +4.0 mag, and M-type stars brighter than 7.5 mag. The principal datum would be the position angle of the stellar rotation axis on the sky, of interest for angular momentum studies of clusters and binary stars.

Summary of Telescope Requirements for Interferometric Imaging

Since S/N varies as θ^{-4} (see above), the primary requirement for speckle interferometry is excellent seeing. In order to avoid smearing the speckles, high-frequency telescope jitter must be kept below $\approx 1/6$ of a speckle diameter during a single exposure. This means that jitter due to tracking errors or wind shake must be $\leq$0.002 arcseconds over times $\leq$0.1s (for 0.55μm) and $\leq$0.01 arcseconds over times $\leq$1s (for 3μm). For infrared speckles scanned with a slit and chopping secondary mirror, the scanning motion of the secondary must be smooth on angular scales of order 0.01 arcseconds.

There is still some debate about the requirements placed by speckle interferometry on telescope aberrations. These may depend on the type of image-reconstruction method used. The standard speckle technique measures only the modulus of the Fourier transform. Full reconstruction is not attempted, but rather comparison with source models. The method is appropriate for simple cases such as binary stars and stellar diameter measurements, where source geometry is well known in advance. The standard modulus technique requires only that telescope phase errors be significantly smaller than the smallest aberrations introduced by the atmosphere (Dainty, 1975). This is satisfied automatically by the phasing tolerances adopted for the primary mirror (Section 3.3).

There are other speckle techniques that attempt to extract phase information as well as the modulus, with the aim of reconstructing the full image. Two types of phase schemes have been proposed: measuring the phase directly by suitable processing of the speckle exposures, and deriving the phase indirectly from the power-spectrum (modulus) and known constraints on the image (it must be real and non-negative). The Knox-Thompson (1974) algorithm is of the first type, the algorithms of Fienup (1982) belong to the second.

The Knox-Thompson algorithm is apparently sensitive to telescope aberrations. Some have claimed that it gives the image reconstructed including all telescope aberrations (Mertz, quoted by Howell, 1983). Others (Barakat and Nisenson, 1981) have concluded that it is sensitive only to odd-order optical aberration, such as coma. The situation with the Fienup algorithm is even less clear. Being a modulus method, it is nominally insensitive to telescope aberrations smaller than the seeing limit. However, in practice it relies on small features in the modulus spectrum to deduce the phase. Concern has been expressed (Howell, 1983) that at this

low level the method may in fact be sensitive to small changes in the aberrations.

In view of the present confusion, it seems appropriate to require at this time that path length errors introduced by the telescope be much smaller than those of the atmosphere in moving between object and point-source calibrator, that is, over a few degrees in angle and over a few tens of minutes of time. This will ensure that requirements for standard speckle interferometry are satisfied. The requirements for full image reconstruction methods are still under study.

3. Telescope Performance Specifications

Contents **Page**

3.1 Science Related Goals

We summarize here the performance goals derived from the scientific projects in Section 2. These form the basis for the specifications of the TMT.

Multiple Object Spectroscopy

a. Excluding the effects of the atmosphere, all light is to fall within a 1 arcsecond diaphragm for images over a field of view (FOV) that must be a minimum of 10 arcminutes in diameter and preferably 30 arcminutes in diameter. A larger FOV would be desirable, but not at the expense of strong compromises on other aspects of telescope performance.

b. No requirement is placed on the f-ratio at this focus.

c. Atmospheric dispersion compensation (ADC) must operate over the entire field. It must maintain all light within 1 arcsecond up to 2 air masses. The minimum bandwidth is 0.33μm to 1.1μm without refocus.

d. The focus must have high optical and fiber transmission from 0.33μm to 2.5μm.

e. A large, stable platform must be located adjacent to the MOS focal plane to mount MOS spectrographs.

f. Compensation for field rotation must be provided.

Thermal Infrared Imaging and Spectroscopy (2.5μm to 20μm)

a. The telescope thermal emissivity must be as low and as stable as possible.

b. Image quality must be diffraction-limited at 10μm for chopping secondary throws of at least $\pm$20 seconds, over a minimum FOV of several arcminutes.

c. The polarization of both transmitted and emitted IR radiation must be low and stable. Residual polarized emission from the telescope as seen by the detector must be less than 1% over a single observing session. Instrumental polarization of transmitted IR light must be less than 0.3% and stable to 0.1%.

d. The chopping secondary must be able to chop at frequencies up to 30Hz and over focal plane chop half-angles of 2.5 arcminutes. At 30Hz we require the ability to chop with at least 80% duty cycle over a chop angle of $\pm$30 arcseconds. The secondary must be undersized such that the geometric projection of the secondary lies completely on the primary for chop half-angles up to 2.5 arcminutes. The shape of the secondary shall be such as to minimize light lost by the undersize dimensions. A two axis chopper is needed.

e. Changeover from the thermal IR to other instruments (and vice versa) must be possible in 20 minutes or less. This includes the removal and installation of optical baffles.

f. Compensation for field rotation is required.

g. An unchopped field of view of at least 10 arcminutes with image quality better than 1 arcsecond is needed.

Wide-Field Visual Imaging

a. The telescope should degrade the best atmospheric seeing (FWHM = 0.50 arcseconds) by no more than 10% over the full FOV.

b. The minimum FOV is 30 arcminutes.

c. The focal ratio should be approximately 2.0 (see Section 3.2.2).

d. The minimum bandwidths are as follows:

   1. Blue camera: The minimum bandwidth ($\Delta\lambda$) should be equivalent to the chromatic width of the photographic J band in a single exposure without refocus over the entire operating image. This implies bandwidths of 0.33μm-0.40μm, 0.39μm-0.54μm, and 0.44μm-0.60μm.

   2. Red camera: A minimum bandwidth of $\Delta\lambda$ = 0.30μm should be achievable anywhere in the range 0.50μm to 1.1μm in a single exposure without refocus.

   3. Both cameras should be able to take high-quality V-band exposures (0.50μm-0.60μm).

e. Both sets of camera optics (except common elements) should be coated with high efficiency anti-reflection coatings, to operate over the following wavelength ranges:

   Blue camera: 0.33μm to 0.66μm
   Red camera: 0.45μm to 1.1μm

   Any optical elements in common should be coated with broadband anti-reflection coatings (0.33μm - 1.1μm) with as high an efficiency as possible.

f. The UV transmission of the blue camera at 0.33μm should be as high as possible.

g. The focal planes of both cameras should be flat.

h. Both cameras should be able to accept plane-parallel elements in the form of detector windows and filters up to a total thickness of 12mm.

i. Both cameras should be able to accept dispersive elements which yield slitless spectra with R = 50-100, based on an image FWHM of 0.55 arcseconds.

j. Each camera must incorporate an atmospheric dispersion corrector that operates over the full FOV and bandwidths specified above and maintains image quality up to 2.0 airmasses.

k. Compensation for field rotation should be provided.

Visual Spectroscopy of Single Objects

a. Excellent image quality must be provided over a 3 arcminute FOV. The telescope should degrade the FWHM of the best atmospheric seeing by no more than 10%.

b. Large, stable platforms must be provided to accommodate high-resolution spectrographs. These must be thermally stable and offer optional light-tight enclosures.

c. At least one focus must be provided for a moderate resolution ($R = 10^3 - 10^4$) spectropolarimeter. The instrumental polarization at this focus must be less than 0.3% and stable to 0.1% over a single observing session.

Speckle Interferometry

a. For modulus algorithms, variations in pathlength errors should be significantly smaller than those introduced by the atmosphere. A specification for full image-reconstruction algorithms is still under study.

3.2 General Optical Configuration

3.2.1 Basic Design Choice: Single Mirror or MMT

The overall telescope configuration is set by the strategy to fabricate the primary mirror. Two choices are possible: a multiple-mirror primary, as in the Arizona-Smithsonian MMT, or a single, contiguous primary, as in conventional telescopes. Both approaches have strengths and weaknesses, but, in our opinion, the single-primary approach is distinctly preferable for a 10 meter telescope. The important advantages of this design are as follows:

(1) To obtain diffraction-limited performance in the infrared and for interferometry, phasing of the sub-elements of the primary is essential. Phasing is conceptually more straightforward with the edge-to-edge contact provided by a segmented single-mirror design. Phasing of an MMT would require monitoring pathlengths through air, with unknown difficulties caused by air turbulence and temperature fluctuations.

(2) Essential sub-systems can be studied and optimized using small prototypes for a segmented, single-mirror telescope. The sub-elements of an MMT-style 10-meter telescope have apertures of order 5m, too large and costly to prototype.

(3) At all f-ratios in the single-mirror approach, light is brought conveniently to a single focus with a minimum of reflection losses and without complicated beam combiners. Only one instrument and detector are required. Although the sizes of single spectrographs are in some cases larger than they are for separate elements of an MMT-type primary, estimates suggest they are manageable (Section 6). For a university setting, single instruments offer the important advantage of lower maintenance and alignment costs. A change of observing programs from one focus to another is also generally less complicated with single instruments at each focus.

(4) Combining beams is essential for diffraction-limited infrared performance. This requires a cryogenically cooled evacuated beam combiner with an MMT but not with a single-

mirror primary (Gehrz 1984). Several technical risks are associated with such a combiner, including the availability of suitable window materials. In addition to risk, a cryogenic beam combiner adds to cost and complexity.

(5) The diffraction patterns of a single primary and an MMT differ. The MMT pattern is narrower in its central lobe, but has more light in objectionable side lobes (Mast and Nelson 1984, TMT Technical Note No. 96). To achieve the same S/N ratio on point sources, the MMT is a factor of 2 slower in the diffraction-limited case, as obtained by a 10-meter telescope under good seeing conditions at 10μm and 20μm. The higher maximum baseline of an MMT does give higher limiting angular resolution. However, in view of the scientific objectives of UC infrared astronomers, the higher efficiency, freedom from side lobes, and lack of complicated beam combiner for a single primary mirror are deemed to give superior overall infrared performance.

(6) The primary mirror is more compact with a single primary and has a smaller outer diameter. For the same dome size, this allows a narrower slit. This is important on Mauna Kea, where protection from wind and wind-blown debris is a design requirement. The primary mirror also sits deeper in the dome, and wind-induced distortion of the mirror figure is reduced (Section 7.8).

(7) The only other major feature offered by an MMT-type telescope that cannot be achieved as well with a contiguous primary is large, well-corrected fields of view of order 1° in diameter (Epps, Angel, and Anderson, 1984). Such a focus would be appropriate to direct imaging and multiple object spectroscopy. In the opinion of the Astronomy Advisory Committee, a field as large as 1° has some scientific value, but the advantage is not overwhelming. The analysis in Section 2.3 indicates that most scientific projects to be carried out with the TMT do not require a field this large. The MMT-style wide field also carries with it three distinct disadvantages:

a. Two major scientific programs, wide-field imaging and MOS, must be carried out at the same focus, which complicates instrument changeovers. The problem is exacerbated by the fact that multiple instruments are required, one for each sub-primary mirror. With the TMT design, three separate focal stations are available for these observations, and easier changeover is possible.

b. The MMT wide-field focus requires a large, three-element corrector lens at each sub-primary. For high performance and to eliminate ghost images, all elements must be coated. However, high efficiency coatings are not now available to cover the entire bandpass from 0.33μm to 1.1μm that is needed for spectroscopy. An additional corrector would also have to be built to cover the wavelength range 1.2-2.5μm, assuming optically transmissive materials can be found. The single-mirror design, in contrast, has three all-reflective foci for spectroscopy, yielding adequate fields of view of 20 arcminutes and requiring no corrector optics (Section 4.3).

c. An MMT-style wide field yields a final f-ratio of about f/5.0 (Epps et al., 1984) and, for four sub-elements in the primary, a final focal plane scale of roughly 8 arcseconds/mm. This provides a good match between detector pixels and the best-seeing images (see below) but requires four times the total detector area to service all four focal planes. Historically, the most advanced astronomical detectors have always been scarce and expensive, and today's silicon arrays are no exception. Given the limited operating budget of a university observatory, this extra factor of four in detector area for direct imaging is a considerable drawback.

In closing, it should be emphasized that many arguments that favor either a single primary or an MMT are specific to the size of the telescope and to the relative weight placed on scientific capability versus cost and complexity. The diffraction argument given above becomes less significant for a 15-meter telescope, for example. Certain aspects of the TMT design also become more difficult at 15 meters, including the prime-focus camera and the segmented primary mirror. Different weight on these considerations could favor a different design choice for a bigger telescope at a national rather than a university observatory.

To summarize, the overwhelming arguments for a single primary mirror are high scientific return coupled with substantially reduced complexity in telescope and instrument design, maintenance, and operation. The weight of all factors together strongly favors a single primary as the logical choice for a 10-meter telescope at a university operated observatory.

The choice of f/1.75 for the f-ratio of the primary mirror is discussed in Section 4.

3.2.2 Wide-Field Imaging: Prime Focus Camera

A single primary mirror telescope offers several natural focal locations, each one well suited to one or more observations described in Section 2.3. The first category is optical direct imaging, which requires a minimum FOV of 30 arcminutes, excellent images, and a suitable image scale. The scale determines how many arcseconds will be imaged per millimeter on the detector. This is important for an efficient match between the angular detail in the image and the resolution set by the pixel size. Adequate sampling is necessary to preserve angular detail and photometric accuracy, but oversampling wastes detector area, which is a scarce and expensive resource. Estimates suggest (Faber 1981, TMT Report No. 61) that a reasonable sampling criterion for Gaussian images is 1.1 pixel per root-mean-square one-dimensional image width. For the best images under excellent seeing (FWHM = 0.55 arcseconds, Section 4.1), this translates to 0.23 arcseconds per pixel. Pixel sizes of typical optical detectors are in the range 15μm to 30μm, implying fast focal ratios for the TMT between 1.3 and 2.6.

Several schemes have been investigated to achieve this f-ratio using focal reducers at the Nasmyth or Cassegrain foci. All of these schemes require bulky and expensive re-imaging optics, which appear difficult to install and remove quickly. The approach finally adopted utilizes a camera at prime focus, containing three silica elements plus an atmospheric dispersion compensator (ADC). The final focal ratio of this camera is f/2.0, comfortably in the desired range. Red and blue cameras containing separate second and third elements cover the entire wavelength range 0.33μm to 1.1μm. The two cameras match well to current optical coating technology, which can achieve high-efficiency optical coatings over one octave in wavelength. Coatings are essential to suppress internal reflections that otherwise result in troublesome ghost images which limit dynamic range.

Both cameras have a 30 arcminute FOV that subtends a compact 180mm. Exposure times for conventional photographic plates will be somewhat shorter than on present telescopes but are still manageable, and available plates easily cover the field. Individual silicon arrays are still not large enough but are increasing in size. A recently announced array by Tektronix measures 60mm by 60mm, and just a few would be adequate to achieve substantial field coverage. The physical size of the TMT prime focus field is comparable to or smaller than prime focus field sizes on existing telescopes.

A major innovation on the TMT at all optical foci is the use of atmospheric-dispersion compensating prisms (ADC) that virtually eliminate atmospheric dispersion. These are essential to maintain the excellent image quality allowed by the atmosphere and optics. The prime focus camera has separate ADCs for the red and blue side. The blue ADC provides compensation to 2.0 airmasses, the red ADC to 3.8 airmasses. (Spot diagrams and further discussion are given in Section 4.2).

3.2.3 Visual Spectroscopy: Nasmyth, Cassegrain, and Bent Cassegrain Foci

Another major class of observations includes moderate- and high-resolution spectroscopy at visible and near infrared wavelengths, including multiple object spectroscopy (MOS). The prime focus is not a suitable location for these observations because the spectrographs are generally too heavy and bulky. Even though the prime focus has a wide field, it is also not optimum for MOS because the wavelength coverage at any one focus setting cannot meet the full requirement of 0.33μm to 1.1μm spectroscopy.

A parfocal system of Nasmyth, Cassegrain, and bent Cassegrain foci is a flexible design that meets the optical and mechanical requirements of spectroscopy, including MOS. There are altogether seven focal positions, six accessible by rotating a tertiary flat in the middle of the

tube, the seventh a conventional Cassegrain behind the primary mirror. The Nasmyth platforms are suitable for the heaviest spectrographs, including an MOS fiber array or mosaic spectrograph (Section 6). The four bent Cassegrain foci are adapted to small instruments such as photometers and low-resolution spectrographs. The straight-through Cassegrain is free of any transverse reflection and is included for polarimetric observations. The tertiary mirror can be removed and the Cassegrain (or infrared) instrument installed on a timescale of 20 minutes (Section 7.10).

Because this system of foci will likely be the most heavily used, and because of the decision to pursue MOS at the Nasmyth foci, the telescope has been designed as a Ritchey-Chretien (R-C) to maximize the Nasmyth-Cassegrain (N-C) field of view. The choice of f-ratio at this focus involves a number of tradeoffs as follows:

a. A faster R-C f-ratio necessitates a more hyperbolic primary mirror. This makes design of the prime-focus camera slightly easier but reduces the FOV at the forward-Cassegrain infrared focus (see below).

b. A faster f-ratio requires a larger, heavier, and more expensive secondary mirror.

c. A faster f-ratio eases the design of the N-C atmospheric-dispersion compensator and yields better images over a larger field of view. The size of the ADC prisms is slightly reduced.

d. A faster f-ratio reduces the focal length of all spectrograph collimators, easing design of Nasmyth instrumentation.

e. A faster f-ratio reduces field curvature at the N-C foci. This curvature is an annoyance for MOS and should ideally be minimized.

As of this writing, an N-C f-ratio of f/15.0 (focal length = 150.0m) has been tentatively adopted, with discussions continuing as to whether this should be decreased to f/12.0. All drawings and calculations in this report refer to f/15.0. An adopted back focal distance of 3.0m for the N-C foci implies a conic constant of -1.0037963 for the primary mirror. A quantitative comparison between the f/12.0 and f/15.0 systems is given in Section 4, where a more detailed description of the optical design may be found.

An f-ratio of f/15.0 yields an ADC-corrected field with geometric image size under 1 arcsecond out to 20 arcminutes diameter and up to 2 airmasses. Limiting image quality is set by the ADC at large airmasses; intrinsic image sizes without the ADC remain under 1 arcsecond out to 26 arcminutes (with vignetting). The ADC is located ahead of the tertiary flat and serves all foci in the Nasmyth-Cassegrain family. It consists of two quartz prisms with a total of two air-glass surfaces. High transmission over the entire range 0.33μm-1.1 μm is ensured with the use of moderate-efficiency broadband coatings. Since no other refractive optics are needed, the N-C foci can be used bare in the region 1.25μm-2.5μm, where the ADC is not needed.

3.2.4 Thermal Infrared: Forward Cassegrain Focus

A third category of observations includes the thermal infrared, where thermal background subtraction is of paramount importance. At limiting integrations for broad-band thermal infrared photometry, signal counts are only 10^{-6} to 10^{-7} as large as the background, necessitating highly accurate background subtraction. This can be achieved only with a chopping secondary mirror, with chopping rates up to 30Hz and throws as large as several tens of arcseconds. This requirement strongly favors small secondaries. At the same time, off-axis image quality is improved with an f-ratio at the forward-Cassegrain that differs as little as possible from the N-C f-ratio. To satisfy both requirements, the IR focal position has been located forward of the primary mirror near the elevation axis. The adopted f-ratio is f/25.0, and the required secondary diameter is only 0.528m. Although this location of the IR focus creates a rather crowded space near the tertiary flat and ADC, and has restricted human access, the other mechanical and scientific benefits outweigh this inconvenience.

The optical performance at this focus is complex, as intrinsic off-axis coma interacts with coma due to chop (Section 4.4). Roughly speaking, diffraction-limited performance is achieved

over a 9 arcminute diameter FOV with no chop, over a 6 arcminute FOV with a ± 10 arcsecond chop, and over a 4 arcminute FOV with a ± 20 arcsecond chop. The performance with an f/12 R-C option is discussed in Section 4.6. Changeover between the IR focus and the tertiary flat on a timescale of 20 minutes is set as an important design goal.

3.2.5 Coudé Focus

All the foci described above are attached to the telescope. Even though the Nasmyth platforms can accommodate large instruments, an earth-stationary coudé focus that can accommodate large or extremely delicate instruments is felt to be desirable. At the moment, no specific scientific program requires the coudé focus, but the design of the telescope allows for its ultimate implementation. A relatively slow beam ($\approx$f/100) delivered to a large, thermally stable, and easily accessible area is needed. The telescope must accommodate the optical train, and the building must provide space for a coudé room.

3.2.6 Comparison with Science Goals

A detailed description of optical performance including spot diagrams and error budgets is presented in Section 4. However, a qualitative comparison is possible now between the expected performance of the present optical design and the science goals set forth in Section 3.1. The present discussion is limited to the optical design itself; separate performance goals for the segmented primary mirror are discussed in the following section.

Most of the minimum science goals are met or nearly met by the present design. The specification on wide-field imaging quality (degradation of excellent seeing by no more than 10%) is met by the prime-focus camera over the inner 15 arcminute FOV and very nearly out to 30 arcminutes, including an atmospheric dispersion compensator. A flexible set of N-C foci is provided for spectroscopy and polarimetry, with ADC provided over an exceptionally wide bandwidth. The 20 arcminute FOV at these foci does not equal the largest needed by all science projects but is satisfactory for the majority. Restrictions on field of view are compensated for by the wide bandwidth and by the fact that the foci can be used here with no additional corrector optics in the region 1.25μm to 2.5μm.

In the thermal infrared, the diffraction-limited FOV for all chop half-angles $\leqslant$20 arcseconds is several arcminutes and is comfortably larger than today's infrared arrays, which cover at most a few tens of arcseconds. For future IR fiber-fed spectroscopy, the available FOV depends on the chop angles and the minimum size of fiber that can be used. For small chop angles of a few arcseconds, the design provides diffraction-limited images over a 9 arcminute field, which is large by today's standards.

Overall, the design appears to be a reasonable balance between simplicity, as regards to arrangement and access to foci, versus image quality and field of view.

Additional focal ratios may be added in the future. For example, it may become desirable eventually to increase the FOV for MOS. At the expense of introducing a multi-element corrector (see above), it would be possible to place a wide-field focus inside the tube to the rear of the elevation axis. Although the maximum secondary size is only 1.43m in the initial design, provision is being made in the telescope and dome to carry secondaries up to 2.0m in diameter. This would allow final f-ratios in the neighborhood of f/6 or f/7 and field sizes with good images over 30 arcminutes or more. Despite the attractions of such a focus, it has not been included in the initial focal complement because its primary application is to multiple object spectroscopy. MOS is sufficiently unfamiliar and challenging that it appears preferable to pursue it initially at the Nasmyth foci, where access and instrument support are more straightforward. Use of a multi-element corrector for spectroscopy from 0.33μm to 1.1μm also depends on improvements in high efficiency coatings that are not yet available.

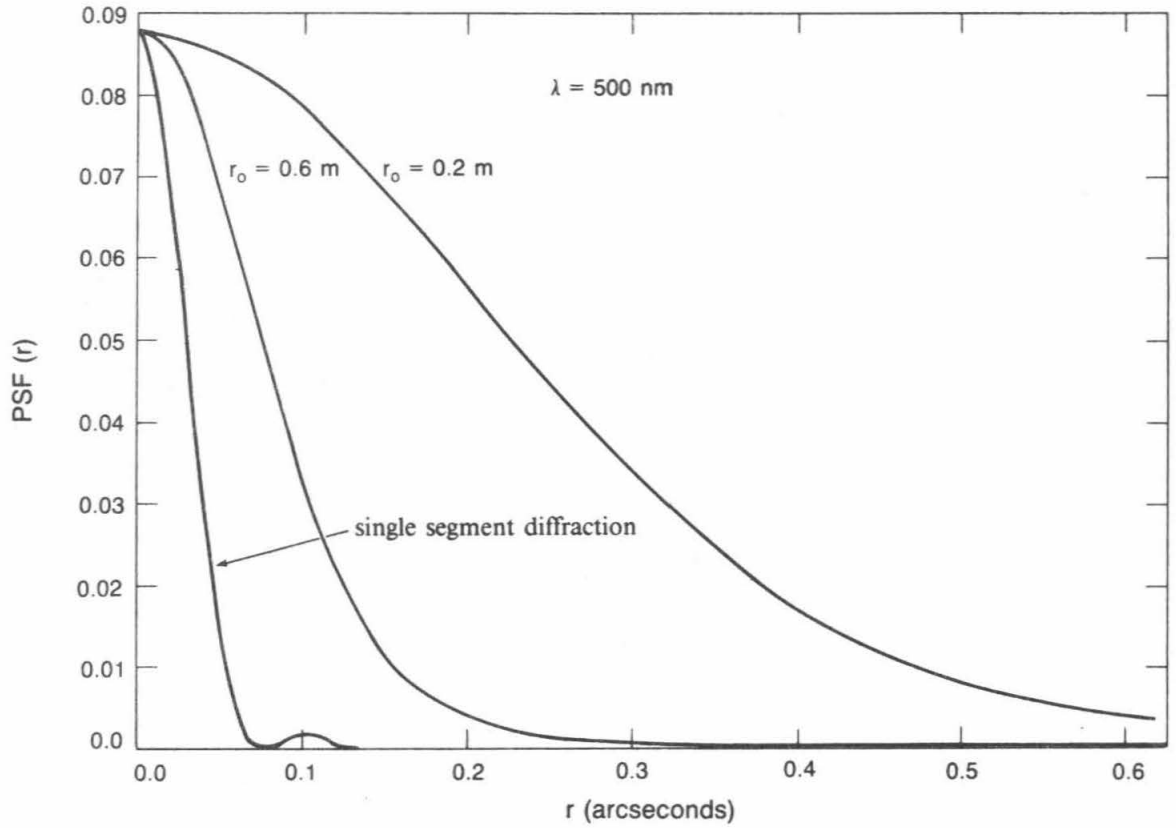

Figure 3-1 The point spread function expected from atmospheric seeing is shown as a function of image radius for λ=500nm. The upper curve is based on an atmosphere coherence diameter of r_o = 0.2m and the second curve is based on r_o = 0.6m. Approximately 10% of the time the Mauna Kea site is expected to have $r_o \geqslant$ 0.2m. The third curve shows the diffraction limited PSF of a single segment.

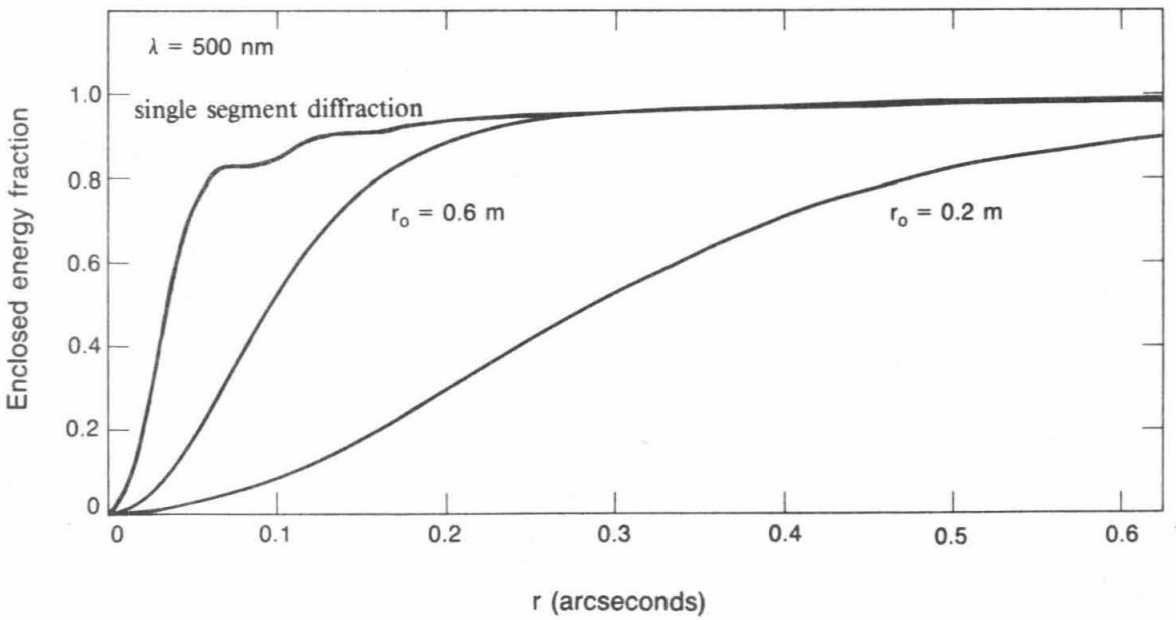

Figure 3-2 The enclosed fractional energy based on the standard model of atmospheric seeing is shown as a function of image radius. This is simply the integral of the point spread function shown in the previous figure. Curves for r_o = 0.2m, 0.6m, and the single segment diffraction limit are given.

3.3 Optical Specifications

3.3.1 Visual and Infrared Image Quality

3.3.1.1 Atmospheric Seeing

The specifications for the system optical quality are based on atmospheric seeing and on diffraction. Typically, seeing measurements are characterized by a single parameter, the Full Width at Half Maximum (FWHM) of the image. To make a more complete characterization of the image degradation of the atmosphere requires use of the theoretical models of atmospheric seeing that have become available in recent years (Fried, 1966, Hufnagel, 1978). These models are based on turbulence theory and agree rather well with observed properties of the atmosphere. Seeing limitations of the atmosphere, both theoretical and experimental, are reviewed by Woolf (1982). Seeing theory predicts that the long exposure atmospheric modulation transfer function is given by

$$\mathrm{MTF(f)}=\exp(-(\mathrm{f}/\mathrm{f}_0)^{\frac{5}{3}}) \tag{3-1}$$

where f has units of image cycles per sky radian, $f_0 = r_0/2.10\lambda$, λ is the wavelength and r_0 is the *coherence diameter* of the atmosphere (Fried, 1966). The point spread function is then given by

$$\mathrm{PSF}(\theta)=\frac{1}{2\pi}\int_0^{\infty} J_0(f\theta)\mathrm{MTF(f)df} \tag{3-2}$$

where θ is the angle in the sky.

This is shown in Figure 3-1.

The FWHM is found to be $0.98\lambda/r_0$. Thus, given r_0 for the atmosphere and the wavelength of the observation, the enclosed (fractional) energy can be determined

$$\mathrm{E}(\theta) = 2\pi\int_0^{\theta}\mathrm{PSF(u)udu} \tag{3-3}$$

This is shown in Figure 3-2.

Atmospheric seeing theory predicts and experiments (Boyd, 1978) show that r_0 is wavelength and zenith angle dependent, with the form

$$r_0 \propto \lambda^{\frac{6}{5}}(\cos z)^{\frac{3}{5}} \tag{3-4}$$

where z is the zenith angle.

3.3.1.2 Global Optical Goal

Given this description of the atmosphere, we can characterize the seeing conditions at the site on Mauna Kea and establish optical performance goals.

Visual observations ($\lambda = 0.5\mu$m) at the Canada France Hawaii Telescope (CFHT) and at the University of Hawaii (UH) 88-Inch Telescope have been compiled to yield a frequency curve of seeing at Mauna Kea (Racine, 1984). This is shown in Figure 3-3. Systematic seeing tests made at the TMT site (Walker, 1983, TMT Reports 123, 124) indicate that the TMT site is at least as good as the Mauna Kea ridge sites exemplified by the CFHT and the UH 88-Inch Telescope. The Walker scale is calibrated against large telescope image size by Woolf and Angel (1980). From the Racine results we expect that roughly 10% of the time, the FWHM seeing at λ = 500nm will be 0.5 arcseconds or better, equivalent to an atmosphere coherence diameter of r_0 = 200mm.

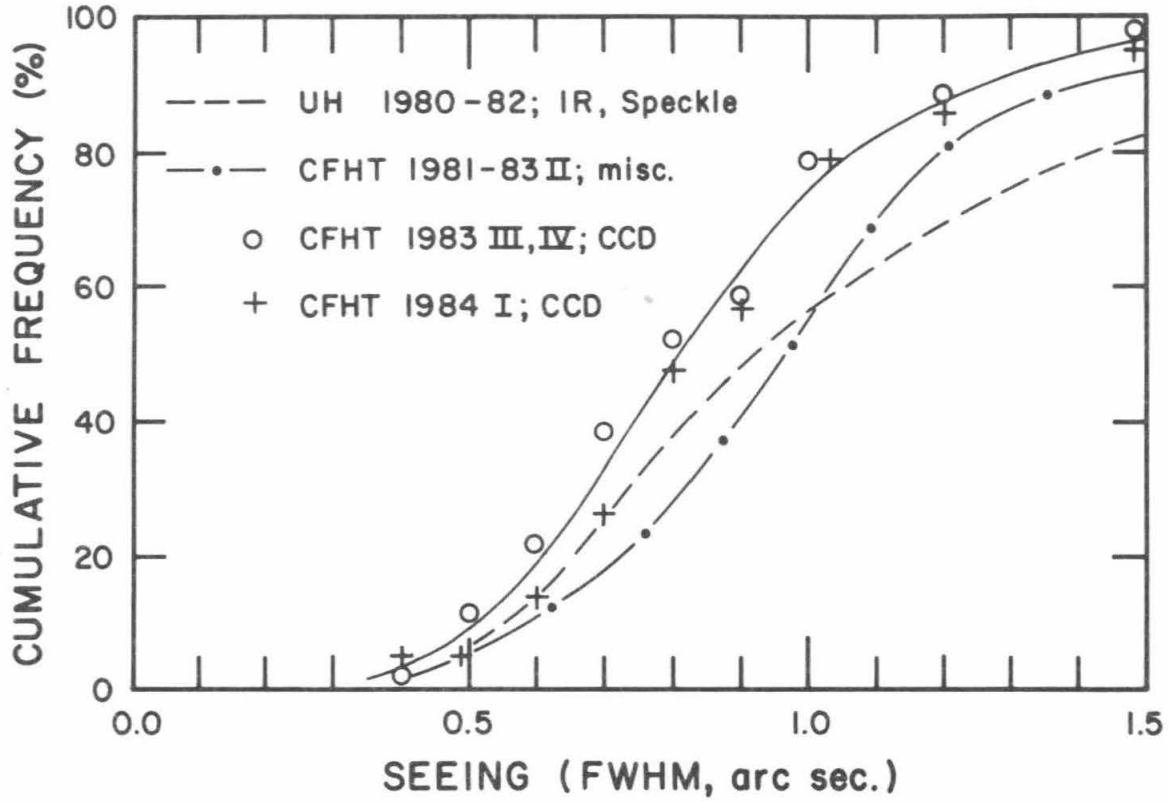

XBL 8411-4945

Figure 3-3 Seeing statistics for CFHT and UH telescopes on Mauna Kea (from Racine, 1984) for visible light ($\lambda \approx 500$nm).

The optical goals are set such that the 0.5 arcsecond seeing (FWHM) is degraded by the optical system by no more than about 10%. Assuming the telescope and atmospheric contributions add in quadrature, the telescope system performance should be limited to 0.23 arcsecond images (FWHM). To match the optical design described in the previous section, this image quality should be maintained in the visual over a 20-30 arcminute field depending on focal position and in the infrared over a 9 arcminute field. The creation of an error budget among the various sources of error is somewhat arbitrary. Roughly half the allowed error is assigned to the primary mirror and the other half to all other sources, including other mirrors, the optical design, fabrication, and alignment errors. Since these are assumed to add in quadrature, the primary mirror is allowed 0.17 arcseconds FWHM for visible light, corresponding to $r_0 = 600$mm. This is one third the aberrations introduced by the best seeing ($r_o = 200$mm). As stated above, it is desirable to characterize our goals more completely than simply by a FWHM. A practical way to do this is to specify a number of enclosed energy diameters. The TMT specifications are set at 50%, 80%, and 90% enclosed energy all based on one-third the best seeing, and they are given in Table 3-1. The enclosed energy curve is shown in Figure 3-2.

Table 3-1
Enclosed Energy Diameter (Arcseconds)

	0.5 arcsecond seeing λ=500nm r_o=0.2m	Segment diffraction λ=500nm	Primary diffraction λ=10.0μm	TMT Primary Mirror Goals 500nm r_o=0.6m	2.0μm r_o=3.2m	10.0μm r_o=22m
FWHM	0.50	$\approx$0.063	$\approx$0.21	0.17	0.13	
50%	0.57	0.068	0.22	0.19†	0.14†	Strehl††
80%	0.95	0.116	0.38	0.32†	0.24†	σ=0.26μm
90%	1.27	0.248	0.82	0.42†	0.32†	
95%	1.70	0.494	1.62	0.57	0.43	

† Formal specifications for TMT primary mirror

† † In the diffraction-limited regime we specify the rms surface error σ as that value which will degrade the peak image intensity 10%. This corresponds to a Strehl ratio(S) of 0.9. The relationship is $S = e^{-(4\pi\sigma/\lambda)^2}$.

3.3.1.3 Optical Goals for the Primary Mirror

The optical goal that the primary mirror should have an error budget about one third of the expected aberrations caused by the atmosphere is to be met at all wavelengths when the telescope is seeing-limited. Since the primary is segmented, it does not follow automatically that if the goals are met at 500nm they will be met at longer wavelengths. This is easily seen by noting that piston errors in the segments do not affect the individual segment's coherent images but will degrade the image quality produced by the entire mosaic. For 500nm wavelength the individual segment images are expected to meet the optical goals, since the diffraction-limited image quality of the individual segment (Shack,1977) is substantially better than our specification, as is seen in Table 3-1. Figure 3-4 shows the 10 percentile atmospheric seeing images along with the diffraction-limited images both for a single segment and for the entire mosaic as a function of wavelength. Also shown is the r_0 = 600mm (λ = 500nm) seeing curve. Adding this curve in quadrature with the diffraction curve for the entire primary yields the lower curve, upon which our wavelength dependent primary mirror specifications are based. The mirror should perform at least as well as this lower curve at all wavelengths.

For practical reasons the image quality of the primary is specified at precisely three wavelengths; 500nm where the individual segment surfaces dictate the image quality, 2000nm where the coherence between neighboring segments is critical to achieve the desired image quality, and 10000nm, where coherence of the primary as a whole will dominate the image quality. The formal specifications for the primary mirror are given in Table 3-1 (daggers). These specifications are consistent with the lower curve in Figure 3-4.

High resolution observations such as speckle interferometry can overcome the image quality limitations imposed by the atmosphere. The telescope optics should also allow these kinds of observations. For many reconstruction algorithms, it is sufficient that the telescope aberrations be smaller than those of the atmosphere, and within this range no particular stability is needed. For other algorithms, absolute stability of the optical system to a small fraction of the observing wavelength may be needed, but some controversy surrounds this. We assume the looser goal is adequate.

3.3.2 Criteria for Thermal Infrared

Successful operation in the thermal infrared ($\lambda \geq 2.5\mu$m) requires extremely accurate control over background noise, since in most instances the background flux will enormously dominate over the signal flux. This background flux comes from radiation from the atmosphere and from the telescope optics and local telescope environment.

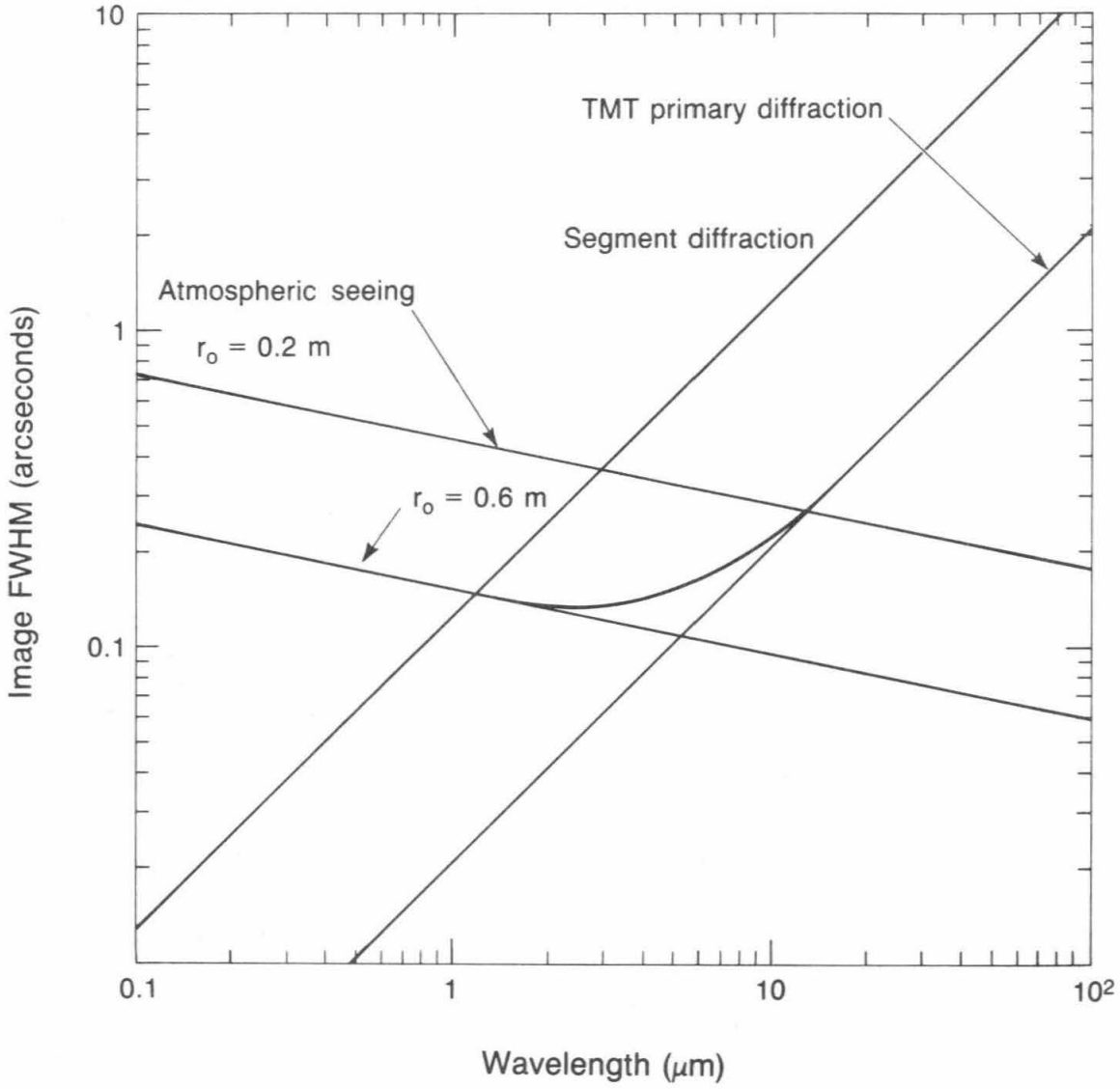

XBL 8412-6443

Figure 3-4 Image diameters (FWHM) are shown as a function of wavelength. The upper descending curve shows the 10 percentile seeing expected at Mauna Kea (r_o = 0.2m for λ = 500nm). The lower descending curve shows the images from a hypothetical atmosphere three times better. This is the basis for the specification for the TMT primary. The upper ascending curve shows the diffraction image diameter from a single optically perfect segment. The lower ascending curve shows the diffraction image diameter from the entire optically perfect primary. The smooth curve that joins the lower two curves gives the expected image size from a perfect ten meter telescope including the degrading effects of the atmosphere with r_o = 0.6m. This curve shows that at short wavelengths (λ = 500nm), image size is set by seeing alone. At 2μm, diffraction effects from single segments would dominate the image size if coherence between adjacent segments were not maintained. At 10μm the diffraction effects of the entire primary establish the image size when r_o = 0.6m.

Experience indicates that the most effective technique for accurate subtraction of the background flux is a chopping secondary mirror. This mirror rapidly switches back and forth between the "source" region containing source and background and an equal area "sky" region containing background alone. To achieve this the science goals call for a chopping secondary that can chop at frequencies up to 30Hz and over image plane chop angles of up to ± 2.5 arcminutes. At 30Hz the ability to chop with at least an 80% duty cycle over a chop angle of ± 30 arcseconds is required.

To achieve optimal performance, the IR background should be small and stable. The direct emission of the optical path should be less than 5% of an ambient temperature blackbody for $\lambda \geqslant 8\mu$m and under 7% for $\lambda = 2-8\mu$m. This emission will come from the primary surface, the secondary surface, and other warm sources in the field of view of the detector. Other sources outside of the direct optical path may diffract some of their energy into the detector, and this should be minimized as well. The stability of these sources is important. Low frequency components of variability are removed by chopping the secondary mirror and by beam switching (moving the telescope so the source moves from one extreme chop position to the other). For this to work successfully, the telescope emissivity must also be highly constant as a function of chop angle. Details are given by Matthews (1981, TMT Report No. 46). Maintaining this low background level will require frequent cleaning and recoating of the optics.

3.3.3 Pointing and Tracking

In order to take full advantage of the excellent imaging properties of the TMT optics and the site, the telescope must deliver the starlight accurately and stably onto the scientific instrument. One of the major impediments to accurate pointing is the presence of uncontrolled thermal gradients in the telescope structure. A technique capable of largely overcoming pointing errors caused by thermal or other perturbations on the telescope is under development by Cudaback (TMT Report No. 136, 1985). This technique involves a laser interferometer metrology system that measures the positions of all optical elements with respect to earth. It should be capable of reducing absolute pointing errors to under 0.5 arcseconds. The TMT design should not prevent implementation of this technique, but at present will not rely on it. Since the TMT will be used during the day as well as at night, the telescope performance must be specified separately for day and night time use.

The absolute pointing accuracy of the telescope should be no worse than 1.0 arcseconds rms over all elevation angles above 20°. This should be achievable over an entire night without recourse to calibration stars. Blind offsets from calibration stars should be accurate to better than 0.1 arcsecond rms over offset angles up to 1°. For daytime observations the absolute pointing should be no worse than 2.0 arcseconds rms during an entire day. Offset requirements should be held both night and day.

Tracking stability should be better than 0.1 arcsecond rms open-loop (without recourse to any guide stars) for at least 10 minutes at night and 5 minutes during the day. Open-loop tracking stability should be better than 0.5 arcseconds for one hour during the night, and should be better than 1.0 arcsecond for one hour during the day. During closed-loop tracking on a guide star, the jitter should be under 0.02 arcseconds rms. Closed loop tracking with an effective bandwidth of 10Hz is desired. Field rotation errors should be held to 0.1 arcseconds rms over a 20 arcminute field of view.

The telescope should also have an unobstructed view down to elevation angles of 15° (3.9 air masses). With vignetting, the telescope should work at the horizon.

3.4 Environmental

3.4.1 Solar

Daytime use of the telescope is considered essential. Many infrared observing programs can be carried out during twilight and daytime hours when visible light observations are impractical. An analysis of likely gains in observing time is given by Nelson (1984, TMT Technical Note No. 108). However, several factors must be considered in evaluating daytime observations. First, daytime observations force a requirement that instrument changeovers be rapid and safe. Second, normal guide stars are not available, so pointing and tracking needs are affected. Third, heat loads caused by the sun can cause adverse thermal gradients in the telescope and also produce heat loads on the interior of the dome that may degrade seeing conditions during the following evening. Finally, the seeing during the day at the site itself will be substantially worse than experienced during the night, at least during the late morning and afternoon.

To minimize the adverse consequences of daytime observing, particularly on nighttime observing, all observations should be made at least 90° from the sun during daylight hours, and in no instance should sunlight be allowed to enter the dome slit. Sunlight in the dome may substantially degrade pointing accuracy and introduce severe dome seeing effects.

3.4.2 Thermal

The optimal seeing conditions and telescope pointing accuracy will occur when the telescope is isothermal and when the telescope and dome are at the outside ambient temperature. Achieving this condition in the face of a varying outside thermal environment, daytime observations, and substantial thermal inertia in the telescope, mirrors, and dome is not possible, but an excellent approximation to this condition is required.

The summit area of Mauna Kea fortunately has quite mild air temperature swings well away from the ground. Measurements made at the top of the Canada France Hawaii Telescope (CFHT) dome indicate that the typical diurnal temperature swing is about 6.5°C (data taken from CFHT weather records). Closer to the ground the diurnal temperature swing is higher, the average being about 12°C (Kaufman & Vecchione, 1981, TMT Report No. 61). During the evening hours from 7pm to 5am the temperature change is quite small, being under 1.5°C on average, and being above 3°C only rarely (Nelson and Bely, 1984, TMT Report 133). Further, the average night temperature is quite constant during the year, with an annual average of about 2°C, and a seasonal variation in the average of only about ±4°C. The maximum temporal gradients in temperature occur near sunset and sunrise and have typical values of 1°C per hour, with gradients above 1.5°C per hour being rare. The historical extremes for the site temperature are -15°C to +20°C. More details are given in Section 10.

Using this summary of thermal properties of the site, the thermal specifications can be given. Electrically and mechanically, the observatory should function over the temperature range −15°C to +20°C. The telescope must meet its operating specifications over the temperature range −6°C to +10°C, which represents 99% of the time.

To ensure an acceptably small seeing effect from the dome, the inside temperature of the dome and the temperature of the telescope structure must be within 0.5°C of the ambient temperature from sunset to sunrise. Numerical modeling of the thermal environment by Carroll and Conners (1984, TMT Report No. 134) indicates that, with a well insulated dome and floor and with the mild thermal swings seen on Mauna Kea, this goal can be met passively, using only forced ventilation of the dome. However, an active floor chiller is also being considered. Since the primary mirror can produce thermal seeing degradation most easily, the primary mirror itself (front surface) should be within 0.25°C of the average ambient dome air during this same time period. Since the natural time constant of the mirror coupled to still air is roughly 9 hours, achieving this goal will probably require some form of active thermal control of the primary. Since the conduction time constant for cooling the back surface is only 45 minutes, a

form of forced ventilation of the back surface will probably be used. The telescope structure will have a thermal time constant in still air of roughly 2 hours. This is sufficiently short that it will likely follow the ambient air temperature to within our specifications without any active control.

3.4.3 Wind, Precipitation, and Dust

The observatory must be capable of surviving the worst expected conditions and of operating successfully under most conditions. Survival should be assured in the worst storms anticipated in a one hundred year period. We assume that the worst case wind is 65m/s (145mph), and that the worst ice loads correspond to 100kg/m^2. Under these conditions the closed dome must protect the telescope from dust and precipitation. Thus the sealing between the shutters and dome, and the dome and stationary dome foundation must be excellent.

In clear weather conditions, the telescope should be capable of meeting its performance goals even in the face of substantial winds. Wind can affect the performance in several ways. First, buffeting on the dome and its foundations can tilt the pier and the telescope. Second, wind can buffet the telescope itself, particularly the top end of the telescope that is exposed by the open slit. Third, wind buffeting can exert varying forces on the surface of the segmented primary that may objectionably distort the surface, even with the active control system in operation. The effects of the wind on the telescope itself will be a strong function of the direction of the wind relative to the dome slit, and also the open size of the slit. It is expected that the best thermal seeing conditions may occur with the slit fully open, but the best wind protection will occur with the slit opening reduced to the minimum needed by the optics. Because of this variability, when wind conditions are unacceptable in one orientation, they may still be acceptable in another. Hence the degradation of telescope performance due to wind will be largely one of restriction on where the telescope can be pointed. Observing with reduced performance should be possible in winds up to 35m/s.

The distribution of wind speeds and directions is a strong function of the exact location of the site on the summit area. Wind speeds appear to be highest along the summit ridge itself, where the CFHT, UH 88-Inch, and UKIRT are located. Our site on the Northwest Cone is substantially less windy. Simultaneous measurements at our site 5m above ground level with measurements 2m above the top of the CFHT dome spanning different times of day, seasons, and wind speeds, indicate a difference in mean wind speed of a factor of 2. Some of this is due to the perturbing effects of the dome itself (about a a factor of 1.5) and some may be due to the height difference, but a real difference of at least 50% is likely. Long term records (about nine years) at the UH 88-Inch indicate the 95 percentile wind is about 20m/s (Kaufman and Vecchione, 1981, TMT Report No. 66). Records at our site covering about one year indicate the 95 percentile wind speed is 14m/s, about 40% less than at the UH 88-Inch. A longer time base is needed to put this value on a secure footing.

The operating specifications for wind are set at the 95th percentile. Thus the effects of a 14m/s wind on the dome and telescope should be so small as to cause image motion that is less than 0.25 arcseconds rms. Although the protection offered by the dome is difficult to estimate, we assume there is a factor of 2 reduction in wind speed at the top of the telescope, and a factor of 6 reduction in wind speed near the primary mirror. This information is converted into a specification on the telescope structure that under a load at the top end of 500N, the telescope pointing shall change by no more than 0.25 arcseconds. Additionally, an axial load at the top end of 250N shall cause defocus or image motion that is under 0.25 arcseconds. The basis for this conversion is described by Nelson (1981, TMT Report No. 47).

The setting of a meaningful wind specification for the actively controlled primary mirror itself is more difficult and requires establishing the power spectrum of the wind perturbations. Suitable measurements have not yet been made, so for the moment a force level at a fixed frequency is set as the goal. With the factor of 6 reduction, wind speeds under 2m/s are expected, so global perturbations will occur at frequencies set by the travel time across the primary, or $\approx$0.2Hz. Wind induced motion at this frequency can be crudely estimated from the static wind

pressure at this speed and the expected stiffness of the mirror cell. From this wind motion, mirror motions of 0.2μm are expected without active control (see Section 7.8).

3.4.4 Seismic

Since Mauna Kea is located in a seismically active area, seismic specifications are required. The telescope need not operate under any seismic loads, but the telescope, instruments, and the rest of the facility must survive the worst seismic load expected in a 100 year period. Mauna Kea is rated as a seismic zone 3. Present buildings on Mauna Kea are designed for 0.3g horizontal loads, which are ample for this zone.

3.5 Operational

3.5.1 Telescope and Dome Slewing

Telescope and dome motion requirements are based on the need to move quickly from one observing program to another, and on the variable tracking speeds needed for an altitude-azimuth telescope. Also, within an observing program some observations require calibration on objects widely separated in the sky or frequent calibration on nearby objects. The telescope, dome and shutter must be capable of motion so the telescope can move to any region in the sky in less than two minutes. The settling time after completion of slewing must be less than 10 seconds. Thus slew speeds for telescope and dome must be over 3°/s in azimuth, and over 0.8°/s in elevation. A blind spot surrounding the zenith is created by slewing limitations with an altitude-azimuth mount. The zenith blind spot should be under 1° in diameter. Specific velocity and acceleration relationships can be found in Nelson (1981, TMT Report No. 49).

3.5.2 Instrument Handling

The ability to change the operating configuration of the telescope from one observing system to another quickly should be a great asset in maximizing the scientific productivity of the TMT. Perhaps the most obvious case concerns the change from nighttime to daytime observing, where one will need to change to and from IR observing procedures. Equally important is the ability to adapt the observing program to changes in the weather and in the seeing conditions.

As a general goal, the TMT should be capable of being configured from one system to another in less than 20 minutes. This procedure may involve changing the secondary mirror, moving the tertiary mirror, removing or installing light baffles, and exchanging instruments. Clearly the more items that must be changed the longer the change will take. To minimize the changing time, all equipment and instrumentation at the prime focus, the forward Cassegrain, and the Cassegrain will be modular in form. For each position, these modules should be identical in their attachment scheme, their mass, and their center of gravity. All electrical connections and mechanical structural connections should be achievable by remote operation, with little or no local human intervention required. To the extent possible, fluid and vacuum connections should be arranged in similar fashion. The modules must also be reproducible in their positioning to minimize instrument recalibration and telescope pointing errors. The characteristics of the instrument modules are listed in Table 3-2.

Table 3-2
Instrument Module Requirements

Characteristic	Prime	Forward Cass	Cassegrain
Weight (kg)	2000	2000	2000
Center of Gravity Position From Vertex (meters)	-16	-3.5	3.5
Axial Error (μm)†		±25	±25
Decenter (μm)†		±112	±115
Rotation (arcseconds)†	23		
Tilt (arcseconds)†		±27.1	±11.3
Maximum Length (m)	3	2	3
Maximum Diameter (m)	2	1.3	1.3
Types of Instruments	Prime Focus Camera f/15 Secondary IR Chopper Coudé Secondary	Tertiary IR Photometer IR Camera IR Spect.	Mod. Res. Spect. Polarimeter

† Errors should be maintained during use and between module changes. A discussion is given in 5.4 and by Nelson (TMT Note 113, 1985).

3.5.3 Mirror Covers

The primary mirror requires a cover that protects the mirror from falling objects, dust, and humidity. The tertiary flat must also have a mirror cover for dust and humidity protection.

3.5.4 Telescope Servicing

Since the primary mirror has 36 segments, and low emissivity is required for IR observing, recoating procedures should be thought through carefully. A triangular wedge of six (different type) segments can be removed and replaced with freshly coated spares during a 24-hour period, but preferably during an 8 hour period. This guarantees that only six daytime periods will be lost in re-aluminizing the entire primary, or, at most, six 24-hour periods. If bare aluminum is deposited on the mirror segments, yearly re-aluminizing is expected. If protective overcoatings are applied, much less frequent coating will be needed.

Cleaning or washing the segments will be done more frequently. We require that the complete primary can be cleaned during an 8 hour day.

The active control system has many components, with 168 sensors and 108 actuators. Particularly because of this multiplicity, ease of servicing of these components is required. Since all actuators must be working for the primary to work properly, their ease of replacement is most critical. It is expected that an actuator can (and should) be replaceable in 30 minutes. Sensors must be partially removed and reinstalled during the recoating process, so their rapid replacement is also needed. A sensor and its electronics should be replaceable in 10 minutes.

4. Optical Design

Contents **Page**

Section 3.1 summarizes the science goals to be met by the optical design, and Section 3.2 discusses the broad considerations that led to the adopted overall design. This section describes in more detail the functional characteristics of the optical design.

4.1 General Layout of Foci

Figure 4-1 shows schematically the general layout of foci in the telescope. Table 4-1 summarizes basic data for each focus, including f-ratio, angular scale in arcseconds/mm, and the fully baffled unvignetted field of view in meters and arcminutes.

Tables 4-2 to 4-5 show the error budgets for visual light for the primary mirror, prime focus camera (for 15 and 30 arcminute fields), and f/15 Nasmyth focus. With these error budgets, we come very close to meeting the desired optical goal of degrading the best-seeing FWHM images ($\theta = 0.50$ arcseconds) by no more than 10%.

Table 4-1 Focal Plane Specifications

Focus	Focal Length (m)	Primary Vertex - Focal Plane Distance[a] (m)	Image Scale (arcsec/mm)	Diam. FOV (arcmin)	Diam. FOV (m)	Radius of Field Curvature (m)	Instrument Dimensions (diam x length)	Maximum Weight Limit (kg)
Prime Focus Camera	20.0	-17.60	10.31	30	.175	Flat	2m x 1.5m	500
Prime	17.5	-17.5	11.79	-	-	-	2m x 3m	2000
Nasmyth	150.0	3.00 ± 0.96	1.38	20	.873	2.180	5m x 8m[b]	10,000
Bent Cassegrain	150.0	3.00 ± 0.96	1.38	5	.219	2.180	1m x 2.0m	500
Cassegrain	150.0	3.00 ± 0.96	1.38	20	.873	2.180	1.3m x3m	2000
IR Forward Cassegrain	250.0	-4.00 ± 2.48	0.83	9.0	.654	.846	1.3m x 2m	2000
Coudé	1000.0	70.0 ± 34	0.206	1.5	.436		10m x 10m	–

a The range of focus is defined as that region having under 1 arcsecond of spherical aberration.

b Roughly rectangular area; 2 platforms.

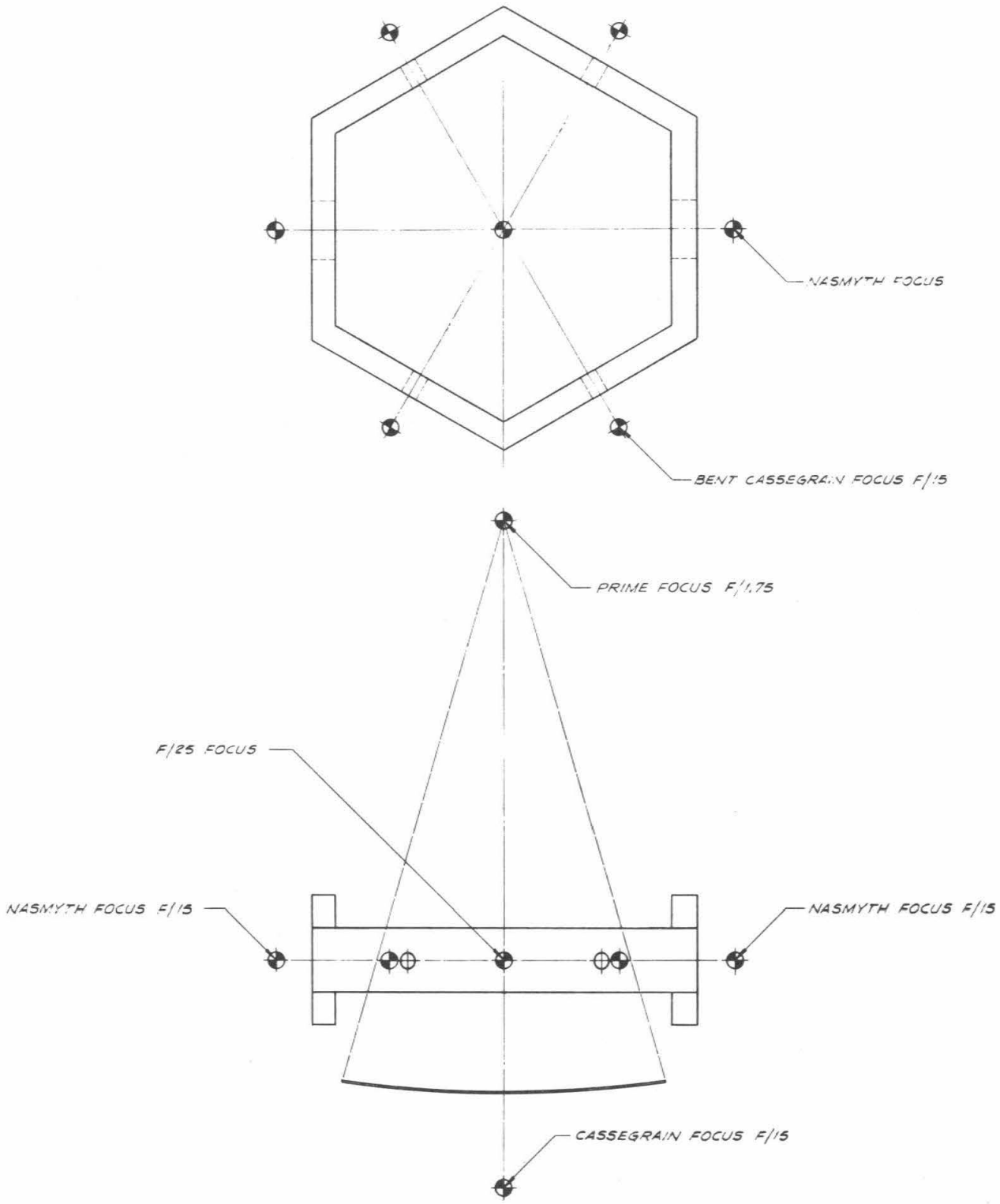

XBL 8411-4922

Figure 4-1 The locations of the various foci of the TMT are shown, excluding the coudé focus. The four bent Cassegrain foci and the Nasmyth foci require the use of a tertiary mirror.

Table 4-2
Primary Mirror Error Budget

Goal: 80% of energy flux in 0.32 arcseconds

Item		Allowed Error (arcseconds)	
Segment figuring (polishing and warping)			0.242
Segment thermal distortion			0.147
Segment support (larger of axial, radial)			0.098
Axial design		0.082	
Axial fabrication		0.05	
Radial design		0.04	
Radial fabrication		0.05	
Thermal effects		0.02	
Segment alignment (passive degrees of freedom)			0.074
Initial alignment		0.05	
Thermal cell expansion		0.045	
Gravity induced segment motion		0.03	
Segment alignment (active degrees of freedom)			0.098
Sensor calibration		0.05	
Thermal effects on sensors		0.004	
Gravity effects on sensors		0.021	
Temporal drift of sensors		0.029	
Control system noise		0.057	
Sensor noise	0.024		
Actuator noise	0.052		
Wind induced motion		0.05	
		Total	0.32

Table 4-3

Error Tree for Prime Focus f/2
(80% enclosed energy diameters in arcseconds)[1]
(For inner 15 arcminutes)

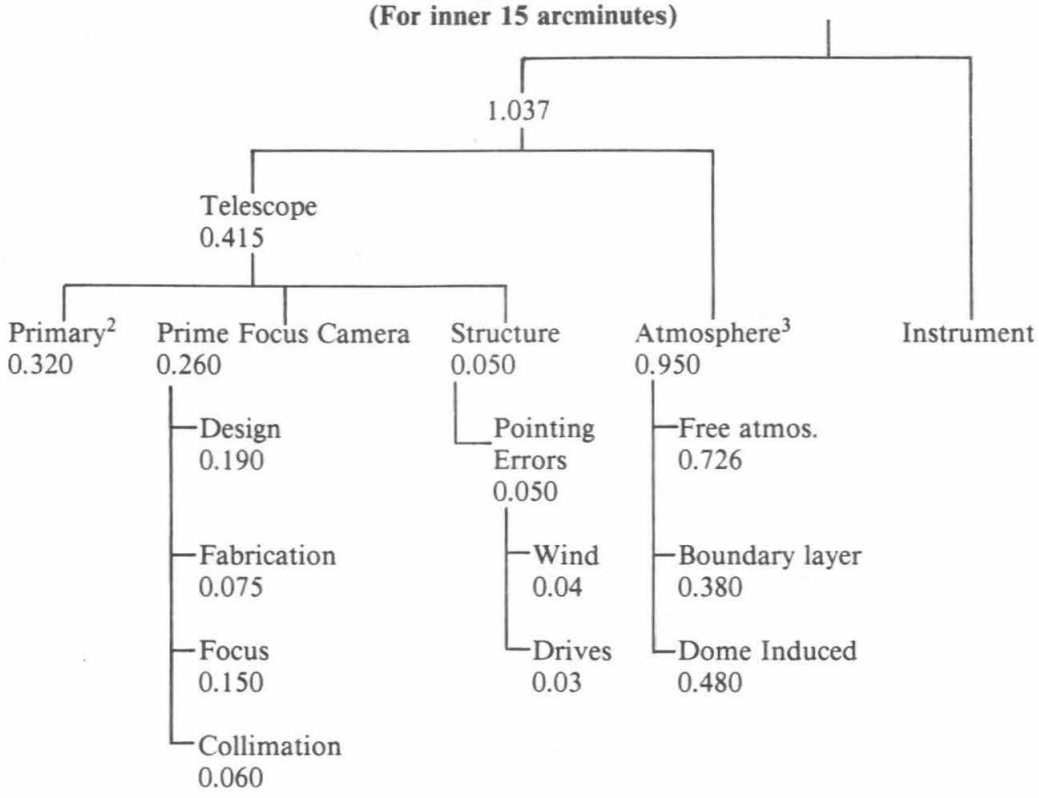

XBL 852-1415

1. Errors are for image diameters that enclose 80% of the incident energy. This relates to FWHM errors in a complex way. Atmosphere errors are assumed to have the form given in Section 3. Other errors are assumed to have a Gaussian distribution. All indicated errors are assumed to add in quadrature.
2. The details of the primary error budget are given in Table 4-2.
3. The atmosphere error budget is somewhat arbitrarily broken up into the indicated categories to show the potential influence local effects have on the error budget. The net atmosphere allocation corresponds to a FWHM of 0.50 arcseconds.

Table 4-4

Error Tree for Prime Focus f/2
(80% enclosed energy diameters in arcseconds)[1]
(For inner 30 arcminutes)

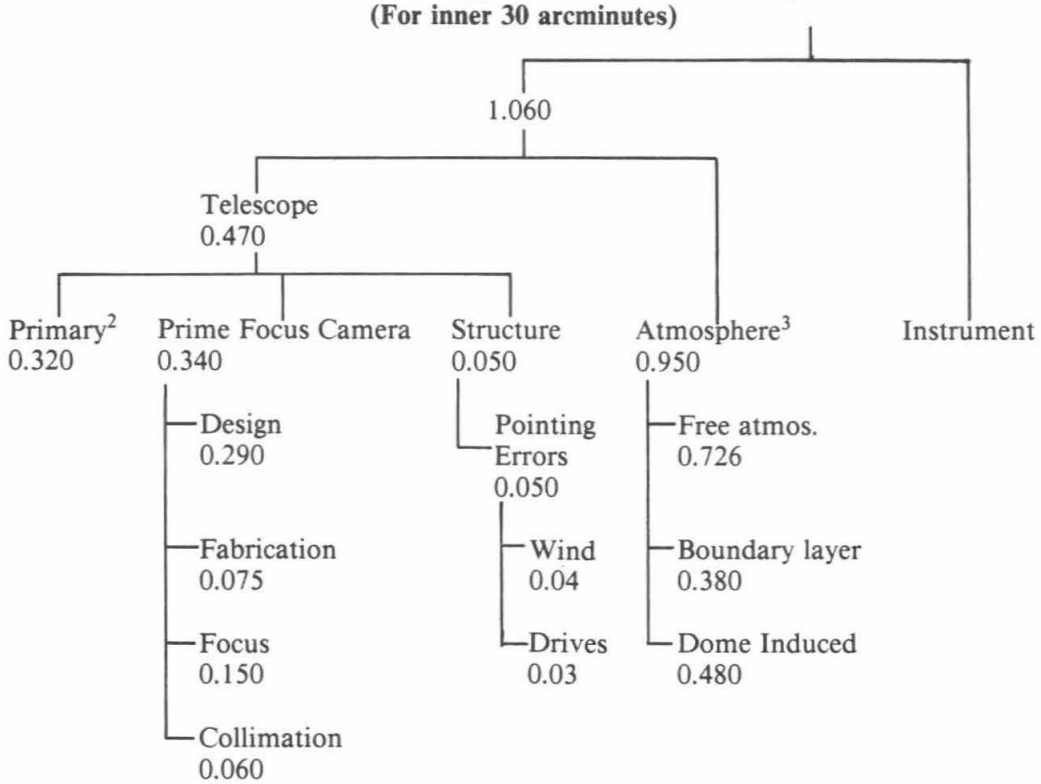

XBL 852-1414

1. Errors are for image diameters that enclose 80% of the incident energy. This relates to FWHM errors in a complex way. Atmosphere errors are assumed to have the form given in Section 3. Other errors are assumed to have a Gaussian distribution. All indicated errors are assumed to add in quadrature.
2. The details of the primary error budget are given in Table 4-2.
3. The atmosphere error budget is somewhat arbitrarily broken up into the indicated categories to show the potential influence local effects have on the error budget. The net atmosphere allocation corresponds to a FWHM of 0.50 arcseconds.

Table 4-5

Error Budget for f/15 Nasmyth[1]
(80% enclosed energy diameters in arcseconds)[2]
λ=500nm

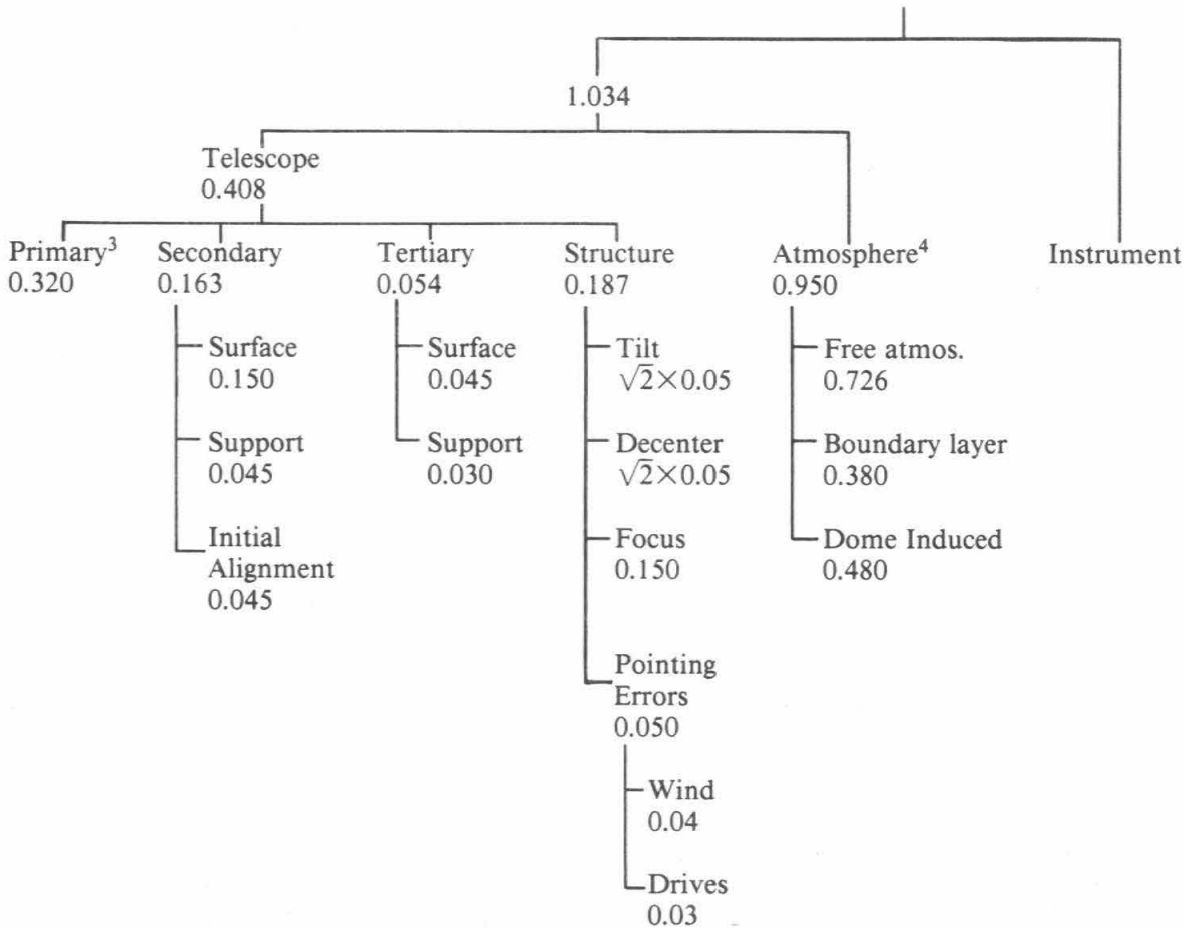

XBL 852-1445

1. The error budget is for on axis images. The Ritchey-Chretian design gives approximately 0.5 arcseconds of image blur 10 arcminutes off axis. This astigmatic blur enters quadratically with field angle.

2. Errors are for image diameters that enclose 80% of the incident energy. This relates to FWHM errors in a complex way. Atmosphere errors are assumed to have the form given in Section 3. Other errors are assumed to have a Gaussian distribution. All indicated errors are assumed to add in quadrature.

3. The details of the primary error budget are given in Table 4-2.

4. The atmosphere error budget is somewhat arbitrarily broken up into the indicated categories to show the potential influence local effects have on the error budget. The net atmosphere allocation corresponds to a FWHM of 0.50 arcseconds.

The adopted design is an alt-azimuth yoke-mounted Ritchey-Chretien with a primary focal length equal to 17.50m. The primary mirror consists of 36 hexagonal segments with a total area of $76m^2$, equivalent to a filled circular aperture (with equivalent central hole) of 10.0m diameter. The maximum outer diameter enclosing the primary mirror is 10.95m. The on-axis beam leaving the primary mirror has a maximum f-ratio of f/1.94 and minimum f-ratio of f/1.60. The prime-focus camera slows this beam from a focal length of 17.5m to 20.0m.

We selected the focal length of the primary mirror after analyzing and weighing several conflicting factors. Two factors argue in favor of a smaller focal length. Perhaps the most important is the need to reduce the length of the telescope and thus the size of the enclosing dome which is a substantial cost item in the total observatory budget. A smaller focal length also gives a shorter stiffer tube. The stiffness increases more rapidly than the required alignment tolerances for the primary-secondary optics as the focal length is reduced, hence maintaining adequate optical alignment should be easier for a smaller focal length. Three factors argue in favor of a larger focal length. First, segment fabrication using Stressed Mirror Polishing (Section 5) varies in difficulty with the difference between the desired off-axis paraboloidal surfaces and the best fitting sphere for each segment. This difference varies as k^{-3}, where k is the radius of curvature of the primary mirror. Hence as the focal length is reduced the optical fabrication rapidly becomes more difficult. Second, the tolerances on the alignment of a segment within the array vary as k^3. Misalignment can result from initial assembly errors, gravitational distortions, and thermal distortions. Third, chopping for infrared observations introduces coma over the field of view that varies as k^{-2}.

Based on these considerations we selected a focal ratio of 1.75 (focal length =17.5m,k = 35m). Since the above considerations are so different in their nature, the selection process is qualitative and the final choice is a compromise. With this choice the alignment tolerances are practical, but not easy, and an appreciably smaller focal length would probably require extensive changes in the mirror cell and segment support structure. At the selected focal length the comatic chopping aberration for infrared observations is already objectionable for large chop angles and reducing the focal length would further reduce the field of view.

A system of Nasmyth and Cassegrain foci offers a total of seven observing stations. Two of these are Nasmyth foci at opposite ends of the elevation axis, each of which is served by a large platform for mounting large or massive instruments. On the four remaining sides of the (hexagonal) elevation ring are four bent Cassegrain foci. Beams are directed to these foci by a tertiary flat mirror in the middle of the telescope tube, which can rotate to any orientation. The tertiary mirror can be removed via an instrument tunnel that extends through a hole in the primary mirror. With the tertiary removed the light comes to a conventional Cassegrain focus behind the mirror.

All Nasmyth-Cassegrain (N-C) foci are parfocal with a primary vertex - focal plane distance of 3m behind the primary vertex, and all are served by a pair of atmospheric-dispersion compensating prisms that sit immediately ahead of the tertiary flat. Because these foci are the workhorse stations on the telescope, they have been designed as Ritchey-Chretien foci to maximize the field of view. The tentative focal length has been set at 150.0m, but discussions are continuing as to whether this value should be reduced to 120.0m. The quantitative impact of the shorter focal length on image quality at various foci is discussed below.

Removal of the tertiary mirror to the rear allows access to a forward Cassegrain infrared focus, which is located in the center of the tube near the elevation axis. This focus is fed by an infrared chopping secondary mirror, which yields a final focal length of 250m. All optical baffles forward of this focus are removed when infrared observations are made.

Figure 4-2 shows a detailed view of the N-C and forward Cassegrain optical components to scale, with sizes and spacings of optical elements indicated. A detailed description of the optical performance at each focus is given below.

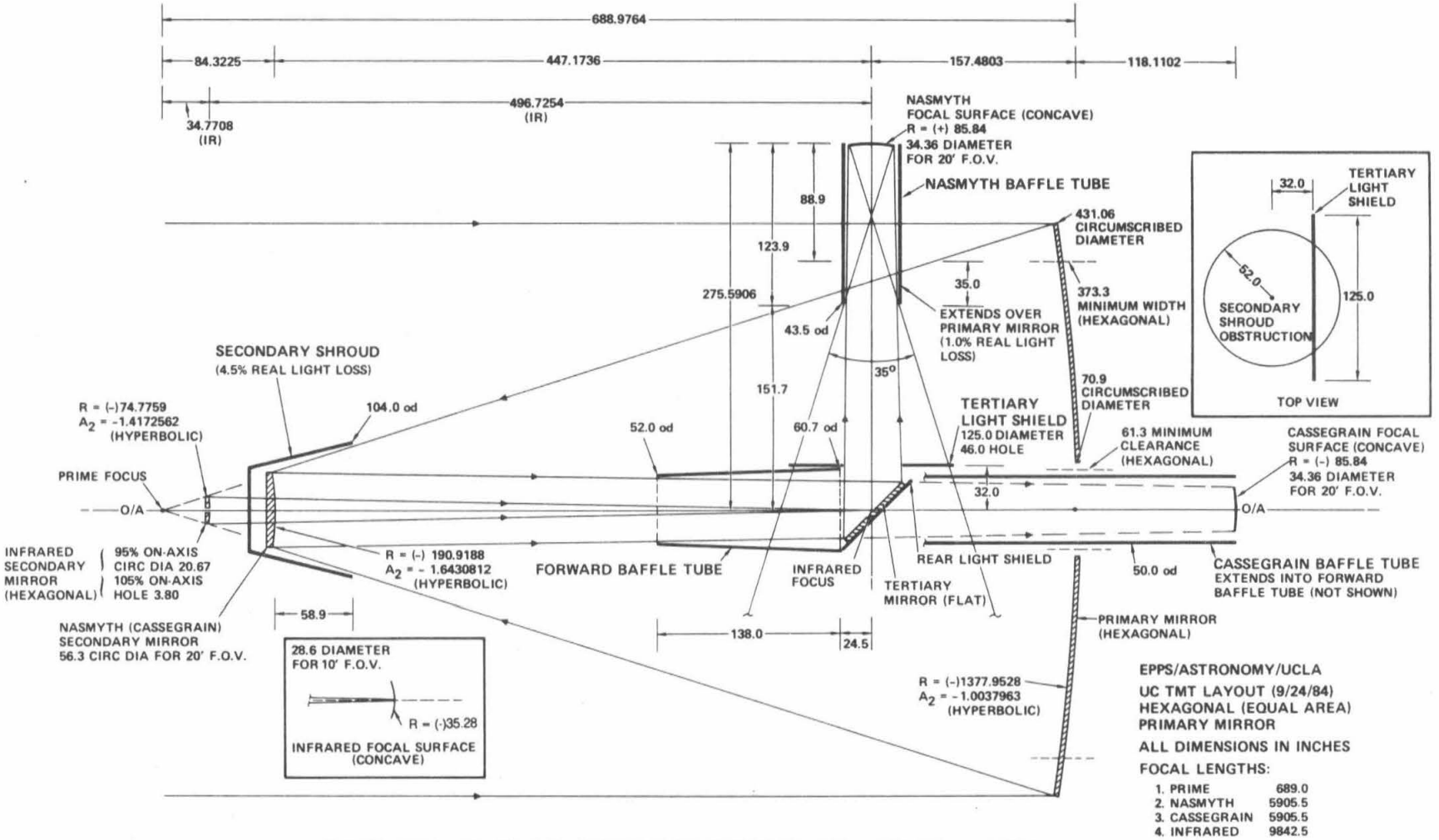

UC TEN-METER TELESCOPE: NASMYTH (CASSEGRAIN) AND INFRARED LAYOUT
WITH LIGHT BAFFLE SYSTEMS FOR 20-ARCMIN DIAMETER
UNVIGNETTED DARK (OPTICAL) FIELDS OF VIEW

XBL 8412-5073

Figure 4-2 Nasmyth-Cassegrain and forward Cassegrain layout, with baffling included.

4.2 Prime Focus Camera

The prime focus camera has been developed to meet the wide-field imaging goals of Section 3.1. For convenience, these goals are repeated here:

a. The telescope should degrade the best atmospheric seeing (FWHM = 0.50 arcseconds) by no more than 10% over the full field of view (FOV).

b. The minimum FOV is 30 arcminutes.

c. The focal ratio should be approximately 2.0 (see Section 3.2.2).

d. The minimum bandwidths are as follows:

   1. Blue camera: The minimum bandwidth ($\Delta\lambda$) should be equivalent to the chromatic width of the photographic J band in a single exposure without refocus over the entire operating image. This implies bandwidths of 0.33μm-0.40μm, 0.39μm-0.54μm, and 0.44μm-0.60μm.

   2. Red camera: A minimum bandwidth of $\Delta\lambda$ = 0.30μm should be achievable anywhere in the range 0.50μm to 1.1μm in a single exposure without refocus.

   3. Both cameras should be able to take high-quality V-band exposures (0.50μm-0.60μm).

e. Both sets of camera optics (except common elements) should be coated with high efficiency anti-reflection coatings, to operate over the following wavelength ranges:

   Blue camera: 0.33μm to 0.66μm
   Red camera: 0.45μm to 1.1μm

   Any optical elements in common should be coated with broad band anti-reflection coatings (0.33μm - 1.1μm) with as high an efficiency as possible.

f. The UV transmission of the blue camera at 0.33μm should be as high as possible.

g. The focal planes of both cameras should be flat.

h. Both cameras should be able to accept plane-parallel elements in the form of detector windows and filters up to a total thickness of 12mm.

i. Both cameras should be able to accept dispersive elements that yield slitless spectra with R = 50-100, based on an image FWHM of 0.55 arcseconds.

j. Each camera must incorporate an atmospheric dispersion corrector that operates over the full FOV and bandwidths specified above and maintains image quality up to 2.0 airmasses (60° zenith angle).

k. Compensation for field rotation should be provided.

Because of limitations on chromatic bandwidth and anti-reflection coatings, the prime-focus camera uses separate red and blue cameras to cover the desired wavelength range. Figure 4-3 shows the camera elements to scale. The philosophy of the design and the balance of aberrations is discussed in more detail by Epps (1984b). The two cameras share a common first element, a large, highly concave lens, which is the most difficult element to fabricate and support. Both surfaces are spherical. Each camera contains separate second and third elements, one surface of which is an aspheric, plus a 12mm thick flat window. Each camera also contains its own atmospheric dispersion compensator (see below). The focal planes of both cameras are flat.

Optical performance is summarized in a series of spot diagrams (Figures 4-4 to 4-6). The entrance pupil corresponds to a hexagonal mask with total area equal to the primary mirror. For the blue camera, monochromatic spot diagrams for three separate wavelength ranges are shown, each for a common focal position. These correspond roughly to the U, J, and V spectral regions (Figures 4-4a,b,c). Two spectral regions are shown for the red camera, 0.44μm-0.70μm and 0.48μm -1.1μm (Figures 4-5a,b). Figure 4-6 shows integrated performance in each wavelength range by superimposing monochromatic spot diagrams. Camera performance is very good; aberrations may be noticed, but only under conditions of excellent seeing, at the

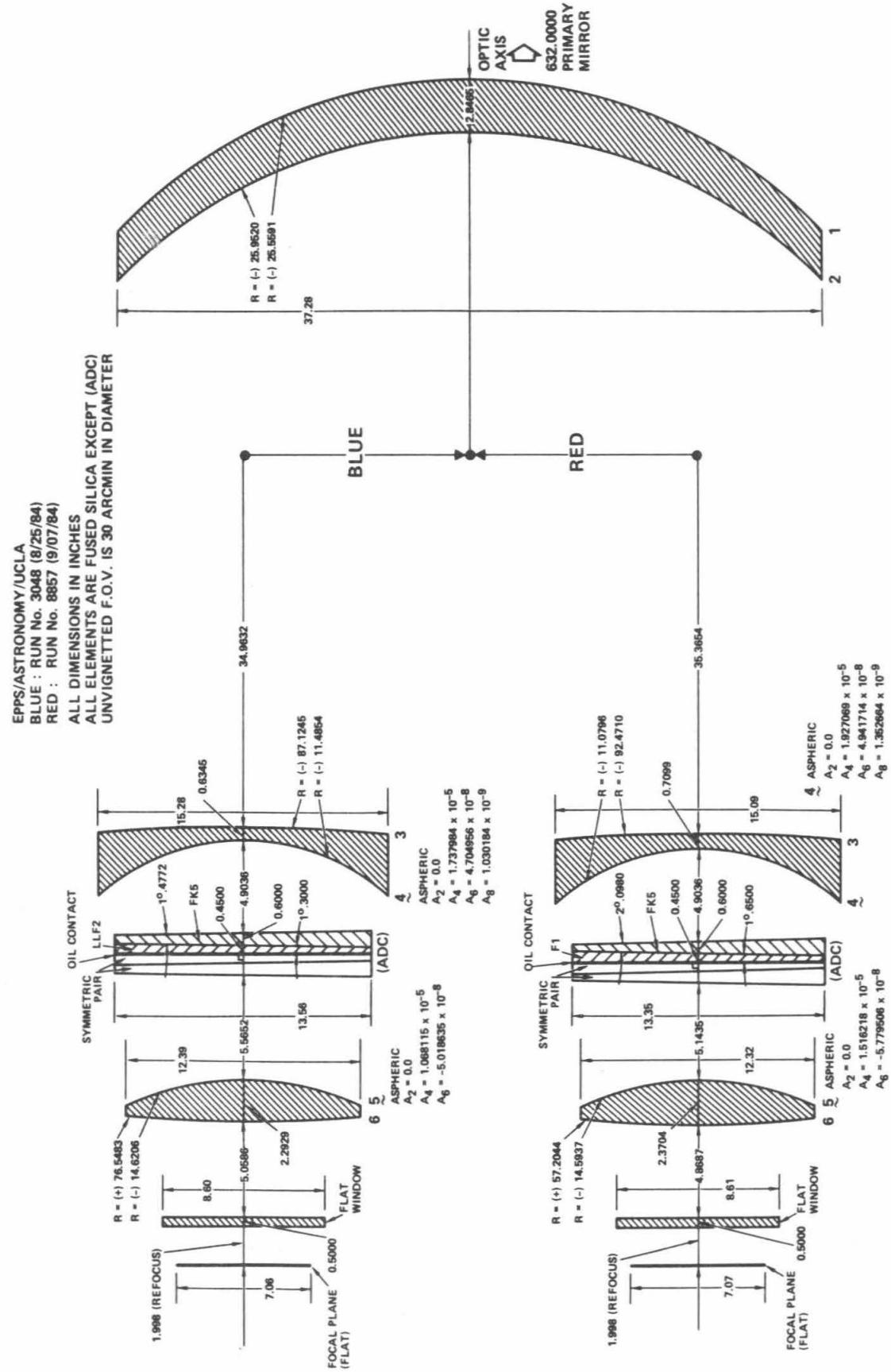

UC TEN-METER TELESCOPE : THREE-ELEMENT *f*/1.86 PRIME FOCUS CORRECTOR SYSTEM (3300 Å TO 11000 Å)

{431-INCH *f*/1.60 (HEXAGONAL) HYPERBOLIC PRIMARY MIRROR, R = (-)1377.9528, A_2 = -1.0037963}

XBL 8412-5072

Figure 4-3 Optical layout for the red and blue prime-focus cameras.

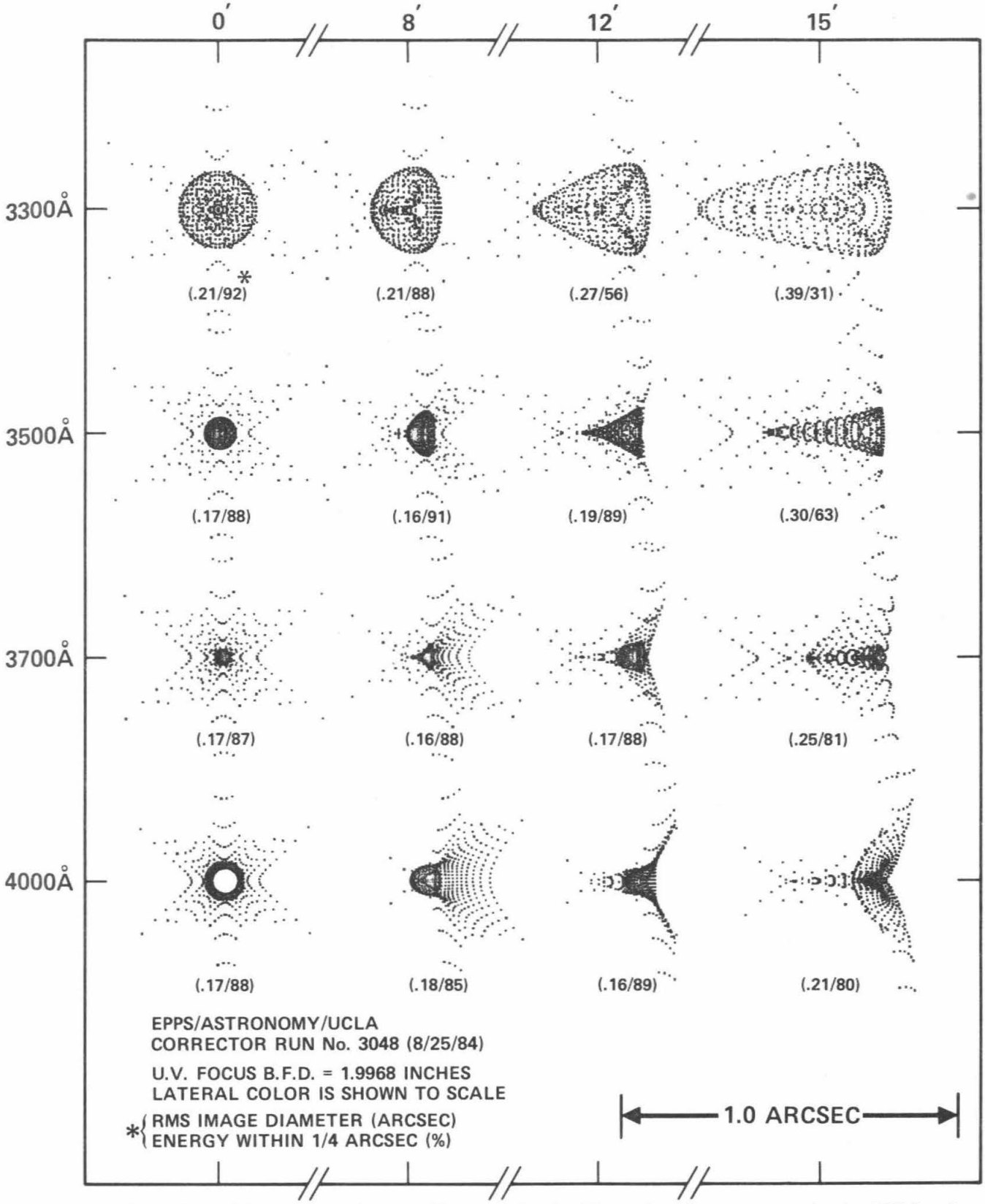

Figure 4-4a Monochromatic spot diagrams for the blue prime-focus camera in the UV band (ADC not included). The entrance-pupil mask is hexagonal with the same total area as the primary mirror. In this and the following figures, rms image diameter is defined as $[\frac{1}{N}\sum_i(\vec{r}_i-\vec{r}_o)^2]^{1/2}$ summed over all rays, where $\vec{r}_o$ is the center of gravity of the image and N is the number of rays.

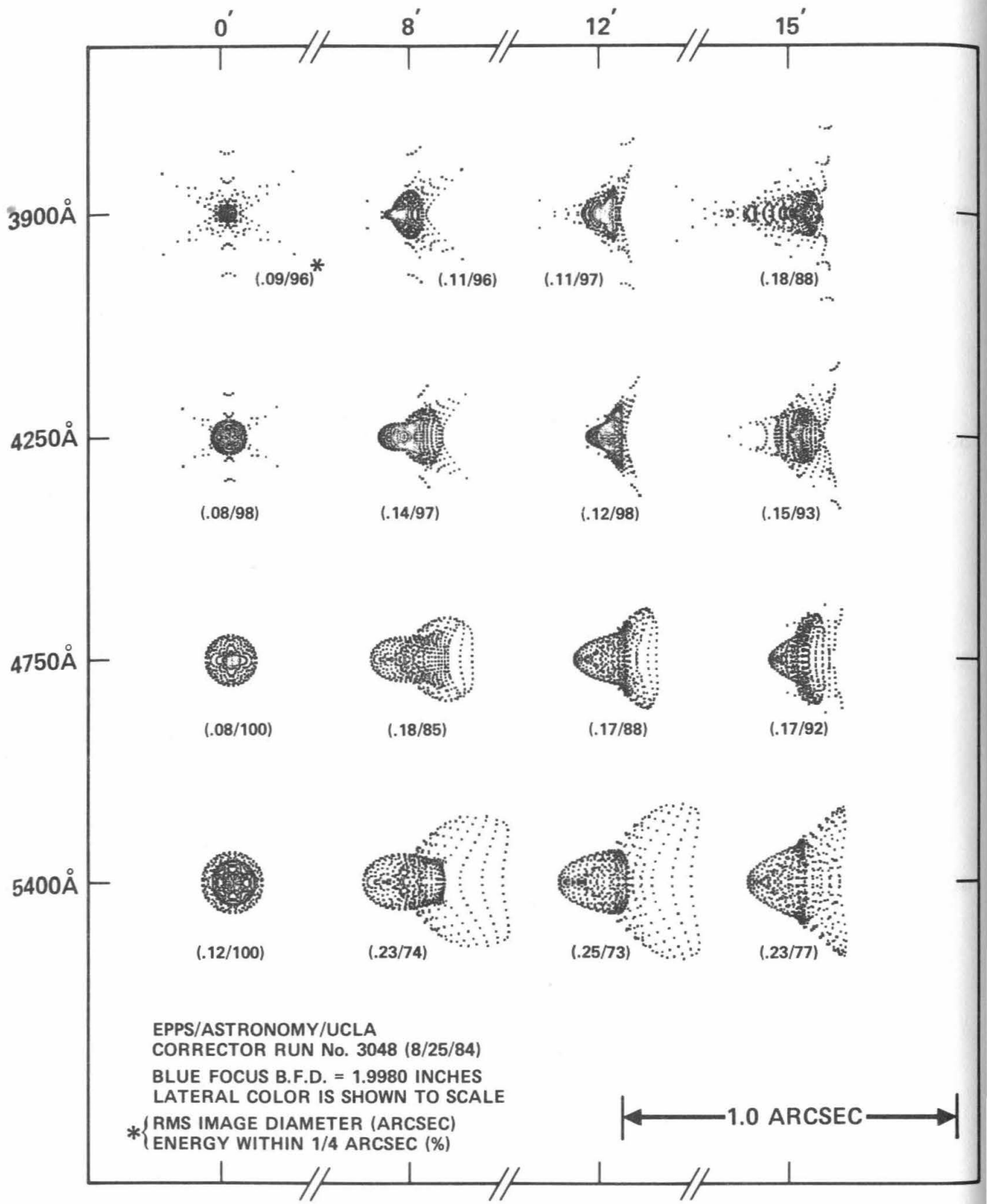

Figure 4-4b Same as Figure 4-4a for the J band.

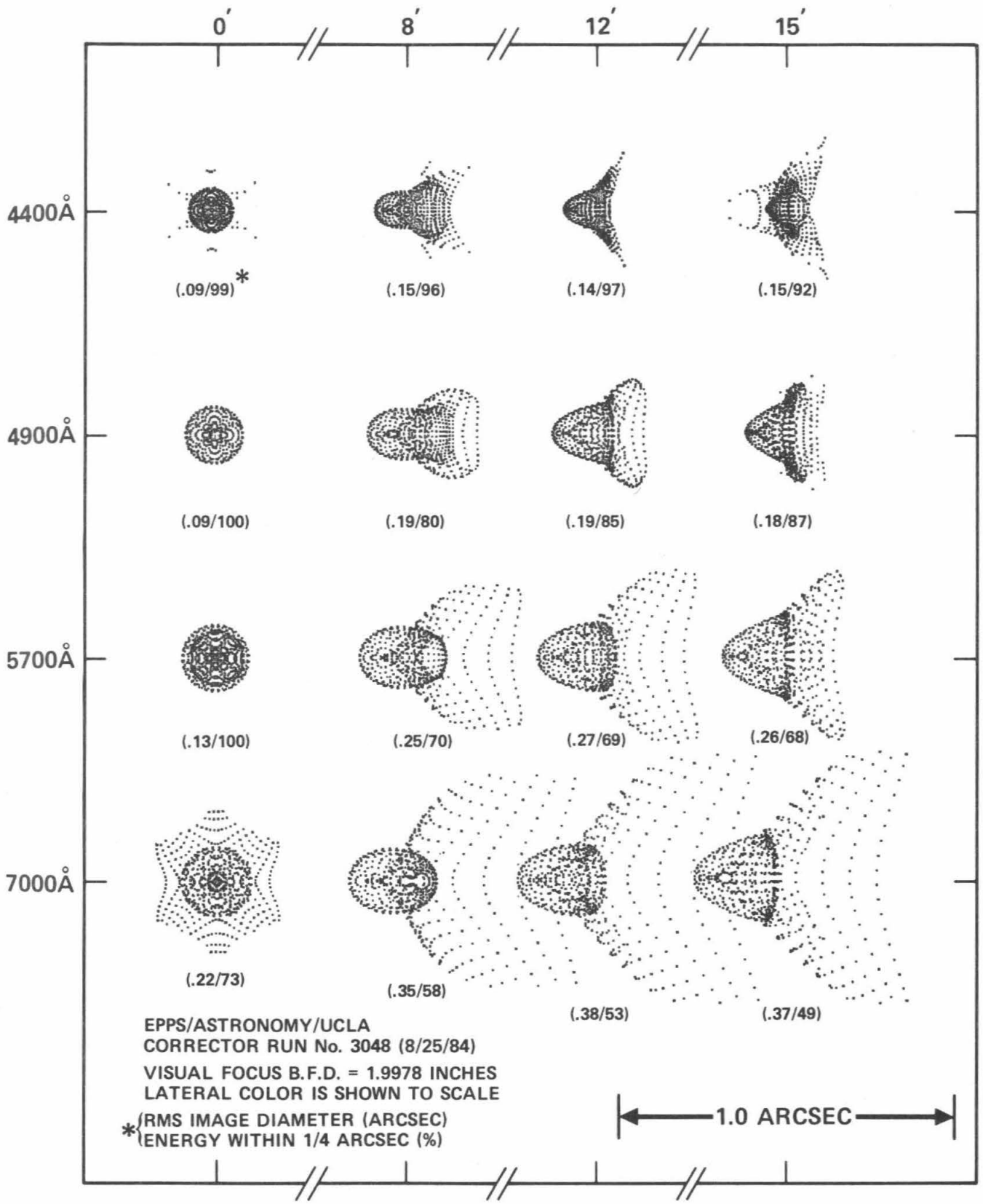

Figure 4-4c Same as Figure 4-4b for the V band. The spots at 0.70μm are included for information only, as the blue camera is not intended for use beyond 0.60μm.

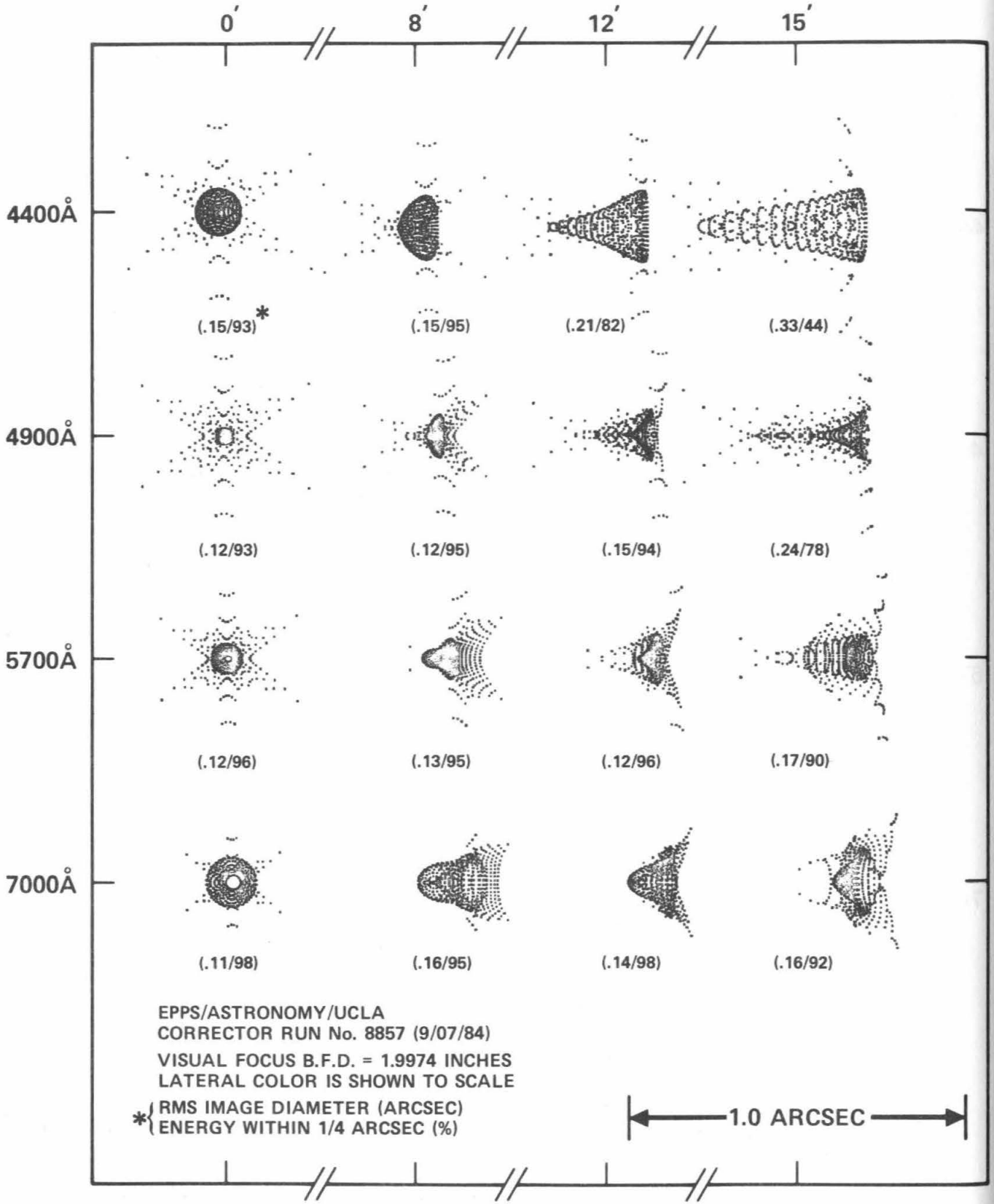

Figure 4-5a Monochromatic spot diagrams for the red prime-focus camera at short wavelengths. See caption to Figure 4-4a.

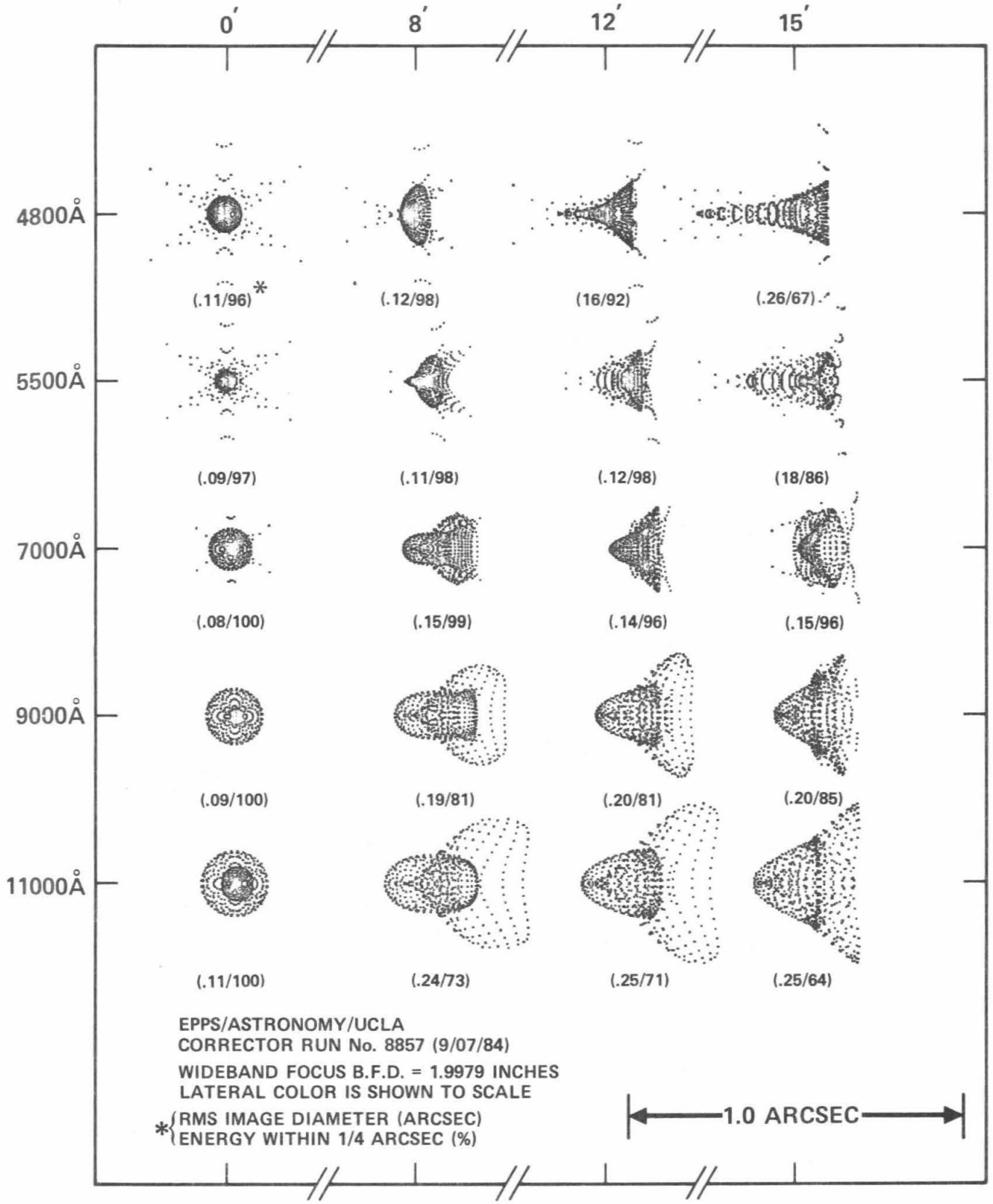

Figure 4-5b Same as Figure 4-5a at long wavelengths.

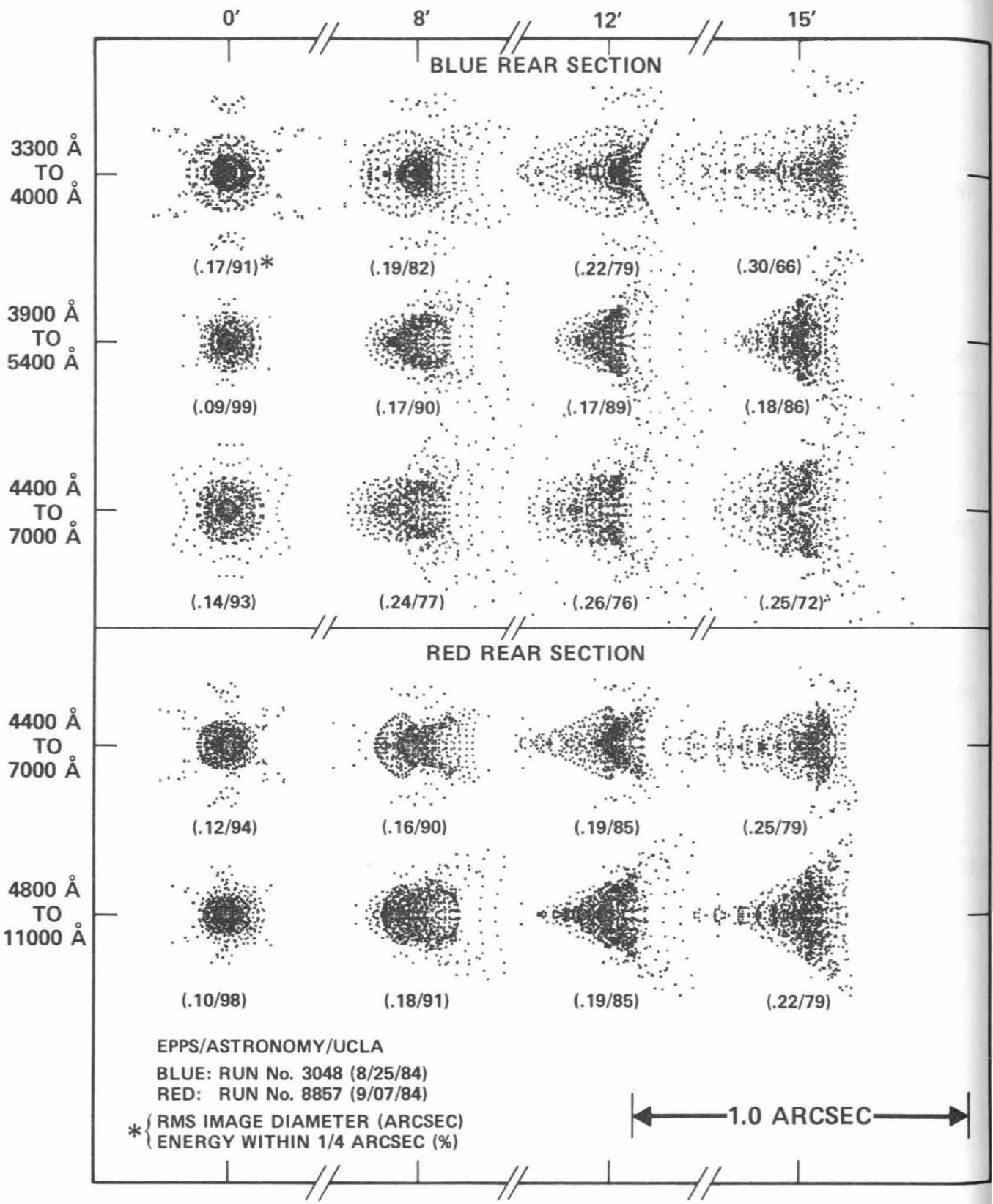

Figure 4-6 Superposed polychromatic spot diagrams for the blue and red cameras.

extreme ends of each wavelength range, and at the edge of the field of view. Reducing the bandwidths of an observation slightly below those shown will significantly reduce the aberrations.

Figure 4-3 shows the location of atmospheric dispersion compensation prisms in each camera. Each ADC consists of two crossed, zero-deviation prisms of crown and flint glass. The glasses are such that the *difference* in their dispersion curves matches atmospheric dispersion well over the relevant color range. Glass pairs were chosen to optimize this match, consistent with other criteria, such as ultraviolet transmission, availability of glass, and stability. The strategy of picking the glass pairs is described further by Epps (1984b).

The prisms operate from the zenith (bucking mode, full off) to a maximum airmass (additive mode, full on). Their success in removing atmospheric dispersion is shown in Figure 4-7, which shows (to scale) polychromatic images at the zenith, the spread in colors at maximum airmass, and polychromatic superposed images after compensation by the ADC. The success of the red ADC is particularly striking. It can operate to a maximum zenith distance of 3.8 airmasses and compensates over 3 arcseconds of atmospheric dispersion to within an accuracy of 0.25 arcseconds. The blue limiting airmass is 2.0.

The prime-focus cameras meet or nearly meet all the minimum wide-field imaging goals of Section 3.1. Based on the error budgets in Section 4.1, the cameras yield 0.56 arcsecond images (FWHM) within the inner 16 arcminute FOV and 0.57 arcsecond images (FWHM) over the remainder of the field for atmospheric seeing equal to 0.5 arcsecond FWHM. This estimate incorporates all known errors, including the primary mirror, camera fabrication and alignment, and very nearly meets the design goal of no more than 10% degradation of excellent atmospheric seeing. The bandwidth, ADC, and coating specifications have also been met. Still unexplored are slitless spectroscopy, a tolerancing study for fabrication and alignment errors, and an estimate of the location and brightness of ghost images.

The large diameter and deep curvature of the first element make it potentially difficult to support. A generic study of the deflections of meniscus lenses has been made by Iraninejad and Nelson (1984, TMT Report No. 135). Their results indicate that with the simplest edge support systems, induced deflections can amount to 400nm with gravity normal to the optical axis and 350nm with gravity along the optical axis. By use of a more sophisticated edge support however, they found that these deflections can be easily reduced by a factor of 10-100. Hence the deflections can be made sufficiently small to cause negligible optical distortions. It should be noted that lenses are fortunately much less sensitive to distortions than mirrors.

4.3 Nasmyth, Cassegrain, and Bent Cassegrain Foci

The second suite of foci are the Nasmyth, Cassegrain, and bent Cassegrain foci. For convenience, the optical goals are restated here based on requirements for multiple object and single-object spectroscopy in Section 3.1.

Multiple Object Spectroscopy

a. Excluding the effects of the atmosphere, all light is to fall within a 1 arcsecond diaphragm for images over a field of view (FOV) that must be a minimum of 10 arcminutes in diameter and preferably 30 arcminutes in diameter. A larger FOV would be desirable, but not at the expense of strong compromises on other aspects of telescope performance.

b. No requirement is placed on the f-ratio at this focus.

c. Atmospheric dispersion compensation (ADC) must operate over the entire field. It must maintain all light within 1 arcsecond up to 2 air masses. The minimum bandwidth is 0.33μm to 1.1μm without refocus.

d. The focus must have high optical and fiber transmission from 0.33μm to 2.5μm.

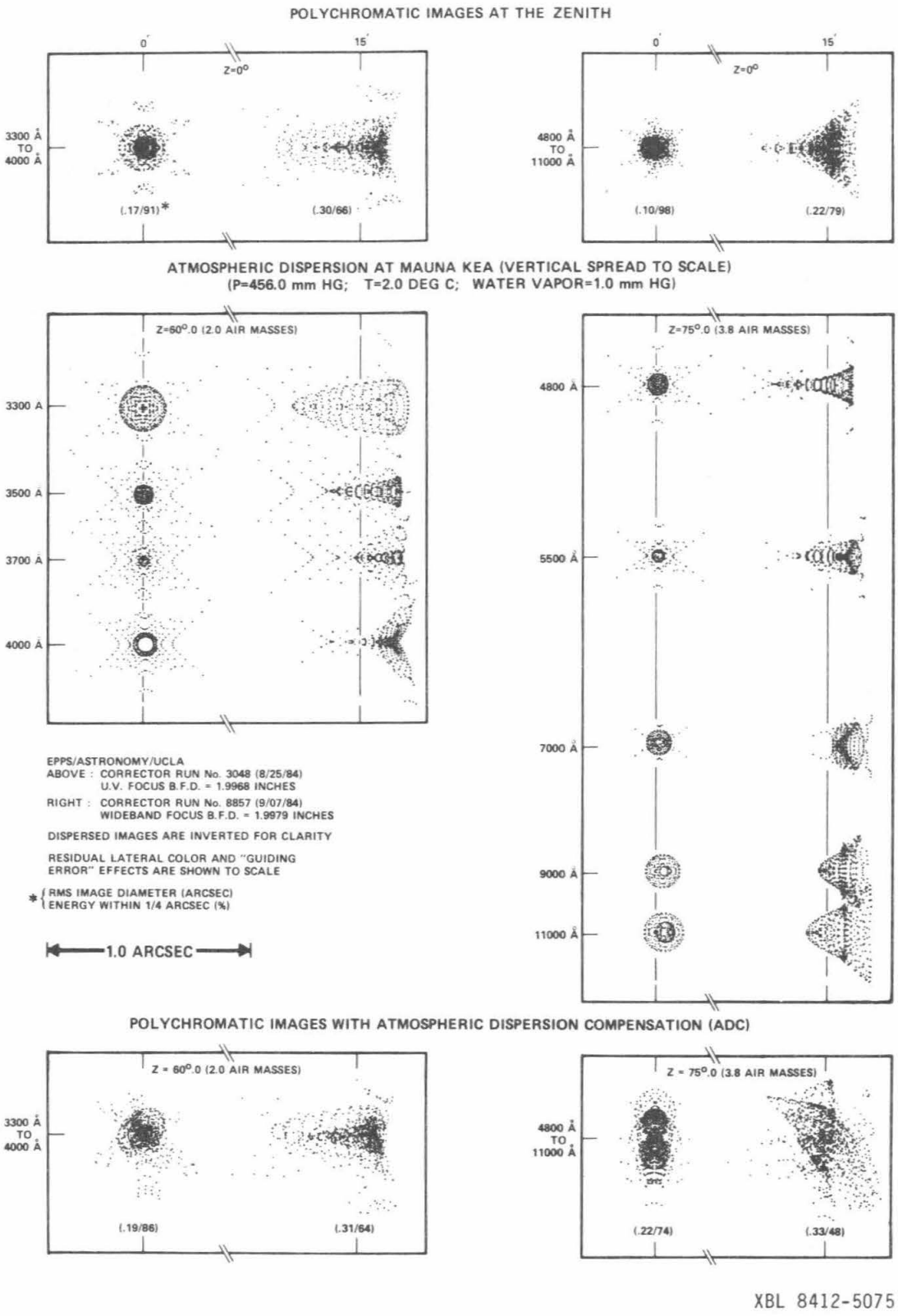

Figure 4-7 Atmospheric dispersion compensation (ADC) for the blue (left) and red (right) prime-focus cameras. The top panels show polychromatic superposed images at the zenith (prisms off). The middle panels show the effect of atmospheric dispersion to scale for the blue (2.0 airmasses) and red (3.8 airmasses). The bottom panel shows how well the polychromatic images are corrected by the ADC (prisms on). Camera aberrations are included in all spot diagrams.

e. A large, stable platform must be located adjacent to the MOS focal plane to mount MOS spectrographs.

f. Compensation for field rotation must be provided.

Visual Spectroscopy of Single Objects

a. Excellent image quality must be provided over a 3 arcminute FOV. The telescope should degrade the FWHM of the best atmospheric seeing by no more than 10%.

b. Large, stable platforms must be provided to accommodate high-resolution spectrographs. These must be thermally stable and offer optional light-tight enclosures.

c. At least one focus must be provided for a moderate resolution ($R = 10^3 - 10^4$) spectropolarimeter. The instrumental polarization at this focus must be less than 0.3% and stable to 0.1% over a single observing session.

Optically, all foci in this family are essentially equivalent. They are Ritchey-Chretien foci, with present plans currently calling for a final focal length of 150m (f/15.0). Image quality is limited by astigmatism, which varies quadratically with field angle. At the edge of the 20 arcminute fully baffled, unvignetted FOV, astigmatic image diameter is 0.5 arcseconds. Optimum input f-ratios for fiber-fed MOS are in the range 4.0-8.0 (Powell, 1983, Hill, Angel, and Richardson 1983). Speeding up the beam to this value could be accomplished using one of several lensing schemes described by these authors.

For lengthy spectroscopic exposures, some form of ADC is necessary to keep images under 1 arcsecond. Three ADC designs were investigated (Figure 4-8). These are based either on zero-deviation prisms, as were used at prime focus, or on finite-deviation prisms using a single kind of glass. The latter approach is possible at the Nasmyth (but not at prime) because of the slower beam and smaller angles of attack at the optical surfaces. Performance for one model of the former type (Model 3) and two of the latter (Models 1 and 2) is shown in Figures 4-9, 4-10, and 4-11. These figures show a layout of the focal plane with images placed in their proper relative locations. Each spot is a superposition of three colors (see inset at right) at the zenith and at 2.0 airmasses. A description of the aberrations and residual color errors is given in the figure captions.

Model 3 is a zero-deviation pair of LLF2 and FK5 prisms located 1.99m in front of the focal plane. It has several serious disadvantages, including the fact that it transmits poorly in the ultraviolet (see inset, Figure 4-8), it corrects only one focal plane, the residual color errors at 0.33μm and 1.1μm are substantial (Figure 4-9), and LLF2 is not ordinarily available in diameters as large as 0.97m.

Finite-deviation prisms introduce astigmatism that increases with airmass and prism wedge angle. This is visible as the horizontal and vertical "moustaches" for Models 1 and 2 in Figures 4-10 and 4-11. This effect is reduced if the prism is located farther from the focal plane, as can be seen by comparing Model 2, which is only 1.99m from the focal plane, with Model 1, which sits in front of the tertiary mirror and is 7.78m from the focal plane. Model 1 has been adopted because of its lower astigmatism and the fact that it corrects all N-C foci simultaneously. Its diameter (1.20m) is somewhat larger than that of Model 2 (0.97m), but fused silica is readily available as large as this. The larger cost is offset by the fact that only one is needed. Being silica, its transmission at all wavelengths is high, and it successfully corrects all wavelengths from the far UV to 1.1μm. No ADC is needed further to the red, as atmospheric dispersion at these wavelengths is very small. A moderate broad-band anti-reflection coating such as MgF will keep reflection losses to 2-3%. No high-efficiency coating is needed, as ghosts should not be objectionable.

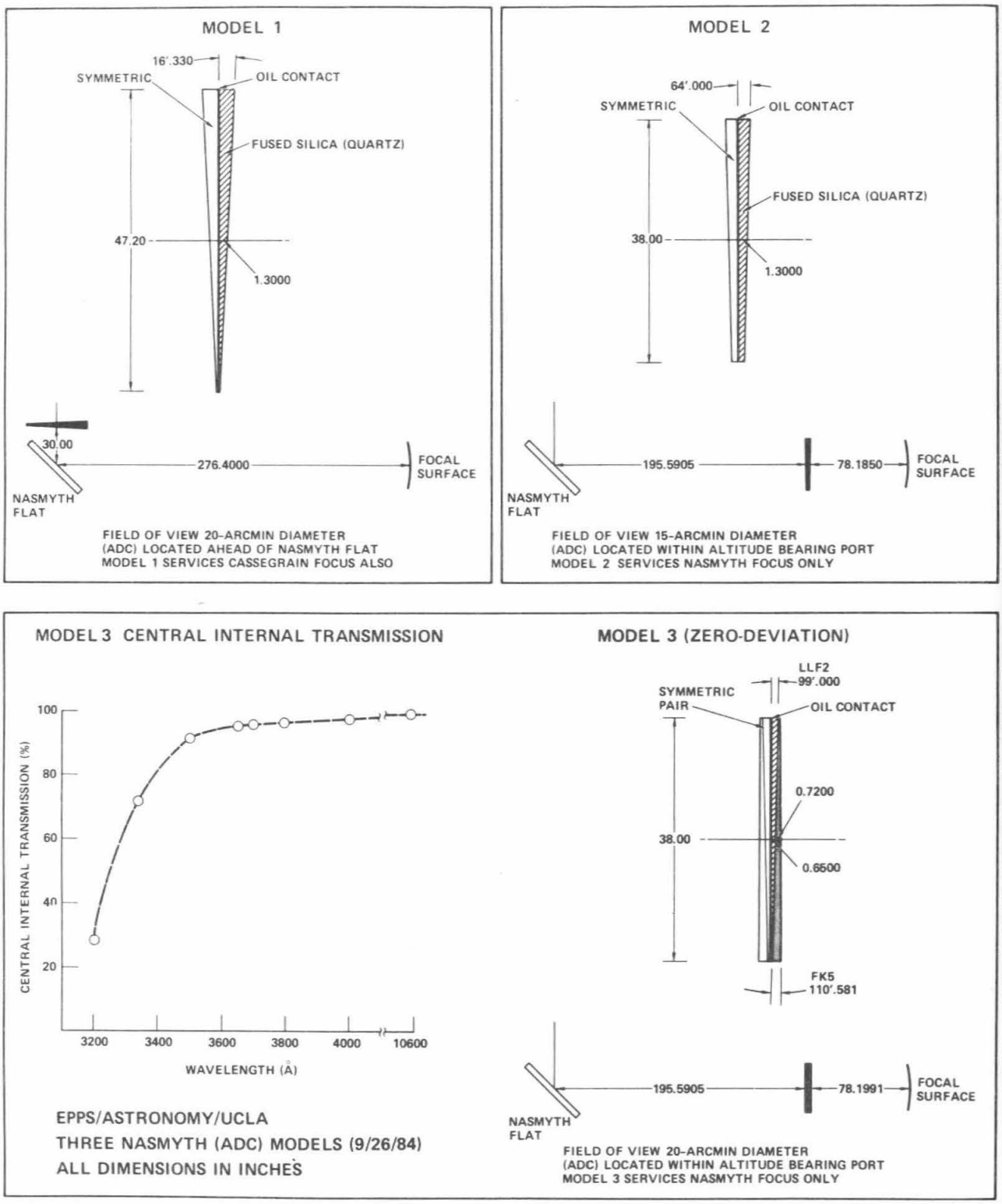

XBL 8412-5074

Figure 4-8 Three ADC designs for the Nasmyth-Cassegrain foci. Models 1 and 2 are finite-deviation designs using two prisms of fused silica. Model 3 is a zero deviation model using LLF2 and FK5. Model 1 is the preferred option for the TMT.

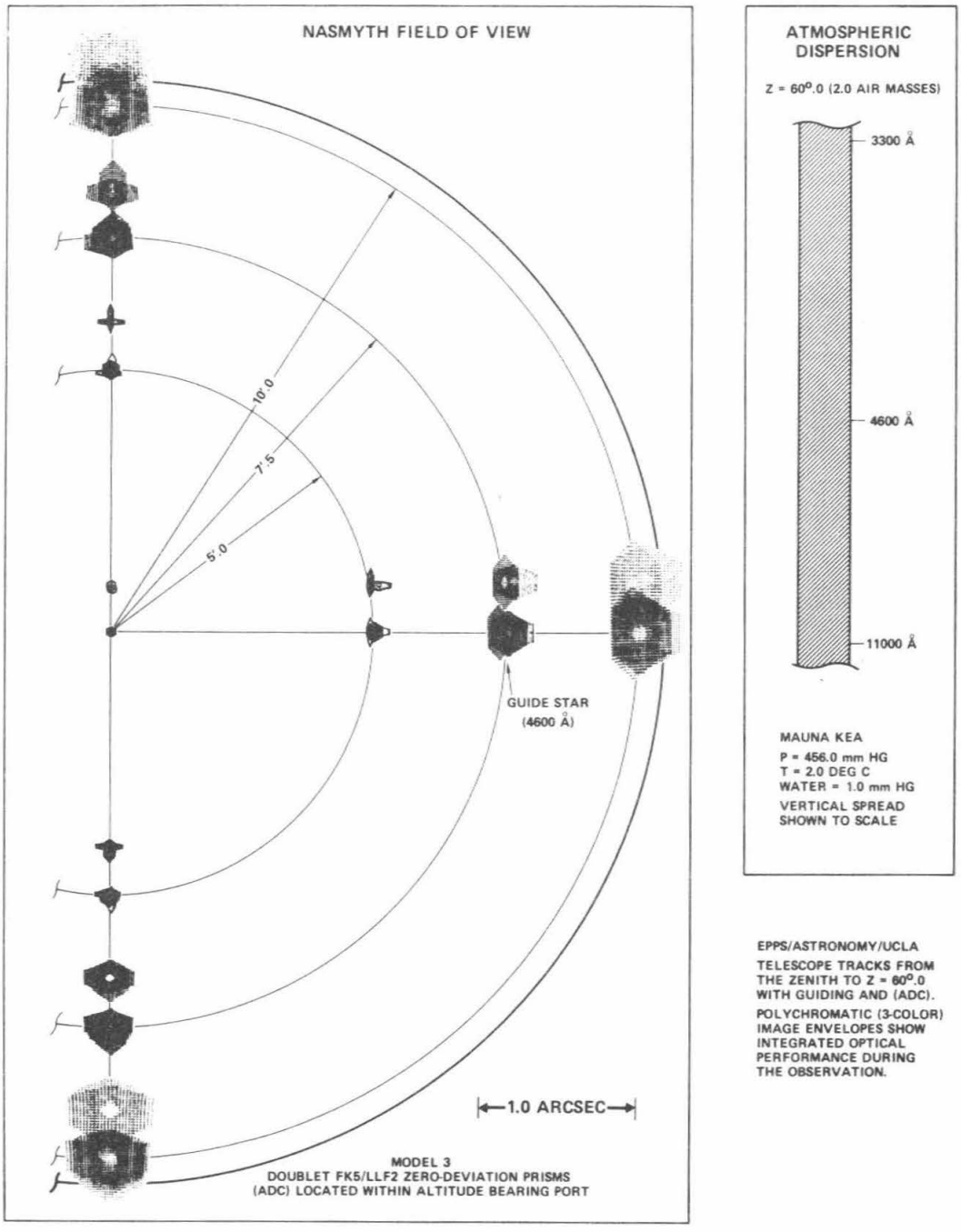

XBL 8412-5078

Figure 4-9 Optical performance of Model 3 ADC shown in the previous figure. The inset at right shows the magnitude of the atmospheric dispersion to scale at the design limit of 2.0 airmasses. The panel at left is a layout of the N-C focal plane with spot diagrams shown in appropriate locations. Each image is a superposition of images at the zenith and at 2.0 airmasses in the three colors shown (six spots in all). The three zenith spots superpose and are visible as the dense patch in the lower half of each image. Compensation at 2.0 airmasses is not perfect, with the result that the 0.33μm and 1.1μm spots superpose but lie slightly above the 0.46μm spot. Guiding was done at 0.46μm, so this spot overlies the image at zenith. The increase in monochromatic image size as (field angle)^2 is due to the off-axis astigmation of the R-C focus, which amounts to $\approx$ 0.6 arcseconds (O.D.) at 20 arcminute diameter FOV.

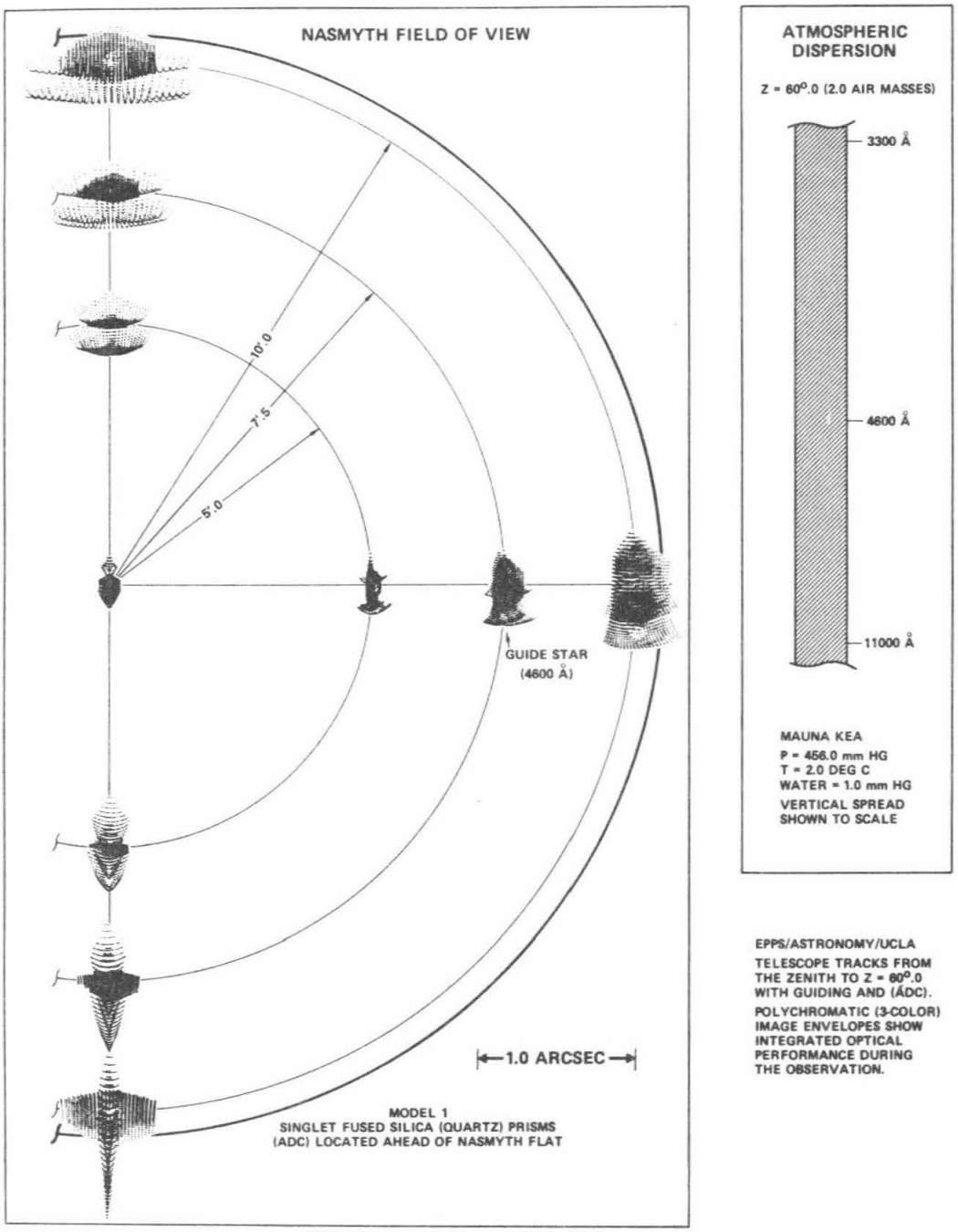

XBL 8412-5079

Figure 4-10 Same as Figure 4-9 for Model 1. A total of six spots (three at zenith, three at 2.0 airmasses) are again superimposed. In this model, the off-axis aberrations are a combination of R-C astigmatism (image at 3 o'clock) and astigmatism introduced by the ADC at 2.0 airmasses (horizontal and vertical "moustaches" in the 12 o'clock and 6 o'clock images). The image structure is most clearly

Figure 4-10 Same as Figure 4-9 for Model 1. A total of six spots (three at zenith, three at 2.0 airmasses) are again superimposed. In this model, the off-axis aberrations are a combination of R-C astigmatism (image at 3 o'clock) and astigmatism introduced by the ADC at 2.0 airmasses (horizontal and vertical "moustaches" in the 12 o'clock and 6 o'clock images). The image structure is most clearly seen in the 12 o'clock image. The dense hexagonal array on top is the zenith image, where all three colors superimpose. The moustaches are the 2.0 airmass spots, the two lower ones at 0.33μm and 1.1μm, and the upper one at 0.46μm. The length of the moustaches vary approximately as (airmass-1.0). The 0.46μm spot was again used to guide. Model 1 is the preferred choice for ADC.

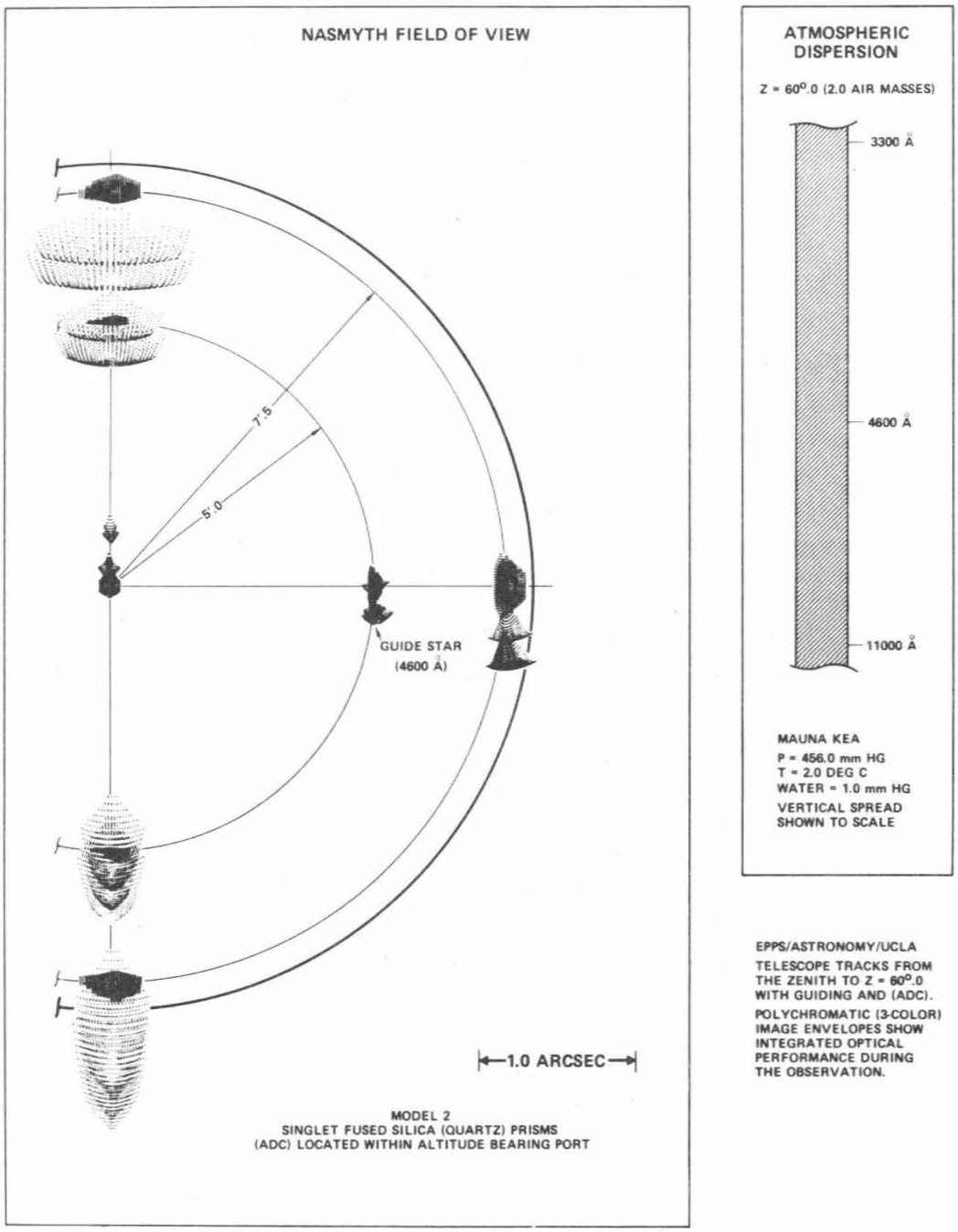

Figure 4-11 Same as Figure 4-10 for Model 2. See description in previous figure caption.

The focal planes at the N-C foci have a radius of curvature of approximately 2.18m. A characteristic of all two-mirror telescopes (when the secondary has magnification) is that the chief ray from the center of the exit pupil is not perpendicular to the focal plane (see for example Figure 4-14). This has adverse implications for fiber-fed MOS, and will mean that the mechanism for moving and holding fibers must also tilt them at an angle appropriate to their position off axis. Optical schemes to flatten the field or restore perpendicularity were considered, but were rejected as too complex and costly.

The N-C foci meet all the minimum requirements for MOS and single-object spectroscopy in Section 3.1. However, it is desirable to have a larger field for certain MOS projects. Field size could be increased somewhat by reducing the N-C f-ratio from f/15.0 to f/12.0. This option is discussed further below, after the IR focus is described.

4.4 Infrared Forward Cassegrain Focus

The optical goals for thermal infrared observations are repeated here from Section 3.1:

a. The telescope thermal emissivity must be as low and as stable as possible.

b. Image quality must be diffraction-limited at 10μm for chopping secondary throws of at least ± 20 seconds, over a minimum FOV of several arcminutes.

c. The polarization of both transmitted and emitted IR radiation must be low and stable. Residual polarized emission from the telescope as seen by the detector must be less than 1% over a single observing session. Instrumental polarization of transmitted IR light must be less than 0.3% and stable to 0.1%.

d. The chopping secondary must be able to chop at frequencies up to 30Hz and over focal plane chop half-angles of 2.5 arcminutes. At 30Hz we require the ability to chop with at least 80% duty cycle over a chop angle of ± 30 arcseconds. The secondary must be undersized such that the geometric projection of the secondary lies completely on the primary for chop half-angles up to 2.5 arcminutes. The shape of the secondary shall be such as to minimize light lost by the undersize dimensions.

e. Changeover from the thermal IR to other instruments (and vice versa) must be possible in 20 minutes or less. This includes the removal and installation of optical baffles.

f. Compensation for field rotation is required.

The strategy of the thermal IR focus is determined entirely by the need for a rapidly chopping secondary mirror to subtract the thermal background. Since high rates of chop up to 30 Hz are needed, the physical size of the secondary mirror must be kept small. However, in a Ritchey-Chretien telescope, one finds that image quality at f-ratios other than the R-C f-ratio is limited by coma. This coma is worse the more the final f-ratio departs from the R-C f-ratio. At the slow f-ratios appropriate for the IR, the comatic image diameter, θ_{coma}, is proportional to

$$\theta_{coma} \propto \theta F(1+K_1), \qquad 4\text{-}1$$

where θ is the radial field angle, F is the final f-ratio, and K_1 is the conic constant of the primary mirror (K_1 = -1.0037963 for R-C f-ratio = f/15). To maximize the IR FOV thus argues for the fastest possible f-ratio (or slower R-C focus), and hence for large secondary mirrors.

To help balance the conflict between small secondary size and fast f-ratio, the IR focus has been moved as far forward as possible. The nominal location is presently at the elevation axis, although this may be altered slightly as mechanical design of the tertiary and ADC mechanisms proceeds.

The infrared secondary mirror must be undersized so that the geometric projection of the secondary on the primary shall be contained within the perimeter of the primary for either chop or field half-angles up to the value θ_{chop}. For a hexagonal primary of edge length a_1, a primary to secondary spacing d, and primary vertex - focal plane distance e, a simple undersized hexagonal secondary mirror has edge length

$$a_s = \frac{d+e}{f} a_1 - d\theta_{chop}. \qquad 4\text{-}2$$

For f = 250m, e =-4m, d = 16.617m, and θ_{chop} = 2.5 arcminutes, we find a_s = 0.250m. Actually, throughput can be maximized further by giving the IR secondary a serrated edge. Current plans call for the design in Figure 4-12, which passes 91% of the light and has a maximum outer diameter of 0.528m. If made of light-weighted beryllium, this secondary weighs only 4kg and is expected to be small and stiff enough to chop rapidly. Additional remarks on the IR chopping secondary can be found in Section 7.11.

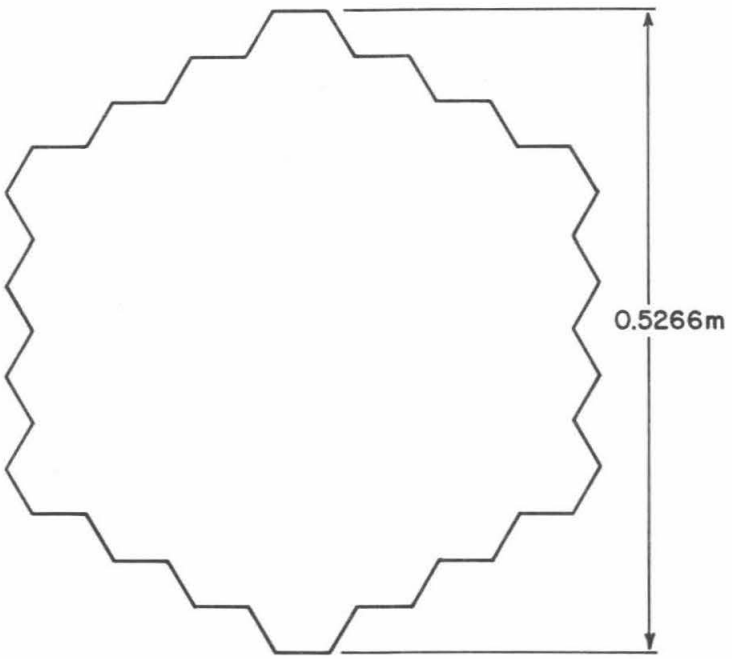

Figure 4-12 The f/25 (nominal) infrared chopping secondary mirror is shown. The mirror is undersized to allow ± 2.5 arcminutes of chop or ± 2.5 arcminutes field of view. The serrations match those of the primary and thus minimizes the loss of light due to undersizing. Only 9% of the light from the primary is lost.

The optical properties of the IR focus are summarized in Figure 4-13. The inset at top shows spot diagrams for the collimated telescope as a function of distance off axis. The upper line shows the off-axis R-C induced coma of the hyperbolic primary, the lower line the essentially coma-free images that would be produced by a classical parabolic primary. More important is how the images look in chopping mode, when the secondary mirror is tilted. These are shown in the lower position for chop half-angles of 20 arcseconds and 40 arcseconds. Chop-induced coma combines with R-C coma vectorially, with the result that net coma varies as a function of position in the field. Chop-induced coma scales roughly as (primary f-ratio)$^{-3}$ and thus is larger for the TMT than in existing telescopes. However, diffraction-limited images are provided over a 9 arcminute FOV for no chop, over a 6 arcminute FOV for a ± 10 arcsecond chop, and over a 4 arcminute FOV for a ± 20 arcsecond chop.

Technically, geometric spot diagrams are not applicable at 10μm, which requires a diffraction calculation. However, the above variation in image quality is undoubtedly real, and its impact on infrared observations is still under study. Present-day IR arrays have an exceedingly small FOV of only tens of arcseconds, within which the influence of R-C coma is completely negligible. Of more concern is the future use of fibers for IR multi-object spectroscopy, which could potentially cover a FOV of many arcminutes. As noted above, the maximum field of view for diffraction-limited images depends on the size of the chop. However, fiber-fed spectroscopy would presumably apply to objects of small angular extent, for which small chop angles might be suitable. Under these circumstances, a full 9 arcminute FOV is available, which is large by the current standards of infrared astronomy. However, the secondary described above will overfill the primary more than 2.5 arcminutes off axis. For a 9 arcminute FOV, a 0.508m diameter chopper is needed, which accepts only 85% of the light hitting the primary.

A major question yet to be addressed is the mechanical design of the chopping secondary, which must be able to chop in any direction to compensate for field rotation. Ordinarily this would be accomplished by chopping in one axis and rotating the entire mechanism. This solution will not work on the TMT, however, as the undersized IR secondary is hexagonal in shape to match the primary (Figure 4-12) and hence cannot be rotated. A two-axis chopper is therefore needed, which complicates the design. Infrared field-of-view requirements must also be balanced against the optical requirements for MOS. This issue involves the choice of the R-C f-ratio for the Nasmyth-Cassegrain foci, and is still under discussion. The various tradeoffs are described more fully in the Section 4.6.

4.5 Coudé Focus

Provision is included for an eventual coudé focus that will be located in the adjoining building. It will be used for large or massive equipment that cannot readily be used on the Nasmyth platforms. The focal length is 1000m (f/100), and the primary vertex - focal plane distance is 70m (Figure 4-14). Light reflects from a total of seven mirrors before reaching the coudé focus, so special high reflectivity mirrors will be needed to obtain appreciable throughput. The beam size with a 90 arcsecond FOV will require folding mirrors with semi-major diameters up to 1.2m. A description of the coudé focus room is given in Section 9.

4.6 Nasmyth-Cassegrain f-ratio

The above spot diagrams and calculations assume a nominal R-C f-ratio for the Nasmyth-Cassegrain foci of f/15.0 (focal length = 150 m). Discussions are still continuing as to whether this should be shortened to f/12.0 (120 m). Such a change would have the following advantages and disadvantages.

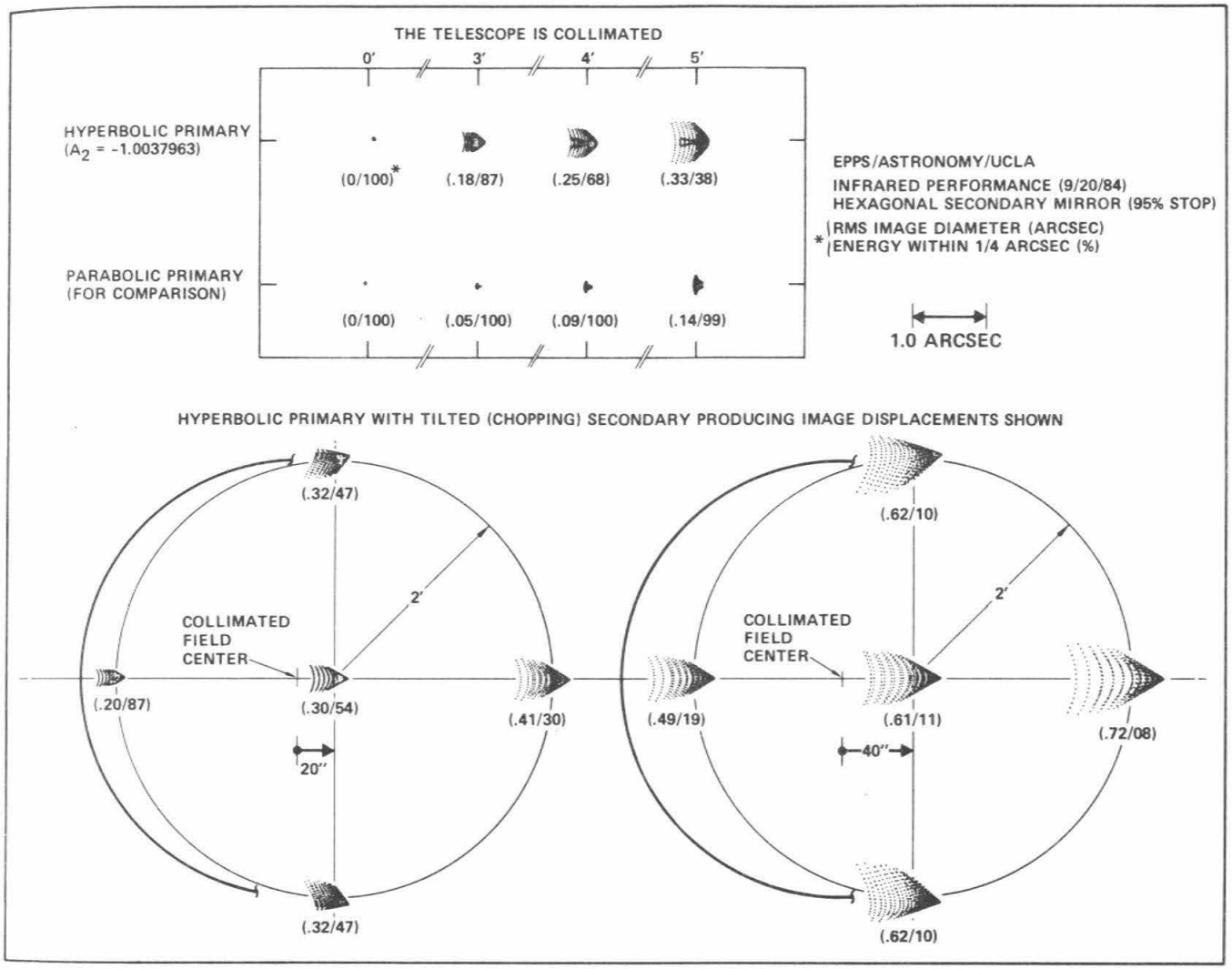

UC TEN-METER TELESCOPE: INFRARED PERFORMANCE IN COLLIMATED AND CHOPPING-SECONDARY-MIRROR OPERATING MODES

XBL 8412-5082

Figure 4-13 Image quality with and without chop for the f/25 forward Cassegrain infrared focus. The upper panel shows spot diagrams with the system collimated for the adopted f/15 R-C hyperbolic primary and for a parabolic primary for comparison. The field angle is field radius off axis. The lower insets show how the system performs for chop angles of ± 20 arcseconds and ± 40 arcseconds. Radially symmetric R-C coma adds vectorially with chop-induced coma to produce a variation in image quality over the field. Diffraction-limited performance corresponds roughly to the central image at lower left, with rms image diameter = 0.30 arcseconds (Faber and Nelson, 1982, TMT Report No. 57).

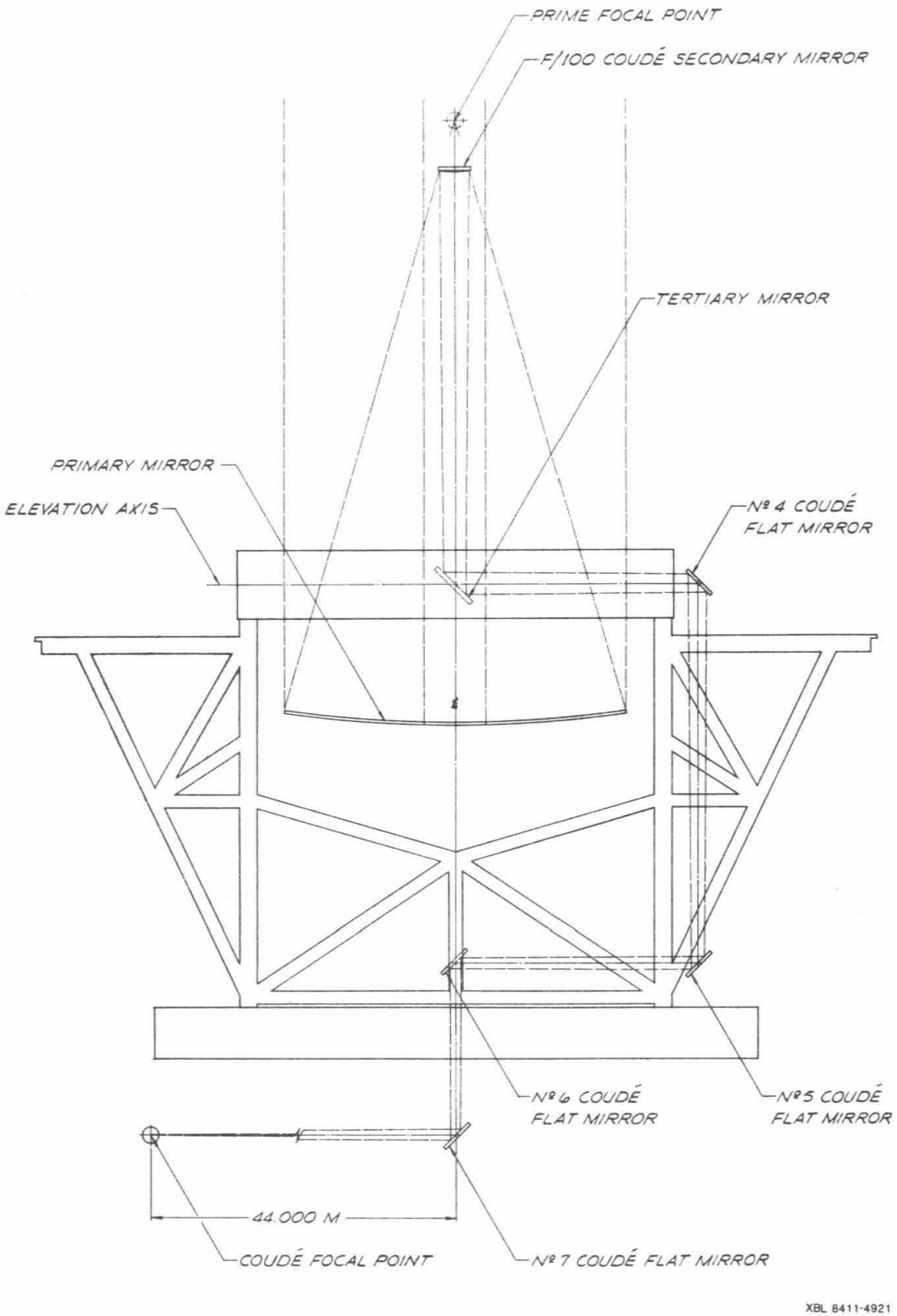

Figure 4-14 The optical path for the coudé focus is shown.

(1) The performance of the ADC at the N-C foci would improve at large airmasses. This is currently limited by astigmatism introduced by the prisms, visible as the "moustaches" in Figure 4-10. The length of this astigmatic image scales approximately as F^2, where F is the R-C f-ratio. A change to f/12 would shrink the "moustaches" by 0.64, giving better performance over the present 20 arcminute FOV. The total usable field would also increase somewhat, but not by a proportional amount. This is because, even without the ADC, the basic FOV is limited by off-axis R-C astigmatism. This already amounts to 0.6 arcseconds at 10 arcminute radius and varies with field angle as θ^2. R-C astigmatism is insensitive to final f-ratio and would be virtually the same at f/12.0 as at f/15.0.

(2) The focal length of all spectrograph collimator mirrors would shrink in the ratio 12/15, easing congestion on the Nasmyth platform.

(3) The deviation of the primary conic constant from -1 would approximately double. This would improve images in the prime-focus camera (Epps, 1985), but at this writing it is not know how big the effect would be.

Against these, there are two disadvantages:

(1) The diameter of the R-C secondary mirror would increase from 1.42m to 1.73m, and it would move farther forward by 0.53m. This would make it heavier, more costly, more difficult to handle, and more difficult to support.

(2) Off-axis coma at the f/25 infrared focus would increase owing to a more negative primary conic constant. This coma would approximately double, and the IR FOV for a ± 20 second chop would shrink from roughly 4 arcminutes in diameter (Figure 4-13) to 2 arcminutes.

These issues are still under discussion, notably the merits of having a somewhat better corrected and slightly larger optical FOV for MOS versus a substantially smaller infrared field.

5. Primary Mirror

Contents **Page**

5.1 Conceptual Design

Segmentation

The idea of constructing a large mirror from segments rather than from a single monolithic blank has been suggested many times in various contexts. Radio and millimeter wave telescopes have for many years had primary mirrors composed of panels or segments. In the optical regime the tolerances are more critical and there has been correspondingly less development. A review of some of the history of this idea has been described in a recent article about the Multiple Mirror Telescope (MMT) (Beckers *et al.*, 1981). The MMT itself is one approach to avoiding a single large mirror. At this time, the MMT is becoming increasingly effective, and its success as an idea is clearly established. Although the segmented design for the TMT shares the concept of using multiple optical elements to make up the primary mirror, in most details, the TMT design is radically different from the MMT. The TMT primary will act as though it is a single monolithic mirror, which distinguishes it from the MMT, in which each mirror acts as an independent primary mirror. It is the intention that except for certain special uses, the astronomer will be able to use the TMT as though it has a single ten-meter diameter primary mirror rather than the 36 segments that actually compose the mirror.

Classical primaries that consist of a single piece of glass have the advantage that the surface is guaranteed to be smooth and continuous and that, at least in principle, it can be polished in a fashion that takes advantage of its axisymmetric properties. On the other hand, scaling up a single mirror to larger and larger size becomes enormously costly, and ultimately becomes physically impossible. Since the optical goals are set by the wavelength of light, larger mirrors must have similar surface accuracy as smaller ones, thus the problems of support become increasingly difficult. Under the effects of gravity, the deflections of a plate under its own weight (a rough model of a mirror blank) scale with the diameter, d, and thickness, h, as

$$\delta = K\frac{d^4}{h^2} \tag{5-1}$$

Thus, as the mirror diameter grows, the thickness must grow even more rapidly-in order to maintain a constant level of gravity-induced deflections. As a result, the volume and weight grow at an even greater rate, soon leading to impossibly massive and expensive mirrors. To circumvent this problem, one must make the mirror thin, or at least have low mass per unit area. But thin mirrors are extremely flexible and fragile, and thus would require a sophisticated active control system to keep the mirror surface in the correct shape. Light-weighted mirrors are much more expensive than solid ones, and are not expected to be available in the size needed. Both on the basis of cost and availability, we find the options involving monolithic mirrors impractical for the TMT. We note, however, that dramatic progress has been made recently on the development of light-weight Pyrex mirror blanks, (Angel *et al.*, 1983a, b). Although Pyrex has a relatively large coefficient of thermal expansion ($\alpha = 3\times10^{-6}/°C$) compared to ceramic glasses ($\alpha=10^{-7}/°C$), it is hoped by these researchers that surface distortion can be avoided by adequate thermal control. In addition, the cost and complexity of handling and coating mirrors grows rapidly with size, hence smaller segments are preferred.

The approach taken for the TMT to avoid the problems of cost and availability for the primary mirror is to make the primary out of segments, the blanks for which are much smaller, and readily available. From Equation 5-1 one sees that the segments can be also much thinner than otherwise, leading to a great reduction in the weight of the primary. However, there are two major challenges that must be met in this design. First, the positions of the segments will have to be actively controlled to maintain the desired surface. This is evident since any support structure will suffer the same gravitational deflections as those of a monolith. Second, the segments must be polished so they are all parts of the same overall mother shape, and since each segment is a non-axisymmetric piece of optics, this fabrication procedure will be unconventional. These critical subjects will be discussed in detail in this chapter.

Segmentation Geometry

We have selected the segmentation geometry shown in Figure 5-1, which shows a plan view of the 36 hexagonal segments as they would appear to a star. There are many possible types of segmentation that could be considered, with hexagonal arrays and annular rings of wedges being the most common. Annular rings are quite common as the geometry of the surface panels in radio telescopes, but the hexagonal pattern has several advantages for our application. Since the mirror material will be expensive, the hexagon's more efficient use of material over a trapezoid is notable. Even with a modest-sized segment, the passive support of each segment is difficult. For a given thickness, the hexagon is more easily supported without undue gravitational deflections. Finally, the control system that we employ takes natural advantage of the hexagonal configuration. Additional discussion of these geometries is given in a Kitt Peak National Observatory study (Shack 1977). Since segmented mirrors are of interest in various space projects, the topological alternatives have been discussed in this literature as well. A recent study by Perkin-Elmer investigating segmentation for a proposed NASA project, the Large Deployable Reflector, discusses segmentation in some detail (Swanson *et al.* 1982).

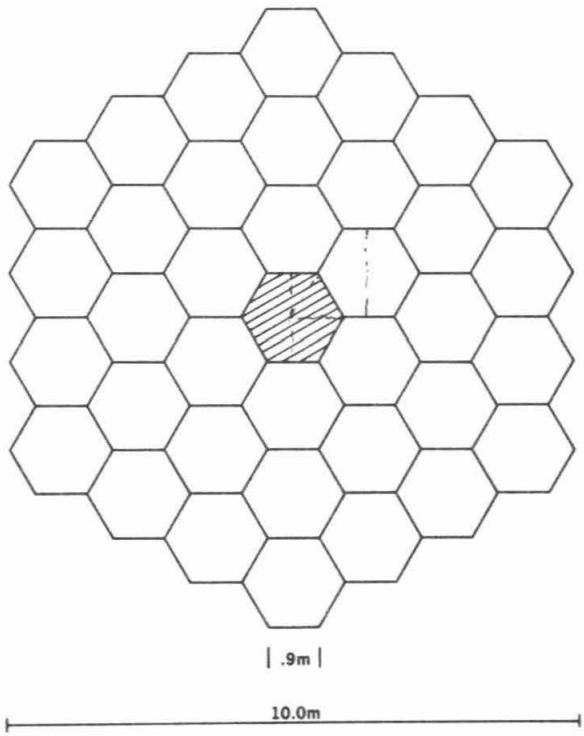

Figure 5-1 The geometry of a segmented primary mirror showing three rings of hexagonal segments. The segment edge length a is 0.9m.

Number of Segments

Having selected the shape of the segments, the size and number must be selected. The arguments favoring smaller segments include the following:

1. The mirror material cost will be reduced since modest sized blanks are less expensive per kg.
2. The segments can be much thinner since their stiffness varies as h^2/d^4. This reduces material cost. The weight of the primary varies as h or as d^2 assuming the stiffness is held constant. Since the telescope weight tends to follow the weight of the primary, the overall cost is reduced.
3. The passive segment support system (both axial and radial) can be simplified by letting the segment stiffness increase rather than holding it constant through reducing the thickness.
4. The individual segment surfaces will more closely approach a sphere, and thus be easier to polish. The deviations from a sphere largely vary as d^2.

5. The tolerances on the passive alignment of the segments are relaxed, leading to easier assembly and fewer thermal problems. The tolerances largely vary as d^{-2}.

On the other hand, the following arguments favor making the segments as large as possible:

1. The number of optical elements to be fabricated is reduced.
2. The number of active control components (sensors, actuators) is reduced, promising greater reliability and economy.
3. The computational power needed for active control is reduced.

These tradeoffs are also discussed by Nelson (1980, TMT Report No. 41). After investigating the relative costs and complexities of these issues, the 36-segment geometry was selected. In our view, the uncertainties over control are the main arguments against more segments. At this point we have no strong assurance that the four-ring geometry with 60 segments is appreciably worse with respect to cost, and we actually expect that in the future, when experience and confidence in the control system is better, the more finely segmented geometry will be preferred. For the TMT however, our desire to simplify the control system as much as possible has led us to select 36 segments.

The selection of 36 segments and the requirement of a 10m diameter equivalent aperture sets the size of each segment. Each segment is a regular hexagon (when viewed from infinity) with a side length $a = 0.900$m. The area of each hexagon is $(3)^{1/2}3a^2/2 = 2.104\text{m}^2$. The total area of the array is 75.8m^2.

Rigid Body Control

A mirror or mirror segment, is a flexible body, and its shape, as well as its position, are candidates for active control. When one considers large, thin monolithic primaries, active control of the mirror shape is an important consideration, and we expect that in the future, thin monolithic mirrors in the 5m to 7m range will have some active control over the surface shape in order to allow their use and to simplify the passive support system.

For the TMT we have chosen to implement the segmented idea in its simplest form, in which the segment position is subject to active control, but its shape is set in fabrication, and its passive support is designed to maintain this desired shape. Thus, only the six degrees of freedom that are needed to define a rigid body in space need to be controlled. With this decision the control system is greatly simplified. This of course makes more stringent demands on the fabrication and support of the segments.

Active and Passive Degrees of Freedom

When treated as a rigid body, each segment in a segmented mirror has six degrees of freedom. We characterize these as piston, rotation about two axes in the segment plane or "tilt" rotation about the normal to the segment, and finally, radial and azimuthal motion of the segment center in the surface of the primary mirror. For the relatively slow focal ratio of the TMT, only the first three motions (piston and two tilts) are in need of active control. The remaining three motions are assumed to be passively constrained by the rigidity of the support structure. An analysis of the thermal and gravitational deformations of the support structure for the Ten Meter Telescope (Nelson and Mast, 1980) shows that the expected small motions in the passively controlled degrees of freedom do not appreciably degrade the image quality. A schematic drawing of the active and passive support structure is shown in Figure 5-2. The passive degrees of freedom are controlled by a central post-diaphragm assembly and an azimuthal restraint assembly. Both assemblies couple the segment to the support structure via flexible elements which allow motions in the active degrees of freedom. The post couples to the segment via a thin flexible steel diaphragm and the azimuthal restraint through a thin rod. This post-diaphragm and azimuthal restraint are described in Section 5.9. The active degrees of freedom are controlled through three actuators attached to the back of each segment. Each actuator is coupled to the mirror via a whiffletree that serves to distribute the gravitational load to 12 points on the back of the mirror. The central post and three actuators are all parallel to each other and parallel to the normal to the segment surface at the center of the segment.

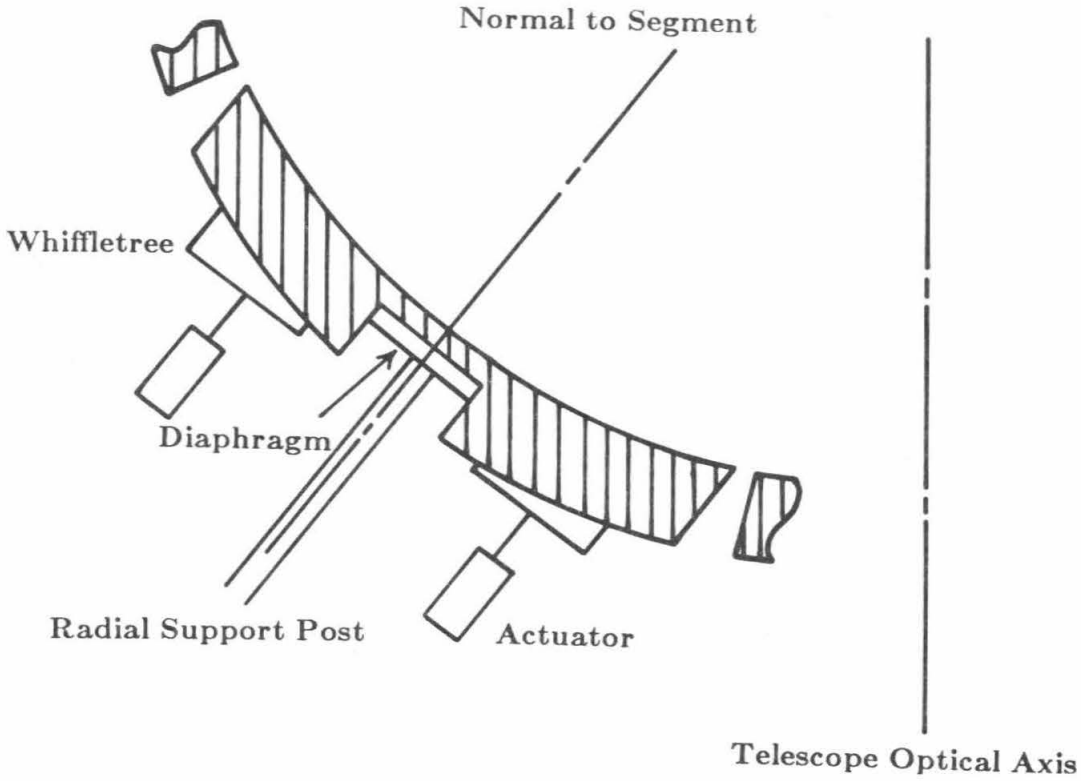

XBL 852-1262

Figure 5-2 Schematic showing the geometry of the elements supporting a segment. Whiffletrees and actuators carry loads parallel to the segment normal. A central diaphragm and post carry loads in the plane perpendicular to the segment normal. The sides of the hexagonal prism, the actuators, and the radial support post are all parallel to the segment normal.

Active Control System

The active control system contains three major components: 1) a system of sensors to measure the relative positions of the segments, 2) a computer and global control algorithm that uses the sensor information to calculate the desired positional changes in the segments and sends commands to, 3) a system of actuators that re-position the segments in response to perturbations. We expect slow perturbations of the segments to occur from thermal changes and gravitational loading changes of the support structure. We expect faster perturbations to occur from wind forces on the segment.

5.2 Active Control Sensing System

Sensing Systems

Two basic approaches to the measurement of the active degrees of freedom are possible. First, one can measure the relative positions of the segments using light from celestial sources, either from the astronomical object of interest or from nearby objects. Second, one can use a secondary reference system, and then periodically check this secondary system using starlight. Although the first method is clearly more fundamental, it may at times be inconvenient. When the object under study is extremely faint (which is usually the case) there may not be enough

light to continuously measure the segment positions. Alternatively, if one relies on using a nearby star, this may be impossible when the object of interest is in a particularly dark and starless region of the sky, when one is observing in the daylight hours, or in times of full moon. Because of these limitations, we selected a secondary reference system. It operates continuously, operates independently of the objects in the field, and operates both night and day. If the secondary system could be designed to have great stability, then a direct reference to starlight would be a very occasional procedure.

In the past segmented mirrors have used a variety of secondary reference systems for sensing the segment orientations. Systems located at the center of curvature using interferometric sensing of the mirror figure have been successful (Crane 1969). However, to limit the size of the telescope structure, we have avoided requiring access to the center of curvature. Other techniques employing light beams reflected from the mirror surface are possible, such as the system initially planned for the MMT (Sanger *et al.,* 1972, Reed, 1979) or the absolute distance interferometry system of Gillard *et al.,* (1980,1983a). However, since many astronomical measurements require extremely low background light levels, we felt it advantageous to avoid shining any light on the mirror surface. Given these considerations we devised a sensing system that monitors the segment positions without using the front surface.

Sensing the Back Surface

For the TMT we have chosen a secondary reference system that measures the positions of the backs of the mirrors rather than the front surface. This has the advantages that 1) there is no light scattering from the optical surfaces and 2) there are no interfering devices such as cube corners in the optical path. However, it is essential that the back of the segment is a reliable measure of the front surface. Since thermal effects are the main potential source of a difference between front and back, the segments need to be made from a material having a very low thermal expansion.

Because we are using a secondary reference system it is necessary to initially align the system, using starlight from a convenient source. Since we can do this, it is not necessary to know the absolute relationship between the back of the mirror and the front surface. This can be calibrated to give the information needed to hold the front surface in the desired location. Methods of initially aligning both the passive and the active degrees of freedom are described in Section 5.9. Thus the active control system described here is actually an active surface stabilization system.

Electronic Stiffness

In practice the control system will have a finite bandwidth. For external perturbations that occur on a time scale long compared with the control system response time, the system will effectively keep the segments in their desired positions to within the noise level of the sensors and actuators. Thus when low frequency perturbations occur, the mirror cell supporting the segments will deflect as a result, but the mosaic of segments will act as though it is perfectly rigid. This will be the case for gravitational and thermal effects and we expect this to be true for most wind perturbations as well.

Within the constraints imposed by the bandwidth of the control servo system, the primary mirror acts as though it is infinitely stiff. This electronic stiffness replaces the mechanical stiffness that conventional thick monolithic mirrors rely upon. This replacement of mechanical stiffness by electronic stiffness is a fundamental concept in understanding the primary mirror of the TMT.

Edge Displacement Sensors

The sensing system designed for the Ten Meter Telescope employs sensors mounted at the edges of the segments, with each sensor bridging the gap between two segments and measuring the relative displacement of the adjacent edges normal to the front surface. All of the sensors are identical in design and they are mounted on the backs of the segments. We have designed a

sensor that measures the relative displacement by measuring a capacitance that is directly proportional to the relative displacement. Early designs and tests of prototypes of this sensor are described by Gabor (1979, 1980, TMT Reports No. 12, 36). A recent detailed description is given in Mast *et al.* (1983, TMT Report No. 107).

The sensors are located (two per intersegment edge) at the positions shown schematically in Figure 5-3. Each sensor is a distance e from the segment vertex. For the TMT $e = 0.1$m. The sensors are on the backs of the segments and each sensor bridges the gap between two segments. Also shown in the inset to Figure 5-3 are the locations of the three actuators on a circle of radius t, where for the TMT $t = 0.47$m.

The number of sensors for a given number of rings of hexagons is

$$N_{sensors} = 18N_{rings}^2 + 6N_{rings} - 12 \qquad (5\text{-}2)$$

Table 5-1 lists the number of control components for arrays with 2, 3, 4, and 5 rings of hexagons.

Table 5-1
Numbers of Control Elements

	Number of Rings			
	2	3	4	5
Segments	18	36	60	90
Actuators	54	108	180	270
Sensors	72	168	300	492

A schematic elevation view of a single sensor is shown in Figure 5-4. A "body" assembly is attached to one segment and a "paddle" assembly is attached to the other. The height displacements are determined using a simple capacitance difference measurement. Two capacitors are formed by plating rectangular areas on the body assembly and larger plated surfaces on the top and bottom of the paddle. For a properly aligned sensor the height difference is measured along a "sensor center line." This line passes through the primary mirror center of curvature and passes through the point between the centers of the capacitor rectangles. The sensor paddle should be very close to being perpendicular to this line. (The exact angle is chosen to minimize the size of lookup table corrections for thermal and gravitational perturbations.) The height of the point at which the paddle plane intersects this line defines the sensor output. The location of the height difference measurement is offset from the edge of the segments by a distance L, typically a few centimeters. Figure 5-5 shows schematically the orientations of the sensors, including the offset. The sensors on each edge are offset in opposite directions.

By design, the sensor is insensitive to displacements of the segments in the plane of the mirror and to any rotation or tilt about the center of the sensing capacitor. The relative displacement of the segments only along the "sensor center line" is sensed. A hinging of two segments about the gap between them thus gives a reading proportional to the lever arm distance L.

The hexagonal geometry has a natural interlocking character. This is illustrated in Figure 5-6, which shows a vertex where three segments meet. If the back two segments (A and B) are correctly oriented with respect to each other, the measurements from the four displacement sensors shown can be used to calculate the orientation of segment C, which is indented between the two. Segment piston is sensed equally by all four sensors. Rotation (tilt) about a line parallel to the line adjoining the centers of the segments A and B is measured by sensor differences. In particular, tilt of the segment C is measured by using the segment's stiff lever arm to convert positional information to angular information. The dimensions a and e define the lengths of two lever arms proportional to $a - 2e$ and $a - e$ for tilts in two directions. This keystone effect operates between all the segments. In principle this single calculation could be used

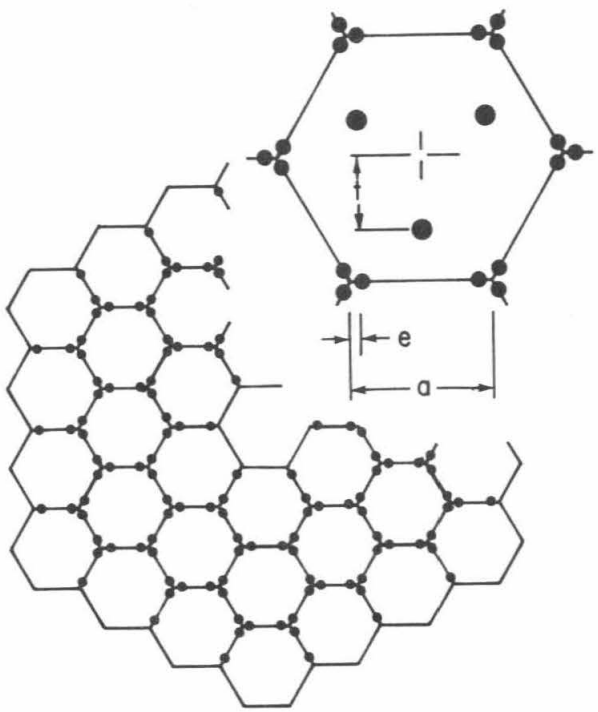

XBL 817-2396

Figure 5-3 The positions of the displacement sensors used for measuring the relative orientations of the mirror segments. The segment edge length is a, the locations of three actuators on a circle of radius t are shown in the insert, and the sensors are located a distance e from the segment vertex.

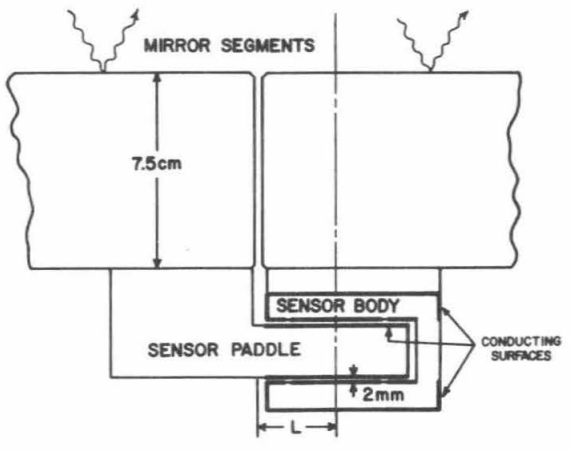

XBL 838-10932

Figure 5-4 Schematic of a sensor (elevation) showing the body assembly and paddle assembly on the back of the segments, with the capacitive sensing region offest from the mirror edges by a distance L.

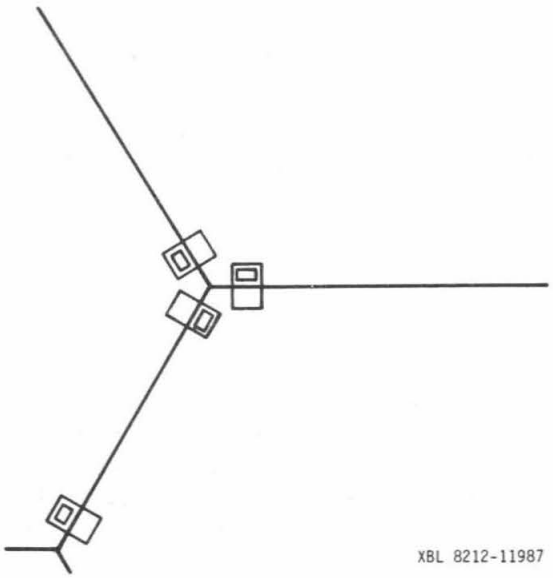

Figure 5-5 Schematic showing the relative orientations of the sensors with their sensitive points offset from the segment edges.

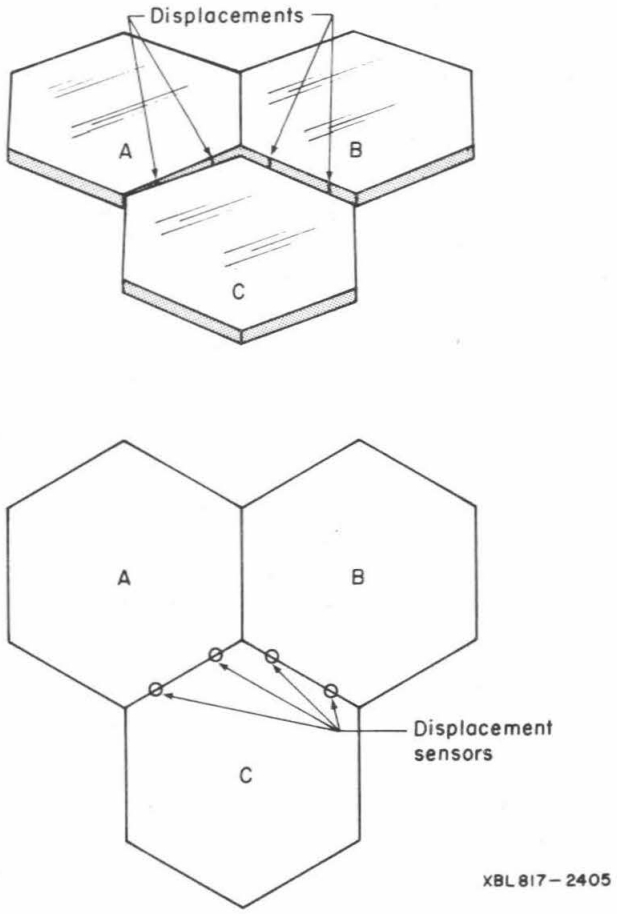

Figure 5-6 Schematic plan and oblique views of three mirror segments illustrating the displacement measurements made by the sensors. If segments A and B are fixed, then the measurements can be used to determine the piston and tilt of C with respect to A and B.

repeatedly from vertex to vertex to calculate the relative orientations of all segments in the array. In practice all of the sensor information is used simultaneously in a global fit, as described in Section 5.3.

In summary, the system geometry is defined by the four dimensions a, e, t, L and the number of rings N_{rings}. For the TMT $a = 0.9$m, $e = 0.1$m, $t = 0.47$m, and $L = 0.06$m (Mast and Nelson, 1984, TMT Report No. 80)

5.3 Active Control Algorithm

The control algorithm uses the sensor readings to determine the actuator motions needed to adjust the segment orientations in response to perturbations from the wind, temperature changes, and changes in the gravitational loading. We emphasize that the control system does not provide the initial alignment of the segments. In the present analysis we assume the initial alignment has been achieved, and the control system described here is used to maintain that alignment. A method for making the initial alignment and phasing is described by Oliver (1983, TMT Report No. 102).

There are $3N_{segments}$ degrees of freedom (3 per segment) that require active control. Three of these simply define the overall orientation of the primary mirror as a whole, and these can be defined by simply locking three of the actuators. Thus there are $3N_{segments} - 3$ degrees of freedom defining the relative orientations of the segments. The system of displacement sensors measures all of these degrees of freedom.

Since there are many more sensors than actuators, the system is highly redundant. Approximately two extra sensors per mirror provide both increased precision and stability. The redundant sensors also allow cross checks of sensor performance during the operation of the telescope. In addition they provide the extra information needed so that individual sensor failures do not disable the system.

For purposes of this discussion, and without loss of generality, we assume that when the mirrors are initially correctly oriented all of the sensors read zero. (In practice one will analyze the difference between the measured value and the desired one.) Perturbations then change the orientation of the segments and generate non-zero sensor readings. In the geometrical optics limit (zero wavelength) each segment of the paraboloid will make its own focal spot and the final image will contain $N_{segments}$ individual spots. Without perturbations or errors these will all superpose to form a single stellar image. With perturbations and errors a distribution of spots will be formed and the rms radius of this distribution is one measure of the image quality and control system performance.

The segment-sensor system is a complex coupled array, and all sensors contribute some information about the orientation of each segment. Thus the calculation of the desired motion of the actuators relies on solving a set of coupled linear equations using all of the sensor measurements. We use a least squares minimization technique to use optimally all of the information contained in this set of equations.

A sensor's reading is given by the difference in the heights of segments at the sensor's location.

$$s_j = z_{body} - z_{paddle} \tag{5-3}$$

Although in general the mirror assembly is curved, for ease in describing the algorithm we assume the mirrors form a flat surface in the x,y plane. We assume that the actuator motion is normal to the segment surface, and that when the segments are in their desired ideal positions all the actuator lengths are zero. Thus $p_{ij} = 0$, where $i = 1,2,3$ refers to the three actuators on segment j (Figure 5-3) and $j = 1,N$ refers to the N segments. Non-zero values of p_{ij} give rise to an error surface, where the height of the error surface at a point x,y is given by

$$z_j = \alpha_j x + \beta_j y + \gamma_j t \tag{5-4}$$

where

$$\alpha_j = \frac{1}{3t}(2p_{1j} - p_{2j} - p_{3j})$$

$$\beta_j = \frac{1}{\sqrt{3}t}(p_{2j} - p_{3j}) \tag{5-5}$$

$$\gamma_j = \frac{1}{3t}(p_{1j} + p_{2j} + p_{3j}).$$

So we see that in a system with no noise the expected reading on each sensor is linearly related to the lengths of only the actuators on the two mirrors that the sensor bridges.

$$s_j^{exp} = \sum_n A_{jn} p_n \tag{5-6}$$

where s_j^{exp} is the expected reading of the j^{th} sensor and p_n is the n^{th} actuator length. The matrix A_{jn} is defined by the geometry (a,e,t,L) and has $(N_{sensors} + 3)$ x $N_{actuators}$ elements. The extra three rows of the matrix provide constraining equations to define the overall orientation of the primary. These three constraining equations can fix any three linear combinations of the actuators.

The A matrix is sparse, that is, most of its elements are zero. Each sensor's reading is defined by the orientation of the two segments that the sensor bridges. Thus it depends only on the lengths of the six actuators on the two segments, and all but 6 elements of every row of the A matrix are zero.

The chi square is then defined

$$X^2 = \sum_j \frac{(\sum_n A_{jn} p_n - s_j^{meas})^2}{(\sigma_j)^2} \tag{5-7}$$

where s_j^{meas} are the actual measured sensor readings and σ_j their expected rms errors. The set p_n which minimizes chisquare is the solution to $N_{sensors} + 3$ coupled linear equations. The exact solution is found by effectively inverting A and has the form

$$p_k = \sum_n B_{kn} s_n^{meas}, \tag{5-8}$$

where the matrix B is completely defined by the geometry (a,e,t,L) (see Figures 5-3 and 5-4) and the σ_j. The matrix B does not depend on the s_n^{meas} or p_n. In principle, one finds the matrix B from A and σ_j just once for the system. Then to find the actuator motions needed to correct any perturbation (either real or due to noise), one takes the measured sensor values and performs the matrix multiplication indicated by Equation 5-8. A more complete discussion of the control algorithm is given by Mast and Nelson (TMT Reports No. 64, 80, and 107, and TMT Technical Note No. 46).

Focus Degree of Freedom

As noted above there are $3N_{segments} - 3$ degrees of freedom which define the relative orientations of the segments. One of these differs in character from the remaining. This is the "focus" degree of freedom. Changes in this degree of freedom lead to changes in the overall focus of the image. Unlike the remaining $3N_{segments} - 4$ degrees of freedom this mode depends strongly on the sensor dimension L for its measurement.

The geometry of the focus mode is most easily understood by imagining first an array of flat hexagonal segments lying in a plane. A focus mode distortion is induced if all the segments are tilted and lowered so that all their centers touch a common mathematical spherical surface, that is the array is "drooped" over a sphere. With this spherically symmetric distortion every set of three segments meeting at every vertex has the same geometry; the three segments form a triangular pyramid with each of the three segment normals tilted away from the vertex by the

same angle. The geometry of this focus mode is such that every segment forms the same dihedral angle with respect to all its adjacent segments. In this distortion adjacent segments are simply "hinged" with respect to each other, leaving all the edges aligned. If the displacement sensors are made such that the offset distance L is zero, then they will be insensitive to the hinging motion and will not change their reading with the hinging. Thus this spherically symmetric distortion of the primary mirror is not measured by an array of displacement sensors with $L=0$. If L is non-zero then the hinging of the segments about the crack between them causes a displacement at the center of the capacitor given by the product of the lever arm L and the hinging or dihedral angle ω. Again, it is the sensitivity of this mode on L that distinguishes it from all the others. Since L is typically only a few centimeters, this displacement is much smaller than that caused by the much longer lever arm motions shown in Figure 3. Thus the measurement of the focus mode by one sensor is not very precise. However, the information from the large number of sensors provides an adequately precise measurement of the focus mode.

5.4 Active Control System Image Quality

An extensive study has been made of the effects of sensor noise, actuator noise, and sensor systematics on the image quality of a segmented primary mirror by Mast and Nelson (1983, TMT Report No. 80). We briefly summarize some of those results here.

To describe the control system performance we characterize its quality by two parameters. First, we calculate the rms image radius (arcseconds) using geometrical optics. The image radius is primarily due to the errors in the tilts of the segments. Second, we characterize the phasing of the segments by an rms surface error, S_{rms}. For observations in the infrared, where near diffraction limited performance may be achieved, the correct phasing as well as the tilt of the segments is important. Noise in the sensors and actuators generates tilt and phasing errors and thus a primary mirror surface which differs from the ideal one. The difference between the ideal and achieved surface is an error surface. To characterize the surface roughness, we define the rms surface error, S_{rms}, to be the rms deviation of the error surface about its mean.

$$S_{rms}^2 = \int_{array} (z_e - \overline{z_e})^2 \frac{dxdy}{\int_{array} dxdy} \tag{5-9}$$

where the error surface is

$$z_e = z_{ideal} - z_{achieved} \tag{5-10}$$

and the integral is over the area of the full primary.

Even without perturbations of the segments, the sensor drift and noise will cause the control program to move the actuators and degrade the image from the ideal. Electronic noise in the sensors, σ_s, and electronic noise and roughness in the actuators, σ_a, will both contribute to image blur and mirror surface roughness. Since the actuators and sensors are independent, their contributions will add in quadrature. Based on the geometry of the focus mode we expect the focus contribution to be only slightly correlated with the contribution from all the other modes. Thus we can calculate those contributions separately and combine them in quadrature. This is confirmed by a computer analysis (Mast and Nelson, 1983, TMT Report No. 80). The image radius and the surface error can thus be written in terms of the different contributions as follows:

$$\theta_{rms}^2 = i_o^2 \left(\frac{\sigma_s}{a-2e}\right)^2 + i_1^2 \left(\frac{\sigma_s}{L}\right)^2 + i_2^2 \left(\frac{\sigma_a}{t}\right)^2 \tag{5-11}$$

and

$$S_{rms}^2 = s_o^2 \left(\frac{a}{a-2e}\right)^2 \sigma_s^2 + s_1^2 \left(\frac{a}{L}\right)^2 \sigma_s^2 + s_2^2 \left(\frac{a}{t}\right)^2 \sigma_a^2 + s_3^2 \sigma_a^2 \tag{5-12}$$

Here i_o and i_1 are the non-focus and focus contributions of the sensors to the image and i_2 is the actuator contribution to the image. The corresponding contributions to the surface error are given by the s_o, s_1, and s_2 and s_3. We have included explicitly here dimensional scaling so that all the i and s coefficients are dimensionless. Since the image depends on angles only, the errors scale as the rms error divided by a lever arm. For the actuators this lever arm is t, and for the focus mode, L. For the non-focus degrees of freedom, the geometry is complicated because there are many lever arms. The shortest of these is $a-2e$, and thus one might expect this to dominate the errors. This assumption is confirmed by the computer analysis described below, and the forms of the scaling in Equations 5-11 and 5-12 are good to a few percent. The coefficients i_o, i_1, s_o, s_1, and s_3 depend on the number of rings and segments. These coefficients have been calculated with good agreement using both analytic methods that are based on the array geometry and computer analysis. The results for systems with 2, 3, and 4 rings are given in Table 5-2.

Table 5-2
Image Radius and Surface Error Coefficients

	Number of Rings		
	2	3(TMT)	4
i_o	3.33	3.44	3.59
i_1	0.405	0.362	0.344
i_2	2.31	2.31	2.31
s_o	2.01	2.60	3.42
s_1	0.162	0.205	0.252
s_2	0.527	0.527	0.527
s_3	0.315	0.324	0.328

Using the coefficients in Table 5-2 and Equations 5-11 and 5-12 we can calculate the effects of sensor and actuator noise for arrays with the dimensions for the Ten Meter Telescope and assumed sensor and actuator noise levels.

$$\sigma_s = 10\text{nm} \qquad \sigma_a = 10\text{nm}$$

$$a = 0.90\text{m} \quad t = 0.47\text{m} \quad e = 0.10\text{m} \quad L = 0.06\text{m}$$

Table 5-3 gives the contributions and total image radius and surface error.

Table 5-3
Image Radius and Surface Errors

	Number of Rings		
	2	3(TMT)	4
θ_{rms}(arcseconds)	0.020	0.019	0.019
S_{rms}(μm)	0.037	0.047	0.059

Assuming the errors are Gaussian, 80% of the flux from a point source would be contained in a diameter $\theta(80\%) = 2.54\theta_{rms}$. For $N_{rings} = 3$ with sensor noise alone of 10nm, $\theta^s(80\%) = 0.041$ arcseconds and $S^s_{rms} = 0.045\mu$m. For actuator noise alone of 10nm, $\theta^a(80\%) = 0.026$ arcseconds and $S^a_{rms} = 0.0106\mu$m.

An important and encouraging feature of this result is the stability of θ_{rms} as the number of rings increases.

5.5 Sensor Specifications and Tolerances

From the previous sections we see that, in principle, the mosaic of segments can be controlled using information from displacement sensors. In practice, various limitations exist on their successful use.

The sensor readings taken on the back of the segment may not represent accurately the front (optical) surface. For this to be true, one must use a dimensionally stable material for the segments and sensors. We will use a glass ceramic material (for example, Zerodur by Schott Optical Technologies) with a thermal expansion coefficient $<1\times10^{-7}/°C$. For our thin segments, temperature differences between adjacent segments of 1°C will cause differential thickness variations of under 10nm. Neighboring segments may also have different coefficients of thermal expansion. Such differences are expected to be $< 5\times10^{-8}/°C$. If the operating temperature is different than the temperature during sensor calibration, a temperature dependent error will result. The temperature at the telescope site (see Section 7) is within $\pm4°C$ of the mean 90% of the time. This will introduce apparent sensor errors $<$ 20nm. This type of error can be readily removed by use of a calibrated lookup table.

The TMT optical error budget calls for an 80% energy diameter of 0.32 arcseconds (see Section 3). The effect of sensor noise is expected to be quite small. If the sensors were allowed the entire error budget, we could allow σ_s = 80nm. Based on prototype sensors the sensor noise is equally set by digitization noise and electrical noise to give $\sigma_s = 1.4nm$. Systematic effects in the sensor are expected to be much larger. Thermal and gravitational effects are expected to require corrections of tens of nanometers. Both of these will be largely removed using calibrated lookup tables. Slow temporal drifts are also expected at the level of 10-20nm. These can be removed by periodic recalibration of the sensors.

The segment alignment procedures will be simplified if the segments can be accurately tilted over angles of about 5 arcseconds. This requirement implies the sensors should have an accurate linear operating range of about 20μm, if they are to tilted independently. If the "tilts" are introduced by defocus of the array, a range of only about 1μm is needed. Assembly of the sensors on the segments to an accuracy of $\pm20\mu$m may be difficult, therefore an even larger operating range could ease the construction and assembly. In addition, adjustment of the position of this range will ease the construction of the sensors and their assembly on the segments. Capability for a discrete but very stable electrical offset with a range up to $\pm20\mu$m is desired to meet these needs. Prototype sensors described in Section 5 have this capability.

Since the mirror cell will undergo gravitational deflections of up to 0.6mm, a mechanical sensor range in excess of this is desired. We selected a capacitor gap of 2mm. A larger gap increases the sensor noise and fringe field effects. A smaller gap increases the chance of damaging a sensor in the event of extreme actuator motion.

The three "passive" degrees of freedom per segment were ignored in the previous description of the control algorithm. Since these motions will not be completely eliminated, it is crucial that small perturbations in these directions not degrade the sensor or the system performance.

To make the sensor insensitive to relative body-paddle motions in the paddle plane, one must ensure that no electrical fringe fields can see the paddle edge. A grounded guard plane on the sensor body will greatly reduce fringe fields. Further reduction can be obtained by making the paddle larger than the body by an amount large compared to the capacitor gap.

System performance may be affected if these "passive" motions cause the sensor readings to change even though no surface figure change occurs. It is essential that the sensors be designed, built, and aligned to make them insensitive to these motions. The sensitivity to these motions are described in detail by Nelson (1980, TMT Report No. 32). In the remainder of this section we summarize those results.

Sensitivity to Paddle Shape

We described in Section 5.2 how the sensors and the interlocking nature of the hexagonal segments are used to determine and thus control the two tilt and the focus or piston degrees of freedom of the segments. That description assumed the segments were fixed in their other degrees of freedom; the effects of motions of the segments in the mathematical surface of the global paraboloid were not discussed. Here we address the sensitivity of the control system to those motions. We first assume that the sensor is perfectly aligned; that is, the paddle is parallel to the mirror surface directly above it as defined in Section 5.2. We consider the effects of paddle misalignment below.

To understand the system behavior under outside influences, such as thermal changes that cause the spacing between segments to change, we begin with a simplified example of a flat segmented array as shown in Figure 5-7a. It is clear that in this case motion of the segments in the plane of the flat mirror will not change the imaging characteristics of the mirror surface. The sensor paddles will not move along the sensor center line as a result of this motion; hence there will be no change in the sensor output.

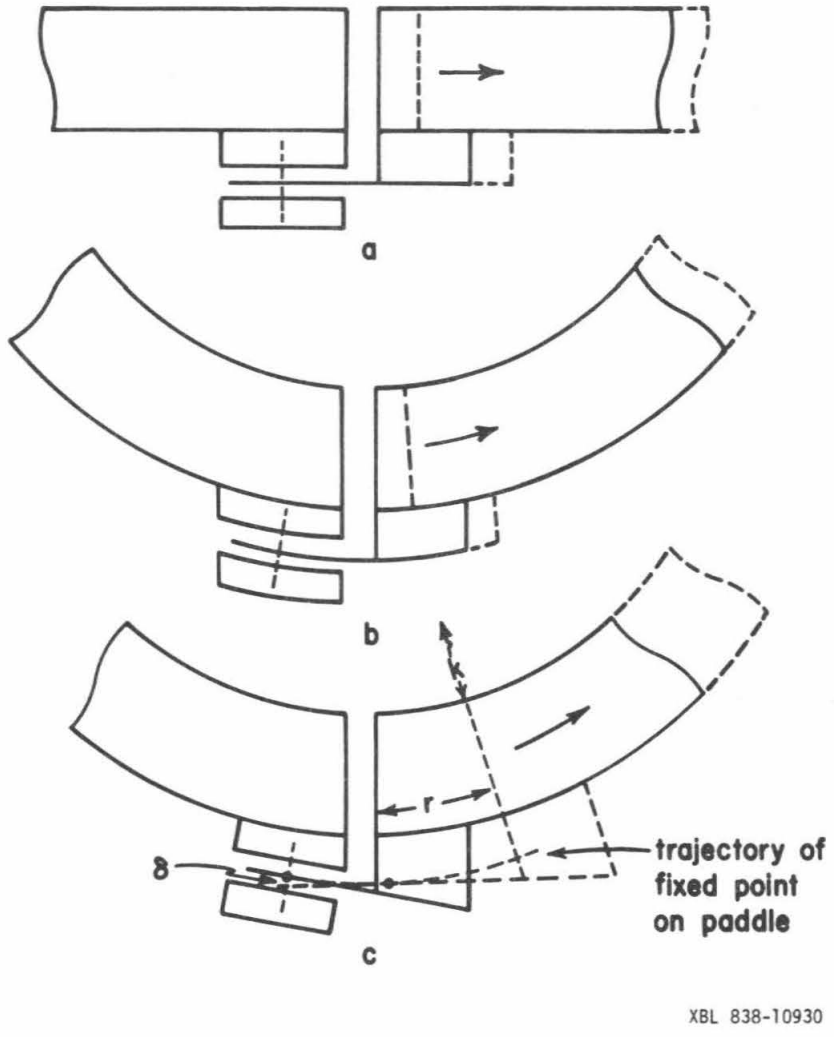

Figure 5-7 Illustrations of the sensitivity of the sensor to in-plane motions of the segments for various paddle shapes. Figure a illustrates a hypothetical flat mirror, b shows the sensor for a hypothetical spherical mirror and paddle, and c illustrates a spherical or parabolic mirror with a flat paddle.

Now consider a spherical mirror surface composed of spherical segments controlled in the same fashion. If the sensor paddle is spherically curved with the same center of curvature as the mirror, then the sensor output will behave in the same way as in the example with the flats. Segment motions which are confined to the spherical surface do not degrade the figure and likewise generate no change in sensor output. This is illustrated in Figure 5-7b. Motions of the segments involving tilt or focus changes will be detected by the sensors, which then allow the control system to correct the figure.

Now, if the paddle is flat instead of curved, a different situation arises. In this case, a transverse motion of the segment in the spherical surface will cause a change in the sensor output, and the control system, in attempting to compensate for it, will degrade the image. For a segment motion r along the surface of the mirror, the sensor paddle moves along the sensor center line a distance

$$\delta \approx r^2/2k \tag{5-13}$$

where k is the radius of curvature. This is illustrated in Figure 5-7c. If the motion along the sensor center line due to the transverse motion r is excessive, one could use curved paddles to eliminate this effect. Expected sources of intersegment motion are mainly thermal and gravitational. A 10°C variation will cause a displacement $r_{\text{"thermal"}} \approx 0.2$mm. Differential motions due to gravity are even smaller. If $r = 0.2$mm, and $k = 35$m, then $\delta \approx 0.5$nm. Thus we see that for the relatively benign environment expected, curved sensor paddles are unnecessary.

Finally, consider a paraboloidal surface composed of mirror segments. The optimal (in the sense of maintaining the overall figure) transverse segment motion would be that which moved along the surface defined by the local radius of curvature. This is just the motion which sensors with curved paddles allow, since it gives no change in sensor output. We note that because the local radius of curvature for a paraboloid varies over the segment surface, then strictly speaking, no such motion is possible. For our f/1.75 primary, however, the local radius of curvature varies only 2% from the nominal 35 m; thus paddles with a 35 m radius of curvature allow almost unlimited transverse motion, while still maintaining local segment-to-segment smoothness. We conclude that paddle shape is relatively unimportant and does not constrain strongly the range of allowed transverse segment motions.

Sensitivity to Paddle Alignment

Having established the behavior of the control system and the perfectly-aligned sensors when the sensors are subjected to transverse displacements, we now turn to the alignment tolerances of the sensor. The sensor body itself has no critical alignment tolerances, but paddle misalignment is potentially troublesome. A possible alignment geometry is to have the paddle aligned perpendicular to the radius of curvature line passing through the sensor body center. Other alignment geometries which differ slightly from this can be used to minimize the size of lookup table corrections for thermal expansion and/or gravitational deflections. For the purpose of this discussion we assume the desired orientation is with the paddle parallel to the segment tangent plane. If the paddle is tilted relative to its desired orientation (parallel to the mirror surface above it) by an angle θ, then transverse segment motion r will cause a change δ in the sensor output

$$\delta = r\theta. \tag{5-14}$$

This is shown in Figure 5-8.

If we assume that the largest source of intersegment transverse motion is thermal change, then we can estimate the needed alignment tolerances. As before, we assume a steel mirror cell ($\alpha = 1.2\times10^{-5}$/°C), to obtain the intersegment expansion for $\delta T = 10$°C of

$$r = 0.19\text{mm}.$$

If we allow $\delta \leqslant 15$nm, then

$$\theta \leqslant 7.9\times10^{-5}.$$

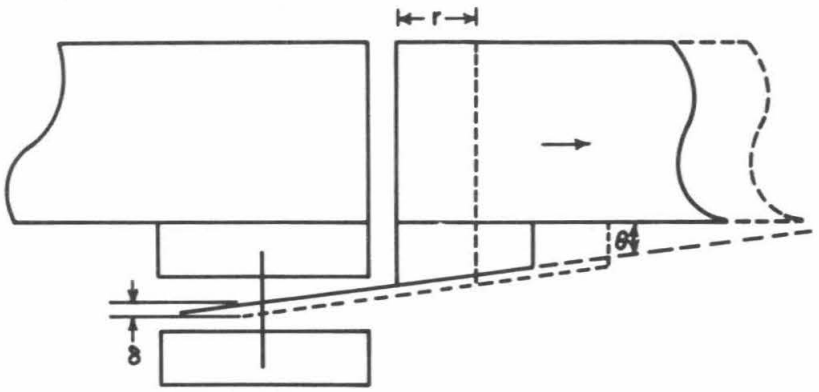

XBL 838-10931

Figure 5-8 Illustrating the effect of paddle misalignment by an angle θ when there is lateral relative displacement of the segments by a distance r.

Assuming the paddle mounting plate is 100mm long, then the tolerance on the total plate wedge is 100mm $\times$ θ or 7.9μm. For ground glass surfaces this precision is readily achieved.

It is worth noting that if this tolerance is not achieved, then corrections based on a lookup table could be made to compensate for known sources of transverse perturbations such as gravity and thermal changes. As a further practical matter, the paddle should be well centered between the body capacitor plates since a variety of systematic effects (sensitivity to temperature, pressure, and humidity) are proportional to the miscentering. The practical centering tolerance is about $\pm 20\mu$m.

5.6 Edge Sensors

The edge sensors described here are based on several generations of prototypes, and closely resemble the sensors built for the engineering test of the active control system described in Section 8.

Mechanical Design

The sensor is constructed from machined plates of the same low thermal expansion ceramic glass as the segment. Figure 5-9 shows a cross section of a full sensor; a body assembly and a paddle assembly. Figure 5-10 is a photograph of the sensor and Figure 5-11 is an exploded view of the sensor parts. The plate-to-plate contacts and the assembly-to-segment contacts are all glass to glass. The contacts take place at three small raised surfaces on plates that serve as kinematic mounts. A layer of epoxy less than 1μm thick is used to bond the pieces together. The base plate is not bonded to the rest and provides the removal interface. The base plates for each sensor location are made to a custom thickness so the distance from the mirror surface to the interface is the same for all sensors. This permits the active parts of the sensors to be interchanged. The assemblies are held to each other and to the segment surface by spring-loaded constant-force mounts. The sensor is protected by a rubber boot (not shown in the figure).

Each assembly is held to the back of a segment by three Invar pads (9.5mm diameter, 3.0mm thick) bonded to the segment. These Invar pieces have tapped holes to receive the constant-force mount rods. The Invar pads are the only pieces bonded to the segment.

The paddle assembly consists of a mount plate, a spacer plate, and the paddle itself. The body assembly consists of a mount plate, two body plates, and three posts. The weights of the body and paddle assemblies are 705 and 900 grams respectively. The dimensions are given in Table 5-4.

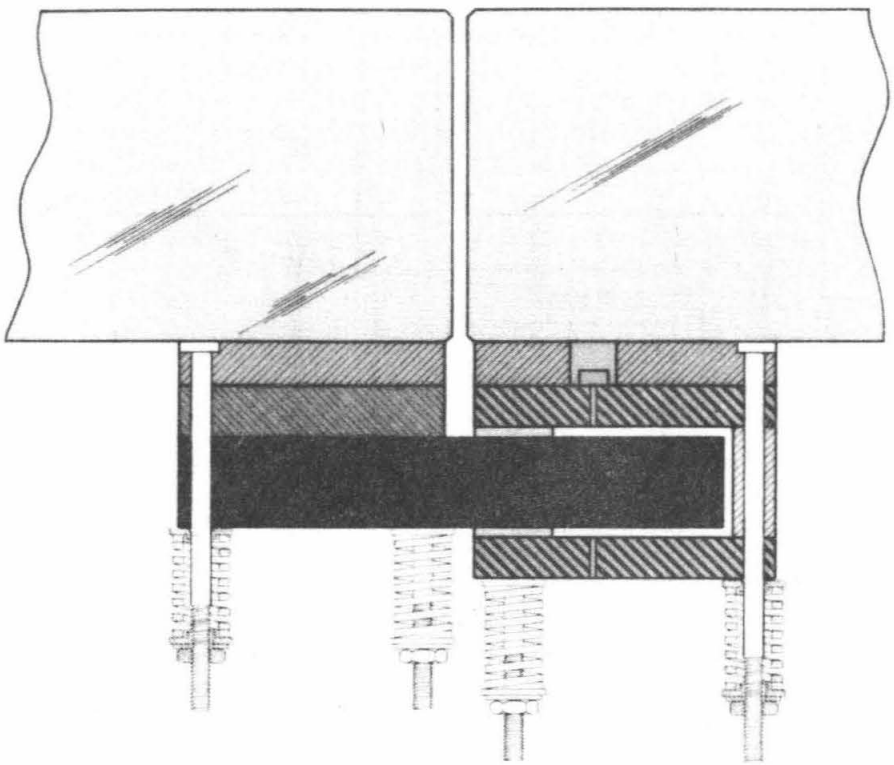

Figure 5-9 Elevation view of the sensor showing the plates of the paddle assembly, the plates of the body assembly, and the constant-force mounts.

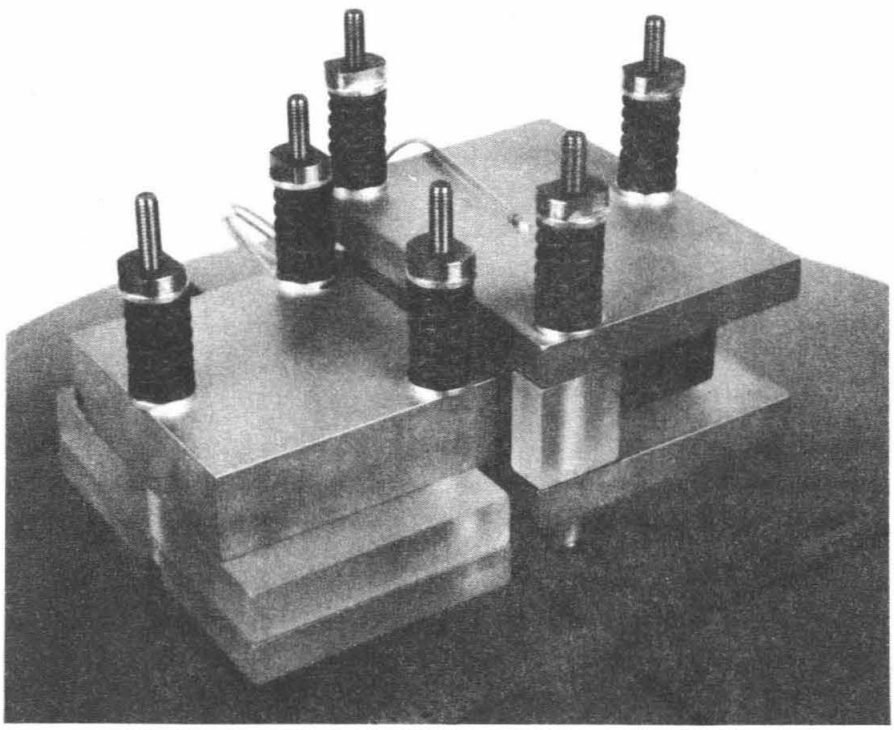

Figure 5-10 A photograph of the sensor. The overall dimensions are about 90mm X 100mm X 130mm.

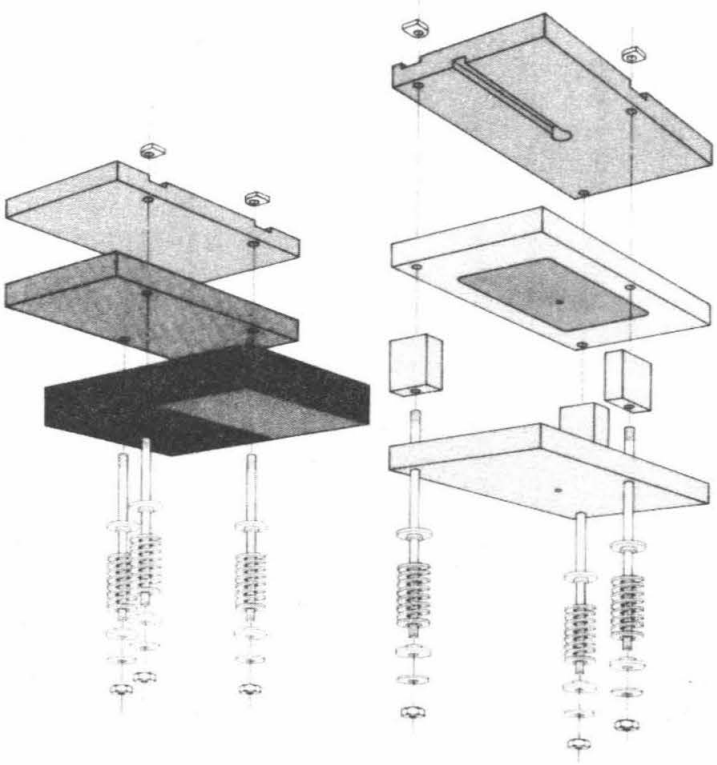

Figure 5-11 Exploded view of a sensor showing the plates of the paddle and body assemblies and the components of the constant-force mounts. The elements are described in the text.

Table 5-4
Sensor Plate Dimensions (mm)

Plate	Height	Width	Length
Paddle Assembly			
Mount	10	90	60
Spacer	12	90	60
Paddle	20	66	123
Body Assembly			
Mount	10	67.5	90
Body	10	67.5	90
Posts	24	20	10

The kinematic mount areas are raised 0.25mm and each has an area of 200mm^2. The gaps between the paddle surface and body surfaces which form the capacitors are each 2.0mm. The top surfaces of the mounting plates that contact the segment are concave to match the segment surface. They are first rough ground to the spherical surface and then lapped on a mehanite tool to the final concave surface. The same tool is used to support both mounting plates during the final flat grinding of the bottom surfaces. This final grind introduces the small wedge needed to have the paddle plane perpendicular to the sensor center line.

The flat surfaces of all plates are first rough ground with a 100 grit diamond wheel and then fine ground with a 320 grit diamond wheel. The tolerance on the vertical dimensions is $\pm 2\mu$m. The parallelism of the surfaces or wedge is held to less than 2μm in 100mm. The edges of all plates have a 0.5mm radius. The holes for the constant-force-mount rods (5.0mm diameter) are drilled with diamond core drills, and are etched with HF for stress relief. Additional feed-through holes in the body plates are made for electrical wires. The ends of these holes have a 0.5mm bevel to allow for a solder joint.

The constant-force-mount rods (Invar, 90mm or 100mm long x 4.42mm diameter) are threaded on each end (10-32 thread). The springs (steel, McMaster-Carr #9623k11) are 25mm long and have a spring constant of 4.8kg/mm. The washers and nuts are of Invar. A third washer made of aluminum is used on each rod to balance the thermal expansion of the rod and further reduce the sensitivity of the force mount assembly to temperature changes. The holes through the blocks are 5mm in diameter, allowing the rods to pass through without contacting the glass. A layer of teflon tape keeps the rod centered and allows smooth motion between the rods and plates. About 12 kg of force are applied to each spring. This is transferred to the back of the segment through an Invar pad. For the engineering prototypes the pad is bonded to the segment with a $250 \pm 50\mu$m thick layer of cyanoacrylic cured at room temperature (thermal coefficient $= 1 \times 10^{-4}/°C$). For the TMT the pads will be bonded into small holes bored in the back of the segment.

Various surfaces of the plates are vacuum coated to provide the capacitor surfaces and ground planes for shielding. The ground surfaces are prepared for coating by ultrasonic and chemical cleaning followed by glow-discharge cleaning in air just prior to coating. The coating thickness is controlled by a shutter and measured with a crystal monitor. The coating is 0.1μm of chrome as an adhesion agent and 2.4μm of gold for the conducting surfaces. The thickness was chosen to avoid a high reactance from too thin a coating and bimetallic effects from non-uniformity in too thick a coating. Gold was chosen for its high conductivity, inert chemical nature, and because it is self-relaxing under thermal cycling. The average thickness is controlled to an accuracy of $\pm 2\%$, and the uniformity to better than 1%. Both the top and bottom surfaces of the plates are coated, and the coating thickness is kept uniform to avoid bending effects at different temperatures.

Some coated areas are etched away to define the capacitor plates and ground-plane conducting surfaces. Conventional techniques of printed-circuit etching are used. A proprietary KI etching agent is used to remove the gold and dilute HCl to remove the chrome. The area of the capacitor is defined by the rectangular region coated on the body plates and is 34mm x 44mm. With the rounded corners the area of the capacitor is 1475mm^2. The area is controlled to within 0.1%. A line 0.5mm thick is etched in the coating to separate this capacitor area from the surrounding guard area. The distance L from the center of the capacitor area to the inter-segment crack is 30mm. For the final sensor design for the Ten Meter Telescope, this will be increased to 60mm to improve the sensitivity to the focus mode displacements. The paddle plate is coated on both sides; then lines are etched defining the top and bottom of the inserted end of the paddle as the second surface of each capacitor. The coated surfaces of the paddle are larger in area than the rectangular areas on the body assembly, thus reducing the sensitivity to relative motion in the paddle plane from fringe field effects. The active coated area of the paddle is 66mm $\times$ 61mm, so the paddle extends outwards beyond the body plate about 5 times the 2mm capacitor gap.

The entire sensor is protected by an RTV (Series 700) boot (200mm x 150mm x 100mm). The boot is made of an upper section that is bonded to the segments and connects the two segments together with a thin membrane above the sensor, and a lower section that completely covers the sensor. The upper and lower sections are connected by a thin rectangular aluminum flange. The boot keeps out dust and moisture and contains a desiccant. Thus the condensation of moisture at the dew point is eliminated, as is sensitivity to differential changes in the dielectric constant as the relative humidity changes.

Electronic Design

A block diagram of the electronics is shown in Figure 5-12. The entire circuit is controlled by a master oscillator that generates a pulse modulated signal at 10MHz. For a segmented mirror with many sensors, a single master clock will be used to control all sensor circuits. The master frequency is twice divided by 16 to give a drive-oscillator frequency of 39.1kHz. This frequency was chosen to avoid commercial and military frequencies and because at this frequency the noise of the FET in the preamplifier front end is minimized. The drive oscillator uses a sine synthesizer to generate a 39.1kHz analog sine wave ($V = \pm 6$V) that drives the paddle sides of the capacitors. This analog signal amplitude is stable to 1 part in 10^4 over the telescope operating temperature. An inversion core (transformer) serves to isolate the sensor and provides signals of 180 degree phase shift difference which are applied to the two paddle sides of the capacitors.

The resulting signals from the body sides of the capacitors are added and the sum is amplified by a charge-sensitive preamplifier (gain $\approx$ 3). The preamplifier output signal is proportional to the difference in the capacitance and thus the relative displacement of the paddle and body assembly. The gain of the preamplifier is controlled by the feedback capacitor C_F (4.7pF) as described below. Because of the high open loop gain (10^6), the sensor body plates are held at virtual ground. The preamplifier contains some band-pass filtering. This filtering is very low Q so that it has a flat phase response and does not produce phase shifts with thermal variations.

The balance circuit adds an additional (adjustable) charge to the input of the preamplifier to balance out up to $\pm 20\mu$m of displacement caused by mechanical misalignment from fabrication and assembly tolerance buildup. The balance circuit is driven by one loop on the inversion core and internally uses two ratiometric cores. The ground point on the cores is used to select the voltage applied to the output capacitor (C_B = 4.7pF). The cores have bifilar windings to reduce mechanical and thermal effects on electrical stability. The capacitor areas on the body act as a virtual ground, and thus the fringe electric fields are pushed out to the edges of the paddle. These fields are thus about 5 times the 2mm gap away from the capacitor areas, which greatly reduces their effects when the paddle experiences in-plane motion.

The signal from the preamplifier is filtered in a band-pass amplifier (1kHz band at 39kHz, gain $\approx$ 10, 12db/octave roll-off). The amplifier contains two stages of amplification, which are designed to maintain excellent phase and gain stability. Jumpers allow reductions of the gain by factors of 2 or 4.

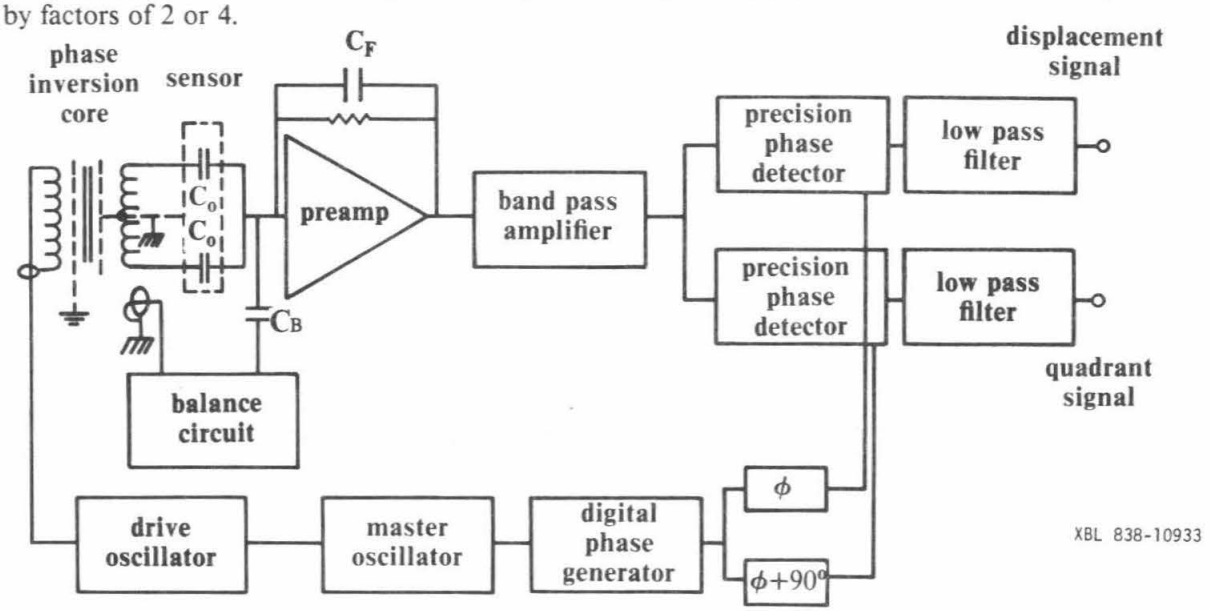

Figure 5-12 Block diagram of the sensor electronics. The functions of the elements are described in the text.

The signal is then split, and each signal is synchronously rectified and integrated by identical precision phase sensitive detectors. The master frequency drives a digital phase generator that in turn drives the two phase sensitive detectors. A balanced bipolar rectifying system gives a stability to better than 100μV. One phase sensitive detector gives a signal proportional to the displacement. The other detector is driven with a 90 degree phase offset to provide a quadrature signal that is used to monitor the performance of the circuit. Finally each signal is filtered through a low pass filter (3db point at 1kHz).

The phase inversion core, the balance circuit, and a portion of the preamplifier circuit are packaged separately and are located next to the sensor on the back of the segment. This allows short leads to be used between the sensing plates and the FET, thus minimizing stray capacitance and noise pickup. The package adds an additional 495g to the sensor load on the mirror and consumes about 100mW. The current in the FET is minimized to minimize this power consumption.

A sensor and its circuitry are electrically isolated as much as possible. All cables are doubly shielded and a single-point ground is used to avoid any direct electrical connections between sensors.

A first-order expression for the output voltage for a displacement d is given by

$$V_{out} = \frac{2d}{X_o} \frac{C_o}{C_F} V G_1 G_2 \tag{5-15}$$

where X_o is the capacitor gap (2.0mm). Each capacitor has a capacitance, C_o, of 6.5pF, and C_F is 4.7pF. The gain of the preamplifier is close to $2C_o/C_F$, V is the voltage applied to the paddle ($\pm$6Vrms), and G_1 and G_2 are the gains of the band-pass amplifier and phase detector ($G_1 \approx 10, G_2 \approx 10$). The sensitivity of the full device is about 1 mV per nanometer of displacement.

For the segmented-mirror control system, the signal is digitized with a 12 bit ADC at 2.5mV/bit, giving a resolution of about 3nm/bit. The ADC has a range of $\pm$ 2048 bits, and thus for a fixed balance point the range of the sensor is $\pm$ about 6μm. The output over a sensor total mechanical range is monotonic. Gain changes in the band-pass amplifier can be used to expand this range by a factor of 2 or 4.

5.7 Position Actuators

The second critical set of components of the active control system are the position actuators. These must make precise movements under a large and variable load, operate reliably, and have a long life. Several generations of actuator prototypes have been built and tested. The performance of the design described here is discussed in Section 8.

Specifications

Minimum specifications for the actuators follow from a variety of objectives, described below.

(1) Optical goals for the Ten Meter Telescope have been established to provide high quality images in the visible and infrared. Analysis of the control algorithm has established the performance characteristics required of the sensors and actuators to achieve these optical goals (Mast and Nelson, TMT Reports Nos. 64 and 80, TMT Technical Note No. 46). In order not to degrade the image size in the visible wavelength region and to allow diffraction-limited performance in the infrared region, the actuators need to position smoothly with an rms uncertainty better than 10nm (Mast and Nelson 1982, TMT Technical Note No. 46).

(2) The range requirements for the actuators are set by the mirror cell deflections. As the telescope moves from the zenith to the horizon the mirror cell and support structure deflect by about 1mm. We have designed the actuators to have a range of about 3mm.

(3) The goal for the control system response time is not yet well established, since it depends on the as yet unmeasured power spectrum of wind perturbations. A program to measure the wind spectra at the telescope site is now in progress. Initial results of this program are described by Forbes and Gabor (1982, TMT Report No. 82) and Gabor (1982, TMT Report No. 77). We have tentatively set the goal for the actuators to have a minimum slew rate of 3μm/sec and small signal bandwidth of 10Hz.

(4) As the telescope moves from the zenith to the horizon the load on the actuator varies. At the zenith each actuator carries one third of the mirror mass (400kg), the mass of a whiffletree (14kg) that connects the actuator to the segment. the segment, and the mass of sensor components (4kg). At the horizon some actuators will need to provide a negative force against gravity since some of the segments forming the curved primary overhang. Thus the above performance requirements must be achieved under a load that varies from -20kg to about +150kg.

(5) Finally, since there is no redundancy in the system of actuators they must operate reliably and have a long life in the observatory environment. The temperature at the proposed site, Mauna Kea, lies in the range 2°C$\pm$8°C for 99% of the time (Kaufman and Vecchione 1981).

Mechanical Design

The selected actuator design is basically a motor driven screw. It can be divided into three major mechanical assemblies, that are nested inside each other: (1) an outer housing with a counter balance spring, a diaphragm, an encoder, drive electronics, and an inner module; (2) an inner precision module with a torque motor, a limit switch, a hardstop assembly, a diaphragm, and an integral roller screw; and (3) an integral bearing roller screw that takes the axial thrust load and converts the rotary torque motor motion into linear displacements.

Outer Housing and Preload Spring Assembly

The actuator is a cylinder 133mm in diameter, 610mm long, and weighs 10kg. The outer housing is split into two sections. Figure 5-13 shows a sectional view. A rigid front cylinder contains the precision module, preload spring, and the encoder assembly. This front cylinder transmits the mirror load back to the subcell. A thin-walled rear section encloses the encoder and drive electronics that mount onto the rear flange. The iridited aluminum outer case has O-rings at both ends and middle, providing a hermetically sealed interior while permitting easy assembly and electrical shielding. Removal of the rear thin-walled cylinder gives access to encoder adjustments and electronics.

The material and machining costs are kept low by use of standard tubing for both pieces. The use of self-aligning vee-step design for the forward section permits machining with a single setup, which makes the needed concentricity and perpendicularity requirements easy to achieve.

The drive electronics are mounted to the rear flange, which also holds the input/output connector. The electronics are split into three sections; a power input filter, a power switching amplifier, and a low level logic signal conditioning section. Each section is electrostatically shielded from the others. The output amplifier FETs are mounted to a heat sink plate which mounts to the rear flange. The power drivers are pulse width modulated and have very low switching losses, but the heat sinks are provided to handle the maximum full power requirement of the torque motor.

An optical shaft encoder (BEI model H25D) is used to monitor the shaft rotation and provide the information required to control the torque motor. The encoder is held rigidly to the forward tube by a flange plate. Four holes through the tube give access for tightening the bellows coupler that connects the encoder shaft to the rear of the roller screw shaft. The bellows coupler yields to any slight angular or displacement machining error yet gives a joint with high torsional stiffness. The torsional resonant frequency of the shaft-encoder-bellows coupler system with a locked roller screw shaft is 1.6kHz, well above the mechanical time constant of the torque motor, but much lower than the drive switching frequency.

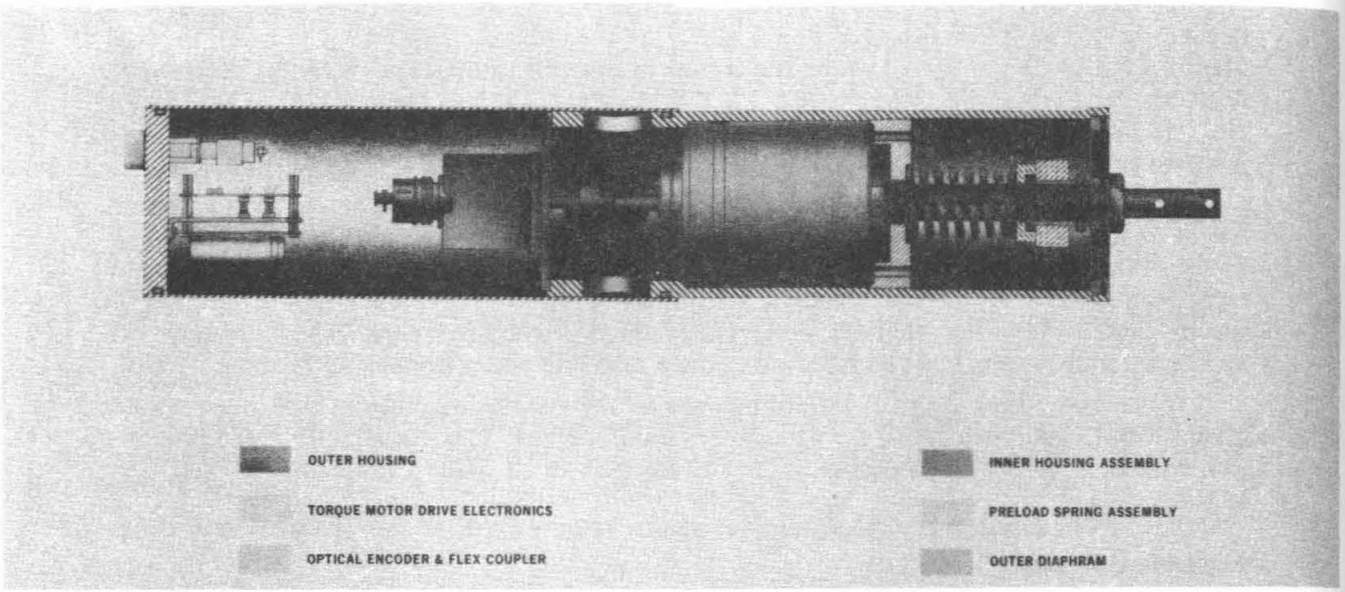

Figure 5-13 Drawing showing the major components of the actuator; the outer housing, preload spring assembly, torque motor-roller screw assembly, optical encoder, and drive electronics.

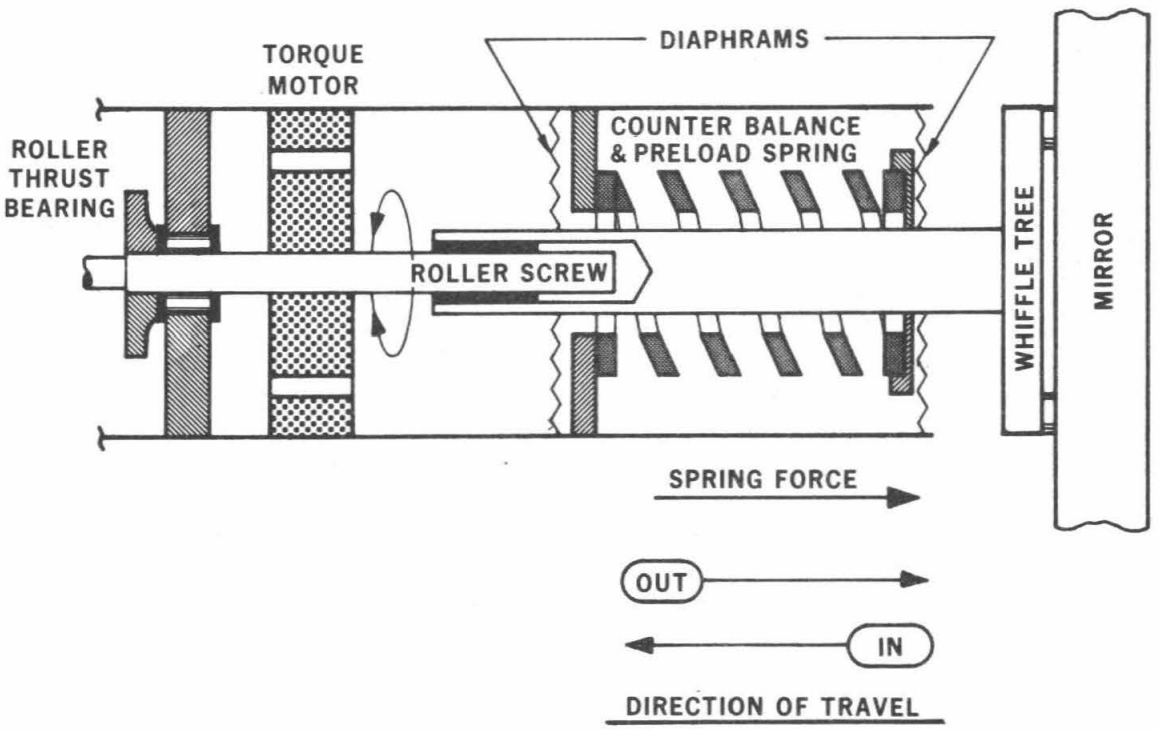

Figure 5-14 A "block diagram" of the actuator load system showing the counter balance spring and the diaphragms which take up any lateral loads.

The inner housing assembly is self-centering when installed in the outer housing. A 45° beveled annular surface at the rear of the inner module engages a sister annular surface in the front outer housing. The rear spring seat is screwed into the outer housing, clamping down on another 45° beveled annular surface at the front of the inner module. This forces the inner module to become centered and normal to the center axis of the outer housing.

The outer diaphragm in the front of the outer housing provides a flexible hermetic seal and, together with the inner diaphragm in the inner module, is a hysteresis-free hinge bearing system for the linear motion of the pusher shaft. The diaphragms are made of 0.125mm stainless steel corrugated with seven equally spaced concentric vee grooves, 0.43mm deep. These corrugations provide flexibility normal to the plane but high in-plane stiffness when the diaphragm is trapped between rigid center and perimeter rings.

Figure 5-14 is a simple schematic showing the major mechanical elements in the front of the actuator with the whiffletree and the mirror. The torque motor turns the roller screw shaft to which it is attached. The rotary motion of the shaft is converted into linear motion by the pitched section of the roller screw pushing on the roller nut fixed to the pusher shaft. The two diaphragms spaced 152.4mm apart suspend the pusher shaft in the center of the outer housing. Along the axis of the shaft the diaphragms only exert a 0.7kg axial load for a motion of 1.5mm, yet normal to the axis they have a spring constant of 1000kg/mm. This prevents lateral loads from disturbing the roller screw function. Each actuator will have to carry the 14kg weight of its whiffletree as a lateral load when the mirror looks at the horizon.

A counter balance and preload spring acts to minimize the load on the roller screw when the mirror faces the zenith. A square wire spring with a free height of 89mm and a nominal rate constant of 140kg/cm is used. The spring force is set to balance the 150kg mirror and whiffletree weight plus a 20kg preload in the outward direction. This will minimize the power required to move the mirror, since the friction, which is proportional to the load, is the major loss component in the screw. At the horizon the load is at the maximum of 170kg. An additional benefit of minimizing the zenith-pointing load is to maximize the screw's life, which varies as the inverse of the cube of the load.

Inner Module

The inner module shown in Figure 5-15 contains the pusher shaft, limit switch and hard stop assembly, torque motor, and integral bearing roller screw. Its shell is made from stock heavy-wall aluminum tubing utilizing a vee design so that the majority of internal machining can be done in a single operation. The shell is hard-anodized to prevent galling during assembly. As a further safeguard all aluminum threads are coated with a light coat of molybdenum disulfide before assembly. One threaded hole is left unanodized so a ground wire can be attached.

The pusher shaft is made from aluminum bar stock with the integral hard stop and limit switch contacts machined in. First copper, then gold plating is applied to the hard stop-limit switch flange before the shaft is iridited. The limit switch contacts one quarter turn of the screw (0.25mm) before either of the hard stops are hit. A simple plate in the limit switch sandwich sets the maximum linear motion of the pusher shaft. In practice the electronic braking, initiated by limit switch contact, will stop the actuator motion before the hard stops are hit. Only motion away from the contact is possible when the pusher shaft is contacting a limit switch. The limit switch electrical return path is through the shaft, the diaphragm, and the outer housing. CMOS logic levels are used to prevent any false readings due to noise.

The prime mover is a direct drive permanent magnet dc torque motor (Inland model T-2950) which has 1.6N-m peak torque, a torque sensitivity of K_T = 0.5N-m/A, an electrical time constant τ_e = 2.1ms and a back emf constant K_E = 0.5 V/rad s. It has a 41 segment commutator and a 5% torque ripple. The motor is capable of dissipating 79W at stall. The armature is clamped directly to the screw shaft with two thick aluminum nuts, which provide a very stiff mechanical coupling as well as stiffening the screw shaft. The nut on the commutator side has a dust deflector machined into it. The nut, together with the roller bearing flange plate groove,

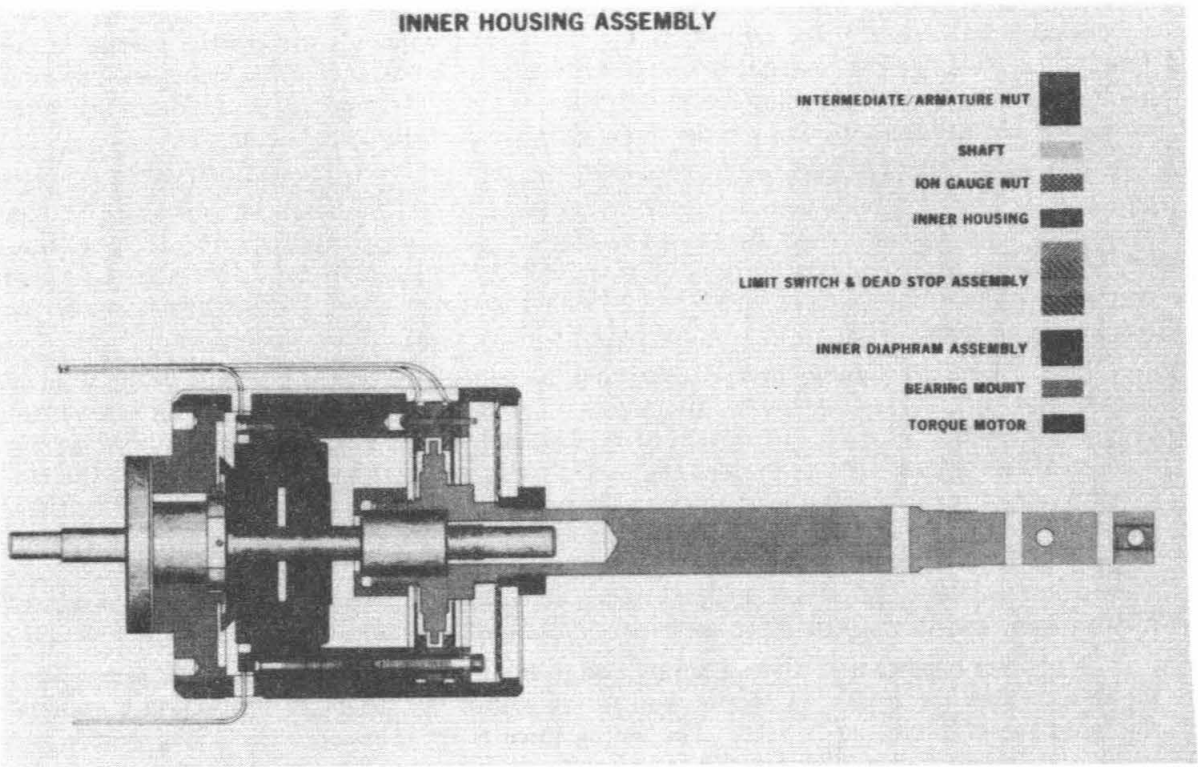

Figure 5-15 An assembly drawing of the precision inner module of the actuator. Shown are the 1) integral bearing roller screw, 2) torque motor, 3) screw bearing of the roller screw, 4) limit switch hardstop assembly, and 5) pusher shaft.

provide an effective dust trap, which prevents dust from getting into the thrust roller bearing. Current for the motor is supplied via a shielded twisted pair thereby electrically isolating the motor from the housing.

Integral Bearing Roller Screw

The heart of the actuator is the integral bearing roller screw. It provides a smooth, low friction, high load capacity mechanism for converting rotary to linear motion with 3mm dynamic range yet resolution at the 4nm level. Roller screws are commercially available from La Technique Integral, a division of SKF, located in France.

The integral bearing roller screw is made of two types of roller bearings on a common shaft. Figure 5-16 is a sectional view of the complete screw. The 1-mm pitched roller nut and shaft convert the rotary shaft motion into linear motion while a zero-pitch roller nut thrust bearing transfers the shaft load to the housing. A detailed description of the pitched nut has been given before (Gabor 1980) but a brief one will be given here.

The roller screw owes its high load capacity and smoothness to the large number of rolling contact points. The screw used in the actuator has a 12mm diameter shaft with a 1-mm pitch in the threaded side. A 90^o thread form is used for both the pitched and unpitched sides. The seven planetary rollers in each nut contact the shaft at 17 points, for a total of 119 points. The screw is rated to have a mean failure travel distance of 2.5×10^4m at 540kg load.

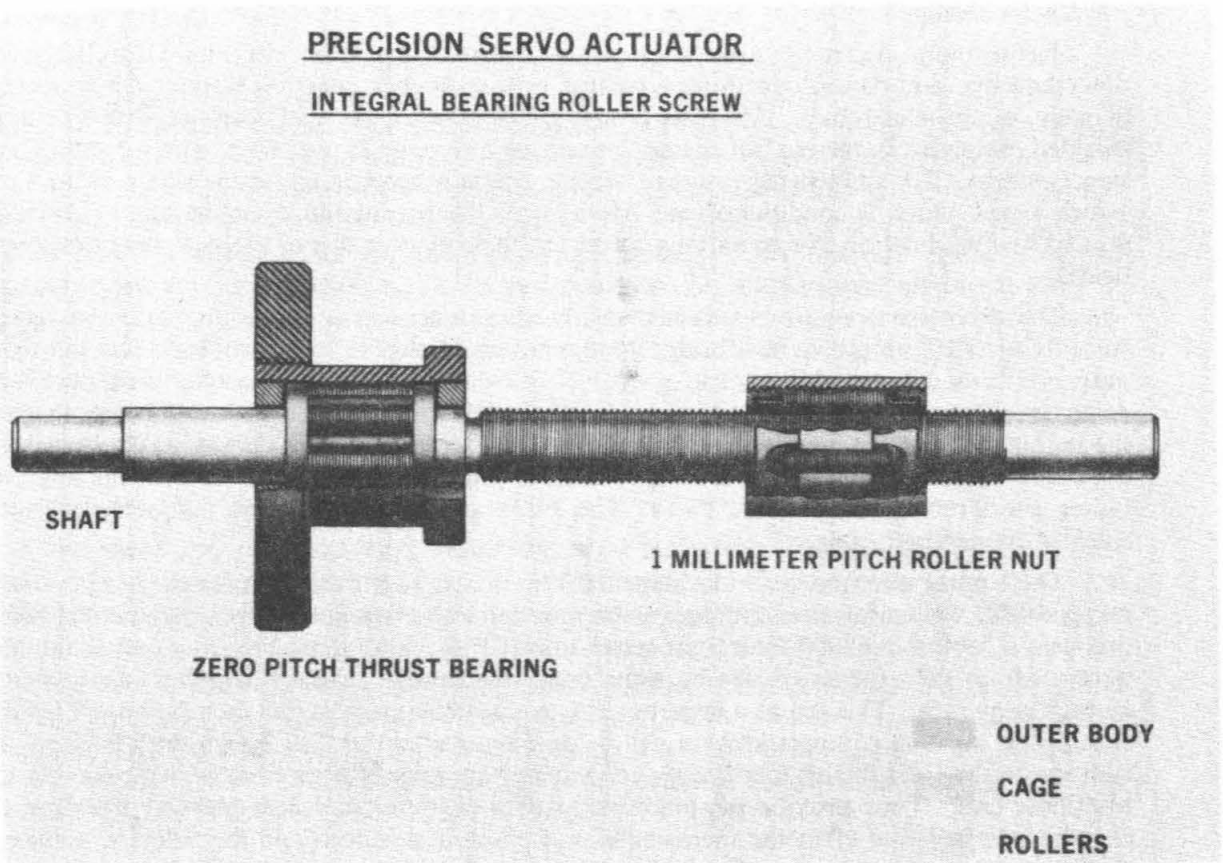

Figure 5-16 Section drawing of the integral bearing roller screw shaft with a roller thrust bearing to the left and the 1mm pitch roller bearing on the right that drives the pusher shaft attached to the whiffletree.

The pitch section uses a nut with an internal 1-mm pitched thread. Unpitched rollers contact the inner and outer threads. A slot in the nut permits each roller to be shifted forward as the nut advances by a cam at the trailing edge of the nut. A cage maintains the roller spacing.

The thrust bearing section was designed by adapting the roller screw concept to a zero pitch shaft and nut. The nut requires no shifting slot. A special free floating cage was designed which contacts the rollers only at their ends, which have been ground to form pins. Holding the rollers by the pins keeps them spaced while reducing the drag on the rollers.

The slow movement of the integral bearing roller screw during normal operation requires a dry lubricant to provide lubrication. An air impinged tungsten disulfide coating is used. In addition, to prevent rusting during handling and assembly, a synthetic oil is used to coat the moving parts.

Despite careful design and lubrication, the integral bearing screw still exhibits stick-slip behavior for fractional arcminute motions ($<$ 50nm). This is within our normal operating range, hence we must cope with this non-coulombic frictional behavior. Since the encoding bit resolution is 5 arcseconds (3.8nm) we have the information needed to control this behavior.

Electronics Design

The actuator electronics are separated into two packages; drive electronics, located in the outer housing, and control electronics, located in a relay rack chassis. Figure 5-17 is a block diagram of the electronics. The two groups of electronics are tied together with a doubly shielded cable set. In the control chassis a single point ground is used for the power supply and signal returns. The only signal returned via the actuator housing and cable shield is the limit switch signal which is conditioned to CMOS levels. This grounding configuration eliminates ground line modulation due to varying current in the torque motor or external electromagnetic fields.

The drive electronics are mounted inside the actuator outer housing on the rear flange. An efficient FET amplifier in a bridge configuration drives the torque motor. The output is pulse width modulated while switching at 19.5kHz which is locked to the system master clock. A low level logic and signal conditioning circuit provides split phase signals and power to drive the output FETs in the amplifier. A two section Pi filter keeps any switching spikes from leaving the drivers via the input power line. The filter mounts directly to the driver heat sink providing short power leads to the FETs. The FETs are connected to the torque motor by a shielded twisted pair cable.

The control electronics are developed around a fast 16-bit microprocessor using memory mapped I/O. In lieu of developing a special microprocessor we purchased a commercial board that uses a Motorola 68000 central processor unit (CPU). Additional time and cost economies were made at the expense of size by using linear regulators, standard Multibuss cages, and a 19-inch relay rack. This led to a large but easy to assemble package for each actuator's control electronics. A more compact package will be developed after the final design is established. In addition to the CPU board, four boards per actuator are presently required, which plug into the Multibuss cage. They provide the following: a data digitizing and data highway interface, an encoder interface that gives the incremental and absolute positions and the velocity, a current monitor, and a precision power supply for the analog circuits.

BLOCK DIAGRAM OF ACTUATOR ELECTRONICS

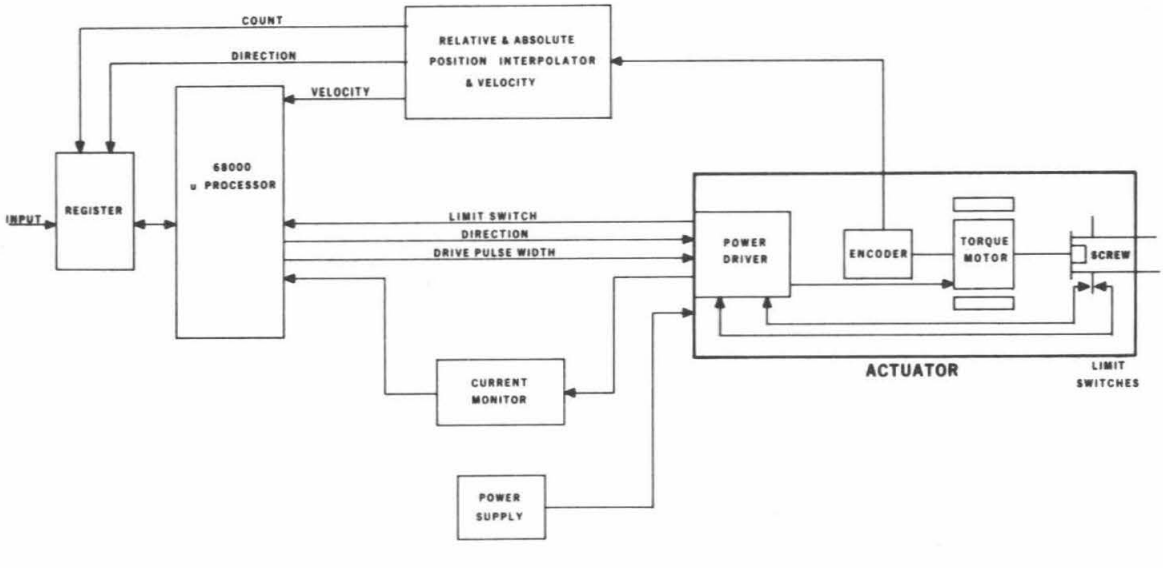

Figure 5-17 Block Diagram of the actuator electronics.

Servo-Control Loop

Compensation for the non-linear behavior of the screw is made using a predictive control algorithm. This algorithm uses the following parameters: the present and immediate past values of the encoder position, the encoder velocity, and the motor current. The control loop makes corrections to the pulse width of the 19.5kHz driving signal. This method is used in order to avoid exciting lower mechanical resonant frequencies and also to provide individual bit motion control on a millisecond time scale. The method then requires that the control parameters be measured at the 19.5kHz switching frequency. This high rate makes measuring the control parameters a challenge. The incremental position must be measured to at least the 10nm level required by the optical error budget. The velocity ranges over 3 orders of magnitude with the lowest being 10^{-5} radians per sample period. The range of the current is quite large due to the changing torque required as the mirror goes from zenith to horizon. The percentage resolution in motor current at any elevation angle remains constant even though maximum current varies by a factor of seven.

Measurement of the Control Parameters

The speed and dynamic range requirements of the system required using special techniques to measure the incremental position, the velocity, and the motor current. An optical shaft encoder was chosen to measure both position and velocity because of its low cost and low inertia.

The optical shaft encoder and its electronics measure the incremental position to 18 bit accuracy (3.8nm) and velocities between 0.001 and 2rad/s (160nm/sec to 0.3mm/sec or 0.008nm/period to 16nm/period). These measurements are made each switching period (51.2μs). Analysis of the effects of actuator errors on the image quality shows that an rms error of 10nm will lead to an 80% image diameter of 0.025 arcseconds.

Encoder Position

Achieving 18 bit resolution from the BEI industrial encoder required using an extrapolation technique. Every revolution of the encoder produces 2048 cycles of a rounded triangle wave that looks roughly like a sine wave as well as a similarly shaped "cosine" wave. In addition, for each revolution an index pulse is provided. The wave forms are differentially transmitted from the encoder to differential receivers to reduce common mode noise pickup. Input circuitry corrects the quadrature phase to 90 degrees and produces equal amplitude "sine" and "cosine" waves and their complements. The wave forms are electrically centered about ground. Eleven bit angular resolution is obtained by detecting each time the sine and cosine wave forms cross ground. Directional information is derived from the phase relation of the sine-cosine crossings.

An additional seven bits of resolution is obtained by dividing each individual cycle using the following method. A resistive ladder bridge is driven at one end by the sine function, the middle point by the cosine function and the opposite end by the not-sine function. Comparators referenced to ground are attached to the taps on the ladder. At each tap when the sum of the electrical vectors of the sine and cosine cross ground the attached comparator changes state. This zero crossing point is equivalent to phase dividing the cycles. The outputs of the comparators are exclusively OR-ed to produce a pulse output each time a comparator changes state. The incremental pulses occur at fixed phase angle intervals set by the resistive bridge ratios.

Encoder Velocity

Velocity is measured by using the almost linear slope of the sine and cosine wave outputs of the encoder between -45 and +45 degree phase angles from each of the four quadrants. Two sample-and-holds are used to measure the voltage change of the sine wave for a fixed time period of 48μs. A sample of the sine signal taken at the beginning of the time period is subtracted from the value of the second sample taken at the end of the time interval. The output voltage is proportional to the angular velocity of the encoder. Velocities between 0.001 to 2.5rad/s are measured to 5% accuracy in 51.2μs. Corrections are made for the harmonic content of the wave form using an analog multiplier fed by a three piece-wise sine wave correction function.

Current Monitor

Motor current is measured by placing a 0.030 $\pm$ 1% ohm metal resistor in a lead of the motor. A differential amplifier amplifies the voltage developed across the resistor and drives a cable to the current monitor in the microprocessor box. The current signals are differentially received, referenced to local ground, and then sampled in a box car integrator for 48μs each switching period. During the time it is open, the sampler has a time constant equal to 1/2 the sampling period, which roughly averages the changing current value. This average value of current is used to calculate the torque of the motor.

All the measured parameters are sampled synchronously and are updated every 51.2μs to the microprocessor just before the control computation that generates the desired motor current.

Servo-Loop Algorithm

The overall control of a segmented mirror is made by the global control loop. It takes the sensor readings, uses them in the global control algorithm, and issues individual correction values to all the actuators. The motion of an individual actuator is carried out by a **local** servo-loop. This allows all actuators to be updated or moved simultaneously rather than sequentially, thus increasing the system bandwidth.

The local actuator servo-loop algorithm will receive actuator correction values every 3.3ms. These will be delayed relative to the sensor sampling time by the global algorithm processing time which will be approximately 100μs. We would like the actuator servo-loop to produce the desired actuator displacement to within 20nm rms of the requested position before the next sensor sampling. During this movement the local loop must compensate for any nonlinear behavior of the bearings and be immune to variations in individual roller screw characteristics.

An actuator servo-loop algorithm that addresses these goals has been developed. The major goal of the algorithm is to correct for non-linear behavior of the roller screw bearing. The roller thrust bearing exhibits a non-linear behavior as follows. If one plots the torque required versus angular displacement of the screw one finds it traces out a curve similar to a BH magnetization curve for iron. Normally, as more torque is applied to a screw, the angular displacement per increment of torque increases until the bearing starts rolling (breaks away), at which time nonlinear behavior disappears. Upon stopping, a new hysteresis cycle begins. It was found that the roller screw bearing does not have to break away if torque is continually applied when the bearing is wound up. It appears as if the bearing moves by relaxing as long as the angular velocity is not too high. Since our largest expected motions during any sensor sampling period is $\leq$40nm (equivalent to a 4μm/s slew rate), a control algorithm was developed to take advantage of this phenomenon. The algorithm takes values from readings of a position

register (PR) and velocity to derive a new drive pulse width and sign every 51.2μs.

The local control loop is implemented as follows. The position register is a bidirectional loadable signed counter that is the equivalent to an error summing node of an analog servo loop. To make a move, a correction value represented by a signed number is loaded into the PR by the global control loop. The actuator algorithm works to keep the PR equal to zero. The sign and duration of the drive pulse are controlled according to the PR offset value. Counts from the encoder either increment or decrement the PR depending on the rotation direction of the screw until the PR reaches zero.

5.8 Global Electronics

The global control loop is an oversampled position loop with 108 individual nested local loops in the actuators. As described above, the actuator uses an optical shaft encoder to measure the relative actuator position. The local servo loop strives to null the difference between the error value provided by the global loop and the position measured by the encoder.

Control System Redundancy and System Checking

Since the active control system has 168 sensors and only 108 actuators, there is redundancy in the control system. Since the rigid body motion of the primary is not sensed by the sensors, there are 63 extra measurements made by the sensors beyond those strictly needed for control of the primary. These extra measurements provide substantial capability for monitoring the health of the control system.

For each control cycle, one can calculate the contribution to chi square from each of the sensors. If the sensors are working properly, then independent of the amount of segment motion desired, each sensor should have approximately the same residual. By simply monitoring these residuals for each sensor, one can immediately determine if a sensor is drifting relative to its calibration, or if the sensor is failing in any other way. Having recognized such failure, one can then note that the sensor electronics or mechanism needs replacement (to be done at a convenient time) and proceed with the control system ignoring that defective sensor. Deleting a sensor requires recalculating the B matrix, and this is readily done.

The actuators can be monitored in a related fashion. By noting the calculated motion expected of each actuator one can study the smoothness and accuracy of each actuator. The externally induced segment motions are not known for each sample, but they will be smoothly varying, and similar for each segment. The signature of an improperly functioning actuator will be its consistently requiring larger corrections than nearby actuators.

For both sensors and actuators, it is thus relatively straightforward to monitor their correct functioning or quantify their degree of malfunctioning. When such malfunctioning becomes excessive the components should be replaced. Whether the actual source of error lies in a mechanical or in an electrical subcomponent is not determined by this monitoring scheme.

Global Loop Stability and Performance

The global loop stability and performance are governed by three characteristics: 1) the loop gain, which is set by a coefficient in the software, 2) the system delays (i.e., calculation times and filter delay), which need to be small compared to the sample time, and 3) the corrective move, which should be made before the next sample is taken.

System delay comes from processing time, communication time, and delay time. These times need to be reduced to a minimum in order to achieve the best global loop performance.

Processing time is reduced by parallel processing. The limiting operation in the processing is the matrix multiplication. The scaler product of the 168 and 108 element vectors can be completed in about 50μs with a dedicated matrix multiplier. Using pipelining and parallel techniques the total processing time (calculations and communications) can be reduced to less than 100μs.

Structural resonances with frequencies that fall in the upper end of the bandpass may be insufficiently controlled to meet the rms error goals. In this case filters will be used to remove these resonances from the sensor signals. The filters will also track the resonance frequency if it changes as the telescope changes elevation angle. The delay due to this filtering will be minimized by using either high Q notch filters or anti-correlation filters. Both methods track the resonance frequency by periodically making an FFT of the sensor output to identify resonance spikes that exceed a threshold amplitude above the noise. The notch filter algorithm uses the measured resonance frequency and Q. The anti-correlation filter requires both the amplitude and phase information from the FFT. Since the mechanical resonances will be stimulated by the actuator motion they will be coherent with respect to the start of actuator motion. The anti-correlation algorithm will remove the resonant portion of the signal. The anti-correlation filter introduces less delay than the notch filter. In addition to the resonance filtering, a hardware anti-aliasing filter is applied to each sensor signal. Since the anti-aliasing filter will introduce a significant delay below the Nyquist frequency it is important that this frequency be high. We thus plan in the full TMT system to sample at 300 times/second, allowing filtering below the Nyquist frequency, and providing enough bandwidth with minimal phase shift to include and possibly affect the lowest mirror cell resonance.

Block Diagram

A block diagram of the global control loop electronics is shown in Figure 5-18. The physical locations of the various modules are indicated on the right side of the figure. The design addresses the potential problems of component multiplicity, influences of environmental factors (thermal, noise, seismic, etc.), diagnostics, and maintenance.

System Flexibility

The global loop is a distributed intelligence system with intercommunication links between special function devices. This approach provides the means to change the loop behavior without hardware changes after the telescope is assembled. As an understanding of the detailed response of the structure and environment is acquired so that information can be incorporated into the relevant software modules of the loop.

Diagnostics

The programmability of the various functions of the control hardware permits the system to run self-diagnostic software. The system self-diagnostic software will be run in real time during normal loop functioning, in idle CPU time, and during normal maintenance procedures. Control and monitor microprocessors are assigned to sensor and actuator electronics and to the signal conditioning and array processor modules. By running set data patterns, the software will pinpoint malfunctions to a specific board, which can be rapidly replaced.

Maintenance

A minimum of electronics is placed in the mirror cell. The majority of the electronics is on the Nasmyth platforms and in an electronics room. This will provide ease of access to any malfunctioning components. In combination with the diagnostics, the ease of access will minimize loss of observing time when electronic components fail.

Failures

The high multiplicity of components allows and demands a particular program for dealing with component lifetime and failures. All components will be put through an initial burn-in process in order to eliminate infant mortality problems. The multiplicity of components will provide identical (and burned-in) replacements should a failure occur. In the detailed design and implementation of the electronics the lifetime of components will be of the highest priority in component selection. Reducing the part count is the first goal in order to improve the reliability. Thermal control will also be essential for reliability.

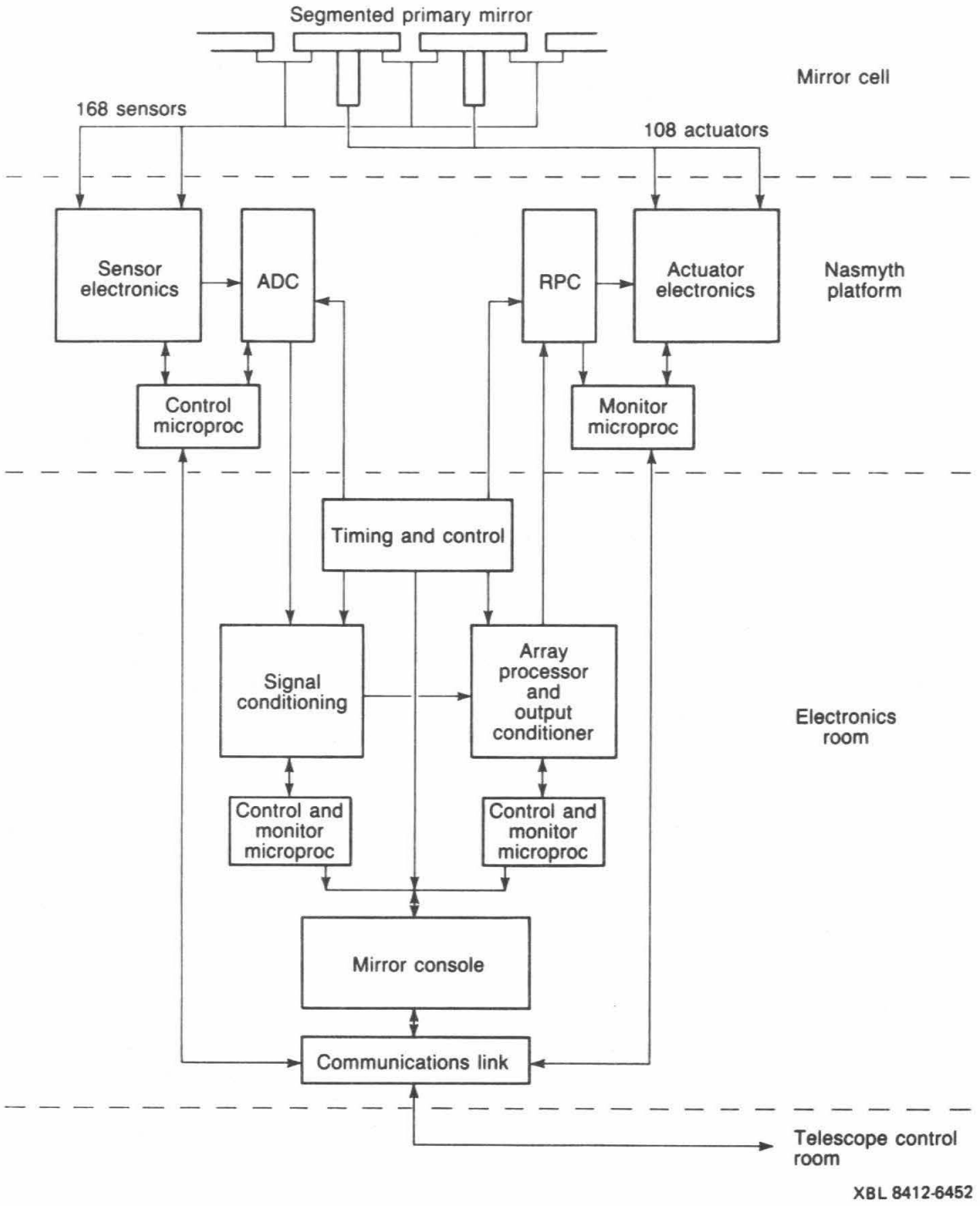

Figure 5-18 Block diagram of global control loop electronics.

Thermal Control

An advantage of having the majority of the electronics on the Nasmyth platforms or in a separate room is the ability to keep a low and constant temperature in the electronics racks. A low chip temperature will be maintained by good component layout and by providing adequate cold air flow between each board. Although there is a high component count, good low temperature thermal control of active component junction temperatures can give several orders of magnitude improvement in device life.

Ground Loops and Noise

Widely distributing the electronics would normally make them susceptible to ground loop and induced noise problems. Fiber optic links and a single point ground system will be used to avoid these problems. Power will be distributed in a star configuration, with local isolation and regulation in each electronics rack. Inter-location communication will be over high bandwidth serial optical links.

Power Dissipation and Cabling at the Mirror Cell

The electronics on the mirror cell consist of those within the actuator housing and the small FET front end of the sensor electronics. This small amount of sensor electronics is housed in a box $35 \times 50 \times 100$mm and weighing 500g. The power used by each of these elements is 100mW. One cable per sensor will connect the sensors to the Nasmyth platform electronics. Each is a 10mm diameter multiconductor cable with about 12 conductors. The total sensor cable cross sectional area is about $0.015 m^2$.

The light in the actuator encoder dissipates 0.5W and the motor at the zenith about 0.25W. At the horizon the actuator dissipates about 2W. At maximum drive conditions the motor has a peak output of 75W. Each actuator is also connected to the Nasmyth platform by a single multiconductor cable with a diameter of about 20mm. Thus the total cross sectional area is $0.037 m^2$. Heat dissipated at the back of mirror cell will be removed using the system which will be designed to maintain the mirror temperature at ambient (see Section 9).

Nasmyth Platform Electronics

On the Nasmyth platforms are the sensor electronics described in Section 5.6 above and the actuator electronics that perform the local loop algorithm. Microprocessors that control and monitor these functions are located there as well. The electronics on the Nasmyth platform will dissipate approximately 5kW and this will be pumped away to the exhaust tunnel. The signals from the Nasmyth platform to the electronics or control room are sent via fiber optic links.

Computer Room

The global loop algorithm and timing control are performed here. A signal conditioner puts in the desired offsets to the digitized sensor readings and periodically makes a Fourier transform of the sensor outputs to seek the mechanical resonances in the system and position adaptive filters to remove them from the sensor data. An array processor makes the global control matrix multiplications and also conditions the signals to the actuators. Both the signal conditioner and array processor are monitored and controlled by separate microprocessors. The entire system can be addressed by a central microprocessor in the mirror console (described below).

Mirror Console

A block diagram of the mirror console in shown in Figure 5-19. The mirror console CPU is the central link for both the sensor calibration procedure and for software modification of the global algorithm. In addition, it monitors the condition of the system during its operation. It gathers archival performance data on all the system components and provides communication links to the telescope operator, giving status information and maintenance instructions. The

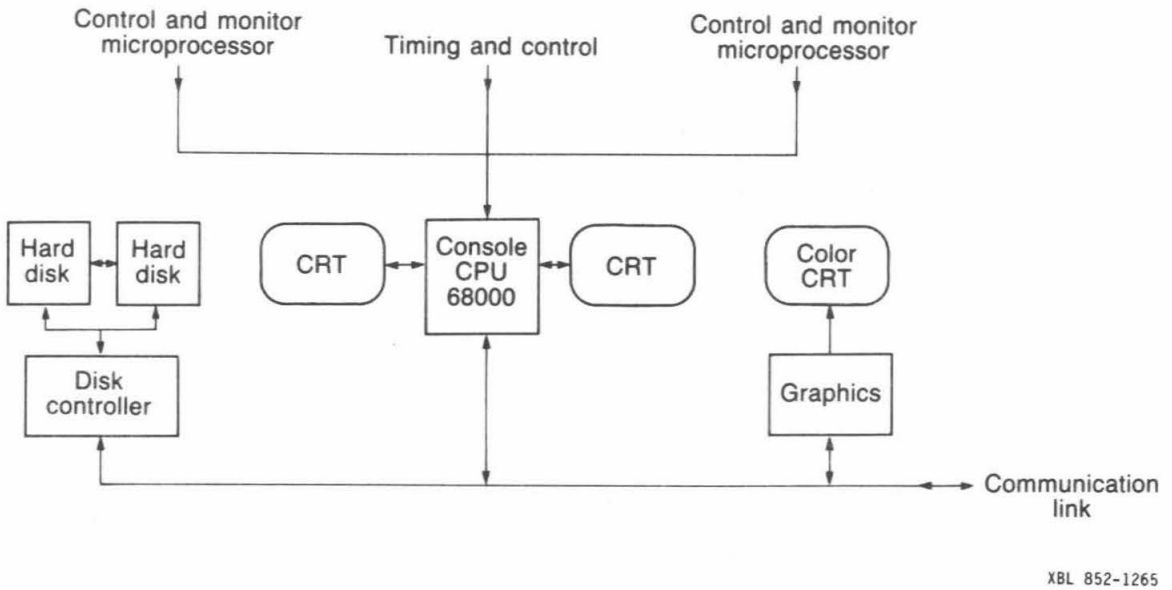

Figure 5-19 Block diagram of the mirror console with a central CPU and peripherals used for communication and control of the active control system.

console consists of a microprocessor with several keyboard monitors, two hard disks for fast bulk storage, a color graphics monitor for diagnostic display, and communication links to the Nasmyth platform and telescope control room. Additionally, the control room CPU will play a vital role during installation of the telescope and development of the control software.

5.9 Segment Support and Surface Correcting Systems

The flexibility of the thin (75mm) segments and the very small tolerances on surface errors make the mechanical support of each segment a challenging problem in mechanical engineering. Since the mirror is much more flexible under axial loads than in-plane (radial) loads, we decompose the external gravitation load into these orthogonal components, and use two independent mechanical systems to accommodate these components. Forces on the segment (mainly gravitational) perpendicular to the surface, axial forces, are balanced by the distributed forces that are provided by whiffletrees. Each whiffletree connects to the segment at twelve points and is supported by a single actuator. This forms the axial support system. Forces parallel to the segment surface are transferred to the mirror cell through a thin diaphragm attached to the segment center and through a thin rod attached to the edge of the segment. The three actively controlled degrees of freedom of the segment are adjusted by actuators through their whiffletrees. The three passively controlled degrees of freedom are constrained by the thin diaphragm and azimuthal restraint rod. These form the radial support system. In principle these are the only two systems required. However, due to the curvature of the segment, gravitational forces in the mirror plane cause deformation of the mirror at the horizon that is in excess of the allowed tolerances. We have thus designed an additional system to apply small forces to the segment to correct for the effects of distorting in-plane forces.

In addition, as described in Section 8.1.2 below, our initial experience was that cutting the mirror into a hexagon after polishing caused about one micron of surface warping. This may have been due to an accidental non-symmetrical treatment of the front and back surfaces of that mirror. If so, this will not happen in the fabrication of the TMT segments. However, the warping could have also been caused by the presence, and release during cutting, of residual internal stress in the mirror blank that was non-symmetrical top to bottom. If this was the case, then we must expect the TMT segments to warp when they are cut into hexagons. In preparation for the latter situation we have designed some mechanical systems that can be used to un-warp the segment and hold the segment to the proper figure during its use in the telescope. These designs are also described below in this section.

Whiffletrees

The axial force of each actuator is distributed to 12 points in order to give a more uniform axial support. Without the whiffletrees, that is if the segment were supported on the three actuator points, the rms surface error caused by the self-weight deflections of the segment under gravity would be about 1.7μm. As the telescope moves from zenith to horizon this surface error decreases to zero. The error budget for the segment surface is roughly 10nm rms, and thus the whiffletrees must make a factor of 170 reduction in the deflections. A formal study of the deflection of thin plates on point supports has been made (Nelson, *et al.* 1982, TMT Report No. 74). From this study we concluded that the rms deflections due to the self-weight could be reduced to 8nm by using a 36 point support system. The locations of these 36 points and the axial forces associated with them have been optimized using finite-element analysis to minimize the rms deflections of the mirror (Budiansky, 1982, TMT Technical Note No. 52).

Several methods are available for applying the forces at the 36 points. Telescopes have been commonly built with counterweight systems or with pressurized flotation pads to apply these forces. We selected whiffletrees because they were kinematic, passive, and lightweight.

The geometry of the whiffletree support is shown in Figure 5-20.

A drawing of a single 12-point whiffletree is shown in Figure 5-21. The mechanical design of the system must satisfy several severe constraints. It should apply the desired forces to the

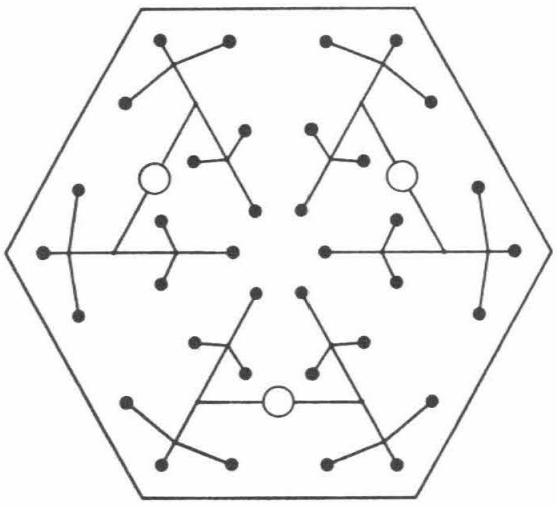

XBL 8212-11990

Figure 5-20 Schematic showing the 36 points of axial support for each segment and the three whiffletrees used to connect those points to the 3 actuators.

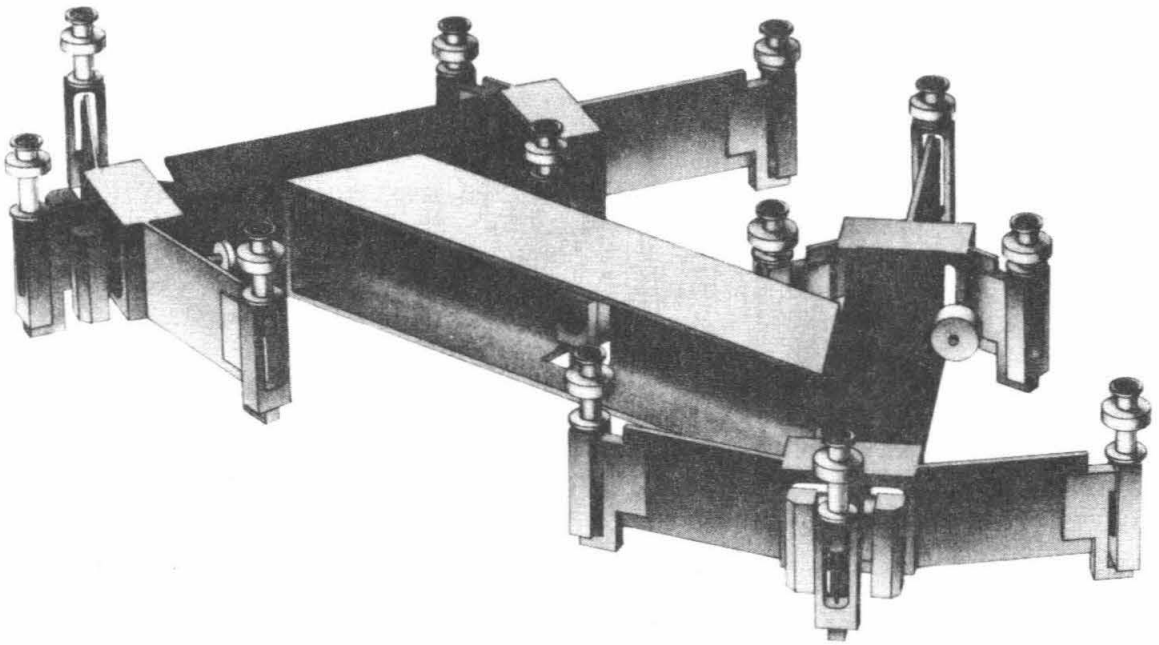

Figure 5-21 Drawing of one of the three whiffletrees used to support each segment. Each whiffletree attaches to the segment at 12 points through flex-rods, and contains 11 flex joints.

mirror with high accuracy and consistency. It should also have low mass, be durable, and require no maintenance. In addition, the forces applied to the mirror should be independent of any thermal expansion of the whiffletrees or small mechanical errors in the construction of the whiffletrees. To accommodate the bandwidth requirements of the active control system, the structure must be very stiff axially. Conversely, to satisfy the need to carry only axial forces with the whiffletrees and only radial forces with the radial support system, the whiffletrees must be very flexible radially. To achieve these goals, the whiffletrees employ aluminum I-beams, flex pivots (Bendix), and flex-rods at each of the 36 points. This system has extremely low hysteresis, no parts to be lubricated, and is axially quite stiff. The whiffletree system weighs 42kg, compared to 400kg for the segment. The flex-rods allow the whiffletrees to expand thermally without putting appreciable additional stress on the mirror at the points of attachment.

Radial Support Post and Azimuthal Restraint

The radial loads, which are orthogonal to the axial loads, are primarily carried by a single post attached to the center of gravity of the segment. This post is attached to the segment with a very thin diaphragm (stainless steel, 0.25mm thick, 0.25m diameter) which provides high radial stiffness, and very low axial stiffness. Figure 5-22 shows the design. The post assembly has hard stops that prevent the segment from moving too far, thus protecting the displacement sensors. The post is also designed to raise and lower the entire segment some 200mm to allow installation and removal of a segment from the mirror cell. The system has high in-plane stiffness against translations, but is rather flexible against rotations. An additional stiffening attachment near the edge provides azimuthal stiffness. This attachment is through a flexible rod which also allows the motion required for the active control.

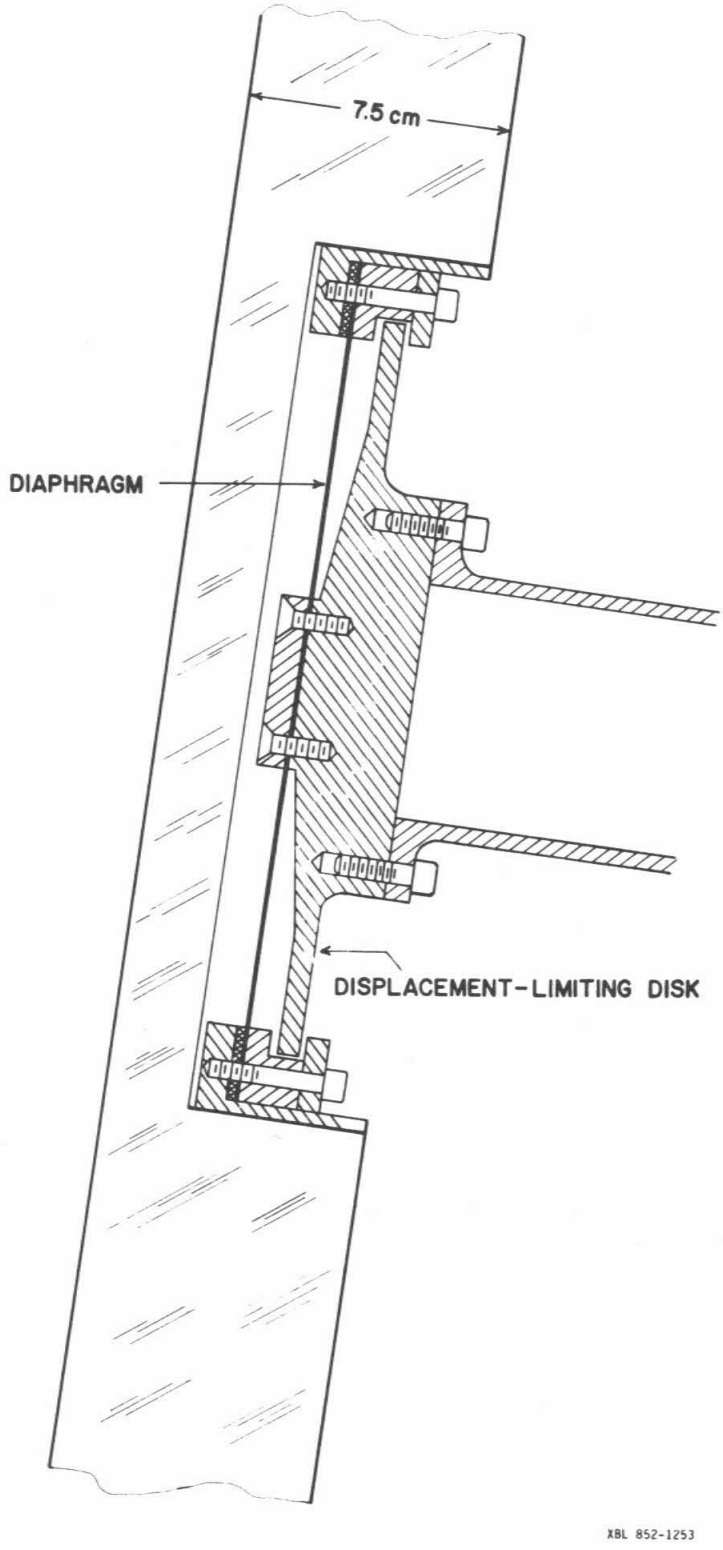

Figure 5-22 Schematic showing the diaphram and radial support post for providing the radial support for each segment. The diaphragm is set in a hole in the back of the center of the segment and allows the small amount of piston and tilt motion required by the control system.

Radial Support Residual Error Correction

When the telescope is pointed at the horizon the load is predominantly carried by the diaphragm at the center of gravity of the segment. Since the segment is a curved meniscus, gravity acts to bend the upper edge forward toward the prime focus and acts to bend the lower edge backward away from the prime focus. This effect is inversely proportional to the radius of curvature of the segment and varies inversely as the square of the thickness. If the segment were flat and held at the center of gravity, then this bending of the upper and lower edges would not occur. A finite-element analysis has been made of the deflections of the hexagonal segment held at the center of gravity (Budiansky,1983, TMT Technical Note No. 74). The surface is comatic, and dominated by the Zernike coefficients $C_{31} = -0.093\mu$m and $C_{51} = 0.048\mu$m. The resulting image blur calculated using geometrical optics yields 80% of the energy in a circle of 0.25 arcseconds. The error varies as $\sin\theta$, where θ is the zenith angle. The atmospheric seeing image size varies as $(\cos\theta)^{-3/5}$. Thus near the horizon the segment surface error can be larger than at the zenith. Unfortunately, since these effects scale differently with θ, one cannot greatly relax the radial support error budget relative to the axial one. Hence the single post support is not quite adequate by itself, and a factor of about 2 improvement is desired. After an exploration of alternatives, we selected a method of reducing this aberration to an acceptable level. We will apply four axial forces to the segment, proportional to the sine of the zenith angle, applied at the upper and lower corners, to unbend the mirror. In addition, the diaphragm will be moved away from the center of gravity slightly. Analysis indicates that this simple application of modest forces (about 0.5kg per point for the TMT) will reduce the aberration by a factor of five, sufficient for our purposes. A simple system of weights and rods has been designed for this task.

Warping Harnesses

Since the segments are to be polished as circles and then cut into hexagons, the mirrors may warp from the cutting. If they warp objectionably, then one possible solution is to use a warping harness to apply permanent forces and moments to the segment to return it to the correct surface shape. If the warping harness method is practical and successful, then it may have substantial effect on the segment fabrication. Since we anticipate that practical warping harnesses can be used to remove up to a micron of surface error, the polishing tolerances on the segments could be considerably loosened, probably resulting in substantial saving in the polishing costs. Unlike the whiffletree system, which applies forces that vary with gravity direction (i.e., zenith angle), the warping harness must apply forces that are independent of gravity. Two types of warping harnesses have been studied.

The first applies forces to the segment at the same 36 points that the whiffletrees apply their forces. In practice the forces could be applied through the whiffletrees themselves. These forces are applied with springs that extend from the whiffletree to the mirror cell. This design has the advantage that its analysis uses the same computer code and results that were developed for the whiffletree. It has the disadvantage that the hardware (springs and adjustments) is somewhat cumbersome and is located in an inconvenient and awkward space behind the segment. A successful test of this scheme was made and the results are described in Section 8.3.3.

An alternative method applies forces and moments at points near the periphery and center of the segment. These forces and moments may be applied with leaf spring devices that lay close to the back of the segment. The advantage of this design is that it is compact, resting in a small volume close to the back of the mirror. In addition, it is independent of the whiffletree and thus any undesired coupling between the gravity-dependent whiffletree system and the gravity-independent warping harness will not arise. To date we have only made some preliminary analysis of this design and some preliminary conceptual hardware designs. The scheme appears promising and will be pursued in the near future.

5.10 Primary Mirror Assembly and Alignment

In this Section we outline the procedures which will be used to make the initial assembly and alignment of the segments in the telescope and to make periodic re-alignments of the actively controlled degrees of freedom.

Array Assembly

The primary mirror cell is a welded space frame and the positions of the nodes are expected to be accurate to ± 4mm. The accurate positioning of the segments will rely on the fabrication and positioning of the precision machined subcells. Each subcell will be placed on the mirror cell, precisely positioned with respect to the global vertex of the primary mirror, and bolted in place. Next the actuators will be inserted into the precision sleeves in the subcell. Then the segment (with whiffletrees, radial post, and azimuthal restraint attached) will be placed on the subcell, and the radial post and azimuthal constraint will be secured to fix the position of the segment. Finally, the actuators will be coupled to the whiffletrees.

At the beginning of the procedure the desired position of the segment and the dimensions of the segment, radial post, azimuthal restraint, and subcell will be used to calculate the desired position of subcell. Precision surveying and metrology will be used to set each subcell at the desired position. Surveying targets will placed in the radial post hole and azimuthal restraint hole and used to define the position of the subcell in three-space. The coordinates (radius and angles) of the subcell with respect to the global vertex will be measured and adjusted to the desired values. Possible instruments for making these measurements include commercial surveying devices which measure angles to $\pm$ 1 arcsecond and commercial distance measuring interferometers with an accuracy better than $\pm 1\mu$m. Given these tools we will survey the subcells into place to an accuracy of ± 0.1mm.

The tolerances on the radial position and on the azimuthal angle of the segment are described in Section 5.15.2 under Hexagon-Surface Positioning. The tolerances are given in Table 5-10 in that section. The tolerances for cutting and positioning are the same. The positioning of the subcells (and their precision fabrication) to ± 0.1mm meets these tolerances.

Initial Segment Tilt Alignment and Phasing

The above procedure positions all degrees of freedom to ± 0.1mm. This is well within the range of the actuators. The next step in the alignment procedure is to set to sensors in the middle of their electronic range while the front segment surfaces are aligned.

This segment surface alignment was achieved on the active control prototype using a small dual electronic gauge spherometer. The same method can be used for this stage of the TMT alignment. During the procedure the actuator servo loops are used to maintain the position of a segment during the measurements. The global control loop is not operating. A small spherometer kinematically rests on the edge of one segment and two electronic gauge probes rest on either side of the gap, one on each segment. This device was used to phase the two pieces of glass in the prototype to $\pm 0.03\mu$m, that is, well within a wave. A device identical or similar will be used to measure the relative height of adjacent segments at positions above each sensor. The measurements are made, sensor position by sensor position and segment by segment. As each measurement is made the corresponding sensor reading is recorded. The measurements are then used to move the actuators to achieve the best least squares alignment of the surfaces. The sensors are then electronically adjusted to be in the middle of their range. This alignment is expected to give roughly 0.12 arcsecond images.

Periodic Re-alignment

Drifts in the sensors will require that periodic re-alignments be made. Tests with the active control demonstration suggest such realignments may be required no more frequently than about every 3 days. However, those tests were made in a hostile thermal environment where the temperatures varied over a range of more than $25^{o}C$. The range of nighttime temperatures on Mauna Kea is $\pm 4^{o}C$ 90% of the time over the year and typically changes less than $4^{o}C$ during a night.

The spherometer procedure was used on the prototype to align and phase the two mirrors. It can be used on the TMT to make the initial phasing and possibly subsequent phasings. However, it has a number of drawbacks. These include risk of damage to the surfaces, awkwardness of positioning the spherometer, sensitivity to particles on the surface, and sensitivity to local surface deformations. Instead of using the spherometer we will use optical methods for periodic re-alignments.

Periodic Segment Tilt Alignment

Alignment of the tilts of the segments will be achieved using an area detector and a bright star. The segment tilts are adjusted using the actuators to spread a stellar image into 36 separate images. This spreading will be done by changing the sensor zero-point lookup table. The centroids of these images will be measured, and sensor changes required to superpose all 36 centroids will be calculated. The final accuracy should equal that of the centroiding, estimated to be 0.05 arcseconds. Although initially manual control may be required to find the images, the stability of the sensors will allow the procedure to be done by computer algorithms after the initial alignment is achieved.

Segment Phasing

An optical method for phasing the segments has been devised by Oliver (1983, TMT Report No. 102). The method measures and allows adjustment of the relative height of adjacent segments. The measurements and adjustments proceed from edge to edge. The diffraction pattern from a region that straddles the common edge between two segments is observed. This diffraction pattern is created using an auto-collimating arrangement. A light source at the prime focus illuminates the segments under test, is reflected up to a collimating flat, and then back through the system to the prime focus. The light is reflected twice from the segments so any phase error is doubled. Since the first reflection off the primary mirror produces a parallel beam, the flat must be as large as the illuminated spot. It must be positioned above the region of interest, and therefore we must be able to move it over the aperture of the telescope. This can be done perhaps using a special prime focus module. It can be located any distance from the primary where it will not intercept the diverging and converging beams. The mechanical design of the system has not been completed. It is also expected that starlight can be used for the same analysis.

The analysis of the optical design shows that, using an optimized beam shape, the relative intensity of the wings of the diffraction pattern is a strong measure of the relative segment height and can be used to measure and set that height to a small fraction of a wavelength. Details of the optical analysis including the sensitivity to beam shape, local seeing, and bandwidth are given by Oliver.

5.11 Control System Dynamics

The description and analysis of the control system in the sections above were based on a "quasi-static" approach. We assumed that the perturbations to the segments changed on a time scale long compared to the active control system cycle. We also assumed that the supporting structure was stiff and well damped. This model of the system may or may not be valid for the real structure and the real perturbations. Experience with the active control prototype shows that structural resonances are very important. Structural analysis of the TMT mirror cell design shows it has its lowest resonance frequencies in a region ($\approx$20Hz) where wind forces may play a significant role. Preliminary very rough estimates of the wind perturbations suggest that significant wind energy might be present at the structural resonances. These realities mean that 1) an accurate picture of the expected wind forces is needed, 2) an accurate understanding of the dynamic properties of the segment support structure is needed, and 3) a proper dynamic analysis of the control system based of these inputs is required. Only with these studies completed will we be able to describe confidently the dynamic response of the TMT to the major high frequency perturbation, wind loads, and confidently choose the required bandwidth for the control system.

Wind Perturbations

Early measurements of the wind spectra on the primary mirrors of existing telescopes (UKIRT and MMT) are described by Forbes and Gabor (1982, TMT Report No. 82) and Gabor (1982, TMT Report No. 77). Unfortunately, uncertainties in the absolute normalization of the spectrum mean that these data are not a solid source of input for the dynamic analysis. A program of more extensive and improved measurements will be undertaken in the coming year to provide the required data. The hardware and part of the software for this program exist. Only limitations of funding and manpower have prevented the data collection up to now.

An alternative input to the dynamics study can be based on calculations of the expected wind effects. Two rough but conservative calculations have been made. The first was made to establish goals for the active control system prototype. This is described below in Section 8.4.2 and by Mast, *et al,* (TMT Report No. 79). Another calculation (also rough and conservative) was made to establish a global wind force. Those results are described in Section 7.8. Both of these calculations suggest that wind perturbations might lead to segment amplitudes as high as 100-200nm and occur at frequencies $\leqslant$ 1Hz. Both of these calculations are conservative and could be too high by a factor of ten. Thus the wind perturbations might only lead to amplitudes of 10-20nm which would be negligible.

Dynamics of the Support Structure

Preliminary analyses of the dynamic performance of the mirror cell are available at the time of this writing, and the lowest resonant frequency of the mirror cell (simply supported at the edge) is about 20 Hz. An analysis of the cell and telescope combination, which will include the effect of the flexibility of the rest of the structure on the cell, will be made in the coming months. We expect the mirror cell resonant frequency to decrease somewhat when this full telescope flexibility is included. In addition to the support structure below the actuators, the flexibility of the whiffletrees between the actuator and glass, and the radial support post, also play a central role in the dynamic response of the system. The whiffletrees in the active control prototype have resonant frequencies in the 20 - 30 Hz range. Measurements of the system response to perturbations showed that the control system pumped energy into these resonances and this limited the bandwidth of the system (See Section 8.4.3). Based on this experience with the prototype we are presently designing a new whiffletree which will have several improved features, including greater stiffness. Calculations based on the design and measurements of the new whiffletree prototypes will provide the required structural input to the dynamic study.

Dynamic Study in Progress

The University has recently contracted with Lockheed Missiles and Space Company in Palo Alto to make a study of the dynamic performance of the TMT active control system. This study is presently in progress. It will be based on a detailed description and modeling of the telescope, mirror cell, and segment support structure. A detailed finite element model will be created from which the frequencies and shapes of the significant modes will be determined. A spatial and temporal power spectral density model of the wind loads will be established and applied to the structural model to determine the statistical motions of the relevant parts of the telescope structure. From these motions the optical performance using geometric optics will be evaluated. The mode shapes and frequencies will be used to construct a State-Space model of the system which will also include the sensors, actuators, and control algorithm. The model will be used for closed-loop performance evaluation of the system.

The low levels of natural damping in the structure may very well lead to inadequate performance of a control system based only on static analysis. Some simple changes, for example addition of active damping, may greatly improve the stability and performance of the system and these changes will be tested in the closed loop simulations.

5.12 Diffraction Effects

The geometry of the primary mirror segmentation will cause a specific diffraction pattern that can be calculated in detail using Fraunhofer diffraction theory. At visible wavelengths the fine structure of the diffraction image will be averaged by the effects of atmospheric seeing and mirror roughness. Thus only a qualitative description of the diffraction image for visible light is warranted and this is given in the first section below. At infrared wavelengths a ten-meter telescope can approach diffraction-limited performance and thus a quantitative description of diffractive effects is of interest. In the second section below we describe the ideal diffraction pattern for the segmented aperture and discuss the pattern as it might appear in practice.

Diffraction Images for Visible Light

In existing telescopes bright stellar images typically show a four spike image pattern resulting from the diffraction effects of secondary support trusses (spiders). With a segmented primary mirror an additional contribution to the diffraction spikes will come from the gaps between the segments. For a mosaic of hexagonal segments (Figure 5-23) there will be a pattern of six spikes instead of the usual four.

Two parameters can be used to characterize the diffraction image:

1. The fraction of the energy incident on the primary that is diffracted by the spiders or gaps:

   f = area of spiders or gaps / area of primary

2. The angular scale of the diffraction pattern:

   θ = wavelength / (thickness of support structures or width of gaps)

We list these characteristic parameters for some existing large telescopes.

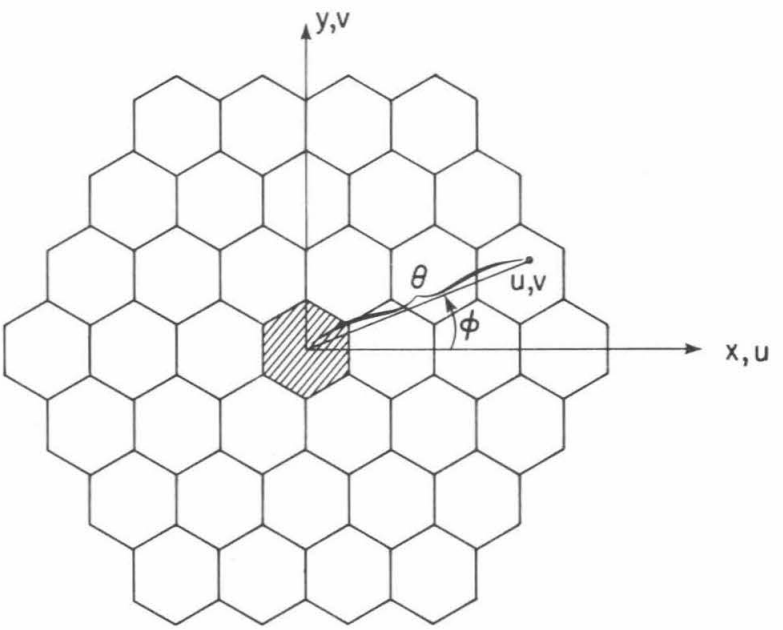

Figure 5-23 The geometry of the primary mirror showing the 36 hexagonal segments. The mirror plane coordinates are (x,y) and the image plane coordinates are cartesian (u,v) and polar (θ, ϕ).

Telescope	Diameter	f(%)	θ(arcseconds)
Palomar	5.0m	0.5	8
KPNO	4.0m	1.0	5
Lick	3.0m	0.9	13
Las Campanas	2.5m	0.9	8

With 10mm wide gaps between the segments these parameters for the geometry of Figure 5-23 are f = 1.0% and θ = 10 arcseconds, i.e., comparable to those from struts in existing telescopes. For narrower gaps there is a proportional decrease in the fractional energy and a corresponding increase in the characteristic angular scale. The TMT will have 7mm wide gaps, 3mm between the segments and 2mm bevels.

Thus the diffraction images from the gaps will be comparable in intensity and size to those seen on existing telescopes with the scattered light distributed among six spikes instead of four.

A diffraction image distribution calculated for the geometry of Figure 5-23 contains structure on three angular scales coming from the three scales of the mirror; the 10m overall aperture, the 1.8m segment size, and a 10mm crack size. For visible light the angular scales resulting from the first two are 0.01 and 0.07 arcseconds respectively. This fine structure is integrated out by atmospheric seeing. The remaining structure then results from a 10mm crack width and the intensity distribution along a spike is given by the simple rectangular aperture diffraction distribution; $(4a^2b^2/\lambda^2)(\sin(kax)/kax)^2$. Here x is the angular image plane coordinate, $2a$ is the spider or crack width, $2b$ is the crack length, and $k = 2\pi/\lambda$.

Note that as the crack width decreases, the energy diffracted into the central part of the diffraction spike decreases, and the angular scale of the diffraction effects increase. An interesting result occurs for angles larger than the characteristic diffraction angle $\theta=\lambda/2a$. There the average intensity in the diffraction spikes becomes roughly independent of the crack width and only depends on the total length of the gaps.

Diffraction Images at Infrared Wavelengths

At infrared wavelengths the size of the diffraction image is larger and the effects of atmospheric turbulence reduced. The fine scale structure is not necessarily integrated over and thus a detailed description of the diffraction image is of interest. The amplitude for the image is given by

$$\Psi(u,v) = \frac{i}{\lambda}\int\int_{aperture} e^{-ik(ux+vy)}dxdy \qquad (5\text{-}16)$$

where (x,y) are the aperture coordinates, (u,v) the image angular coordinates, and $k=2\pi/\lambda$ (Born and Wolf, 1980). Since the aperture is a regular array of hexagonal apertures this can be written

$$\Psi(u,v) = \Psi_{hex}(u,v)\left[\sum_{j=1}^{36} e^{-ik(x_j u + y_j v)}\right] \qquad (5\text{-}17)$$

where x_j, y_j are the coordinates of the segment centers, and the summation is over the 36 segments. Ψ_{hex} is the amplitude for a single hexagonal segment and is calculated by integrating Equation 5-16 over the area of a hexagon.

$$\Psi_{hex}(u,v)=\frac{\sqrt{3}a^2}{4\lambda}\left[\frac{\sin(3\beta+\alpha)\sin(\beta-\alpha)}{\beta(\beta-\alpha)}+\frac{\sin(3\beta-\alpha)\sin(\beta+\alpha)}{\beta(\beta+\alpha)}\right] \qquad (5\text{-}18)$$

where $\alpha=\sqrt{3}kau/4$, $\beta=kav/4$, and a=the segment edge length (0.9m). The coordinate system is defined in Figure 5-23.

The irradiance distribution for a *single* hexagon, $|\Psi_{hex}|^2$, is plotted along a spike (on the u-axis) in Figure 5-24 and between the spikes (at 30^o from the u-axis) in Figure 5-25. The distribution is plotted over the ranges 0 to 5, 50, and 500 arcseconds to illustrate the structure on various scales. It is normalized to 1.0 at $\theta=0$. The distributions are plotted for a = 0.9 m and for a wavelength of 10μm. For other wavelengths the angular scale changes proportionally. In the distribution along the spike there is structure on the scale of 1.3 arcseconds ($kax\sqrt{3}/2=\pi$) and the average intensity falls off as $1/\theta^2$. Between the spikes the average intensity falls as $1/\theta^4$. A circular aperture has a diffraction intensity that falls off as $1/\theta^3$.

The irradiance distribution for the *full array* (with the central hexagon absent), $|\Psi|^2$ is shown along the u-axis (direction of largest angular scale spike) in Figure 5-26, again for λ = 10μm. Figure 5-27 shows the intensity distribution at 30^o from the u-axis, between the spikes. Figure 5-26a covers the distribution out to 5 arcseconds and shows the 0.25 arcsecond structure from the overall 10m aperture. The first maximum away from the central maximum is 2.1% as bright as the central maximum. A circular 10m aperture with no gaps gives the usual Bessel function diffraction pattern in which this maximum is 1.8% of the central brightness. The next highest maximum is then down in brightness by more than a factor of ten, falling faster than the diffraction pattern for a circular aperture. Figure 5-26b covers the distribution out to 50 arcseconds and shows 2.6 arcsecond structure from the segment spacing. The segment spacing in the x-axis direction is effectively 0.78m because of the staggered setting of the hexagons in the array (see Figure 5-23). Finally Figure 5-26c gives the distribution along the spike out to 500 arcseconds and shows the 200 arcsecond structure from the 10mm crack width. There is sharp structure on the 2.6 arcsecond scale, which, if it were brighter, could possibly be mistaken for stellar structure. However, it is 4 orders of magnitude or 10 stellar magnitudes reduced in brightness. In addition, this structure is only sharp in one dimension and thus does not produce point-like images. Given the dynamic range of infrared detectors this structure is unlikely to cause any problems.

The discussion and equations above, and the associated figures, are based on monochromatic light. In practice observations may be made with a significant bandwidth that will average over the fine scale structure in the irradiance distribution. In addition, the fine structure will be further averaged over by any aberrations in the optical surfaces, by atmospheric seeing, and field rotation. We conclude that there will not be artifacts in the infrared image due to diffraction from the segmentation geometry. Finally, we note that the large scale spikes from the gaps arise from the very special relationship between the phases of the segments given by the phases of the unit vectors in Equation 5-17. Any phase errors in the positioning of the segments will alter these phases and thus strongly affect the size and even the existence of the diffraction spikes.

Diffraction Effects of Segment Phasing

Although long term stability of the phasing is expected, it is worthwhile to establish the consequences of partially or completely unphased segments.

The amplitude given in Equation 5-17 is modified to include the effect of the segment tilt and phasing as follows

$$\Psi(u,v) = \sum_{j=1}^{36} \Psi_{hex}(u+2\alpha_j, v+2\beta_j) e^{-ik(x_j u + y_j v + 2\gamma_j)}, \tag{5-19}$$

where α,β, and γ are defined for each segment by the error surface describing the deviation of the surface from its ideal position.

$$\delta z = \alpha_j(x-x_j)+\beta_j(y-y_j)+\gamma_j \tag{5-20}$$

To understand the effects of phasing alone we can make the assumption that the tilt errors α and β are small. For visible light this is not a good assumption since the diffraction limit θ(80%) is about 0.019 arcseconds and the geometric optics calculation of segment tilt errors in Section 5.4 gives θ(80%)= 0.027 arcseconds. At 10μm it is better since the diffraction limit is

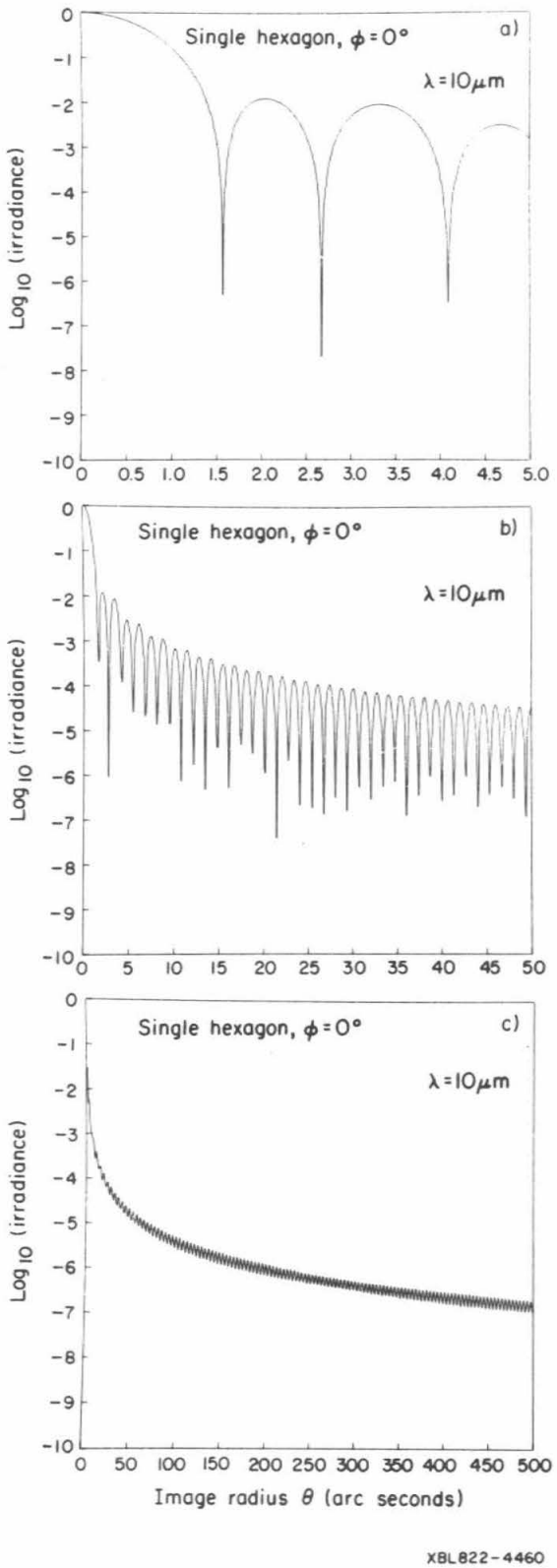

Figure 5-24 The intensity of the diffraction pattern along the u-axis from a single hexagon. The hexagon is 0.9m on a side and the pattern is plotted for a wavelength of 10μm.

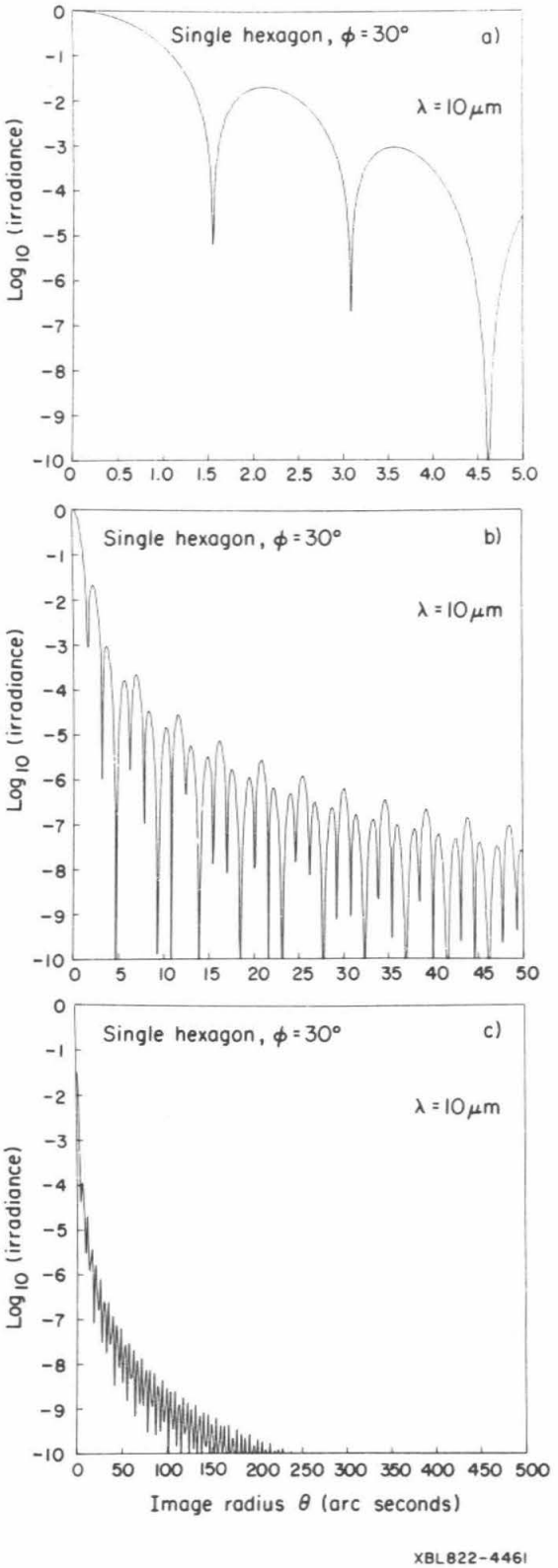

Figure 5-25 The intensity of the diffraction pattern along a line at 30^o from the u-axis for a single hexagon. The hexagon is 0.9m on a side and the pattern is plotted for a wavelength of 10μm.

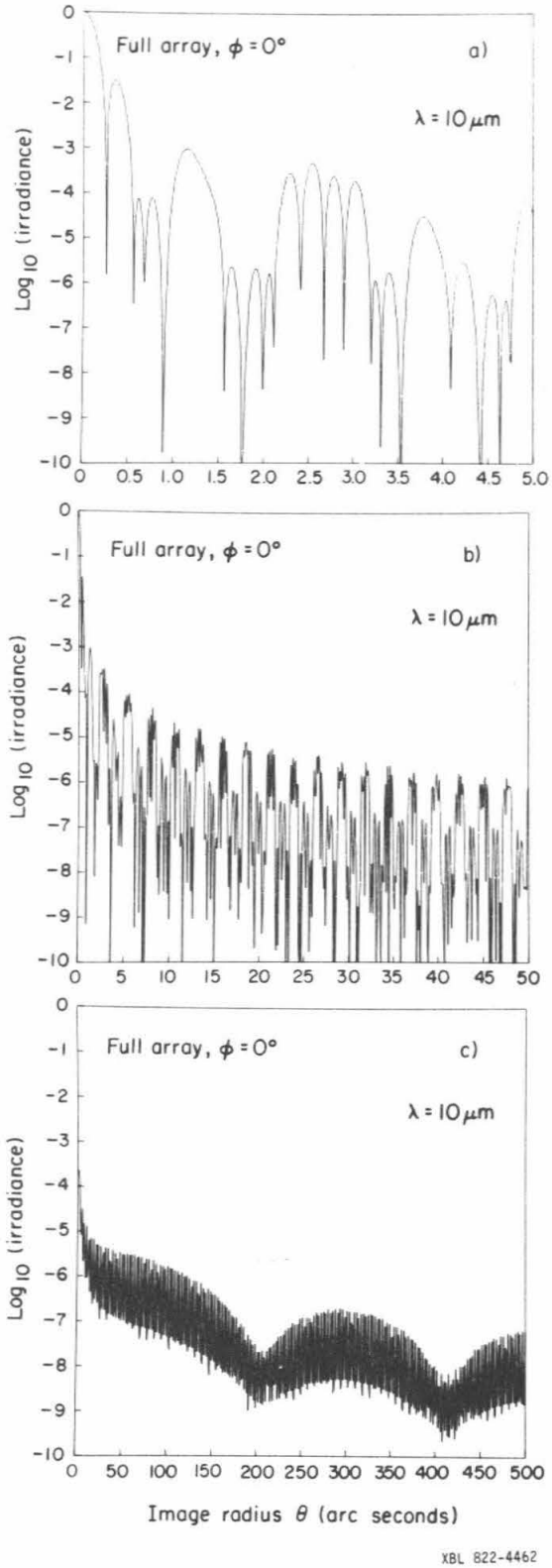

Figure 5-26 The intensity of the diffraction pattern along the u-axis from the full array of hexagons plotted for a wavelength of 10μm.

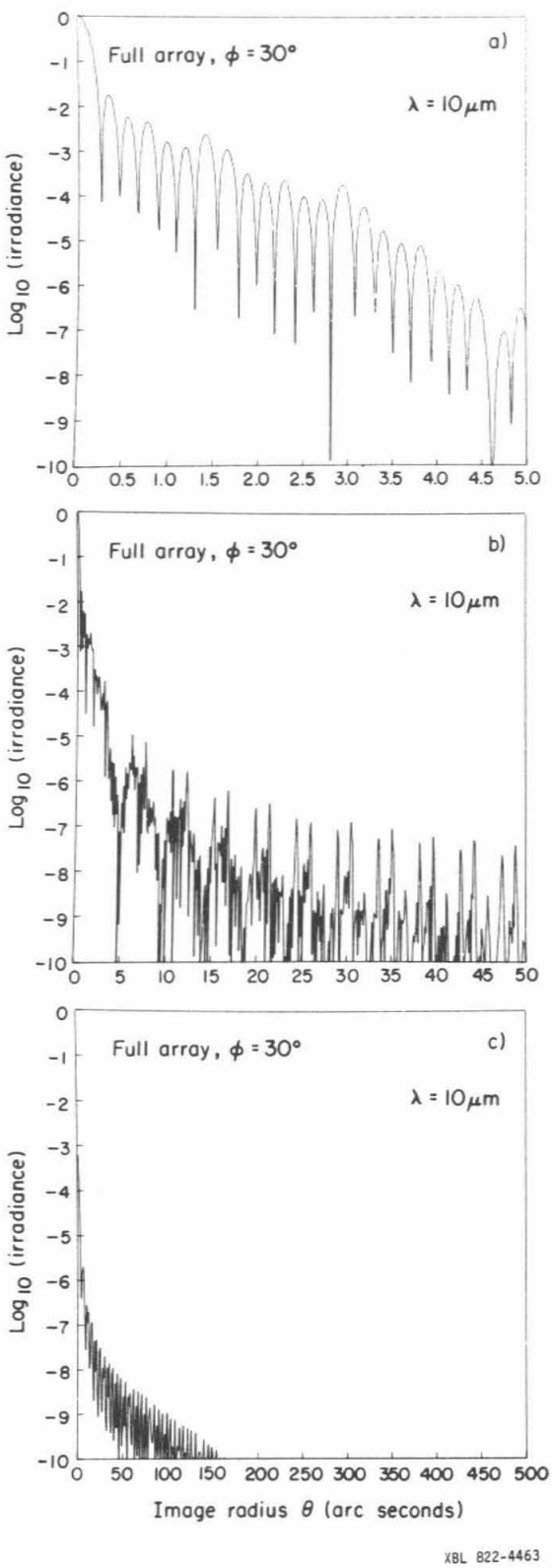

Figure 5-27 The intensity of the diffraction pattern along a line at 30^o from the u-axis for the full array of hexagons plotted for a wavelength of 10μm.

$\theta(80\%) = 0.38$ arcseconds.

The calculation of the irradiance distribution from Equations 5-19 and 5-20 for the hexagonal array with cracks and with the expected tilt and phasing noise requires a monte carlo computer calculation. We describe here an analytic calculation of the effects of only the phasing errors in order to give a qualitative understanding of their effects. With the assumption that there are no tilt errors the irradiance then reduces to

$$|\Psi(u,v)|^2 = |\Psi_{hex}(u,v)|^2 \left| \sum_{j=1}^{36} e^{-ik(x_j u + y_j v + 2\gamma_j)} \right|^2, \tag{5-21}$$

where the final factor is the amplitude squared of a sum of unit vectors with random phases. The statistics of the sum of random vectors is treated in wonderful detail by Beckmann and Spizzichino (1963). We have used their treatment to derive the irradiance including the effects of the cracks between the segments. We derive the irradiance for two different possible distributions of phases. The first is with the segment heights random over a range of heights that exceeds a wavelength, i.e. all phases in the interval $(-\pi,\pi)$ are equally probable. The net irradiance is then given by

$$|\Psi_\sigma(u,v)|^2 = N\,|\Psi_{hex}(u,v)|^2. \tag{5-22}$$

It is noteworthy that the parameters of the array are absent from this expression; that is, it doesn't depend on the crack width. It only depends on the dimensions of a single hexagon.

A second possibility is a Gaussian distribution of phase errors. If the phase errors have the Gaussian distribution then

$$w(\phi) = \frac{1}{\sigma_\phi \sqrt{2\pi}} e^{-\phi^2/2\sigma_\phi^2}, \tag{5-23}$$

where $\phi = 4\pi\gamma/\lambda$. The relationship between the rms surface height, σ_γ, and the rms phase, σ_ϕ, is simply

$$\sigma_\phi = 4\pi\sigma_\gamma/\lambda, \tag{5-24}$$

which includes a factor of 2 from the reflection from the surface. Again using the results of Beckmann and Spizzichino the irradiance is given by

$$|\Psi_\sigma(u,v)|^2 = |\Psi(u,v)|^2 e^{-\sigma_\phi^2} + N\,|\Psi_{hex}(u,v)|^2 (1 - e^{-\sigma_\phi^2}) \tag{5-25}$$

The first term contains the irradiance of the perfectly phased array and is thus defined by the array parameters, including the crack width. The total irradiance $|\Psi_\sigma(u,v)|^2$ is just a fraction of the image from a perfectly phased mirror added to a fraction of the image from a completely randomly phased mirror. Thus the transition from one extreme to the other is smooth.

The fractional energy contained in a circle of radius θ' is given by

$$F_\sigma(\theta') = (e^{-\sigma_\phi^2}) F(\theta') + (1 - e^{-\sigma_\phi^2}) F_0(\theta'), \tag{5-26}$$

where $F(\theta')$ and $F_o(\theta')$ are the fractional energies for the phased array and individual segment respectively. The fractional energy for the phased array, $F(\theta')$, includes the effects of the large diffraction spikes from the cracks between the segments.

Based on the budgeted sensor and actuator noise (Table 5-9) and Equation 5-2, the rms surface error is only 0.012μm. Initial phasing of the segments will probably dominate the rms surface error although this can potentially be done to high accuracy (Oliver, 1983, TMT Report No. 102). We estimate that the initial phasing of the segments can be made to $\lambda/20$ for visible light, or about 0.025μm. If the total $\sigma_\gamma = 0.030\mu$m, then for visible light observations, $e^{-\sigma_\phi^2}$ is about 0.5 and the contributions from the two terms are about equal. Thus, for this phase error we expect the diffraction spikes from the cracks to to be substantially reduced. The diffraction image will approach that due to a single hexagon. At a wavelength of 10μm $\sigma_\phi^2 = 0.0014$ and the phased array makes the dominant contribution to the diffraction image. We have found no tractable analytic expression for the fractions F for the array or for an individual hexagon. So again to get a qualitative understanding of the unphased system we use the fraction for a

circular aperture. If we assume a circular aperture of radius R we can calculate the functions $F(\theta)$ and $F_0(\theta)$ (Born and Wolf, 1980):

$$F(\theta) = 1 - J_0^2(kR\theta) - J_1^2(kR\theta)$$

$$F_0(\theta) = 1 - J_0^2(ka\theta) - J_1^2(ka\theta). \qquad (5\text{-}27)$$

Now using Equations 5-26 and 5-27 for a given F_σ we can relate $kR\theta'$ to σ_γ, and this is plotted in Figure 5-28 for $F_\sigma = 0.8$ and 0.9. For $\lambda/50$ or less there is only a small degradation of the diffraction-limited image. For rms surface errors larger than $\lambda/50$, however, the image size (θ') containing 90% of the energy in particular grows quite rapidly. If the segments are phased to an rms of 0.26 μm, then the performance specified in Section 3.3.1.2 can be achieved at 10 μm.

The image diameter containing 80% of the energy is shown as a function of wavelength in Figure 5-29 for various values of rms piston error. The change from segment diffraction limit (the upper straight line) to full primary diffraction limit (the lower straight line) as the wavelength increases is illustrated. The wiggles in the curves come from the zeros of the Bessel functions in Equation 5-27. Again, an rms surface phasing of 0.26μm gives near diffraction-limited performance at a wavelength of 10μm. The expected surface error for the TMT is about 0.03 μm, far less than required.

5.13 Infrared Characteristics

The performance of the TMT in the infrared has been analyzed and described by Matthews (1981, TMT Report No. 46) and by Jones and Matthews (1982, TMT Report No. 78). They treat those aspects of the telescope design which affect infrared performance. We review here briefly only the effects of the primary mirror. This discussion is based on the above reports and on some calculations given by Mast (TMT Technical Note No. 112).

The goals for optimum infrared performance are 1) to minimize the IR background and 2) to minimize the fluctuations in the IR background. The segmented mirror has a source of background that doesn't exist with a monolith; the gaps between the segments. This background can vary since the segments move independently. Small transverse motions will change the gap width and thus the IR background.

Background Contribution from the Gaps

The gaps between the segments are 3mm wide and there is a 2mm wide bevel on each segment. Thus the total non-reflecting gap is 7mm wide. The total gap area is 0.7% of the total mirror area.

Telescope sources of background (emissivity x fractional area) are:

spiders:	0.7% (assuming emissivity=1)
gaps:	0.7% (assuming emissivity=1)
primary surface:	2.0% (assume coated with aluminum)
secondary surface:	1.0% (assume coated with gold)
top socket shadow:	0.0% ($3m^2$ eliminated by cone in secondary)
total	4.4%

The fractional area of the gaps is equal to that of the spiders. Thus they do not present any new problems for IR observations. In addition, the contribution from the gaps does not significantly increase the telescope emissivity. The total estimated emissivity of 4.4% is typical of the IR backgrounds in existing IR telescopes.

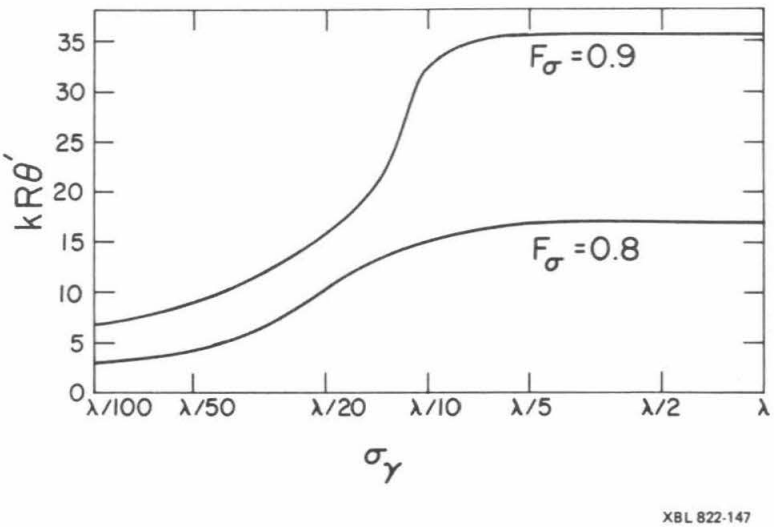

Figure 5-28 The image "radius" $kR\theta$ versus rms piston error which contains 80% and 90% of the image energy. For small piston errors the angles are those of the diffraction limit for the full primary. For large piston errors the angles correspond to the diffraction limit of a single segment.

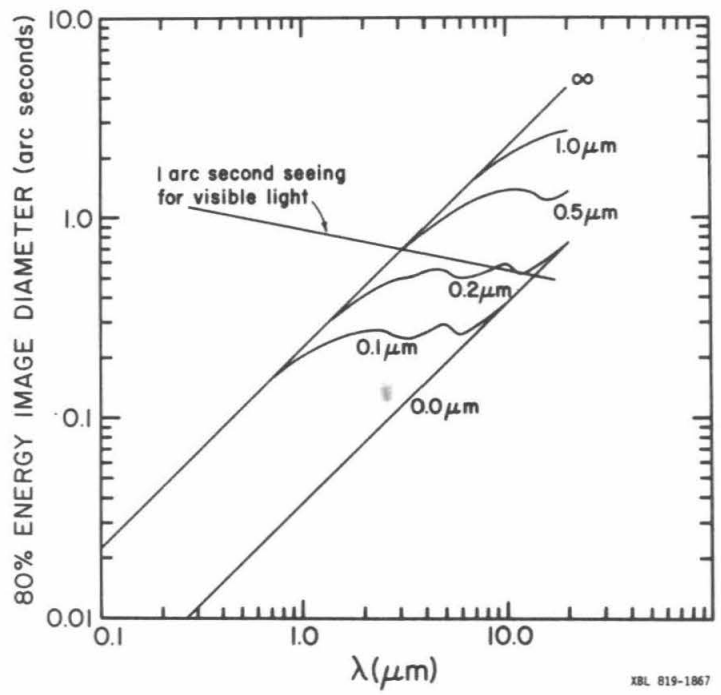

Figure 5-29 The image diameter (80%) for various rms piston errors as a function of wavelength. As the wavelength increases the image diameter changes from the single segment limit (rms = infinity) to the full primary limit (rms = 0.0).

Variations in the Background

The goal of IR telescope design is to limit the background variation to a value that is smaller than the photon statistical fluctuations. Thus we must examine each source background variation and compare it with the square root of the number of detected photons. In estimating the number of photons we have made a worst case analysis. We consider broadband observations at 10μm where the atmosphere emission is often very low and the background is thus dominated by the telescope emission. We assume a warm telescope ($10^{o}C$) and a large aperture (15 arcseconds diameter). To estimate the number of photons we assume $10^{o}C$, wavelength = 10 microns, bandwidth = 6 microns, a 15 arcsecond diameter aperture, and emissivity 4.4%. This is a worst case with broadband and a large aperture. The calculations are based on an assumed chopping frequency of 40Hz and nodding frequency of 0.05Hz.

Changes in the gaps occur due to the following effects:

1) Active control motion of the segments: Since the mirror is curved and the actuators move the each segment normal to its surface, actuator motions will cause the gap width to vary by small amounts.

2) Chopping induced transverse motions of the segments: The chopping of the secondary might be made at frequencies in the 20-40Hz range. The transverse resonant frequency of the segments is also in this range. Telescope motions induced by the chopping secondary could excite transverse motions of the segments and cause the gap widths to vary.

3) Wind induced transverse motions of the segments: Wind forces on the top of the telescope will cause the telescope to shake and this motion will excite transverse motions of the segments.

4) Thermal expansion of the steel: Expansion and contraction of the steel support structure will vary the gap widths.

5) Gravitational deflections of the support: As the telescope moves in altitude the gravitational deflection of the mirror cell causes the segments to move small transverse distances.

6) Chopping moves the beam over the primary mirror exposing different portions of the segments and gaps.

These changes will occur as a function of time and will each have a frequency power spectrum. Variations in the background flux on time scales small compared to the chopping period will be averaged during the data collection. Variations in the background flux on time scales long compared to the chopping period can be removed by the nodding and data analysis. Of most concern are variations in the background that are at frequencies close to the chop frequency and its harmonics or in resonance with the nod.

We will not reproduce here the calculations of the sizes of these effects. They are given in the reports and note mentioned above. Those calculations show that effects 1, 3, 4, and 6 have variations in the background that are negligibly small compared to the photon statistical fluctuations.

The chopping frequency of the secondary is near the transverse resonance frequency of the segments and induced segment motions could vary the gap sizes. An estimate of effect 2 shows that it will be important to balance and isolate the secondary motion from the telescope. It will be important to make the segments stiff against in-plane motions and to choose a chopping frequency that will not excite these motions.

Effect 5, the gravitational deflections of the support, could cause the gap size to vary in phase with the nodding, if the nodding is in the zenith angle direction. A worst-case, rough calculation suggests this effect is about a factor of 10 larger than the photon statistical fluctuations in a single nod period. This worst-case calculation assumed a nod throw of 5 arc minutes. It was based on a very rough estimate of the change in the overall gap area as the telescope moves from zenith to horizon. A more detailed calculation will be made using the final mirror cell design and structural analysis results.

In general, neither the gaps between the segments nor the active control of the segments will degrade the infrared performance of the telescope. The possible ability to overcoat the segments, and therefore clean them frequently without surface degradation, may significantly improve the IR performance of the segmented mirror over a monolithic one.

5.14 Segment Surface Maintenance

Frequent refurbishment of the primary mirror segments is important in achieving the maximum performance of the telescope. To facilitate continuous operation of the instrument, six spare segments are included in the inventory, one for each mirror surface type. The spares will be mounted while the originals are re-aluminized. By this procedure the surface maintenance program causes only a minimal interruption of the observation program.

Segment Removal and Handling

A system has been designed to accommodate frequent and safe segment changes. In so doing, the number of parts and systems were minimized, enhancing safety and reliability. The system is based upon a conventional horizontal boom and trolley with hoist. The minimum capacity of this system is 2000kg. Due to the precise calibration necessary for mirror handling, the crane should be used only for loads and service similar to those imposed during mirror handling.

Several mechanical devices will be used during the procedure of segment removal. Some of these have been designed and tested, and others are still in the preliminary concept stage.

In general, the edges and perimeters of all parts that operate within the telescope frame will be padded to avoid damage to either system.

The system is designed to be operated by two persons, a crane operator at the crane control point at the Nasmyth level, and a mirror installer at the underside of the segment. The sequence of events is as follows:

1. The crane boom (50 feet) and traveling hoist are normally parked above the Nasmyth level in the horizontal operating position (Figure 5-30). The telescope is pointed at the zenith and rotated to the entry position, Figure 5-31. The crane boom is swung from the parked position into the interior of the telescope frame, Figure 5-32. The telescope is then rotated to the desired azimuth for extraction of a pre-determined mirror segment. Several segments may be removed from an area without further movement of the telescope.

2. The crane operator aligns the hex frame to the recorded bearing angle, Figure 5-33.

3. The talons are raised or lowered on the frame for the varying edge height known for the segment in question, Figure 5-34. Multiple holes in each talon strut provide the means of adjustment. The talons are held open by compression springs.

4. The boom is aligned to the recorded angle over the selected segment.

5. The hex frame is lifted to the underside of the boom, and traverses a fixed length to the point directly over the segment. This is determined by visual confirmation of the number of turns on the drive drum, or by reference markings on the drive cable.

6. The hex frame is lowered to the pick-up position, again by the crane operator's visual confirmation of drum or cable travel.

7. The installer below the segment removes the sensors (up to 12) associated with the segment. At present this requires for each sensor removal of nuts and springs from six threaded rods. We believe that future modifications of the sensor design can reduce this to just two mounting nuts. Following the sensor removal the whiffletrees are decoupled from the actuators, the radial post and azimuthal anchor are released, and then a screw jack is used to raise the mirror using the radial support post. The mirror is pushed up against gravity parallel to the local segment normal.

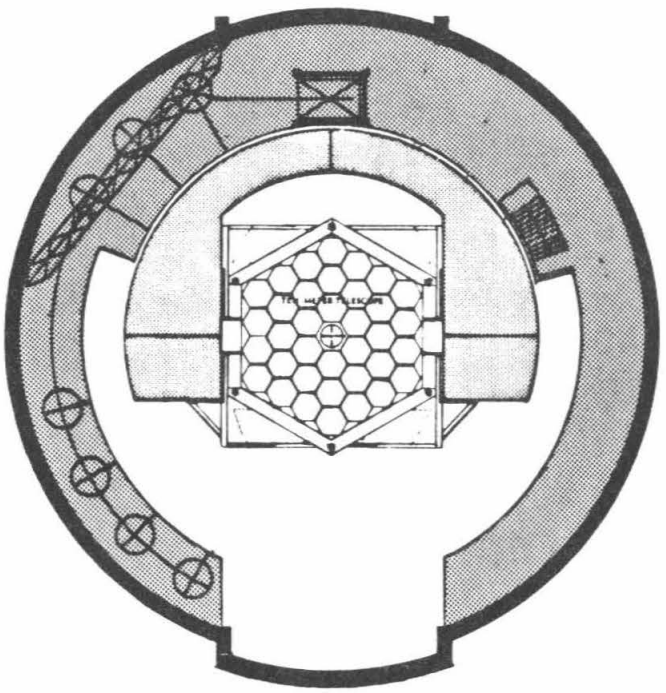

XBL 8410-4470

Figure 5-30 The 50' boom and traveling hoist are parked above the Nasmyth deck in the horizontal operating position.

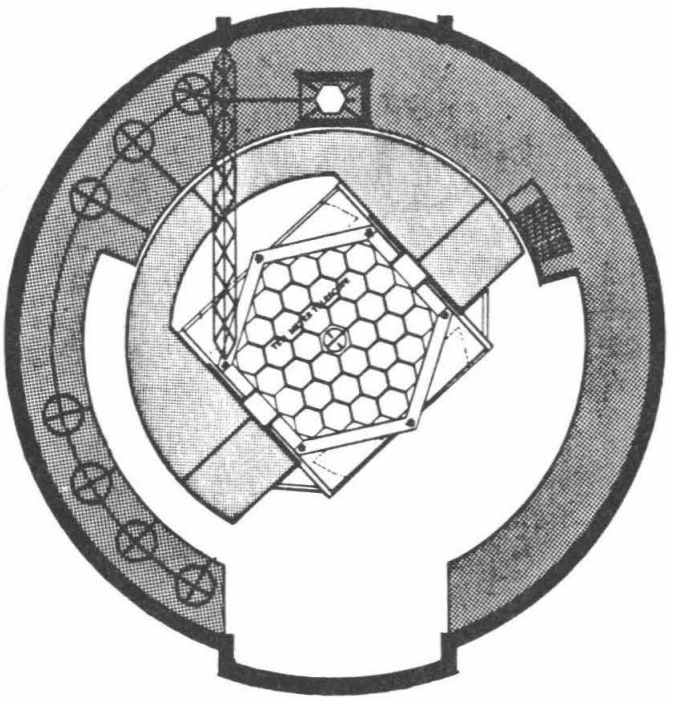

XBL 8411-4947

Figure 5-31 Crane entry at the northwest section the telescope is shown. The telescope is rotated 43^{o}. The boom is then swung east to center through a frame diamond.

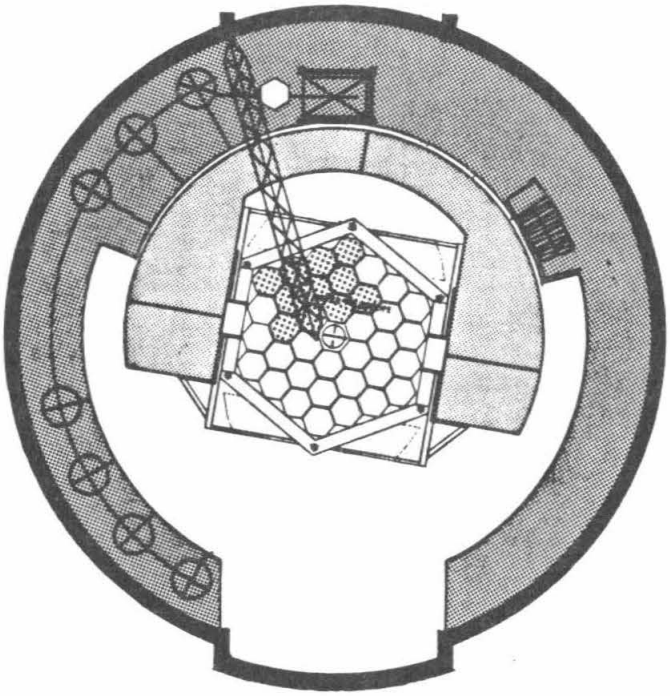

XBL 8411-4946

Figure 5-32 Mirror segments which may be reached in the northwest section are shown shaded. With the telescope 9^o west of south the boom will traverse from 12^o to 30^o east of south. A mirror segment is shown on its monorail cradle near the hoist.

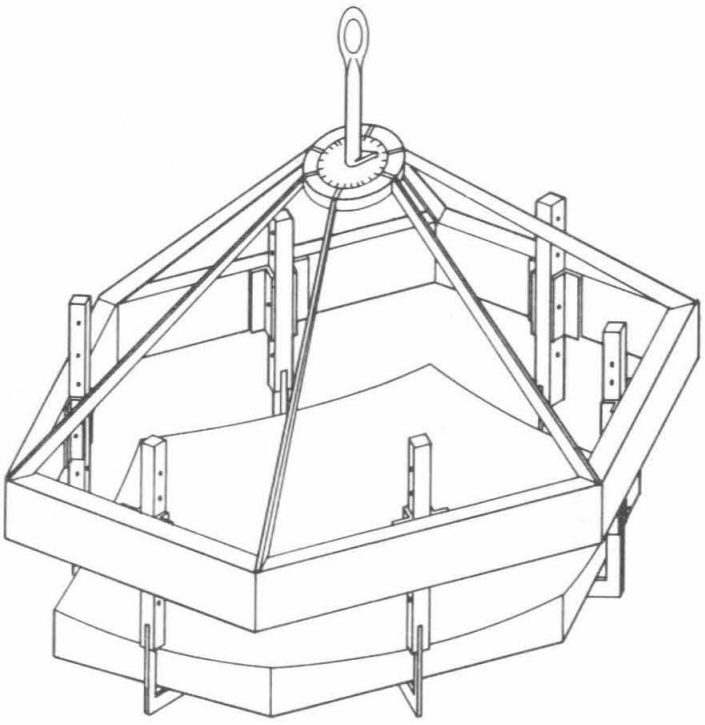

XBL 8410-4476

Figure 5-33 Talon device with mirror segment. Six adjustable talon struts and bearing angle adjustment are shown.

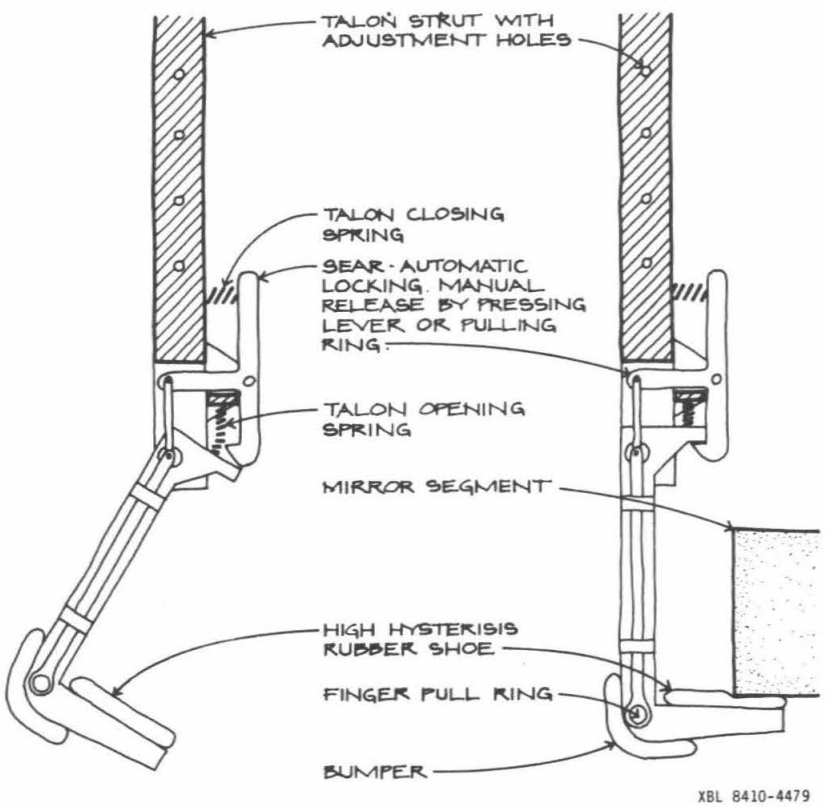

Figure 5-34 Talon struts in opened and closed positions.

8. As the segment clears the surface, the worker below can observe the overall alignment of the segment to the opened talons. In the event that cable fatigue or differential settling have occurred, instructions can be given to the crane operator to adjust the location of the suspended hex frame. The segment is boosted to the full 300mm extension above the primary mirror surface when adequate alignment is achieved. Allowable clearance could be as much as 50mm all around between the segment and the talon tips in the open position.

9. The talons are closed manually from below by the mirror installer. A locking sear positively holds the talon closed for lifting, Figure 5-34. At this point the radial support post is decoupled from the diaphragm-insert assembly (this coupling has not yet been designed).

10. The mirror is lifted vertically, at which time it reaches lateral equilibrium between the axis of symmetry of the talon device and the center of mass of the segment. It is then traversed to the exterior of the telescope frame. The sears are manually released by the crane operator after placing the segment in a cradle.

11. The segment in its cradle is moved to the Aluminizing Room on a monorail truck similar to that used for instrument modules.

12. The identical replacement mirror segment is rolled out and loaded into the hex frame. The process is reversed and repeated with the installation of each replacement.

13. Upon lowering the mirror segment onto the fully extended central screw jack, the mirror installer pulls the finger ring to release each sear. He then lowers the segment onto the support. The radial post and azimuthal anchor are locked, the whiffletrees are connected to the actuators, and the sensors are reinstalled.

Surface Overcoating

Ideally one would like to cover the surface with a broadband durable protective coating. This would give a long lifetime to the surface and allow it to be washed often. To our knowledge no such coating has been developed and demonstrated. However, research to develop such a coating is in progress. Thus we plan to design and build the coating facility to accommodate the equipment and operations that are needed for multi-layer dielectric coatings.

A vertical chamber in which the mirror is on top looking down will be required. The stainless steel chamber will be about 2.5m diameter and 2.5m long. The chamber will sit in an area of the facility with a sunken floor to allow easy entry of the segment to the top of the chamber from the floor level. The chamber will provide a high quality vacuum, and have the capability of rotating sources and/or segment and have sufficient height to achieve highly uniform coatings. The facility will be a well-lighted, clean, low dust environment with a crane for handling the segments. It will require about 100kW of power for coating, pumps, and various electrical outlets.

Aluminizing and Cleaning

The segments will be re-aluminized using conventional procedures. HNO_3 in a 10:1 dilution will be used to strip the Al coating. De-ionized water will be used for rinsing. Aluminizing will done at 10^{-6} torr after a final cleaning using glow discharge. We expect to periodically wash the segments while they are in the telescope. A detailed procedure for doing this has not been developed. Since the sensors are protected by a sealed rubber boot, we believe that a practical and safe procedure can be developed.

5.15 Segment Manufacture

The material for the mirror blanks must satisfy those criteria usually needed for optical mirrors, and in addition it must satisfy special requirements resulting from our special polishing technique and mirror design. We describe the selection of the blank material in Section 5.15.1.

The specifications for the mirror blanks, the generating of the meniscus shapes, and the polishing and cutting of the segments are described in detail in a series of notes (Mast *et al.* 1984, TMT Technical Notes 88, 89, and 90). We review these specifications in Section 5.15.2 below.

Because of the difficulty normally associated with fabrication of non-axisymmetric optics, we have invested substantial effort into selecting and testing an efficient and accurate fabrication technique. The method proposed for grinding and polishing the segment concave surface, Stressed Mirror Polishing, is one that we have developed since 1979. This method is described in Section 5.15.3, and the tests of the technique are described in Section 8. Those tests show that the technique can be used to rapidly create the off-axis surfaces needed for the TMT segments.

5.15.1 Selection of Material

Non-Glass Materials

The conventional requirements of polishability, durability, stability, and high strength have made glass-like materials the traditional choice for high quality telescope mirrors. Occasionally, metal mirrors, particularly nickel coated metal mirrors, have been used in special circumstances, but the reputed instability of these materials has made them a poor choice for most applications. Their high coefficient of thermal expansion has been a liability, but since their thermal conductivity is also quite high, their thermal properties have been viewed as acceptable. It is still possible that casting techniques will be developed that will make metals such as aluminum acceptable blank materials, but because there is presently no direct evidence that such materials can be used we have rejected them. We note however encouraging work underway at European Southern Observatory (Mischung, 1984, Noethe, *etal,* 1984). Other non-glass like materials such as graphite-epoxy composites exhibit creep and poor polishability due to their grainy nature. Thus, only glass-like materials were considered for the mirror blanks.

Homogeneity and Isotropy

In applications where weight reduction is of overwhelming importance, e.g. space applications, light-weight mirror blanks have been used. These have either been solid blanks that have been cored by machining, or egg-crate blanks that have been fabricated by the mechanical assembly and subsequent fusion of thin sheets of glass material. Both of these types of light-weight blanks have been very much more expensive than a solid blank of the same overall thickness. This large increase in potential cost makes these types of light-weight blanks unattractive for our application. Casting of light-weight blanks is presently being developed by Angel (Angel and Hill, 1983, and Angel, *et al,* 1983) and the prospect of inexpensive large egg-crate blanks is promising. Lightweighted mirrors have the advantage that their thermal inertia is reduced.

In addition, we wish to polish our surface shape while warping the blank by the external application of shear forces and bending moments around the periphery. A blank with the non-uniform elastic properties of a light-weight blank would make the use of the method substantially more difficult. For this reason, and the present unavailability of lightweighted blanks, we have chosen a blank that is homogeneous and isotropic.

Thermal Requirements

The blank material must perform adequately in the thermally hostile environment of the observatory mountain top. Thus in the face of a range of temperature (± 10°C) and thermal gradients the mirror segments must still maintain their correct surface shape. In addition, since our active control sensing system measures the position of the back of the mirror, we require that the distance from the back to the front be adequately stable.

Thermal Expansion Coefficient

For thermal analysis, the shallow shell form of a segment can be approximated by a flat plate with a thickness h and radius a. Assume the midplane of the segment is the x-y plane. We specify the coefficient of expansion throughout the segment by

$$\alpha(r, \theta, z) = \alpha_0 + \frac{z}{h}\delta\alpha + \cdots \tag{5-30}$$

We can also specify the temperature field in the segment by

$$T(r, \theta, z) = T_0 + \frac{z}{h}\delta T + \cdots \tag{5-31}$$

where δT is the front to back temperature difference, T_0 is the temperature change from the figuring temperature to the operating temperature, α_0 is the average coefficient of thermal expansion and $\delta\alpha$ is the average front to back difference in the coefficient of expansion. If only the first two terms of each expression are present and if α and T have no r,θ dependence, one can readily show that the mirror deflection caused by thermal effects is given by

$$\delta z(r, \theta, z) = -\frac{r^2}{2h}(\alpha_0\delta T + T_0\delta\alpha) \quad , \tag{5-32}$$

or writing this in terms of Zernike polynomials,

$$\delta z(r, \theta, z) = C_{20}Z_{20} \tag{5-33}$$

$$C_{20} = -\frac{a^2}{4h}(\alpha_0\delta T + T_0\delta\alpha) \tag{5-34}$$

A more detailed calculation including α and T with a dependence on r and θ is given by Nelson (1984, TMT Report No. 52).

One can estimate the image blur resulting from such distortions using geometric optics. For a circle of radius a a fraction ξ of the energy will be contained in an image diameter given by

$$\Theta_{dia}(\xi) = 16\frac{C_{20}}{a}\xi^{1/2} = \frac{4a}{h}(\alpha_0\delta T + T_0\delta\alpha)\xi^{1/2} \tag{5-35}$$

For a hexagon the 80% enclosed energy diameter is given by

$$\Theta(80\%) = 13.3\frac{C_{20}}{a} \tag{5-36}$$

We consider an example for each term in Equation 5-34 using $h = 0.075$m and $a = 0.9$m. If $\alpha_0 = 5\times10^{-8}$/°C and $\delta T = 0.25$°C, then $\Theta(80\%) = 0.10$ arcseconds. If $\delta\alpha = 3\times10^{-9}$/°C and $T_0 = 4$°C, then $\Theta(80\%) = 0.10$ arcseconds. If all segments undergo the same change in C_{20} then the global aberration can be removed by tilting the segments and refocusing the telescope. Thus the quantities in these examples should represent the deviations within the array about some mean. The details of this statistical calculation can be found in Nelson and Mast (1985, TMT Technical Note No. 113).

Thermal Gradient

For a temperature difference δT and a material conductivity k, there will be an average flow of heat through the segment of

$$P = \frac{k\delta T}{h} \tag{5-37}$$

The rms surface change (due to a change in curvature) caused by a linear thermal gradient inside the mirror resulting from a net power flow into one side of the mirror is given by

$$\sigma = \frac{a^2\alpha_0 P}{(3)^{1/2}4k} \quad , \tag{5-38}$$

where P is the power incident on one side of the mirror, and k is the thermal conductivity of the material. Note that this result is independent of the mirror thickness.

For Zerodur the conductivity is $k = 1.64\text{W/m}^o\text{C}$. so for $\delta T = 0.25°\text{C}$ and h=0.075m we obtain

$$P = 5.5\text{W/m}^2$$

We expect that in the normal telescope environment $P < 6\text{W/m}^2$.

Typical heat flow rates are about $5\text{W/m}^2\,°\,\text{C}$ for radiative coupling (emissivity = 1) and roughly $2\text{W/m}^2\,°\,\text{C}$ for free convective coupling. Since in the dome environment, temperature differences of several degrees between parts of the structure and the air temperature may be common, it appears unrealistic to assume that the asymmetric flow of heat into the segments can be controlled to a level much below 0.5W/m^2. The amount of image degradation is shown in Figure 5-35 as a function of the expansion coefficient of the mirror segment for a variety of assumed asymmetric heat loads. From this we see that Pyrex is unacceptable. Since this warping is basically a change of focus, the final image of the telescope will be degraded if all segments do not experience the same heat load.

This discussion loses its validity if the internal thermal time constants of the segments become large compared to the time scale of thermal variations in the environment. For a uniform thickness plate the characteristic time for the interior to come to equilibrium given an initial front to back thermal gradient is given by

$$\tau = \frac{h^2}{\pi^2\,\beta} \quad , \tag{5-39}$$

where β is the diffusivity of the material. This assumes heat transfer through both the front and back surface. For our segments (h = 75mm, $\beta = 0.8 \times 10^{-6}\ \text{m}^2/\text{s}$) the time constant is about 10 minutes, hence the assumption of short internal time constant is valid. For more conventional large telescopes of the 4m class, the mirror thickness is typically 500mm, resulting in an internal time constant of about 9 hours. Thus for those mirrors the internal temperature gradients may not be linear and the above analysis may not apply.

Thermal Coefficient Gradient

Linear variations of α through the thickness may be more serious, since the availability of blanks with a small value of $\delta\alpha$ is not known. If for example $T_o = 18^o$, (perhaps typical of the difference between the operating temperature and the optical fabrication and test temperature) and $\delta\alpha = 3 \times 10^{-9}/^o\text{C}$ yields Θ_{80}=0.44 arcseconds. Measurements of α are not commonly made even to this accuracy. One potential mirror material, Zerodur, is made by Schott Glass Co. Schott measures α with an uncertainty of $\pm 5\times 10^{-9}/°\text{C}$ for a single measurement. They have suggested making a series of 9 measurements on each side of the blanks. Statistically, this would allow measurement of $\delta\alpha$ to about $\pm 2\times 10^{-9}/°\text{C}$. If such measurements detect a gradient, we can reduce the image blur by a factor of two by simply orienting the blanks so the gradient has the same sign for all segments. Such measurements have been made by Schott of

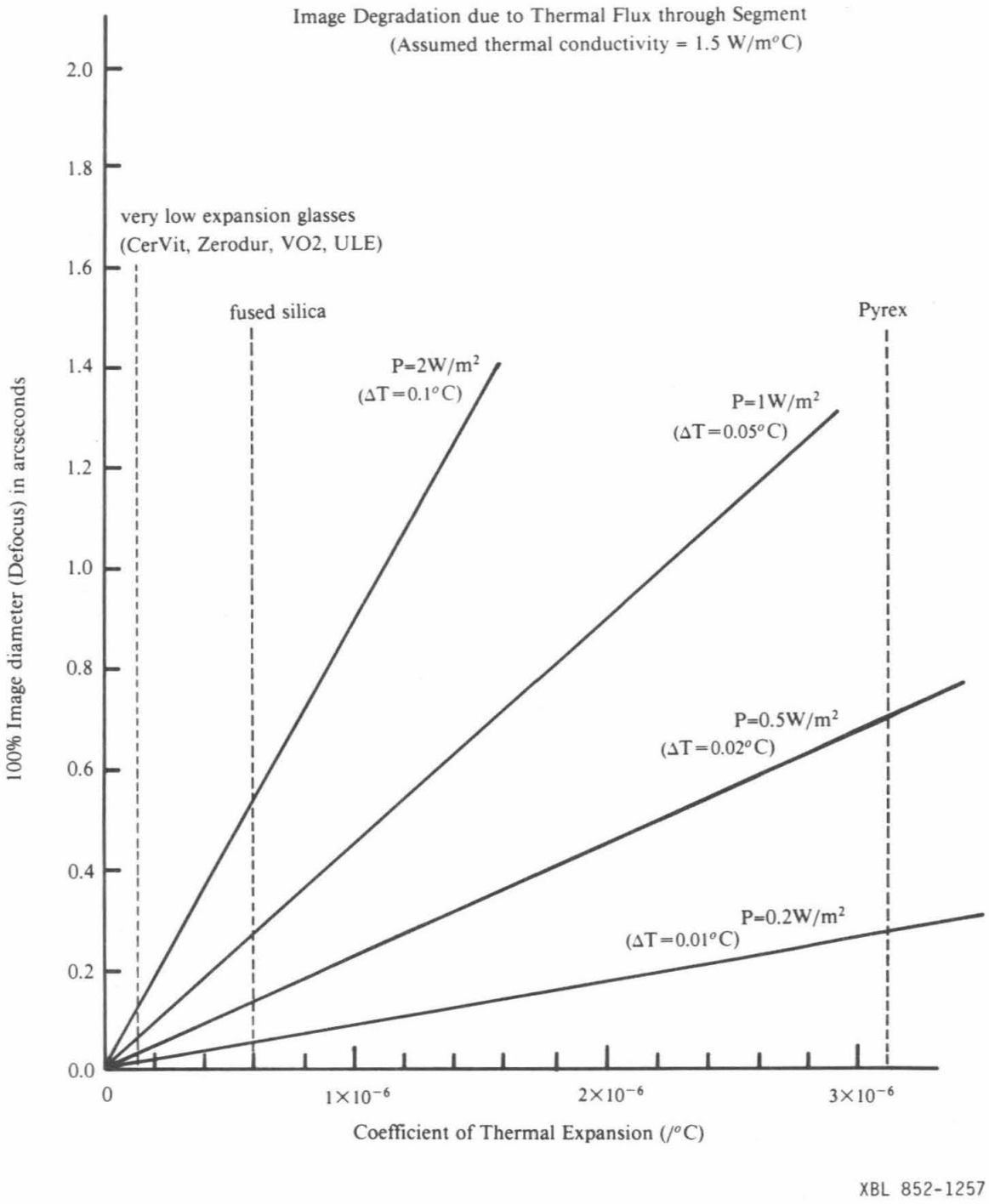

Figure 5-35 Image degradation due to thermal flux through segment with thickness h=0.075m and radius a=0.9m.

much thicker Zerodur blanks, and these results indicate $\delta\alpha$ over 7.5cm is $<$ about $1\times10^{-9}/^{o}$C.

Two samples from the Zerodur mirror used in the control system prototype (Section 8.1.2) were specially measured by S. Jacobs at the University of Arizona. The samples from near the top and bottom surfaces differed in coefficient by $1.3\times10^{-9}/$℃. This is encouraging, but a direct measure of the linear variation averaged over the entire mirror would give us more confidence in the size of the gradient. We plan to measure additional samples in order to obtain some estimate of the variation of the gradient in α over position in the mirror.

The only other measurement we know which relates to this effect is that of Shaffer and Bennett (1984). In the process of measuring the dimensional stability of Zerodur as a function of temperature they heated a 0.147m diameter, 0.030m thick optical flat to 100^{o}C and saw no change in the focus at the level of about $\lambda/100$. This measurement and Equation 5-34 imply an average linear variation of coefficient over our segment thickness less than about 10^{-9}.

In the event that the gradient in the coefficient or its measurement uncertainty is larger than allowed by the optical error budget, one possible option is to perform the final segment fabrication tests at the mean Mauna Kea nighttime temperature, 2^{o}C. This would remove the effect of manufacturing the segments at 20^{o}C and using them at 2^{o}C. Then the remaining concern would be the temperature variations occurring on Mauna Kea. Ninety percent of the time the nighttime temperature is within $\pm4^{o}$C of the mean (See Section 10.2.1). By this procedure the tolerance on the gradient can be loosened by a factor of 18/4 or 4.5.

Front-Back Stability

The displacement edge sensors measure the difference between the displacements of the back surfaces of adjacent mirrors. In principle, when no thermal effects are present, this is equivalent to measuring the relative displacement of the front surfaces. When thermal effects are included this is no longer strictly true. The sensor reading will be changed by

$$\Delta s = h_1 \alpha_1 T_1 - h_2 \alpha_2 T_2 \tag{5-40}$$

where $T_{1,2}$ is the temperature difference between the operating temperature and the temperature at which the sensor was calibrated, and the subscripts refer to the segment number. For small differences between adjacent segments in the relevant parameters, we can write this as

$$\Delta s = \Delta h\ \alpha\ T + h\ \alpha\ \Delta T + h\ \Delta\alpha\ T \tag{5-41}$$

The effective thickness of the mirror h is 0.105m, measured from the front surface to the midplane of the sensor. We assume $T = \pm4^{o}$C, the ninety percentile temperature range at the site on Mauna Kea. We expect Δh to be well below 1mm, and thus the first term implies that for $\Delta s < 1nm$ we need $\alpha<2.5\times10^{-7}/$℃. If we assume that ΔT could be 0.05℃ (which could possibly be caused by a heat flow difference of 1W/m^2), then the second term implies that for $\Delta s < 1nm$ we need $\alpha < 1.9\times10^{-7}/$℃. Finally, the third term implies that if we want to keep $\Delta s < 1nm$, then we need $\Delta\alpha < 2.4\times10^{-9}/$℃. Thus the most serious potential problem is maintaining a sufficiently tight control over the uniformity of α from segment to segment. This number is about an order of magnitude small than what can be achieved in the manufacture of ceramic glass. Thus we expect roughly 5nm/℃ temperature variation in the calibration of the sensors. This is comparable to the measured thermal coefficients of the prototype sensors. Consequently we may need to apply a temperature correction to the sensors, and the accuracy of this correction will need to be within about 10%.

Internal Stress

We plan to polish circular mirrors and then cut the segment from them. When the polished circular mirrors are cut into hexagonal pieces, the segments may warp to a certain extent (Section 8.1.2). This occurs because the stress component in the glass normal to the surface must vanish at the edge of the segment. Hence the warping will be that resulting from the

imposition of bending moments and in plane forces along the hexagonal edge that just cancel this internal stress component along that edge. Roughly speaking, the longer the correlation length in the internal stress pattern the greater the warping will be. Thus, materials that have a highly randomized internal stress pattern are preferred over materials with systematic internal stress patterns. This issue is discussed more fully by Lubliner (1982, TMT Technical Note No. 48).

Ceramic Glass

The thermal coefficients for some glass like materials given in Table 5-5. Based on the above discussion and the material properties we will assume that a ceramic glass such as Zerodur or V02 will be used for the mirror segments.

Table 5-5
Material Thermal Coefficients

Mirror Material	α(/°C)	$\delta\,\alpha$ (/°C)
Pyrex	3.2×10^{-6}	$< 10^{-7}$
Fused Silica	0.56×10^{-6}	5×10^{-9}
ULE	$\leq 0.1 \times 10^{-6}$	$\leq 20 \times 10^{-9}$
Ceramic-glass	$\leq 0.1 \times 10^{-6}$	$\leq 5 \times 10^{-9}$

Dimensional Stability

Recent tests of Zerodur have shown dimensional hysteresis upon thermal cycling. (Jabobs, *et al,* 1984 and Shaffer and Bennett, 1984). Jabobs *et al.* cycled Zerodur samples between 200°K and 300°K at a rate of 6°K/hour. They found the samples permanently changed length by about 1 part in 10^7. This is a very large temperature range and relatively rapid rate of change compared to the thermal conditions we expect for the segments. The dimensional change corresponds to about 10nm for the segment thickness.

Jacobs *et al.* also cycled samples between 300°K and 480°K and observed no dimensional changes upon returning to 300°K. Shaffer and Bennett cycled a Zerodur optical flat between 0°C and 300°C. At about 250°C they saw large permanent changes in the figure. Both of these groups expressed concern about Zerodur being placed in environments where rapid thermal changes occur and where large thermal gradients can exist. The only environment where this might happen is in a coating chamber where mirrors are sometimes heated as part of the process of applying multi-layer dielectric coatings. Further study of these effects and careful development of procedures will be made before the segments are given such coatings.

5.15.2 Segment Specifications

Mirror Blank Specifications

The primary mirror requires 36 segments, six each of six types. An extra segment of each surface type will be made; thus a total of 42 segments will be fabricated. In addition, a few blanks will be acquired for tests and breakage. The mirror blanks are of low-thermal-expansion ceramic glass. Each blank is 2000 ± 3mm in diameter, 96 ± 3mm thick, has a volume of $0.302m^3$, and weighs 763kg. The specifications call for a thermal coefficient of expansion within the range -1×10^{-7} to $+1\times10^{-7}$ per degree centigrade (See Nelson, 1984, TMT Technical Report No. 52). In order to limit the variation of the segment radius of curvature with temperature, and meet the segment error budget, we need a linear variation in the thermal coefficient through the blank thickness to be $< 0.6\times10^{-9}/°C$. If the delivered blanks have larger coefficient gradients, then procedures in the segment fabrication and testing can be used to reduce the tolerance by a factor of 5 to 10 as outlined in Section 5.15.1. The limit on mean birefringence is set at 3nm/cm with a maximum for any one measurement of less than 10nm/cm.

The delivery of the blanks will begin one year after receipt of order. We expect the order to be placed at the beginning of 1985. The total shipment is to be completed in 3.5 years from receipt of order with a blank delivered, as an average, once every three weeks.

Segment Generating Specifications

From each blank a meniscus is generated with a uniform thickness of 76.0 - 76.2mm. Both surfaces will be spherical. The average radius of curvature of the best fitting spheres for Types 1 through 6 is 35.350 meters. The convex radius is this average concave radius plus the thickness, $k_{convex} = 35.427$ meters. The diameter will be 2000 ± 0.5mm with out-of-roundness held to less than 0.1mm. The wedge between the concave and convex surfaces shall be less than 0.2mm over the full diameter.

Global Primary Mirror Surface Shape

The coordinate system for the overall segment array is shown in Figure 5-36. The horizontal plane coordinates are X and Y and the optical axis of the array is in the positive Z direction. The array of segments is a mosaic of regular hexagons when projected on the global X, Y plane, i.e. as seen by the incoming parallel light of a star.

The surface desired for the overall primary mirror is a hyperboloid of revolution. The vertex of the hyperboloid of revolution is at the point X, Y, Z = 0,0,0. The general expression for a conic surface of revolution is given by

$$Z(X,Y) = \frac{1}{K+1}\left\{ k - [k^2 - (K+1)S^2]^{1/2} \right\} \tag{5-42}$$

$$= \frac{S^2}{2k} + (K+1)\frac{S^4}{8k^3} + (K+1)^2\frac{S^6}{16k^5} + \frac{5}{128}(K+1)^3\frac{S^8}{k^7} + \cdots$$

where K is the conic constant, k is the radius of curvature, and $S = (X^2 + Y^2)^{1/2}$. For the Ten Meter Telescope primary mirror

$$K = -1.003796, \text{ and}$$

$$k = 35.000 \text{ m}.$$

The difference between this surface and a paraboloid ($K = -1.0$) is less than 7 μm at the outer edge.

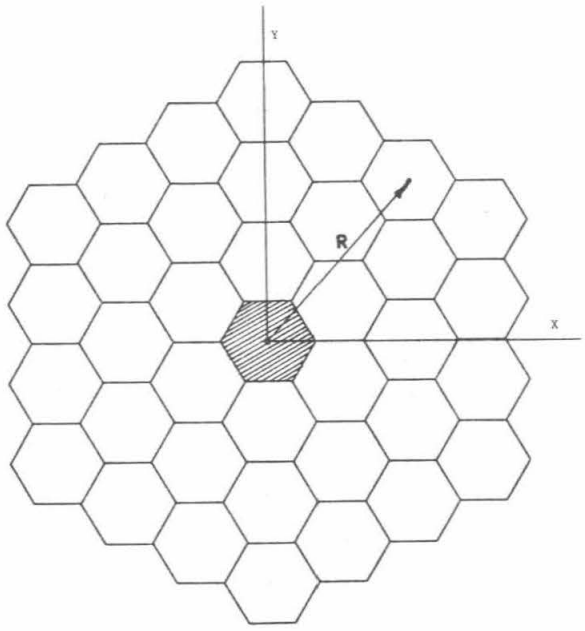

Figure 5-36 The coordinate system for the overall segment array. The center of a projected hexagon is at radius R in the X-Y plane.

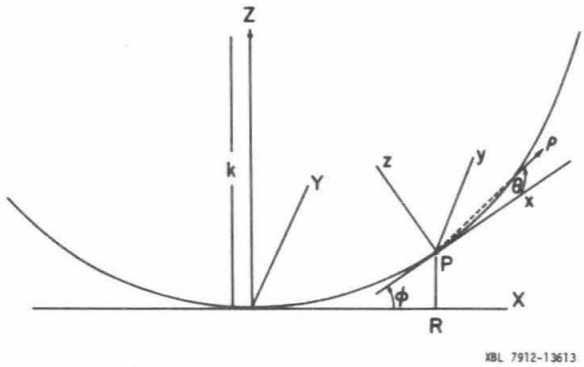

Figure 5-37 Diagram showing the relationship between the global coordinates (X,Y,Z) and the local coordinates (x,y,z = ρ,θ,z). The distance to global surface center of curvature is labeled k. The center of the segment is point P and the plane tangent to the segment surface at the center makes an angle ϕ with respect to the global X-Y plane. The polar coordinates ρ,θ are in the local x-y plane.

Segment Concave Surface Shape

The surface of each segment can be described by a series of Zernike polynomials. These surfaces are calculated using the equations by Nelson and Temple-Raston (1982, TMT Report No. 91), and are given by Nelson (1983, TMT Technical Note No. 78). For completeness we repeat that information here and give additional clarifying details.

A local coordinate system is defined for each segment. The origin of this coordinate system is at the center of the segment. The center of the segment is on the concave surface. It is located at the intersection of the surface with a line parallel to the global Z-axis that passes through the center of the projected hexagon in the X-Y plane. The center of the projected hexagon is at a radius R in the X-Y plane; $R = (X_c^2 + Y_c^2)^{1/2}$. The coordinates of the local system are shown in Figure 5-37. The local x-axis is along the radial direction of the global coordinate system and tangent to the segment center. The local z-axis is perpendicular to the hyperboloid surface at the center of the segment. The local y-axis is that of a right-handed coordinate system using the x and z axes. Polar coordinates ρ, θ are defined in the x, y plane. We use the dimensionless polar variables $\rho = (x^2 + y^2)^{1/2}/a$, $\theta = \tan^{-1}(y/x)$, where a is the projected segment radius ($a = 0.900$ meters). Figure 5-38 shows these polar coordinates in the x, y, z coordinate system. Note that in the local coordinate system the segments are not regular hexagons.

In the local coordinates the segment surface can be written:

$$z(\rho,\theta) = \sum_{ij} \alpha_{ij} \rho^i \cos j\theta \quad ; i \geq j \geq 0, \quad i-j \ \ even \tag{5-43}$$

The off-axis expansion of the general conic equation given above has been made by Nelson and Temple-Raston (1982, TMT Report No. 91). The local coordinate expansion coefficients, α_{ij}, are given in terms of the conic parameters.

$$\alpha_{20} = \frac{a^2}{k}\left[\frac{2 - K\epsilon^2}{4(1 - K\epsilon^2)^{3/2}}\right] \qquad (focus)$$

$$\alpha_{22} = \frac{a^2}{k}\left[\frac{K\epsilon^2}{4(1 - K\epsilon^2)^{3/2}}\right] \qquad (astigmatism)$$

$$\alpha_{31} = \frac{a^3}{k^2}\left[\frac{K\epsilon[1 - (K+1)\epsilon^2]^{1/2}(4 - K\epsilon^2)}{8(1 - K\epsilon^2)^3}\right] \qquad (coma)$$

$$\alpha_{33} = \frac{a^3}{k^2}\left[\frac{K^2\epsilon^3[1 - (K+1)\epsilon^2]^{1/2}}{8(1 - K\epsilon^2)^3}\right] \tag{5-44}$$

$$\alpha_{40} = \frac{a^4}{k^3}\left[\frac{8(1+K) - 24K\epsilon^2 + 3K^2\epsilon^4(1-3K) - K^3\epsilon^6(2-K)}{64(1 - K\epsilon^2)^{9/2}}\right] \qquad \begin{pmatrix} spherical \\ aberration \end{pmatrix}$$

$$\alpha_{42} = \frac{a^4}{k^3}\left[\frac{K\epsilon^2[2(1+3K) - (9+7K)K\epsilon^2 + (2+K)K^2\epsilon^4]}{16(1 - K\epsilon^2)^{9/2}}\right]$$

$$\alpha_{44} = \frac{a^4}{k^3}\left[\frac{K^2\epsilon^4[1 + 5K - K\epsilon^2(6+5K)]}{64(1 - K\epsilon^2)^{9/2}}\right]$$

where $\epsilon \equiv \dfrac{R}{k}$.

In general,

$$\alpha_{ij} \approx \left(\frac{a^i \epsilon^j}{k^{i-1}}\right) \tag{5-45}$$

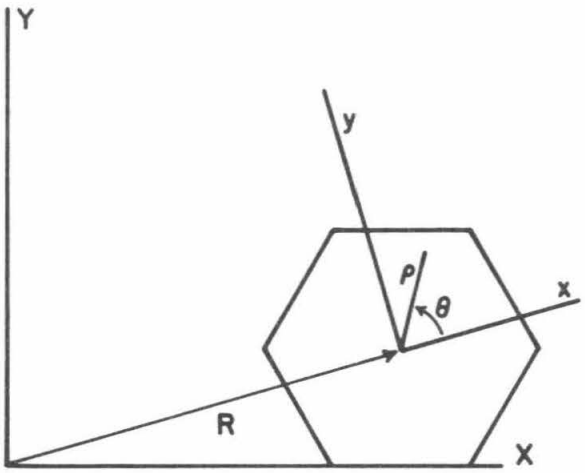

XBL 8410-4478

Figure 5-38 Projected view showing the relationship between the global coordinates (X,Y,Z) and the local coordinates (x,y,z = ρ,θ,z) and the distance R from the vertex of the global system to the center of the projected hexagon.

For the segments of interest, all terms with $i > 4$ are negligible.

For a sphere, $K = 0$, and equation (5-44) reduces to

$$\alpha_{20} = \frac{a^2}{2k} \tag{5-46}$$

$$\alpha_{40} = \frac{a^4}{8k^3}$$

The segment surface can also be written in the local coordinate system:

$$z(\rho,\theta) = \sum_{ij} C_{ij} Z_{ij}(\rho,\theta) \;\; ; i \geq j \geq 0, \quad i-j \;\; even, \tag{5-47}$$

where $Z_{ij}(\rho,\theta)$ are the Zernike polynomials given in Table 5-6. The relations between the polar monomial coefficients, α_{ij}, and the Zernike coefficients, C_{ij}, are given in Table 5-7.

The Zernike coefficients, C_{ij}, for the hyperbola, K = -1.003796, are given in Table 5-8. In this table we have given the off-axis distance, R, to the center of each segment type, and all significantly non-zero coefficients. The coefficients are given for a circular mirror with a radius of 0.900 meters, that is, $\rho = 1$ at 0.900 meters. Note that 0.900 meters defines the circle over which the coefficients are calculated. The real physical segments may fall slightly within or outside of this circle depending on the segment type. The surfaces for segment types 4 and 5 are identical over the 0.9m diameter circle. These types differ only in the orientation of the hexagon cut from the circular mirror.

Table 5-6 Zernike Polynomials Z_{nm} †

n	m	Polar	Cartesian
0	0	1	1
1	-1	$\rho\sin\theta$	y
1	1	$\rho\cos\theta$	x
2	-2	$\rho^2\sin2\theta$	$2xy$
2	0	$2\rho^2-1$	$2x^2+2y^2-1$
2	2	$\rho^2\cos2\theta$	x^2-y^2
3	-3	$\rho^3\sin3\theta$	$3x^2y-y^3$
3	-1	$(3\rho^3-2\rho)\sin\theta$	$3x^2y+3y^3-2y$
3	1	$(3\rho^3-2\rho)\cos\theta$	$3x^3+3xy^2-2x$
3	3	$\rho^3\cos3\theta$	x^3-3xy^2
4	-4	$\rho^4\sin4\theta$	$4x^3y-4xy^3$
4	-2	$(4\rho^4-3\rho^2)\sin2\theta$	$8x^3y+8xy^3-6xy$
4	0	$6\rho^4-6\rho^2+1$	$6x^4+12x^2y^2+6y^4-6x^2-6y^2+1$
4	2	$(4\rho^4-3\rho^2)\cos2\theta$	$4x^4-3x^2-4y^4+3y^2$
4	4	$\rho^4\cos4\theta$	$x^4-6x^2y^2+y^4$
5	-5	$\rho^5\sin5\theta$	$5x^4y-10x^2y^3+y^5$
5	-3	$(5\rho^5-4\rho^3)\sin3\theta$	$15x^4y+15x^2y^3-12x^2y-5x^2y^3-5y^5+4y^3$
5	-1	$(10\rho^5-12\rho^3+3\rho)\sin\theta$	$10x^4y+20x^2y^3+10y^5-12x^2y-12y^3+3y$
5	1	$(10\rho^5-12\rho^3+3\rho)\cos\theta$	$10x^5+20x^3y^2+10xy^4-12x^3-12xy^2+3x$
5	3	$(5\rho^5-4\rho^3)\cos3\theta$	$5x^5+5x^3y^2-4x^3-15x^3y^2-15xy^4+12xy^2$
5	5	$\rho^5\cos5\theta$	$x^5-10x^3y^2+5xy^4$

† Born & Wolf (1980) convention is used for the indices n,m.

Table 5-7 Relations Between Zernike Coefficients and Polar Monomial Coefficients.

C_{ij}		α_{ij}
C_{00}	=	$\alpha_{00} + \frac{\alpha_{20}}{2} + \frac{\alpha_{40}}{3} + \cdots$
C_{1-1}	=	$\alpha_{1-1} + \frac{2}{3}\alpha_{3-1} + \cdots$
C_{1+1}	=	$\alpha_{1+1} + \frac{2}{3}\alpha_{3+1} + \cdots$
C_{2-2}	=	$\alpha_{2-2} + \frac{3}{4}\alpha_{4-2} + \cdots$
C_{20}	=	$\frac{\alpha_{20}}{2} + \frac{\alpha_{40}}{2} + \cdots$
C_{2+2}	=	$\alpha_{2+2} + \frac{3}{4}\alpha_{4+2} + \cdots$
C_{3-3}	=	$\alpha_{3-3} + \cdots$
C_{3-1}	=	$\frac{\alpha_{3-1}}{3} + \cdots$
C_{3+1}	=	$\frac{\alpha_{3+1}}{3} + \cdots$
C_{3+3}	=	$\alpha_{3+3} + \cdots$
C_{4-4}	=	$\alpha_{4-4} + \cdots$
C_{4-2}	=	$\frac{\alpha_{4-2}}{4} + \cdots$
C_{40}	=	$\frac{\alpha_{40}}{6} + \cdots$
C_{4+2}	=	$\frac{\alpha_{4+2}}{4} + \cdots$
C_{4+4}	=	$\alpha_{4+4} + \cdots$

Table 5-8 Zernike Coefficients for Segments
Hyperbolic primary (a = 0.9m, k = 35m, K = -1.003796)

Type	R(m)	$C_{2,0}(\mu m)$	$C_{2,2}(\mu m)$	$C_{3,1}(\mu m)$	$C_{3,3}(\mu m)$	$C_{4,0}(\mu m)$	$C_{4,2}(\mu m)$
1	1.5589	5774.221	-11.481	-4.410	0.007	0.001	0.002
2	2.7000	5751.397	-34.238	-7.556	0.034	0.004	0.005
3	3.1177	5740.060	-45.515	-8.677	0.052	0.006	0.007
4,5	4.1243	5706.351	-78.949	-11.294	0.118	0.012	0.012
6	4.6765	5684.125	-100.910	-12.669	0.170	0.015	0.016

The segment surfaces are almost paraboloidal. The difference between a paraboloidal primary and the hyperboloidal one over a segment is largest for the outermost segments. For Type 6 this difference is 235nm rms and is almost entirely focus and astigmatism.

Concave Surface Tolerances

The tolerances on the polished concave surfaces are set by the optical goals for the primary mirror.

For visible light: must have 80% of the light from a point source in a circle of diameter 0.32 arc seconds.
For infrared light at 10μm: must have a diffraction limited surface (Strehl ratio $\approx$ 0.9).

Based on these goals and our present experience with mirror fabrication, support design, and fabrication, we have assigned the error budget given in Table 5-9.

Table 5-9
Primary Mirror Error Budget

Goal: 80% of energy flux in 0.32 arc seconds

Item		Allowed Error (arc seconds)	
Segment figuring (polishing and warping)			0.242
Segment thermal distortion			0.147
Segment support (larger of axial, radial)			0.098
Axial design		0.082	
Axial fabrication		0.05	
Radial design		0.04	
Radial fabrication		0.05	
Thermal effects		0.02	
Segment alignment (passive degrees of freedom)			0.074
Initial alignment		0.05	
Thermal cell expansion		0.045	
Gravity induced segment motion		0.03	
Segment alignment (active degrees of freedom)			0.098
Sensor calibration		0.05	
Thermal effects on sensors		0.004	
Gravity effects on sensors		0.021	
Temporal drift of sensors		0.029	
Control system noise		0.057	
Sensor noise	0.024		
Actuator noise	0.052		
Wind induced motion		0.05	
		Total	0.32

We define the concave surface tolerance over two areas.

1. The "edge area" comprises the 4mm wide outermost strip. The edge area contains about 1% of the segment surface area.

2. The "inner area" contains the surface within 4mm of the edge of the final bevel.

Edge Area Tolerances

Within the edge area we require

1. The deviation from the desired surface should not exceed 500nm over more than 25% of the area. This should be measured with a test plate.

2. The deviation from the desired surface should not exceed 1000nm over more than 10% of the area. This should be measured with a test plate.

Inner Area Tolerance

Over the inner area we place the following surface requirements.

The point spread function from the surface should match that of an atmosphere with a coherence diameter of r_0=0.6m, and must meet the following fractional enclosed energy goals.

image diameter containing 50% of the energy = 0.144 arc seconds
image diameter containing 80% of the energy = 0.242 arc seconds
image diameter containing 90% of the energy = 0.318 arc seconds

These specifications include **all** surface errors **including** focus or radius of curvature errors **as well as** segment location errors. The division of the error budget among the different aspects of the the surface is arbitrary as long as it meets the above enclosed energy goals.

Error Budgeting

We now give a plausible budgeting of the errors amongst the three categories, segment alignment, radius of curvature, and figure (non-focus). We describe the budget using the 80% image diameter. Although there is nothing fundamental to motivate this particular division we present arguments for the plausibility.

Segment Alignment Tolerances

Fixturing for the mechanical alignment tolerances should be inexpensive, and thus we assign a small part of the error budget to these terms. We make the tightest azimuthal and tightest radial tolerance about the same. We assign 0.035 arc seconds to the radial error and 0.070 arc seconds to the azimuthal error. An approximate relationship between $\theta(80\%)$ and δR and $\delta\theta$ has been calculated by Nelson (1983, TMT Report No. 32) and is given by

$$\theta(80\%) = \frac{8KRa\delta R}{k^3}\left[1+\frac{a^2}{16R^2}\right]^{1/2} \tag{5-48}$$

$$\theta(80\%) = \frac{3.58KR^2a\delta\theta}{k^3}\left[1+\frac{0.31a^2}{R^2}\right]^{1/2} \tag{5-49}$$

Actual ray tracing of these misalignments leads to the following mechanical segment alignment tolerances.

Table 5-10. Segment Position Tolerances (a=0.9m)

Segment Type	R (m)	a$\delta\theta$ (mm)	δR (mm)
1	1.5589	1.75	0.68
2	2.7000	0.61	0.39
3	3.1177	0.40	0.34
4	4.1243	0.26	0.25
5	4.1243	0.26	0.25
6	4.6765	0.20	0.22

These tolerances give the accuracy that the segment center and orientation need to be defined relative to the primary mirror vertex during fabrication and testing. The segment center is defined by the location of an Invar ring bonded into the central hole described below. The segment azimuth should be defined by a permanent fiducial near the edge.

Radius of Curvature

This assignment of alignment errors (0.078 arc seconds total) leaves 0.229 arc seconds for the radius of curvature error and figure error. The best choice of budgeting this between these two sources will depend on the metrology technique used by the manufacturer to measure the radius of curvature. We tentatively suggest dividing the error equally between the two. This budgets 0.163 arc seconds to radius error corresponding to a value of C_{20} of 53nm (106nm peak-to-valley surface power) over the 1.8m diameter circle that circumscribes the hexagon. The can alternately be expressed as a radius of curvature error of δk = 322μm. This error allowance is for the relative radius of curvature errors among the segments. The absolute radius tolerance for the primary as a whole is $\pm$4mm.

Figure Errors

The remaining 0.162 arc seconds is budgeted amongst low and high spatial frequency errors.

Low Spatial Frequency Figure Errors

If the entire 0.162 arc seconds for θ(80%) is contributed to by a single Zernike coefficient up to and including 4th order, then the allowed rms surface error is between 38nm rms and 19nm rms depending on the particular coefficient. The approximate relationship between rms surface and enclosed energy for single Zernike coefficients is given in the Tables below.

Table 5-11
Image Blur Caused by Zernike Aberrations on a Segment

We tabulate the geometric image blur that results from a single Zernike aberration occurring on a TMT segment with a = 0.9m. The Zernike coefficient is normalized over a 0.9m radius circle. The image blur diameter is based on an 80% enclosed energy and is calculated using ray tracing. All numbers are approximate. Note that the rms for $C_{3,-3}$ and $C_{3,3}$ are different while their ray tracing is identical. In all cases we assume that C_{ij} = 1.0μm.

C_{ij} (=1μm)	rms (μm)	θ (80%)(arcseconds)
2,-2	0.357	1.52
2, 0	0.510	3.04
2, 2	0.357	1.52
3,-3	0.253	1.88
3,-1	0.299	2.21
3, 1	0.299	2.20
3, 3	0.324	1.88
4,-4	0.245	2.09
4,-2	0.287	2.24
4, 0	0.409	3.48
4, 2	0.287	2.28
4, 4	0.245	2.10

Table 5-12
Size of Single Aberrations That Give 0.2 Arcsecond Images

ij	C_{ij} (nm)	rms (nm)
2,-2	132	47
2, 0	66	34
2, 2	132	47
3,-3	106	27
3,-1	90	27
3, 1	90	27
3, 3	106	34
4,-4	96	23
4,-2	89	26
4, 0	57	24
4, 2	88	25
4, 4	95	23

The point spread function should be calculated using data uniformly sampled over the mirror. The sample spacing should be no greater than 20% of the smallest diameter tool used, or 3cm, whichever is greater. In no case should the spacing exceed 10cm.

High Spatial Frequency Figure Errors

Should the mirror fabrication require small tools, then it will be important to measure the high frequency errors. The high spatial frequency errors should not exceed 10nm rms. The surface should be sampled with a 150mm diameter test plate at 13 locations. The interferograms should be fitted to Zernike polynomials and the aberrations expected from the difference between the test plate and surface should be removed. The expected aberrations (astigmatism and focus) will be below 500nm rms. The remaining rms surface errors should be no more than 10nm. A test plate with a spherical surface and radius of curvature of 35.35m will serve all segments.

Peak to Valley Limits on Figure Errors

In addition to the above errors the following tolerances must be met

1. The deviation from the desired surface should not exceed 200nm over more than 1% of the area.

2. The peak-to-valley deviation from the desired surface should not exceed 500nm.

Convex Surface Shape

The convex surface is spherical and the same for every segment. The radius of the sphere is 35.427m. The convex surface should lie within an envelope that is +0.2mm and -0.2mm on either side of the desired spherical surface.

Hexagon Dimensions

The mathematical geometry of the primary mirror is an array of regular hexagons when seen from star, i.e., when projected on the X-Y plane. Each hexagon has a side length $a = 0.900$m. The physical segments will project to be regular hexagons when in the primary

and viewed from a star. The physical segments have a smaller side length since there is a gap between the segments of $t = 3.0$mm. Thus the projected side length of the physical segments is $a - t/(3)^{1/2} = 898.27$mm.

Only the projected outline is regular. The segments themselves are irregular hexagonal prisms because the segment is oriented at an angle with respect to the Z-axis and the upper and lower surfaces are curved. The detailed dimensions of the prisms are given by Mast *et al.* (1985c).

Hexagon Dimensional Tolerances

The fabricated segments should lie within an envelope that is 0.3mm inside and 0.3mm outside the desired hexagon dimensions.

Central Support Hole

The radius of the central hole is 127.0mm. The depth of the hole at the center is 55.0mm. The axis of the hole passes through the center of segment ($\pm$ 0.1mm) and is parallel to the normal to the segment surface. The inside corner of the hole has a 3mm radius. The hole should be within an envelope that is 0.1mm inside and 0.1mm outside the desired hole.

Final Surface Treatment

The concave and convex surface will be pitch polished with the an rms surface finish of 3nm (30 angstroms). The edges of the segment and the surfaces of the hole will be stressed relieved by etching. There will be a nominal 2mm bevel on all edges.

5.15.3 Stressed Mirror Polishing

Motivation

The fabrication of high-quality non-axisymmetric optical surfaces has traditionally been vastly more difficult than producing axisymmetric surfaces. Among the axisymmetric surfaces, the sphere is the easiest to fabricate, with commonly desired surfaces such as paraboloids and hyperboloids being substantially more difficult. Even with the advances in computer-controlled polishing, made by some of the large optical firms, non-axisymmetric surfaces are a challenging task, one very much more difficult than polishing spheres.

The mirror segments must be off-axis sections of a hyperboloid. Because of the great difficulty in making even a single off-axis hyperboloid by traditional methods, the construction of a matched set of 36 mirrors appeared quite formidable when the project began. Our desire to produce these mirrors accurately, quickly, and economically was the impetus for developing the technique described in this section.

Concept

In general, the idea is to apply an appropriate set of forces to a mirror blank such that after a sphere has been ground and polished into the blank, the forces can be removed and the polished spherical surface will deform elastically into the desired non-axisymmetric surface. We call this method Stressed Mirror Polishing. If the material behaves elastically, with no hysteresis, and the desired surface is smooth, there will exist a force function capable of producing the desired deformation. Thus, in principle, one can reduce the difficulty of polishing non-axisymmetric mirrors to the much simpler task of polishing spheres. For circular mirrors of uniform thickness, a very general class of surfaces can be created by an extremely simple force distribution. The theoretical basis for Stressed Mirror Polishing was derived by Lubliner and

Nelson (1979, TMT Report No. 21).

History

Historically, this general idea was first used by Bernard Schmidt in making an axisymmetric correcting lens for a Schmidt telescope, and the theory and method for this technique is described by Everhart (1966). An interesting variant of the method adopted here is described by LeMaitre(1974), where variations in plate thickness are deliberately introduced to attempt to achieve a set of desired deflections under external loads. A related idea, that of bending a given mirror into another shape by the use of a warping harness to adjust astigmatism has been described by Leonard(1969) and Alvarez(1978). In these applications, no polishing during warping was attempted; rather, the warping harness was a permanent part of the desired mirror.

Elastic Response

The material should behave elastically for this procedure, so some materials may not be suitable for this technique; but at least one material, glass, is known to have nearly ideal elastic properties. If the material responds linearly to the imposed forces, the resulting deflections are independent of the internal stresses of the original blank and of changes in the internally generated stresses caused by grinding and polishing.

Iterations

An attractive feature of the technique is the ability to produce the desired surface iteratively. If the applied forces are only approximately correct, due to approximations in the theory, incomplete knowledge of the blank's elastic properties, or systematic errors in the application of the desired forces, then the surface produced will not match the desired one. Measurements of the errors in the fabricated surface can then be used to calculate corrective forces, which, when reapplied along with the original set of forces, can be used as the basis for a second spherical polish and test cycle, and so on. Thus, if the results of a single polish contain errors of order ϵ and the desired deflection is of order d, one can expect the error after n polish cycles to be

$$\epsilon_n \approx \left(\frac{\epsilon}{d}\right)^n d \tag{5-50}$$

If $\frac{\epsilon}{d} < 1$ the technique converges to produce the desired surface. In practice, $\frac{\epsilon}{d}$ is of order 10^{-2} and accurate convergence to the desired surface is achieved in two or three polishings. Appreciable changes in the thickness of the blank from the grinding and polishing will of course affect the deflections caused by the applied forces, but in a predictable fashion. In practice these changes are small and do not strongly affect the convergence of polishing iterations. In practice we expect the stability of the applied forces will determine the limits of the technique.

Desired Deflections

The deflections that need to be induced in the surface by the application of moments and forces is the difference between the desired off-axis section of the hyperboloid and the sphere being polished into the glass. The best single sphere is that which minimizes the maximum rms difference between the sphere and any segment. The radius of this sphere is l_s = 35.53m (Nelson 1983, TMT Report No. 98). The best sphere has coefficients:

$$C_{2,0} = \frac{a^2}{4l} + \frac{a^4}{16l^3} = 5700.323\mu m \tag{5-51}$$

$$C_{4,0} = \frac{a^4}{48l^3} = 0.305\mu m \tag{5-52}$$

To calculate the desired deflections these coefficients are subtracted from those in Table 5-8. The peak-to-peak deflection is largest for segment Type 6 and is about 215 microns.

The desired deflections can thus be written in terms of Zernike polynomials or in terms of the polar monomials. For the calculation of the forces and moments we use the polar monomials:

$$w = \alpha_{20}\rho^2 + \alpha_{22}\rho^2\cos 2\theta + \alpha_{31}\rho^3\cos\theta + \alpha_{33}\rho^3\cos 3\theta \tag{5-53}$$

$$+ \alpha_{40}\rho^4 + \alpha_{42}\rho^4\cos 2\theta + \text{neglected terms.}$$

Plate Bending

The determination of the forces necessary to produce a given deflection pattern in a glass plate constitutes a straight-forward problem in elastic plate theory, since glass is nearly perfectly linearly elastic at sufficiently low stresses. The deflection w of a uniform, linearly and isotropically elastic, thin plate is governed by the partial differential equation

$$D\nabla^4 w = q\ , \tag{5-54}$$

where q is the transverse load per unit area (measured as positive in the same direction as the deflection); ∇^4 is the operator $(\partial^2/\partial x^2 + \partial^2/\partial y^2)^2$ (where x and y are cartesian coordinates in the plane of the plate); and $D = Eh^3/12(1 - \nu^2)$, where h is the plate thickness while E and ν are respectively, the Young's modulus and Poisson's ratio of the glass. (for ceramic glass $E = 9.1\times10^5$ kgf/cm^2, $\nu = 0.24$). Fortunately, all the terms in Equation 5-53 can be generated by applying shear forces and bending moments to the periphery of a uniformly supported mirror.

The solution to the problem relates the bending moments and shear forces to the deflections. The distributions of bending moments $M(\theta)$ and shear forces $V(\theta)$ can be represented by Fourier series:

$$M(\theta) = M_o + \sum_{n=1}^{\infty}(M_n\cos n\theta + \overline{M}_n\sin n\theta)\ , \tag{5-55}$$

$$V(\theta) = V_o + \sum_{n=1}^{\infty}(V_n\cos n\theta + \overline{V}_n\sin n\theta)\ ,$$

The pressure on the back of the plate can be either uniform or linearly varying.

$$q(r,\theta) = q_o + q_1 r\cos\theta + q_2 r\sin\theta\ , \tag{5-56}$$

Equilibrium of transverse forces, moments about the y-axis and moments about the x-axis requires that

$$V_0 = -q_0/2$$

$$M_1 + aV_1 = -q_1a^3/4 \tag{5-57}$$

$$\overline{M}_1 + a\overline{V}_1 = -q_2a^3/4$$

Moment/Force - Deflection Relations

The equations which relate the series coefficients of the moments and forces to the series coefficients of the surface defections follow

$$M_o = \frac{D}{a^2}[2(1+\nu)\alpha_{20} + 4(3+\nu)\alpha_{40}]\ ,\quad V_o = -\frac{D}{a^3}(32\alpha_{40})\ ;$$

$$M_1 = \frac{D}{a^2}[2(3+\nu)\alpha_{31} + 4(5+\nu)\alpha_{51}]\ ,\quad V_1 = -\frac{D}{a^3}[2(3+\nu)\alpha_{31} + 4(17+\nu)\alpha_{51}]$$

$$n > 1$$

$$M_n = \frac{D}{a^2}[(1-\nu)n(n-1)\alpha_{nn} + (n+1)[n+2-\nu(n-2)]\alpha_{n+2,n}] \qquad (5\text{-}58)$$

$$V_n = \frac{D}{a_3}[(1-\nu)n^2(n-1)\alpha_{nn} + n(n+1)(n-4-\nu n)\alpha_{n+2,n}],$$

$$q_o = 64D\frac{\alpha_{40}}{a^4}, \quad q_1 = 192D\frac{\alpha_{51}}{a^5}, \quad q_2 = 192D\frac{\beta_{51}}{a^5}.$$

More details are given by Lubliner and Nelson (1980, TMT Report No. 21).

Maximum Stress

The maximum stress induced in the glass by the forces and moments will occur for the segment Type 6 and at the outer edge of the segment. That stress is calculated using equations given by Lubliner and Nelson (1980, TMT Report No. 21) to be $2.4\times10^6 N/m^2$. This is 12% of the breaking tensile strength of the glass, $2\times10^7 N/m^2$.

Force and Moment Calculations

The equations from the work of Lubliner and Nelson have been coded by Hunt (1983, TMT Note No. 53) into a program called OMNI. This code generates desired forces and moments at 24 uniformly spaced points on the periphery to a surface described in terms of Zernike polynomials. This code was used in the fabrication of the two off-axis mirrors described below in Sections 8.1.1 and 8.1.2.

Application of Forces and Moments

Two mirrors have been fabricated using the Stressed Mirror Polishing method. For both of these a simple mechanical jig was used to apply the forces and moments. Invar blocks were bonded to the outside edge of the blank and then a horizontal arm was attached to each block. A system of levers and lead weights were then used to apply a force and moment to each arm. The configuration is shown schematically in Figure 5-39.

The method of Stressed Mirror Polishing has been tested in the technology development program described in Section 8.1.

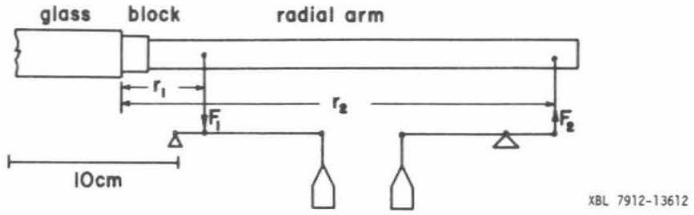

Figure 5-39 Schematic showing mirror blank, Invar block, radial arm and lever and weight system used to apply forces F_1 and F_2. Twenty-four such assemblies produced shear forces and moments to stress the mirror.

6. Instrumentation

Contents **Page**

6.1 Initial Instrument Complement

From among the scientific projects described in Section 2, a small number of key instruments can be targeted that should be ready for operation when the TMT itself is completed. These may be divided into the visual and thermal infrared instrument complements.

6.1.1 Visual Instrumentation

Multiple Object Spectrograph

Among visual instruments, a clear choice is some form of moderate resolution multiple object spectrograph (MOS). Basic alternatives involve fiber feeds, multiple slits, of some combination of both. A moderate resolution instrument would be well suited for most spectroscopy of distant galaxies, QSO's, and stars in clusters, the Galactic halo and bulge, and nearby galaxies are discussed in Section 4.3.3.

High Resolution Spectrograph

Certain MOS studies would usefully employ very high resolution, notably fundamental abundance studies of stars in clusters and the Galactic bulge. If restricted to just a few order, this could be accomplished with today's detectors by placing an order -selecting interference filter in a high- dispersion echelle spectrograph, as discussed in Section 4.3.4. Such a spectrograph would also give full spectral coverage for single objects and would be the workhorse instruments for all high-resolution visual studies, including detailed stellar composition studies, stellar seismology, and QSO absorption lines.

Prime Focus Spectrograph

A third possibility discussed in Section 4.3.5 is a low-to-moderate dispersion spectrograph located at prime focus. This location offers maximum throughput for spectroscopy and polarimetry of one or a few objects at a time over a small field of view. Such a spectrograph would utilize high-efficiency coated lenses and thus have very high transmission, but over a limited bandwidth. The advantage over MOS at the Nasmyth would depend on the number of objects to be observed and the bandwidth required. Major applications would include spectropolarimetry of QSOs and AGNs and long-slit spectra of extended sources and as galaxies and emission-line regions.

Prime Focus Cameras

A fourth principle instrument is the wide-field imaging camera. The major portion of the camera is the optical assembly. This is considered an integral part of the telescope and is discussed in Section 4.1.2.

The initial visual instrument complement will emphasis the spectral range 0.33μm to 1.1μm. As detectors improve in the near infrared, future instrumentation will exploit the range 1.1μm to 2.5μm.

6.1.2 Infrared Instrumentation

Infrared instrumentation is divided into the same basic categories as visual instrumentation, with the additional complication that separate devices may be needed to cover the separate atmospheric windows. Photometers are also included, owing to the relatively less advanced state of IR array detectors for direct imaging.

IR Photometers

These systems give sensitivity from the near IR through 30μm and will provide a simple technique for obtaining the colors of a source. Primary applications will include stars, the Galactic center, other Galactic point sources, QSOs, and active galactic nuclei. The ability to achieve high time resolution and measure several colors simultaneously will be useful for the study of spatial flux distributions and source sizes during occultations.

IR Low to Moderate Resolution Spectrometers

The spectral region from the near IR to 30μm contains a wealth of atomic and molecular emission lines, many from ionic species which have no optical lines and which may frequently represent the most highly populated states. These lines are also much less subject to uncertainties due to extinction than their optical counterparts. There are also recognizable features from dust emission and absorption, *e.g.,* silicate compounds. Likely targets for study include solar system objects, stars, regions of star formation, the galactic center, IRAS sources, QSOs, and active galactic nuclei. The use of a long slit enables spatial information to be collected simultaneously with the spectra. At longer wavelengths the slit can be narrowed under good seeing conditions to the diffraction limit of the telescope, giving the most detailed information achievable by any available technique on these sources.

IR Cameras

These systems require the most advanced technology envisioned for the first generation of instruments. The 2-D arrays currently available (1984) can already be used to exploit the unique advantage of the TMT in sensitivity and high spatial resolution for IR imaging. Further developments in technique will result in larger fields of view. Scientific uses are many, and include the study of regions of star formation, which are usually complex and require the best spatial information, the Galactic center, external galaxies, IRAS sources, etc. Imaging in conjunction with other techniques such as polarimetry offers an additional important tool.

IR High Resolution Spectrometers

These instruments require the most sensitive detectors since the thermal background and its associated noise component can be reduced by a large factor compared with low spectral resolution instruments. High spectral resolution has been achieved by the use of echelles, Fourier Transform spectrometors and Fabry-Perot spectrometers which all offer some advantages in specialized applications. Applications include observations of line profiles and velocity distributions in shocked regions to study the kinematics of star formation processes, stellar atmospheres, the interstellar medium, planetary atmospheres, and many others.

IR Polarimeters

IR polarimetry is already revealing details of the nonthermal emission processes responsible for much of the radiation from active extragalactic objects (eg. BL Lacs, Optically Violent Variables, etc.). Thermal IR radiation arises from emission or scattering from dust grains. These are frequently asymmetrical in shape or in spatial distribution around the associated energy source. This produces radiation which is frequently polarized, with characteristic wavelength or spatial dependence giving details on source structure and energetics. Wire grid polarizers are relatively simple devices which can operate throughout the wavelength region accessible from the ground. A cooled wire grid (or some other more sophisticated polarizing device) will make a powerful addition to any of the above mentioned instruments.

6.2 Wide Field Imaging

Wide field visual imaging will be performed at the prime focus of the telescope. The prime focus camera will provide fields up to 30 arcminutes in diameter at a final f-ratio of f/2.0. This camera is considered an integral part of the optical design of the telescope rather than a separate scientific instrument, and details of its design and performance are given in Section 4.2. An alternative scheme for wide-field imaging involving a mosaic camera at the Nasmyth platform is discussed in the following section.

6.3 Multi-Object Spectrograph

Many of the scientific programs outlined in Section 2 of this report are feasible only with a multi-object spectrograph. A general purpose MOS spectrograph will be a high priority first generation instrument for the TMT. Such a spectrograph will of necessity be large and therefore most suitable for the Nasmyth focus. The discussion of an MOS spectrograph naturally breaks into three aspects: the pre-slit optics, the spectrograph itself, and the detectors. In the following paragraphs we discuss these in reverse order.

Detectors

The format of a detector for an MOS spectrograph must be two dimensional, and should be as large as possible, consistent with very low noise. Recent developments in CCD technologies may at long last yield the essential device for large telescopes. Tektronix, Inc., is currently developing 2048 by 2048 element arrays, 530mm on a side (26μm pixels); they have already achieved a readout noise as low as two electrons. In the next five years this device, or others

like it, should become available for astronomical use. We can take encouragement that Tektronix has other uses in mind for such a detector, so the development of this detector is not dependent on the minuscule astronomical market. CCD's combine high quantum efficiency, low noise, linearity of response, and positional stability, and are essentially ideal as astronomical detectors. For spectroscopy it is essential in addition that the CCD have good charge transfer efficiency at low exposure levels.

If the final spectrograph camera operates at a focal ratio of f/1.5, a 1 arcsecond slit will project to 3 pixels and so will be well sampled. Using the full length of the detector will yield 680 independent resolution elements in one order, which is competitive with the best spectrographs on smaller telescopes. The height of the slit projected onto this detector would subtend 10 minutes of arc, or perhaps 300 separate 1 arcsecond fibers at the slit. If we decide to use image slicing or narrower slits on the MOS, perhaps we should move to a slower spectrograph camera so as not to undersample the slit image. A slower beam would make it easier to implement a pyramid beam splitter to divide the spectrum between two detectors and so extend the number of resolution elements.

An alternative detector for the MOS would be a large microchannel multiplier followed by a coded anode readout device. The microchannel plate could be in proximity focus to a photocathode, or the photocathode could be deposited directly onto the front of the microchannel array. This type of device could provide 50μm spatial resolution; arrays of size up to 100mm have been fabricated. This detector would not have the high quantum efficiency of a CCD but it would be a photon counting device. The counting rate limit in an individual pixel cannot exceed 100 sec^{-1} because of limitations of current flowing in the microchannels; however its total count rate could be in the megahertz range, which should be fully adequate for spectroscopic applications.

Spectrograph

A preliminary design for the MOS spectrograph would scale up the recently completed double spectrograph on the 5m telescope (Oke and Gunn, 1982). This spectrograph features a 6-inch beam and is intended for detectors up to 40mm in size. Let us for the sake of definiteness simply scale up this design by a factor of two. The spectrograph has a dichroic mirror to separate the red and blue light so that the optics can be coated for higher throughput over the entire visible spectrum. The large beam is likely to necessitate the use of mosaic gratings. The spectrograph would contain an assortment of grating selections, so that the astronomer can operate at resolutions ranging from 500 to 10000. There should be a cross-dispersion element available, to permit echellete observation of one or a few sources.

We should consider whether this spectrograph can be combined with the high resolution spectrograph discussed below; it could share many common optical elements. Furthermore, there are a number of scientific projects that could benefit from high resolution spectroscopy of multiple objects over a limited spectral range (one echelle order). Such a project would be feasible by using an echelle grating in the MOS combined with an order selecting interference filter.

The double spectrograph uses Cassegrain Schmidt collimators, a prime focus f/1 Schmidt camera on the red side, and a folded f/1.5 Schmidt camera on the blue side. The MOS spectrograph should have as large a field of view as possible, and a detailed study of the spectrograph design has not yet been done.

Pre-slit Optics

The front end of the multi-object spectrograph should be able to accommodate a variety of observational programs. The size of the spectrograph dictates that it be stationary, yet the focal plane of the Nasmyth platform will rotate about the optical axis as the telescope traces a source. Counter-rotation is therefore required at the front end of the spectrograph. For long-slit observations, the counter-rotation could be done conveniently with a dove prism preceding the slit. The f/15 focal plane is sufficiently slow that the prism will introduce minimal

distortion. In addition to a long slit, there will be a multi-slit that separates into segments that are independently translatable in direction perpendicular to the slit axis. Such a scheme is the simplest adjustable MOS scheme. The use of drilled or etched aperture plates customized to a specific field is now common on large telescopes. With the Tektronix CCD detector at f/1.5, the total usable slit could be up to 10 arcminutes in length. This is extremely desirable to achieve in practice as it is adequate for spectroscopy of distant galaxies (see Section 2). However, the spectrograph optics would have to be extremely large to avoid vignetting the edges of the field. Furthermore, the curvature of the focal plane may prove impossible to correct over so large a field.

By steering segments of the primary mirror individually, it should be possible to perform image slicing in a variety of modes. The goal of such a scheme is to provide an effectively narrow slit in conditions of less that perfect seeing. The primary mirror would be deformed to produce multiple images of each star, all lined up on the slit axis. Below each element of the slit, a small piece of lens deflects and speeds up the individual beam segment, and the effect is to give increased slit demagnification on the detector.

Another method of multi-object spectroscopy will use an array of fiber-optic filaments to bring the light from a number of sources (10-150) in the field of view to a long slit on the spectrograph. This is the only method that is likely to be able to utilize the full 20 arcminute field. For each source there will be one fiber, plus one or more separate fibers to sample the sky at adjacent locations. This method has been under intensive investigation for a number of years and appears promising. (Powell,1983; Hill, Angel and Richardson, 1983). The fibers will be mounted on a frame that will rotate to counteract the field rotation of the telescope. In one possible design, each fiber will be separately movable on the frame to adjust to the location of interesting sources in any field of view. The motion of the fibers would be under computer control. A simpler but less flexible scheme would involve fibers set into holes in a drilled plate. The focal surface of the Nasmyth focus is curved, and the principal rays of sources off the center of field may be curved with a different radius of curvature. The fibers must be aligned so that the principal ray is perpendicular to the fiber face, and the holding jig for each fiber pair will need to compensate for this field curvature.

Multiple-object spectroscopy is intended for application to faint sources that frequently will have a brightness considerably less than that of the sky. Experience has shown the importance of careful sky subtraction to remove systematic transmission variations of the different fibers. The normal mode of operation with multiple fibers will be to obtain pairs of observations with the sky and object fibers reversed between exposures. This would be most easily accomplished by a telescope displacement if the separation and alignment of all the fiber pairs are identical.

Fiber-fed spectroscopy requires lens coupling of each fiber, since an f/15 beam is too slow to be preserved within the fiber. Focal ratios in the range of f/3 to f/5 would be ideal. It is unclear what the best method for coupling the fiber output into the spectrograph will be. It would be best if the fibers could replace the long slit, but another option would be for the fibers to emerge at the prime focus of the Schmidt collimator camera. This latter scheme would be difficult to implement in a double spectrograph. There are additional questions of stability of the throughput of the fibers as the front end of the fiber feeds rotates. Many questions are yet unanswered regarding fiber-fed spectroscopy; we intend to closely follow the developments of fiber-fed spectroscopy over the next several years.

An Alternative Concept: A Mosaic Fly's Eye Spectrograph

The above discussion indicates that a multi-object spectrograph using multiple entrance slits does not easily achieve a wide field of view. For a camera f-ratio of f/1.5, the Tektronix CCD or its equivalent can in principle cover a 10' FOV. However, this field subtends 0.44m in the focal surface and would require very large spectrograph optics to avoid vignetting. It is also deeply curved. An alternative scheme using smaller components might employ a mosaic "fly's eye" camera with a transmission grating in each imaging module. Such a scheme was first

explored for direct imaging, but the prime-focus camera gives better throughput and better images (Epps and Faber 1983, TMT Report No. 113). The fly's eye device might be better suited to low dispersion spectroscopy, however.

A generic design (Epps 1984) is illustrated in Figure 6-1a. The heart of the device is a semi-solid Schmidt camera. This particular version is tailored to a detector that is 16.7mm in its largest (diagonal) dimension. Each module covers a field that is approximately 3.5 arcminutes in diameter. The distinctive feature is that each module sits in the shadow of the region of the focal surface it covers. The field lenses can therefore be trimmed in principle to provide nearly contiguous coverage of the focal surface if this is important.

Figure 6-1a illustrates a slight difficulty caused by the curved Nasmyth focal surface. As shown in the upper panel, for locations off-axis the principle ray is not perpendicular to the focal surface. Since, for adequate optical performance, the module axis must be aligned with this principle ray, the detector must be tipped to compensate for the tilted image surface seen by the module. This tipping is fairly successful at compensating for the effect, as is seen in the off-axis spot diagrams in Figure 6-1b. Off-axis performance is limited by the intrinsic off-axis astigmatism of the RC Nasmyth focus, and is adequate to approximately 20 arcminutes in diameter, which is the nominal full Nasmyth field. Sixteen modules could subtend a field roughly 16 arcminutes by 16 arcminutes and provide roughly 60% areal coverage. Since the area of the focal plane imaged by each individual module is small, defocus due to field curvature within each module field is a small effect.

The fly's eye could be converted to a low-dispersion spectroscopic device by inserting transmission prisms into each module between the field lens and the Schmidt corrector, and by inserting an appropriate mask into the Nasmyth focal surface with slits. Performance with the prism has not yet been explored quantitatively but is expected to be good because the beam is slow (f/15.0). This is a major question for future investigation.

Note that field rotation for the fly's eye in all likelihood cannot be achieved with a Dove prism, as the field is too large (in excess of 0.5m). It will therefore be necessary to rotate the entire array of modules.

6.4 High Resolution Visual Spectroscopy

A detailed design study was carried out for a high resolution, wide spectral coverage optical spectrometer for the TMT. Though the needs of high resolution coudé-style spectroscopy will almost certainly require a variety of spectrometers, an instrument which could deliver a spectral resolution of 60,000 and spectral coverage from 0.3 to 1.0μm single exposure would undoubtedly become the workhorse of the high resolution facility. It would go a long way toward meeting anticipated needs for high resolution optical spectroscopy of point sources.

To properly design such a spectrometer, one must carefully match the optical parameters of resolution and field size to the pixel size and overall dimensions of the detector. First light of the TMT is at least 5 years away, and until it is known exactly what the detectors of that era will look like, it will not be possible to do a meaningful final design of the spectrometer. However, it seemed useful to carry out a preliminary design study to see what might be accomplished with today's detectors and technology. This study has provided an "existence proof" for such an instrument, and explores its capabilities in detail. It establishes requirements on the spatial resolutions and linear dimensions of optimum detectors. The resultant design is intended to be used only as a "strawman" to identify any potential conflicts with the telescope and dome design, and to point to areas where further design studies or technological development are required. A comprehensive write-up of this study is available as UC TMT Report No.101. Only a brief summary is given here.

It is clear that this instrument should be of the cross-dispersed reflection echelle variety, and that it should reside on one of the two Nasmyth platforms. The strawman design is shown in Figure 6-2. It consists of two separate spectrometers, one for the "blue" and one for the "red" The incoming beams are separated immediately behind the slit with a dichroic. Each

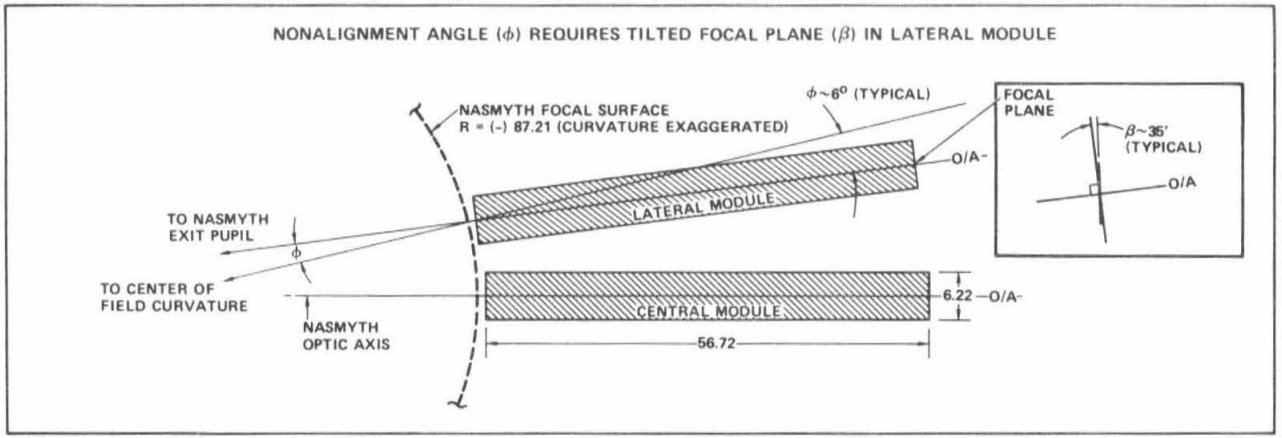

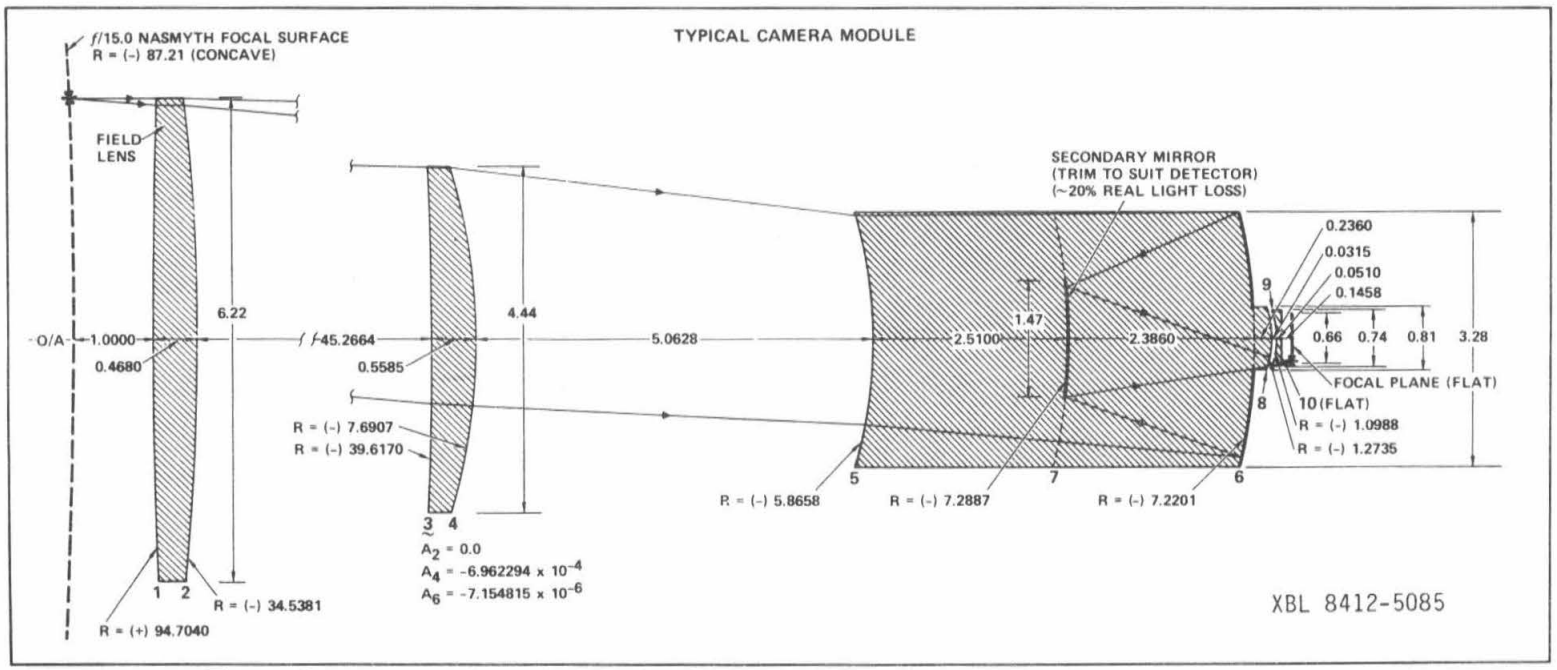

Figure 6-1a A generic optical design for a direct imaging reducing fly's eye camera at the Nasmyth focus. The design is modelled on a similar design by Gunn for the Palomar 5m telescope. The upper panel illustrates the lack of perpendicularity between the principal ray (to center of the Nasmyth exit pupil) and the focal plane off-axis. To compensate for this, the focal plane of the camera is tipped, in this case by 35 arcminutes.

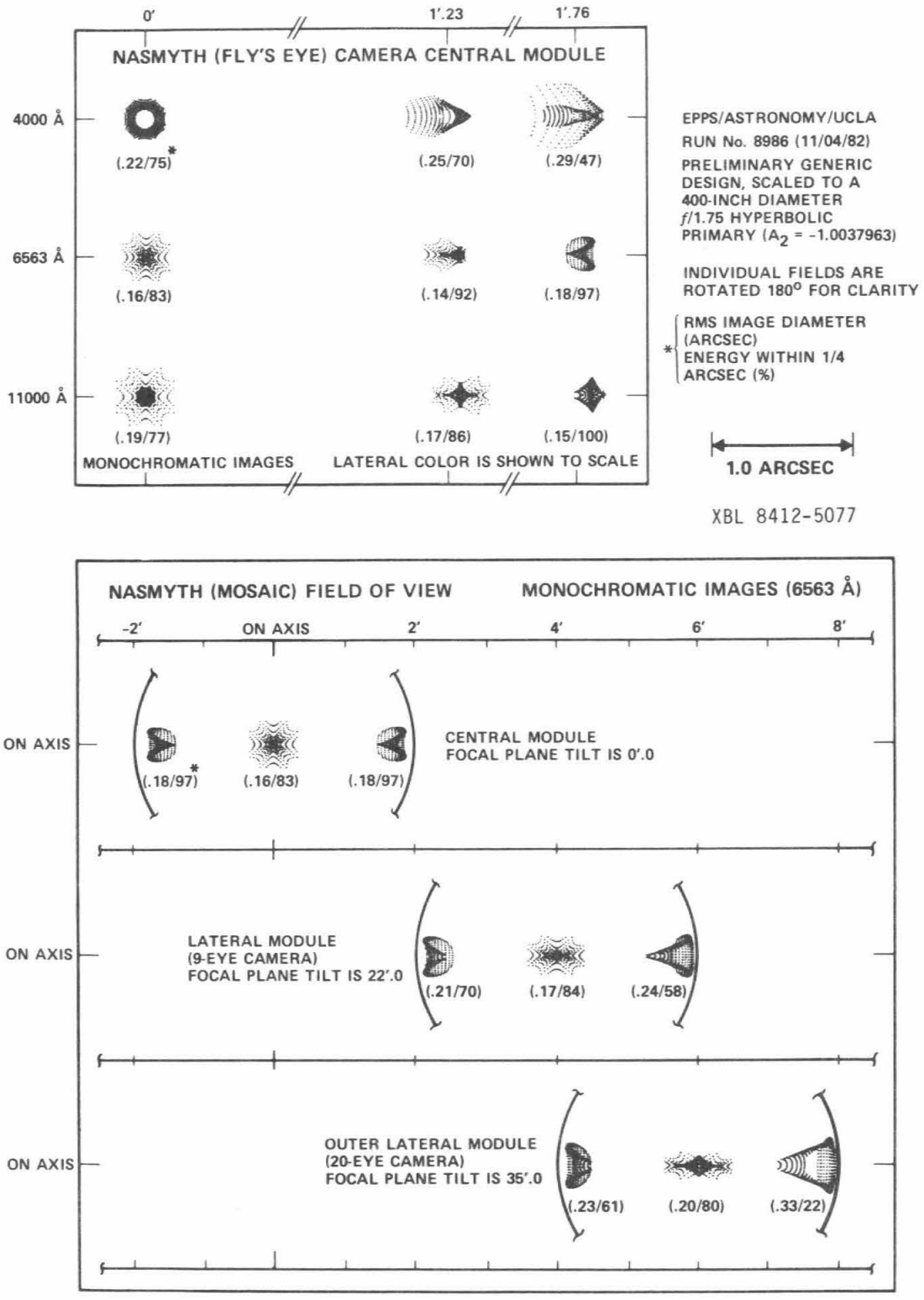

Figure 6-1b Spot diagrams for the camera design in Figure 6-1a. The upper panel shows the performance of the on-axis module as a function of color. The lower panel shows images at 0.6563μm for modules centered on-axis, 4 arcminutes off-axis, and 6 arcminutes off-axis. Most of the off-axis degradation is due to Nasmyth R-C astigmatism. The maximum field radius within each module is 1.76 arcminutes. As in previous figures, rms image diameter is the average rms distance of all rays from the center of gravity of the image. (For a Gaussian distribution, it is $\sqrt{2}$ times the one dimensional rms sigma.)

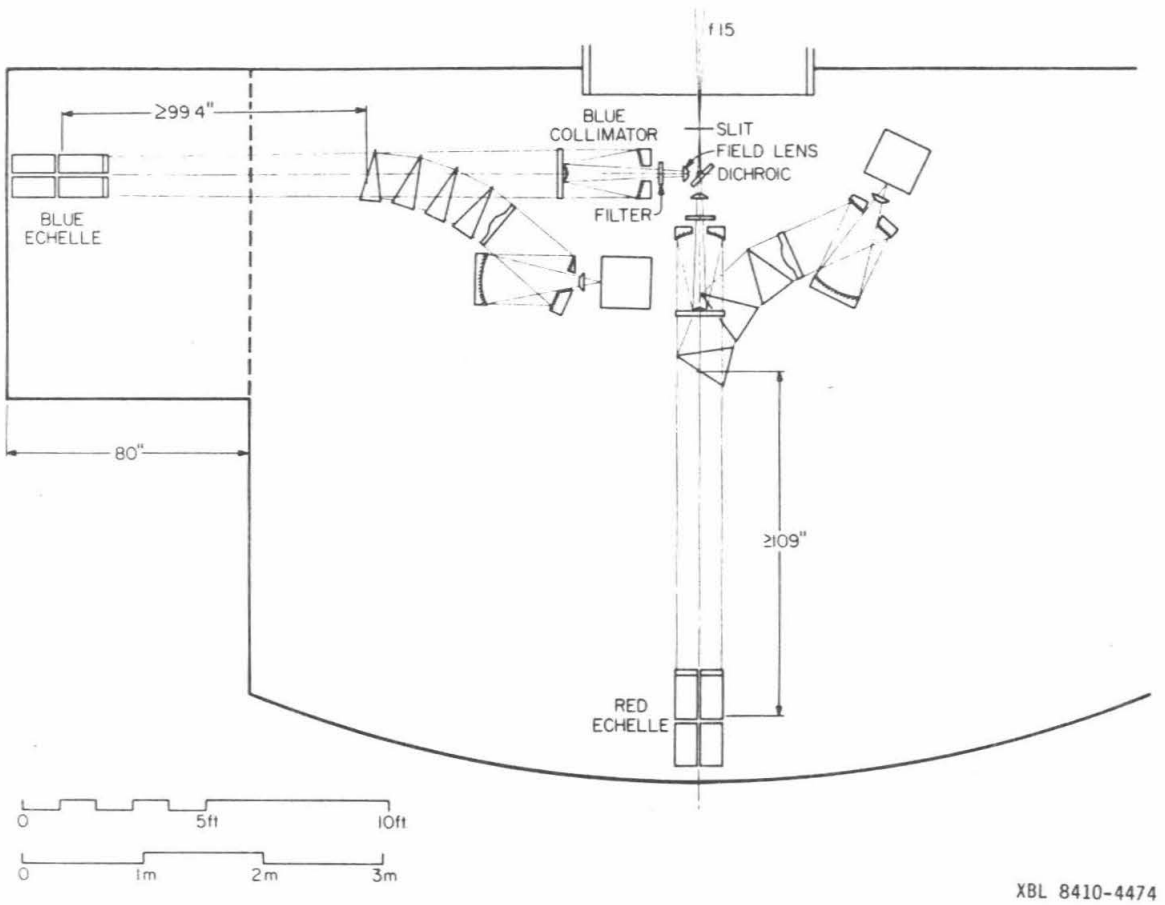

Figure 6-2 The Nasmyth dual echelle layout.

spectrometer consists of an inverted Cassegrain collimator of 16″ aperture, a mosaic of four 8″x16″ R-2 echelles (31.6 gr/mm), cross-dispersing prisms, and a folded Schmidt camera feeding a flat, external focal plane. The blue side covers 0.32 to 0.54μm in one exposure, while the red side covers 0.54 to 1.0μm. As shown in Figure 6-1, an 80″ extension to one side of the Nasmyth platform seems necessary to accommodate the blue echelle mosaic; however this extension could easily be eliminated by adding one extra folding flat. The inverted Cassegrain collimators could also be avoided by folding the beams and using conventional off-axis parabolic collimators.

The required detectors have 30μm pixels and field diameters of 36 and 40mm respectively for the blue and red sides. Such detectors are presently obtainable in Ranicon technology. The largest available CCD's of today are still only 12x12mm, but promising developments are already underway at Tektronix (unveiled at the August, 1984 meeting of the S.P.I.E in San Diego) to produce CCD's as large as 60x60mm, which feature 30μm square pixels on a 2048 by 2048 format.

The blue camera is simply a scaled up version of a design already ray-traced by H. Epps and under construction for the Lick Observatory Hamilton Spectrograph. The red camera is faster, and may prove troublesome to design. However, if detectors as large as the Tektronix CCD become available, the red camera could be slowed down to the same f-ratio as the Hamilton camera, and should then be relatively straightforward. Due to non-uniformity in real optical materials, camera designs cannot simply be scaled up to larger sizes without sacrificing performance. Detailed camera design studies will have to be worked out. As larger detectors with more pixels become available, the camera design becomes easier. With detectors as large as 60mm on a side, it might be possible to do the entire spectrometer with only one set of optics, rather than splitting it into red and blue sides. This approach would give up the possibility of optimizing coatings and quantum efficiencies throughout, but would be less expensive and easier to set up and maintain.

The spectrometer features a 0.9 arc-sec slit at a resolving power of 60,000 (slit projects onto two 30μm pixels). This is large enough to minimize the need for image slicing under many conditions. Often though, a modest amount of image slicing (2 to 3 slices) would be desirable. With a shot-noise limited detector of 20% Q.E., the spectrometer will reach V=18 in 1.3 hours at S/N=30 per resolution element, and a resolution of 0.1 A at 6000 A.

The study has pointed out a number of critical areas where careful thought must be given. It is essential that the Nasmyth platform be totally enclosed in an insulated, light-tight, clean-room enclosure to insure thermal stability and cleanliness. It seems almost inevitable that one of the two Nasmyth platforms will have to be permanently committed to high and moderate resolution spectrometers. The former, due to their large size and critical alignment tolerances, must remain essentially undisturbed. The light-tight enclosure must be thermally insulated and designed to minimize seeing effects within the spectrograph. Spectrograph supporting structures should be as stiff, light-weight, and as thermally stable as possible. Graphite-epoxy I-beams seem a likely technology for this need.

Atmospheric dispersion and field rotation will need to be dealt with, and studies to design some sort of Risley prism arrangement and field rotator must be undertaken. Often, a small amount of image slicing will be desirable, and slicer designs need to be worked out in close coordination with the final spectrometer design. Slicer design will be a difficult, yet important component of the overall spectrometer design. The next most critical optical design problem will be the cameras. These will be fast optical systems with relatively large optical elements. Alternatives to the standard Schmidt variety of camera designs should be explored. A system of sensors and actuators for aligning the echelle mosaics will also be required. Ideally, this should be a closed-loop scheme which requires no intervention from the observer. Technology developed for the primary mirror segment actuators could be exploited for this task.

CCD detectors with larger formats should be developed. The needs of the strawman design would be nicely met by detectors with 30μm square pixels covering a 60mm diameter field. Since much of the use of this spectrometer would be for spectroscopy of point-like

sources, with only a very small field of view required, it would be nice to implement a system of small, turret- selectable mirrors for the Nasmyth tertiary mirror. Most of Nasmyth secondary size is not due to FOV.

Since this spectrometer does not fill all the needs of high resolution spectroscopy, an investigation of ways to incorporate other spectrometer combinations into the design must be done.

6.5 Prime Focus Spectrograph

It would be inappropriate to make a detailed design study for a faint object spectrograph for the TMT at the present time because detector technology is in a rapid state of change. Considerations of detector size and pixel size are fundamental starting points for the design of any spectrograph, and one can only guess what might be available in a few years. However, it is possible to make some general remarks.

For spectroscopy with large telescopes, light losses at the entrance slit are an extremely important consideration. It is simple to show that the principal figure of merit in the design of a spectrograph where slit losses are important is the speed of the camera; small focal-ratio cameras ($\leq$ f/1.0) are essential. Furthermore, the overall efficiency of the instrument must be maximized to the fullest extent. When observations are background dominated, as they will be for the faintest objects, the speed gain of the TMT compared to smaller telescopes will be proportional to the diameter of the primary mirror, not its area. The most efficient place to do faint object work would be the prime focus, since there would be only one reflection in the telescope. Highly reflective special coatings on secondary mirrors could relax the need to go to the prime focus, but they remain to be developed.

We suggest that careful consideration be given to designing a spectrograph with refractive optics. With modern optical glass and multi-layer coatings, it is possible to produce lenses that are extremely fast ($<$ f/1.0) and also highly transmissive. Even with seven optical elements, lenses can transmit over 90% of the light in a broad spectral range. Additionally, lenses offer the advantage of external focal plane, so that mating to detectors is considerably simplified compared to Schmidt cameras. Careful consideration should also be given to splitting the beam with dichroic mirrors, so that two (or even more) cameras and detectors, each optimized for a different wavelength region, could operate simultaneously. Finally, employing prisms for the dispersive element rather than diffraction gratings would allow for high efficiency for this crucial component of the spectrograph.

We suggest that a spectrograph using lenses for the collimator and camera, a prism for the dispersing element, and a CCD for a detector could approach 50% in quantum efficiency from slit to detector. This would be at least twice as efficient as any spectrograph now in use on a large telescope, and the TMT would be capable of truly major advances in faint object spectroscopy compared to existing telescopes.

6.6 Infrared Spectroscopy and Imaging

We consider the IR for TMT applications to be divided into the "thermal" region (in which the dominant noise source is $N^{1/2}$ where N is the photon arrival rate from the thermal emission from telescope structure, mirrors, etc. in and close to the beam) and the near IR (for which the noise is dominated by other sources, eg. detector, sky, etc.). Thermal IR work will be done at the Forward Cassegrain f/25 focus within the telescope tube, forward of the primary mirror. This focus will be served by a chopping secondary and will offer the lowest background available on the telescope. Applications including imaging, low and moderate resolution spectroscopy, and polarization studies from 2.5 to 30μm will be located at this focus. This is the only focus available for low background work requiring chopping and apart from prime and Cassegrain, the only focus not suffering a 45 degree reflection. Short wavelength imaging and

Table 6-1 Photometers with Discrete Detectors

	#1 Photometer $0.9 < \lambda < 2\mu m$	#2 Photometer $1 < \lambda < 5\mu m$	#3 Photometer $5 < \lambda < 30\mu m$
FOV	1 - 10″	1 - 10″	1 - 10″
Focus	Prime	IR[1]	IR
Spectral resolution	atm window special filter CVF[2]	atm window special filter CVF	atm window special filter CVF
Spatial resolution	defined by aperture	defined by aperture	defined by aperture
Detectors	Si or Ge or InSb	InSb or Si:XX	Si:XX or bolometer
Weight & size	25kg 0.5m cube	25kg 0.5m cube	25kg 0.5m cube
Technology status	established	established	established

[1] IR focus means f/25 forward Cassegrain focus with chopping secondary

[2] circular variable filter

Table 6-2 Moderate Resolution Array Spectrometers

	#4 Spectrometer $0.9 < \lambda < 2\mu m$	#5 Spectrometer $1 < \lambda < 5\mu m$	#6 Spectrometer $8 < \lambda < 13\mu m$
FOV	slit 1-10″ long 0.5-2″ wide	slit 1-10″ long 0.5-2″ wide	slit 1-10″ long 0.5-2″ wide
Focus	Prime	IR	IR
Spectral resolution	10 - 500	10 - 500	10 - 200
Spatial resolution	defined by slit	defined by slit	defined by slit
Detectors	Si or Ge or InSb CCD	InSb or Si:XX	Si:XX
Weight & size	50kg 0.5m cube	50kg 0.8m cube	50kg 0.8m cube
Technology status	detectors can be purchased	detectors can be purchased	detectors exist but hard to acquire expect situation to improve

Table 6-3 Imaging Systems (IR Cameras)

	#7 Camera $0.9 < \lambda < 2\mu m$	#8 Camera $1 < \lambda < 5\mu m$	#9 Camera $8 < \lambda < 30\mu m$
FOV	1 arcmin square per InSb CCD	1 arcmin square per InSb CCD	30×15 arcsec for butted array
Focus	prime	IR	IR
Spectral resolution	selectable filters	selectable filters	selectable filters
Spatial resolution	~ 0.25″/pixel	~ 0.25″/pixel	~ 0.25″/pixel diffraction limit
Detectors	Si or Ge or InSb CCD	InSb or Si:XX	Si:XX
Weight & size	50kg 0.5m cube	50kg 0.8m cube	50kg 0.8m cube
Technology status	detectors can be purchased	detectors can be purchased	detectors exist but hard to acquire expect situation to improve

spectroscopy where the detector or sky dominates the noise will be done principally at the prime focus, and high resolution spectroscopy which involves the use of large instrumentation susceptible to changing gravitational loads will be done at the Nasmyth focus.

The advantages of a "forward" Cassegrain focus compared to a more conventional focus behind the primary are a faster beam and better plate scale, easier to match to expected image sizes. Access to the focus will not present a problem due to the large scale of the overall project. Typical detector arrays operating at 10μm and currently available have 100μm square pixels and 16x32 pixels per array unit. It is expected that larger arrays may be assembled from basic units similar to this. With good atmospheric seeing of 0.25 arcseconds (FWHM) and diffraction effects of 0.21 arcseconds, we expect an image FWHM of 0.33 arcseconds. According to Faber (1981, TMT Report No. 61) image sampling at a density of 2-2.5/FWHM is adequate, so we assume 0.15 arcsecond pixels. Thus using 100μm pixels, we need to speed up the beam by a factor of approximately 2, and an 11x32 element array will cover a 2.4x4.8 arcsecond area with good sampling. A larger field could currently be implemented by either combining several unit arrays or by placing several single array systems over the field to sample astronomically interesting positions, or for fine guiding, or possibly some type of active image reconstruction using a bright source in the field.

6.6.1 Detectors and Atmospheric Windows

Infrared detector arrays with fully multiplexed readout have recently become available for astronomical uses with sensitivities for each pixel comparable to the best single detector. The manufacturers of these devices are advancing the technology, increasing array sizes, increasing quantum efficiences, decreasing readout noise, and exploring the use of different detector materials and multiplexing schemes.

At shorter wavelengths, intrinsic silicon CCDs are useful to 1.1μm. CCD readouts can be used for detectors sensitive at longer wavelengths by coupling a 2-D array of detectors to the CCD by "indium bump bonding" Arrays of this type using InSb are currently in use. The CCD readout cannot be used for the longer wavelength IR however, since at the low temperatures required for the successful operation of the detectors, the readout ceases to function. At wavelengths around 10μm, 2-D arrays have been constructed using switched FET multiplexing with doped silicon used for the detecting element. The high background flux in the thermal IR requires that these arrays must be read out frequently and requires some sophistication in resulting data handling. The full implementation of IR arrays in astronomy will have far reaching effects on the science achievable with this telescope.

A summary of detectors and their characteristics is given in Table 6-4. The IR atmospheric windows and the standard photometric bands are given in Table 6-5. A more detailed view of the atmospheric transmission is given in Figure 2-2.

Table 6-4 Infrared Detectors

Material	Wavelength (μm)	Comments
Si CCD intrinsic	$\lambda < 1.1$	CCD technology currently up to 1000x1000, 22 μm pixels, available now or within months
Ge intrinsic	$\lambda < 1.7$	1 D arrays now becoming available, 2D arrays likely in near future
Si:In	$1 < \lambda < 7$	Comments relate to all Si:xx. Long λ cut-off
Si:Bi	$4 < \lambda < 18$	hard, short not well defined. Si:Bi best developed
Si:As	$7 < \lambda < 24$	FET MUX 2D arrays up to 16x32, (100μm pixels) exist
Si:Sb	$18 < \lambda < 32$	and are buttable 2 sides. CCD techniques not useful since detectors must operate at T $\approx$ 10K
InSb	$1 < \lambda < 5.5$	80% QE single detectors 0.25 - 2.0mm dia 2D arrays available both CCD & FET readout FET arrays currently 58x62, 75μm pixels
Hg:Cd:Te Pb:Sn:Te	selectable	These materials are currently under development; future astronomical applications uncertain. Useful wavelength range tunable by doping.

Table 6-5 Atmospheric Windows

Symbol	Wavelength μm	Bandwidth μm	Atmospheric Transmission	Absorbers & Emitters
R	0.7	0.6 - 0.8	good	H_2O airglow
I	0.9	0.8 - 1.1	good	H_2O airglow
J	1.25	1.17 - 1.3	good	H_2O
H	1.65	1.5 - 1.8	good	H_2O CO_2
K	2.2	2.0 - 2.5	good	H_2O CO_2
L	3.6	3.4 - 4.2	good	H_2O CO_2
M	4.8	4.5 - 5.2	poor	H_2O
N	10.2	7.7 - 13	good	H_2O O_3 CO_2
Q	20.	17 - 25	poor	H_2O
X	30.	25 - 38	very poor	H_2O

6.6.2 Photometers

Although arrays will probably be used for the majority of telescope time allotted to IR there are likely to remain requirements for simple, single (or few) detector photometers with selectable apertures and filters. Apart from scientific applications, photometers will provide useful data on the IR performance of the telescope. Since high time resolution can be easily achieved they may also be preferred for occultation studies. Their high precision of calibration will also be needed in some applications.

6.6.3 Imaging

Infrared imaging of complex regions at the high sensitivities and spatial resolution achievable with the TMT will probably provide some of the most spectacular scientific results. To date, higher spatial resolution continues to reveal further details in the structure of many sources such as regions of star formation, etc. Working at or close to the 10μm diffraction limit, the TMT equipped with 2-D imaging arrays will provide a unique capability. Arrays presently available provide only small coverage of the focal plane ($\leq$1 square arcminute) (see Table 6-4) but future developments will improve this situation. At the shorter wavelengths, ($\lambda \leq 2\mu$m) where airglow or detector noise dominates the thermal background, larger CCD arrays will probably be implemented at prime focus similarly to present plans for the visual prime focus camera. In the thermal infrared, chopping is necessary for background subtraction, and at least in the near future, the forward Cassegrain focus with its 5 arcminute chopped field will be the preferred focus for thermal IR imaging. A summary of IR camera characteristics is given in Table 6-3.

6.6.4 Moderate Resolution Spectrometers

The use of the long slit and 2-D detector arrays for spectroscopy provides spatial information in the cross dispersion direction again enabling the TMT to exploit its advantage of high sensitivity and spatial resolution. Similar to the imaging instruments, the shorter wavelength spectrometers may be able to benefit from the faster beam at either prime or Nasmyth foci, whereas the thermal IR systems will continue to need a chopped IR focus.

IR fibers are currently available out to $\lambda \approx 5\mu$m and the technology is being developed rapidly (Harrington, 1984). Although no IR astronomical instruments presently use fibers, it seems highly likely that the situation will change in the near future. This will enable the IR analog of visual multi-object spectroscopy to become reality and reinforces the requirement for a large, low background field at the IR focus.

6.6.5 High Resolution Spectrometers

Fabry-Perot Spectrometers

Fabry Perot interferometers may be used to obtain resolutions $\approx 10^5$ in the 1 - 20μm wavelength range. To achieve the lower background appropriate to the higher resolution the FP must be cooled and the grating or filter used for order selection also must be cold. Imaging is possible through these devices, so detectors, fields of view, and pixel sizes appropriate to the imaging instruments are appropriate here. Since the background radiation is lower due to the higher spectral resolution the cross-over between thermal and non-thermal operating regimes will be different, and lower noise is achievable. The detectors may be easier to acquire and operate since there are similarities with SIRTF requirements and read-out rates will be lower. The instruments will not be significantly larger than the cameras for those wavelengths.

Fourier Transform Spectrometers (FTS)

In the range out to 4μm where the system is not background or signal noise limited FTS instruments are usefully employed. These may be large high resolution instruments designed for a stable focus (Nasmyth), or smaller devices carried at Cassegrain. Spectral resolutions of 10^3 to 10^5 can be achieved.

Heterodyne Spectrometers

This technique yields very high spectral resolution R $\approx 10^7$. The instrumentation required is massive and would be appropriate for the Nasmyth focus.

6.6.6 Polarimeters

In most cases polarimetry will be done with the addition of a polarizing element ahead of the appropriate detection system (instruments #1 through #9). This unit will need to be cooled for most applications and should be designed such that the window at the rear of the polarizer and the window for the instrument can be removed to form one vacuum system without the losses inherent from two extra windows in the optical path. Techniques available include polaroid film and wire grids (for systems designed to measure large polarizations in faint sources) and photo-elastic modulators (which have low instrumental polarization and are suitable for measuring low polarization sources). Optimum design should not require that 3 separate polarimeters be built for each of nine instruments but that each polarimeter should be usable with each appropriate system. The Nasmyth focus is unlikely to be used for polarization studies because of the 45 degree reflection at the tertiary. The polarimeters will vary from extremely simple small devices to complex systems of approximately the size and weight of the camera or spectrometer they serve.

6.6.7 IR Instrument Priorities

Given a situation of finite time and funding within the project the approximate order of priority of the above instrument complement is:

1. Photometers - these systems are relatively simple, inexpensive, and present no new technological problems. They can be used for testing the TMT's IR performance, and have strong scientific justifications.

2. Low/moderate resolution spectrometers for the 2 - 4μm region and the 8 - 13μm region, each using arrays currently available.

3. Cameras covering the 2 - 4μm and 8 - 13μm windows. Development work is required for astronomical use of 2-D arrays at 10μm. The funding agencies should be encouraged to support this type of activity and UC should ensure that it has access to these techniques.

4. Development of other IR instrumentation will rely on the active participation of the astronomers concerned. There are strong scientific merits for offering as complete as possible a set of instruments for use on the TMT.

7. Telescope Structure

Contents **Page**

7.1 General Approach and Design Goals

The fundamental tasks of the telescope structure are to support the optics and scientific instruments, to maintain their alignment, and to point the optical system to astronomical objects with extremely high precision and accuracy. The structural design should take advantage of the abilities of modern computer controlled systems to compensate for certain predictable structural and optical misalignments, and should take advantage of the simplicity and symmetry inherent in the altitude-azimuth mounting chosen for the TMT. Further, the structure must perform these goals in a relatively hostile environment in which the telescope is subject to variable wind and thermal loads. Finally, because of the special needs of the actively controlled primary mirror, it is important that the structure not exhibit appreciable resonant coupling to the actively controlled primary mirror segments. To achieve these high performance goals for the structure in an economical fashion is the challenge to the designer.

In the design process, the weight of the structure was often used as the merit function in deciding among alternate geometrical, but otherwise equivalently behaving structures. We assume that weight reduction will lead to economical structures, which in turn will minimize any thermal disturbance of nearby air (hence enabling better seeing conditions), and to superior or more economical drive systems. Various practical concerns such as instrument dimensions and wind loads constrain the lowest possible weight. The practicality of fabrication is also a strong consideration in the design process, with standard materials and material sizes being used whenever possible. Alternate structural designs were modeled and analyzed in quantitative detail, often using structural analysis programs such as SAP-4. The overall design, analysis, and optimization of the telescope structure is being carried out by Medwadowski and will be

described in a series of TMT Reports. (Presently available TMT Reports include numbers 59, 70, 71, 72.)

The design goals are given in Section 3. The telescope must move smoothly over essentially the entire sky, and must be able to move to any point in less than two minutes. Since the Mauna Kea site is rather windy, the goal of holding wind-induced image motion to under 0.25 arcseconds in 14m/s winds is a critical factor in the design. Image degradation caused by thermal and gravitational perturbations on the collimation and focus must be negligible as well.

Since the primary mirror is actively controlled, and the primary-secondary alignment may be actively controlled as well, we considered relaxing the specifications for the passive structure. However we felt that any cost savings would be minimal, and further, that weakening the structure would lower resonant frequencies in the structure and thus add complexity to the active control systems. Hence our design goals are generally to be met by the passive structure, much in the manner of more traditional optical telescopes.

For structures the size of the TMT it is impractical, if not impossible, to hold the optical elements in a structure that does not deform excessively under the influence of gravity. However, a structure that provides equal and parallel displacements of the primary and secondary mirrors will provide proper optical alignment even with large deflections of the elements. The system developed by Serrurier to accomplish this has become the classic system for telescopes. For our design, we have followed the same principle, that gravitational loading should not degrade optical alignment.

The performance of an active control system is typically limited by resonances in the structure being controlled. Hence, a telescope with the highest resonance frequencies will have the most potential for excellent active control and compensation. Resonant frequencies in a structure are generally related to deflections (under gravity here for example), as

$$2\pi f = \omega = \left(\frac{g}{\Delta}\right)^{1/2} , \tag{7-1}$$

where f is the frequency, g is the gravitational acceleration, and Δ is the deflection under gravity. Hence it would be advantageous to minimize deflections, both to increase the allowed bandwidth of the active control systems, and to reduce the range of active control that is needed.

For many kinds of structures, deflections can be decomposed into those that the structure experiences due to its own weight and those caused by external loads. Self-weight deflections are often independent of the mass of the structure. For example, deflections of a space frame under its own weight depend upon the geometry, but are unaffected by proportional increases in cross sectional areas (hence mass) of its elements. Deflections due to external loads vary inversely with the mass of supporting structure, for a fixed geometry. From this one can see there is a point of diminishing returns in attempting to decrease gravity deflections by increasing the weight and stiffness of the supporting structure. Often the self-weight deflections approximate the external load deflections when the structural mass is approximately equal to the load mass.

As a consequence, we made particular efforts to minimize the weight of the primary mirror, and all other equipment mounted on the telescope. Segmentation and the 36-point support system for each segment allow the primary mirror to weigh only 14 tons, about the same as the primary mirror in the Hale 5m telescope. Equally important, we have limited the weight of any equipment at the top end of the telescope to 2 tons, thus limiting the external load carried by the telescope tube. For the same reasons, and because the Nasmyth platforms can carry large loads up to 10 tons, the Cassegrain instruments were also limited to 2 tons.

A further goal of the design is that the telescope be parfocal, that is, the Cassegrain and Nasmyth foci have the same back focal length of 3m. Placing both foci at reasonably accessible locations has dictated that the elevation axis be located 4m above the primary vertex. Fortunately, with minor adjustments in the telescope structure we can arrange that the telescope

center of gravity is located on this axis, thus minimizing the counterweights needed for a balanced tube.

7.2 Primary Mirror Cell

General Objectives

The mirror cell performs the task of supporting the primary mirror segments, supporting the Cassegrain instrument module, and supporting the instrument module at the elevation axis, which can carry either the tertiary mirror or IR instrumentation at the forward Cassegrain focus. The cell is attached to the elevation ring. The primary mirror covers will be attached to the elevation ring.

The active control system for the primary imposes additional requirements on the mirror cell. To minimize the amplitude of the motions that the control system must correct for, we wish to minimize the gravitationally induced deflections of the segments. Further, to maximize the allowed bandwidth of the control system, we want the lowest resonant frequencies of the cell to be as high as possible. Both of these requirements are met by maximizing the stiffness of the cell. It should be noted that if the cell could be made infinitely stiff (and thermally stable), then an active control system for the segments would not be needed. In fact the maximum achievable stiffness is roughly four orders of magnitude too low to allow passive support of the segments.

A segment position is defined by six parameters. Three of these must be actively controlled, and three are adequately determined passively by the dimensional stability of the mirror cell. The three adequately determined parameters represent motions of the segment in its own plane. In-plane motions under gravity of the outermost segment must be under 1mm, and segment rotation must be held to under 0.0003 radians. Differential motions between adjacent segments should be appreciably smaller.

Servicing of the segments will be necessary, and this will require reasonable access to the back of the segments. Access to the sensors and actuators will be required in case of failure and for removal and installation of the segments for aluminization.

Cell and Subcell Topology

Since the segment support system must be positioned relative to the segment with high accuracy, and since the gross cell structure (of some 10m diameter) will be built to relatively crude tolerances, a precision subcell that accurately holds the actuators and radial support post for each segment is desirable. This subcell defines the relative positions of the actuators and the radial support post, and carries the weight of the segment. The proper positioning of the segment within the primary will then be accomplished by translating each subcell as a single entity. Once the subcell is positioned on the cell, it is permanently attached, and the subcell defines the segment position when it is installed. The three segment in-plane coordinates will be established by tapered pins that locate the segment relative to the radial support post, which is in turn located relative to the cell as a whole by the subcell. To maximize axial stiffness, the nodal points in the subcell that hold the actuators will also attach directly to the cell. Figure 7-1 shows the subcell geometry.

For the cell as a whole, a number of configurations were considered. A space frame was adopted for the general form, and numerous topologies were examined and quantitatively analyzed to maximize the stiffness to weight ratio of the cell. Some of the candidate cell configurations are described by Medwadowski (1981, TMT Report No. 59 and 1982, TMT Report No. 70). The final configuration developed by Medwadowski (1984 TMT Technical Note No. 109) consists of a three-layered cell with the top and bottom surfaces curved as shown in Figure 7-2. The top layer has nodes at each of the actuator locations (to which the subcells are tied), and nodes along the edge to allow attachment to the elevation ring. The middle layer consists of a hexagonal grid, and is flat to ease the actual fabrication and to provide the basis for a flat

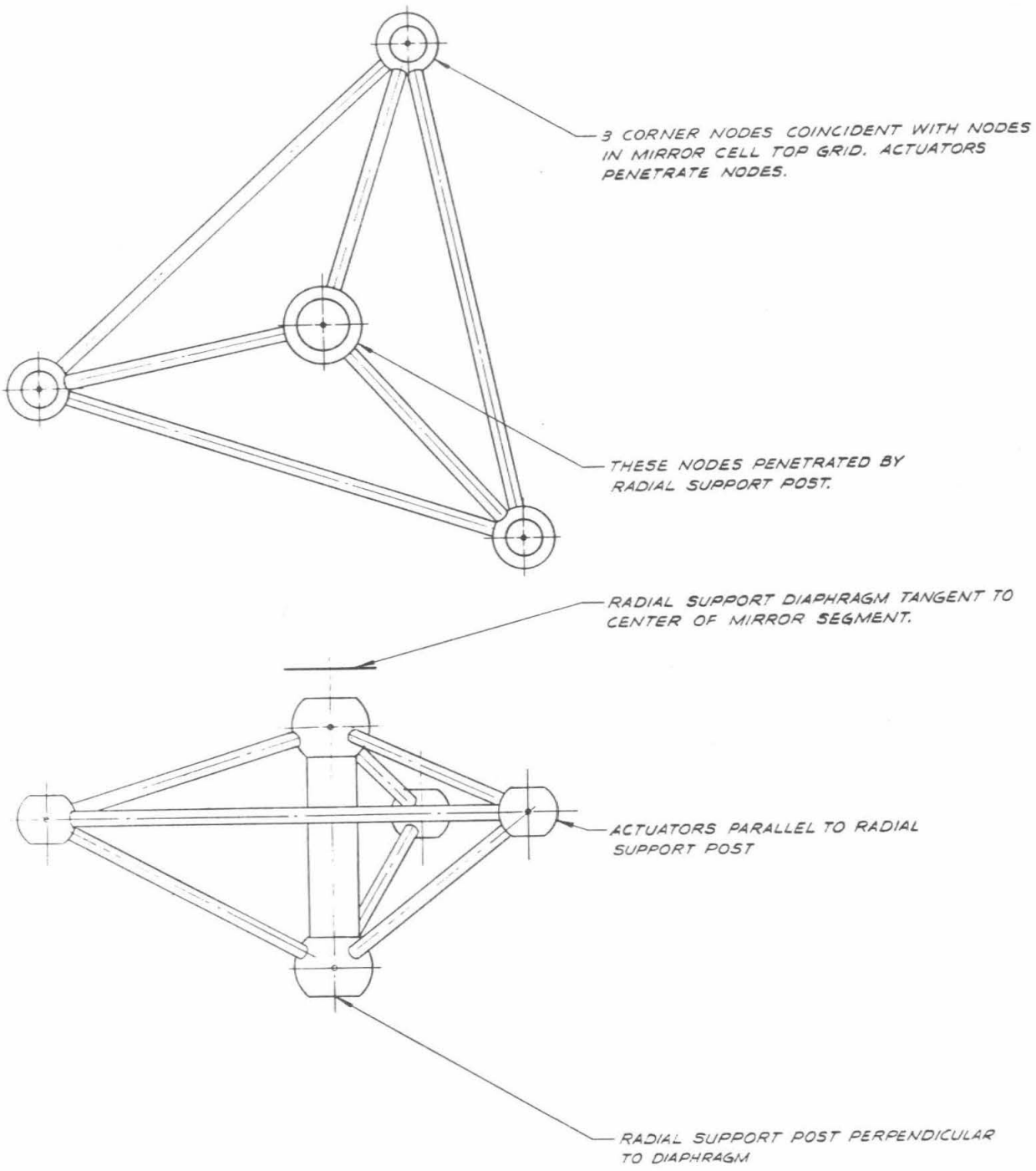

Figure 7-1 Typical Sub-Cell. Note that the actuator nodes and the radial support post nodes are all aligned normal to the tangent plane of the segment.

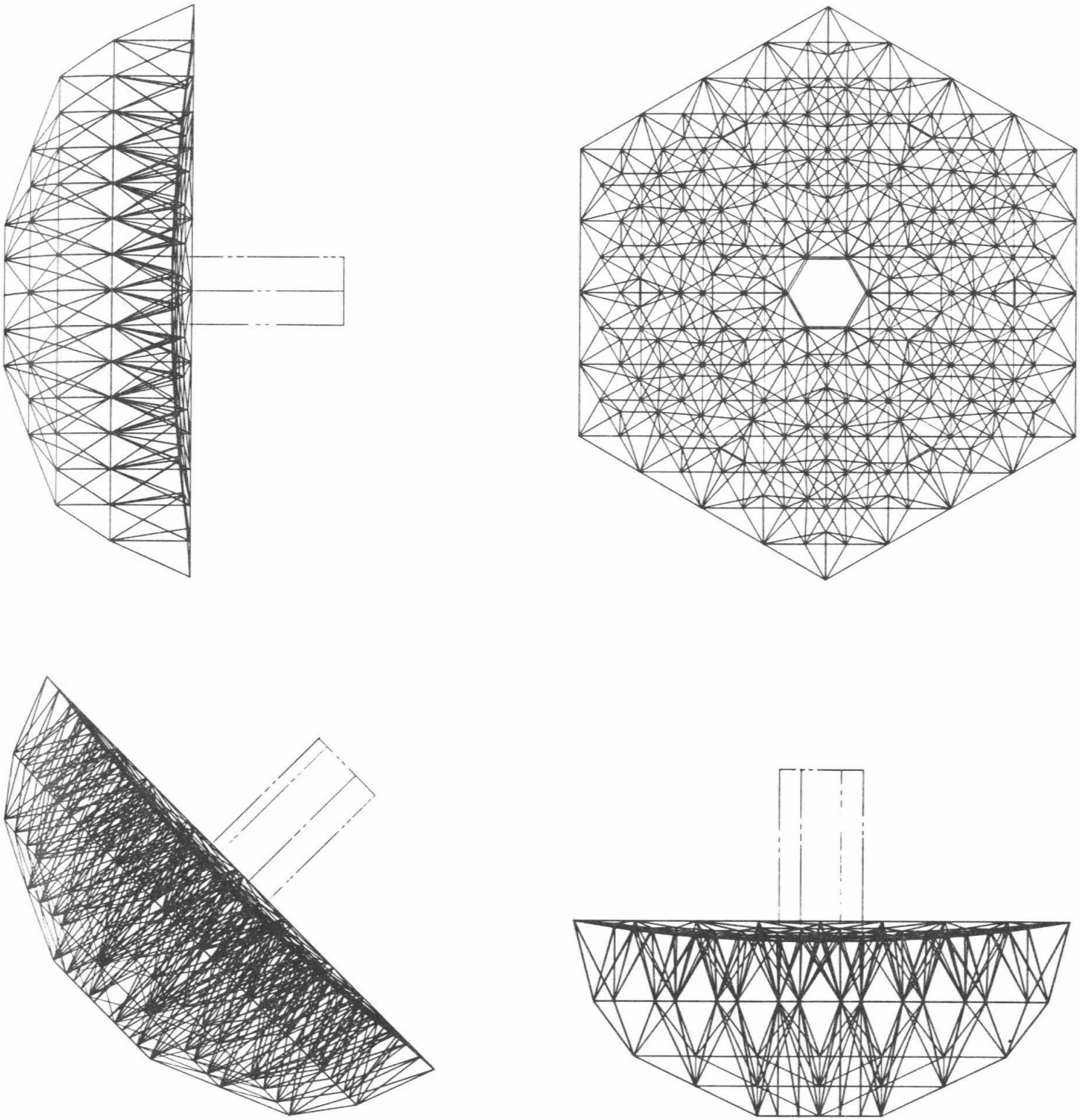

XBL 8411-4923

Figure 7-2 The primary mirror cell is shown in several projections to reveal some of its structure. It is a space from designed to hold the 36 segments quite stiffly. The tertiary support structure is indicated in outline.

surface to be used during servicing. The bottom layer is an equilateral triangular grid in projection. The layers are connected to each other by suitably located struts interconnecting the nodes. Plan views of the cell are shown in Figure 7-3. A detailed description of the cell design is in progress (Medwadowski, 1985).

The cell design will also accommodate a tubular tower extending above the cell in the center that will support instrumentation at the forward Cassegrain position or the tertiary flat that directs the beam to the Nasmyth and bent Cassegrain focal planes. This will be hexagonal in cross section, roughly the area of a segment and about 3m high. This is indicated in Figure 7-2. Near the rear of the cell, attachment for the Cassegrain module will be accommodated. These two instrument stations are not yet incorporated into the structural design.

Cell Dimensions and Performance

The mirror cell supports 14 tons of glass, roughly 6 tons of segment support and control system apparatus, and 4 tons of instruments (Cassegrain and Forward Cassegrain). The cell will be a welded steel structure with a weight of 5 tons. Near the center the cell depth is about 3.8m and near the edge the thickness tapers to about 2.9m. Under the expected thermal operating range of $3^{o}C \pm 12.5^{o}C$ the outermost segments will displace radially $\pm$ 0.7mm, within the optically allowed limits. Under the weight of the mirror etc., the cell, when supported at 12 solid points on its periphery, has a maximum deflection of 0.64mm, and is expected to have a lowest resonant frequency of roughly 20 Hz. When attached to the elevation ring the stiffness of the cell will be somewhat reduced due to the finite stiffness of the rest of the telescope. The weight of the tertiary and Cassegrain instruments will also degrade these performance figures somewhat and, as compensation, an increase in the cell stiffness (mass) is contemplated.

Attachment to the Elevation Ring

The cell is attached to the rest of the telescope structure by 18 struts that connect between the corners and midpoints of the edges of the cell and the elevation ring. This is shown in Figure 7-4. Since the elevation ring is slightly larger than the edge of the cell, these struts will form a slightly "conical" envelope. These struts have cross sectional areas that are adjusted to minimize gravitationally induced optical misalignment between the primary and secondary. This is discussed in the next section.

7.3 Telescope Tube and Elevation Ring

The telescope tube structure supports the top-end instruments for the telescope (prime focus cameras, secondary mirrors, etc.) and the mirror cell and transfers these loads to the elevation ring. The elevation ring in turn transfers the load of the telescope to the yoke through the elevation bearings.

Absolute rigidity and alignment of the optical elements cannot be maintained in a structure of this size. A solution allowing carefully matched motion of the primary and secondary optics under the influence of gravity was first developed by Serrurier for the 200-inch telescope. It maintained proper collimation of the optical system even though the absolute motions of each component were far in excess of the miscollimation tolerances. By using a structure consisting of isosceles triangles for the upper and lower tube (the Serrurier truss) parallel motion of both the top and bottom ends of the tube was achieved, and no miscollimation due to secondary tilt was introduced. By then adjusting the relative stiffness of the upper and lower tube one could achieve equal deflections and eliminate decenter errors due to gravitational forces perpendicular to the optical axis. Additional adjustment of the stiffness of the structure in the direction along the optical axis is also necessary in order to maintain adequate focus as the telescope tracks from the zenith to the horizon. This is commonly done by adjusting the stiffness of the secondary support spiders and by the addition of members parallel to the optical axis in the lower cell. These members can give substantial increase in the axial stiffness, but since they act only as bending elements for loads perpendicular to the optical axis, they provide little

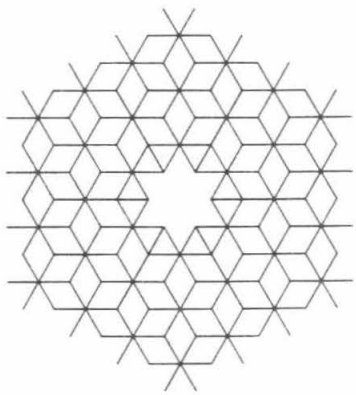

LOWER CONNECTIONS

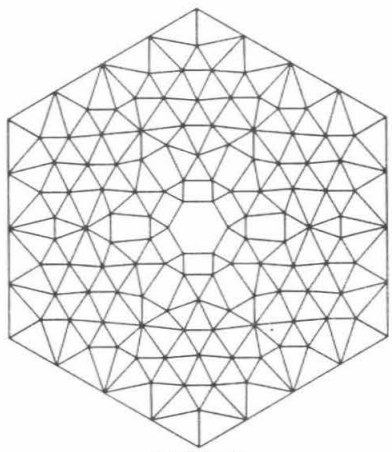

TOP GRID

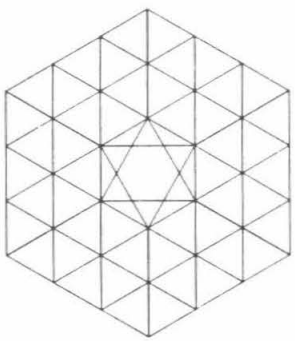

BOTTOM GRID

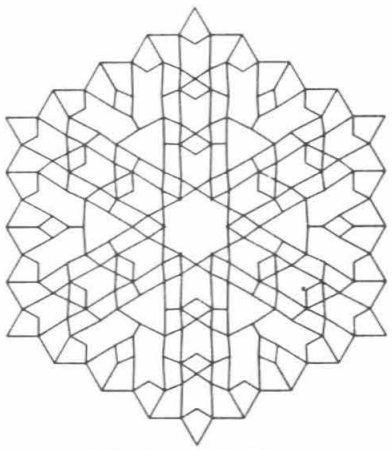

UPPER CONNECTIONS

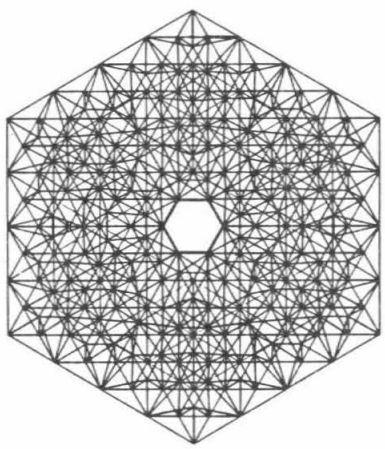

PLAN VIEW OF CELL

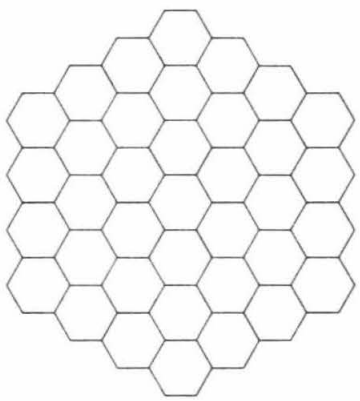

MID PLANE

XBL 8411-4927

Figure 7-3 Details of the primary mirror cell are shown. Each of the three layers is shown along with the two sets of diagonal struts that connect the three layers together.

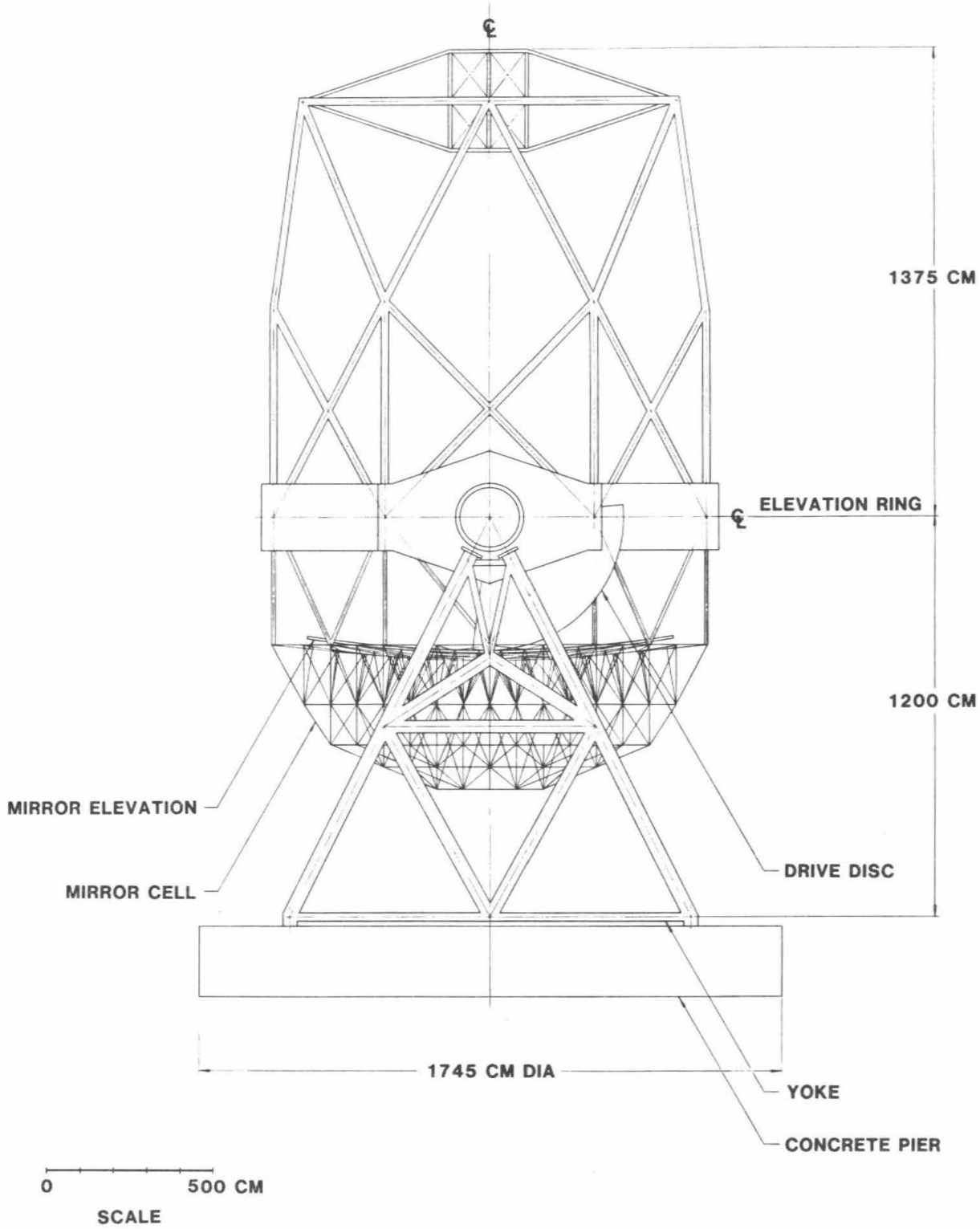

XBL 8411-4920

Figure 7-4a An elevation view of TMT structure is shown looking along the elevation axis. The Nasmyth platforms are not shown.

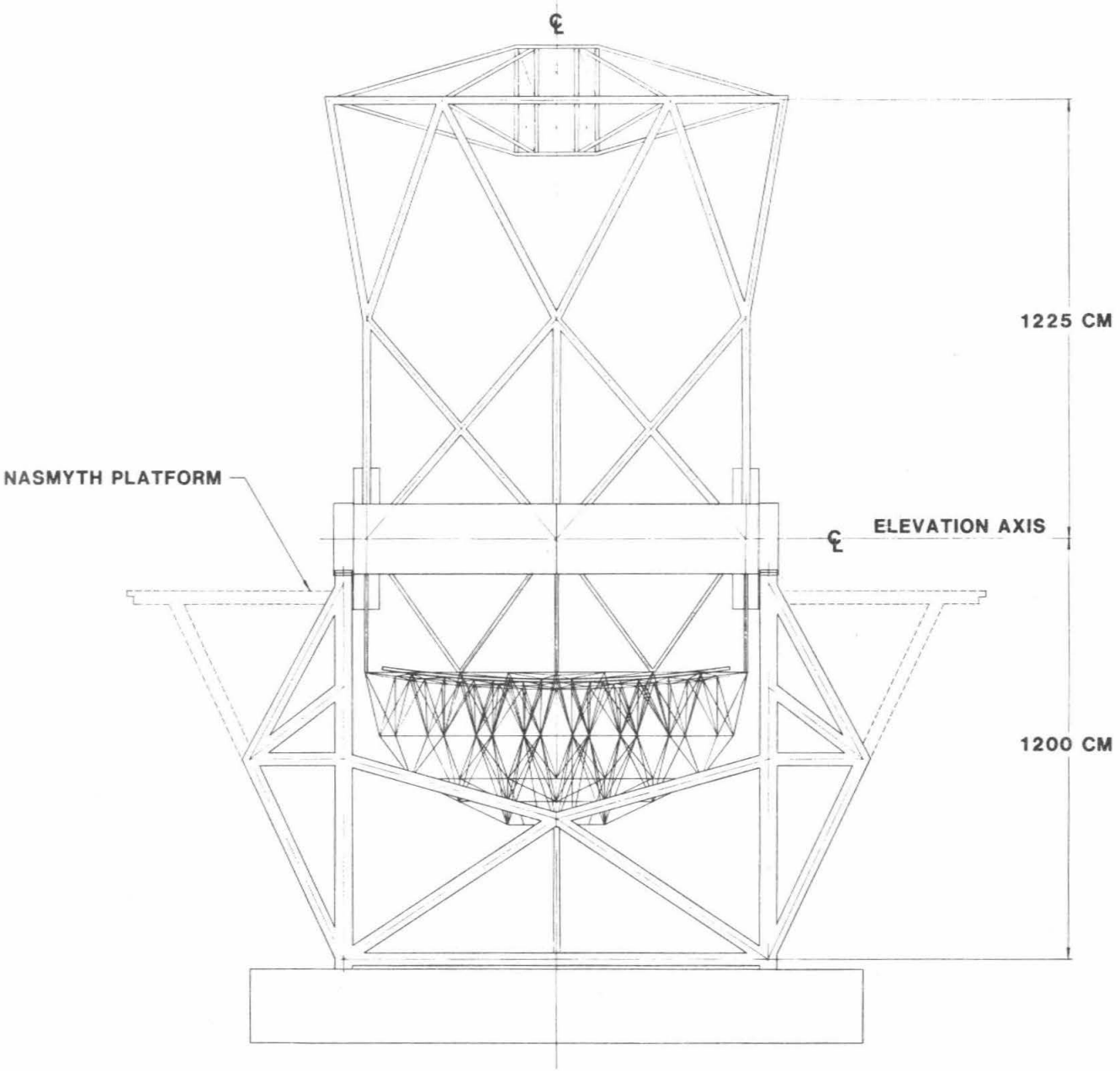

Figure 7-4b An elevation view of TMT structure is shown looking normal to the elevation axis. Here the Nasmyth platforms are shown.

change in the deflections in that direction.

Since the Ten Meter Telescope has an actively controlled primary, the requirements on the telescope structure to maintain primary-secondary collimation under the varying influence of gravity could be greatly relaxed. Nonetheless, we have elected to follow the more "conservative" approach, and attempt to design the tube so that proper alignment of the primary and secondary is maintained under the effects of gravity without any active intervention. As we will see, this has not led to any compromise in structural performance.

Upper Tube

The characteristics of a variety of tube designs were examined analytically, and a structure was developed by J. Lubliner (TMT Report No. 50). It has the basic characteristics of the Serrurier truss but, for the base to height ratio of this telescope (and most other optical telescopes), provides a noticeably stiffer structure for the same weight. Because of this obvious advantage, we have adopted this design configuration, as shown in Figure 7-4. The structure is a two-tiered one, with a set of nodes halfway between the elevation ring and the top ring. We note that a recent re-examination of the upper tube by Medwadowski has led to a new, more efficient geometry that is being considered.

The configuration of this telescope is somewhat unusual in that the primary is basically hexagonal in shape. This suggests that the most compact tube geometry should also be hexagonal, and that the elevation ring should be hexagonal as well. An additional peculiarity of this primary is seen in the diffraction pattern caused by the thin gaps between the segments (cracks) and the segment beveled edges. These 7mm wide non-reflecting strips cover 0.7% of the primary. The diffraction pattern is basically that of a six pointed star. In order to minimize any additional diffraction effects on the images, we have decided to orient the secondary support spiders so that their diffractive effects will have the same alignment as those caused by the segment cracks. The 25mm (1 inch) wide spiders obscure an additional 0.7% of the primary. A detailed discussion of the diffractive effects of segmentation is given by Mast *et al,* (1982, TMT Report No. 68).

The diffractive effects of the spiders and those of the segments will rotate relative to the star field since the mounting of the telescope is alt-azimuth rather than equatorial. This field rotation will occur at a variable rate, but a typical value is the earth's rotation rate of 15 degrees/hour. Thus for observations of several hours duration, the diffractive effects are blurred out substantially, and the choice of the orientation of the spiders may not be particularly important for these cases. If the orientation of the spiders were of no significance, one might elect to orient them perpendicular to the cracks. This would cause 12 clear diffraction spikes to be present instead of 6. The tube structure would be rather different in this case.

The proposed spider orientation has six spiders attached to a hexagonal upper ring that is rotated 30 degrees relative to the primary hexagon. Thus the upper ring is a hexagon that must circumscribe the primary hexagonal shape and is therefore larger by about 15% than its minimum size without the 30 degree rotation. In addition, this rotation gives a geometry where the two-tiered structure becomes desirable. Without the rotation, an upper tube with more resemblance to the Serrurier truss would be possible, with similar performance to the two tiered structure.

The design of the tube has been arranged to minimize the gravitational deflections resulting from the 2-ton instrument package or the deflections resulting from wind loads. With an upper tube weight (including the upper ring and spiders) of about 12 tons we find that the deflections due to gravity with the telescope pointing toward the horizon are about 1.7mm. The self-weight deflections of the upper tube (the deflections of the structure without the 2-ton instrument package) are about 1.3mm, which gives the lower bound for the deflection, independent of the actual amount of structural material assigned to the telescope tube. Of course, adding more steel to the structure will increase its stiffness under external loads such as wind loads. The upper tube described in TMT Report No. 59 has a specific stiffness of roughly 5tons/mm (the amount of external load that gives an additional deflection of 1mm), normal to

the optical axis.

Elevation Ring

The elevation ring should rigidly hold the upper and lower tube, and transfer the weight of the telescope through the elevation stub axles to the yoke. The design of the elevation ring is constrained by the hexagonal shape of the primary, the desire to allow large optical beams through it to the Nasmyth platforms, and the requirement that wind-induced deflections be held to a low level. Because of the primary shape, the most compact ring design is basically hexagonal in shape. The 1.8m hole in the elevation ring allows a 40 arcminute field of view at the f/15 Nasmyth foci.

Several geometries were analyzed, including a variety of space frame and plate designs. We found that the plate ring designs were noticeably stiffer for the same weight than were the space frame designs; consequently a welded plate elevation ring was chosen. The hexagonal ring was tapered around the elevation axis to accommodate the 1.8m hole for the Nasmyth platforms. Both the depth of the ring along the optical axis, and its thickness normal to the optical axis affect its stiffness. As one increases these dimensions the flexure of the ring under wind loads will decrease, but for a given ring weight, one must devote an increasing fraction of the material to stiffeners in order to avoid buckling of the plates. Hence, a compromise geometry was selected which had about a quarter of the steel used to stiffen the plates against buckling. This ring is tapered from 4m down to 2m along the optical axis and is 750mm wide. Figure 7-4 shows the elevation ring. The elevation ring transfers loads primarily in bending and in torsion and only to a minor extent in axial loads, whereas the rest of the telescope structure transfers in compression and tension only. The mass contributing to the structural stiffness of the elevation ring is about the same as the upper tube (12 tons). The total mass of the ring including stiffeners, drive sectors and elevation journals is 18 tons.

The contribution to the image motion (caused by wind forces) of the elevation ring is about the same as that of the upper tube. Hence, the ratio of the upper tube weight to elevation ring weight is nearly optimized: shifting material from one to the other will increase the wind-induced deflections.

Mirror Cover

The primary mirror cover is expected to be attached to the underside of the elevation ring. It will be composed of six articulated leaves and will weigh roughly one ton. Details of the design are currently being investigated.

Center of Mass

The telescope tube center of mass should be on the elevation axis. Since we have placed this axis 4m in front of the primary vertex to allow a parfocal optical design, it does not follow that the center of gravity will be located there. In fact, the thin segments and the lightweight cell allow the center of gravity to be quite close to the desired position, so that only modest structural modifications will be needed to satisfy this requirement. We may increase the weight of the upper tube to reduce wind-induced distortions. A corresponding increase in the cell may then be desirable both to balance the telescope and to further increase the stiffness of the cell to improve the performance of the active control system.

Lower Tube

The lower tube is not exposed to any appreciable wind loads, hence its important characteristics are defined by its response to gravitational loads. Roughly speaking, we wish to adjust the lower tube diagonal and axial member stiffnesses to equalize the upper and lower tube deflections under gravity. For force components normal to the optical axis and elevation axis, we wish to control the secondary mirror net decenter and tilt relative to the primary so as to minimize the induced aberrations, while at the same time minimizing image motions. This is discussed more fully in the next section. With gross deflections of about 1.7mm, we have

limited the net decenter to about 0.1mm, probably comparable to the uncertainties in the structural modeling. With the telescope pointed toward the zenith, the axial stiffness was adjusted to minimize the defocus. Both the secondary and the primary will move downwards about 1mm, and the stiffness of the axial members of the lower truss and the support spiders for the secondary can be adjusted to equalize these deflections. Since the axial range of the primary active control system exceeds $\pm$1mm, and the cell itself has a sag of 0.64mm, it is somewhat arbitrary how we define the axial deflection of the primary. It is convenient to choose the average of the deflections of the structural nodes under each segment. With this definition we balanced the deflections to within 0.05mm. If uncorrected, this defocus would give an image blur of 0.3 arcseconds. Since the amount of defocus is only a function of elevation angle, it can easily be mapped out and removed by use of a focus correction table. Far more serious in this regard is the effect of thermal change on the focus. A temperature change of the structure of only 0.25^{o}C will give the same 0.3 arcsecond image blur. Thermal effects are discussed in more detail in Section 7.9. The lower tube consists mainly of 3-inch pipe and its weight is 2 tons.

Secondary-Primary Motion

Because the upper and lower parts of the telescope tube do not consist of planar surfaces that are perpendicular to each other, the deflections are not strictly of parallelogram form. Hence under gravitational forces normal to the optical and elevation axes, some rotation of the top end occurs about a line parallel to the elevation axis. As we shall see, this rotation is rather small and is not a noticeable liability to this tube design. Of interest is the **net** rotation of the secondary relative to the optical axis defined by the displaced and rotated primary mirror and the **net** displacement of the secondary relative to the optical axis. Thus the rotation and displacement depend on the behavior of the upper and lower tubes. This rotation due to gravity has been calculated analytically (Lubliner, 1981, TMT Report No. 50) and also with SAP-4 (Medwadowski, 1981, TMT Report No. 59) with good agreement. The upper end rotates about 19 arcseconds due to gravity, and the net rotation of the secondary relative to the primary optical axis is reduced to about 17 arcseconds when rotation of the primary is included.

Decenter and tilt will cause two objectionable phenomena. First, there will be image motion, which must be compensated for by guiding or by use of a calibrated correction table. Second, miscollimation will cause optical aberration of the stellar images. Image motion from gravitationally induced decenter δy (see Section 5 for sign conventions, or TMT Technical Note 86) and from tilt $\delta\epsilon$ ($\delta\epsilon$ is positive for a clockwise rotation about the +x axis) is given by:

$$\delta\theta = 2\delta\epsilon\left(\frac{1+\Delta}{m+1}\right) + \frac{\delta y}{f_1}\left(1 - \frac{1}{m}\right) \tag{7-2}$$

Image aberration diameter (mainly coma) is given (Faber, 1981, TMT Report No. 55) by:

$$\delta\phi = \frac{3}{32}\left(\frac{m-1}{F}\right)^3\left[K_2 - \left(\frac{m+1}{m-1}\right)\right]\frac{\delta y}{D_1} - \frac{3}{16}\frac{(1+\Delta)(m-1)}{F^2}\delta\epsilon \tag{7-3}$$

where

f_1 = focal length of primary

f = final focal length

D_1 = nominal primary mirror diameter

F = nominal focal ratio

$m = \dfrac{f}{f_1}$

$$\Delta = \frac{e}{f_1} \qquad \text{(e is the back focal length)}$$

and

K_2 = conic constant of secondary.

The resulting image displacement and image blur as a function of decenter and tilt is shown in Figure 7-5. The circled dot shows the present design, and the black dots along the dashed line show the effect of tilting the primary ± 2 arcseconds ($\pm 50\mu$m at the edge of the primary). Also shown are curves of constant image blur and image motion. From the analysis and optimization of the preliminary TMT design by Medwadowski (1981, TMT Report 59) we expect that a net decenter of < 0.1mm and a net tilt of < 20 arcseconds will be achieved, which for the f/15 focus would yield an image motion of under 5 arcseconds and an image blur of under 0.05 arcseconds. Consequently, it is expected that passive alignment may suffice for the TMT. Since the primary is actively controlled, its tilt is readily adjusted over a range of ± 20 arcseconds. This allows the possibility of collimation using the primary.

7.4 Yoke

The telescope tube rests on hydrostatic bearings that define the elevation axis. The bearings are attached to the top of the yoke, with the elevation journals being attached to the elevation ring. The yoke carries the load of the telescope tube down to the pier by way of the azimuth hydrostatic pads that are attached to the yoke, and onto the azimuth journal, which is attached to the top of the pier. The motion drives are also attached to the yoke and, with frictional force, control all motions of the telescope. Figure 7-6 shows the yoke.

In addition to carrying the telescope tube, the yoke must be adequately stiff to resist wind loads on the telescope, and should have a relatively high resonant frequency in order to minimize any adverse coupling with the telescope drive servomechanisms while at the same time allowing for them maximum bandwidth. The Nasmyth platforms are also supported by the yoke. Each platform has a planned load capacity of 10 tons. The telescope will also have the capability of a Coudé focus, and this light beam must be able to traverse the yoke without obstruction. This beam will be reflected from the tertiary mirror to the Nasmyth platform, and then be reflected vertically downwards toward the #5 mirror on the base of the yoke, which in turn directs the beam to the #6 mirror positioned on the azimuth axis. This mirror sends the beam vertically downwards to the stationary #7 mirror which sends the beam horizontally to the Coudé room. The arrangement is shown in Figure 7-7.

Space frame designs were considered to be most advantageous for the yoke. To provide the greatest stiffness and stability, it was decided to make the azimuth journal quite large, approximately 17m in diameter. This design occupies more floor space than those where the yoke joins a small pedestal, and thus requires a much larger bearing surface, but the added stability and stiffness were viewed as more important than compactness.

The mass of the yoke is determined both by the requirements for stiffness against wind loads and for a high natural resonant frequency. Since the telescope tube weighs 70 tons, the resonant frequencies of the entire assembly will rise rapidly with the yoke mass until the yoke mass is roughly that of the telescope tube itself. This follows from the arguments given in Section 7.1. Since the stiffness requirements against wind loads are for fixed wind forces that have little to do with the mass of the telescope or yoke, no simple scaling law suggests what the needed mass will be. The more massive the yoke, the smaller will be the wind-induced pointing errors due to the yoke.

The present yoke design was developed by Medwadowski (TMT Report 72) and is based on previous yoke studies (Medwadowski, TMT Report 59, 71). The design has been optimized by minimizing the wind-induced pointing errors allowed by the yoke for a given yoke mass. Having optimized the space frame topology and the mass distribution, one can then achieve the

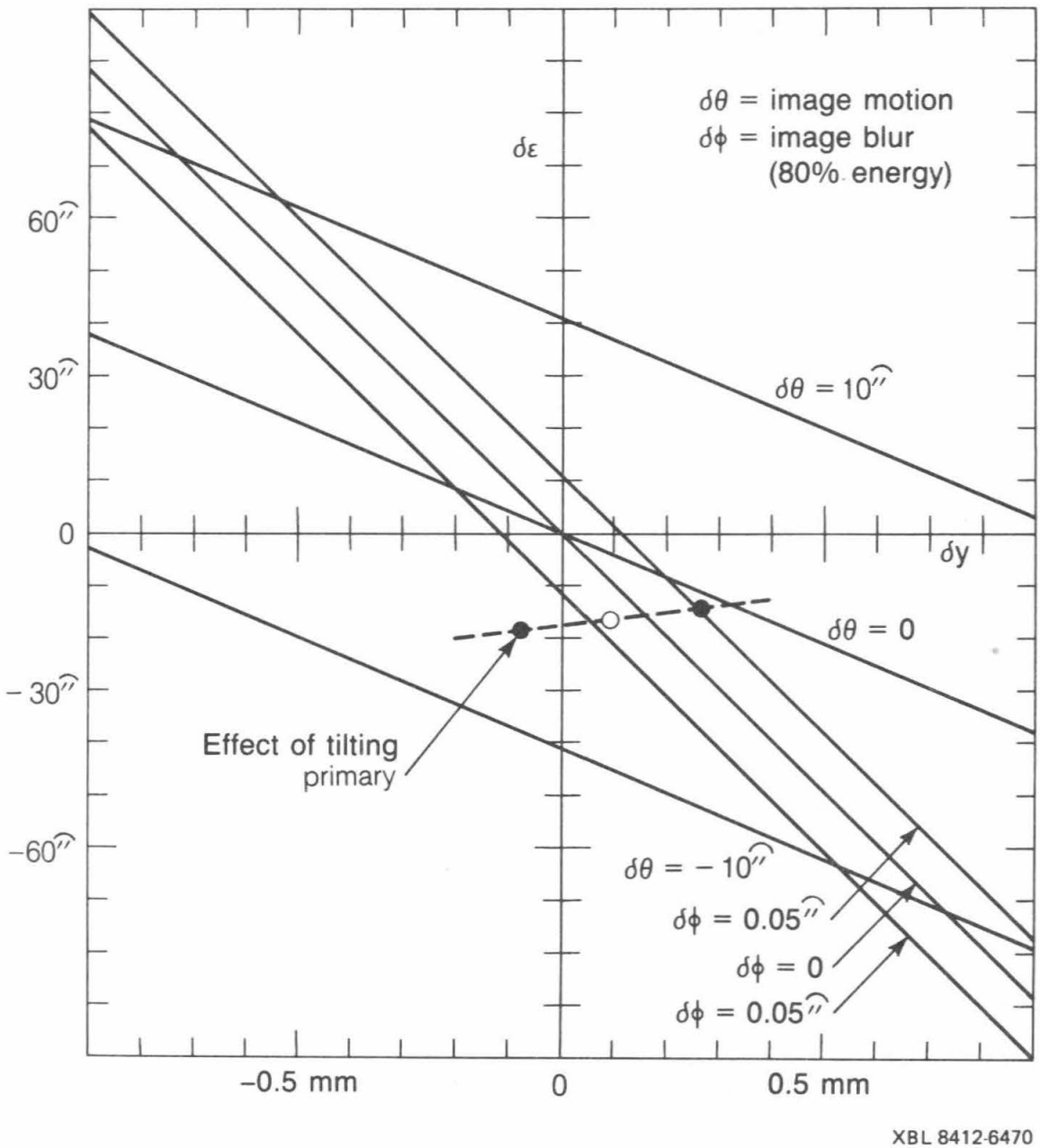

XBL 8412-6470

Figure 7-5 The effects of secondary mirror decenter and tilt on the image quality and on image displacement can be found from this graph. The circled dot shows the present design, and the black dots along the dashed line show the effect of tilting the primary ±2 arcseconds (±50μm at the edge of the primary). Note that for any given tilt, there is a displacement that will make the image blur vanish, hence perfect alignment is not needed.

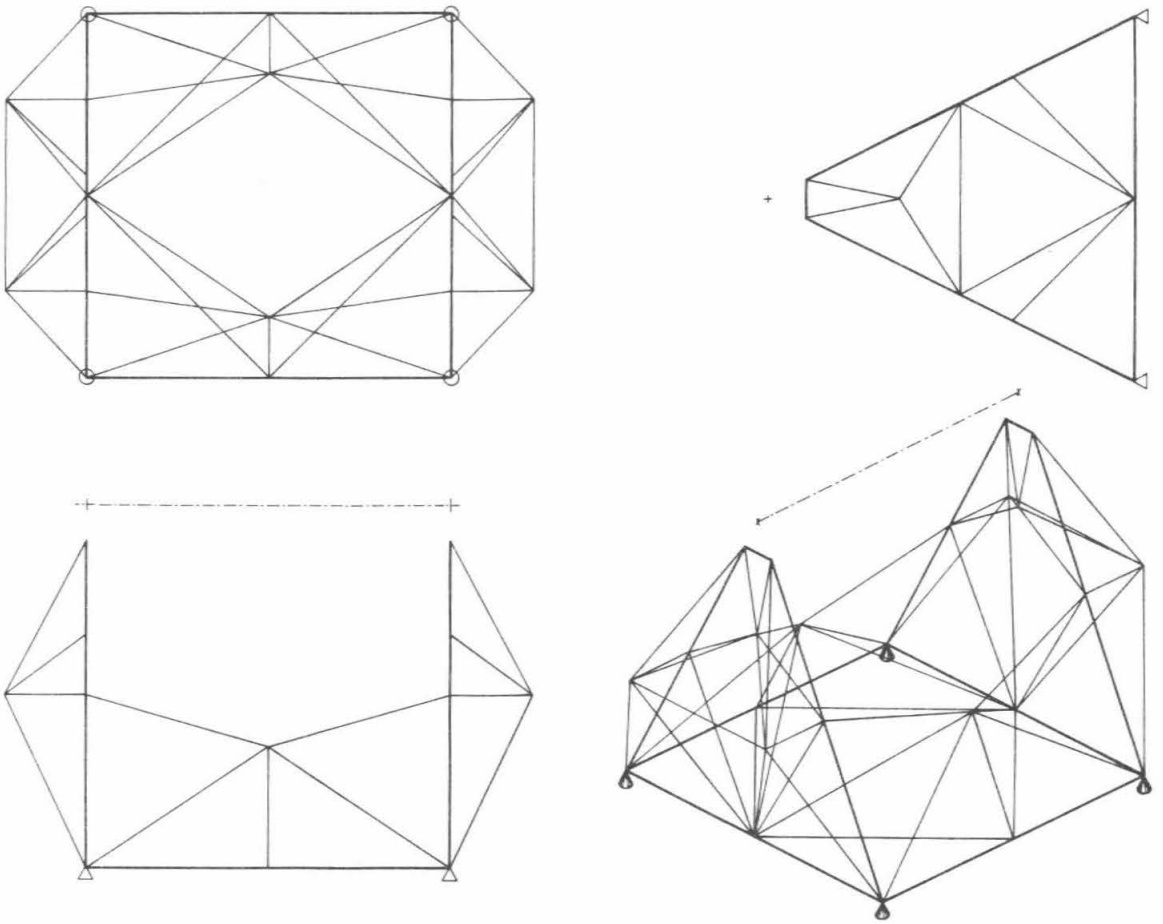

Figure 7-6 The structure of the TMT yoke is shown to indicate the connections of the space frame. Note the large open region along the azimuth axis.

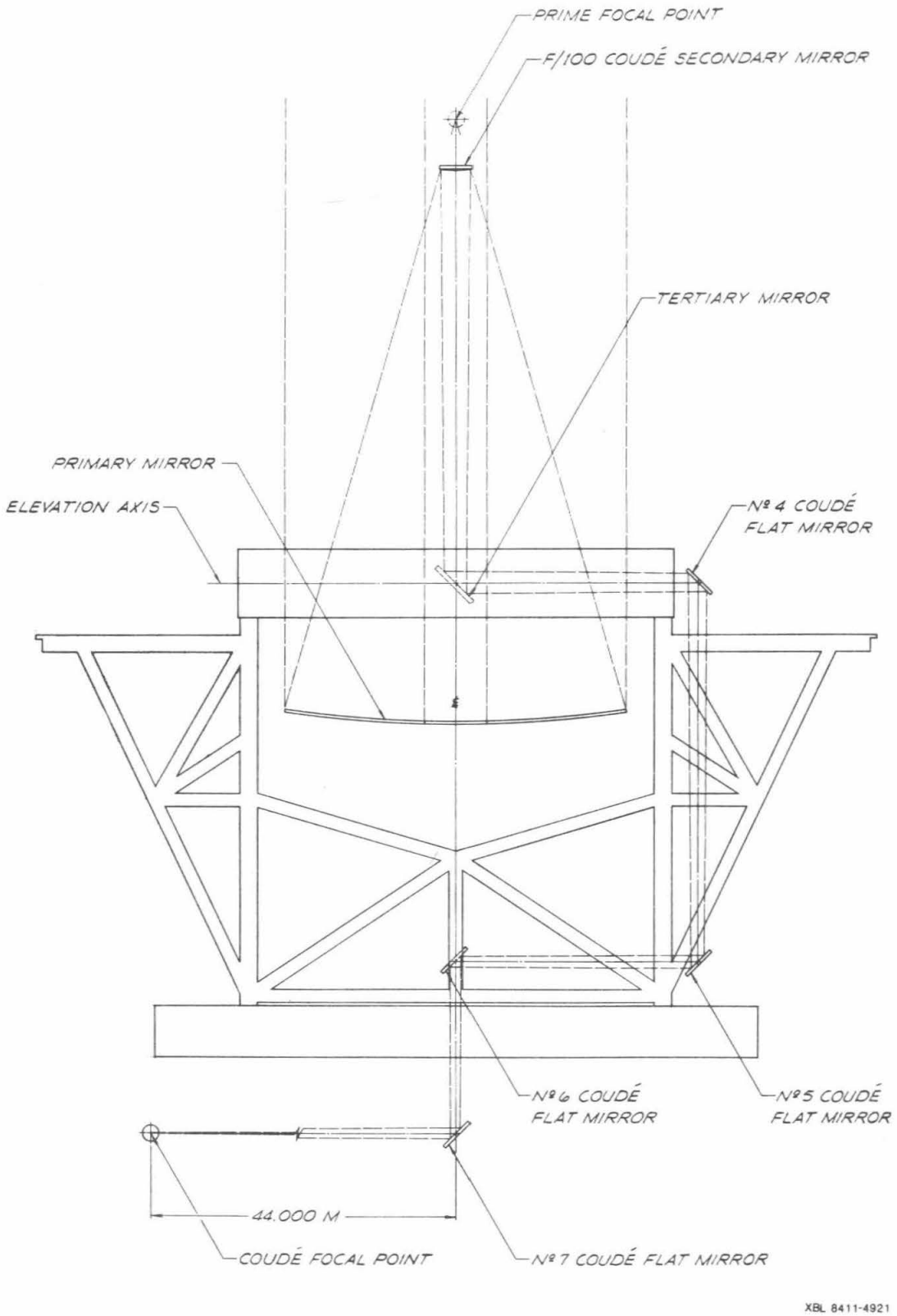

Figure 7-7 The optical train of mirrors for the coudé focus in indicated showing schematically how the beam passes through the TMT yoke and into the coudé room.

desired stiffness by scaling up the mass of the yoke. Six wind cases were studied, for three directions of wind with the telescope pointing to the zenith, and for three directions of wind with the telescope pointing to the horizon. The largest pointing errors occur with winds perpendicular to the elevation and optical axes and with the telescope pointing to the zenith. As designed, with a wind force at the top of the telescope of 50kgf, the yoke will contribute 0.07 arcseconds to the image motion. More details of the structural response are given in Section 7.8. The mass of the yoke totals 90 tons (78 tons of structure and 12 tons for the Nasmyth platforms and their support structure).

The geometry of the yoke is arranged so that there are no structural elements located near its center. This is done to provide open space in the interior of the yoke to allow for access to Cassegrain instruments or for other needs. At first thought a central bearing may seem necessary to maintain centering, but the design of the drive system is such that each of the four feet of the yoke is independently driven, and is quite stiffly defined tangentially to the azimuth bearing ring. This tangential definition serves to hold the yoke effectively centered on the azimuth bearing.

7.5 Pier

The pier is designed to provide a stable base for the telescope. It provides a relatively rigid and broad coupling to the earth as well as providing inertial mass for the telescope to act against during momentary telescope accelerations. The azimuth journal will be attached to the top of the pier, and a central hole in the pier will accommodate the Coudé optics and light beam. Since seeing studies have indicated that the telescope can be placed close to the ground, the pier need not elevate the telescope substantially above ground level. Soil studies and analysis of foundation tilts suggests that sinking the pier deeply into the earth will have no particular value unless it were to be sunk tens of meters into the ground. Thus a relatively shallow and solid pier is contemplated. Further soil studies will be made before a final pier design is made.

The pier has not yet been designed, so its parameters are not known, but it is likely that it will be a solid, reinforced concrete cylinder (density $\rho = 2.5\times10^3 \text{kg/m}^3$) with a radius of approximately 9 meters and a depth $h = 1.5$ meters giving a total mass of about 1000 tons. Including all instrumentation, the TMT should not exceed a maximum weight of about 180 tons, so such a pier has a mass of about five times the telescope mass. The moment of inertia, I, of this pier is 19,300 m^2-ton, about three times the telescope moment of inertia of 6000 m^2-ton.

The extremely broad footing of this pier gives it outstanding stiffness against external torques in spite of the rather low elastic modulus of the volcanic soil, and also gives it a rather high natural frequency of rotation (tilt). The soil under the pier is expected to have a subgrade modulus $K = 5.5\times10^7 \text{N/m}^3$ (200 pci) according to Mauna Kea soil studies (TMT Technical Note 110). Assuming the pier is rigid, rotation of the pier by an angle e in this soil will require a torque τ given by

$$eR = \tau \tag{7-4}$$

where for a rigid disk of radius a, $R = \pi K a^4/4 = 2.83\times10^{11}\text{N}-\text{m}$. Under wind forces at the top of the telescope (25m high) of 50kgf (external wind of 14m/s), a torque of roughly 1.23×10^4N-m will be applied, producing a tilt of the pier of $e = 0.009$ arcseconds. The resonant frequency of the pier tilting in the soil is given by

$$2\pi f = w = \left(\frac{R}{I}\right)^{1/2} = \left(\frac{K}{\rho}h\right) \tag{7-5}$$

For the values given above, $f \approx 19$Hz.

7.6 Bearings

Hydrostatic bearings have been selected for both elevation and azimuth axes. These provide excellent smoothness, high load carrying capacity, very low friction, high stiffness, low maintenance costs, and relatively low installed cost. They are widely and successfully used on many large telescopes. Since we selected a large base for the yoke, roller bearings were not feasible for the azimuth bearings. Although roller bearings may be adequate for the elevation bearings, the additional cost of hydrostatic bearings here appears small, and hence they have been tentatively selected because of their superior performance.

A detailed description of the design and performance of the bearings is given by Osborne (1984, TMT Report No. 93). The basic parameters are currently undergoing revision, and those given here are only representative of the final parameters. Figure 7-8 shows schematically the location of the bearings. Eight elevation bearing pads located on the top of the yoke support the telescope tube. The elevation ring has a pair of 2m diameter stub axles that carry the weight of the telescope and transfer it to these eight pads. Four additional bearing pads located at the bottom four corners of the yoke transfer the gravitational load of the entire telescope assembly to the flat azimuth bearing journal that is mounted on top of the pier of the telescope.

Bearing pad parameters were selected to give the necessary performance and to conform to conventional bearing design and experience with such bearings at large telescopes. Oil bearings have extremely low frictional coefficients, and even at our maximum slew speeds the effective frictional drag coefficient is only 1×10^{-4}, roughly ten times lower than one might obtain with roller bearings.

We will use a single oil pump station with an oil supply pressure (liftoff pressure) of $6.9\times10^{6}N/m^{2}$ (1000psi). By using flow restrictor valves for each pad, all pads can operate successfully from the single pumping station. When the pads have lifted, they will operate with a pressure drop of $4.83\times10^{6}N/m^{2}$ (700 psi).

The elevation pads are spherical to match the 1m radius of curvature of the elevation axis journals. These eight pads must support the 70 ton weight of the telescope. With the above pressures and loads, the elevation pads require an inside diameter of 133mm and an outside diameter of 186mm, and can work with an oil thickness of 0.1mm. The flow per pad is then $1.26\times10^{-5}m^{3}/s$, and the heat dissipated is 60W.

The azimuth pads are flat, and operate at the same pressure. These four pads must carry the weight of the telescope, yoke, and Nasmyth instruments, for a maximum total of 180 tons. The pads require an inside diameter of 284mm and an outside diameter of 402mm. Because the maximum azimuth slew rate will be rather large, 0.4m/s, the film thickness must be increased to 0.15mm to avoid the pads overtaking the outflowing oil. The flow rate varies as the cube of the film thickness, hence this increased film thickness leads to greater oil flow rate and larger heat dissipation. The flow per pad is $4.09\times10^{-5}m^{3}/s$, and the heat dissipated is 198W.

The total system flow rate will be $2.64\times10^{-4}m^{3}/s$ (4.2 gallons/min). The total heat dissipation will be 1276W. To reduce the adverse effects of this heat loss, we plan to precool the oil. Cooling the oil by $3.6^{o}C$ will cancel this heat loss so the oil exits the pads at the ambient temperature.

Proper alignment of the bearing pads with the journals is critical to the operation of hydrostatic bearings, consequently all bearings will have self alignment features. In addition, the yoke may spread under varying Nasmyth platform loads. To accommodate this motion we are considering additional bearings that can slide along the elevation axis.

In practice the journals, particularly the azimuth journal, may not be perfectly shaped. The azimuth pads have substantial vertical flexibility due to innate vertical flexibility in the yoke structure, so height differences between the four pads due to non-flatness of the azimuth journal could be several millimeters without appreciably affecting the azimuth bearings.

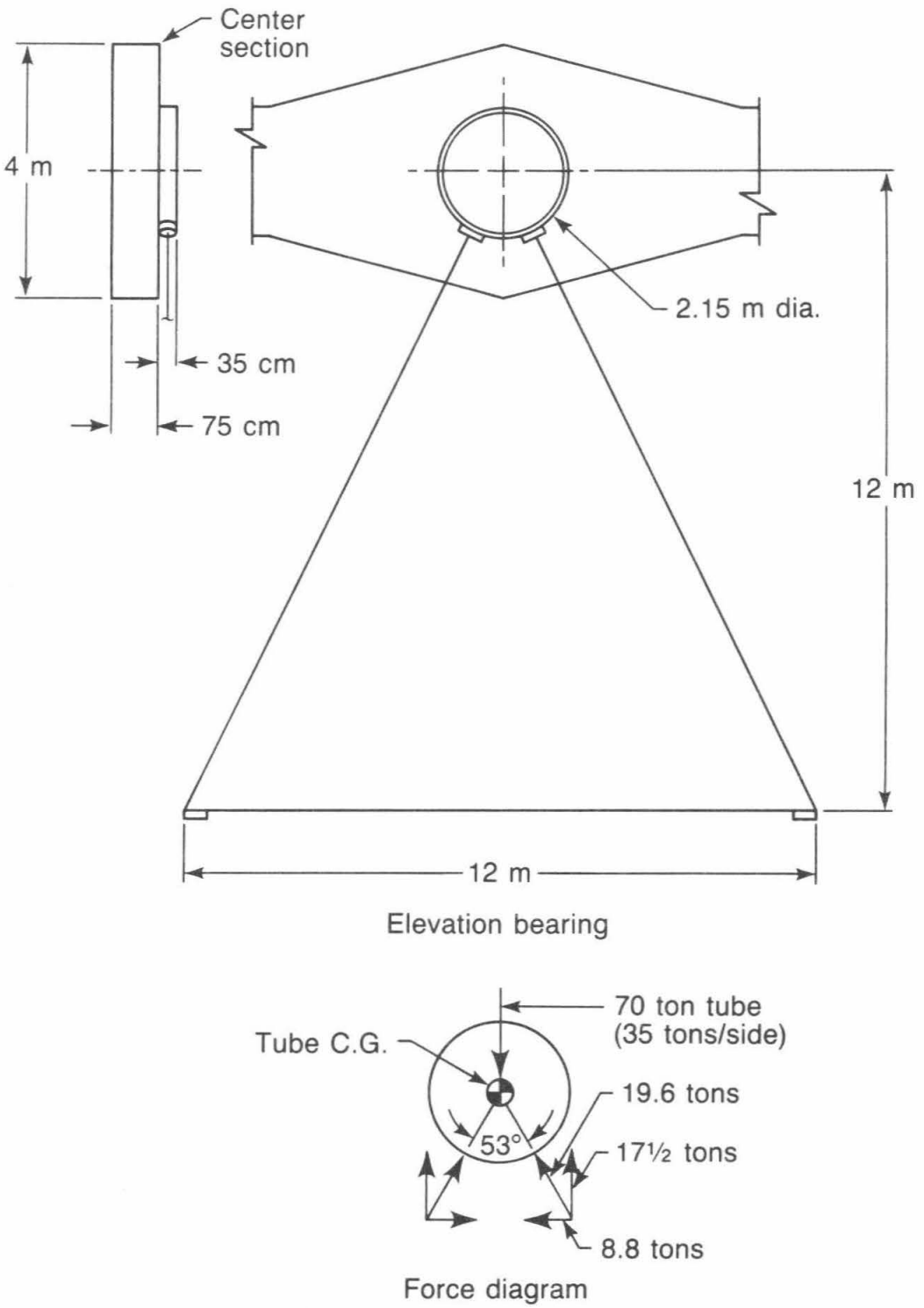

Figure 7-8 A schematic showing the locations of the elevation axis bearings.

7.7 Drives and Encoders

Friction drives will be used for both axes of the telescope. They exhibit superior smoothness compared to gear-driven drive systems, and do so without the expense of large gears. By using relatively small drive rollers, the drive motors can directly drive the shaft, without the necessity of any gear reduction. The drive system is described by Osborne (1982, TMT Report No. 93).

Since friction drives use contact friction to transmit the necessary drive power and torque between the driving and driven element, the cylindrical elements must be pressed together with sufficient force to avoid any slippage under normal operation. This preload is applied by use of springs for both axes. The contact (Hertzian) stresses between the rollers represent a key issue in the design of the friction drives. One must keep this stress at an acceptably low level to avoid damaging the rollers while maintaining sufficient frictional force. The maximum contact stress s between two cylinders of the same material, with Poisson ratio of 0.3, is given by

$$s = 0.418 \left(\frac{PE(\frac{1}{r_1} + \frac{1}{r_2})}{L} \right)^{1/2}$$

where P is the contact load, E is the material elastic modulus, r_1 and r_2 are the radii of curvature, and L is the length of the contacting cylinders. As a result, a large drive reduction (the ratio of the curvatures) will lead to a small drive shaft and high contact stresses.

The elevation drive consists of 4m radius drive sector disks mounted to opposite sides of the elevation ring, each driven by a drive roller 150mm in diameter and 50mm long to produce a drive reduction of 53. This is shown in Figure 7-9b. Assuming a steel-to-steel coefficient of friction of 0.15 and a contact force of 1.27×10^4N per sector, the maximum elevation axis drive torque is 1.52×10^4N-m. The maximum contact stress is 3.47×10^8N/m^2 (50,000 psi). The torque motor is in line with the drive shaft as shown in Figure 7-10.

The azimuth drive consists of a 150mm diameter, 50mm long drive roller mounted at each corner of the yoke and pressed against the inside vertical edge of the 17m diameter azimuth journal as shown in Figure 7-9a. The drive reduction is 113. With a preload of 1.27×10^4N, the maximum azimuth axis torque is 6.48×10^4N-m. The maximum contact stress is 3.46×10^8N/m^2(50,000psi).

One of the key characteristics of the azimuthal drive system is that each of the four drive motors will be independently controlled by its own local position or velocity encoder. These controls must have a high frequency bandwidth (well above 5Hz) since the stiffness of the yoke and telescope assembly is critically dependent upon the four corners of the yoke being stiff azimuthally. It is this local azimuthal stiffness that maintains the centering and squareness of the yoke against high frequency perturbations. On thermal time scales the spacing of these four drives may change, which will generate large error signals in the drives. To prevent this, the azimuthal drives will be filtered so they are independently controlled only for frequencies above, say, 10^{-2}Hz. For lower frequencies, the average of the four encoders will establish the drive control and pointing.

The drive rollers and drive systems must not slip against wind loads on the telescope. The design wind load is 50kgf at the top of the telescope, yielding a torque about the elevation or azimuth axis of 5.9×10^3N-m. The slipping torque for the elevation axis drive is about 2.5 times this torque and about 11 times this for the azimuth axis. In light of our uncertainty about wind forces it may be prudent to modify the design parameters to increase the safety margin between slipping torque and the expected wind induced torque, particularly for the elevation axis. In addition, a safety brake may be included.

The slewing requirements for the telescope require that the elevation axis motors apply a maximum torque of at least 10^3N-m and a shaft speed of at least 7RPM, and that the azimuth drive motors apply a maximum torque of at least 10^4N-m and a shaft speed of at least 60RPM.

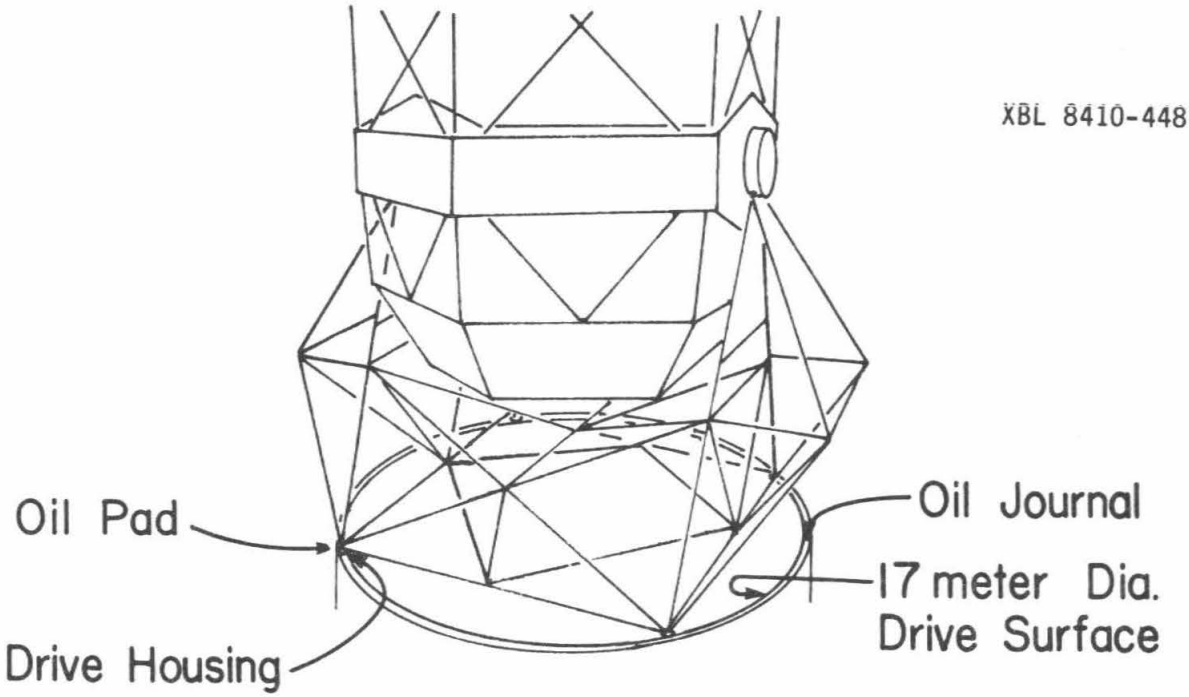

Figure 7-9a A schematic indicating the locations of the 4 azimuth friction drives on the TMT yoke.

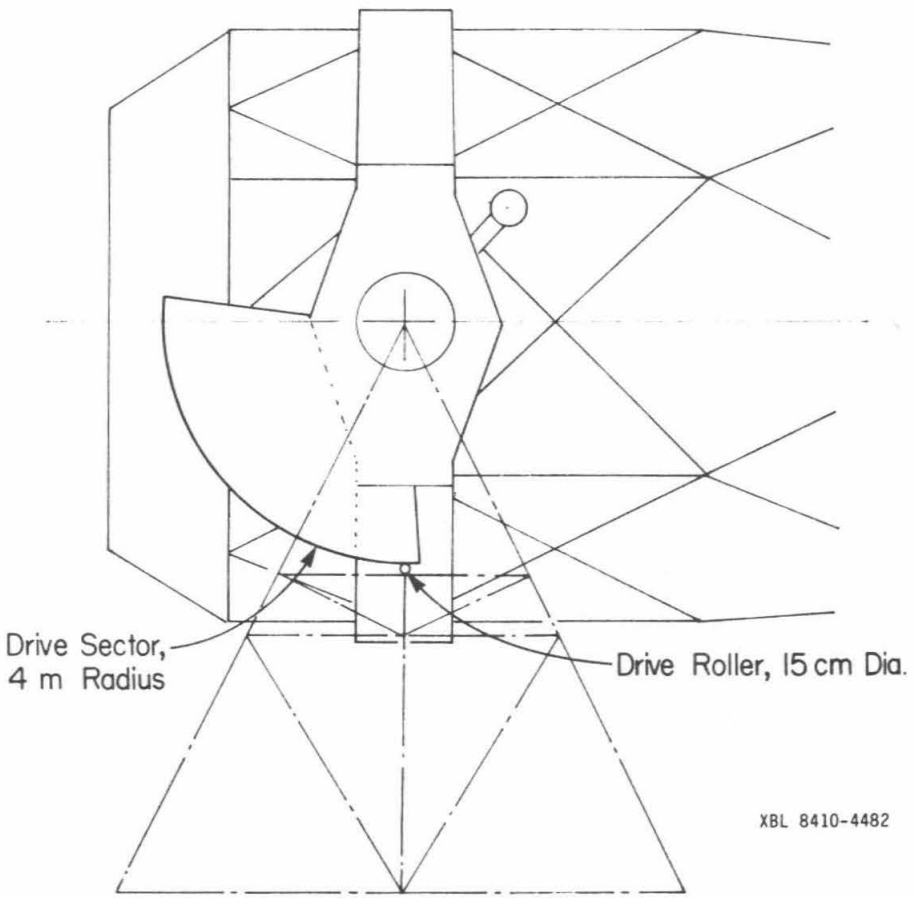

Figure 7-9b A schematic showing the location of the two elevation axis friction drives.

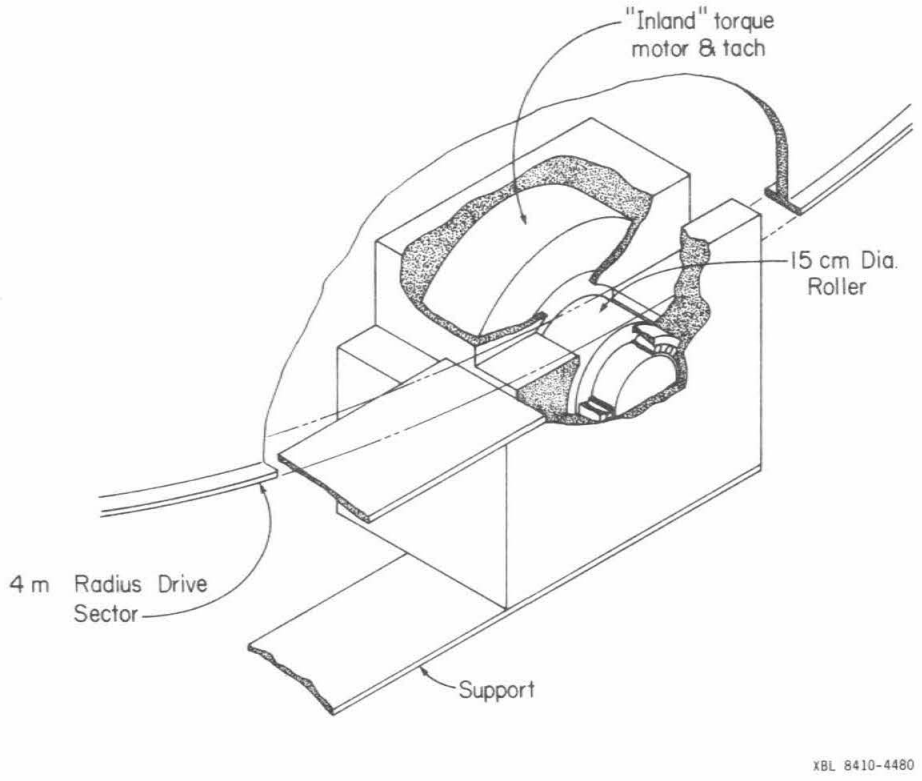

Figure 7-10 A schematic showing the details of the elevation axis friction drive system. Note the drive motor is in line with the friction drive shaft.

Encoding for both axes will be by use of absolute tape encoders located near the surface that the friction drive shafts press against. Encoder strips with a resolution of $\leq 1\mu$m are available in lengths suitable for the elevation and azimuth axes. The elevation encoder will have a resolution of ≤ 0.052 arcseconds with this encoder. The azimuth axis will have a resolution of ≤ 0.024 arcseconds. Since there are two elevation axis encoders and four azimuth encoders, the final resolution can be somewhat improved. These encoders will not have perfect linearity, but this can be removed by suitable lookup tables to allow us to achieve our absolute pointing and offsetting requirements.

The most extreme tracking requirements for the TMT involve visual speckle imaging where short term stability suitable for diffraction limited imaging is needed. Since the atmospheric wavefront errors change on a timescale of 0.01 seconds, it is likely that the inertia and relatively low resonant frequency (5Hz) of the telescope will allow sufficient stability without a special encoding system. For this time period, image motion needs to be under 0.01 arcseconds.

7.8 Static and Dynamic Response

Adequate stiffness against external loads such as wind is essential for the TMT. Structural resonances should have as high a frequency as possible to allow the maximum bandwidth for the primary mirror active control system, and for the telescope drive control system. We do not yet have an adequate model of the external perturbations or the response of the telescope and its active control systems to the perturbations. Some insight can be gained however by noting the static response of the structure and examining structural resonances.

External winds in excess of 14m/s are expected 5% of the time. Under these conditions wind loads at the top of the telescope are expected to reach 490N (50kgf) normal to the optical axis (Nelson, 1981 TMT Report No.47). Under this load, telescope deformations will lead to pointing errors. Analysis of the present design (Medwadowski, TMT Reports No. 59, 71, 72, Osborne, 1982 TMT Report No. 93) indicates the worst deformations occur while pointing to the zenith, with wind loads normal to the elevation and optical axes. With the simplifying assumption that the wind loads are static, net image motion is 0.34 arcseconds, arising from

Telescope	0.177
Elevation Drive Sectors	0.080
Yoke	0.073
Pier	0.010
Total	0.340

Wind forces acting directly on the primary may objectionably distort the primary. Under the 20-ton weight of the segments and segment support system, the cell has a maximum deflection of 0.64mm. The range of cell deflections under the segments will be substantially less, approximately 0.3mm. Axial wind forces of $1.6N/m^2$ corresponding to 2.0m/s (4.5 mph) wind speeds may be experienced at the primary under the previously stated external wind conditions. These will introduce peak deflections of roughly 200nm. Deflections and segment tilts caused by this uniform axial force will introduce an image blur diameter of 0.07 arcseconds. Non-uniform forces on the primary should result in smaller deflections since the cell behaves more stiffly under higher spatial frequency perturbations.

The lowest resonant frequency of the cell (when rigidly supported) is expected to be about 20Hz. The telescope yoke assembly has noticeably lower resonances starting at about 5Hz. The low frequency modes do not involve appreciable distortion of the mirror cell, hence we expect the coupling between the primary active control system and these low frequency modes to be small.

The top end socket is attached to the upper telescope tube by thin radial prestressed members (spiders). Because the members are radial, rotations about the optical axis are resisted only by the pretensioning of the members. We expect a torsional resonant frequency for the socket and module of about 4Hz (Medwadowski, 1981 TMT Report No. 59). We anticipate only very weak coupling of this mode to the rest of the structure.

7.9 Thermal Response

There are three major temperature-dependent phenomena that can affect telescope performance. Temperature variations within the telescope structure can affect the pointing accuracy of the telescope. Temperature changes with time can potentially affect the focus of the telescope as well as the primary mirror support and active control system. Finally, temperature differences between the telescope and the ambient air can cause locally induced degradation of the seeing.

The effects of temperature variations within the structure can be characterized by a few examples. The top end of the telescope is relatively exposed to wind and sky radiation variations. If a lateral temperature gradient develops across the top end of the telescope producing a

maximum difference of 1^{o}C (a probable maximum based on thermal modeling of the dome), the top-end instrument will decenter by about 15μm, assuming a steel structure. This produces pointing errors of about 0.2 arcseconds. Since these are slowly varying, they are well within allowable errors. A more important case involves a lateral gradient across the entire telescope tube rather than just the top end. Assuming the yoke is isothermal, a total difference of 1^{o}C will tilt the primary about 1 arcsecond, and the secondary by about 3 arcseconds. The net effect of tilting the primary and tilting and decentering the secondary is a pointing error of about 3 arcseconds. If the yoke is subject to the same gradient as the telescope, the net pointing error is reduced (by chance) to below 1 arcsecond. To maintain absolute pointing errors below 1.0 arcsecond, we must ensure that systematic large scale temperature gradients are below 0.3^{o}C.

Changes in the absolute temperature will change the length of the telescope and defocus the image to a blur diameter of about 1.4 arcseconds/^{o}C. This large effect will be corrected by manual or automatic refocusing (using a star), or by use of temperature sensors and a lookup table. Expansion of the primary mirror cell can also degrade performance if the sensors are misaligned. Lookup tables will correct these effects. Details are given in Section 8.5 and 8.15.

If the telescope is hotter or colder than the ambient air by ΔT, thermal turbulence will be generated. Seeing degradation will occur when these bubbles of hot or cold air enter the optical path. The quantitative relationship between seeing and ΔT is complex, and depends upon the details of the telescope geometry and orientation, and the character of air currents set by the outside winds and the dome shape. Nonetheless, it is commonly agreed that seeing is noticeably degraded if $\Delta T > 1^{o}$C (Murdin and Bingham, 1975, Gillingham, 1978, Beckers, 1981). Woolf (1979) has developed a model that indicates seeing is degraded 0.5 arcseconds/^{o}C.

A detailed numerical thermal model of the telescope and dome has been made by Carroll and Conners (1984, TMT Report No.134) and some of the modeling results are given in Section 9.3.1. At night we expect to generally keep the telescope within 0.25^{o}C of the ambient air temperature.

7.10 Instrument Changing System

Rapid, reproducible, and safe instrument changes are key performance goals for the TMT. To achieve this we have adopted the view that instruments shall be in identical interchangeable modules. The modules will have identical weight and center of gravity to maximize pointing accuracy and to eliminate the need to rebalance the telescope after instrument changes. Standard attachment mechanisms will be used. Structural connections will be kinematic for maximum pointing reproducibility, and accurate electrical connections will be ensured by using tapered guide pins for alignment.

The top end of the telescope will contain a socket that will accommodate 2-ton modules and optics up to 2m in diameter. The module center of gravity will be 1.5m in front of prime focus. These modules will be exchanged with the telescope horizontal, by use of a deck and a rail system attached to the dome. The telescope will be locked down in this position, and differential vertical motion as the modules move from the dome to the telescope will be small, under 1 mm. Details of this system are described by Weitzmann (1983, TMT Note No. 67) and are shown schematically in Figures 7-11, 7-12 and 7-13.

Possible top end modules include:

(1) Prime focus camera with field rotation mechanism

(2) Prime focus spectrograph

(3) f/15 secondary (with light baffle)

(4) f/25 IR chopping secondary

(5) f/100 Coudé secondary

(6) 2m diameter secondary for future wide field imaging

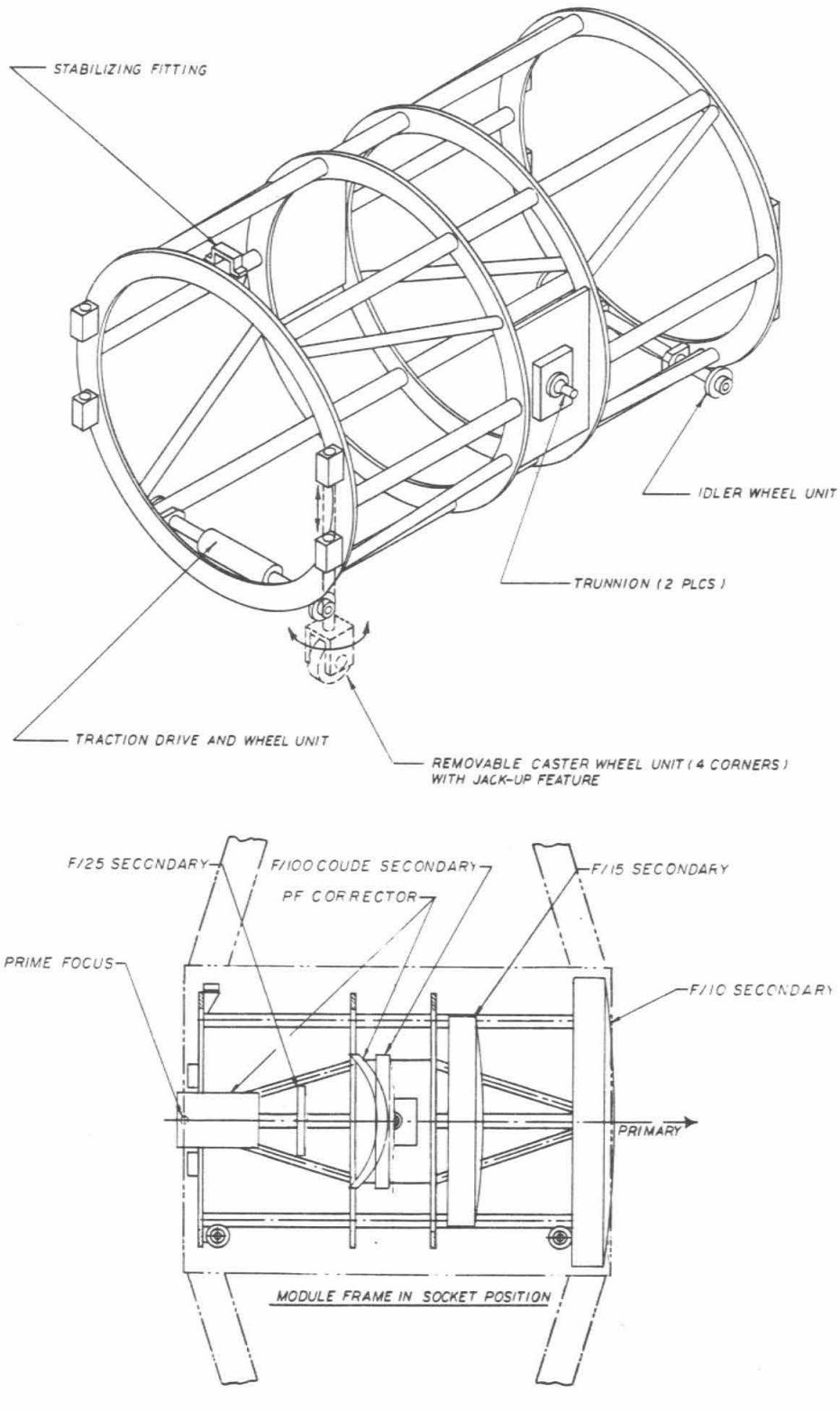

Figure 7-11 A schematic indicating the rough geometry of the TMT top end modules and the kinematic mounting system. The locations of the major optical elements that will be carried by such modules is indicated. The structural details are not correct.

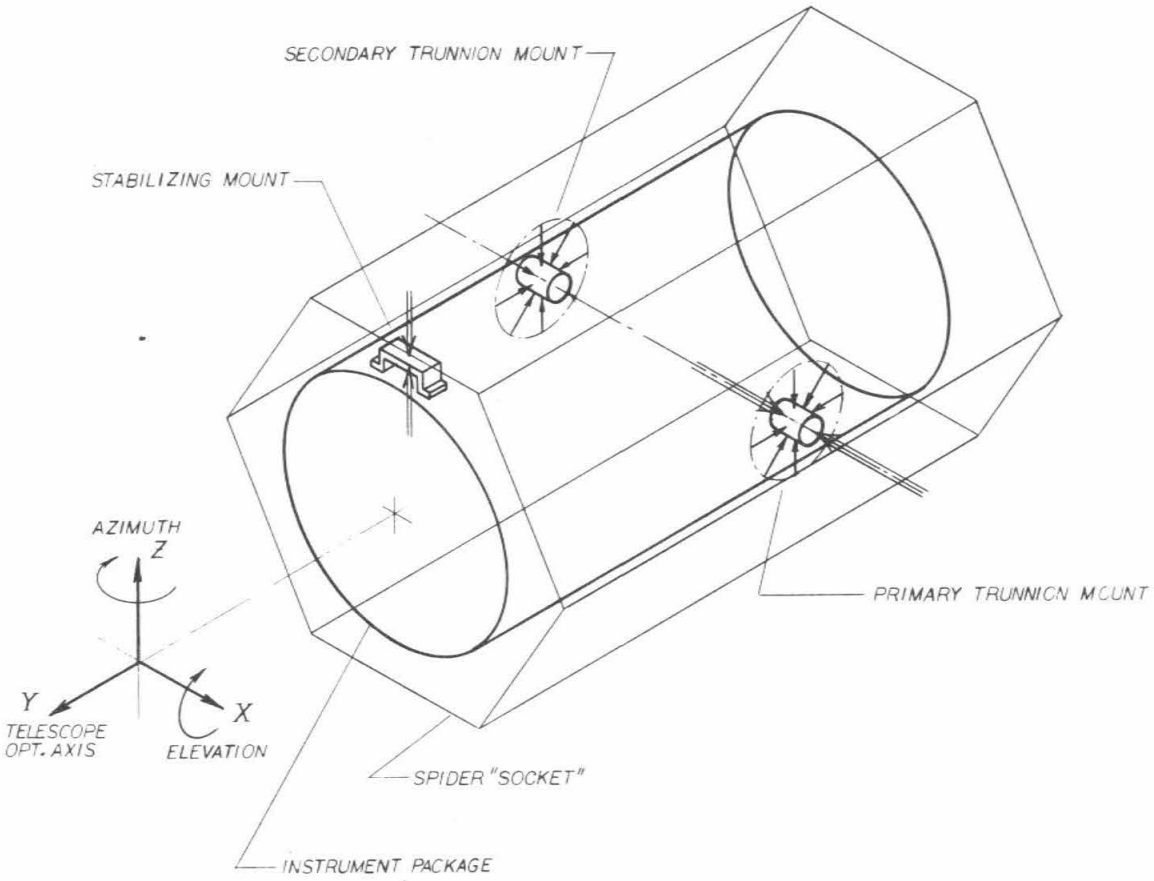

Figure 7-12 A schematic showing in more detail the kinematic mounting system for the exchange of the instrument modules in the socket. This mounting system serves to allow modules to be installed and reinstalled with a very high degree of reproducibility, as is needed for the pointing and image quality requirements of the TMT.

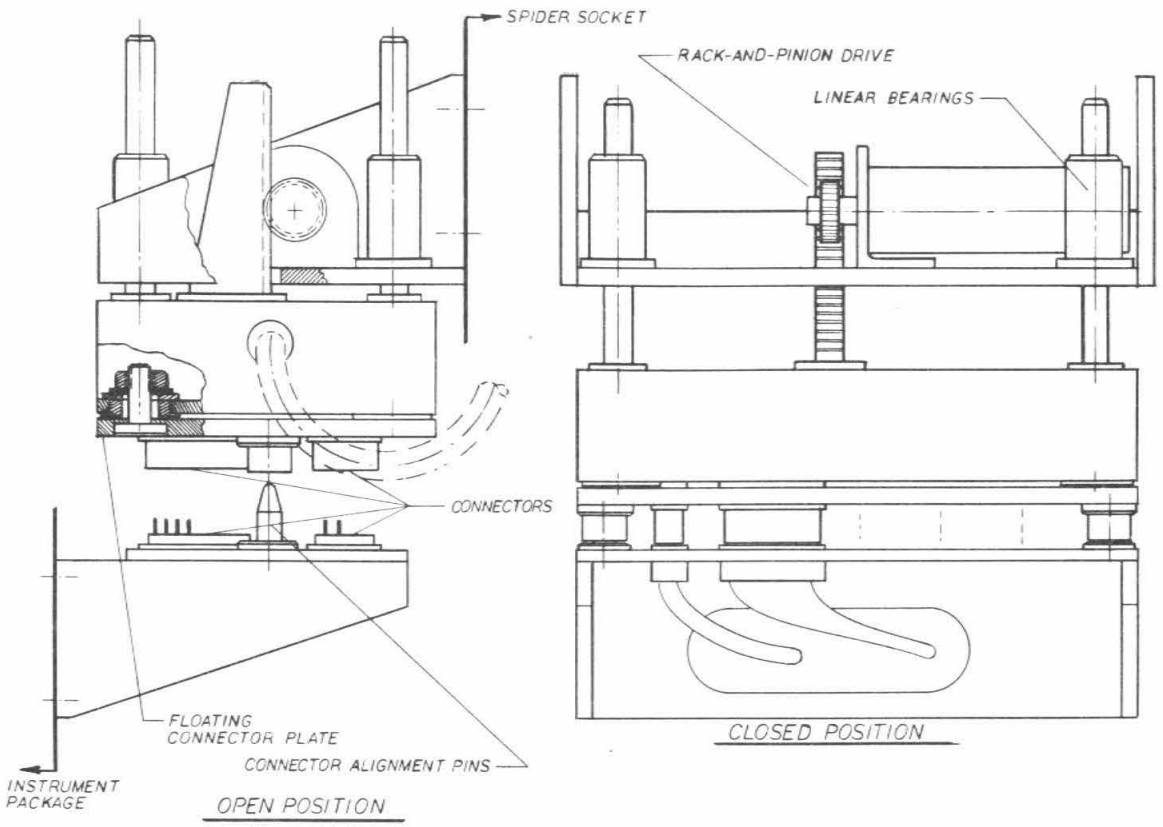

Figure 7-13 A schematic showing a self aligning electrical connector system that may be used with the top end sockets to allow the automatic installation and removal of these modules including electrical connections. Such a system is very desirable if rapid and safe changes are to be made.

The forward Cassegrain position will be developed in similar fashion. Two-ton modules with their centers of gravity +3.5m from the primary vertex will be rolled on and off the telescope through the central hole in the primary, with the telescope horizontal. The socket will be able to accommodate optics up to 1.3m in diameter. Possible modules include:

(1) tertiary mirror, rotation mechanism, baffle for f/15, atmospheric dispersion corrector for f/15

(2) IR spectrometer

(3) IR imager and field rotation mechanism

(4) wide field camera/multiple object spectrograph (future)

The Cassegrain position will have a standard socket and accept 2 ton modules with centers of gravity 3.5m behind the primary (1m behind the f/15 focal plane). These will be exchanged with the telescope horizontal. Possible modules include:

(1) f/15 low/medium resolution spectrograph

(2) f/15 polarimeter

Details of the related dome and building parameters are given in section 6.3.2

7.11 IR Design Considerations

For optimal IR performance the telescope needs low and very stable emissivity and a high quality chopping secondary. The net system emissivity arises from several sources:

(1) Intersegment gaps and beveled edges total 0.7% of the primary area. A method for establishing low or at least uniform emissivity for these strips has not yet been selected. At worst we will have e=1.

(2) Top end spiders will block 0.7% of the primary. Low emissivity, high reflectance surfaces may be placed on their underside. The optical consequences of such an action have not yet been established. At worst we will have e=1.

(3) The primary mirror will be aluminum coated. A clean surface will have an emissivity of roughly e=0.02 and, unless cleaned frequently, will degrade appreciably.

(4) The chopping secondary will be gold coated to give emissivity of roughly e=0.01.

(5) Diffractive effects allowing the detector to "see" beyond the edge of the undersized secondary to additional telescope structure are unknown but expected to be small since the 0.5m diameter secondary is only supported by quite thin (< 5mm) spiders out to the roughly 2m diameter of its top end module. Thus the detector sees only sky up to 3^o off axis.

(6) Background from the emissive region defined by the hole in the primary (2.7% of the primary area) will be reduced either by putting a hole in the secondary or by using a shallow cone at the center of the secondary. This cone would serve to direct light from this region away from the detector and instead allow the detector to see the sky reflected from the primary. Both techniques have been successfully used on other IR telescopes.

Based on estimates of the above sources we expect the system emissivity to be under 5%.

In the thermal infrared ($\lambda > 2.5\mu$m), background photons from the sky and the telescope dominate the flux from typical program objects. Hence stability of the background is critical. Matthews (1981 TMT Report No. 46) has studied in detail possible mechanisms for variability associated with the segmented primary and the telescope in general. No objectionable variability is expected.

The chopping secondary for the TMT will be quite large by today's standards. As indicated in Section 4.4 and shown in Figure 4-12, the chopping secondary is roughly hexagonal and about 0.53m in diameter. To successfully chop such a mirror at high frequencies and large chop angles will require extreme care in the design and optimization of the chopper and its drivers. To help achieve these goals the chopper is expected to be lightweighted beryllium mirror. If lightweighted by a factor of 10, its weight may be roughly 4kg. To minimize the affect of chopping on the telescope structure, the mirror will be chopped against an equal mass so the system will be reactionless.

Chopping the mirror over large angles is difficult, but perhaps more important, it will degrade the images. Faber and Nelson (1982, TMT Report No. 57) have shown that full chop angles in excess of 45 arcseconds will substantially degrade the diffraction-limited image quality of the TMT at 10μm. Ray tracing by Epps (1984b) confirms this comatic degradation.

7.12 Control of Secondaries

Continuous control of the focus of the telescope is needed and is most readily done by pistoning the secondary. Although not clearly needed, control over secondary tilt may also be desirable. We plan to provide this three-axis control over the secondary with three actuators similar to those supporting the primary segments.

The f/25 IR chopping secondary requires rapid and accurate three-axis control to meet the specifications. Preliminary calculations have been made that suggest the chopper is practical, but no detailed design has yet been undertaken.

7.13 Field Rotation and Other Effects of Alt-Az Mount

While an altitude-azimuth mounting system for the telescope allows important simplifications in the structural design, it adds complications to the telescope drive system, and it introduces a rotating field of view at all of the focal positions.

The telescope drive requirements are made more complex in two ways. The first and simplest is that the drives must perform at substantially nonuniform rates, rather than the essentially constant drive rates that are needed on equatorially mounted telescopes. With the use of computer-controlled drive motors, this is a minor complication. The second complexity arises when the telescope is operating near the zenith. As the telescope approaches the zenith, the azimuth and field rotation drive rates become infinite, as do the azimuth, elevation, and field rotation drive accelerations. Practical limitations on any drive motor system will then introduce a "blind spot" around the zenith in which the telescope is not able to perform adequately.

The characteristics of the drive motors are partially established by the slewing specification for the telescope because the friction drive system will be responsible for both tracking and slewing. The slewing performance requires moving from any star to any other in under two minutes. This requires maximum angular velocities of $\geqslant 3^o$/sec and accelerations $\geqslant 0.1^o/\text{sec}^2$. If tracking rates can be successfully maintained at rates even 10 times lower than the slewing rate requirements, the blind spot at the zenith will be under 1^o in diameter. Note that for a 1^o blind spot, the tracking rate must be about 100 times the sidereal rate. From this we expect that the zenith blind spot will be quite small, and given proper drive design, will not be an appreciable consideration in the operation of the TMT. For a 1^o blind spot, only 2% of the sky will ever be affected by its presence. Mathematical details are given by Nelson (1981, TMT Report No. 49).

The effect of field rotation appears far more troublesome. Here the difficulty arises when one is studying a finite area, rather than a single point source. Field rotation effects require one to either unrotate the optical beam by some optical technique such as rotating Dove prisms, or to physically rotate the scientific instrument. Since the field of view may be large in some instances, or the observation may cover a substantial wavelength interval or be at IR wavelengths, a Dove prism may not always be an adequate solution. Hence we must provide for mechanical rotation of many of the instruments in the TMT, particularly for those at the prime and Cassegrain foci. Although this introduces mechanical complexity, it appears practical. Some of the largest instruments that may be on the Nasmyth will not be capable of rotation, and if field derotation is needed, it will have to be performed by optical means. The accuracy required for field derotation is modest, but depends on the field of view. For a 20 arcminute field of view, a rotation angular error of 35 arcseconds will introduce an image error at the edge of the field of 0.1 arcseconds. Mathematical details are given by Nelson (1981, TMT Report No. 49).

8. Technology Development Program

Contents **Page**

Introduction

From the inception of the project in 1977 to the present, the vast majority of effort was spent on the development of the technology for the segmented primary. That work fell into two general and interrelated categories; segment manufacture and segment support.

The method proposed for the segment manufacture, Stressed Mirror Polishing, has been described above in Section 5.15. In Section 8.1 we describe the program that demonstrated that method. A critical aspect of the segment fabrication is the optical testing of the surfaces. Measurement of the off-axis surfaces, including the focus or radius-of-curvature term, is unusual in conventional mirror fabrication. We therefore describe separately in Section 8.2 the surface measurement methods used in the development program.

Mirror support is a critical aspect of any telescope design and for a segmented mirror the active control is an additional critical technology. Each segment in the primary is assumed to behave as a rigid body and therefore has six degrees of freedom. Three of these are passively controlled and three are actively controlled. The development programs for the passive and active support systems are described in Sections 8.3 and 8.4 respectively.

Summary and Conclusions

Since the contents of the different aspects of the technology development program are so different, we give a summary and conclusions at the beginning of each of the four subsections below.

8.1 Segment Fabrication

Summary and Conclusions

The technology development program for segment fabrication began in 1979 with a survey of possible techniques. The concept of Stressed Mirror Polishing appeared feasible and economical.

The analytical and numerical theoretical basis of the method was then developed and this was described above in Section 5.15.

The demonstration of the method began with the fabrication of a quarter-scale (360mm diameter) mirror in 1979, and this work is reviewed in Section 8.1.1. The target surface was a section of a paraboloid with a radius of curvature of 3688.0mm and off-axis distance of 350.0mm. The desired surface was 10μm rms different from the spherical one to be polished into the blank. The achieved surface had a radius of curvature of 3688.3mm, an off-axis distance of 350.7mm, and an rms surface error of 0.03μm. Thus the surface quality was excellent and the radius error was 1 in 10^4.

The demonstration then moved to two full-scale mirror projects in the years 1981 to 1984. Starting in 1980, in collaboration with Kitt Peak National Observatory, we began a program to demonstrate the method on a full-sized 2.0m mirror. That program at KPNO is concluding as this report is being written and the results are described in Section 8.1.3. The target mirror was a section of a paraboloid with a radius of curvature of 40.5m and an off-axis distance of 4.3m. This mirror is comparable to the most aspheric of the TMT segments. The program did not include an effort to precisely control the radius of curvature. The radius achieved was about 1mm from the 40.5m. As of this writing only a single iteration of Stressed Mirror Polishing was completed. The blank was stressed in a fixture, a spherical surface was ground and polished (about 150 machine hours), and releasing the forces and moments yielded a surface that differed from the target surface by only 0.187μm rms.

In 1981 a 1.9m-diameter blank was purchased to make the segment and reference mirror for the active control system prototype. The surface polished into this blank was spherical and not an off-axis parabola. Thus, the Stressed Mirror Polishing technique was not used. However, a number of other aspects of the required segment fabrication technology were demon-

strated in the making of this mirror. These included accurate measurement and control of the radius of curvature, polishing to the surface quality required for the TMT, cutting the mirror into a hexagon, and boring the radial support-post hole. This work is described in Section 8.1.2. The target surface for the mirror was a spherical surface with a radius of curvature of 10000mm and a surface quality better than 42nm rms surface error. This allowed surface error includes the focus or radius of curvature contribution. The goal for the radius of curvature was thus 10000.000 ± 0.032mm. Supports for the mirror to be used during polishing and testing were developed. A precise and accurate method of measuring the radius of curvature was developed and used to control the radius during polishing. The final surface achieved was 45nm rms from the target surface and the radius was 10000.009 ± 0.014mm.

The hexagonal segment was cut from the circular mirror and then tested. The cutting caused a substantial change in the figure, 538nm rms surface error. This distortion was dominated by focus and also contained 86nm of astigmatism and coma. Possible causes of the warping are discussed in the Section 8.1.2 and methods for correcting the problem are discussed in Section 8.3.3. The central hole for the radial support post was successfully bored and the mirror is presently in use in the active control system.

8.1.1 Quarter-Scale Stressed Mirror Polishing Test

In 1979 the method of Stressed Mirror Polishing was used to fabricate a quarter-scale mirror. This demonstration is described in detail in Nelson *et al.*, (1979, TMT Report No. 22).

The CerVit blank for the mirror was 358.8mm in diameter and uniformly thick at 25.4mm. The diameter-to-thickness ratio is 14 to 1.

The convex surface was ground and polished to a radius of 3.77m. The concave surface was ground to a radius of about 3.74m.

We selected for the target surface an off-axis section of a paraboloid with radius of curvature k = 3.6880m and off-axis distance R = 0.350m. The spherical surface to be polished into the stressed blank was chosen to have a radius l = 3.7380m.

A simple jig using levers and lead weights was used to apply the forces and moments to 24 Invar blocks glued to the edge of the blank. The compression of a rubber pad beneath the blank provided a uniform pressure distribution to the back.

The deflections applied by the stressing jig were calculated using the equations in Section 5.7 above. The major terms in the jig-applied deflections were focus ($C_{20} = -8.93\mu m$), astigmatism ($C_{22} = 19.34\mu m$), and coma ($C_{31} = 6.55\mu m$). The peak-to-peak deflection was 60μm. To achieve these deflections the forces varied from block to block over the range -19kg to +19kg. The moments varied from -2.37kg-m to +2.77kg-m.

The grinding of the concave surface proceeded through a series of grit sizes (30 μm, 12 μm, and 3 μm) and required about 7 hours of machine time.

During the polishing with the forces and moments applied, the spherical surface was tested with a 200mm diameter test plate.

With the forces and moments removed, the paraboloidal surface was tested interferometrically using the paraboloidal null configuration in Figure 8-1. The mirror was relatively thin and flexible and therefore supported vertically on edge for the test. By folding the focal point of the interferometer onto the vertex, the laser was autocollimated by adjusting the tilt and displacement of the flat. The resulting perpendicular distance from the vertex to the flat is $k/4$. The desired vertex location relative to the mirror was established by surveying. The distance $k/4$ was measured with an accuracy of 0.05mm using a calibrated rod and dial indicator. The interferograms were digitized and the data fitted through fourth order to a series of Zernike polynomials. The Zernike coefficients were then used to calculate the best-fitting paraboloid. The rms deviation between the desired paraboloid and the achieved one is minimized by the following changes in R the off-axis distance and ϕ the angle of rotation of the mirror about its own axis.

$$\delta R = R\frac{8C_{22}\delta C_{22} + 3C_{31}\delta_{31}}{16C_{22}^2 + 3C_{31}^2} \tag{8-1}$$

$$\delta\phi = -\frac{8C_{22}\delta C_{2-2} + 3C_{31}\delta C_{3-1}}{16C_{22}^2 + 3C_{31}^2}$$

Approximations and errors in the procedure necessitate iterations of the polishing and test cycle. The rate of convergence was such that after two polishings the rms surface deviation from the desired surface was 0.03μm. A summary of the results of the progress to the final surface is given in Table 8-1.

Table 8-1

Parameter	Desired Parabola	First Polish	Second Polish
$k(m)$	3.6880	3.6868	3.6883
$R(m)$	0.3500	0.3579	0.3507
$\phi(radians)$	0.0	0.0043	-0.0060
$(Z-Z_{desired})_{rms}$	-		0.55
$(Z-Z_{best})_{rms}$	-	0.08	0.03

The first polish required about 25 hours of polishing and the second polish required about 30 hours. The best fitted surface corresponds to what one would achieve by moving the mirror to a slightly different off-axis distance $R + \delta R$ and rotating it about its own axis ($\delta\phi$).

After the second polish and the calculation of the best-fitting parameters, we then moved and rotated the mirror to the best-fit values. Interferograms were taken, digitized, and as calculated the Zernike coefficients yielded an rms surface error of 0.03μm. The final mirror has a measured radius of curvature k=3.6883m, which differed by 0.3mm from that desired. The off-axis distance of R=0.3507m differed by 0.7mm from the desired value.

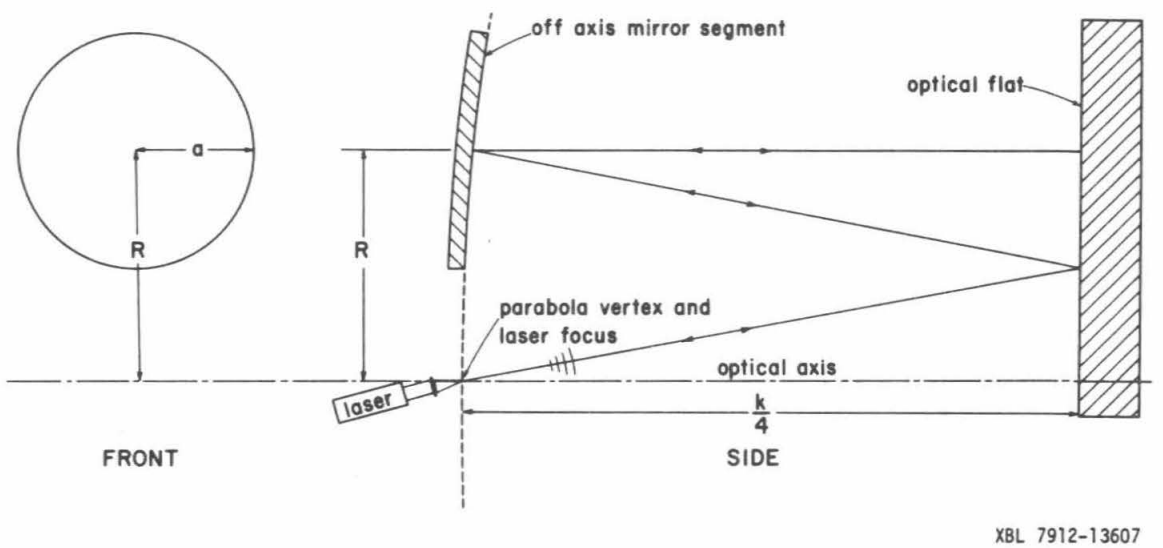

Figure 8-1 Schematic diagram showing geometry of the parabolic null test. The focus of the Twyman-Green interferometer is located at the vertex of the global paraboloid. The mirror section under test is fixed 35.00 cm from vertex.

8.1.2 Control Prototype Mirror Fabrication

The prototype test of the active control system is described below in Section 8.4. Two of the components required for this test were a full-sized hexagonal segment and a portion of another segment which we call the "reference mirror." The fabrication of these two mirrors provided an opportunity to develop some techniques for segment fabrication. The two mirrors were cut from a single circular mirror as shown in the plan view in Figure 8-2. The circular mirror was 1.9m in diameter and 0.076m thick.

The fabrication of this mirror gave us experience with many aspects of segment fabrication including: meniscus generation, blank support during grinding and polishing, grinding, polishing, cutting the hexagon, boring the radial support hole, and supporting the hexagonal segment. In addition, considerable experience was gained measuring the radius during the grinding, measuring the surface including the radius of curvature during the polishing, and measuring the surface including the radius in the final surface tests. The testing methods are critical in the fabrication of segments, and we describe them separately in Section 8.2 below. We describe here the mirror fabrication operations and the results of the optical tests of the figure quality. The details of the fabrication and testing can be found in the TMT Technical Notes Nos. 42, 66, 71, and 92.

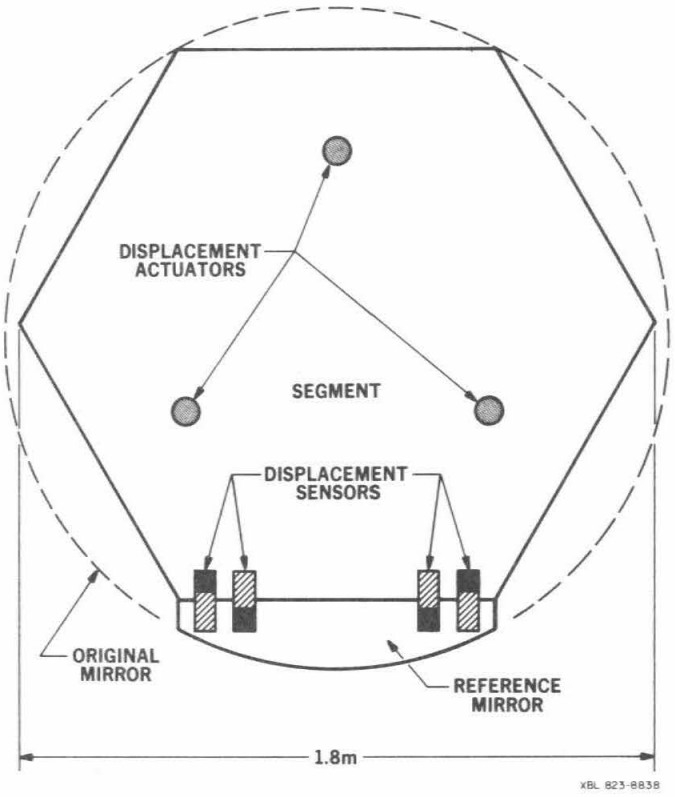

Figure 8-2 Plan view geometry of the optics of the active control system prototype. The piston and tilts of a full-sized segment are controlled with respect to a portion of a neighboring segment called the reference mirror. The positions of three actuators and four displacement sensors are shown. Both mirrors were cut from a circular mirror shown by the dashed circle.

Goals

The surface goals for the circular mirror were set to be the same as those required for the TMT segments. These are described by Mast and Nelson (1982, TMT Note No. 42) and summarized in Table 8-2. The mirror for the prototype was required to have a spherical surface with a radius of curvature of 10m. Since it was not an off-axis section of a paraboloid, the method of Stress Mirror Polishing was not required. The radius of curvature was set by the size limitations of the active control prototype. The 10m radius is considerably smaller than the 35m radius of the TMT segments. This placed more stringent tolerances on some parts of the radius of curvature measurement than will be required for the TMT segments. The total error budget for the mirror was 42nm rms surface error. This was budgeted according to the categories in Table 8-2.

Table 8-2
Prototype Mirror Error Budget

Test and analysis errors	10nm
Non-focus surface errors	25nm
Focus surface error	31nm
$\delta k = 32\mu$m	
Total rms surface error	42nm

The error contribution from the testing and analysis of the interferograms was budgeted at 10nm rms. The non-focus term contributions to the surface error were budgeted at 25nm rms. Since the measurement of the radius of curvature required a separate distance measurement in addition to the interferogram analysis it was budgeted separately at 31nm. This rms surface error corresponds to a measurement of the radius of curvature error of 32μm. Thus the goal for the radius of curvature was 10,000.000 $\pm$ 0.032mm.

Blank Preparation

Table 8-3 summarizes the history of the fabrication process. A Zerodur blank 120mm thick was purchased from Schott Optical Technologies (Mainz, Germany). A 10m radius uniform thickness meniscus was generated from the blank by Kodak (Rochester, New York). The diameter was 1903.5mm and the thickness 76mm. The meniscus was then annealed in order to reduce the internal stress and to make any residual stress symmetric top to bottom. This required about 3 weeks at $\approx$ 600 °C. The annealed meniscus was then shipped to Tinsley Laboratories (Berkeley, California) for completion of the fabrication process.

Table 8-3
Fabrication Process

Date	Process	Machine Time in a Centered Hexagon (hours)	(μm rms)
Sep 81	Ordered blank		
Jan 82	Generated meniscus	≈40	≈ 50μm
Feb 82	Annealed meniscus		
Apr 82	Shipped to Tinsley		
May 82	Grind/shine convex surface	14/19	
Aug 82 - Apr 83	A series of grind/shine cycles to establish test methods, test environment, and support.		
Apr 83 - May 83	4 grind/shine cycles	25/10	0.5
May 83	7 machine polish/test cycles	47	0.1
Jun 83	6 final polish/test cycles	2	0.04
Dec 83	Cut segment	≈ 70	
Feb 84	Bored hole	≈24	

Grinding Convex and Concave Surfaces

The grinding and polishing were done on a 72-inch diameter standard arc-stroke machine with a power pin. The tools were 1.37m in diameter and thus 72% of the blank diameter.

The convex surface was ground through a series of grits (30, 12, 3μm) and shined with Cerox 1650. Many months later we realized that this grind/shine procedure for the convex surface had been inadequate. Since the surface was only shined and not polished out, surface stress remained in the convex surface. Release of this stress when the mirror was cut into a hexagon may have been the cause of the surface warping that was observed on cutting.

The radius of the back surface was measured with an 18-inch spherometer to be $k_{convex} = 10075 \pm 10$mm.

The radius of the concave surface was measured with a 48-inch spherometer during the grinding and the radius was measured to be $k = 10000.5 \pm 1.4$mm, where the error is dominated by the repeatability of the calibration of the spherometer using an optical flat and gauge blocks.

Tests to Establish Support, Test Methods, and Test Environment.

A lengthy period (about 9 months) were required to develop the support and test methods to be used. This process required about 9 grind/shine cycles and the analysis of about 1500 interferograms. Details of the support and testing are described below. The axial support of the mirror during the grinding and polishing was provided by 36 rigid aluminum posts. During testing the mirror support was provided by a 36-point whiffletree. The test environment at Tinsley was extremely hostile, highly subject to background vibrations from operating machinery and nearby freeway traffic, and highly coupled to intense heating by sunlight. This drove us to make many of the tests at night and to enclose the test tower in an outer shroud of polyethylene sheet and an inner shroud of "warm window," a commercial insulated curtain. At the end of this development period we had achieved a marginally adequate support and test environment and we proceeded to try to achieve the above surface specifications. We wished to meet these objectives by 1 July 1983 in order to allow delivery of the mirrors for the active control prototype in time to meet the schedule for the active system tests.

Final Grinding of the Convex Surface

A final series of four grind shine cycles were made to remove astigmatism that had been introduced by earlier poor support configurations and to achieve a radius close to the desired radius. About 25 machine hours of grinding and 10 machine hours of shining were made in this series of 4 cycles. The rms surface error (rms of difference between measured and desired surfaces, including the focus term) was 0.5μm.

Polishing Concave Surface

A series of seven polish/test cycles were then made in order to "polish out" the surface, i.e., to polish deep enough to remove the subsurface damage left from the grinding and to improve the figure. The rms surface error at the end of this stage was 0.1μm.

Final Figuring

The final figure was established with six additional polish test/cycles. The first three were made with a 24-inch diameter tool with the pitch surface cut into a star pattern. These cycles required 5 hours of machine time. The final three cycles were made by hand with an 8-inch diameter tool. These three cycles totaled 122 minutes of hand polishing.

Final Polished Surface Quality

The surface was measured with the mirror on the same whiffletrees used in the grinding and polishing procedure. The surface within a central hexagonal region (side length 900mm) differed from the desired surface by 45nm rms. This is to be compared with our goal of 42nm rms. The radius of curvature was measured to be 10,000.009mm $\pm$ 0.014mm, where the error is based on the rms spread of eight independent measurements. The surface of the flat that was removed from these measurements was based on an average of measurements of the flat made over several months.

The circular mirror was then transferred to a new whiffletree designed to support a hexagonal segment. The tests were repeated, and the difference between the surface on the polishing whiffletree and the surface on the segment whiffletree was compared to the change expected from finite element calculations. The rms surface change expected was 1.577μm and the rms difference between measured and predicted was 0.066μm. This difference is consistent with errors due to mesh effects in the finite element calculation.

The measurements on these whiffletrees were more complete than those on the polishing whiffletrees. The included rotations of the sphere and support in order to remove the effects of the flat and whiffletree induced aberrations. The surface differed from the desired surface by 33nm rms and a spot diagram of the image formed by this surface is given in Figure 8-3. The 80% energy circle diameter is 0.30 arcseconds.

The hexagonal segment was cut off-center from the circular mirror as shown in Figure 8-2. The surface within this off-center hexagonal region was measured in a series of tests on the segment whiffletree. This series included rotations of the mirror with respect to the whiffletree in order to remove any whiffletree-induced surface distortions. (These whiffletree-induced distortions were 19nm rms over the hexagonal region, and thus the whiffletree does not presently meet the desired error budget. This is discussed below in Section 8.3.1.)

Cutting the Hexagon and Warping

The specifications for the cut segment and central radial support hole, and the procedures for cutting and boring are described in detail by Mast (1984, TMT Technical Note No. 66).

The mirror was supported for cutting on a convex wood mandrel (diameter 2032mm, 4 to 6 inches thick). Felt pads (diameter 1 inch) were soaked with pitch and placed on the mandrel in a 2.5-inch square grid, which provided a uniform and surface-matched support for the mirror. Slots cut in the mandrel accommodated the passage of the saw blade.

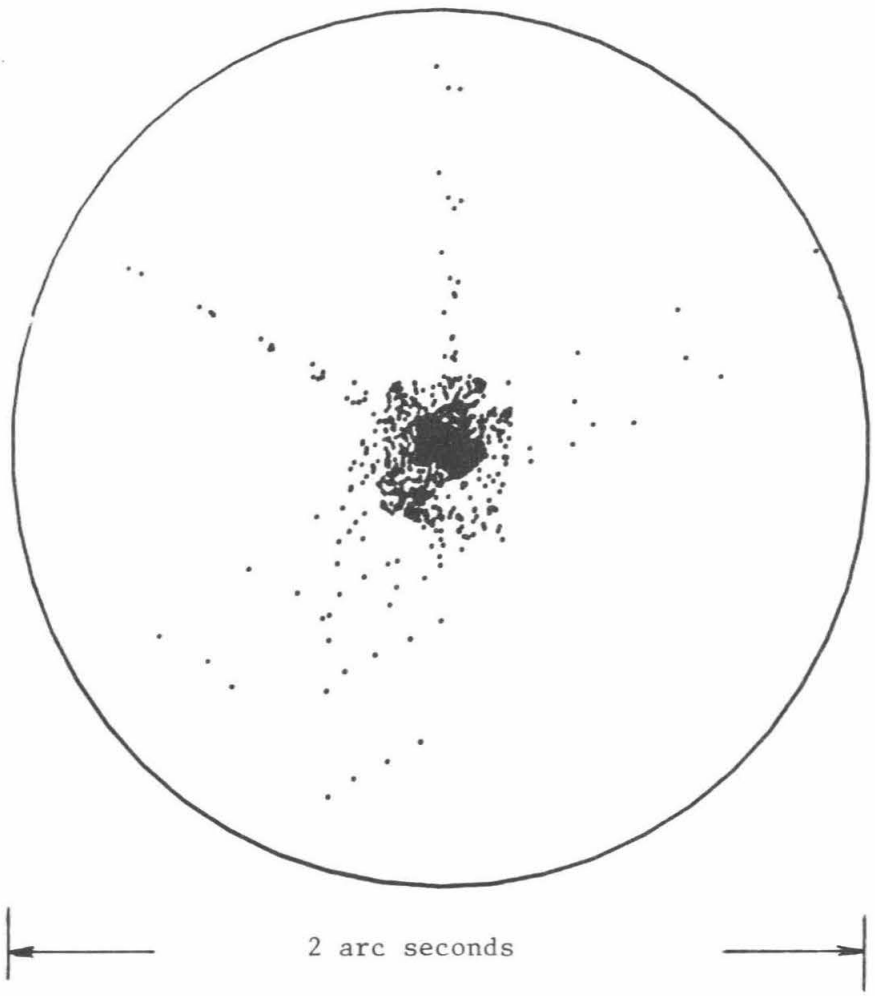

XBL 852-1267

Figure 8-3 A ray-traced spot diagram of the image formed by the central hexagon of the circular mirror polished for the active control system prototype. The surface differs from the desired spherical surface by 33nm and 80% of the energy from a point source is contained within a circle of diameter 0.30 arc seconds.

The mirror was positioned off-center of the mandrel by about the required 58.9mm offset of the hexagon.

The cutting was accomplished in nine working days using a 14-inch diameter circular saw blade operating at 7000feet/minute. Each side of the hexagon was cut using three 1-inch deep cuts in succession at a feed rate of 22 inches/hour. A problem arose because of the flexibility of the mandrel. As material was cut from the mirror, the load on the mandrel changed, the mandrel flexed and exerted a moment on the section being cut. This caused fracturing in the region of the cut. Most of the fracturing occurred in the piece removed. The segment was undamaged except for a small hairline crack 1/4 inch deep and about 1.5 inches long on the face of the first cut. In response to this effect we bolted the mandrel to the polishing table beneath it. During the subsequent cutting the internal stress at the cut was monitored with crossed polaroids and the relative heights of the two pieces were measured with a spherometer. The spherometer measurements were used to flex the mandrel by adjusting bolts, and no further fracturing occurred. The crack on the initial face has not increased in size during subsequent use of the mirror.

The hexagonal segment was then tested on the same segment whiffletree, and these tests showed the surface had warped substantially in the cutting process. The hexagonal surface warped 538nm rms. This warping was dominated by a change in focus. The additional aberrations were dominated by astigmatism and spherical aberration. Without the focus contribution the warping was 86nm rms. The detailed test methods and results are given by Mast (TMT Technical Note Note No. 92). A spot diagram of the image formed by the aberrations due to warping is shown in Figure 8-4. The 80% image diameter is 2.91 arcseconds. In Section 8.3.3 we discuss possible methods of dealing with this very substantial deformation of the surface.

There are two possible causes of this warping. The first possible cause is the inadequate treatment of the convex surface that was mentioned above. The convex surface was not polished out and the concave surface was. If the residual surface stress left in the convex surface was not uniform, then cutting the off-center hexagonal shape would release stresses that would warp the segment. Tests subsequently made with a small flat showed that stresses large enough to cause substantial warping are induced in a surface by grinding (Nelson and Schaefer, 1984, TMT Technical Note No. 111). The second possible cause is the release of internal stress remaining in the blank after the annealing. Although the measured birefringence in the blank suggest low stress levels in the blank in general, those measurements do not indicate directly whether warping will occur or not. Substantial warping can occur with stress levels smaller than associated birefringence measurement uncertainty. In addition, the particular integrated components of stress measured by the birefringence measurements are completely different from the combination of stress components that can cause a mirror to warp.

The warping of the segment can be addressed There are several options for dealing with the problem of warping. One option is to place a mechanical fixture on the back of the segment and apply forces and moments to remove the warping aberrations. This fixture would remain with the segment in the telescope and possible fixture designs are described in Section 8.3.3. It is also possible to polish out the aberrations of the warped hexagon using either conventional polishing methods or computer assisted polishing methods. This option is being explored with commercial optical manufacturers. A third option is to cut the hexagonal shape first and then use Stressed Mirror Polishing. The theoretical basis for this option is described by Lubliner (1982, TMT Report No. 87). The disadvantages of this option include possible high forces and stresses at the vertices of the hexagon and the fact that polishing will give a rolled edge and local scalloping at the edge. By polishing the circular mirror and then cutting, the rolled edge and edge scalloping is largely removed.

Boring the Hole for Radial Support Post

The mandrel used to support the segment for cutting was also used during the boring of the hole for the radial support post. The boring was done using a tool 3.125mm in diameter with a diamond edge (180MD grit with M100 concentration). The tool was rotated from above

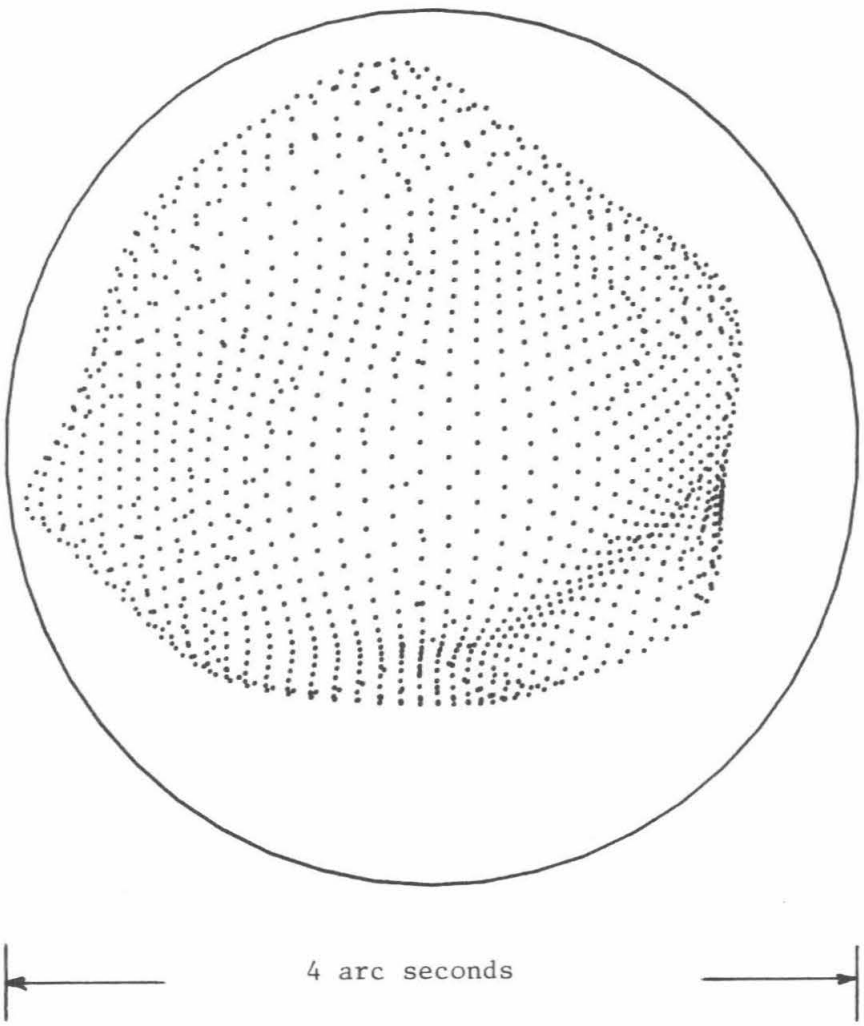

Figure 8-4 A ray-traced spot diagram of the image formed by the aberrations introduced by cutting the hexagon. The rms surface error is 538nm and is dominated by focus. The remaining aberrations(86nm rms) are dominated by astigmatism and spherical aberration. 80% of the energy from a point source is contained in a circle of diameter 2.91 arcseconds.

at about 2800rpm. The turntable was rotated at 40s/revolution. The feed rate varied up to 23mm/minute. After setup and alignment the boring required about 5 days. The final hole dimensions were 253.87mm diameter and 61.19mm depth. The desired hole dimensions were 254.00 ± 0.5mm diameter and 61.20 ± 0.13mm deep at the edge.

The hole was stress-relieved by etching with hydroflouric acid. An Invar ring was bonded into the hole to receive the radial support assembly.

The surface was then retested. The test results showed additional warping of the surface from the boring, etching, and gluing operations. A total of 53nm rms surface change was measured, dominated by astigmatism, focus, and spherical aberration.

8.1.3 Full-Scale Demonstration of Stressed Mirror Polishing

In 1980 the Kitt Peak National Observatory began a program to use the method of Stressed Mirror Polishing to fabricate a full-scale 2-meter mirror. The KPNO documentation of that work is being completed, and we describe here results based on interim publications and private communications (Golden, *et al,* 1982, and Barr, *et al,* 1983). Figure 8-5 shows the phases of the program.

Goals

The target surface was an off-axis section of a paraboloid with a radius of curvature k = 40.5m and off-axis distance 4.30m. These values are close to those required for the outer segments of the TMT (k = 35m and R = 4.67m). Thus the project provides information applicable to the TMT segment fabrication.

The error budget for the surface was set at 32nm for all terms in the Zernike expansion excluding the focus term. The radius of curvature (or focus term) was budgeted for 88nm corresponding to an error in the radius of curvature < 1mm.

The spherical surface to be polished into the stressed blank was chosen to have a radius of l = 41.0m.

The Zernike coefficients of the desired surface are given in the first column of Table 8-4.

Table 8-4
Zernike Coefficients of Desired Surface

Coef	Parabola (μm)	Deflections (μm)	Desired HARTMN Results (λ)
2,+0		−5.690	
2,+2	−68.393	68.393	87.533
3,−3			0.101
3,−1			12.049
3,+1	−10.461	10.461	
3,+3	0.088	−0.088	
4,+0	0.010	0.292	−0.302
4,+2	0.010	−0.010	−0.010

The first column gives the coefficients for the desired off-axis parabola in microns. The second column gives the deflections in microns to be induced by the stressing fixture, i.e., the difference between the sphere and parabola. The last column gives the coefficients expected by the KPNO test analysis program HARTMN, which 1) evaluates only in the inner 90% radius of the mirror and normalizes the Zernike polynomials to this radius, 2) uses a coordinate system rotated by 90° from that used to calculate columns 1 and 2, 3) expresses the coefficients in waves (λ = 0.6328μm), and 4) subtracts a reference sphere with a 41.0m radius of curvature.

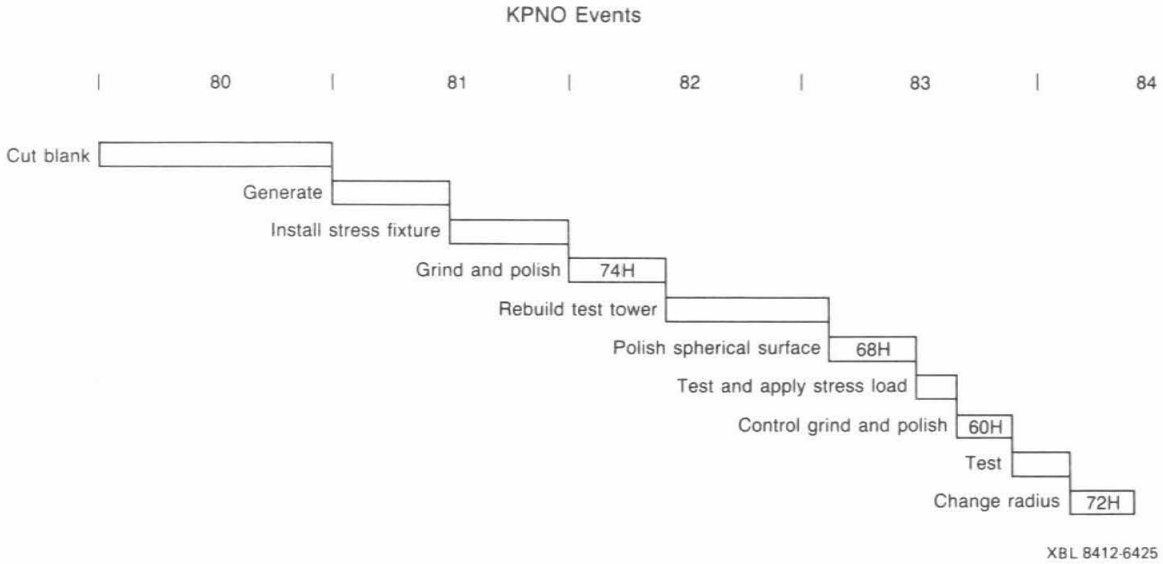

Figure 8-5 Sequence of operations in the Kitt Peak National Observatory program demonstrating Stressed Mirror Polishing. The machine hours for the optical manufacturing tasks are given.

Blank Preparation

The blank was cut from a thick CerVit blank using a band cutter. The diameter was 2.1m and the thickness 121 ± 6mm. Birefringence measurements gave rough estimates of about 30nm/cm. These high levels of stress in the blank suggested that warping upon cutting into a hexagon was probably inevitable and therefore the operation was not included in the program.

A uniform thickness meniscus was generated from the blank using a step generating method with a 12-inch diamond wheel. The thickness was 76mm, the diameter 2000mm, and the radius of both sides was 41 ±0.5m.

The convex surface was fine ground (but not polished out). The radius was measured using a 0.2m bar spherometer.

Stressing Fixture and Blank Support

The stressing fixture design followed that used in the fabrication described above in Section 8.1.1. Figure 8-6 is a drawing of the fixture. Lead weights and lead pellets placed in buckets were used to apply forces and moments to the edge of the blank. At 24 equally spaced locations around the mirror groups of four Invar blocks were cemented to the edge using a 1000 psi burst strength adhesive (Helor Hi Water by Epoxy Coatings Inc.). The CerVit has a 3000 psi burst strength. Each Invar block contains a horizontal pin; plates are used to clamp the four pins together. The horizontal levers which are used to apply the forces and moments are then bolted to the clamp/block assembly.

A 54-point support was used to carry the axial loads of the mirror in the fixture (Figure 8-7). The 54-point support consisted of three 6-point whiffletrees, a disc mounted on a ball joint on each of the 18 whiffletree points, and three rubber blocks on each disk. Compliance occurred through the 54 rubber blocks between the blank and the whiffletree. When the mirror was ground or polished, 18 lockstands were brought up pneumatically under the whiffletrees. These were locked and provided a solid support for the grinding and polishing. Thus the whiffletree mount provided the means of locating and setting the lockstand heights. During optical testing of the surface the lockstands were lowered and the mirror was supported kinematically on the whiffletree mount.

The radial support of the blank was provided by the stressing fixture.

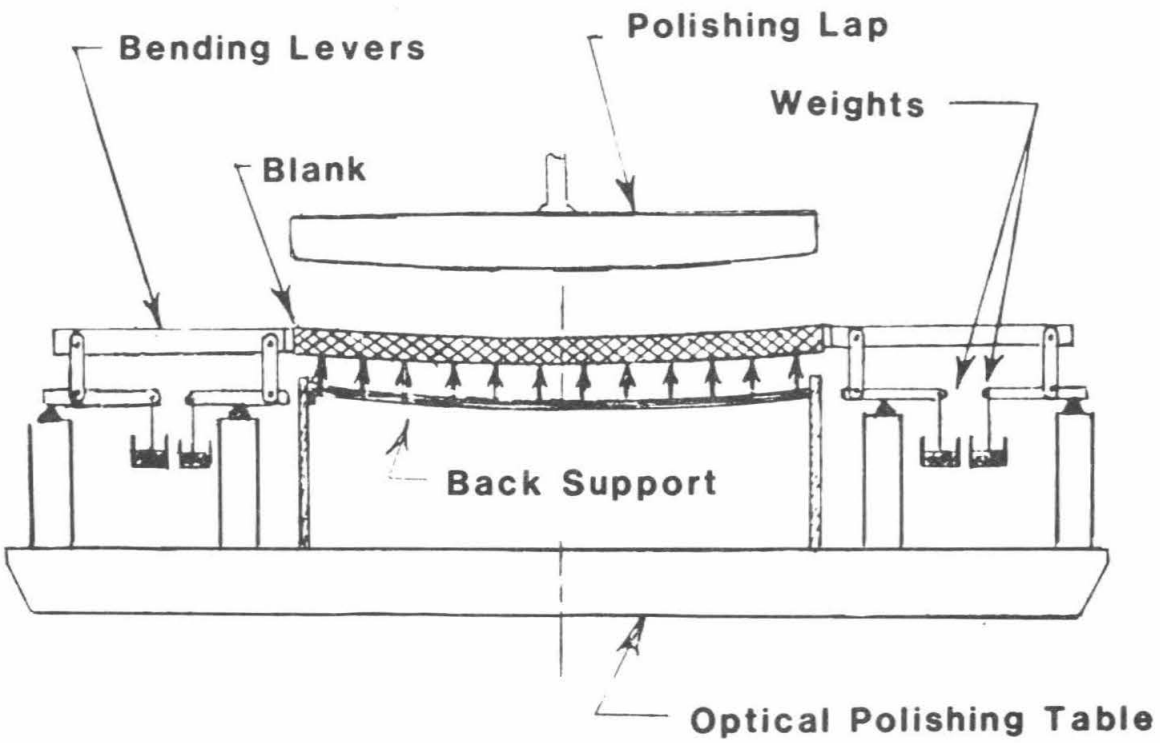

Figure 8-6 Schematic showing the configuration used for Stressed Mirror Polishing. Weights are applied to levers bonded to the edge of the blank in order to apply forces and moments around the edge of the blank. These in combination with a nearly uniform back support warps the blank in a controlled manner during the polishing process.

Grinding Concave Surface

The machine used to grind and polish the mirror is hydraulic with a straight stroke. It has a 4m diameter capacity and also has a tool off-load feature that can reduce the weight of the tool on the blank during operation. In all the work reported here the tool was allowed to bear on the mirror with its full weight or less.

The tools used were roughly 9/10, 1/2, and 1/4 size and weighed 500kg, 200kg, and 25kg. The bearing surface of the grinding tools were covered with round ceramic tiles such that the bearing surface on the mirror was 50% of the full surface of the tool. This reduced the working area but increased the surface pressure.

The mirror was placed in the stressing fixture concave side up. The weight of the Invar blocks, clamping plates, and stressing fixture lever arms were counter-weighted so as to put no forces or moments into the glass. The mirror was then ground and polished to a spherical surface. In this process a large amount of astigmatism was introduced into the surface (about 6 waves) and it was found that it could not be removed using the large tool alone. The mirror was then polished with an 18-inch star lap and the full-sized tool was used for smoothing. This ultimately yielded a surface with an rms surface error (excluding focus) of 36nm rms. The conclusion was that a sphere of required surface quality could be polished in the stressing fixture and associated support.

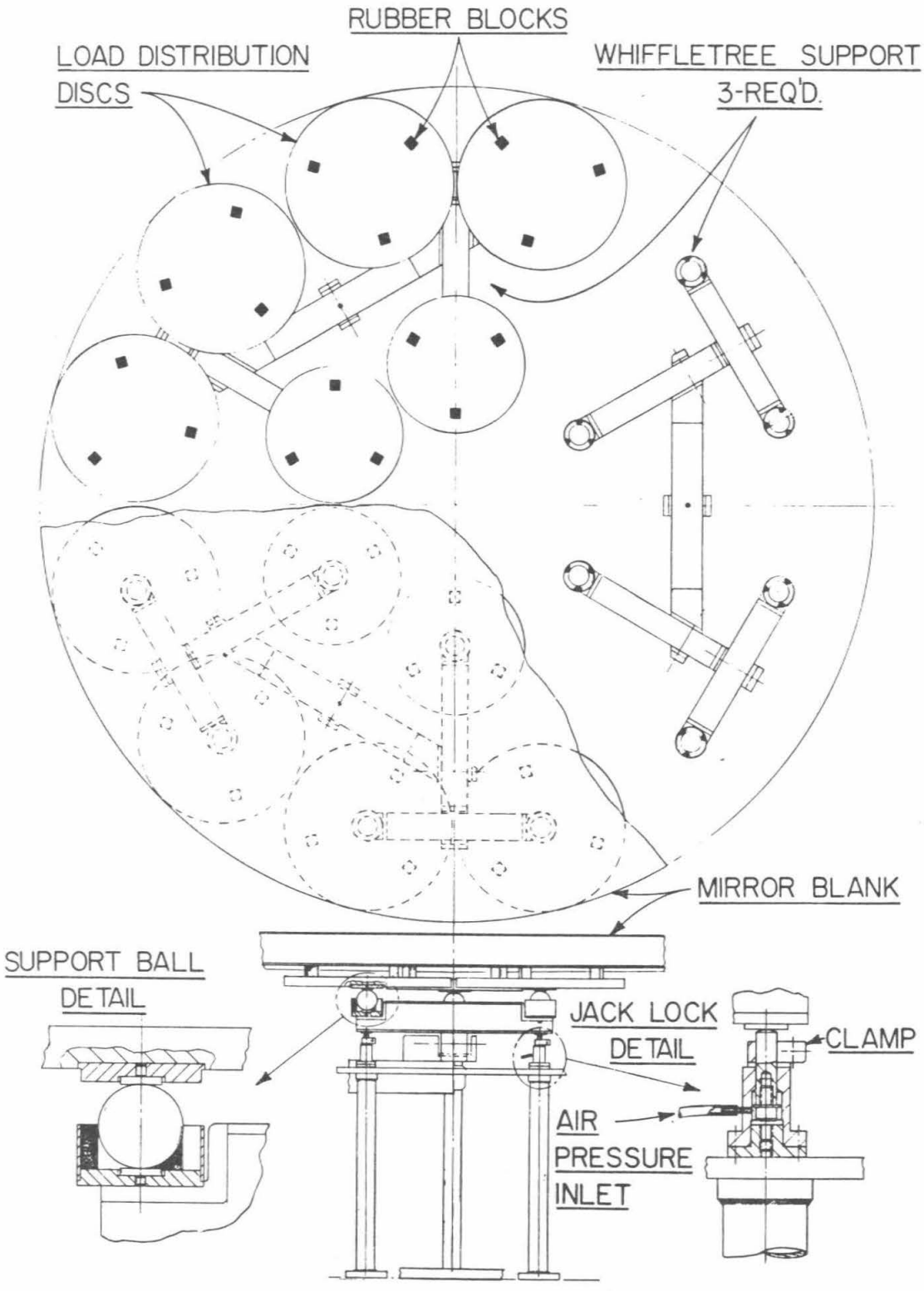

XBL 8411-4926

Figure 8-7 The mirror support system used under the thin KPNO 2-meter diameter meniscus mirror during figuring and testing. The mirror is contacted by 54 rubber blocks mounted on an 18-point whiffletree system. Stiff supports (Jack locks) lock any motion of the whiffletrees during the polishing, transferring the support force at each of the 18 points directly to the polishing table. During optical testing the locks are lowered and the mirror is supported kinematically by the whiffletrees.

Development of Test Environment

During and after the fabrication of this sphere extensive work was required to establish an adequate test environment and test procedures for the interferometric testing of the surface. This work, the test procedures, and test sensitivities are described below in Section 8.2.1. The reproducibility of the interferometer tests showed that a set of 10 interferograms gives an rms surface error of about 30nm.

Qualification of Hartmann Test

The development of the Hartmann test which was required to test the parabolic surface is described below in Section 8.2.2. The results of the qualification tests showed that the Hartmann test was reproducible to 10 to 20nm rms surface error.

Tests of Stressed and Unstressed Surface

The repeatability of the application of the stresses was tested with a series of Hartmann tests with the stress applied and removed. The forces and couples applied were calculated by the program OMNI to induce the deflections given in Table 8-4. The forces varied from −27kg to +33kg and the moments varied from −1500kg-cm to +2700kg-cm. The rms surface differences between the unstressed measurements (Hartmann Plates 28, 32, 34, and 35) are typically 110nm. This spread in the surfaces is a measure of the repeatability of the system including the fixture and the testing. Other tests of the Hartmann test repeatability suggest that most of the variation seen here is due to variations in the support and stressing fixture. The rms surface differences between the stressed surface measurements (Hartmann Plates 29, 30, 31, and 33) are typically 200nm. This larger spread in the stressed measurements is largely due to a larger variation of the astigmatism coefficients. It is assumed that the larger variation in the stressed surface results comes from stiction in the stressing fixture. This spread then is an indication of the possible ultimate surface quality that can be achieved with the present fixture configuration. Known improvements can be made in the fixture to reduce stiction effects. However, the level of effort available for this program does not allow for major changes in the fixture to demonstrate the improvement.

First Aspherization of Stressed Mirror Polishing

With the forces and moments applied the first aspherization proceeded with the same grinding and polishing tools used to figure the initial sphere. The machine hours per grit are shown in Table 8-5.

Table 8-5
Grinding and Polishing Data for First Aspherization

	Tool (in)	Hours	PSI
80 grit (150 sieve)	80	4.5	0.3-0.4
30 μgrit	80	7.0	0.4
12 μgrit	80 & 48	15.0	0.4-0.6
5 μgrit(W-9)	48	29.0	0.5
Barnesite	68	4.0	0.5

After the four hours of Barnesite polishing the mirror was tested in the stressed spherical configuration. The radius was measured with an Invar chain. There was more than a wave of spherical aberration and the radius was 7mm too long. This large error in radius occurred simply because no attempt was made to measure the radius up to this point. (Experience with measuring and controlling the radius in the fabrication of the TMT control prototype mirror showed that measuring the radius allows control of the rms surface to ±15nm. The surface of the mirror was shined except for the outer 10% in radius that was lightly grey to very grey at the outer edge. Thus the mirror was not "polished out."

An additional four cycles of polishing were then made in order to change the radius and improve the figure. Table 8-6 describes these cycles.

Table 8-6
Grinding and Polishing Data for Changing Radius of Curvature

Dates	Tool Diam. (in)	Grit	Hours	Purpose
3/21-4/5	39	Barnesite	49	shorten radius
4/9 -4/24	68	Barnesite	12	smooth
4/25-5/4	39	Barnesite	18	shorten radius
5/8 -5/11	68	Rouge	9	smooth

The final radius was within 1mm of 41m. These additional cycles demonstrate control over the radius for a mirror in the stressing fixture and on the mount. To control the radius to a better precision requires a series of calibrated measurements. The measurement of the radius of neither the sphere nor the parabola was pursued to a better precision in this program. (In the fabrication of the TMT prototype segment the radius of a sphere was measured to the precision required for the TMT segment fabrication.) No attempt was made in this program to measure the radius of the off-axis parabolic surface.

Surface Quality after First Aspherization

The surface was tested using the Hartmann test both in the stressed spherical configuration and the unstressed parabolic configuration. The HARTMN output Zernike coefficients are given (in waves) in Table 8-7 (Hartmann Plates 94,95,96,97).

In the parabolic configuration the test was made with the mirror on the mount with the lockstands lowered. In addition, the Invar blocks, clamping plates, and lever arms were still attached to the mirror. The weight of these components change the spherical aberration (C_{40}). This effect has been calculated ($C_{40} = 0.627\lambda$) and removed from the data in Table 8-7.

The final column gives the error surface, the difference between the measured and desired parabolic surfaces on the first iteration. The rms error is 187nm in the region of the desired hexagon. This is a remarkably small error for this first iteration. We note again, however, that it does not include the focus or radius of curvature term since no attempt was made to measure or control the radius precisely. Nonetheless, given the small number of machine hours of conventional polishing used to achieve this very strong aspheric surface, we believe this demonstrates that Stressed Mirror Polishing is a very efficient and economical method of fabricating the TMT segments.

Second Aspherization

Comparison of the final column of Table 8-7 with the column for the sphere shows that except for astigmatism, the errors in the final surface would be reduced substantially by having polished a better spherical surface. In particular, all of the C_{40} error in the final figure would have been removed. Thus the fixture performed exactly as expected as far as C_{40} is concerned. Since the figure of the sphere can be improved and the overall rms error is still a factor of two larger than the test repeatability, a second iteration will be made. This second iteration is in progress at the time of this writing.

Table 8-7
HARTMN Output Zernike Coefficients (waves)
After the First Aspherization

Coefficient	Measured Sphere	Measured Parabola	Desired Parabola	Difference of Measured – Desired
2,–2	–0.449	0.126		0.126
2,+2	–0.069	87.058	87.533	–0.475
3,–3	0.203	0.598	0.101	0.497
3,–1	0.100	12.468	12.049	0.419
3,+1	–0.151	–0.175		–0.175
3,+3	0.027	0.012		0.012
4,–2	–0.017	–0.014		–0.014
4, 0	0.296	–0.003	–0.302	0.299
4,+2	0.048	0.014	–0.010	0.024
5,–1	–0.061	–0.087		–0.087
5,+1	0.038	0.050		0.050
6, 0	–0.166	– .167		–0.167

8.2 Segment Surface Testing

Summary and Conclusions

The development of adequate interferometric testing environments and procedures was a substantial effort both at Tinsley and KPNO. These programs are discussed in Section 8.2.1. Adequate thermal control was finally achieved and methods of removing the effects of the test optics and support were successfully applied. The equipment, environment, and procedures finally allowed measurements of the surface that were reproducible at the 20nm rms level. This was at great cost of calendar time, human effort, and dollars. The processing time for the data analysis was typically a few days. The conclusions from this experience are given in Section 8.2.1. The test method, test environment, and analysis methods will need to be substantially improved to be used for the fabrication of the TMT segments. In Section 8.2.2 we describe the Hartmann testing of the off-axis parabola mirror at KPNO. This test was successfully developed and showed excellent repeatability at the 10nm level. In Section 8.3 we describe the method used to measure the radius of curvature of the mirror at Tinsly Laboratories. The method uses a fringe counting laser interferometer to measure a distance related to the radius of curvature. A "single" measurement of the surface typically included seven measurements of the radius of curvature. The rms spread in these measurements was about 0.030mm.

8.2.1 Interferometric Testing

Experience was gained with interferometric testing in both the fabrication of the sphere for the control prototype and the fabrication of the off-axis parabola at KPNO. We describe each of these programs in turn. Conclusions are discussed at the end of each section.

8.2.1.1 Interferometric Testing at Tinsley Laboratories

Test Geometry

The optical surface testing was done *in situ* using a tower built above the grinding and polishing table. A small crane attached to this tower was used to handle the grinding and polishing tools. During testing this crane was swung out of the light path and secured. The lockstands used for axial support during grinding and polishing were lowered, and the axial support of the mirror during testing was provided by the 36-point whiffletree. The eight braces that provided radial support were also backed away from the mirror. Fiducials were placed on the mirror to define the coordinate system of the interferogram. Initially a light-weight triangular fiducial frame of 6mm diameter rods was kinematically placed on the mirror. Later crossed pieces of photographic tape on the concave surface served as fiducials. These stayed on the mirror through the process of cutting the hexagonal segment.

The geometry of the optical test is shown in Figure 8-8. The center of curvature of the sphere is folded by an optical flat to near the edge and the surface of the sphere.

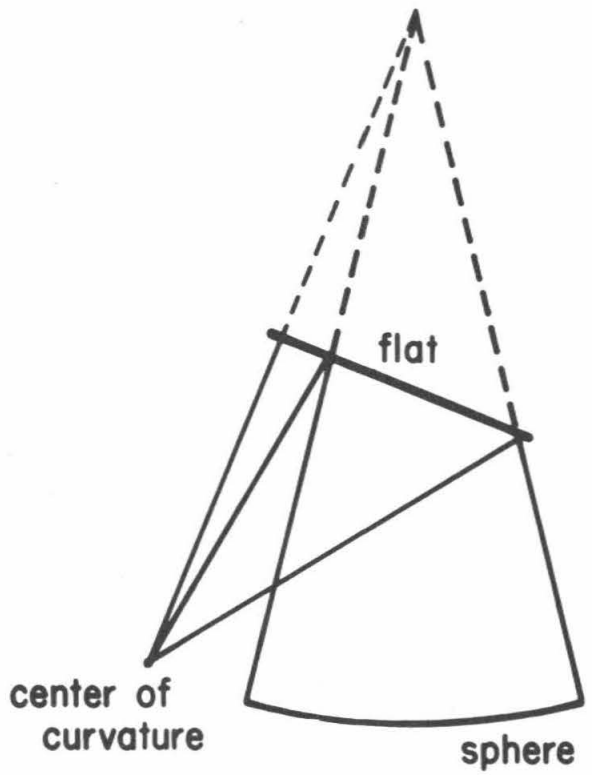

Figure 8-8 The geometry of the optical test at Tinsley Laboratories. The center of curvature of the sphere is folded by an optical flat to near the mathematical extension of the spherical surface. The perpendicular distance from the center of curvature to the flat is 1/2 of the radius of curvature of the sphere.

Folding Flat

The flat was mounted in an aluminum annulus using a layer of silastic. Thus the mirror was only supported around the edge. A calculation using a finite-element analysis program determined the amount of focus and spherical aberration introduced into the surface due to the self-weight deflections. These were removed in the subsequent analysis of the interferograms. The intrinsic focus and spherical aberration in the surface were not removed and were assumed to be stable. These were potentially known from Ritchey-Common tests of the flat made earlier, but the analysis of those tests was never made. The non-azimuthally symmetric aberrations were measured during each test by rotating the sphere with respect to the flat. Measurements were made with the flat rotated 0, 105, and 0 degrees. Using these sets of data we separated the sphere and flat contributions (Budiansky, *et al,* 1983, TMT Technical Note No. 83). Tests showed that the surface of the flat did change with temperature (and time) and the data was interpolated in time to achieve the most accurate removal of the flat.

Piston and tilt of the flat were precisely controlled by three motors.

Interferometer

All of the optical testing during the development of the support and fabrication of the hexagonal segment for the control prototype was done with a Twyman-Green interferometer. The interferometer was manufactured by Tinsley and was mounted via an x-y-z stage on the steel framework of the polishing machine. To photograph the fringe pattern we used a standard commercial 35mm camera (Minolta X-700) with a Motor Drive for film advance and a Data Back to record the roll and frame number on the interferogram. The shutter speed was 1/500 of a second with Tri-X film.

Testing Environment: Thermal

The thermal environment of the test was also hostile. Large diurnal changes in the temperature inside the building initially caused turbulence which often prevented any testing in the daytime and sometimes even at night. A plastic sheet shroud surrounded the tower and polishing machine. An insulating curtain of a commercial material called "warm window" was used to cover the conical volume of the optical beam and the flat. With these modifications tests could usually be made in daytime.

Testing Environment: Vibrational

The vibration environment of the test was also hostile. The test tower and interferometer were not vibration-isolated from the building. During the day many grinding and polishing machines operated in the building. The test tower was about 20m from an active machine shop. In addition, heavy traffic on the nearby freeway could often be seen in the vibrations of the fringes. Taking pictures at 1/500s, testing at night, and judicious choices of when to open the shutter of the camera by the operator were used to reduce the effects of the vibrations.

Analysis of Interferograms

A single test consisted of taking 18 interferograms and selecting 10 to be digitized. After developing the 35mm film, we made paper prints with an electrostatic printer (3M - 500 Reader Printer). This was fast and inexpensive and a comparison with regular photographic printing showed the paper prints did not degrade the final surface measurement accuracy or precision. The fringe positions were digitized by hand using a digitizing tablet (Summagraphics), a graphics terminal (Imlac), and an interactive program running on a VAX computer. There were typically 15 fringes per interferogram and 200-400 points digitized per interferogram. The data were fitted using a least squares fitting program to a series of 48 Zernike polynomials. Additional programs allowed adding, subtracting, or averaging vectors of Zernike coefficients, separating sphere and flat contributions from sets of data with rotated elements, and interpolating data sets in the time domain. Additional programs generated contour maps that were used to inform the optician of the surface status, and geometric optics programs to generate image spot diagrams.

The rms surface difference between individual interferograms was typically 30 to 40nm.

A measurement of the surface usually consisted of a series of 6 to 21 single tests. This series consisted of rotations to take out the flat and/or the effects of the support. For example, eight series on separate days over a period of several months gave series test results for the flat that differed from the mean surface by 12nm to 35nm with an average variation of 23nm.

A set of five series of tests gave results for the whiffletree-induced aberrations that varied from the mean surface by 14nm to 25nm, with an average of variation of 19nm rms. The Zernike vectors for many tests are given by Mast (1984, TMT Technical Note No. 92).

Processing Time

The schedule of processing the sphere at Tinsley was completely dominated by the time required for testing, processing the test data, and interpreting the results. These activities took place at the Lawrence Berkeley Laboratory under the TLC of B. Schaefer and the devotion of the always understaffed Science Office. A series of tests that included rotations to remove the flat and support effects typically took 2 days to perform. The longer times were required if the radius of curvature was being measured (see Section 8.2.3). Then 3 to 4 days were required for the film development, printing, and digitizing of the interferograms. Typically an additional day or two was required to interpret the results and make a decision about how to proceed. It is abundantly clear that the testing time must be reduced to a few hours in order to meet a reasonable TMT segment fabrication schedule.

Conclusions from Tinsley Tests

We conclude from the experience at Tinsley that for the fabrication of the TMT segments it will be highly desirable to 1) **not** use a folding flat in the optical test 2) make the tests in vacuum, 3) have the test equipment vibration-isolated from the environment, 4) have the support completely proven before the optical fabrication relies on its use, and 5) develop or buy an automatic data analysis system such as a phase measuring interferometer.

8.2.1.2 Interferometric Testing at KPNO

Test Geometry

The test geometry is shown in Figure 8-9. A folding flat at the top of a 20m tower is used to fold the center of curvature back to a point above the stressing fixture. There a test table is mounted which supports either the interferometer or the Hartmann camera. The coordinate system for the interferograms was established by fiducial bars. During a test the lockstands were lowered and the mirror was supported by a 54-point whiffletree system. In the unstressed configuration the fixture was disconnected from the radial arms. In this configuration the weight of the Invar pads, dowels, clamping blocks and radial arm were applied to the edge of the mirror.

Folding Flat

An 82 inch diameter folding flat was mounted at the top of the tower. The flat (fused silica, 250mm thick) was supported by a six point whiffletree that left a central circular region large enough to not obstruct the optical beam. The aberrations in the flat were measured during the testing by taking interferograms with the polishing table rotated to different angles. The orientation of the flat was not readily controlled and small adjustments for alignment were made by moving the interferometer.

Interferometer

A scatterplate interferometer was used and a small flat folded the beam horizontally into the interferometer. The interferograms were made with a 35mm camera (Canon) on Tri-X film with exposures of 1/100 to 1/200s.

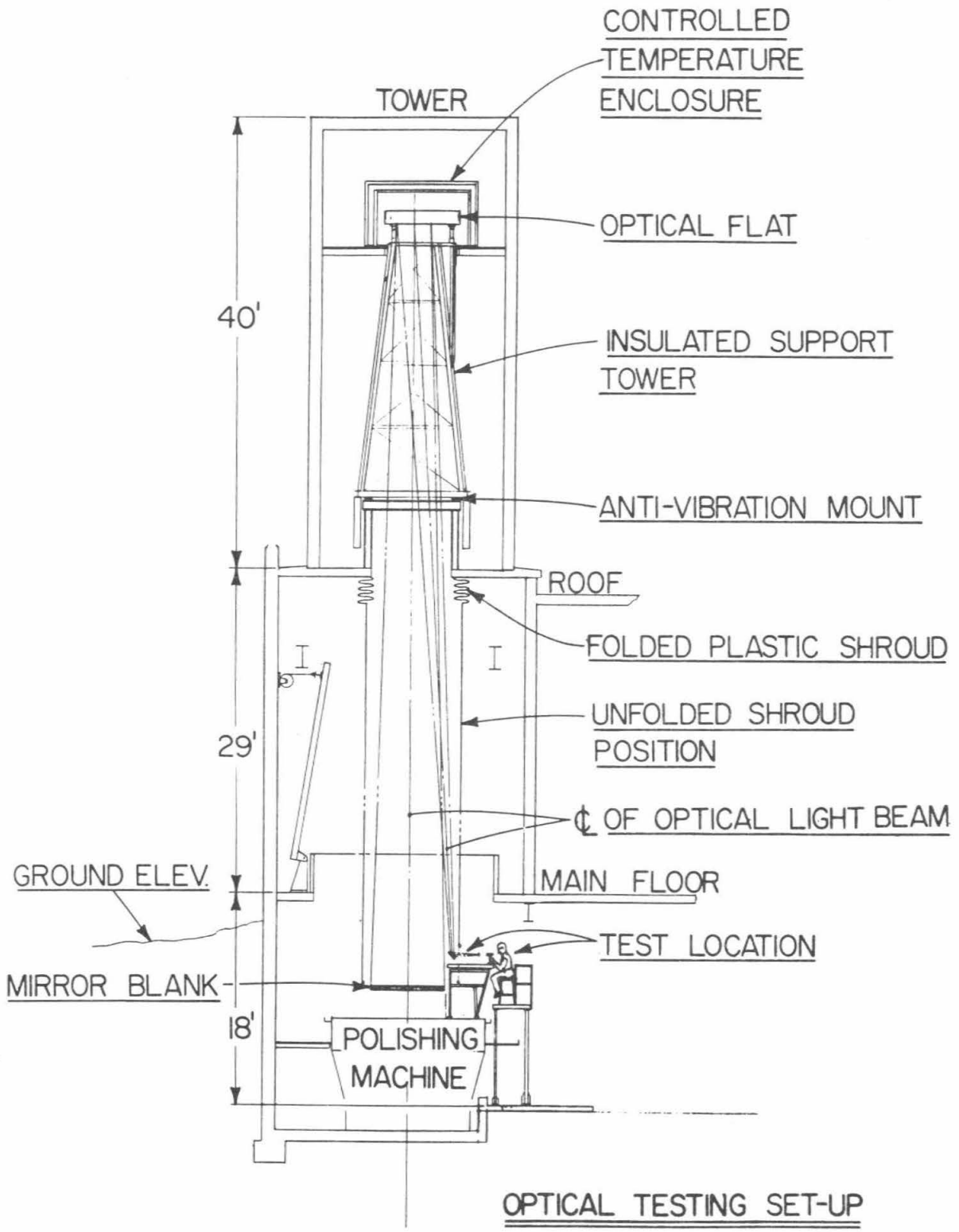

XBL 8411-4925

Figure 8-9 The optical testing configuration used in the fabrication of the 2-meter off-axis mirror at Kitt Peak National Observatory. The mirror rests on the polishing machine below ground level. An optical flat at the top of the 40-foot tower folds the beam back down to a test location just above the mirror where an interferometer or Hartmann camera can be used. Temperature and vibration control elements are illustrated.

Testing Environment: Thermal

The thermal environment was very hostile and considerable time and expense were required to improve it to the point of being marginally adequate. A folded plastic shroud was added to the lower portion of the tower. The upper section of the light beam was surrounded with insulating panels. The flat was particularly sensitive to the large temperature variations at the top of the tower, so the flat was surrounded by a double layer insulating box and the air temperature in the box was controlled.

Analysis of Interferograms

A typical test consisted of selecting 10 interferograms from a roll of 30 to 36 exposures, enlarging these to 8 x 10 inches in size, manually digitizing the photographs using a digitizing tablet, and then processing the data using the program FRINGE on a DEC-10 computer. Each interferogram contained 12 to 15 fringes and about the same number of data points was measured along each fringe. Data was analyzed from the area inscribed by a circle with 90% of the mirror diameter.

Measurements of the surface made closely spaced in time give a measure of the error introduced by the interferometric test process and data reduction. The surfaces from two tests (rolls 157,158) differed by only 6nm rms over a central hexagon. This is very small compared to the day to day test variations and thus the intrinsic test noise is quite small. The variations seen over longer periods of time were dominated by changes in the flat and changes in the support structure and stressing fixture.

Processing Time

A typical test was conducted at night to avoid shop and street vibrations. Photographs were made the following day and about 20 minutes were required to digitize each photograph. This resulted in about a two day delay between testing and results. If many tests were made, it was common for a week to elapse between testing periods.

Conclusions for KPNO Tests

From the effort at KPNO the following conclusions are drawn.

1. A folding flat in the optical test configuration is not desirable. If used, it must be calibrated for each critical test. Calibration of the axis symmetric aberrations is an unsolved problem.

2. Controlling the thermal environment is important if testing is done in air.

3. Automated testing is very desirable.

4. Repeatability at the level of 0.03μm rms was obtained from day-to-day tests using an average of 10 interferograms. Using more than 10 did not significantly improve the results.

8.2.2 Hartmann Testing

The fabrication of the off-axis section of the parabola at Kitt Peak National Observatory (KPNO) required a method of testing the off-axis figure. The Hartmann test was selected because it could be made within the existing test tower, because KPNO had considerable experience with Hartmann testing, and because it averages over the thermal turbulence in the tower that limited the results from the interferometric tests. This test can also be readily used to test the TMT segments. We first describe the geometry of the test and then tests made of the spherical surface of the mirror (before the first asphérization) to characterize the sensitivity and repeatability of the test and compare the results to those with the interferometer. The spherical mirror deviated from a perfect sphere by about 110nm rms.

Test Geometry

The overall geometry of the test was similar to that for the scatter-plate interferometer tests described in the previous section (see Figure 8-9). The small folding flat near the focus was not used in the Hartmann test.

The Hartmann screen contained 177 holes 38.1mm in diameter spaced 120mm center to center on a square grid. The screen rested on three kinematic mounts near the edge and was 52mm above the mirror surface at the center.

The Hartmann plate in the camera was 40m from the mirror center and 1m inside the focus. The overall size of the spot pattern on the plate was about 60mm by 100mm. The spots on the plate varied from 0.6mm diameter to 0.5mm $\times$ 0.9mm. The positions of the centroids of the spots were digitized using a PDS microdensitometer. The rms error in measuring a single spot position was 1μm.

Sensitivity to Screen Sag

The Hartmann screen sagged about 15mm under its own weight, giving a cylindrical surface deformation of the screen. At night on 30 June 1983 a test was made to measure the effect of this sag by rotating the Hartmann screen by 90 degrees. The rms surface difference between Plate 11 (0 degrees) and Plate 13 (90 degrees) is 14nm over a central hexagonal region. This is also a measure of the repeatability of the Hartmann test at night.

Hartmann Test Repeatability

On 27 July 1983 three consecutive Hartmann tests (Plates 18, 19, and 20) were made between two interferometric tests (rolls 157 and 158). The three surfaces from the Hartmann tests differed from each other by from 8 to 9nm rms.

Since it was desirable to make tests during the day instead of night, two plates (P16,17) were taken on the afternoon of 1 July 1983. The rms surface difference between the two surfaces over a central hexagonal region was 11nm.

These tests showed the intrinsic error in the Hartmann test to be quite small and thus it was not necessary to average many plates.

The above tests were made on the same day within an hour or two. Tests made on different days measure both repeatability of the test procedure and the stability of the support. A series of such tests (Plates 28 to 35) are described above in Section 8.1.3 and they typically show a scatter from test to test of 100-200nm. Since this is considerably larger than the short term repeatability the variations in the support dominate the variation in the results.

Comparison with Scatter-plate Interferometer Results.

Shortly after Plate 11 was taken the Hartmann screen was removed and Roll 152 was taken with the interferometer. The rms surface difference between the Hartmann test and the interferometer test was 27nm over a central hexagon.

The average of the three Hartmann plates 18, 19, and 20 differed from the average surface of rolls 157 and 158 by 36nm rms over the central hexagon. The difference was dominated by astigmatism. This astigmatism difference is primarily due to the small folding flat that is used in the interferometric test, but not in the Hartmann test. This flat has residual power of about 0.1λ, which introduces astigmatism of this order when used in 45 degree incidence.

Conclusions

The Hartmann test results show that only a single spot diagram is needed to make a measurement. The repeatability of the test is 10nm rms or less. Comparison of the Hartmann test and interferometer tests show a difference of 30 to 35 nm rms and this is consistent with known effects and statistics.

8.2.3 Radius of Curvature Measurements

The fabrication of the segments for the TMT differs substantially from conventional mirror fabrication, not only in the surface shape required, but also in the need to match the radii of curvature very accurately. The optical error budget requires the 35m radius of curvature to be controlled to ± 0.390mm. In order to control the radius to this precision we will need to measure it to about ± 0.1mm.

Measurement and control over the radius of curvature is identical to measurement and control of the Zernike expansion coefficient C_{20}

$$C_{20} \approx (1/4)a^2/k$$

where a is the effective radius of the segment (0.818m) and k is the radius of curvature (35m). Thus the error in radius is related to the error in C_{20}

$$\delta C_{20} = (1/4)(a/k)^2 \delta k \quad .$$

The rms surface error (σ) for an error in C_{20} is

$$\sigma = \frac{\delta C_{20}}{\sqrt{3}}.$$

For δk = 0.390mm, σ = 31nm.

Controlling the radius of curvature of a mirror is not unusual. It occurs whenever an optical flat is made. Although the radius for a flat is infinite, the rms surface error control exercised in making a good flat is comparable to the surface control needed for the segments. The unusual aspect for the TMT segments is the method required to measure the radius. In making a flat the power in the flat can be measured as part of the optical tests of the other aberrations. For the segments we need to supplement the optical test with additional very precise measurements of distances between the optics and test elements.

KPNO Off-Axis Segment Radius of Curvature

A method to measure the radius of curvature was designed and analyzed at KPNO. The method is described by Golden, *et al.* (1982) and a detailed error analysis was made by Radau (1981). Several precise distance measurements are required, the longest being about 20 meters, the distance from the folding flat to the segment. KPNO has designed and built a temperature-compensated Invar chain to make this measurement. Unfortunately, due to limitations in manpower and schedule, the system has not been implemented to make precise radius measurements. The method is nonetheless still a viable candidate for use in the TMT segment fabrication, and we refer the reader to the KPNO for further details.

Active-Control Prototype Mirror Radius of Curvature

For the purposes of the active control tests there was no requirement for an accurate radius of curvature. Nonetheless, in order to gain experience with measuring and controlling the radius, we set an error budget for the mirror to be comparable to that required for the TMT segments, i.e., the radius error should lead to an rms surface error $\sigma \leq$ 31nm. Due to the faster f-ratio of this mirror compared to a segment, this placed very stringent limits on the error in the radius of curvature. The error budget called for $\delta k \leq$ 0.032mm, i.e. k = 10000.000 ± 0.032mm.

Test Geometry

As described above, the test geometry used a folding flat to place the center of curvature at a point near the edge and surface of the sphere (Figure 8-8). If the center of curvature were exactly on the mathematical extension of the spherical surface, then the perpendicular distance from this point to the flat is exactly half of the radius of curvature. It is this distance (≈5m) that we measured to determine the radius of curvature. Since the center of curvature was not

folded back exactly to the mathematical extension of the spherical surface, additional measurements of distances were required to make small corrections.

The method of measuring the radius is described in detail by Mast (1983, TMT Technical Note No. 42). It utilizes several pieces of specialized equipment. The primary tool for measuring the distance is a Hewlett-Packard 5526A measurement system that utilizes a fringe counting interferometer to measure the absolute distance between two points to a precision of less than 0.1μm. The distance is based on the known wavelength of the helium-neon laser. The measurement required a number of corrections for temperature, temperature changes, atmospheric pressure, and relative humidity. Additional equipment served to locate each end of the H-P distance measurement with respect to the spherical surface and the folding flat. A point in space close to the spherical surface that we call the "extended point" was fixed in space using two specialized pieces of equipment, a sphere extender and a retroreflector assembly. The sphere extender is a frame that rests on the mirror at its edge, hangs about 200mm over the edge and holds the retroreflector assembly. The retroreflector assembly contains a bearing ball, the center of which is the "extended point," and a cube corner to retroreflect the beam from the H-P laser interferometer. A third piece of equipment is a rail with a carriage. By pulling a string on pulleys, the operator moves the carriage to carry the retroreflector from the sphere extender to the flat. As the retroreflector assembly moves, the H-P system counts the fringes moved in the interferometer.

This measurement process required about 40 minutes. Although some of the data recording could be automated, it seems unlikely that the time required could be reduced by more than a factor of 2.

Data Analysis

Part of the measurement also requires information (specifically C_{20}) from interferograms. The analysis time was dominated by the time required to develop, print, digitize, and fit the interferograms. (These same interferograms gave all the other aberrations in the surface.) After acquisition of the interferogram fit, then a ten minute pocket calculator computation was required to combine all the components of the measurement to derive the radius of curvature. The processing of the interferogram typically required 2 to 3 days. This time can be, and will need to be, substantially reduced for the TMT segment fabrication. A method called phase-measuring interferometry appears to be feasible for this application, and would reduce the analysis time to much less than an hour. The development and use of this technique or a comparable one will be invaluable for the segment fabrication.

Measurement Error

A determination of the radius was usually based on a series of measurements that included rotations of the whiffletree support to different angles. A series of seven measurements of the circular mirror on the polishing whiffletrees gave an rms spread in the radius measurements of 0.041mm. A series of seven measurements of the circular mirror on the whiffletrees for the segment gave an rms spread of radius values of 0.017mm. And a series of seven measurements of the hexagonal segment on the segment whiffletrees gave an rms spread in values of 0.031mm. Thus the statistical error in the mean radius from each series (rms/$\sqrt{7}$) was much smaller than the budgeted $\delta k \leqslant 0.032$mm. A detailed error analysis is made of the method by Mast (1983, TMT Technical Note 42). We show there that systematic effects are removed to a level comparable to these statistical errors.

Conclusions

We conclude from this experience that modifications of the method used for the spherical mirror can be made to extend the measurements to the longer distances required and to reduce substantially the data processing time. With these modifications the method can be readily used to measure and thus control the radius of curvature of the segments to the required precision.

8.3 Passive Support System

Summary and Conclusions

We describe in this section the support systems that constrain the segments in the passively-controlled degrees of freedom: the whiffletrees and the radial support post. We also describe designs and tests of systems that may be used to "unwarp" the segments should we choose to not polish out aberrations introduced by cutting.

The whiffletrees that have been built and tested as of this writing are shown to be inadequate in two respects. They introduce about 19nm rms surface deformation in the segment which gives an image blur of $\theta(80\%) = 0.106$arcseconds. This is a factor of 2 larger than the budgeted 0.05 arcseconds (Table 5-9). The resonant frequency under piston is about 20Hz and this is about a factor of 2 lower than desired. A new whiffletree is being designed and the design is addressing both of these deficiencies. Design calculations show the new design to be substantially stiffer and significantly more tolerant of fabrication errors. Three whiffletrees of the new design will be built and tested in the coming months.

The radial support built for the active control system prototype has functioned to constrain the segment in the passive degrees of freedom, but as of this writing no optical tests have been performed to test its effect on the segment surface.

Cutting of the hexagonal mirror for the prototype caused it to warp 538nm rms. A number of approaches to address this problem are being explored. One possible approach is to permanently attach a fixture to the hexagonal segment to correct the surface. A number of designs have been considered for fixtures to achieve the "unwarping." A primitive design using helical springs that pull on the whiffletree has been designed, built, and tested. Calculations show that the design is capable of reducing the warping from 538nm to 27nm rms residual error. The optical error budget goal is to achieve a 39nm rms surface. Tests of the system showed the deformations were reduced from 538nm to 48nm. The achieved deformations differed from the predicted deformations by 42nm rms. The rms error in the measured surface is about 8nm. This successful "unwarping" was achieved by simply applying the calculated forces. In practice, improvements could be made with a series of test-and-adjust cycles. Although the helical spring design is successful and could be used in the TMT, the design is somewhat awkward mechanically. A less bulky design employing leaf springs close to the back surface will be designed in the coming months.

8.3.1 Axial Support - Whiffletrees

The segment support design calls for a system to carry the axial load of the segment. By axial we mean the load of the mirror in a direction parallel to the local normal of the segment. Since the normal of each segment is at an angle (varying from 2.55 to 7.65 degrees) with respect to the optical axis of the telescope, the force direction in the global coordinate system varies from segment to segment.

The aspect ratio (diameter-to-thickness) of the segments is 24 to 1. This is unusually large for telescope mirrors and the segments are quite flexible. The self-weight deflections of a plate supported around the edge vary as d^4/h^2, where d is the diameter and h the thickness. The self-weight rms surface deflections of a circular plate 1.8 meters in diameter and 0.075m thickness which is supported around the edge is 6.7μm. This rms surface deflection is a measure of the natural deflection of a mirror with this aspect ratio and diameter.

The support for the TMT segments must reduce this natural deflection to less than 10nm. Thus a factor of $\approx 10^3$ reduction is required. This places very stringent requirements on the design and tolerances of the support.

Point Support

Ideally, a continuous support of the segment would provide an efficient support. In practice, support at a number of discrete points is used to approximate a continuous support. The

number of support points required to achieve a given level of support can be calculated analytically. We have made several general studies of this subject (Nelson, *et al.,* 1982 TMT Report No. 72, Nelson, 1983, TMT Technical Note No. 69). Based on these studies we selected a 36 point support for the segments. The positions of the support points and the forces to be applied at each point need to be established. There is some arbitrariness allowed in the general symmetry of the point positions and in a tradeoff between the point positions and forces. We have made a number of optimization studies and tolerance studies. These were performed first for the support of the circular blank during polishing (Budiansky 1983,TMT Technical Note No. 54, 72, and 76) and then for the hexagonal segment (Budiansky, 1983, TMT Technical Notes No. 52, 73 and 82). These analyses were made with a finite element method and included shell effects from the meniscus shape, the effect of the central hole, the ring for the support post, and the effect of the sensor weights. The forces applied at the points vary over the range from 5.95kgf to 15.0kgf. With these forces the rms surface deflections are 9nm. The tolerance to a variety of changes in the force positions and moments are described in the TMT Technical Notes listed above. In general, motions of 1mm in a group of forces (one or more whiffletrees) produce about 20nm of astigmatism or focus. Errors of 1mm in the positions of the pivots cause force changes that also induce about 20nm of astigmatism. Moments of the order 1000g-cm induce comparable aberrations. Errors of 1mm in the actuator positions cause from 50 to 200nm of astigmatism. The true tolerances depend in detail on the specific configuration of the errors in positions, forces, and moments.

Whiffletree Supports

A common device for applying point supports in a kinematic fashion is the whiffletree. This is a set of pivoting beams that successively spread the force from a single support point at the actuator to the 12 points of contact with the mirror. Considerable experience with whiffletrees exists in industry and they are successfully used to support mirrors during polishing and in application. Figure 8-10 shows a stick model in plan view of the geometry of the pivoting beams. Each pivot allows a rotation about an axis that lies in the plane of the whiffletree. At the actuator a single pivot allows the primary beam to rotate in one degree of freedom. At the ends of the primary beam are single-axis pivots that allow the secondary beams to rotate. At each end of the secondary beams is a two-axis pivot (a universal joint) that allows each rigid tripod to rotate. The heights of the 36 points represent 36 degrees of freedom. The whiffletree must convert these to the three heights of the actuators. Thus 33 degrees of freedom (or 11 per whiffletree) need to be flexible. There are 11 pivot degrees of freedom per whiffletree.

At the juncture of the actuator and primary beam, the whiffletree allows rotations of the coupling to match small errors in the angle of the actuator post. These rotations are accommodated in the primary and secondary pivots of the whiffletree. Small errors in the transverse position (x and y) of the actuator post and error in the rotation of the actuator about its own axis, however, must be accommodated by flexibility elsewhere, and these are accommodated in the flexibility of the couplings between each force point of the whiffletree and the mirror.

Mechanical Design

We have designed and constructed two different sets of three whiffletrees. The first set was used for grinding and polishing the prototype mirror and used a less symmetric geometry than the final set used to support the hexagonal segment. The mechanical design of both the first and second version was similar and we only describe the second version here. A drawing of a whiffletree is shown in Figure 8-11 (BBC 838-7549). The beams of the whiffletrees and tripods are fabricated from 4-inch aluminum I-beams. The commercially available pivots (Bendix Corporation) are made of pairs of crossed spring plates supporting rotating sleeves. Flexing of the stainless steel spring plates gives frictionless and hysteresis free motion over a limited angular travel. Each pivot is located in the beam web and held by 1 or 2 small yokes. They are positioned using an assembly fixture and then locked in place with set screws. The universal joint for a tripod is made of a pair of flex pivots holding a third flex pivot at a right angle.

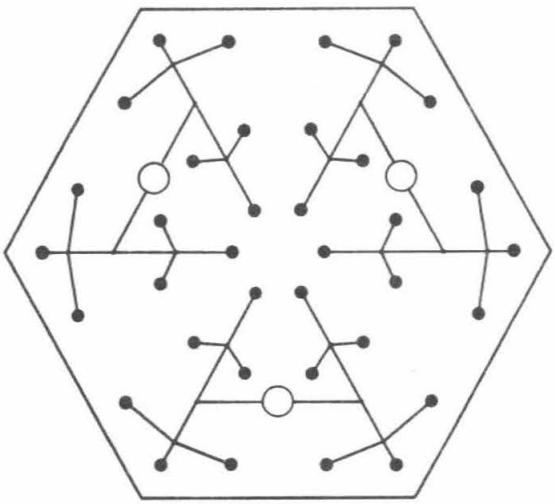

XBL 8212-11990

Figure 8-10 Schematic showing the 36 points of axial support for each segment and the three whiffletrees used to connect those points to the three actuators.

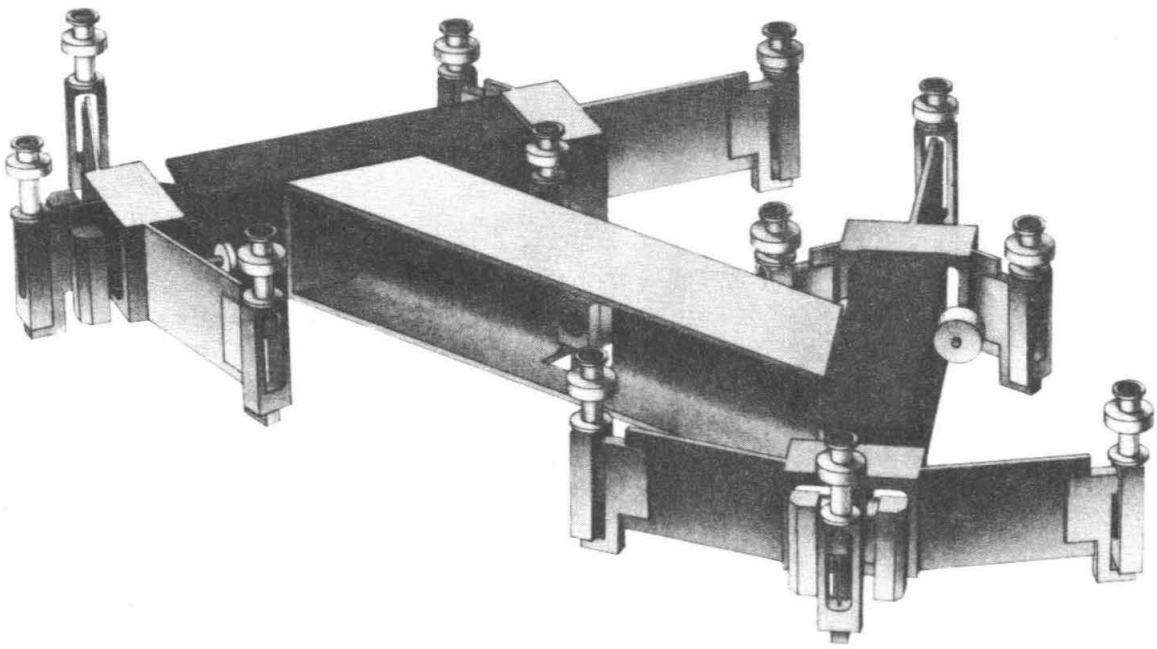

Figure 8-11 Drawing of one of the three whiffletrees used to support each segment. Each whiffletree attaches to the segment at 12 points through flex-rods. Flex pivots connect a primary beam to two secondary beams which in turn connect to four tripods.

The coupling of each of the 36 points to the mirror is provided by a flex-rod assembly (Figure 8-12 BBC 836-5531). This assembly uses a piece of drill rod (1.3mm dia and 50mm length) in tension and allows the mirror to literally hang from the whiffletree at 36 points. These flexible rods then serve to 1) allow for differential thermal expansion of the whiffletree and 2) allow for small misalignments in the x-y positions and rotation orientation of the actuators. A small conical post is glued to the glass at each attachment point and the top of the flex-rod assembly then clamps to this post via a spring-loaded snap clamp. The conical post and associated gluing pad are positioned using a precision machined radial arm that rotates about the normal to the segment. The azimuthal rotation angle is measured with an optical shaft encoder. The pads are glued to an accuracy of ± 0.1mm

Performance

Many interferometric tests were made of the circular and hexagonal mirrors on these whiffletrees. The tests measured both the surface of the mirror and also measured the properties of the whiffletrees. For most of these tests the mirror was rotated with respect to the whiffletree support. In addition, some tests were made rotating the mirror-whiffletree combination with respect to the three posts supporting the whiffletrees. These rotations allowed us to measure the aberrations introduced into the mirror by the support, and to separate the component of the support aberrations due to misplacement of the three posts. An extended series of tests on the hexagonal segment showed the rms surface error introduced by the support is 19nm over the hexagon (see Mast 1984, TMT Note No. 92). A spot diagram of the image formed by these aberrations is shown in Figure 8-13. The 80% image diameter is 0.106 arcseconds, a factor of 2 above that budgeted in Table 5-9. The aberrations due to the support were dominated by astigmatism. This support-induced aberration can have two possible causes. Either the whiffletrees themselves cause the aberrations or the position of the support posts induce aberrations.

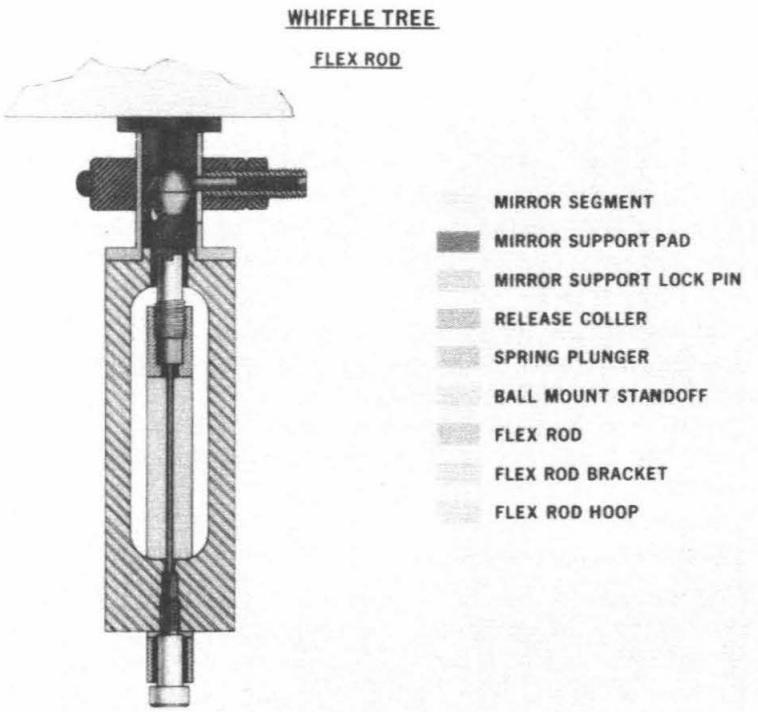

Figure 8-12 Flex-rod assembly used to couple the whiffletree to the glass. Differential thermal expansion of the whiffletree and glass is accommodated by bending of the flex-rods.

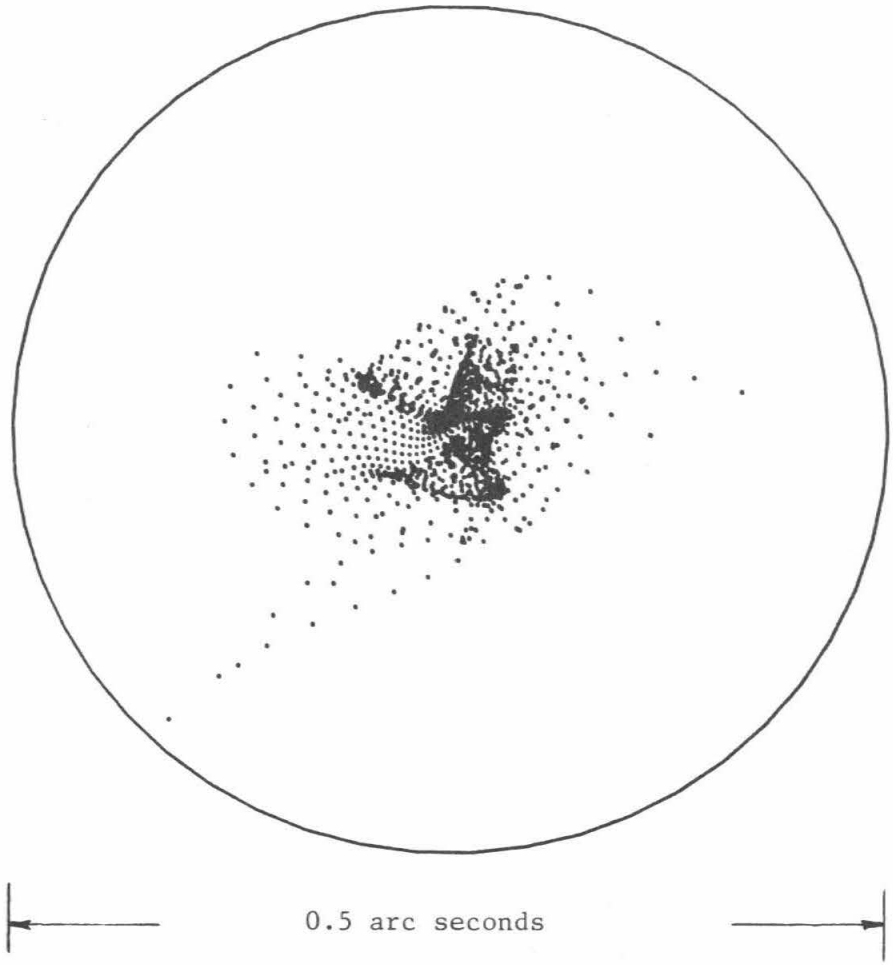

Figure 8-13 A ray-traced spot diagram of the aberrations introduced by imperfections in the whiffletrees. The surface error is 19nm rms and 80% of the energy from a point source is contained in a circle of diameter 0.11 arcseconds.

Post versus Whiffletree-Induced Aberrations

With the circular mirror on the whiffletrees, a set of measurements showed there was astigmatism introduced by the whiffletree support-post misalignment. In addition, the amount and direction agreed very well with that predicted using the finite element method and measured errors in the post positions. The angle of this astigmatism was different from that induced by the combination of the whiffletrees and posts. Thus the whiffletrees themselves also introduce astigmatism. After these tests the mirror support was disassembled and the hexagon was cut and bored. After reassembly of the support, the extended series of tests of the segment was made. These tests showed 19nm rms surface error due to the support and an amount and direction of astigmatism that was consistent with that measured before.

Whiffletree Stiffness

Since the whiffletree is between the actuator and the mirror its resonant behavior is of critical important to the bandwidth of the active control system. The present whiffletree-segment combination has a lowest resonant frequency of about 20Hz. This comes from a variety of sources, but is dominated by the primary flex pivot. The flex pivots are not as stiff as desired under loads perpendicular to their rotation axis.

Future Improvements

At the time of this writing an improved whiffletree is being designed. The improvements are focusing on two aspects; the flex pivots and the flex-rod assembly.

An alternative design for a flex-pivot is being studied. The pivot for the tripod consists of simply two vanes machined into a rod of steel. For the primary and secondary (one degree of freedom) pivots, a single vane is used. The two vanes are at a right angle to each other. The advantages are 1) greater transverse stiffness, 2) simplified design, 3) lower cost, and 4) the ability to design and fabricate specifically to the needs of our application. The second improvement is in the flex-rod assembly. The proposed new design uses thicker rods under compression instead of tension. In addition, the rods will be attached to inserts glued into holes in the glass and located in the central plane of the segment. The advantages are 1) a reduced part count, 2) greater stiffness and 3) less stringent fabrication tolerances because transverse forces introduce negligible moments into the mirror. Having the attachment point in the central plane should remove any moments presently being applied by transverse forces at the attachment point on the surface. This may be the cause of the aberrations described above.

In the coming months we plan to finish the design studies, fabricate, install, and test a new whiffletree.

8.3.2 Radial Support

Degrees of Freedom

A separate mechanical system is used to carry the in-plane mirror loads. This system constrains the segment in the three passive degrees of freedom; in-plane positions (x and y in the local coordinate system) and rotation about the segment normal (local coordinate z-axis). At the same time it must allow almost completely free motion in the three actively controlled degrees of freedom; piston and two tilts. These motions may be as large as $\pm$ 0.3mm of piston and $\pm$ 0.05 degrees of tilt.

Mechanical Design

This combination of constrained and unconstrained degrees of freedom is achieved by holding the segment with a flexible disk or diaphragm at the center of gravity. A schematic drawing showing the concept is given in Figure 8-14. A detailed drawing of the radial support post assembly is shown in Figure 8-15. The design is described by Weitzmann (TMT Technical Note No. 114). A hole (254mm diameter) is drilled in the back of the segment and a threaded Invar ring insert is bonded into the hole. A steel diaphragm is bolted to the end of the radial support post. A threaded Invar clamping ring is centered and clamped to the diaphragm. The clamping ring is screwed into the insert. The two rings and screw threads are shown as a single ring in the Figure 8-14. The threads allow adjustment of the depth of the diaphragm in the hole and easy installation and removal of the post from the segment. The diaphragm is of high-strength steel. Concentric with the diaphragm is a displacement-limiting disk that uses a circular cavity in the clamping ring to safely limit the segment motion. This limits the diaphragm excursion to $\pm$2mm. The surfaces are dimensioned to prevent deformations of the diaphragm in excess of the design elastic limit.

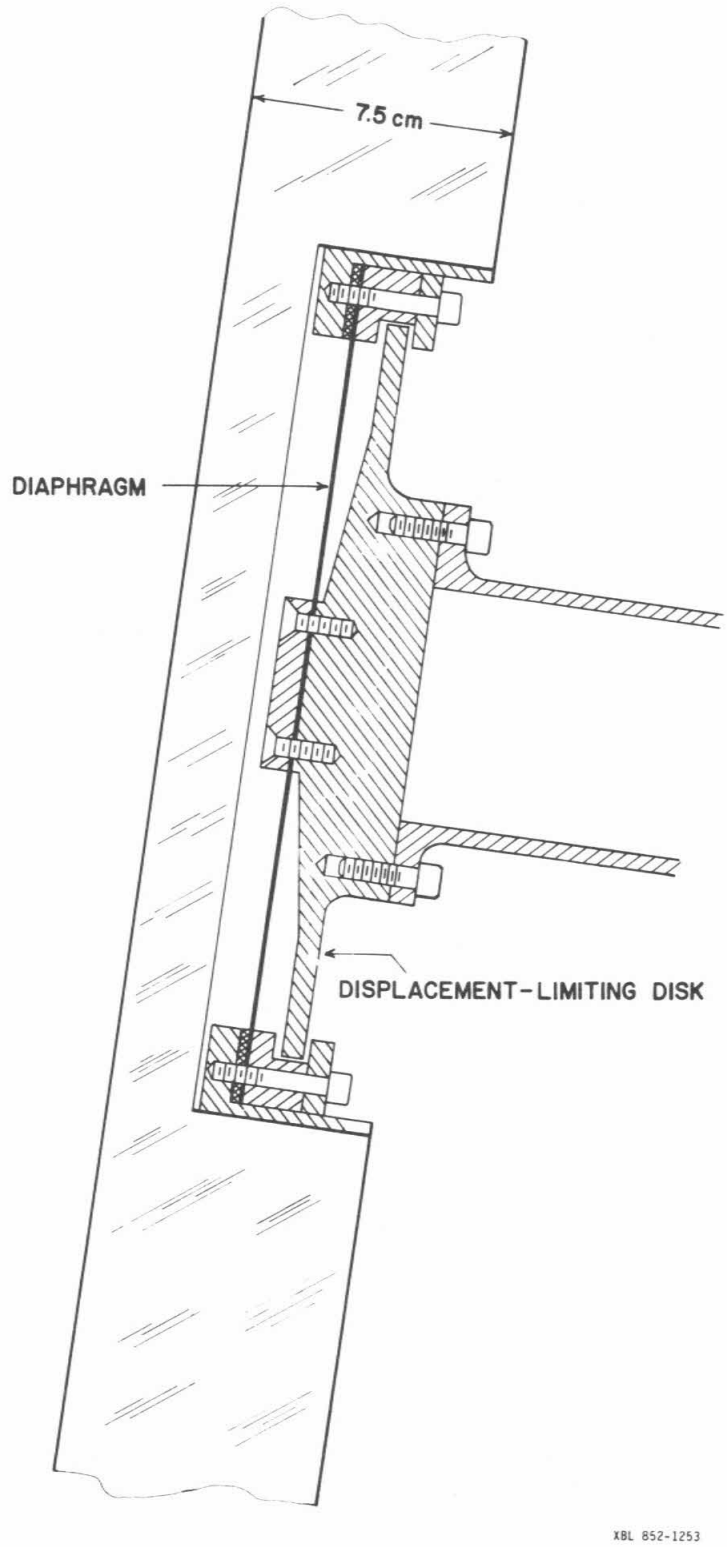

Figure 8-14 Schematic showing the diaphragm and radial support post for providing the radial support for each segment. The diaphragm is set in a hole in the back of the center of the segment and allows the small amount of piston and tilt motion required by the active control system.

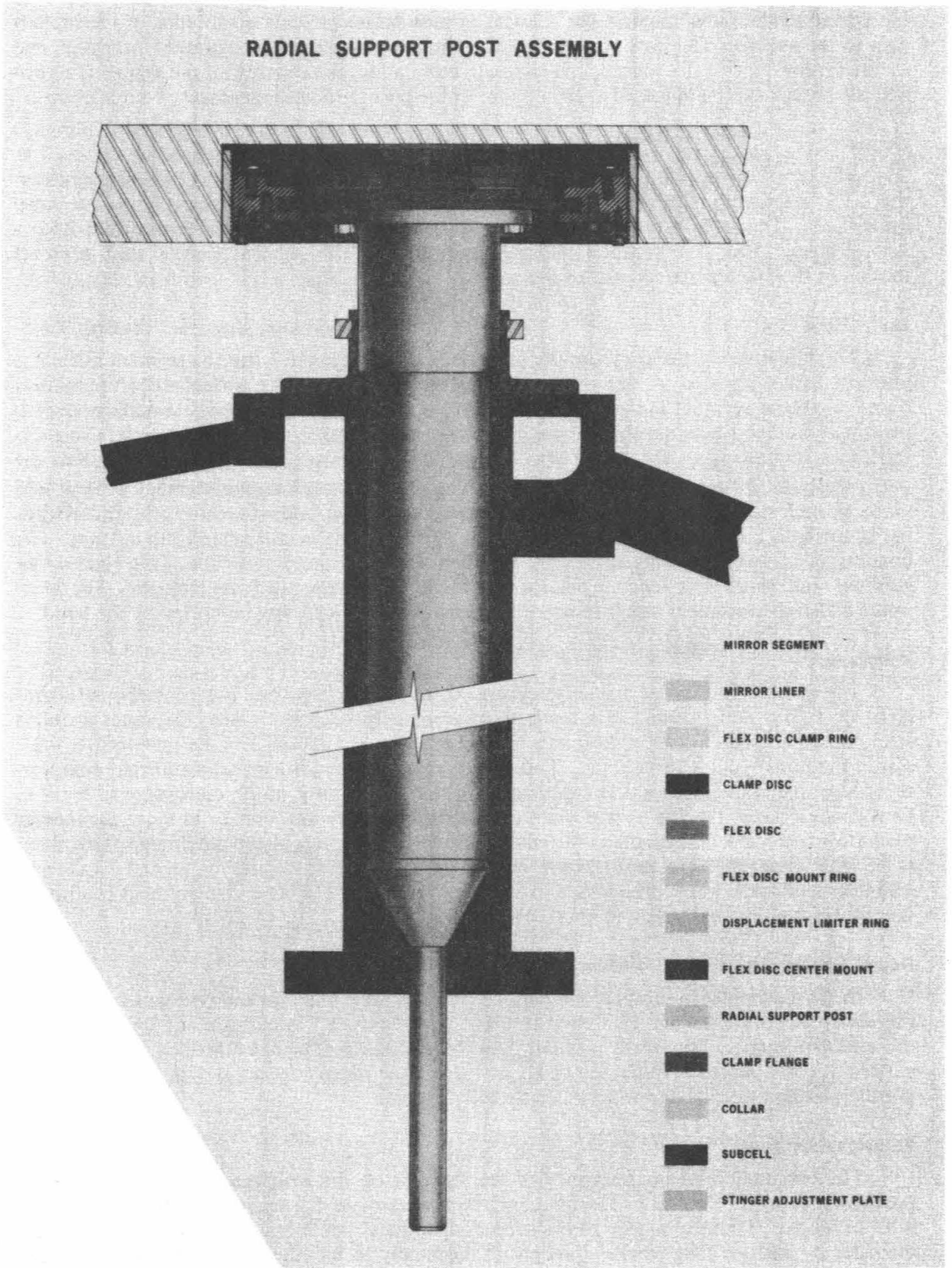

Figure 8-15 Detailed drawing of the radial support post assembly used in the active control system prototype.

Transverse loads from the diaphragm and/or displacement-limiting disk are then transferred to the radial support post. Locating pins assure accurate positioning of the support post to the subcell. The post (xxm long and 76mm in diameter) is constrained near each end by the central tube of the subcell. To facilitate installation and removal of the segment, a portable screw jack can be mounted at the bottom of the post to raise the segment about 200mm.

Geometry

Motion of the post and segment when using the screw jack is along the local segment normal. The diaphragm is tangent to the segment plane and thus is not perpendicular to the global optical axis. The angle between the global optical axis and segment normal varies from 2.55 to 7.65 degrees. This configuration allows motions along the segment normal and prevents motion in the plane perpendicular to the normal.

Insert Bond

The radial support post carries the entire load of the segment when the segment normal is pointing to the horizon. A finite element analysis was made of the surface distortions introduced when the segment is looking at the horizon. It showed that significant surface error is present if the bond between the ring insert and the glass is made over the full circle. This distortion is minimized to the extent that the bond can be made at only two points that are horizontally on either side of the hole axis. For the control prototype segment a bond was made on each side of the axis, extending 30 degrees above and below the midplane, and extending 38mm into the hole. The total bond area is $1.03\times10^4 mm^2$ and the bond gap is 1mm. The bonding agent was a Silicone elastomeric adhesive (Dow Corning series 700). This bond configuration was tested in a separate fixture and found to provide adequate strength. The maximum radial displacement was 0.16mm when the full mirror load was supported by the bond.

Diaphragm

The diaphragm is a flat disk of thickness 0.25mm. The inner and outer attachment diameters are 0.05m and 0.10m. It is made from grain-oriented cold-worked 300 series stainless steel (tensile strength = $17\times10^3 kgf/cm^2$, yield strength = $14\times10^3 kgf/cm^2$, Poisson ratio = 0.27, elastic modulus = $2.1\times10^6 kgf/cm^2$. This thin diaphragm cannot support significant compressive loads; the segment weight is supported by essentially a strip of the diaphragm in tension. Only modest forces ($\approx$ 5kgf in the worst case) are required by the actuator to make the 0.6mm piston displacement. Calculations of the operational stress levels in the diaphragm show them to be well below (20%) the fatigue limit, resulting in an expected infinite life for the diaphragm. Life tests have been made of the diaphragm under maximum load and displacement conditions and no degradation was apparent after 10×10^6 load cycles.

Radial Support Resonance Behavior

In the assembled prototype, measurements have been made of the resonant behavior of the radial support when the azimuthal restraint was removed. Impulses made on the edge of the segment excited transverse motions that were measured with an accelerometer. These yielded a lowest resonant frequency of about 13Hz. The radial support system for the TMT is presently being designed and will be substantially stiffer.

Azimuthal Stiffness

The torsional resonant frequency of the segment on the whiffletrees and radial support post was measured to be 5Hz. The frequency is dominated by the torsional stiffness of the subcell. In the active control prototype the azimuthal stiffness was increased by means of a 3.8mm diameter by 300mm long steel rod attached tangentially to the underside of the segment near the outer edge and anchored to the mirror cell. This azimuthal support rod increases the resonant frequency to 25Hz. As the rod flexes laterally when the actuators drive the segment, an axial force component is introduced into the segment at the rod attachment point. This force is less than 0.1kgf for maximum segment displacements.

Alignment

Alignment and load interfaces between the radial support post and the concentric tubular support element are provided at three locations in Figure 8-15. An adjustable axial position collar ensures proper elevation height of each segment above mirror cell nodes. Two close-tolerance alignment pins are press fitted into the segment radial support post assembly. These are spaced 180 degrees apart to ensure azimuth and radial x-y position alignment and also act as the primary radial load transfer components. A further radial x-y position adjustment point is located at the radial support post extremity. The required radial adjustment motion is accommodated by an oversized internal diameter in the tubular support element. To absorb seismic loads, the radial support post is secured axially to the tubular support by means of a bolted plate as shown in the figure.

8.3.3 Surface Correcting Systems

As described above in Section 8.1.2, the mirror for the active control prototype warped substantially (about 0.5μm rms) when it was cut into a hexagon. Although this warping may have been caused by the mistake made in not removing the grinding stresses in the convex surface, this cannot be proved. Thus we must assume that in the fabrication of the TMT segments we will see comparable warping of the surface due to cutting. In addition, some warping was also caused by the boring of the radial support hole. There are several ways of addressing this possibility, and we describe one of those methods here.

This approach is to proceed with the proposed fabrication process, and then if the mirror warps, we will add a mechanical device to the glass or support which "unwarps" the mirror. This device remains in place forever.

The method has both positive and negative features. It is a complication which, of course, we would prefer to avoid. It is additional hardware on the back of the segment which 1) is already crowded and 2) may require maintenance. In general we would prefer to have the correct surface polished into the glass. On the positive side however is a potentially large cost savings. If a warping fixture can adjust the final figure from about 0.5μm down to the 30nm level, then the final expensive stages of polishing can be eliminated. In fact as seen above in Section 8.1.3, KPNO achieved with stressed mirror polishing a surface this good with only one stage of polishing. In addition, such a warping fixture could be used to reduce support aberrations.

In the light of the above we decided that at least one method of solving the warping problem needed to be proved before proceeding with this report and the project. The particular fixture explored here is not the most elegant that has been designed. However, it could definitely be used in the TMT. Other mechanical designs (for example flat leaf springs on the glass) are being studied. Only limitations of manpower and schedule have delayed their development.

We have designed, built, and tested a warping harness that uses springs to apply forces at the whiffletree contact points in order to correct the figure. The surface correcting system needs to be gravity independent as opposed to the whiffletree system which is gravity dependent. So springs are suitable. The desired reduction in rms surface error is from about 0.5μm to about 0.030μm, or about a factor of 17. Thus the spring system needs to be stable over a long period of time, and over a temperature range -10^{o}C to $+15^{o}$C, to better than 6%. This is quite feasible with springs. Several spring systems have been discussed and two have been tested.

Leaf Springs on Whiffletrees

The first system used leaf springs to apply moments across the flex-pivots of the whiffletrees. This system failed to achieve the desired surface (See Mast, 1984, TMT Technical Note No. 92). The design of the system was simple. But the implementation relied on introducing forces throughout the whiffletree system, moments transverse to the flex-pivot axes, and moments into the actuator. These moments caused rotations of the whiffletree beams about axes other than the usual flex pivot axes. We surmise that these small rotations may have been

the cause of the failure to achieve the desire surface correction. However, we were unable to prove this. We abandoned this design and proceeded to a system that relied less on the internal rigidity of the whiffletrees.

Leaf Springs on the Back of the Segment

An alternative system using leaf springs has been proposed but has not yet been analyzed or tested. This system would apply forces and moments directly to the back of the mirror. The leaf springs would be low profile strips of steel lying close to the back surface and attaching to the glass at each end. Thus the warping harness and whiffletree systems would be independent of each other. This system will be studied further and will be tested if feasible, since it promises to have high resonant frequencies, require less volume, and eliminate any potential interactions with the whiffletrees.

Helical Springs on Whiffletrees

The second system tested used helical springs between the bottom of the whiffletree tripods and the mirror cell. A spring on each tripod applied a force at a point slightly offset from the tripod universal joint. Twelve spring forces and the x and y offsets thus provided the means to apply 36 forces to the mirror at the whiffletree pads.

A preliminary test of the method was made using weights instead of springs. To partially test the feasibility of applying forces at the whiffletree pads, we hung a set of weights from shoulder bolts of the whiffletrees (Mast 1984, TMT Technical Note No. 94). A set of 11 weights were used that applied forces of the approximate magnitude to remove the warping. No attempt was made to remove the exact values of the real warping that occurred. It was felt that agreement between predicted and observed deflections for an arbitrary set of weights of the same magnitude was sufficient to prove the method. The weights applied varied from 3.3 to 6.7kg. The weights required to remove the warping due to cutting are of comparable size. The rms deflections expected from the 11 weights was 406nm. We expected 586nm of C_{20}, 719nm of $C_{2\pm2}$, and 64nm of $C_{3\pm1}$. The difference between the deflections achieved and those desired was 35nm. Much of this is attributable to measurement noise. Thus we were strongly encouraged that this method could work.

The warping from cutting was primarily a change in focus, which required compression of the springs on the inner ring of tripods and tension on the outer ring. Thus mechanisms to apply both were designed, built, and tested. The spring mechanisms are very simple, easily calibrated and by calculation are stable to much better than the 6% required.

Interferograms were taken in a series of tests with the springs alternately on and off. Finite element calculations predicted that the 36 forces could reduce the rms surface error from 538nm to 27nm (Budiansky 1984, TMT Technical Note No. 95). The difference between the measured deformation and that predicted was 42nm rms. The difference between the measured deformation and the deformation required to remove all of the warping was 48nm rms. The rms uncertainty in the measured is about 8nm. Thus without iteration the achieved deformation is consistent with the predicted deformation and the deformation required to meet the TMT error budget of 39nm rms.

8.4 Active Control System

Summary and Conclusions

An assembly to test the proposed active control system has been designed, built, and operated. The design, goals, and results are described in the following three sections. The assembly contains a single full-sized hexagonal segment supported by whiffletrees and a radial support post and controlled by three actuators. The piston and tilts of the segment are measured with respect to a portion of a neighboring segment using four displacement sensors.

The goals for these tests were set by the performance requirements for the TMT active control system. These goals include limits on sensor noise levels, sensor stability, system stability, and active control reduction of external perturbations.

Measurements of the prototype assembly show that sensor noise levels are about 1nm, i.e., negligibly small. Sensor thermal dependence is about 2nm/^{o}C. This is marginally at a level needing correction, and thus only a rough temperature correction lookup table will suffice. The long term sensor stability tests (over a month) show variations of about 3nm per day, suggesting calibration using a star would be required about every three days. The sensitivity to transverse motions of the segments is also at a small enough level to allow for elevation angle correction using a lookup table.

The response of the active control system to piston forces applied to the mirror has been measured under a variety of conditions using control sampling frequencies up to 38Hz. The resonance characteristics of the whiffletree and flexibility of the reference mirror support structure limit the performance of the system. In the process of reducing the amplitude of the driven frequency the system excites the structural resonances that leak into the control via a hinging motion of the reference mirror. The structural elements oscillate at frequencies in the 20 to 30 Hz range. With these limitations the control system reduced the rms amplitude of perturbations at 0.2Hz by a factor of 3.

The structural resonances in the prototype are different from those expected in the TMT. Additional tests of the system were made with the structure stiffened and some of the resonances damped. Under these conditions the rms sensor reading was reduced by a factor of 3 at 1Hz. These results were then limited by delay in the control response from a phase shift induced by a notch filter used to remove a remaining resonance and by delay induced by the control calculation time. The measured results agree with a mathematical model of the system.

From the measurements with the active control assembly we draw the following conclusions.

1. The active control components, algorithm, and system performs as designed.

2. The performance of the control system in the present prototype configuration is limited by the presence of resonances in the segment support structure. The greater symmetry of the TMT mirror cell will eliminate some of the problems observed with the prototype in which the reference mirror and segment are supported on different structures. The stiffness of the support elements now being designed for the TMT segments must be emphasized in that design.

3. If the prototype structure is made stiffer, then the performance is limited by computation delay time and phase delays introduced by filters to remove remaining resonances. The computing hardware designed for the TMT will reduce the computation time to a level, at which it will introduce negligible delay (100μs). If resonances in the support structure are moved to higher frequencies, then control can be achieved without filters and their associated delays.

8.4.1 Active Control System Prototype: Design

The design of the prototype assembly needed to test the active control system concepts was based on many considerations. It was apparent that the more closely the prototype approximated the TMT design, the more confidence we could develop in the overall design. Initially, a design using three full-sized segments was proposed. The piston and tilts of two segments would be controlled with respect to a fixed third. This would test what might be viewed as a single "unit" of the primary mirror, with the whole primary viewed as an assembly of such units. Later this design was scaled down to a single full-sized segment controlled with respect to a fixed portion of a neighboring segment. This was selected because of the considerably smaller cost and fabrication time. The design selected of course tests the actuators, sensors, and passive support system proposed for the TMT. In principle the design also tests all of the mathematical aspects of the TMT control system. However, in practice we have discovered a number of important differences between the prototype design and the TMT design. The lack

of symmetry in the prototype means that it is not a "unit" of the TMT primary. There are differences in the dynamic characteristics. In the prototype the reference mirror and the segment are supported on quite different structures. This makes their resonant behavior different. In addition, experience with the structure shows resonances in the structure that were not originally thought to be there and that affect the active control system performance. These are described below with the results of the active control tests.

Active Control Design

A plan view of the primary mirror is shown in Figure 8-2. The system has three actuators and four sensors. Three sensors are sufficient to measure the three degrees of freedom under active control, thus four sensors provide redundancy, which is also an important part of the full TMT system. The difference between the TMT geometry and prototype geometry leads to a difference in the precision of the measurements of the different degrees of freedom. Since sensors surround each segment in the full TMT, all three degrees of freedom are measured with lever arms on the order of a meter. Only a global focus degree of freedom is measured with the small sensor lever arm L (center of sensor capacitor to center of segment gap distance). In the prototype, however, one of the tilt degrees of freedom (hinging of the segment with respect to the reference mirror) is measured by only the small sensor lever arm. Thus this degree of freedom is about ten times more sensitive to sensor noise. A quantitative description of the control algorithm for the prototype and the expected performance is given by Mast (1983, TMT Technical Note No. 60)

Optics

Limitations of the budget and schedule, and the ease of testing dictated that the surface should be spherical rather than the off-axis section of a paraboloid. (The program at KPNO was relied upon to demonstrate the fabrication of off-axis segments.) The limited size of the building available for the test motivated the choice of a 10m radius of curvature. Both the reference mirror and segment were cut from the same circular mirror; and thus, in principle, the fringes across the gap should be continuous when the control system is aligned and operating. Warping of the two pieces due to cutting and improper support would degrade the quality of this fringe continuity. Since these effects are small and since we are primarily looking for fringe stability, this is not a problem.

The optical system folds the center of curvature back to a point on the Nasmyth platform (Figure 8-16). A Twyman-Green interferometer is mounted on the Nasmyth platform. The interferometer beam passes through the elevation bearing, reflects from a tertiary flat, and is folded to the sphere by the same secondary flat used in the tests at Tinsley. This system allowed interferograms to be made of the segment and reference mirror combination (Figure 8-17). These were used to quantitatively measure the tilts ("hinge" and "roll" and piston of the segment. The fringe pattern of the interferometer could be recorded either with the 35mm camera used in the tests at Tinsley or with a video camera and recorder (Panasonic).

Optics Support

The segment in the prototype is mounted on whiffletrees and radial support post designed for the TMT. Thus the prototype assembly also serves as a test facility for the passive control systems. The unusually shaped reference mirror requires a rather specialized support and is described by Budiansky (1983, TMT Technical Note No. 80) and Osborne (1983, TMT Technical Note No. 85). The actuators and radial support post are mounted in a precision subcell (Budiansky, 1982, TMT Technical Note No. 44). The segment support structure is illustrated in Figure 8-18. The subcell and reference mirror are mounted on a steel space-frame mirror cell (Budiansky, 1983, TMT Technical Note No. 59). The mirror cell is in turn part of a quasi-telescope shown in Figure 8-16 and Figure 8-19. The design and structural analysis of the design are described by Nelson (1981, TMT Technical Note No. 26) and Budiansky (1982,

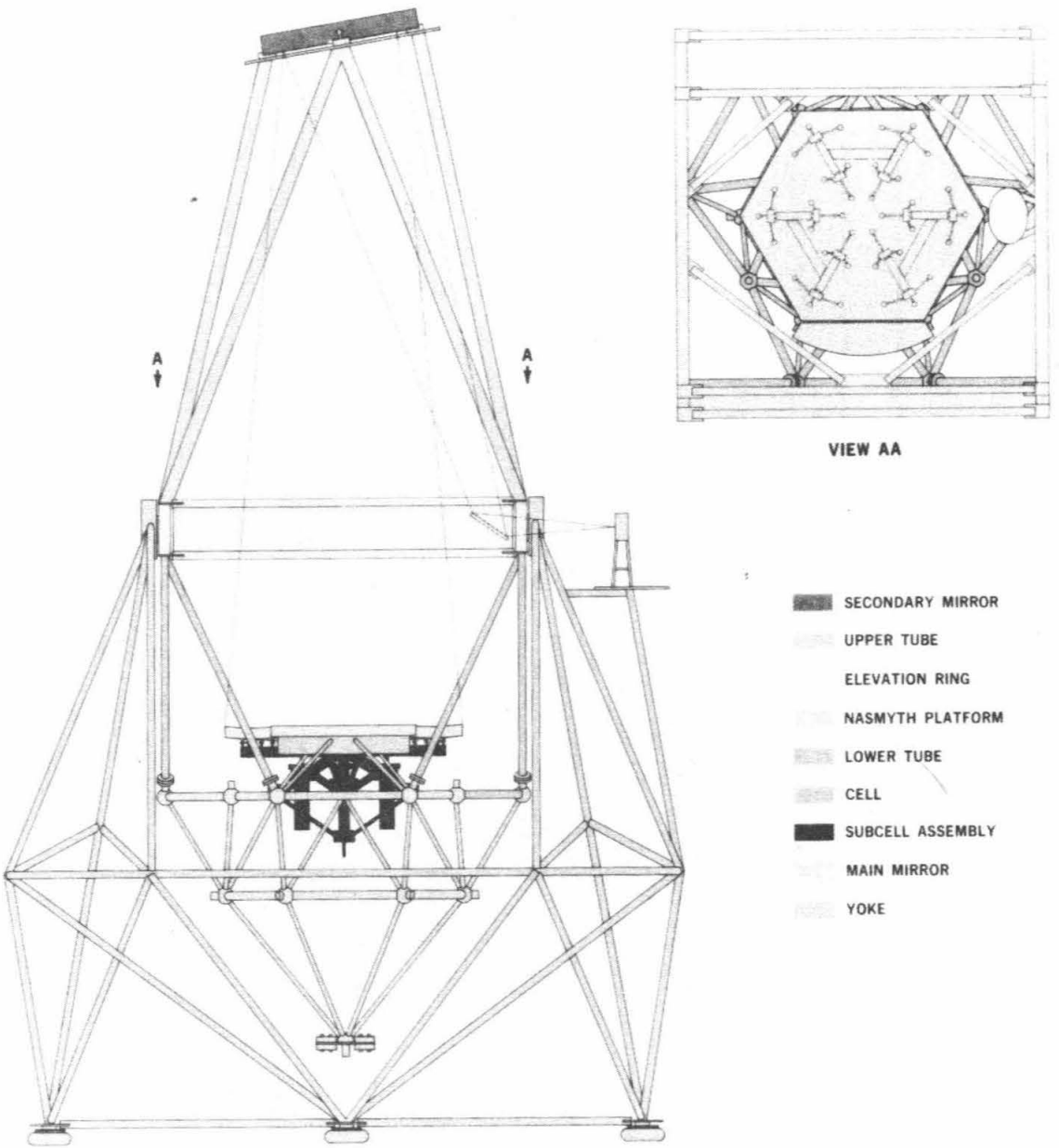

Figure 8-16a Schematic of the "telescope" structure and optics of the active control system prototype. The optical elements (segment, reference mirror, secondary flat, and tertiary flat) are shown. The beam is folded through a hole in the elevation bearing. An interferometer is used at the center of curvature.

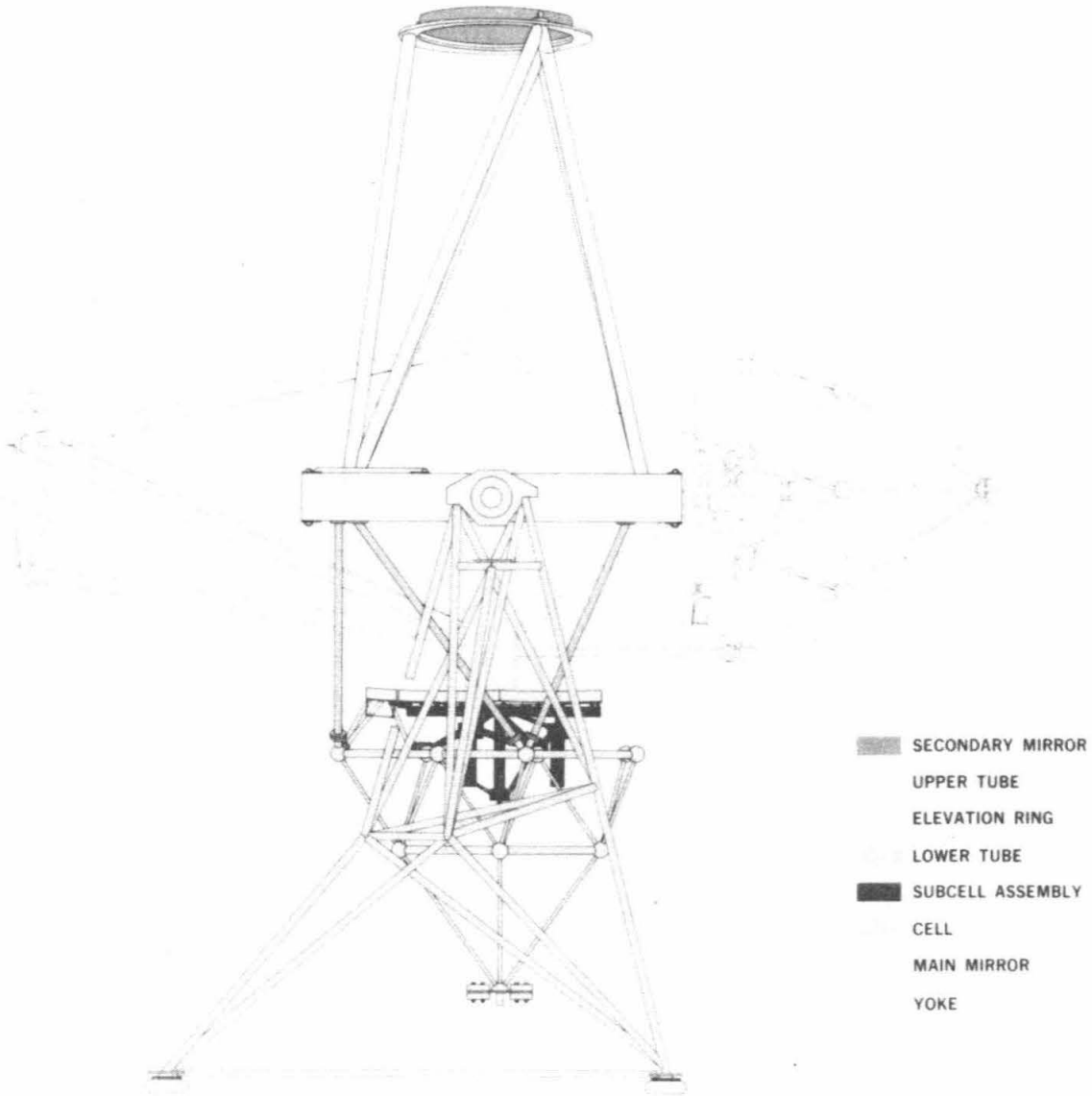

Figure 8-16b A view of the active control system prototype showing the yoke which supports the telescope structure and allows elevation angle changes.

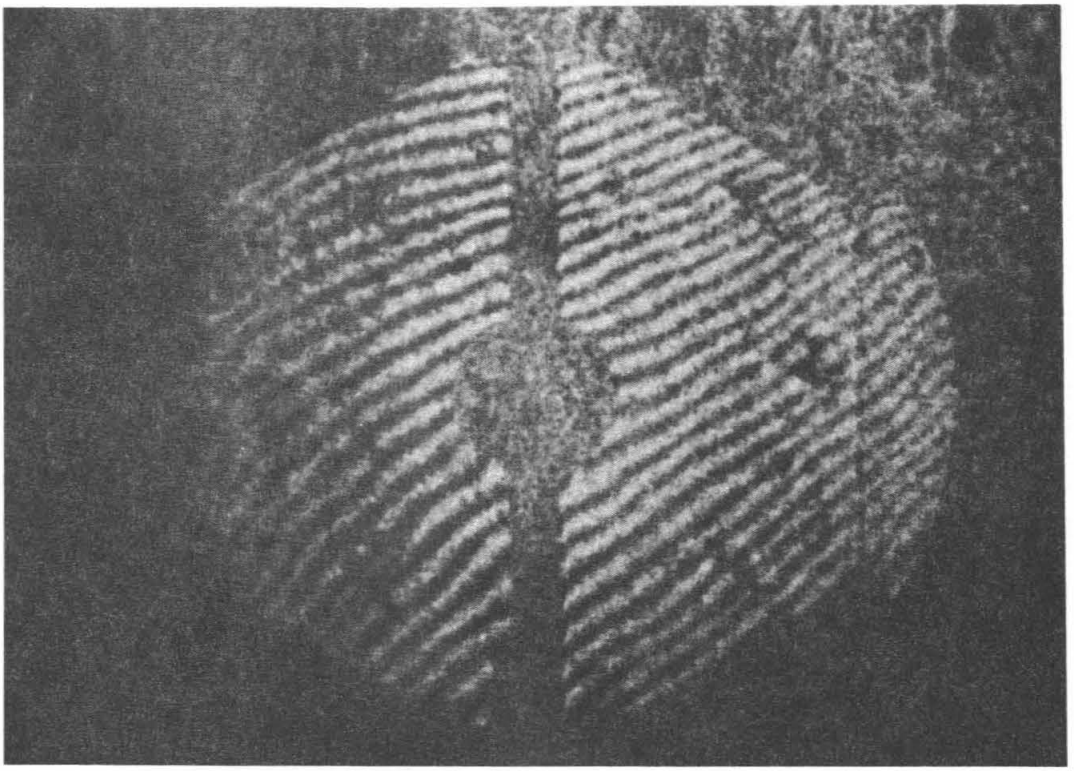

Figure 8-17 A photograph of an interferogram of the segment and reference mirror combination in the active control system prototype. The segment and reference mirror have been aligned and the control system is operating.

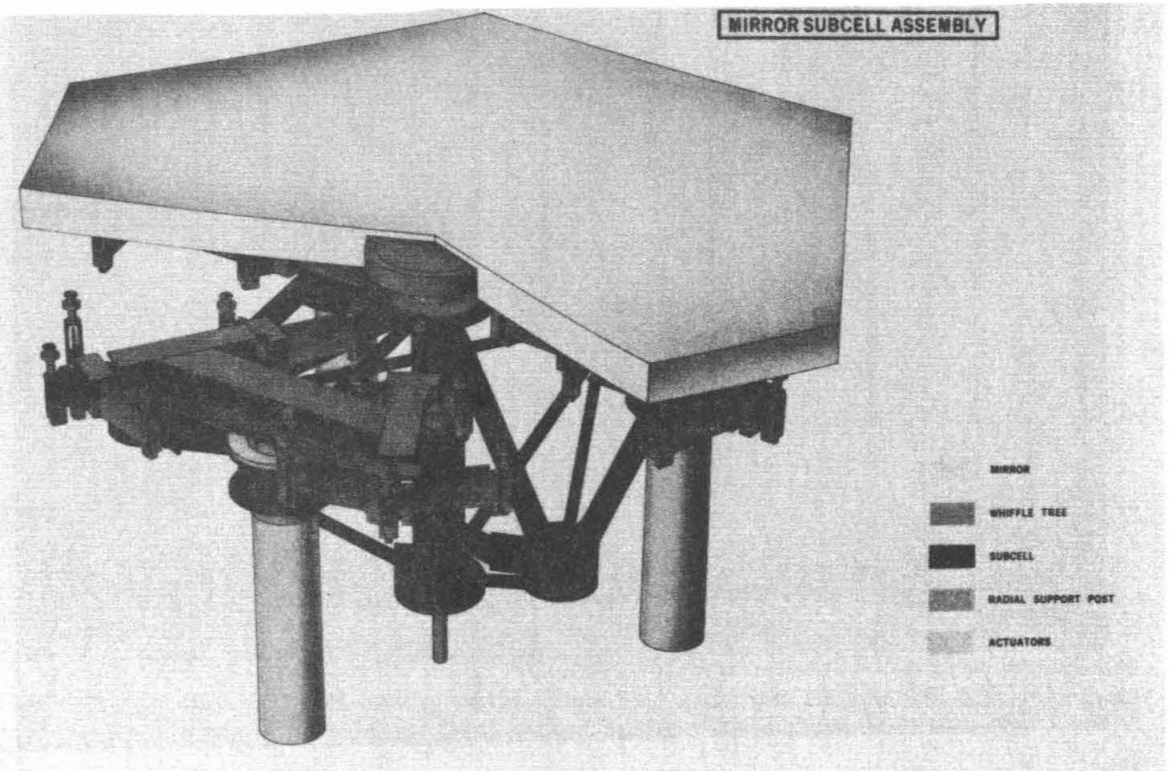

Figure 8-18 A drawing of the subcell assembly with a mirror segment. Shown are the welded steel subcell, three actuators, three whiffletrees, and the radial support post.

Figure 8-19 The telescope structure of the active control system prototype shown with the glass hexagonal segment and reference mirror installed.

TMT Technical Note No. 29). The telescope supports the optics and allows slewing the system from zenith to horizon. The entire structure rests on three inflated tube vibration-isolation pads.

The structure is housed in a sheet metal building with overhead crane. The thermal environment is extremely severe compared to that expected on Mauna Kea. On many days of the tests the temperature has reached 40°C, diurnal variations of 15°C or more are common, and a vertical gradient of 10°C or more is present during the day. These conditions stressed the electronics and often made optical testing difficult. A set of sensors was used to monitor the temperatures of the air and the top and bottom of the mirror.

Vibrations from a large motor generator at the nearby Bevatron, nearby air conditioning systems, and construction of an adjacent building made significant contributions to the segment motion.

Electronics

Electronics for the system are mounted on one of the Nasmyth platforms. This includes the sensor electronics, power supplies for the actuators, and power supplies for logic circuits. A computer (LSI/11/23, 256 kilobytes memory) for operating and monitoring the control system is in an adjacent room. The computer system includes a dual floppy disk drive, a hard disk (10.4 megabyte RL02), a graphics terminal, and a printer. A separate terminal was used to communicate with the M68000 microprocessors used to control the local loop of each actuator.

8.4.2 Active Control System Prototype: Goals

The goals for the active control performance are defined in Mast, *et al.*, (1984, TMT Technical Note No. 97). They are derived from the error budget for the TMT primary mirror. The control system is budgeted for a contribution to the rms surface error that would give 80% of the energy from a point source in a circle of diameter less than 0.084 arcseconds (Table 5-9).

Sensor Noise

Using the equations in Section 5.4 relating sensor noise and image blur, we find the rms sensor noise is required to be $\leqslant$ 14nm.

Using the geometry of the prototype we can translate this sensor noise into rms segment motion in the prototype. The resulting goals for hinge (α), roll (β), and piston (γt) are:

$$\alpha_{rms} \leqslant 0.046\text{arcseconds}$$

$$\beta_{rms} \leqslant 0.005\text{arcseconds} \qquad (8\text{-}2)$$

$$\gamma_{rms} t \leqslant 176\text{nm}$$

The actuator motion is digitized in counts of 3.8nm and we have assumed that actuator noise is negligible. The large allowed error in hinge in the prototype is due to its only being measured by the small lever arms of the sensors. The large apparent piston is simply an artifact of the hinging motion. The goal for the relative vertical displacements of the two pieces at the gap is $\leqslant$ 7nm.

Sensor Stability

In the TMT, variations of the sensor readings with temperature and elevation angle can to some extent be corrected with lookup tables. Thus we require that the residual drift after these corrections are made be $<<$ 14nm. This should hold true over a temperature range $\pm 10°$C, over the full elevation angle range 0° to 90°, over in-plane segment motions of 0.25mm, and preferably over time periods of 8 hours or more.

Control Loop Stability

Without perturbations, but with the control system operating, the rms surface motions should meet the requirements of Equation 8-2. Thus activation of the control loop should not itself degrade the image.

Control System Response to Perturbations

Wind forces are expected to be the highest frequency perturbations driving the segments. We have made a very conservative estimate of the magnitude and frequencies of these forces (Mast, *et al.,* 1984 TMT Technical Notes No. 97). We assumed a 30mph wind at the slit, reduced it by a factor of 10 at the primary mirror, assumed a drag coefficient of 1.0, and assumed a worst case where adjacent segments are alternately loaded and not loaded. These assumptions give a force of 0.016kgf on the segment. Using a measured resonant frequency of the segment support system of 26Hz, we calculate a motion of 130nm. To derive a typical driving frequency we simply took the time for the wind to cross a segment, to get 0.7Hz. Based on these estimates we set a conservative specification for the dynamic response to be a reduction by a factor of 10 at 1Hz for amplitudes less than 200nm.

8.4.3 Active Control System Prototype: Results

Presently the tests and improvements of the active control prototype are still in progress. Nonetheless, many tests have been made and some of the goals outlined above have been achieved.

Sensor Noise

If the control system is not operating, each of the four sensor readings shows a random scatter during a data collection period of a second to a minute. This scatter is typically 10 to 20nm and these readings are dominated by actual motion of the segment. This motion is induced by seismic motion of the structure. We can remove this motion mathematically to measure the intrinsic noise in the sensors. We fit the four sensor readings by removing the best fitting segment position and then look at the sensor residuals to this fit. The scatter in the residuals is then a measure of the intrinsic sensor noise. Over many tests and in a variety of conditions this noise is 1nm rms or less. Its value is approximately that expected from the digitization noise of the ADC. Thus the intrinsic sensor noise is an order of magnitude smaller than the limit set in Section 8.4.2 above.

Sensor Stability

The sensor stability as a function of temperature has been studied on many occasions. The data taken during weekend runs of the prototype over a period of several months shows a thermal coefficient of about 1nm to 3nm per degree centigrade. Figures 8-20 and 8-21 show the data from a typical run. Figure 8-20 shows the air temperature as a function of time during a 60 hour run. A diurnal variation of about 9^{o}C is seen. The control system was operating to maintain the segment position with respect to the reference mirror through this period. Figure 8-21 shows one of the four sensor residuals. The diurnal variations in the residual are 8nm. Since the control system moves the segment to achieve the minimum residuals, the residual is smaller than the true intrinsic change in sensor reading. Since we have only one redundant measurement we cannot tell which or how many of the sensors have a thermal sensitivity. If all sensors have random and independent thermal coefficients, then the magnitude of the drift is about 1.6 to 2.7 times the residual (Mast, 1984, TMT Technical Note No. 60). Under these assumptions, the thermal coefficient is about 2nm/^{o}C.

Tests of the thermal sensitivity of the electronics in operation have been made by disconnecting the sensors and monitoring for 60 hours the variations in the output. These variations are small compared to those observed from the sensors and thus the thermal variation is caused by a sensitivity in the sensor itself.

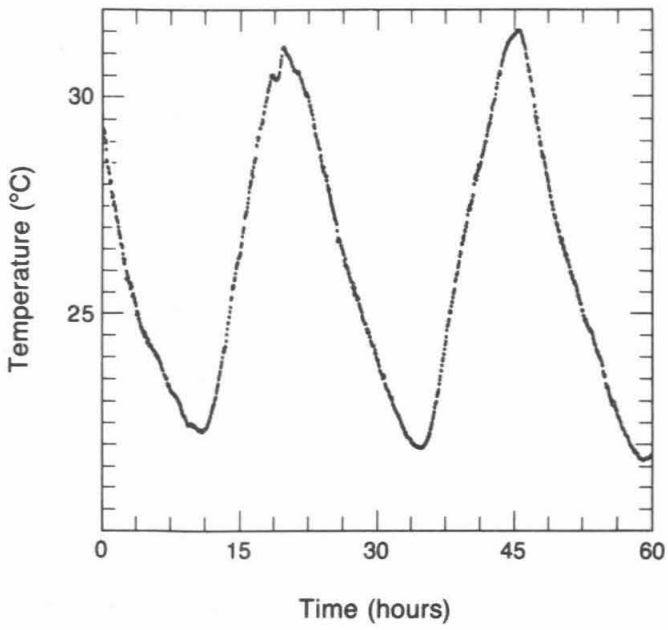

Figure 8-20 Air temperature as a function of time during a 60 hour sensor stability test. A diurnal variation of about 9^{o}C is seen.

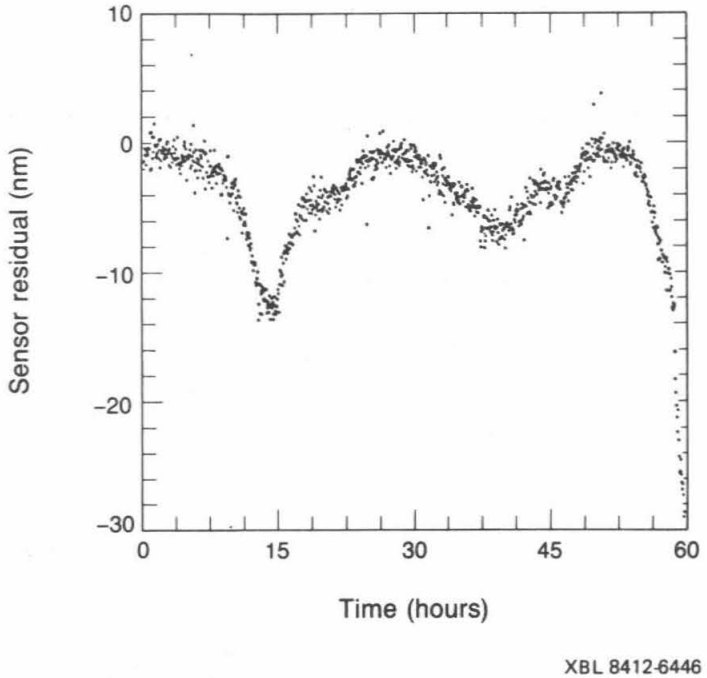

Figure 8-21 Data from the 60 hour test shown in Figure 8-20. To measure the stability of the sensors the sensor readings were fitted to remove rigid body motion and the residual of a single sensor is plotted versus time. There is a correlation with the temperature variations shown in Figure 8-20 indicating either a dependence of the sensors on temperature or temperature gradients or a differential warping of the two mirrors caused by thermal gradients.

Experience with the sensors in the laboratory shows that 1) the thermal sensitivity is close to 1nm/^{o}C, and 2) that the sensor is sensitive to thermal gradients. In the environment of the prototype tests the temperature changes rapidly. At Mauna Kea the temperature will change more slowly, and thus the thermal gradients induced in the sensors should be reduced. For a range of 10^{o}C we expect a change in sensor readings of about 20nm. This can be easily reduced to much less than the 14nm goal with only a rough open loop correction for temperature by the control computer.

To test the sensor stability over a longer period of time we collected data with the control system operating under identical conditions about 20 times during a month-long period. Over the month the sensor variation was about 90nm. There is a general correlation with temperature that suggests a thermal coefficient of about 3nm/^{o}C. The discrepancy between this coefficient and the thermal coefficient measured during a shorter period is not presently understood. The variation is larger than expected and the origin is not yet known. Without future improvement in the long term stability, the data implies the sensors would have to be recalibrated using a star about every 3 days.

A second stability goal addresses the sensitivity to transverse segment motion. As the TMT moves from zenith to horizon we expect the segments to move relative to one another (i.e., the gaps open and close). An early study of the mirror cell predicted relative motions of the segments of 0.1 to 0.25mm. Similar studies have not yet been made of the present cell-subcell and mirror support system. To test the system sensitivity to in-plane motions we shifted the reference mirror away from the segment by 0.45mm. Interferograms taken before and after the shift and the control system operated throughout the test. Analysis of the interferograms showed the following segment motion induced by the shift:

$$\text{roll} = 0.04 \pm 0.04\text{arcseconds}$$

$$\text{hinge} = 0.45 \pm 0.04\text{arcseconds}$$

$$\text{piston} = 12 \pm 37\text{nm}$$

These motions are sufficiently small that even a rough lookup table correction for temperature and elevation angle will leave negligible residual errors.

Control System Stability

With the local and control loops turned off we typically observe 10nm rms sensor motion. This is due to ground vibrations inducing relative motion (typically tilt) between the segment and reference mirror. When the local loops in each actuator are turned on there is no significant increase in this rms motion. Thus the local loops do not add noise to the system. When the global loop is turned on there is no significant change in the sensor readings.

Control System Response to Perturbations

In order to test the response of the system to external perturbations a speaker coil was mounted over the segment at the center and was used to drive a rod that was bonded to the mirror. The force as a function of time could be either a sine wave or square wave of various amplitudes and frequencies. Typically a sine wave with an 80nm rms amplitude and varying frequency has been used as a forcing function to test the system response.

Some results are shown in Figure 8-22. The rms sensor amplitude is plotted versus the frequency of the applied perturbation. A horizontal line at 80nm shows the rms perturbation of the sensors by the forcing function when the control is turned off. The dashed line is the rms sensor reading with the control loop operating. The control system sampling frequency was 38Hz. Since the sensors are a very sensitive measure of the segment position their readings are a better measure of the system response than interferometric analysis. The solid line is the rms residual amplitude of the driving frequency as determined from a Fourier analysis of the sensor

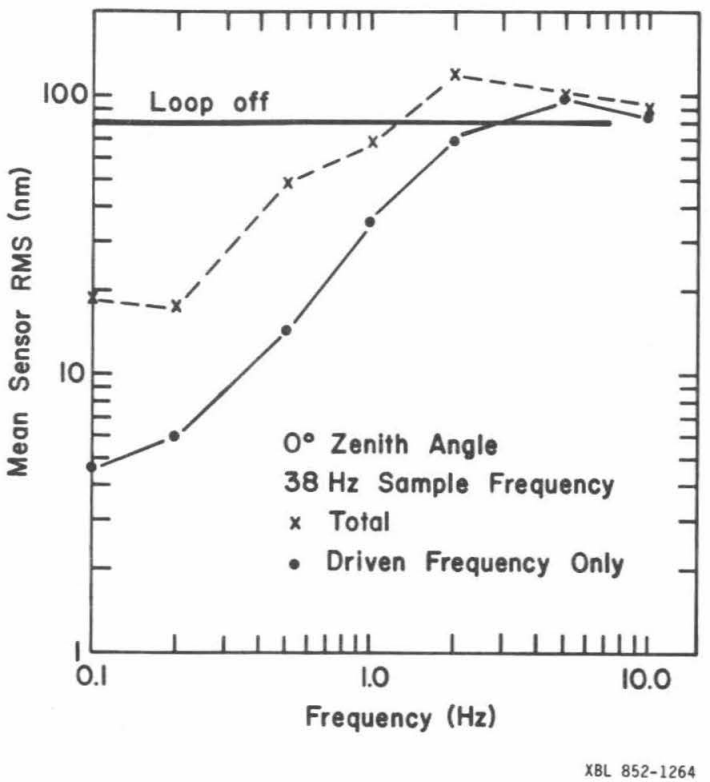

Figure 8-22 The response of the system to a sine wave piston perturbation of the segment. The mean of all four rms sensor motions is plotted as a function of the perturbation frequency. With the global control loop turned off the perturbation induced 80nm rms sensor readings. The dashed line is the total rms sensor readings and the solid line is the rms motion at the driving frequency derived from a Fouier transform.

outputs. The data show that the amplitude at the driven frequency is reduced by a factor of 17 at 0.1Hz and 2.3 at 1.0Hz. However, the data and Fourier transform show that power is pumped into the mechanical resonances of the system and the total rms motion is only reduced to the background noise level (about 20nm rms for this run) below about 0.2 Hz. At 1.0 Hz there is essentially no reduction in rms mirror motion. Figure 8-23 shows the sensor readings with the control system off and with a 0.2Hz sine wave perturbation. The Fourier transform of one sensor is shown in Figure 8-24. The main power is at 0.2Hz, however a small amount of power is in the 20 to 30Hz region where the mechanical resonances of the structural elements lie. Figure 8-25 shows the sensor readings with the control system operating during a 0.2Hz sine wave perturbation. Most of the 0.2Hz signal has been removed. Present, however, is increased motion in the 20 to 30Hz region. This is also seen in the Fourier transform of one sensor in Figure 8-26.

Analysis of the source of the structural resonances lead to the discovery that the reference mirror is very compliant in a hinging motion. This couples bending moments in various cell struts into rotation of the reference mirror. The large magnitude of the effect is an artifact of the particular design and fabrication of the prototype assembly. The reference mirror is narrow and thus has a short baseline for its support. The space frame structural concept of having the force vectors of all struts meet at points in space was poorly implemented. In the lower tube-elevation ring interface, struts are offset from each other, resulting in bending of the elevation ring structure.

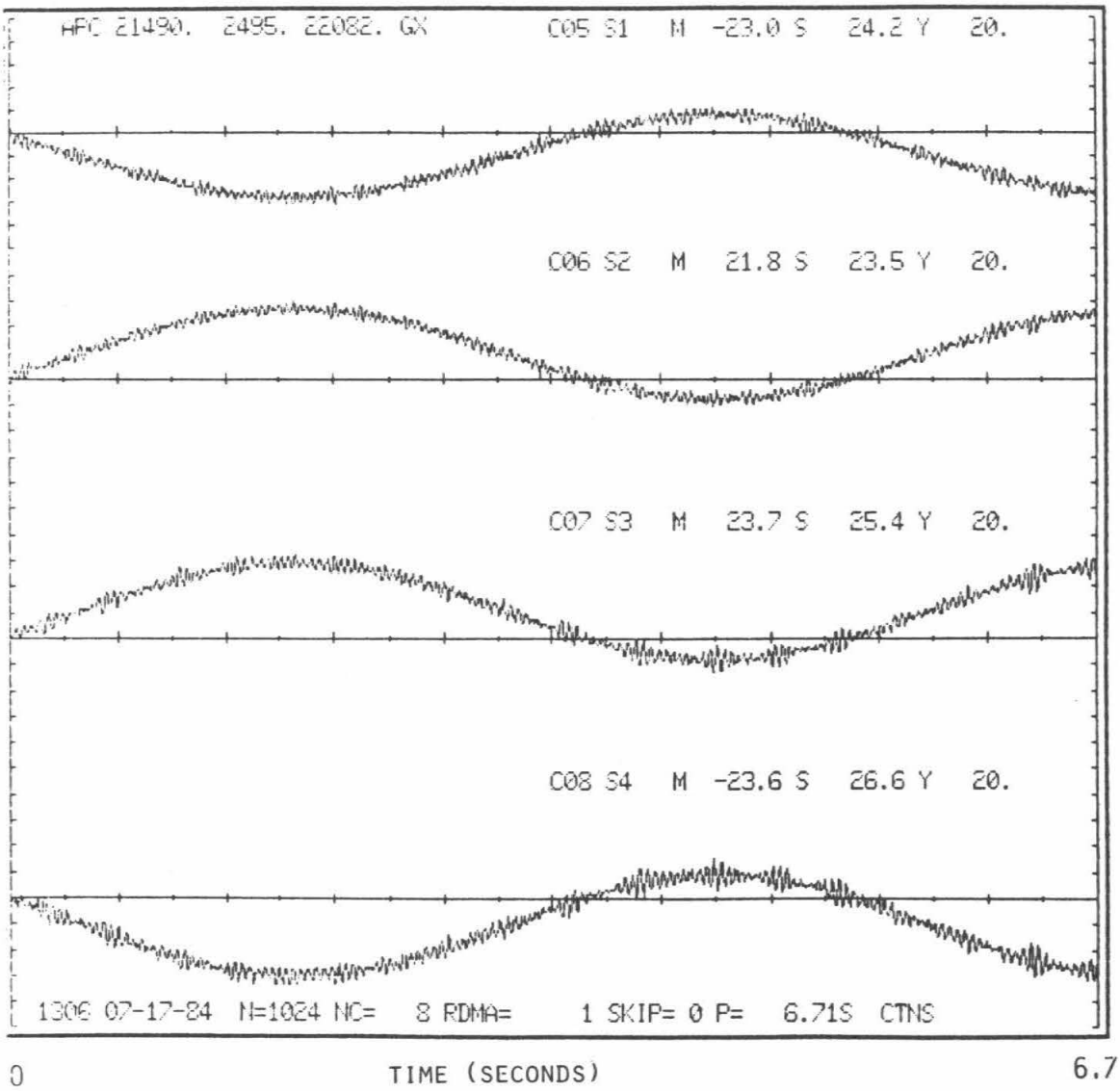

XBL 852-1261

Figure 8-23 A time series of sensor readings when the segment was perturbed with a 0.2Hz sine wave. The control loop is turned off and the small high frequency motions are from oscillations in the 20-30Hz region due to resonances in the segment support structure. The vertical scale is 60nm per division. The rms amplitude is about 75nm.

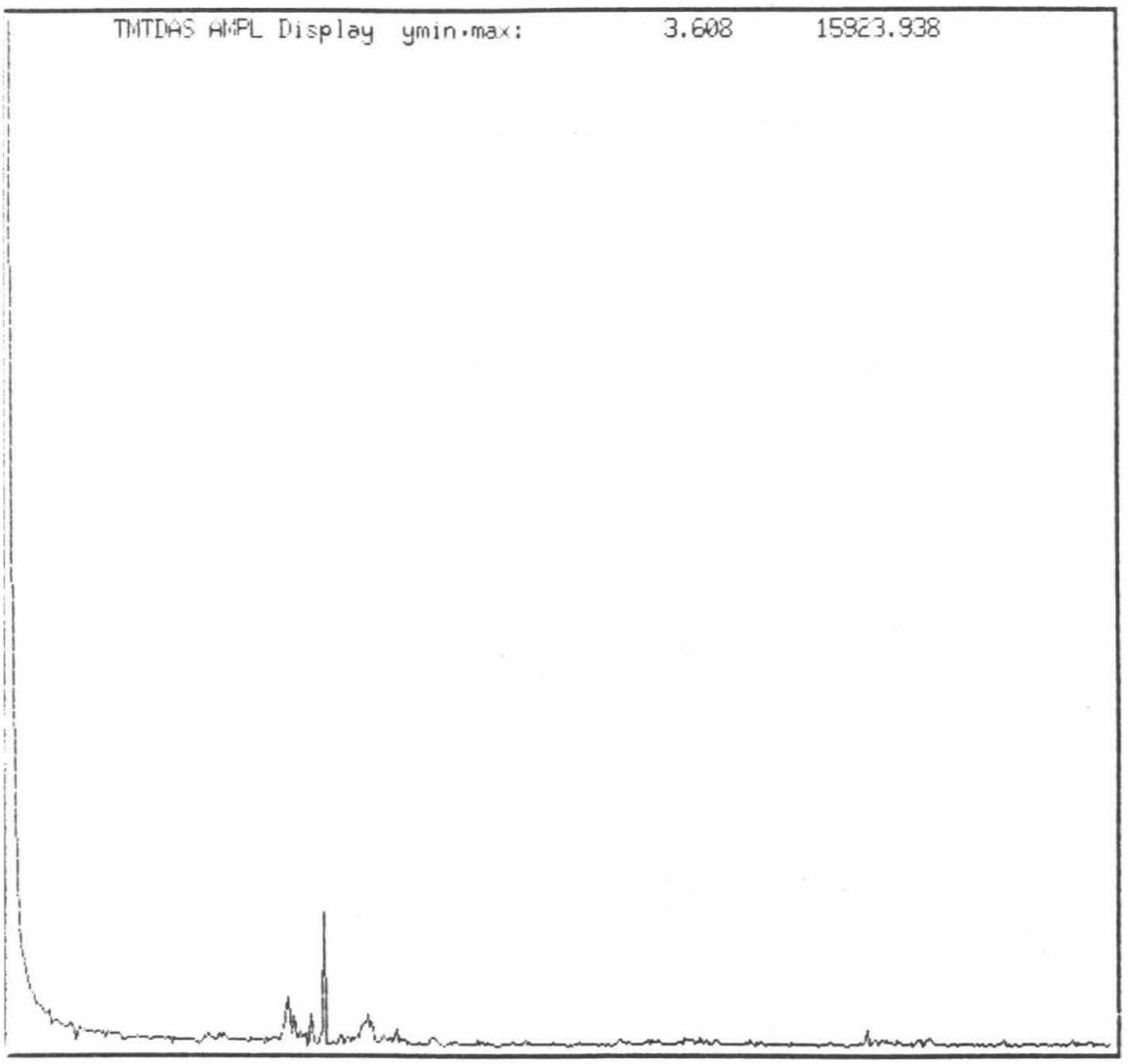

XBL 852-1258

Figure 8-24 A fourier transform of the signal shown in Figure 8-23. The large signal at the left edge is the 0.2Hz perturbation. The peaks in the 20-30Hz region are from resonances in the segment and support structure.

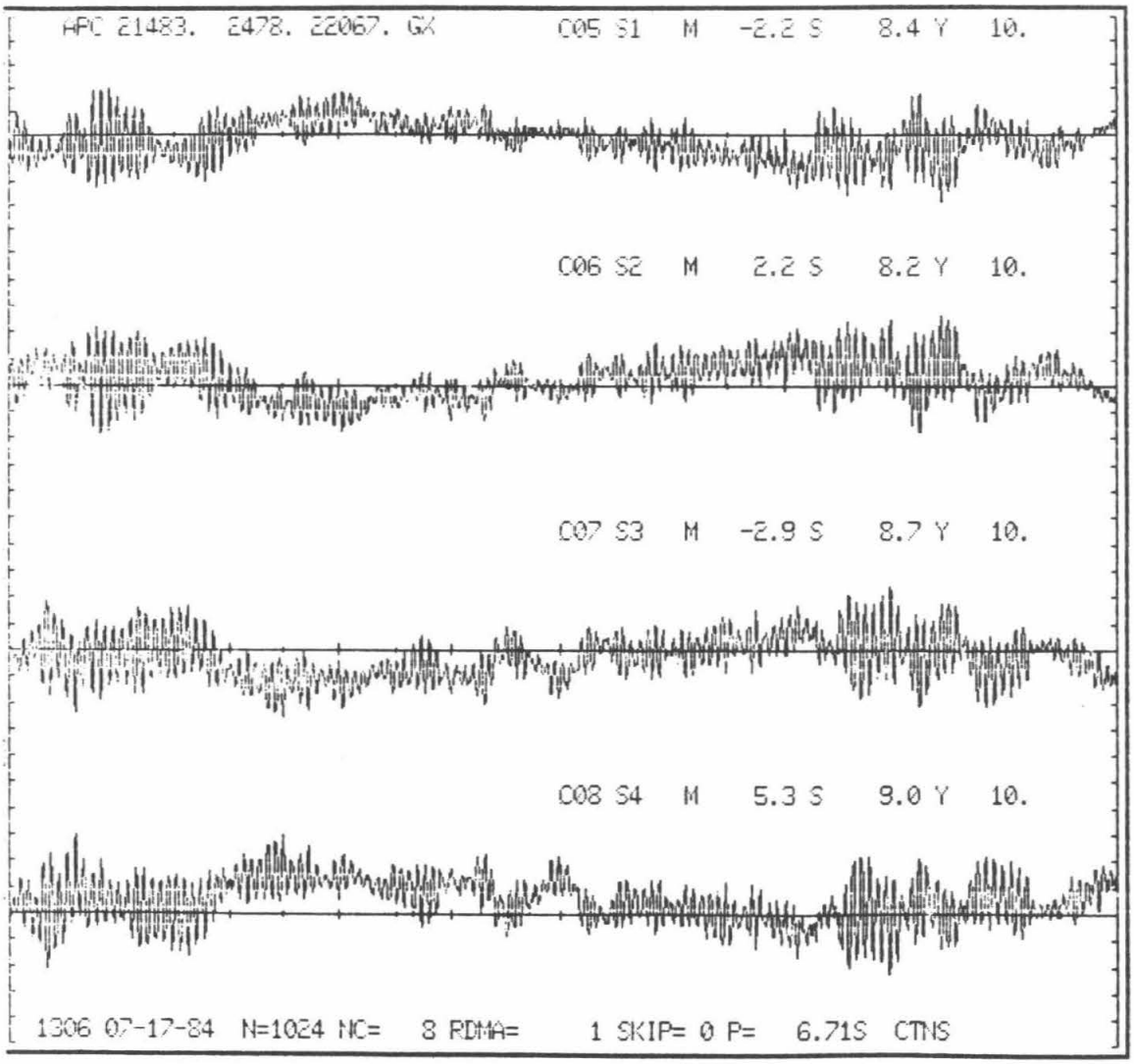

XBL 852-1260

Figure 8-25 A time series of the sensor readings with the control system operating and the segment being perturbed by the 0.2Hz sine wave described in Figures 8-23 and 8-24. The amplitude of the sensor reading is greatly reduced and the remaining motion is segment support resonance motion excited by the control system. The vertical scale is 30nm per division. The rms amplitude is about 25nm.

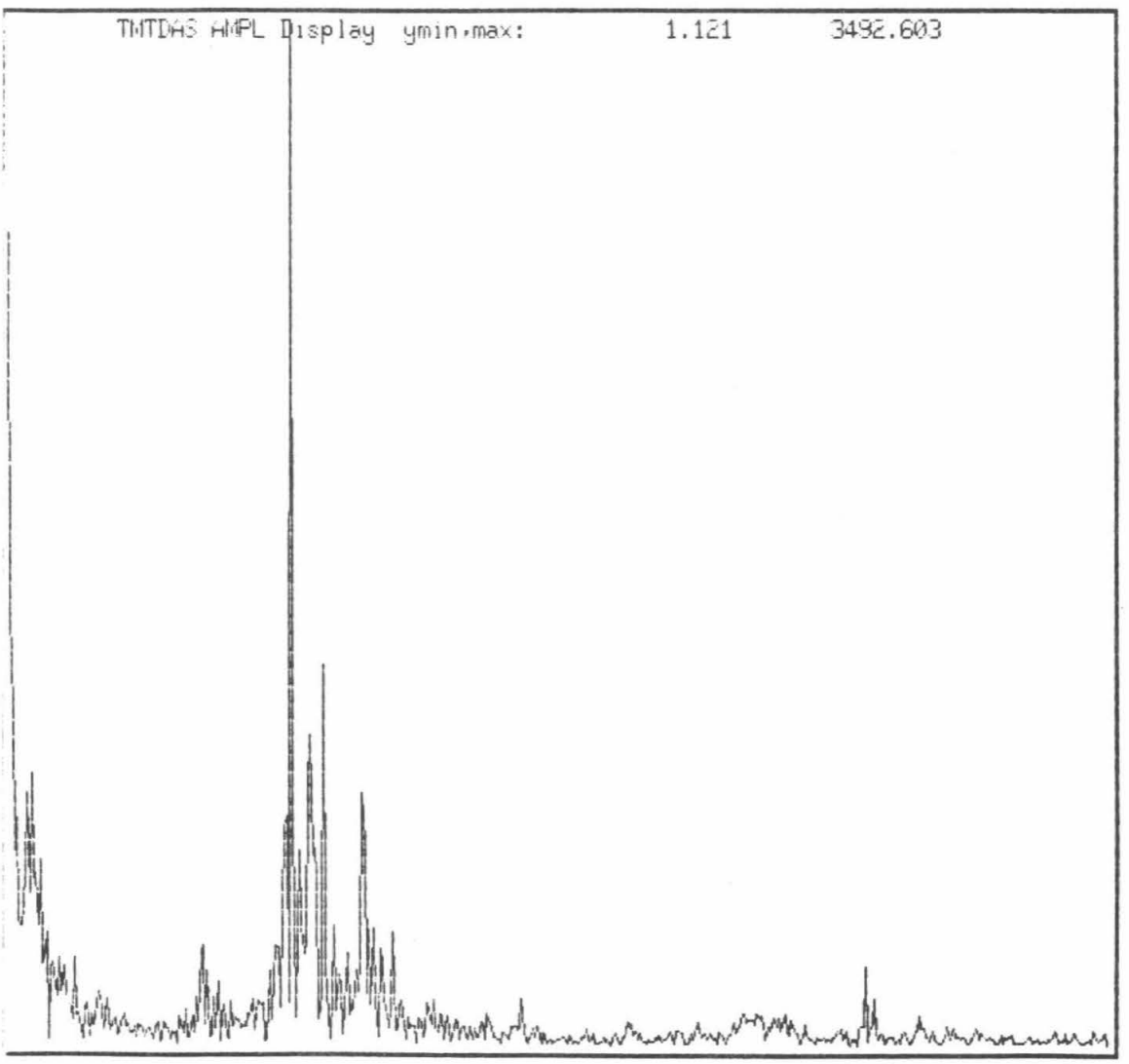

XBL 852-1259

Figure 8-26 A fourier transform of the time series in Figure 8-25. The control system is operating and the amplitude at the 0.2Hz perturbation frequency is greatly reduced. The residual power is dominated by the motions in the 20-30Hz region.

The system response does not presently meet the original bandwidth goal described in Section 8.4.2. We are in the process of making a number of improvements. The mechanical resonances are being identified and the responsible components are being stiffened and/or damped. The phase delay in the system has been measured and is found to be longer than expected. Phase delay in filters applied to the sensor signals are being reduced and the computation time for the global control algorithm is being reduced. These reductions in time will reduce the delay between sensor reading and finishing the actuator motion by a factor of about 2. Thus the bandwidth for reducing the driven amplitude will increase and shift the solid curve in Figure 8-22 to the right. Raising the resonant frequencies in the structure makes it less likely they are excited, and damping reduces the amplitude of those excitations. Thus we expect the total rms amplitude in Figure 8-22 to fall closer to the driven frequency rms amplitude.

The effect of some of these improvements have been tested without actually designing and building new whiffletrees and support structure. The most compliant component in the whiffletree, the primary flex pivot, was removed and replaced with a solid bar. This of course destroyed the kinematic character of the whiffletree and introduced distortions in the surface. However, this was unimportant for the control tests. A number of additional struts were added to the cell and lower tube structures to make them stiffer and also add damping. These changes did remove several resonances and reduced the excitation of others. A single resonance remained and this was removed from the analog sensors signals using a notch filter. The performance of the control system under these conditions is summarized in Figure 8-27. The excitation of the structural resonances has been eliminated and the mirror motion is dominated by the uncontrolled driving frequency. This response curve and others taken at different control sampling frequencies agree with a mathematic model of the system. Thus we believe the control system loop and algorithm are operating as designed. Its ability to reduce perturbations in the TMT will depend on the structural stiffness and resonance behavior. In the coming months the supports for the TMT segments (cell, subcell, whiffletrees, support post) will be redesigned and analyzed for their dynamic properties. New whiffletrees will be built and tested. Throughout this final design work emphasis will be placed on improving the stiffness of the elements that contributed to the resonances observed in the prototype assembly.

The bandwidth of the system will be further improved in the near future by reducing the calculation time. Additional improvement could be made by removing the notch filter at the remaining 28Hz tube resonance. This introduces a phase delay of about 10ms.

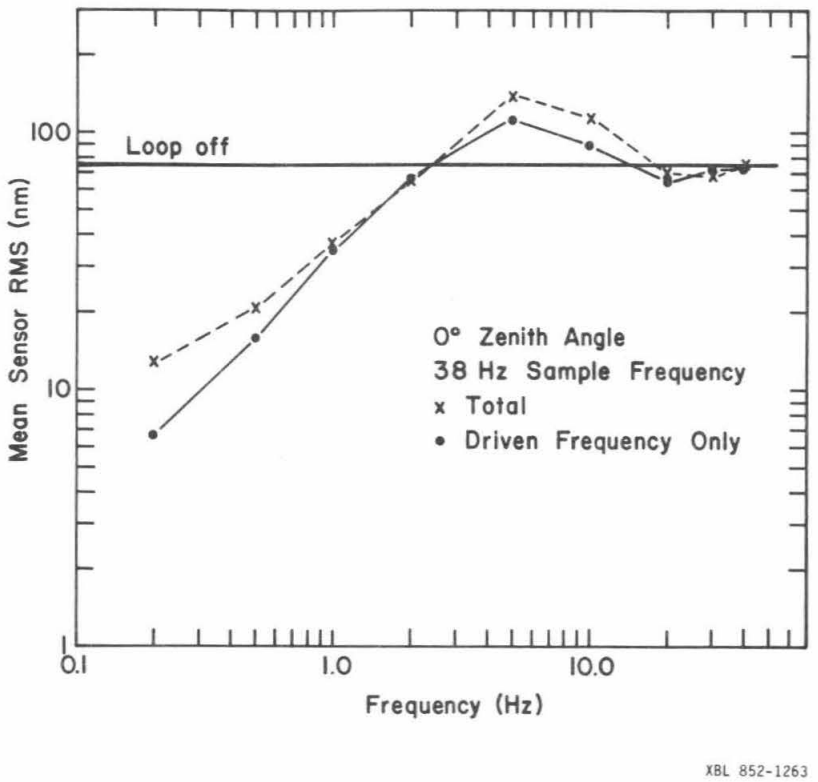

Figure 8-27 The response of the control system to sine wave piston perturbations of various frequencies. The system differs from that used to create Figure 8-22 in that many of the structural resonances in the 20-30Hz region were removed by stiffening and damping the structure. As a result the total rms motion is not substantially larger than the residual motion at the perturbation driving frequency.

9. Observatory Building and Dome Design

Contents **Page**

9.1 Site Acquisition and Preparation

9.1.1 Environmental Impact Statement and Complex Development Plan

The summit area of Mauna Kea, a dormant volcano on the island of Hawaii, is owned by the State of Hawaii and designated a conservation district. The State's Board of Land and Natural Resources (BLNR) has leased this area, known as the Mauna Kea Science Reserve, to the University of Hawaii (UH), which manages it through its Institute for Astronomy (IFA). The Reserve was established as "a scientific complex, including without limitation thereof an observatory, and as a scientific reserve being more specifically a buffer zone to prevent the intrusion of activities inimical to said scientific complex" (General Lease No. S-4191).

To guide the development of this scientific complex, UH produced a programmatic master plan for astronomy development to the year 2000. This document is known as the "UH Research Development Plan for the Mauna Kea Science Reserve and Related Facilities" and was adopted by the UH Regents in January 1982. The BLNR then requested that UH produce a development plan for the Reserve describing the contemplated development that would be necessary to implement the academic master plan. The Mauna Kea Science Reserve Complex Development Plan (CDP) was the response to this request, and was issued in its final form in February 1983. The TMT project was described in some detail in the CDP, which indicated that the site chosen for the TMT was a cinder cone named Pu'u Hau Oki, but usually referred to as the Northwest Cone.

The CDP represented a unique departure from past practices in that it marked the first time a comprehensive plan had been produced for Mauna Kea. Previously, individual observatory projects secured their permits to build in the Reserve by preparing individual Environmental Impact Statements (EIS) and submitting individual Conservation District Use Applications (CDUA). The BLNR allowed UH to prepare a single EIS based on the CDP. This was done while the CDP was in draft form, and the EIS was accepted by Hawaii Governor Ariyoshi in January 1983.

The way was now clear for UC to submit a CDUA for the TMT development on the Northwest Cone. This was accomplished in December 1983. After a period of review within the state and a public hearing, the BLNR approved our CDUA and issued a permit on August 24, 1984. UC has one year within which to commence work on this site, or to apply for an

extension to this condition of the permit.

9.1.2 University of Hawaii Agreements

Official UH relations with the TMT project commenced with the signing in November 1981 of a Memorandum of Understanding (MOU). The MOU secured a commitment from UH for the site of TMT, subject to the issuance of a permit by the BLNR and the negotiation of a sublease among UC, UH, and BLNR. The sublease is being prepared in accord with UH's General Lease S-4191, and is in the process of finalization. The sublease will expire, unless renewed or extended, on December 31, 2033. The sublease also secures for UC the continued right to the site should UH either give up or default on General Lease S-4191. The annual lease payment is a nominal $1.00.

UC and UH are also negotiating an Operating and Site Development Agreement (OSDA). The OSDA includes UC's obligations to contribute approximately $2 million to the major infrastructure improvements that will provide public electric power and road improvements to the summit and the Midlevel Facility. UC will also be required to contribute a prorated share of the capital costs of the common areas at the Midlevel Facility, a contribution currently estimated to be about $2 million.

In addition, and perhaps of greater interest, are the provisions of the OSDA linking the UC and UH astronomy programs. In recognition of UH's efforts in originally developing Mauna Kea as a premier site for astronomy and in order to take advantage of their special knowledge of the conduct of astronomy at Mauna Kea, UC will provide UH astronomers special access to TMT.

First, UH will, on the basis of the scientific merit of their proposals, normally be granted 10% of the assignable observing time. Second, UH will participate in the TMT committee structure. UH will have one voting member on the Astronomy Advisory Committee, one voting member on the Time Assignment Committee, and one nonvoting participant on a Policy Advisory Committee if UC has such.

The third area of cooperation will permit UC faculty or research staff members to be appointed for a one year term at UH each year. These appointments will be at UC expense and the individuals will have full access to all UH telescopes and research facilities. Normally, there will be one such appointment each year. Up to two research students may be appointed each year also.

The term of the OSDA is the same as the sublease and will expire, unless renewed or extended, on December 31, 2033.

9.2 Building and Dome Design

9.2.1 Design Criteria

Three goals were foremost in establishing the building and dome design. First, we sought a design that would minimize the locally induced degradation of the seeing. In recent years, it has become increasingly clear that the telescope dome, while providing necessary protection from the elements, is often itself a major source of seeing degradation, due to the adverse thermal properties of the enclosure. Thus we sought a dome design that would have minimal adverse thermal effects on the telescope environment. Second, we sought a facility that would allow us to make frequent, rapid, and safe instrument changes, to allow optimal use of a wide variety of observing conditions. Third, we required that the facility allow straightforward procedures for the realuminizing of the primary mirror segments. Finally, we sought a design that would be particularly convenient for astronomers, allow easy maintenance of the facility and telescope in particular, and a design that would minimize the restrictions on future, unplanned uses for the telescope.

9.2.2 History of the Design

Originally, we explored the possibility of eliminating the dome entirely, a practice common for radio telescopes. However, after some investigation, it became clear that the severity of the storms and the generally windy conditions on Mauna Kea precluded this option. Further, the large cost and risks in using wind fences for protection from wind buffeting on the telescope structure, made even temporary full exposure appear unattractive. Thus, we explored the more traditional range of telescope enclosures. The classical optical telescope enclosure has a stationary circular building covered by a rotating hemispherical dome. In recent years, the Multiple Mirror Telescope (MMT) in Arizona has pioneered an unusually economical, functional, and thermally effective design that has a box-like rotating building that serves both as the dome and the building, and always co-rotates with the telescope. On two occasions, under the guidance of two different architectural and engineering groups, we explored this configuration for the TMT. Somewhat to our surprise, we found that for the size needed for the TMT the design was more expensive, and provided less functional performance than other designs. In addition, it was felt that surrounding the telescope by all of the heat-producing sources of the facility would unacceptably increase the risks of thermal degradation of the seeing. Thus we once again found ourselves resorting to conventional enclosure configurations.

It was decided that rapid instrument changes would be most readily allowed if we used standard instrument modules that would be exchanged as entities. The handling of top-end modules is a major issue, and allowing for suitable devices and space has been an important driver of the design of the dome.

In the original architectural development work by John Wells (TMT Report No. 35) a platform was used to carry top-end modules. The building was located under the dome, and a special elevator gave access to the platform. This design idea was developed and detailed in the work by Rose and Hoggan (TMT Report No. 85).

More recently, we re-examined the design ideas and the architects, MBT Associates, have developed another scheme to satisfy our requirements. The present design has many similarities to the earlier ones, but the building is now basically separate from the dome, instead of being underneath it. During the formulation of this design it was discussed and reviewed by the Astronomy Advisory Committee and other astronomers within the University. At the time of this writing the community is being solicited its input to the next stage of the architectural design.

9.2.3 Observatory Design

Specifications for the TMT are given in TMT Technical Note No. 57 and specifications for the enclosure are given in TMT Technical Note No. 79. These are the basis for the architectural design of the observatory. The enclosure for the telescope has several major requirements.

1. The enclosure must survive 65m/s (145mph) winds, and operate (seals, slit, and dome motion) in winds up to 30m/s. Shutters and enclosure must operate in temperatures from -20^{o}C to +30 ^{o}C and seal against wind, dust, and precipitation.
2. The telescope and pier must be well isolated statically and dynamically from the enclosure.
3. The enclosure must be well insulated and air-sealed from heat-producing equipment and personnel areas. Surfaces surrounding the telescope chamber should have low thermal inertia.
4. A forced ventilation system must exhaust air from the enclosure at more than ten volumes per hour, bringing outside air in through the slit.
5. Easy access to the Nasmyth platform for personnel and heavy equipment during operation is required.

6. Rapid and safe instrument changes at the prime focus and Cassegrain focus with the telescope pointed at the horizon is required.
7. A segment-handling crane must be available for removing all segments. This crane should have a 5-ton capacity. Construction of the telescope will require other cranes in the enclosure with a capacity of 20 tons.

One of the key parameters needed for the design is the height of the telescope above ground level. Originally, we planned to raise the telescope above ground level to reduce ground-caused seeing degradation. A detailed study of the vertical distribution of seeing degradation at the site has been made by Cudaback (TMT Report No. 131). These results show that the seeing degradation caused by the first 10 or 20 meters above ground is negligible, and we now plan to place the telescope essentially on the ground.

The site plan for the observatory is shown in Figure 9-1. We will extend the present road that serves the IRTF to reach the site. The maximum grade will be 7.7%, less than the present maximum 16% grade of the road that reaches the summit. The building extends to the north of the telescope and dome. The flattened area is approximately 7700m^2. The loading dock will be at the north end of the building, and in addition, when necessary, trucks can enter the dome area directly on the east side when large items must be transported to the telescope. The normal entrance for the staff and for visitors will be on the east side of the building.

The building is a one story structure that will be located adjacent to the dome. This is shown in elevation in Figure 9-2. This drawing shows some of the important features that allow access to the telescope. The telescope rests on its pier close to ground level. Attached to the dome is an elevator that provides access to the Nasmyth deck level around the telescope. It is at this level that instrument changes take place at the top end and at the forward and normal Cassegrain positions. The elevator has the capacity to carry not only passengers but the standard instrument modules as well. A lightweight crane is attached to the wall of the dome. This crane serves for segment handling and some instrument handling. The coudé beam pipe is also shown in Figure 9-2. This begins at the center of the pier and then extends horizontally underneath the building to the coudé room.

A plan view of the building is shown in Figure 9-3. The areas assigned for various rooms/functions are given in Table 9-1.

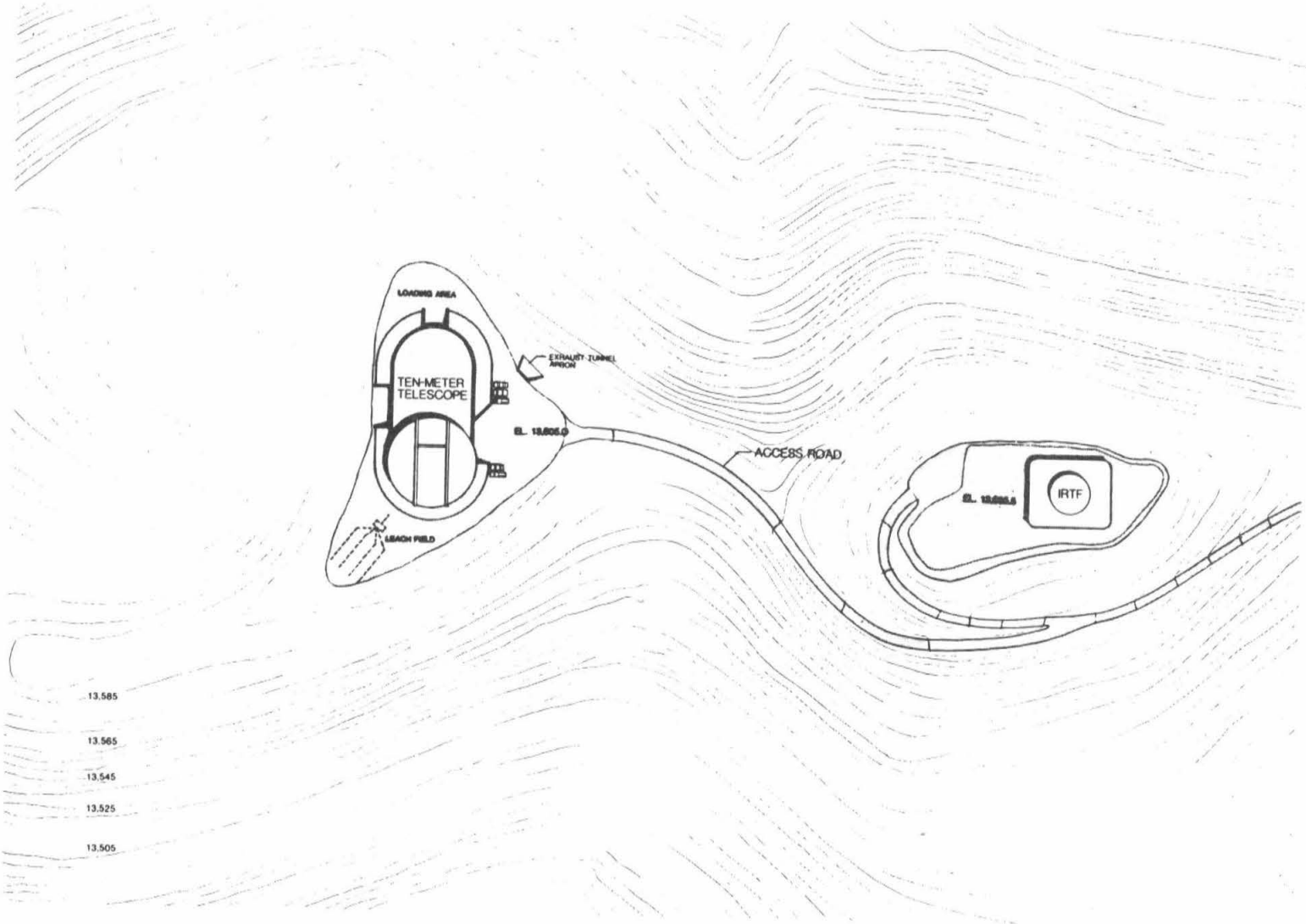

Figure 9-1 The site plan for the observatory.

XBL 8410-4468

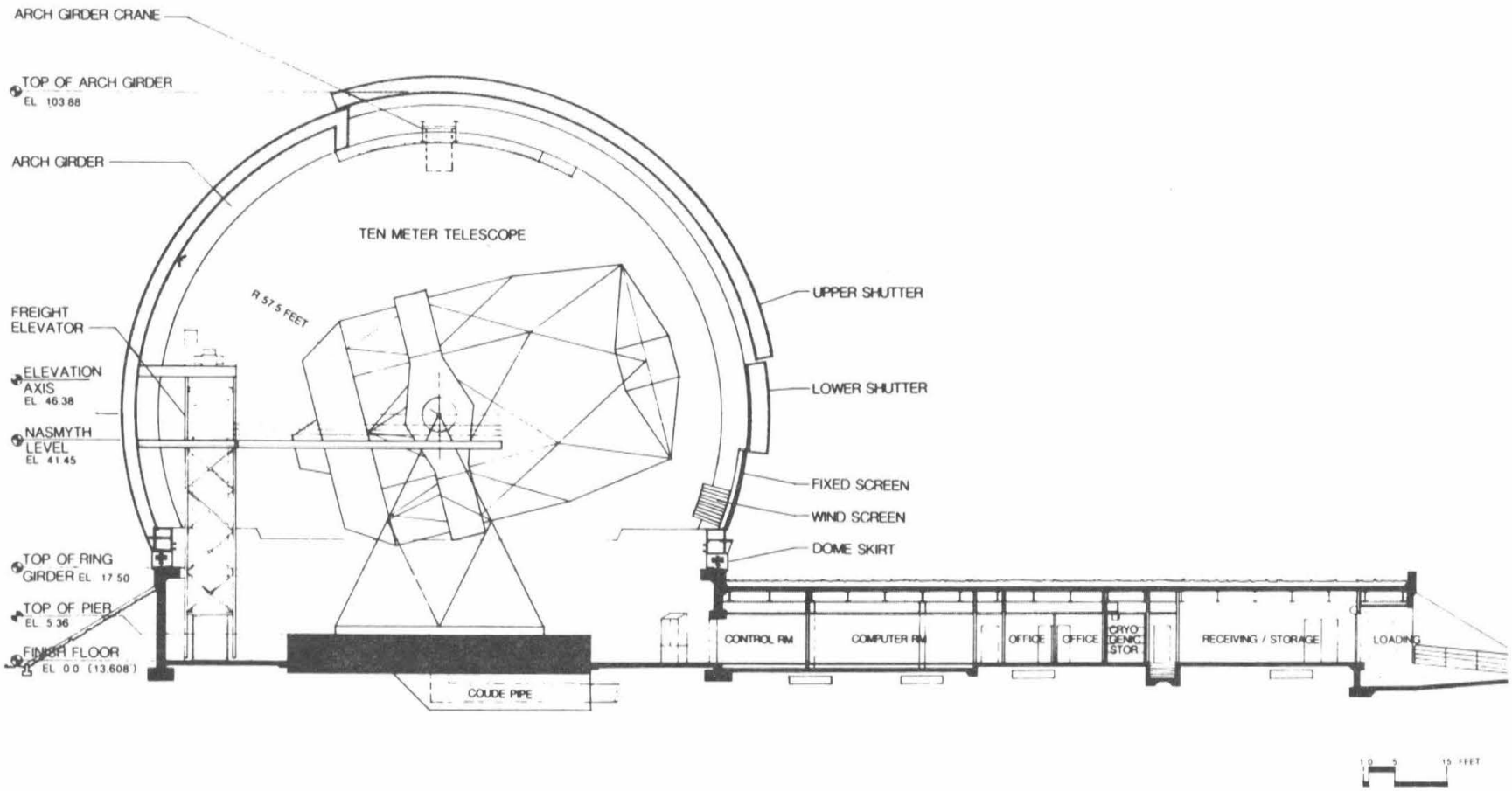

Figure 9-2 Elevation view of the telescope dome and support building.

XBL 8410-4472

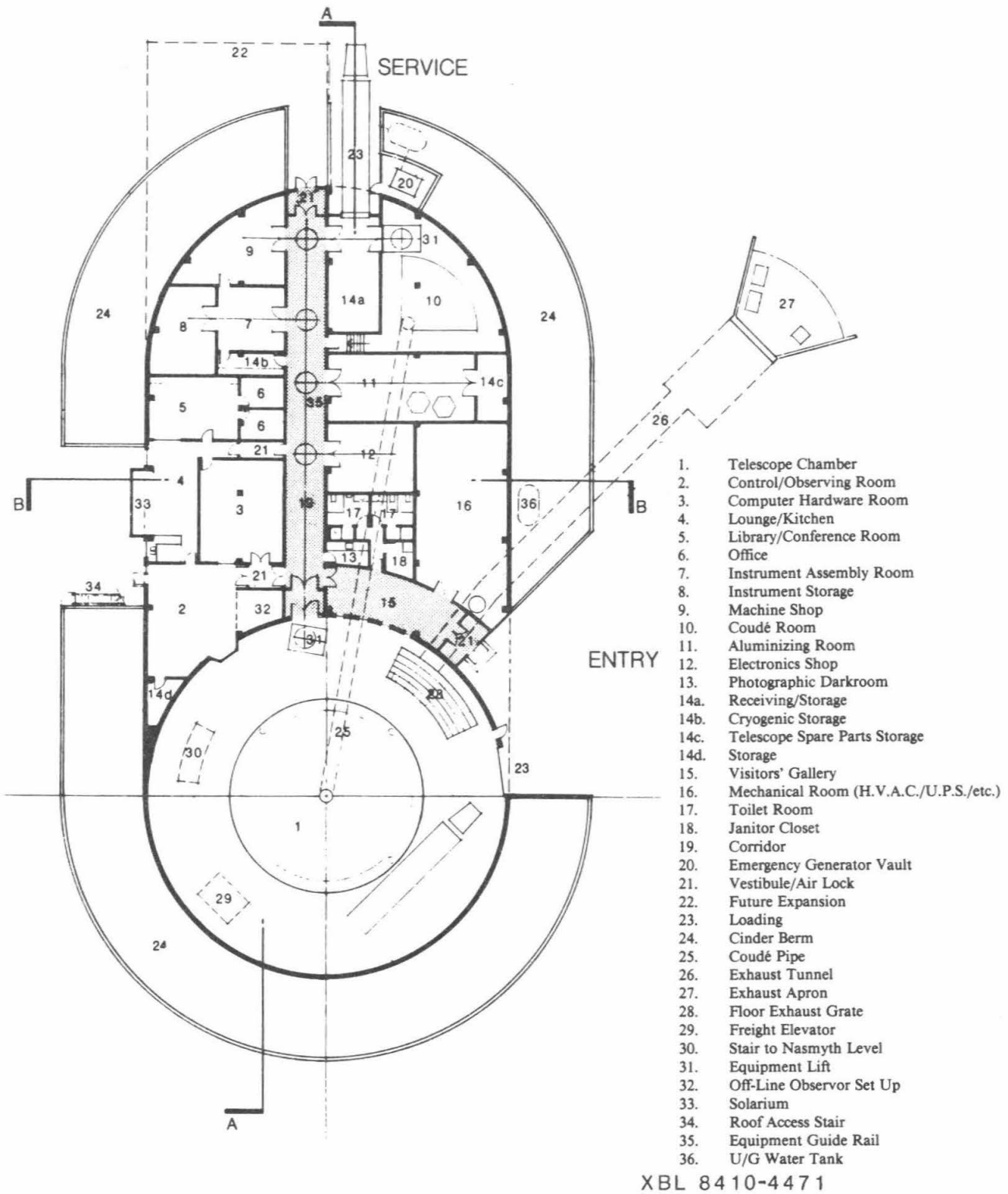

Figure 9-3 The plan view of the observatory building.

Table 9-1 Area Allocations

Room/Functions		Net Area (sq. ft.)
1. Telescope Chamber		9760
Floor	5760	
Nasmyth Deck	4000	
2. Telescope Support and Maintenance		4865
Aluminizing Room	900	
Electronics Shop	500	
Machine Shop	600	
Mechanical Room (H.V.A.C./U.P.S./etc.)	1470	
Storage		
Instrument Storage	470	
Receiving/Storage	525	
Cryogenic Storage	130	
Telescope Spare Parts Storage	180	
Other Storage	90	
3. Observing Support:		3620
Control/Observation Room	980	
Computer Hardware Room	800	
Coudé Room	1200	
Instrument Assembly Room	400	
Observer Setup Room	150	
Photographic Darkroom	90	
4. Personnel Support:		2215
Library/Conference Room	500	
Lounge/Kitchen	550	
Offices (two)	240	
Restrooms (two)	300	
Janitor Closet	75	
Visitors' Gallery	550	
Total of all areas		20,460 ($1901 m^2$)

The normal entrance is on the east side of the building and the first room is the visitors gallery. A display, a view of the telescope, and rest rooms are available here. Adjacent to the gallery is the equipment room that contains much of the general mechanical equipment needed for the observatory. This includes the H.V.A.C., the uninterruptible power supply for the computers, the high pressure oil system for the telescope bearings, vacuum pumps, compressors, and refrigeration equipment if needed for cooling the dome floor.

The southwest area of the building is the area that will be most frequented by astronomers. This region includes the control room, the computer room, the lounge, and the library/office area. This region will have particularly careful acoustic control for the convenience of observers. This area will also be enriched with oxygen to reduce the mentally degrading effects of the high altitude. The control room will have a clear view of the telescope through windows that can be thermally sealed and optically opaqued when not needed. Temporary instrument electronics will be located in this room. Adjacent to this room is the computer room that will house the main computer facilities needed to control the primary mirror, the

telescope, scientific instruments, and handle data processing that is done at the site. Both of these rooms will be equipped with access flooring for ease of cabling, and will also have ample overhead racks for additional cabling. The lounge area adjoins the control room and will be equipped with a modest kitchen and an eating area with a solarium to provide a pleasant environment during meals to contrast with the stark environment of the mountain top. There is also a library with two offices adjoining it. The library serves as the document storage area and meeting room as well.

The northwest area of the building contains the instrument storage area, the instrument assembly room, a cryogenics room, and the machine shop. The instrument areas and connecting doors are designed to accommodate the standard instrument modules and allow their servicing. The cryogenics will provide for LN2 and LHe for scientific detectors, etc. The central hallway that connects the rooms of the building to each other and to the telescope area is sufficiently wide (3.66m (12ft)) to allow easy maneuvering of the instrument modules and other bulky equipment.

The northeast area of the building contains an electronics shop, the mirror coating facility and segment storage area, the receiving and storage area, and the coudé room. The electronics shop can accommodate an instrument module for servicing, will provide storage for spare electronics parts and modules, and will be able to provide servicing for the computers and other electronics in the facility. The coating area will be able to store the six spare segments, and have a coating chamber that can apply state of the art high reflectance coatings to the segments and to other optical surfaces in the facility. The coudé room is designed to accommodate experimental apparatus that is too bulky or is too delicate to place on the Nasmyth platforms. To match the beam, the floor of the coudé room will be 2.4m below ground level. The coudé room will have crane access over most of its area so instruments can be installed or assembled. Also in the northeast area is the emergency power generator that can provide a minimum of 150kW of electricity, should the main power be interrupted for any reason. The preceding areas will not be provided with oxygen enrichment for reasons discussed in Section 9.3.4.

Both the building and dome will be surrounded by a cinder berm. This berm serves to protect and insulate the walls, and will have similar thermal properties to the original undisturbed ground. The roof of the building will also have a 0.3m thick layer of cinders. This should provide a durable and well insulated roof material and provide a surface that closely approximates the thermal and visual properties of the undisturbed site. The dome space will be ventilated by exhausting air through floor vents and out through a tunnel.

As seen in Figure 9-2, there is a Nasmyth deck attached to the dome itself. A plan view of this deck is shown in Figure 9-4. It is at the same height as the Nasmyth platforms themselves, thus providing direct horizontal access to Nasmyth instruments. It also contains an auxiliary control room where the essential functions of the main control room will be available when immediate access to the telescope or Nasmyth platforms is required. This room is immediately adjacent to the elevator that brings both people and equipment up to the deck. The deck is the location of prime focus and Cassegrain instrument modules that are ready for use on the telescope. Instrument handling is described more fully in the next section.

9.3 Operational Aspects of the Design

9.3.1 Thermal Control of Telescope Environment

In this section we will describe the general ideas concerning the thermal environment of the telescope. First we discuss the basic physical effects and parameters of the thermal environment, then we discuss the results of a specific detailed computer analysis and optimization of the telescope thermal environment.

Ideally, the telescope and its local environment should be at the ambient air temperature. In this case, there will be no thermal turbulence, no temperature variations in the air, and no index of refraction variations in the air, hence no seeing degradation caused by the local

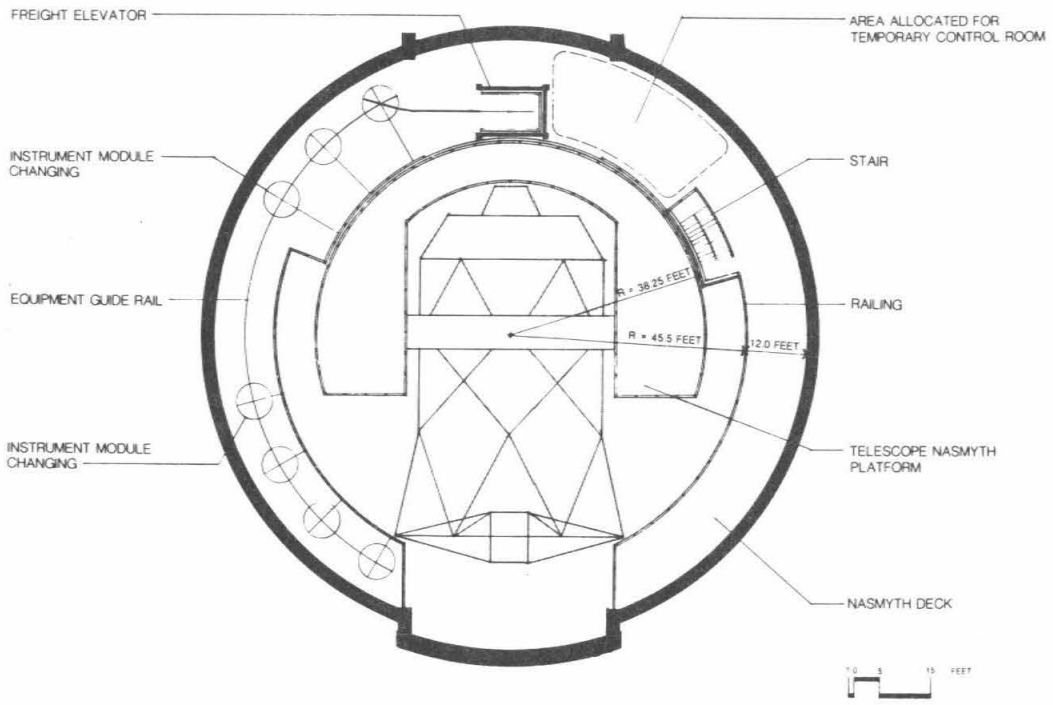

Figure 9-4 A plan view of the Nasmyth level of the dome. The Nasmyth deck attached to the dome is at the same level as the Nasmyth platforms. Most of the frequently used prime focus and Cassegrain instruments will be held on the Nasmyth deck.

environment. Since the ambient air temperature varies both on diurnal and seasonal time scales, achieving this goal is effectively impossible. It is now widely held that for most high altitude observatories the locally induced seeing is in fact the major contributor to the observed seeing quality of the site. Since good seeing is so important to the productivity of the telescope, we will make special efforts to reduce local seeing degradation by minimizing the temperature variations in and around the telescope. Thus we want all objects and surfaces to have low thermal inertia, short thermal time constants, and excellent insulating properties.

By placing all the commonly occupied or heat-generating spaces in a building adjacent to the telescope and dome, we effectively eliminate these heat sources as sources of seeing degradation. The common wall between the building and dome will be heavily insulated, with insulated window shades as well. The foundation wall of the dome will also be heavily insulated. Since the dome is exposed to solar insolation during the day, and is coupled radiatively to an extremely cold sky at night, the dome skin experiences substantial temperature variations. Titanium dioxide based white paint on the dome gives a low solar absorbtivity (0.2 to 0.4), which greatly reduces the daily heat load. Unfortunately, this material has high emissivity in the thermal infrared, so the dome skin cools well below the ambient air temperature during the night. This may have adverse effects on the seeing, so alternate coating are being considered. To reduce the heat loads on the telescope from these variations, we expect to insulate the wall of the dome, and place a low thermal inertia skin on the interior.

The floor of the dome is another potential source of heat imbalance. A high thermal inertia floor such as concrete will tend to stay at constant temperature, thus either act as a heat source or sink, depending on the current ambient temperature. Temperature difference of

either sign is potentially troublesome, although a colder floor will cause less turbulence, hence be less troublesome. The dome floor must also be a load-bearing surface, which tends to increase its thermal inertia. We plan to use rigid foam insulation covered with a thin plywood layer for this purpose. The use of active floor chillers to control the floor temperature is also being considered. The floor will be strongly coupled radiatively to the dome walls and to the telescope itself, so one can effectively add or subtract heat in the dome area by controlling the temperature of the floor. The floor has an area of $800m^2$, and at 0^oC, temperature differences allow a radiative heat flow of $4.6W/^oCm^2$. Thus the floor can emit or absorb at rates up to 3.7kW for a 1^oC temperature difference between the floor and the rest of the interior of the dome. The major drawback of an actively controlled floor is the expense of the electricity needed to provide the cooling.

The steel structure of the telescope provides a key benchmark for thermal inertia and heat transfer requirements. With a mass of roughly 130 tons, the telescope has a heat capacity of $6.1\times10^7J/^oC$ or 17kW-hr/^oC. In still air, the telescope heat transfer will be largely due to radiation, rather than convection. Although the steel members vary considerably in their thickness, if we assume the telescope is made of tubing with 10mm wall thickness, there will be a total steel area of $1700m^2$. This will cool radiatively with a time constant of about 8000s or 2.2hr.

The primary mirror itself has a mass of 14 tons and has a heat capacity of $1.2\times10^7J/^oC$ or 3.2kW-hr/^oC. Since the front surface is directly in the optical path, its surface temperature is the most critical one in the entire observatory. Since its front surface is aluminized, its radiative coupling is extremely poor. If we assume the front surface is completely isolated thermally, and all heat must enter the **back surface only,** then the thermal time constant for the front surface to come to equilibrium is set by the diffusivity β of the glass and is given by

$$t = \frac{4h^2}{\pi^2\beta} \quad .$$

For our segments, t = 48 minutes. Thus the front surface will lag the back surface by almost an hour. Assuming the back surface can radiate as a black body, and that the internal conductivity is very large, the radiative time constant of the mirror is 9.3 hours. Since the ambient temperature changes around sunset and sunrise with a characteristic time of roughly 2 hours and changes by 3^oC the mirror will not readily match the air temperature to within the desired tolerances of 0.25^oC. To achieve this temperature control of the primary will require active heating and cooling of the back of the primary. This will be done by enclosing the back of the mirror and using forced ventilation of temperature controlled air. The maximum heat removal rate is expected to be about 5kW. A thermal flux of this size is expected to noticeably warp the segments (see section 5.15.1) by changing their focal lengths. If uncorrected, image blur of roughly 1 arcsecond may occur. Since the temperature gradient will be the same for all segments, much of this effect can be removed by lookup tables which allow proper segment tilt adjustment and telescope refocus. Even so, these large fluxes on one side of the mirror will degrade image quality, so this form of primary mirror control will require careful management.

Whenever possible, heat sources will be removed from the dome area to the adjacent building. Any heat sources introduced into the dome, such as electronics for the primary mirror and scientific instruments, will be insulated and fluid cooled. The heat will be dumped to a location outside the dome by way of the exhaust tunnel.

Whatever the cause of heat leaks into the dome region, we will minimize their influence by strongly flushing the dome cavity with ambient air. The cavity has a volume of $21000m^3$ and contains an air mass of about 15 tons with a heat capacity of $1.7\times10^7J/^oC$ or 4.2kW-hr/^oC. The floor vents going to the exhaust tunnel and the exhaust fan will provide an air change capacity of $60m^3/s$ or 10 air changes per hour. At a temperature difference of 1^oC, one can carry away 42kW with this venting system.

Thermal Design Study

Because of the potential for the observatory structure to adversely affect the seeing of the telescope, a detailed thermal design study was initiated. The primary thermal design goal is to maintain all interior surface temperatures, and particularly that of the mirror, at the exterior air temperature. The criteria used in the study to determine the "goodness" of any strategy are based on temperature differences between the outside air and the interior air, the telescope structure and mirror. The thermal design goals chosen for the TMT are nighttime root-mean-square temperature differences between outside air and various components as follows: the interior air and all inside surfaces within 0.5^{o}C; and the mirror within 0.25^{o}C.

A series of computer simulations of the observatory building and the enclosed telescope structure was used to determine whether designs could be found that met the thermal goals stated above. A detailed description of the simulation model, its application, and the results are contained in Carroll and Connor, TMT Report No. 134. We summarize the approach and results here.

The simulation model used was developed for building energy research, and simulates in detail the dynamic thermal performance of all building components. The simulation utilizes detailed descriptions of the structure geometry, materials, operating conditions, and external weather. Weather variables used in the simulation include air temperature, wind speeds, insolation, infrared sky radiation temperature, and ground temperature. Using a detailed heat balance method, all heat flows and temperatures for each building component are determined on an hourly basis throughout the desired simulation period.

In the current application, the observatory dome, walls, and floor were all accounted for separately, as was the telescope structure and the mirror itself. Weather conditions for several kinds of diurnal profiles (typical, extreme, summer, winter, *etc.*) were determined from measured on-site data and used to drive the simulation. The thermal impacts of a number of observatory designs were determined by a systematic variation of several selected building design parameters, namely insulation levels, surface radiation properties, operating schedules, and ventilating rates.

Analysis of the results of the parameterized simulations described above clearly indicate that the overall thermal performance is controlled by a complex interaction of the various thermal driving forces and the design parameters, and changing one parameter has interactive effects with the others. However, examination of the results have led to the identification of a number of thermal strategies that when applied in concert yield a thermally optimal design minimizing detrimental seeing effects.

> *Building Insulation*: Insulating all interior surfaces of the observatory building is extremely important. Surfaces include the dome, the lower load-bearing wall, and the floor. For all surfaces, 100-150mm is recommended. This insulation isolates the interior from conductive losses or gains due to external heat sources or sinks, such as daytime solar gains, and infrared radiative heat losses to the sky and the ground. The insulation also isolates the interior environment from the thermal mass of the various structural components. At night, the insulation causes all surface temperatures to come closer to the outside air temperature, which is the basic thermal design goal.
>
> *Telescope Structure Insulation*: All telescope structural elements should be insulated with approximately 20-30mm of standard industrial pipe insulation. This insulation also causes the surface temperature of the structure to more closely track the outside air temperature. In particular, it lessens the amount of stored heat that must be removed from the structure at the beginning of the nightly observing session.

Ventilation: The observatory interior should be mechanically ventilated all night at a rate of about ten volumetric air changes per hour. The ventilation should be started as early as several hours before sundown, whenever the outside air temperature is lower than the inside air temperature, and heat removal can be accomplished. When observing continues after sunrise, ventilation should also continue.

Slit Control: While avoiding any solar gains, the slit should be opened about two hours before sundown. This provides a radiative heat loss mechanism that allows heat gained during the day to be dissipated. During the night, some fine tuning of interior temperatures can be accomplished by controlling the area of the slit opening, consistent with viewing and weather protection needs.

Surface Infrared Emissivity: Interior surface infrared emissivities should be high (0.9), except the interior surface of the dome insulation, which should have a net effective emissivity of about 0.3. The high emissivities ensure good radiative coupling. The relatively low dome interior emissivity serves to reduce the radiative losses to the night sky through the slit. Establishing the optimal exterior emissivity involves tradeoffs that have not yet been carefully investigated. So far as the interior optimization is concerned, a high exterior emissivity is slightly better, but since the dome is slightly insulated, the effect is modest. A low exterior emissivity has the virtue that the shedding of cold air from its surface at night is reduced. This cold air could potentially enter the dome or otherwise enter the telescope light path and degrade seeing. It may also be useful to consider covering strips along the slit with low emissivity material for this reason, and leave the rest of the dome exterior with a high emissivity coating.

Dome Solar Absorptivity: The solar absorptivity of the dome affects the net solar heat gain, and may have a significant impact on interior thermal conditions. Thus, the dome solar absorptivity should be made as low as possible. A well insulated dome, as recommended here, however, decreases the negative impacts of solar gains.

Design Robustness: The parametric variations involving the weather data indicate that while the thermal performance of the optimal design degrades somewhat with season and different (and more extreme) diurnal patterns, this degradation is minor, and the optimal design in fact appears to be relatively robust to such changes.

An example showing the thermal performance for two observatory designs, a basic one and an optimized variation is shown in Figure 9-5. This figure shows how well the average of the inside surface temperatures and the telescope structure temperatures track the outside air temperature for the two designs. It is clear that the optimal design tracks much better than the basic design, with rms nighttime differences of 0.17°C for inside surface temperatures and 0.13°C for the telescope structure itself. For the above modeling, the primary mirror itself has been ignored, work that included the primary is in progress.

9.3.2 Instrument Handling

Planning for the rapid, safe, and repeatable exchange of instruments is a key item for the TMT. In Section 3.4.2 we describe the requirements for the instrument changing system. In Section 7.10 we describe the instrument changing system that will be used. In this section we will describe how the design of the building and dome are arranged to accommodate the proposed instrument changing system.

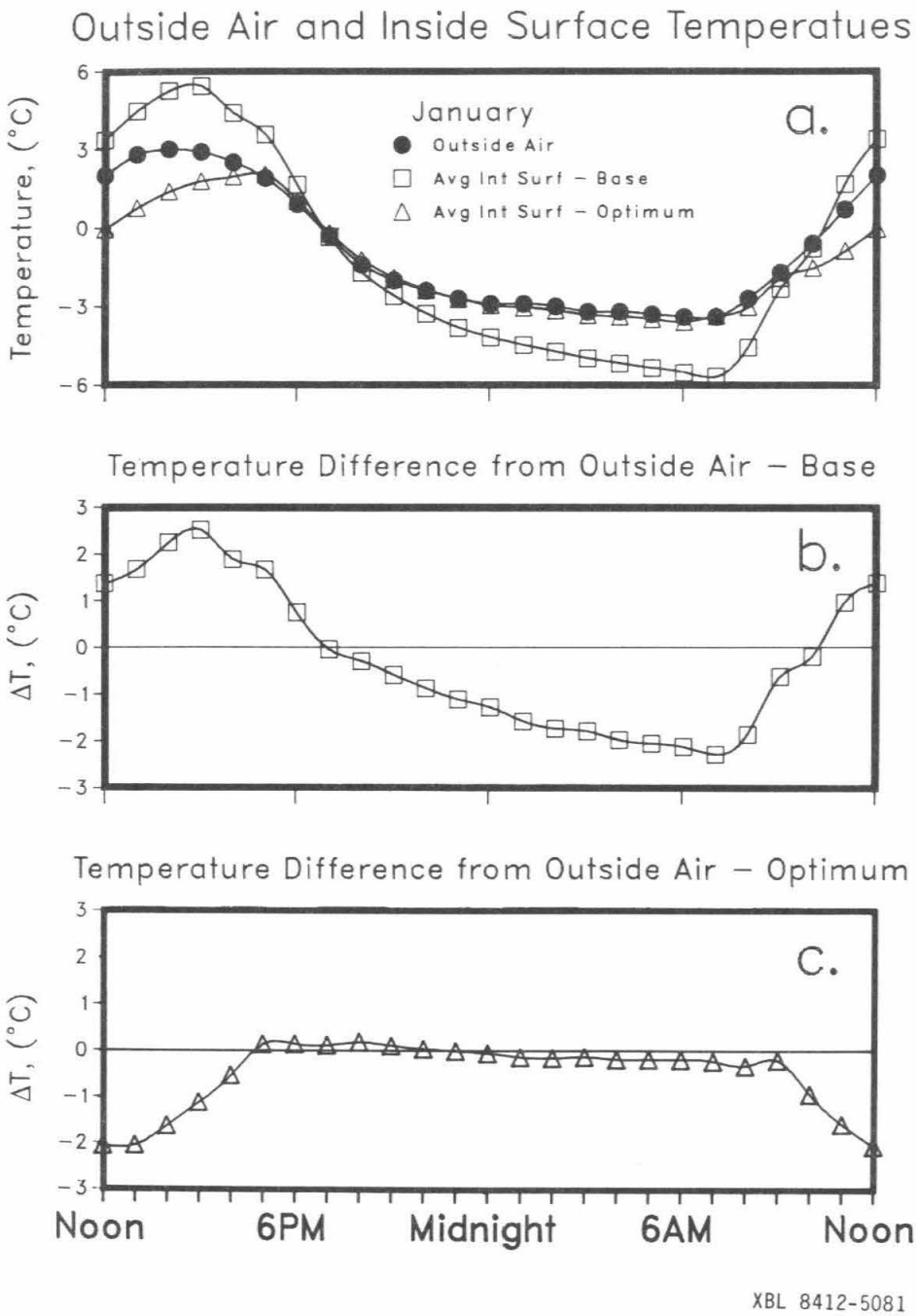

Figure 9-5

a. Simulation results for "basic" and "optimal" observatory designs comparing typical January external air temperatures and average interior surface temperatures

b. average interior surface temperature for "basic" observatory design plotted as a difference from external air temperature

c. average interior surface temperature for "optimal" observatory design plotted as a difference from external air temperature; The horizontal time scale is in hours preceding or following midnight.

The Nasmyth deck on the dome will hold most of the frequently used prime focus and Cassegrain instruments. This layout can be seen in Figure 9-4. A guiderail track will be built into the building floor to allow the safe handling of the modules from the building out to the dome elevator, and then along the Nasmyth deck to the standard positions for instrument exchange. The elevator can accommodate modules with a 3m length, a 2m diameter, and a weight of 2 metric tons.

Since the elevator rotates relative to the floor of the dome area, there will be a small gap between the bottom of the elevator and the top of the dome floor. Thus, a strictly horizontal transfer between the dome floor and elevator is not possible, and a special system is needed to transfer instruments into the elevator. An equipment lift with a vertical range of about 0.3m will be built into the floor of the dome at the doorway between the building and dome. Instruments being transported from the building to the dome are rolled onto this lift, and the lift then raises the instrument until it is level with the floor of the elevator so it can be rolled into the elevator. At the Nasmyth deck the module can simply be rolled on or off the elevator. The elevator and guiderail system details are shown in Figure 9-6.

Up to four top-end modules can be accommodated in the dome. With the four positions, three modules can be stored, with the fourth one in the telescope. Switching modules consists of locking the telescope in a horizontal position and moving the dome so the radial exchange of modules can be made. If one of the modules needs to be removed to the building for servicing, it can, with the aid of the telescope, be positioned in the instrument slot closest to the elevator and then rolled to the building. Alternately, a crane on the dome wall above the modules can lift any module and either lower it directly to the dome floor or swing it over to the guiderail close to the elevator, where it can be rolled to the building. The use of such a crane on the right hand Nasmyth deck will allow additional top end modules to be placed there as needed in the future.

Cassegrain and forward Cassegrain modules are stored in the three slots available on the Nasmyth deck. Module exchange is carried out essentially as for the top ends, except here the module must be rolled across the back extension of the Nasmyth platforms which acts as a bridge between the telescope and the Nasmyth deck. These modules have enough space so they may be rolled forward to allow free passage of the top end modules between their stow positions and the elevator.

Instrumentation for the Nasmyth platforms can also be handled with the elevator for sufficiently small pieces. Bulkier or more massive pieces will be handled by use of cranes, either attached to the dome walls, or to the Nasmyth platforms themselves.

9.3.3 Mirror Segment Handling

Mirror installation and removal is more critical than usual for an observatory since 36 segments, rather than a single primary mirror, must be periodically recoated. A detailed description of the procedures for segment removal and handling are given in Section 5.14. A set of six spare mirror segments will be available and we will exchange a triangular wedge (a sector) of six segments at a time. To perform this safely and quickly, a special crane and set of handling equipment will be used. The crane is attached to one of the main arch girders of the dome, and will have a 5 metric ton capacity.

9.3.4 Effects of Altitude

The TMT site on Mauna Kea has an elevation of 4150m, and it is well known that the reduced atmospheric oxygen (about 60% of sea level) causes a reduction in the performance capability of persons at this altitude. Many people are unaware of this reduction in their performance. Cudaback (1981, TMT Report No. 51) made a major review of the literature on the effects of high altitude and consulted with many experts in the field, and Forster (1984) carried out a study primarily of medical effects at Mauna Kea.

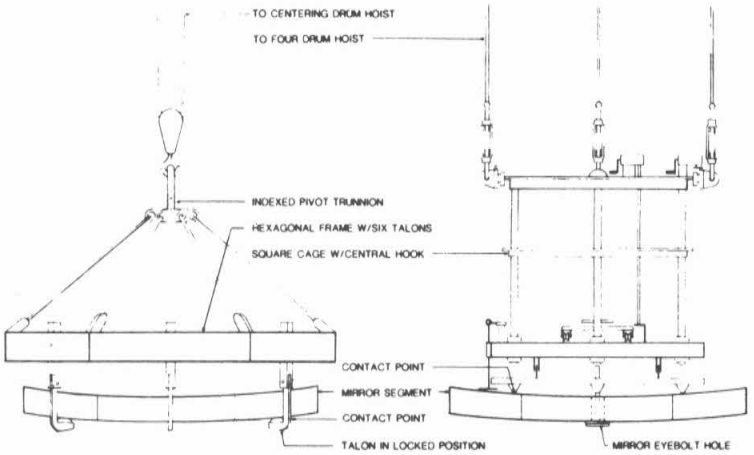

TALON DEVICE (UNMANNED)
(N.I.C.)

LANDER DEVICE (MANNED)
(N.I.C.)

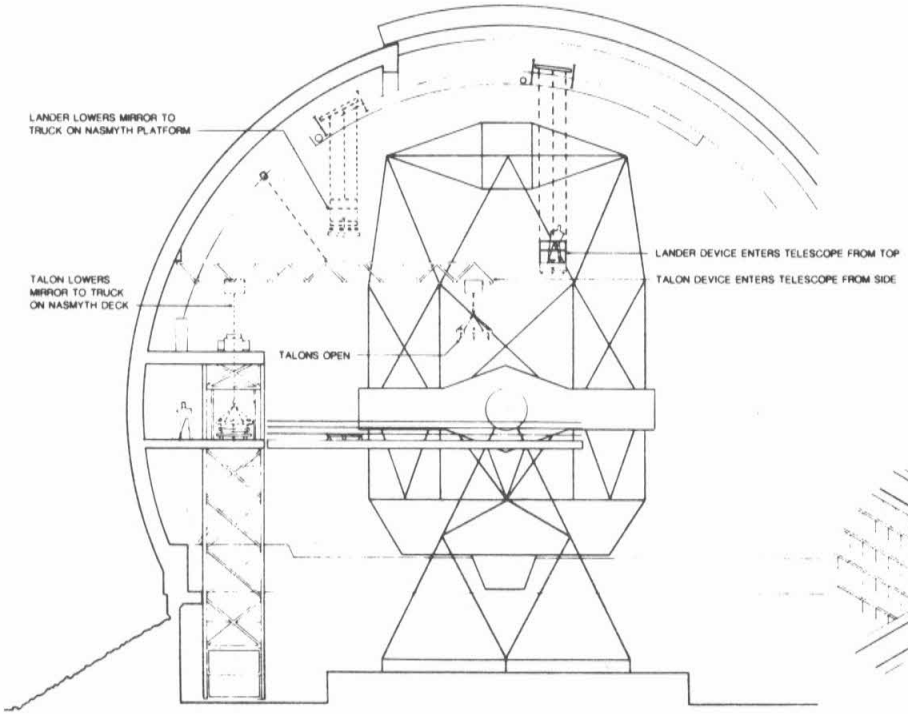

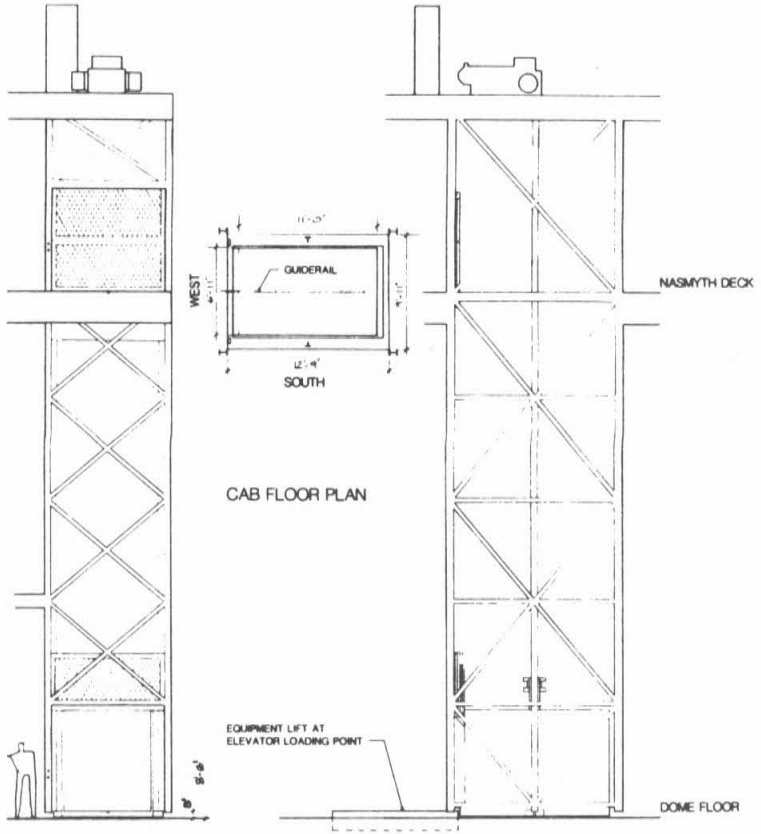

CAB FLOOR PLAN

WEST ELEVATION

SOUTH ELEVATION

FREIGHT ELEVATOR

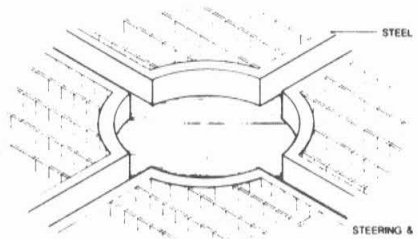

GUIDERAIL JUNCTION

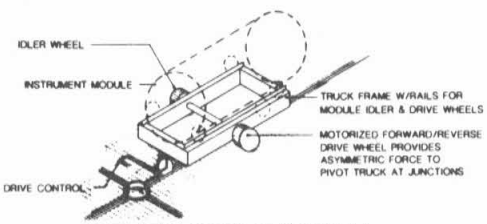

INSTRUMENT MODULE TRUCK (N.I.C.)

Figure 9-6 Details of the elevator and guiderail system.

XBL 8410-4473

The degradation in performance depends on the tasks, and apparently is highly variable from person to person. Indeed, excellent scientific work is done at all the major observatories at Mauna Kea without recourse to any additional oxygen, except for acute medical problems. However, this requires about a day acclimatization at Hale Pohaku before working at the summit. Therefore to maximize the scientific productivity of the TMT and remove the need for acclimitization, and to minimize risks to personnel and equipment, some form of supplemental oxygen will be available for mountain personnel.

Current experience on Mauna Kea suggests that masks and bottled oxygen (available at the present observatories) will not be widely used, and therefore will not be generally effective in reducing problems arising from the reduced oxygen. On the other hand, oxygenating the entire building would be prohibitively expensive. Operating under the assumption that subtle reduction of intellectual performance may occur, and that these will have the largest effect on the scientific productivity of the TMT, we have set as the highest priority the oxygenation of the spaces most commonly occupied by astronomers and telescope operators. For the time being we therefore have restricted our oxygenation requirement to the control room, the computer room, the lounge, the library, and the two offices, a space of about $300m^2$. Oxygen can be provided by masks or tents at the Nasmyth platforms.

The intent of the oxygenation is to provide an environment similar to that of the midlevel facility, Hale Pohaku, at 2832m, where the astronomers and operator eat and sleep. Thus needed acclimatization is reduced, and most astronomers and staff will experience an essentially constant oxygen environment throughout their stay at the mountain. This should allow the broadest spectrum of scientists access to the mountain. To provide this, the oxygen level will be raised from about 20% to 26% to match the partial pressure of oxygen at Hale Pohaku.

These rooms are expected to have only moderate traffic to the unoxygenated spaces. The spaces will be sealed with membrane finishes on the walls, and carefully sealed doors. This is necessary since the higher partial pressure of oxygen will cause it to diffuse outwards from the oxygenated areas. Assuming the minimum legal requirement for ventilation, the oxygen demand has been estimated as a maximum of 125 gaseous liters of oxygen/minute.

Achieving this oxygen flow 24 hours per day by use of liquid oxygen (LOX) would be rather expensive. Assuming LOX is \$2/liter, the annual cost of oxygenation is about \$150K. On-site oxygen-generating equipment looks more promising. Oxygen can be separated from the atmosphere either by molecular sieve or by liquefaction followed with separation by boiling point. A pressure swing absorption system using molecular sieves to separate O_2 from N_2 is commercially available for medical applications. It appears that this system can be scaled up for the needs of the TMT to provide oxygen at an annual cost more than a factor of two below that of the LOX system. In addition, this system avoids having any high concentration of oxygen, so adequate safety precautions are easily provided. More details of this oxygenation system are given in TMT Report No. 129.

10. Site Description and Characteristics

Contents **Page**

The Ten Meter Telescope will be located on the island of Hawaii near the summit of the 4205m (13,796ft) dormant volcano Mauna Kea. The site is located within the Mauna Kea Science Reserve Area, managed by the University of Hawaii. The Science Reserve is currently the site of several major optical and infrared observatories including the Canada-France-Hawaii 3.6-meter telescope (CFHT), the NASA 3.0-meter Infrared Telescope Facility (IRTF), the United Kingdom 3.8-meter Infrared Telescope (UKIRT), and the University of Hawaii 2.2-meter telescope (UH). In addition, the Caltech 10.4-meter and United Kingdom-Netherlands 15-meter millimeter-wave telescopes are under construction near the summit. The TMT location is shown in Figures 10-1 and 10-2 and the site itself is shown in Figure 10-3.

10.1 Site Selection Process

A Site Selection Committee, chaired by Dr. R. P. Kraft with members from the University of California campuses at Berkeley, Los Angeles, Santa Cruz, and San Diego, was charged with finding the best scientific location for the Ten Meter Telescope. The principal site selection criteria adopted were:

1) minimal cloud cover;
2) low background sky light;
3) excellent astronomical seeing; and
4) low water vapor opacity and infrared sky noise.

Wind speed and accessibility of astronomical objects of particular importance were also considered in the committee's deliberations.

Without funding for a comprehensive site survey program, the committee necessarily limited consideration to known astronomical sites for which comparable meteorological and seeing data were available from an extensive survey by Dr. M. F. Walker. One additional potentially promising site, Mt. Bancroft (near White Mountain), California, was added to the list and a nine month seeing survey was carried out. Of the thirteen sites with comparable data, seven were initially rejected as failing to satisfy the astronomical criteria; sites in Chile, notably Cerro Tololo, were rejected at the chairman's request as being politically unsuitable. Five remaining

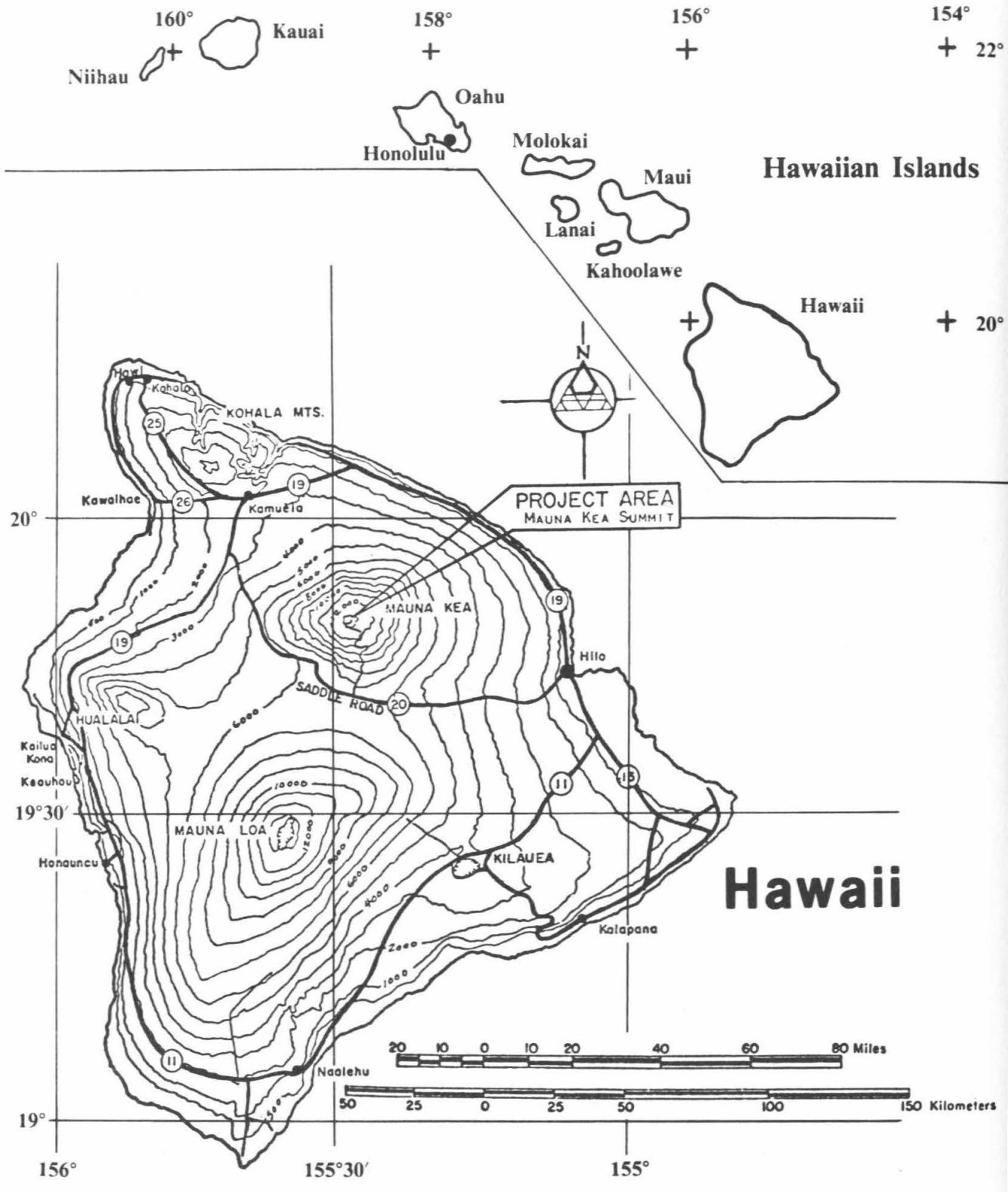

Figure 10-1 Mauna Kea, the site for the TMT, is shown on the Island of Hawaii. The inset shows the relationship of Hawaii to the other islands in the Hawaiian Chain.

XBL 852-1266

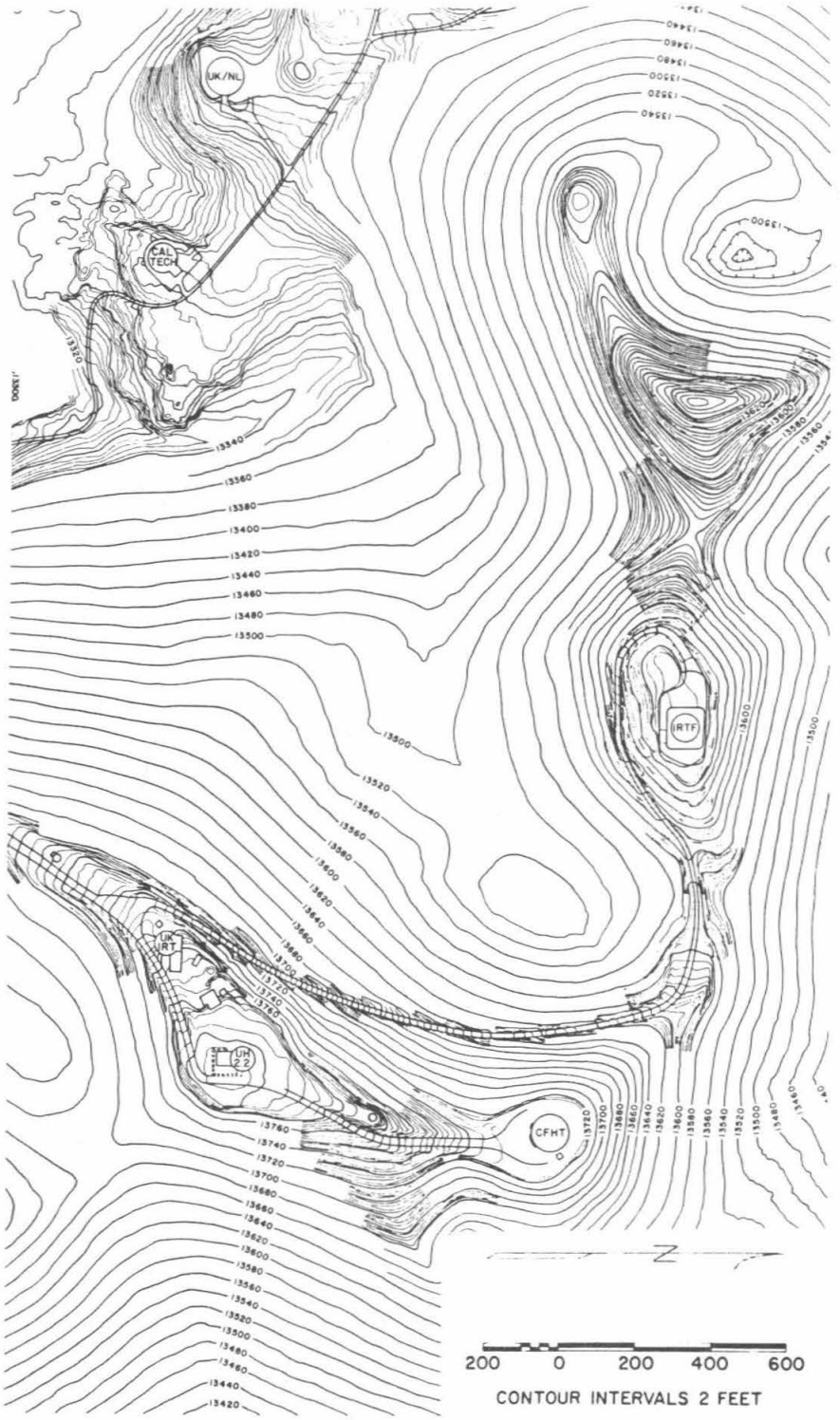

Figure 10-2 A contour map of the summit area of Mauna Kea shows the existing telescopes. The TMT site (the Northwest Cone) is the hill (pu'u) west of the IRTF. Note that north is to the right in this figure.

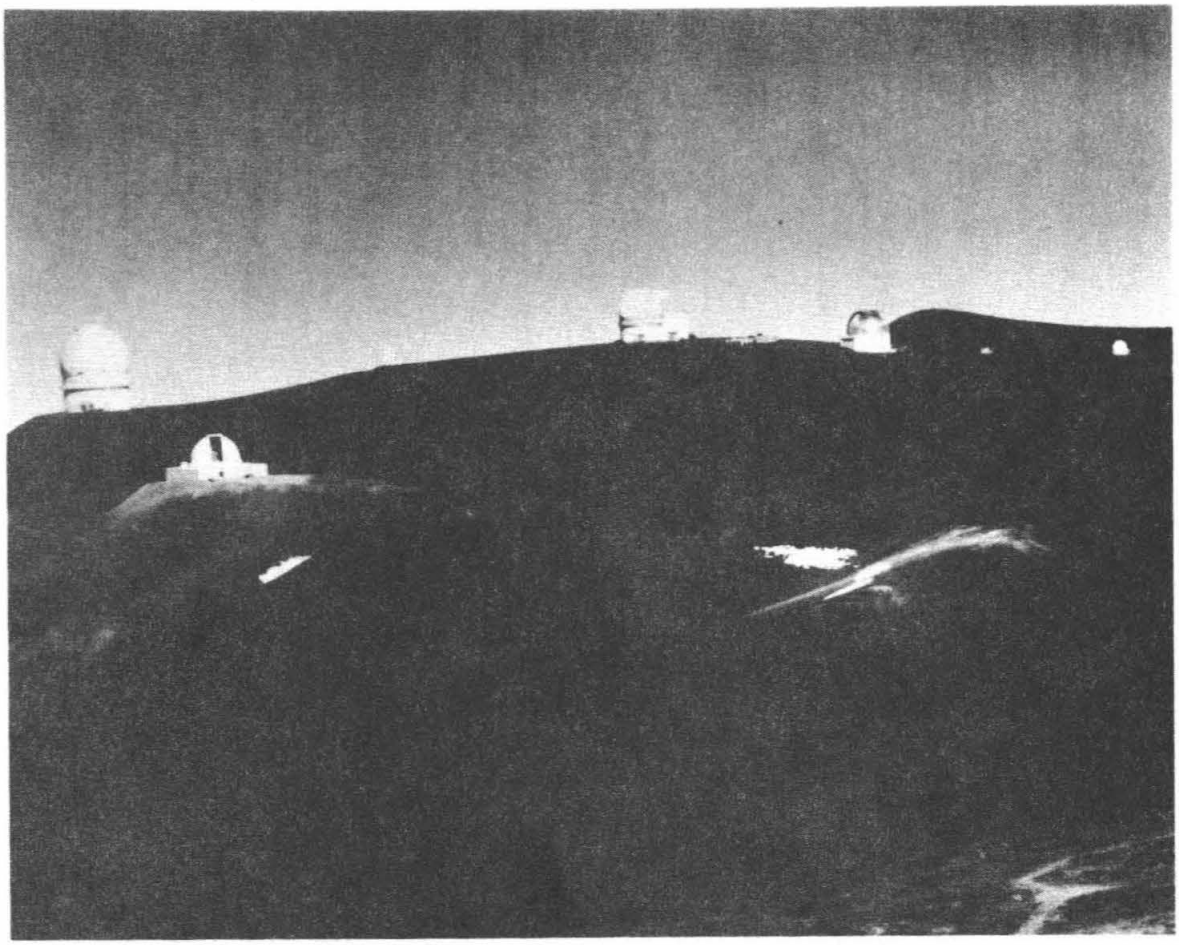

Figure 10-3 A photograph of the summit of Mauna Kea shows the existing telescopes and the TMT site (cinder cone in center).

sites were given more detailed consideration: 1) Fuente Nueva, La Palma (Canary Islands), 2) Encumeada Alta, Madeira (Spain), 3) Junipero Serra Peak, California, 4) Mauna Kea, Hawaii, and 5) Mt. Bancroft, California.

After several meetings in which the relative merits of the five sites were compared and the relative importance of the above criteria were discussed, the following conclusions were reached and documented in TMT Report No. 132:

1) All five sites would be acceptable sites for a large telescope;

2) None of the five sites emerged as clearly superior with respect to every criterion; however,

3) Overall, Mauna Kea, Hawaii, was judged clearly the best site, being at or near the top of the list for all principal criteria. In addition, the low northerly latitude of Mauna Kea (20^{o} N) offers the astronomer access to the Galactic Center in the southern sky.

Finally, the committee noted that long term climatic cycles have a dominant effect on site quality. Since the site quality data for the various sites were, in nearly all cases, obtained over an interval of several months there is some risk in the selection of a particular site as "best". Subsequent information suggests that Mauna Kea is probably an even better site than originally determined by the site selection subcommittee.

10.2 Site Description

Mauna Kea ("White Mountain" in Hawaiian; longitude 155° 28′ 20″ west, latitude 19° 49′ 34″ north), a dormant volcano, together with its still active neighbor Mauna Loa make up the bulk of the Island of Hawaii, the largest and easternmost island of the Hawaiian archipelago. Its summit, at an altitude of 4205m is the highest point in the Pacific. Above 3000m there is little vegetation and the summit area, consisting of several cinder cones rising 200 to 300m above the volcano shield, is a barren alpine desert. The surface is very dark, compacted volcanic cinder, partially cemented at depth by a layer of permafrost. The last volcanic activity on Mauna Kea occurred some 4000 years ago on the southern slopes, with one active region being about 3km north of Hale Pohaku. The cinder cones forming the summit ridge and the TMT site itself were formed during the Pleistocene era, in the Kuupahaan Stage about 40,000 years ago as determined by K/Ar dating. Mauna Kea is the only Hawaiian volcano with known glaciation. Glacial moraines that formed about 25,000 years ago form a skirt around the summit at an elevation of about 3500m. A geological summary of Mauna Kea has been published by Porter (1979a) who also published a geologic map of the area (Porter 1979b).

The mountain above 3660m (12,000ft) is managed by the University of Hawaii as a science reserve on long term lease from the State of Hawaii. The site selected for the Ten Meter Telescope is a cinder cone northwest of the Mauna Kea summit at an altitude of 4156m (13,636ft), shown in Figures 10-2 and 10-3. The TMT site is generally visible from the northwest of the island, including Waimea, and is invisible from the major urban areas of Kona and Hilo and most of the southern and eastern areas of Hawaii.

The Observatory is reached by a paved road running across the Humuula saddle between Mauna Kea and Mauna Loa which connects the population centers on the eastern (Hilo) and western (Kona and Waimea) sides of the island. At the 2000m level a paved road leads up the southern slope of Mauna Kea for about 10km to Hale Pohaku at 2832m. Here are located the mid-level dormitory and living facilities. The final 10km ascent to the summit is currently accomplished by 4-wheel drive vehicle over a steep graded dirt road. Plans exist for partially paving the summit road from the observatory down the mountain a few kilometers.

The principal non-astronomical activities on Mauna Kea are ranching (the famous Parker Ranch is on the slopes of Mauna Kea), hunting, and skiing.

A detailed account of the University of Hawaii's experience with Mauna Kea as an observatory site is given by Morrison *et al.*, (1973).

10.2.1 Weather

Briefly stated the summit of Mauna Kea is cold, somewhat windy and frequently clear. Weather data for Mauna Kea comes mainly from four sources. The most long term set of published data for the Mauna Kea summit ridge has been summarized by Kaufman and Vecchione (1981, TMT Report No. 66). They give a compilation for the years 1970-1978 from the UH 2.2m telescope. The basic data are quite limited, being single data entries for each day. More limited records of observing conditions on the NW cone have been published by Walker (1983, TMT Report No. 123) and consist of occasional nighttime measurements made by observers responsible for the seeing tests at the site. These data cover a six month period in 1981. Continuous observations of wind speed and direction at the NW cone are now available for about 12 months in 1983 (Budiansky and Nelson, 1984, TMT Report No. 130). Although wind conditions appear to vary considerably over the summit area, temperature conditions are expected to be more uniform. An excellent set of continuous temperature and other weather data exists (for the twelve months of 1983) that were taken on top of the CFHT dome, some 30m above the ground (Bely and Nelson, 1984 TMT Report No. 133). This height is particularly valuable in assessing air temperature well away from thermal ground effects that may strongly influence the UH 2.2m data set. They may, however, be influenced by the dome. The temperature sensor is 1.5m from the top of the shutter.

Temperature

Kaufman and Vecchione report maximum and minimum recorded temperatures of 24°C (75°F) and -15 °C (5°F) with a typical range from 10°C (50°F) to -1°C (30° F). Figures 10-4, 10-5, and 10-6 show the average monthly minimum and maximum temperatures and extrema, the distribution of minima and maxima, and the distribution of diurnal temperature variation. Air temperature variations on Mauna Kea are relatively mild as shown by the CFHT data. Figure 10-7a shows the distribution of temperature occurrences over the 24 hour period and the integral of the distribution. The average temperature is about 2.5°C and 90% of the time the temperature is within ±4°C. Figure 10-7b shows the same distributions but for the nighttime hours of 19:00 to 05:00. The average is about 2.0°C and the width of the distribution is almost unchanged.

Of particular importance for astronomical observations is the stability of the temperature during the prime nighttime hours. The CFHT data indicate that the average change in temperature during the nighttime hours (19:00 to 05:00) is only about 1.5°C and is under 3°C about 90% of the time. These results are shown in Figure 10-7c. The measurements by Walker give essentially the same result at the TMT site. A typical two day temperature profile from the CFHT is shown in Figure 10-8.

Wind

The winds recorded for the Mauna Kea summit ridge are principally from due east (35%) or west (20%), with calm or light and variable winds occurring 12% of the time according to the UH 2.2m telescope records. A wind rose for the summit ridge is shown in Figure 10-9. The wind direction is seasonal, being primarily westerly in the first half of the year and easterly in the second half. The recorded speeds for the summit ridge indicate that the wind speed is below 20m/s (45mph) 95% of the time and less than 11m/s (25mph) 84% of the time. Maximum wind velocities occur in January and minimum velocities in September with a nearly sinusoidal variation.

More recently, limited studies of the wind at the TMT site itself have been made. These studies suggest that the wind speeds are generally substantially lower on the northwest cone than on the summit ridge. Analysis of 5903 hourly wind speed samples obtained between October 1982 and November 1983 indicates that the 95 percentile wind speed for the TMT site is only 14m/s (31mph) (Budiansky and Nelson, 1984, TMT Report No. 130). The design criterion for the TMT is to maintain high quality (less than 0.25 arcsecond image blur) performance at wind speeds up to 14m/s, and to be operational up to 30m/s. The wind velocity distribution for the northwest cone is shown in Figure 10-10. The wind speed distribution and the integrated wind speed distribution for the northwest cone are shown in Figures 10-11 and 10-12. These records show a more uniform distribution of wind direction than the UH 2.2m data; however, there is some concern about whether the wind direction indicator was functioning properly during the entire period. Analysis of nighttime wind direction records on the TMT site from July 1981 to January 1982 (Walker, 1983, TMT Report No. 123) show a strong maximum in the frequency of wind direction in the NE-E with a secondary maximum in the SW. Figure 10-13 compares the 24hr/day site wind direction data with the nighttime wind data of Walker.

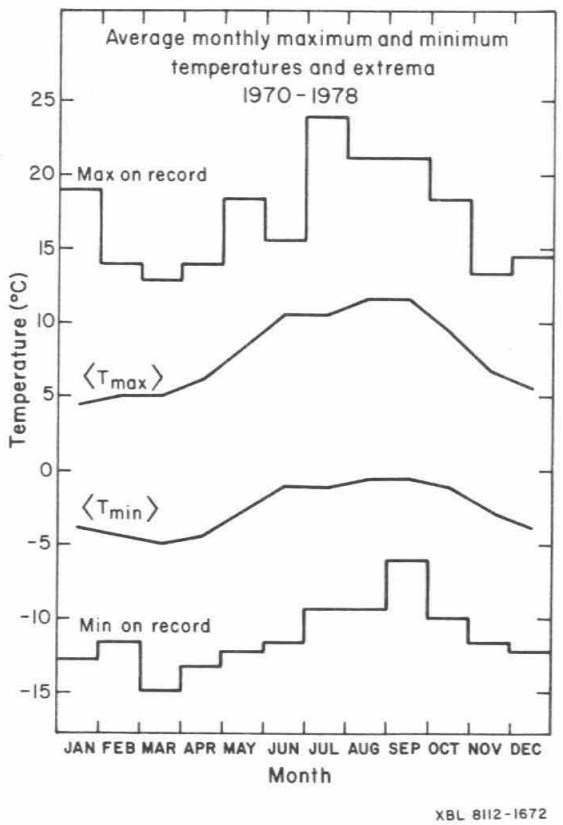

Figure 10-4 Average monthly maximum and minimum temperatures and extrema. 1970 to 1978.

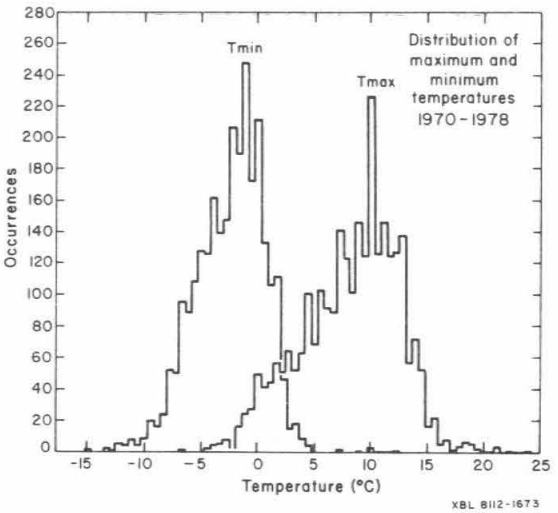

Figure 10-5 Distribution of maximum and minimum temperatures. 1970 to 1978.

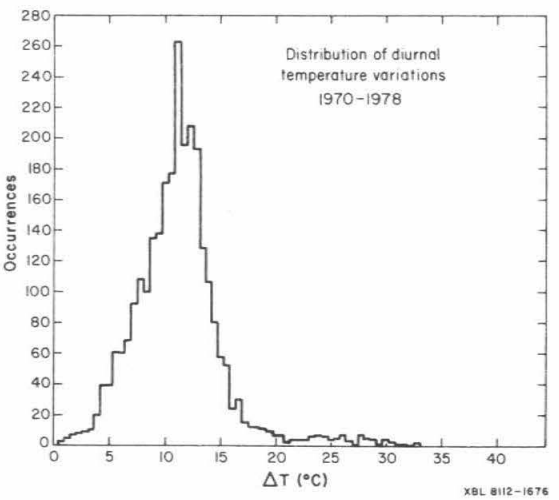

Figure 10-6 Distribution of diurnal temperature variations. 1970 to 1978.

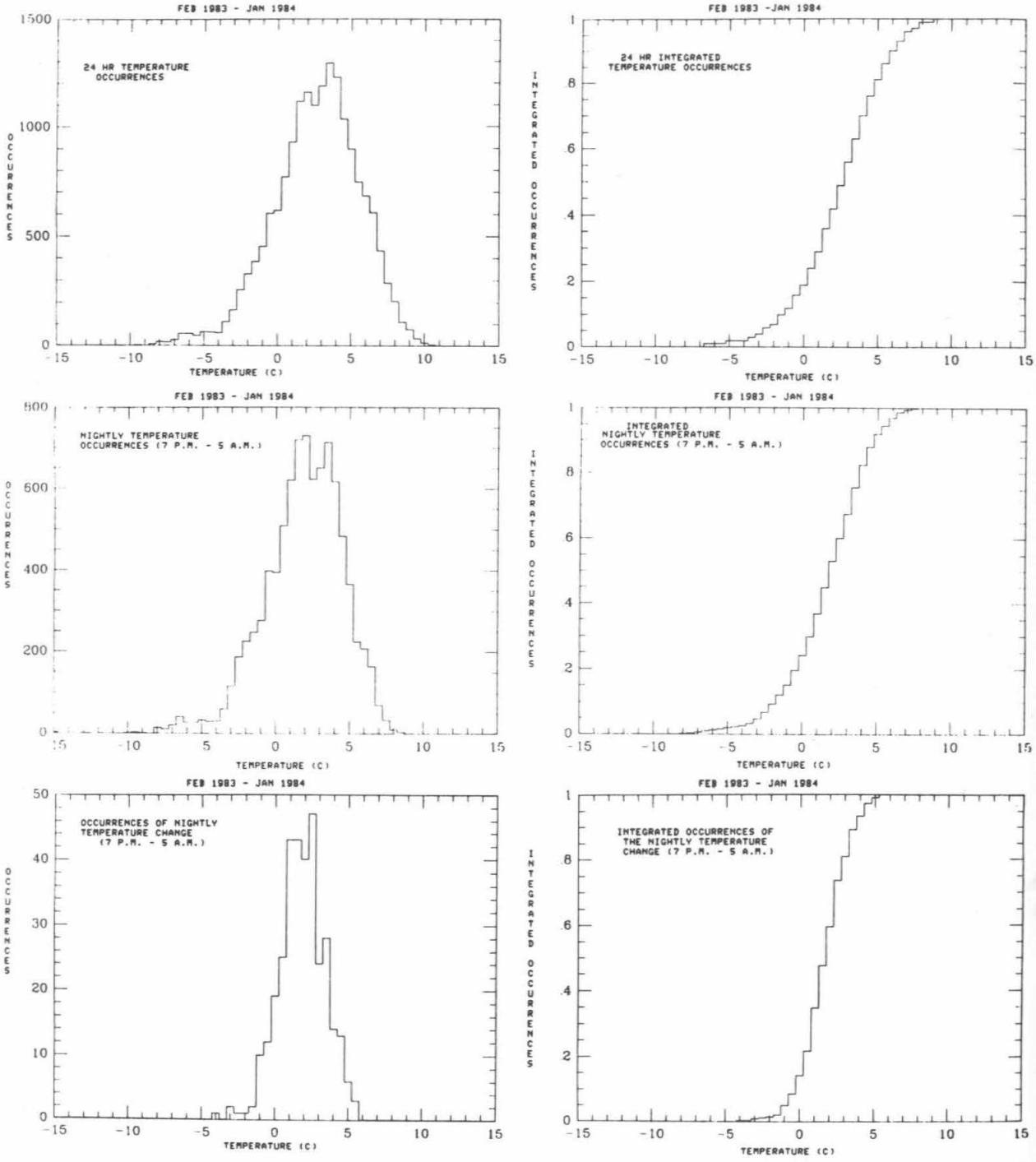

XBL 8412-5087

Figure 10-7 CFHT data show that temperature variations on Mauna Kea are relatively mild.

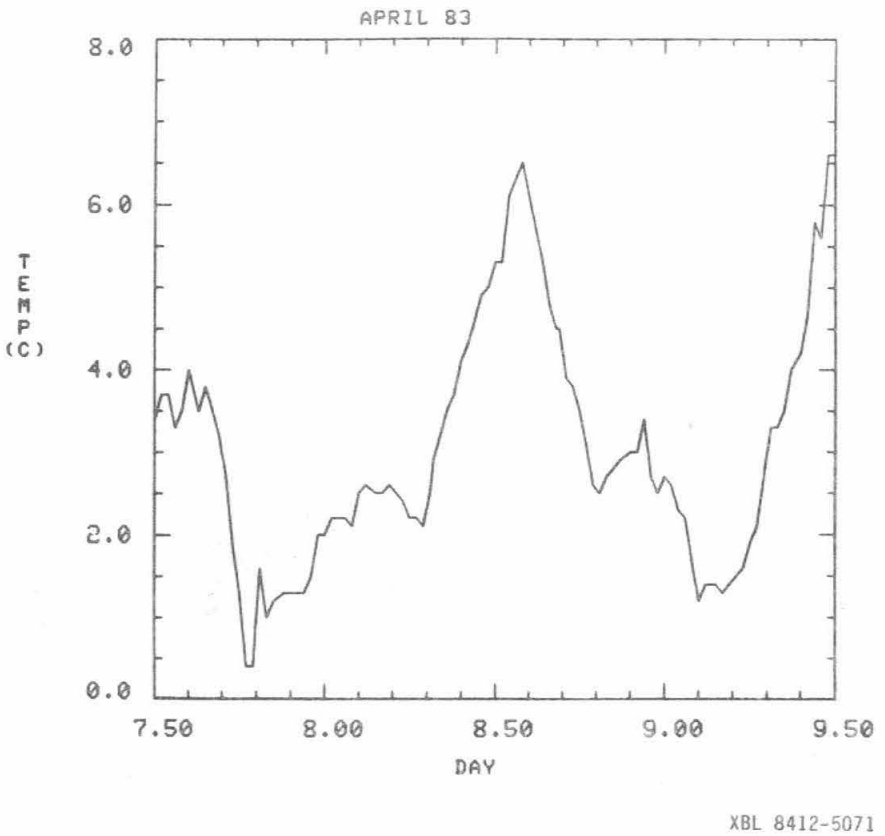

Figure 10-8 A typical 2 day temperature profile from the CFHT.

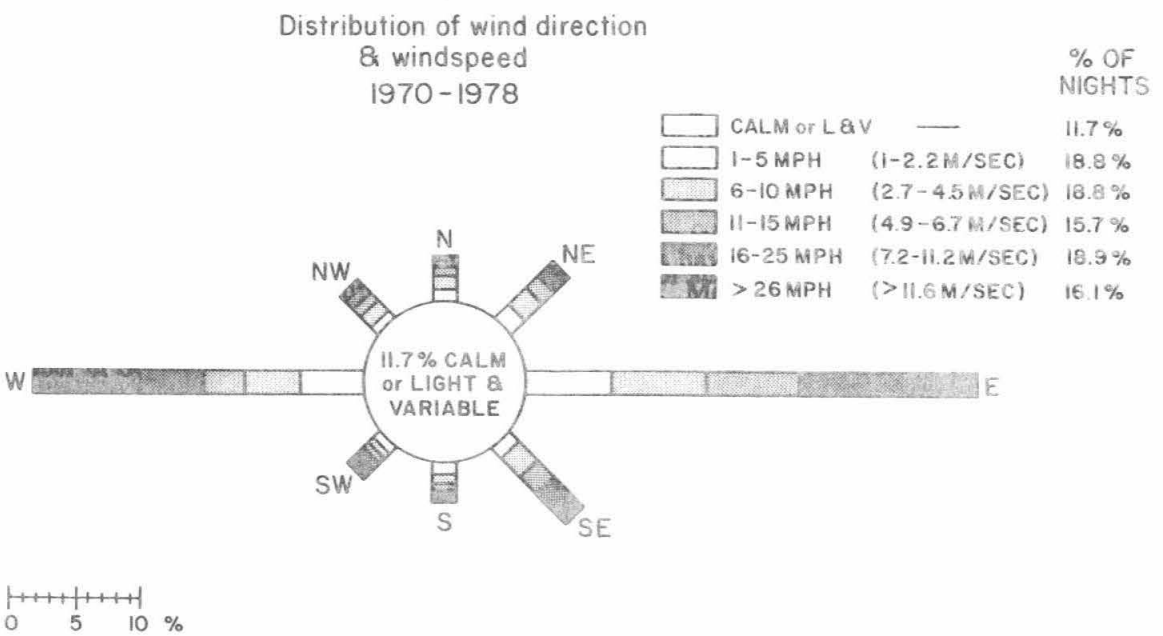

Figure 10-9 A wind rose for the summit ridge.

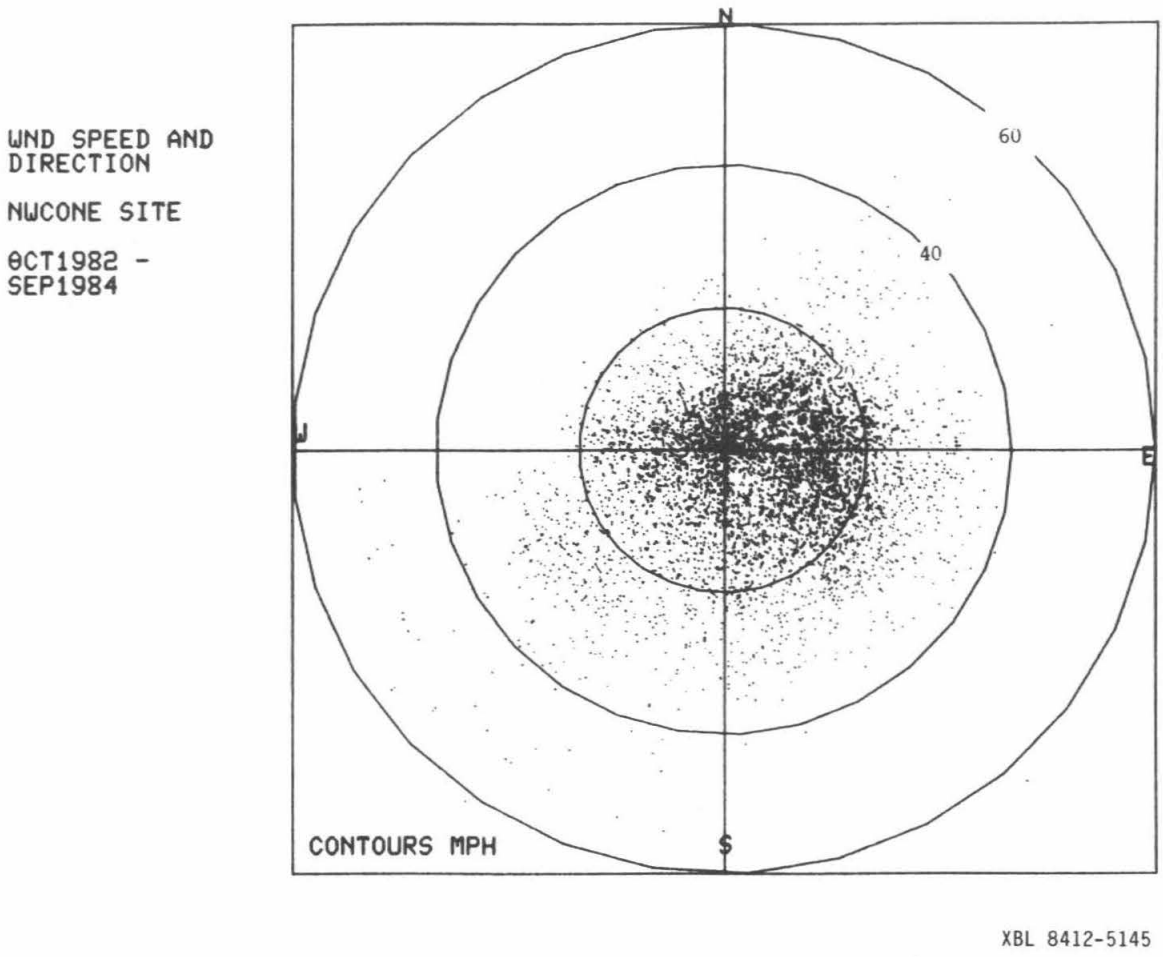

Figure 10-10 The wind velocity distribution for the northwest cone.

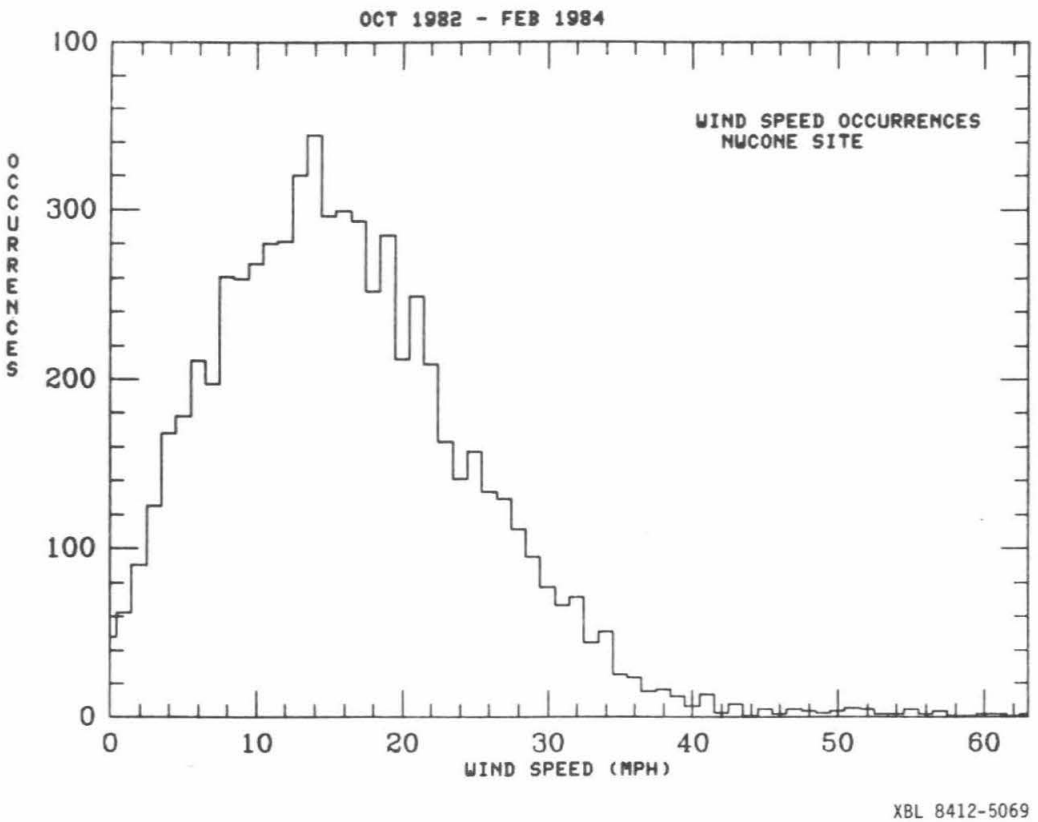

Figure 10-11 The wind speed distribution for the northwest cone.

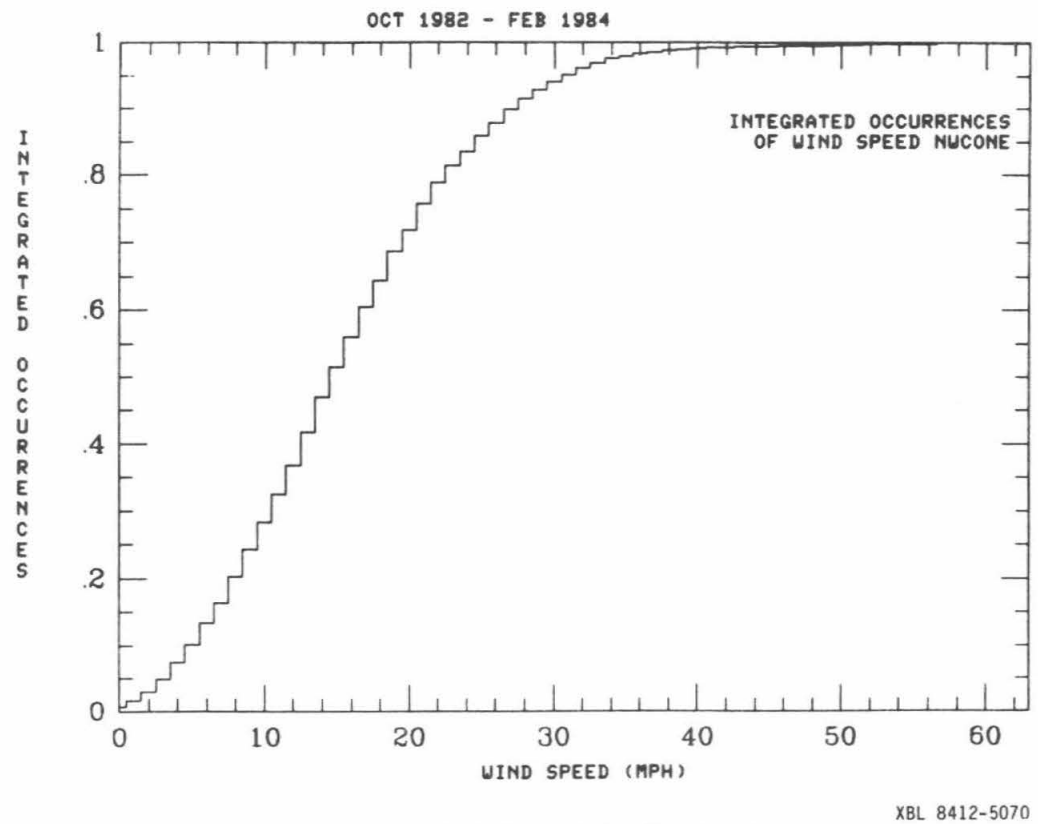

Figure 10-12 The integrated wind speed distribution for the northwest cone.

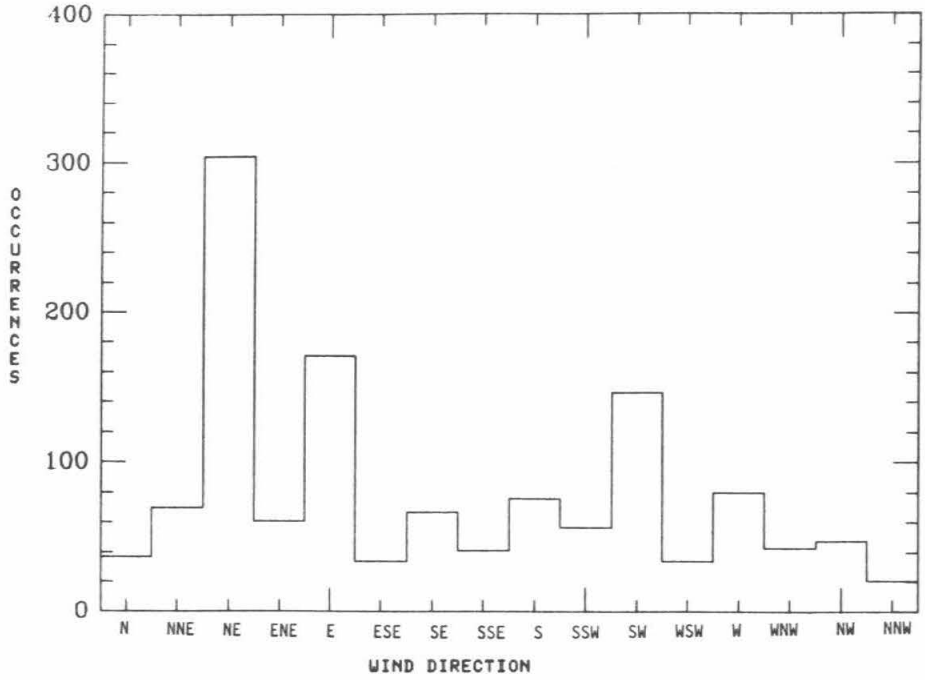

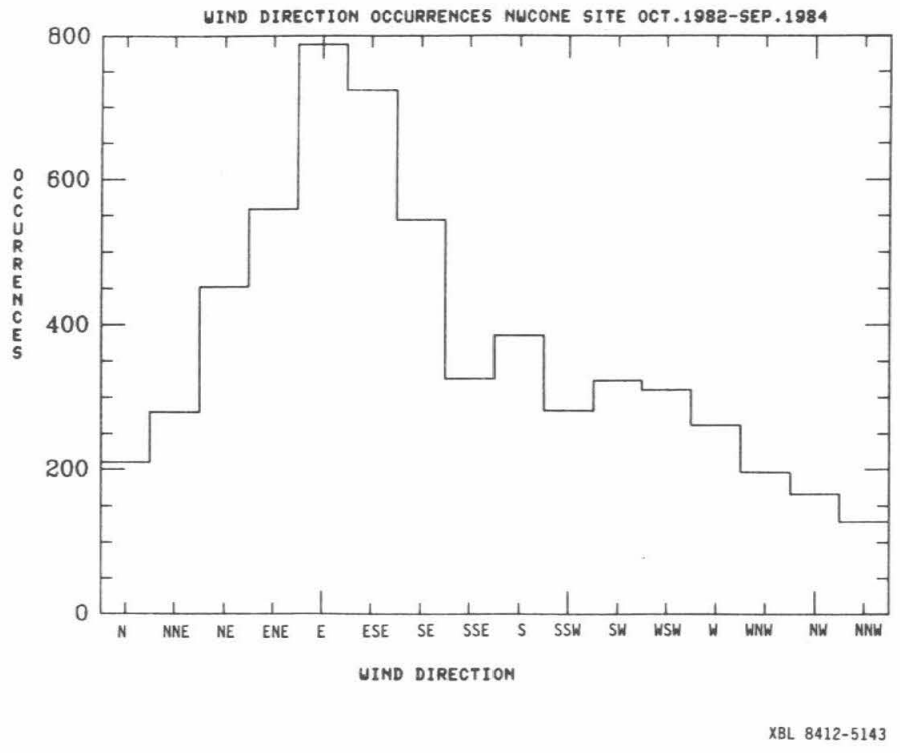

Figure 10-13 The nighttime wind data for the northwest cone (top, Walker) is compared with the 24hr/day data (bottom).

Precipitation

Most of the precipitation at the observatory is freezing fog or snow, which can fall at any time of the year. Only between December and March is there likely to be significant accumulation of ice or snow. Heavy snowfalls (100 to 400mm) typically occur two to five times each winter, but conditions vary from year to year. Some years, deep snow drifts have limited access to the summit, while in others, little snow has accumulated. Access to the summit is expected to be improved with the new paved road. Detailed precipitation records are not available.

Cloud Cover

The most important weather statistic is the fraction of clear nights for observations. Kaufman and Vecchione report that the sky at Mauna Kea is photometric (no cloud cover) on 45% of the nights with an additional 30% spectroscopic (thin cirrus or intermittent 10 - 40% cloud cover) so that 75% of all nights are usable for observing. The distribution of cloud cover through the year is shown in Figure 10-14.

10.2.2 Astronomical Seeing

Seeing measurements on Mauna Kea have been published by McInnes (1981) and Walker (1983, TMT Report No. 123) for the period July 1981 to January 1982. The seeing measurements by McInnes and Walker establish Mauna Kea as among the very best of the world's well studied sites. Data taken simultaneously in 1974-1975 at the northwest cone (the TMT site) and the summit ridge, where the other optical and infrared telescopes are located, indicate that the seeing on the northwest cone is somewhat better even than that on the ridge (Walker, 1984, TMT Report No.124). Under most conditions the seeing at both sites is comparable; however, when the wind is from southerly directions (approximately 15% of the time) the seeing deteriorates somewhat at both sites and becomes wind dependent. (Walker's studies show no correlation between seeing and wind velocity for other wind directions and anecdotal accounts describe excellent seeing at wind speeds up to 60mph.) When the wind is southerly however, the magnitude of the seeing degradation is larger on the summit ridge by up to several arcseconds, suggesting a local origin for the turbulence.

The above measurements have been made with a small telescope on Polaris (70^o zenith distance) and thus are not directly comparable with the expected images at the zenith with a large telescope. With the use of atmospheric seeing theory these measurements can be related to large telescope measurements. Racine (1984) has compiled imaging data from the CFHT and the UH 2.2m telescope. Overall the data suggest that one may expect visible wavelength images better than 0.5 arcseconds (Full Width Half Maximum) 10% of the time and images better than 1 arcsecond approximately 50% of the time. This is shown in Figure 10-15. When corrected for zenith angle effects using atmosphere seeing theory (Fried, 1966), the Polaris data is in good agreement. Several groups familiar with Mauna Kea suggest that at times of very good seeing, image wander, rather than image blur, is the dominant contributor to image size. In these cases there has been some success in improving the seeing over small fields by adaptive optical techniques (Thompson and Ryerson, 1983). Unfortunately, theories of atmospheric seeing (Fried, 1966) suggest that as the aperture increases substantially beyond r_o (the atmospheric coherence diameter), the relative contribution due to image wander will decrease, hence these adaptive optical techniques may be less useful for the TMT.

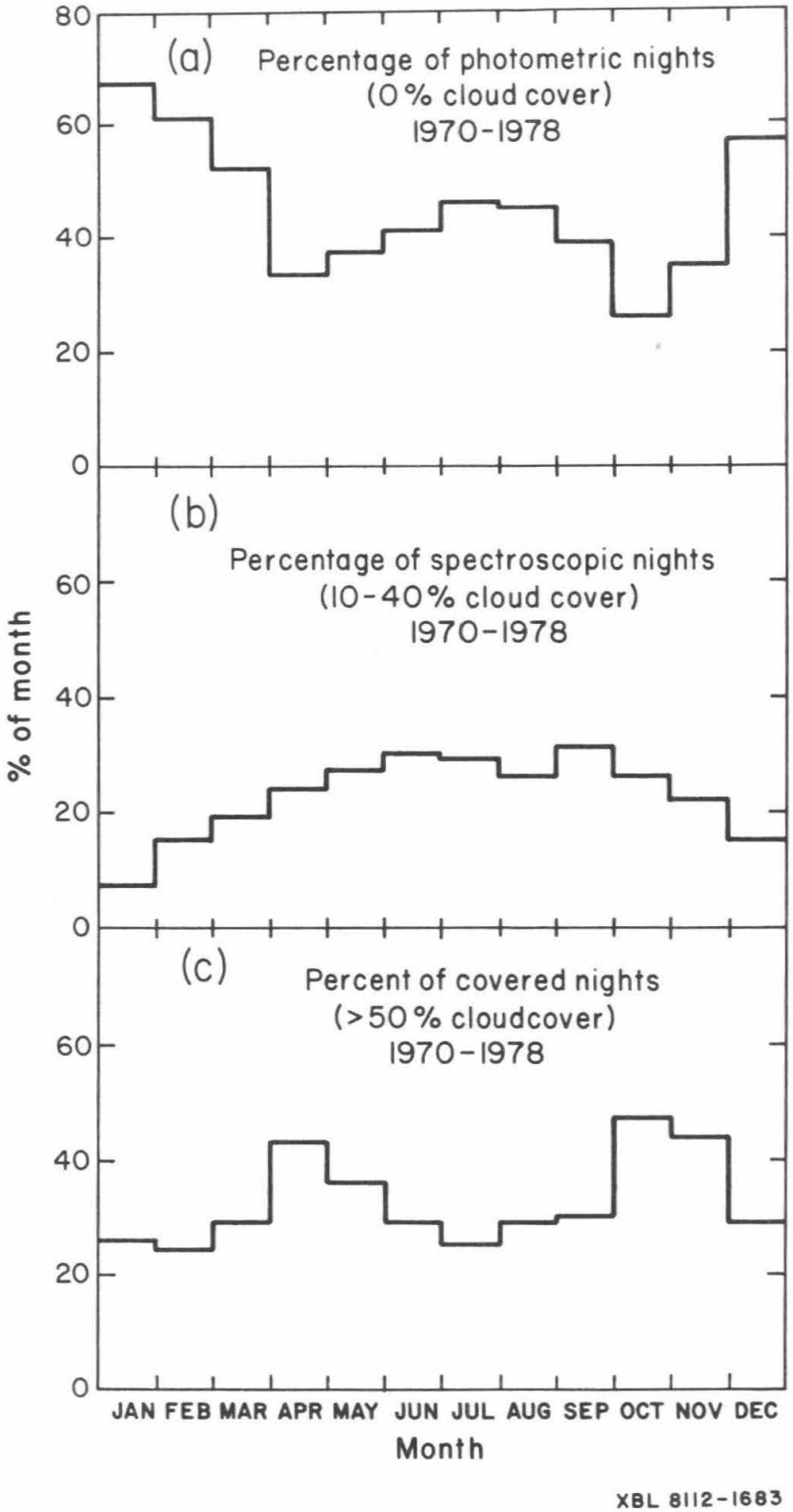

Figure 10-14 The distribution of cloud cover through the year.

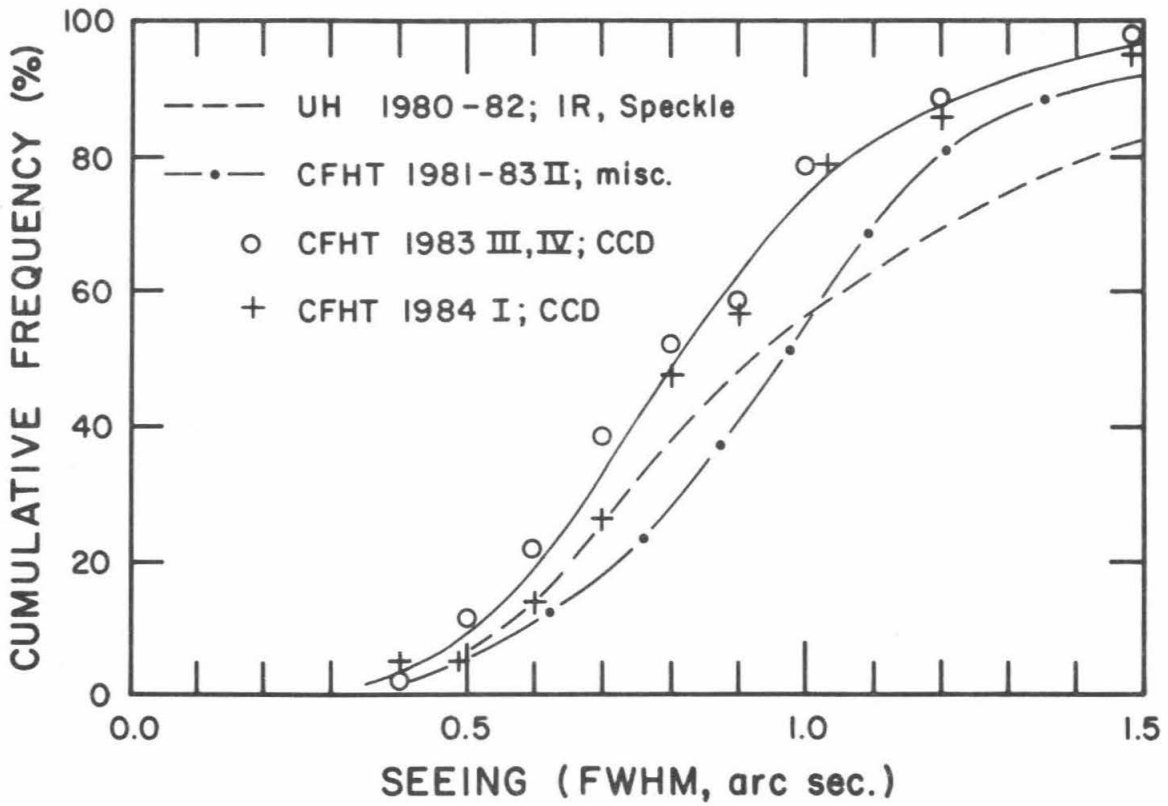

Figure 10-15 Seeing statistics from CFHT and UH telescopes on Mauna Kea from Racine, 1984.

10.2.3 Infrared Astronomical Considerations

An ideal infrared site is cold, to reduce background emission from the telescope and sky, and dry, to minimize infrared water vapor absorption/emission. The generally low temperatures and high thermal stability on Mauna Kea clearly satisfy the first criterion. Westphal (1972) has conducted a NASA sponsored study of water vapor content of the atmosphere at Mauna Kea and seven other observatory sites during the interval June 1971 and July 1972. Woolf (1985) has described a classification scheme for infrared sites based on the amount of precipitable water vapor in the atmosphere above the site:

Class A: $<$ 1.5mm precipitable water vapor. Observations are possible in all infrared windows and in the submillimeter region of the spectrum.

Class B: 1.5mm - 4.5mm H_2O. Observations are possible to 25μm in the infrared and at some wavelengths short of 1mm.

Class C: $>$ 4.5mm H_2O. Observations are possible at 3.5μm and 10μm but there is some absorption even at the centers of those bands. Longer wavelength observations are not possible and some shorter wavelength windows are compromised.

The average precipitable water vapor at Mauna Kea reported by Westphal is 2.04 $\pm$ 0.47mm. 16% of nights have less than 1mm H_2O, 51% have less than 2mm and 83% have less than 3mm. These numbers come from daytime measurements of 10μm absorption, and it is recognized that there may be calibration errors and that the nighttime water vapor may be lower.

Nonetheless they place Mauna Kea as one of the driest sites in the world and among the best in the Westphal survey. More recent measurements of water vapor emission have recently been undertaken. While analysis of these data is incomplete they tend to corroborate the previous measurements (Merrill, and Forbes, 1984)

Other confirmation of the quality of Mauna Kea as an infrared site exists in the considerable literature of successful infrared observational projects carried out at Mauna Kea and the fact that NASA and the United Kingdom have erected their respective national infrared facilities on Mauna Kea.

10.2.4 Optical Sky Brightness

A sky brightness $m_b \approx 23.0/\text{arcsecond}^2$ has been measured by Dr. S. C. Wolff (Morrison *et al,* 1973) which is as dark as any known astronomical site. The island nature of Mauna Kea and the limited potential for major population growth suggest that Mauna Kea will maintain such dark skies for the foreseeable future. A county lighting ordinance has been enacted to control public lighting. Low pressure sodium vapor (LPS) lamps favorable to astronomical observations have been nearly uniformly installed where public lighting exists. Finally, a working group is being established among Mauna Kea users, including TMT representatives, to anticipate potential problems before they develop and to lobby for stricter control in areas of concern.

10.2.5 Site Latitude

One notable advantage of Mauna Kea is its low latitude of 20^o. If we restrict ourselves to observations through less than two air masses, 81% of the celestial sphere is accessible to Mauna Kea, whereas only 69% is available from Lick Observatory. At up to three air masses, 89% of the heavens are visible. The center of the galaxy ($\alpha = 17^h49^m$, $\delta = -28^o55'$) can be seen through as little as 1.5 air masses.

10.2.6 Altitude

The high altitude of the site (4150m) has several important consequences. The mean air temperature ($\approx 2^o$C) is low, and along with the effects of the scale height of water in the atmosphere, leads to a very low precipitable water vapor content. This is a notable virtue for some infrared observations. Unfortunately, the atmosphere oxygen partial pressure is only about 60% of that at sea level, and this can lead to physiological difficulties. Although only very rarely life-threatening, this reduction can reduce the mental and physical performance of personnel at the site. Some of these problems are discussed by Cudaback (1981, TMT Report No. 51) and Forster (1984). Oxygen enrichment schemes are discussed in Section 9.3.4.

10.3 Continued Site Testing

In order to confirm the quality of the northwest cone site and in order to make decisions regarding site-specific design considerations (e.g., telescope height with respect to ground turbulence), testing has continued in four specific areas:

1) Acoustic echo tests of atmospheric turbulence around the site,
2) studies of the microthermal turbulence as a function of altitude above the site employing a 50-foot test tower (being carried out by UH for UC),
3) wind tests on the northwest cone cited above, and
4) soil tests.

Results from studies 2) and 4) are not yet available. Preliminary results from the acoustic sounding tests are given below.

10.3.1 Acoustic Sounder Measurements

Telescopes often have been placed on towers at least 20 meters above ground level, with the belief that they would be above sources of locally induced poor seeing. Further analysis shows this not to be true at all sites. The stellar image is broadened by turbulence in the free atmosphere without ground effects, in the boundary layer next to the ground, and in effects of man-made structures and heat sources. Under best conditions the boundary layer effect is small compared to the free atmosphere effect, and there is little value in raising the telescope above the ground. In mid-day the boundary layer turbulence gives a much bigger effect than the free atmosphere, but then the turbulence is so deep that a 20 meter tower below the telescope is too short to improve seeing noticeably. We have seldom seen conditions at Mauna Kea in which such a modest increase in telescope elevation would be of appreciable benefit.

Recent free atmosphere turbulence studies at Hawaii give a mean image diameter of 0.37 arcseconds from the free atmosphere alone, (Bely, 1984) and the total image size can never be less than that. An acoustic sounder has been operating for 7 months to determine boundary layer seeing. The acoustic echo strength is measured as a function of height above ground, and the image size is calculated with this. Details are given by Cudaback (1984, TMT Report No. 131). The image size is calculated as would be seen with a telescope at various heights above ground. During the night the boundary layer contribution to image size is always less than 0.25 arcseconds (seen from the surface), so the free atmosphere dominates. During the day the boundary layer contribution is always greater than 0.25 arcseconds. The exponential scale height for the reduction above the surface is always greater than 40 meters and is typically 100 meters. Consequently, elevating the telescope $\leq$ 20m cannot help significantly.

11. Summary of Design Parameters

Contents **Page**

In this section the design parameters of the telescope, building, dome, and site are summarized in tabular form. For more details, the reader should refer to the relevant sections.

Table 11-1
Primary Mirror

Geometry	
Effective collecting area	$76m^2$
Number of hexagonal segments	36
Segment diameter	1.80m
Spaces between the segments	3mm
Non-reflecting gap including bevels	7mm (0.75% of total surface)
Primary focal length (f/1.75)	17.5m
Primary conic constant	-1.0038
Segments	
Segment thickness	75mm
Thermal expansion coefficient	less than $10^{-7}/^{o}C$
Segment sagittal depth	11.6mm (max)
Surface deviation from the best fitting sphere for the most extreme segment	42μm rms
Segment weight	400kg
Thermal time constant (internal)	12 minutes
Segment Support	
Individual segment axial support[†]	36 point (3 whiffletrees)
Individual segment radial support[††]	1 central post with diaphragm + supplement
Passive support deflections (axial)	8.6nm rms
Passive support deflections (radial)	8.0nm rms
Support resonant frequency	50Hz (both axial and radial)
Control Elements	
Sensors (total 168)	capacitive displacement sensors
Material	low expansion glass
Mechanical range	± 2 mm
Linear operating range	$\pm 6.1\mu$m (ADC resolution: 3.0nm)
Adjustable offset	$\pm 20\mu$m
Total operating range	± 1.5mm
Power dissipation	100mW
Noise level at 1KHz	0.8nm rms
Drift (time and temperature)	less than 10nm per day
Weight	2kg
Sampling rate	300Hz
Paddle offset	60mm

Actuators (total 108, 3 per segment)	torque motor driven roller screw
Range	±1.5mm
Incremental step size	3.75nm
Positioning noise	±10nm
Power consumption	
At zenith	0.75W
At horizon	2W
Peak available	75W
Maximum slew rate	1cm/sec
Update rate	300Hz
Weight	10kg
Length	600mm
Diameter	130mm
Motor time constant	2.1ms
Active control system	
Update frequency	800Hz
Computation time	$<300\mu s$
Computation operations	4×10^4
Computer	Parallel processor

Mirror Cell	
Maximum gravitationally induced segment motion	0.64mm
Lowest resonant frequency	20Hz

Weights	
Glass	14.4 tons
Sensors	0.3
Actuators	1.1
Subcells	1.8
Whiffletrees	1.5
Cables, Electronics	1.5
Forward Cassegain/Tertiary	2
Cassegrain instrument	2.0
Mirror Cell	≈5
Total weight	29.6 tons

†Axial support is the support in the direction normal to the plane tangent to the segment.

††Radial support is in the plane tangent to the segment.

Telescope Structure

Two major objectives defined the structure. First,under an assumed wind load of 50kgf at the top of the telescope,total image motion is required to be under 0.25 arcseconds. This places minimum stiffness requirements on the telescope tube and on the telescope yoke, and thus sets their weights. This wind force will result from a 14m/s (30mph) wind outside the dome, with an assumed factor of 2 reduction in speed due to dome shielding. The second major objective is that the gravity induced mirror cell deflections at the segments should be no greater than 1mm. This extremely stiff cell reduces the range requirements of the sensors and the actuators, and maintains a relatively high resonant frequency in the mirror cell. This constraint sets a minimum weight to the cell. These constraints, along with the weight of the primary mirror itself, determine the location of the center of mass of the telescope and thus set the size of the dome,etc.

Table 11-2
Telescope Structure

Telescope Tube	
Length	22m
Elevation axis to mirror vertex	4.00m
Elevation axis to ground level	12m
Weight	70.6 tons
Forward Cass./Tertiary	2
Cassegrain Instrument	2.0
Primary Mirror Assembly	25.6
Mirror Cover	1.2
Bottom Tube	2.0
Elevation Box + Drives	22.8
Upper Tube	9.6
Top Ring	3.4
Prime Focus Instrument	2.0
Yoke and Nasmyth Platforms	
Height (elevation axis to pier)	12m
Base	12m × 12m
Weight	90 tons
Total Telescope Moving Mass (excluding Nasmyth instruments)	161 tons
Nasmyth Platforms	5 × 8m
Weight limit	10 tons/platform
Lowest resonant frequency	5Hz
Bearings	hydrostatic, 8 elevation, 4 azimuth
Drives	friction, direct, 4 azimuth, 2 elevation
Slew Rate	$\geqslant 3^{o}$/s(anywhere to anywhere < 2 minutes)
Pointing error	less than 1 arcsecond (rms at night) less than 2 arcsecond (day)

Tracking stability (open loop)	0.1 arcsecond over 10 minutes 0.5 arcsecond over 1 hour at night 1.0 arcsecond over 1 hour during day
Zenith blind spot	less than 1^o diameter
Horizon limit	$< 15^o$ from horizon

Table 11-3
Optics

Primary	
f/1.75 hyperbola	K=-1.003796 (RC at f/15)
Maximum diameter	10.95m (hexagonal, minimum f-ratio = 1.59)
Radius of curvature	35m
Error budget to give 80% of energy in circle 0.32 arcseconds in diameter (See Table 4-2)	
Prime focus	f/1.75
Scale	11.8 arcsecond/mm
Field of view	$\approx$ 1 arcminute uncorrected
Field of view	uncorrected: 1.5 arcseconds sph. ab. on axis 1.8 arcseconds coma at 30 arc seconds field radius
Instrument weight limit	2 tons
Available space	2m diameter $\times$ 3m long cylinder focus near top
Prime focus camera	
Scale	10.3 arcseconds/mm
Field of view	30 arcminutes
f/15 focus	7 positions: Cassegrain, Nasmyth, Bent Cass
Back focal length	3m
Scale	1.38 arcseconds/mm
Field	30 arcminutes/1.30m (images $<$ 1 arcsecond)
Range of focus	$\pm$0.96m, images $<$ 1 arcsecond (limited by spherical aberration)
Baffling	near secondary, diameter 2.6m
Space and weight	
Cassegrain	
Weight limit	2.0 tons
Space	1.3m diameter x 3m long cylinder
Available distance behind focal plane	2.0m
Unvignetted field	20 arcminutes(0.87m)(with baffles)
Bent Cassegrain	
Weight	250kg
Space	1m diameter $\times$ 2.0m long
Available distance behind focus	1m
Field of view	5 arcminutes
Nasmyth (one each side)	
Weight limit	10 tons
Space	platform 5 x 8m
Beam height	1.5m above platform
Focal point	1m from vertical centerline of elevation bearing
Unvignetted field	20 arcminutes (0.87)(with baffles)

f/25 focus (IR)	Forward Cassegrain
Back focal length	-4m
Scale	0.825 arcseconds/mm
Field	20 arcminute/1.45m (images less than 1 arcsecond)
Range of focus	±2.48m (images less than 1 arcsecond)
Chopping secondary	30Hz at ±30 arcseconds
Space and weight	1.3m × 2m 1000kg
f/100 Coudé	
Scale	0.206 arcseconds/mm
Max field	90 arcseconds/0.44m
Back focal length	70m

Table 11-4
Secondary and Tertiary Optics

f/15 Ritchey-Chretien focus (Nasmyth, Cassegrain, Bent Cassegrain)	
Secondary Mirror	
Clear aperture	1.429m (20 arcminute FOV)
Radius of curvature	-4.8493m
Conic constant K_2	-1.64308
Distance to primary	15.358m
Primary vertex - focal plane distance	3m
Displacement tolerances†	
Tilt (0.05, 0.05 arcseconds)(coma)	± 11.3 arcseconds
Decenter (0.05, 0.05 arcseconds)(coma)	± 115μm
Axial (0.15 arcseconds)	± 25μm (single exposure)
Tertiary Mirror	
Clear aperture	1.04m × 1.43m (20 arcminute unvignetted field)
Distance to primary	-4.0m
Displacement Tolerances	
Tilt	<3 arcseconds
Piston normal to surface	1.3mm (0.15 arcseconds of defocus)
In plane of mirror	∞
f/25 IR focus (Forward Cassegrain)	
Secondary Mirror	
Clear aperture	0.5266m diameter hexagon
Radius of curvature	-1.8993m
Conic constant K_2	-1.41725
Distance to primary	16.6168m
Primary vertex - focal plane distance	-4.0m
Displacement tolerances†	
Tilt (0.05, 0.05 arcseconds)	± 27.1 arcseconds
Decenter (0.05, 0.05 arcseconds)	± 112μm
Axial (0.15 arcseconds)	± 25μm (single exposure)
f/100 Coudé focus	
Secondary Mirror	
Clear aperture	0.9485m
Radius of curvature	-3.0634m
Conic constant K_2	-1.11906
Distance to primary	15.9951m
Primary vertex - focal plane distance	70.0m

†Tolerances shown are calculated assuming an initially perfectly focussed image. Values given correspond to displacement which would cause a defocussed image such that 80% of the light would lie within a circle having the indicated diameter. Tilt and decenter tolerances are displacements from nominal design values which must be met during all operating conditions. Axial displacements usually induce only defocus errors which can be compensated by moving the secondary mirror. Axial tolerances must therefore be held only during "single exposures" between telescope refocussing.

Table 11-5
Building and Dome

Building	
Telescope support and maintenance	$452m^2$ ($4865ft^2$)
Observing support	$336m^2$ ($3620ft^2$)
Personnel support	$206m^2$ ($2215ft^2$)
Elevator (2m × 3m capacity)	3 tons
Cranes	
Instrument handling	10 tons
Mirror handling	5 tons
Dome	
Floor	$535.1m^2$ ($5760ft^2$)
Nasmyth deck	$371.6m^2$ ($4000ft^2$)
Inside radius	17.5m (57.5ft)
Outside radius	18.3m (60ft)
Spring line height	14.0m (46ft)
Overall height	31.7m (104ft)
Slit width	10.9m
Thermal control	all surfaces exposed to inside air are insulated

Table 11-6
Site - Mauna Kea

Elevation	4150m
Latitude	19^o 49'
Longitude	155^o 28'
Temperature	$2.5^o \pm 4^oC$ (90% of time)
Air pressure	454mm Hg
Air density	$0.764kg/m^3$
Nighttime temperature variation	2^oC
Wind speed	≤ 6m/s (14mph) 50% of time
	≤ 14m/s (31mph) 95% of time
Humidity	< 15% (50% of time)
Cloud cover:	
Photometric	45%
Spectroscopic	25%
Covered	30%
Sky brightness	B about 23.0 mag/arcsecond^2
Precipitable water	Frequently less than 2mm

W. M. Keck Observatory Reports and Technical Notes*

Description of Report Designations

AV **AVAILABLE.**

HO **HISTORICAL** interest **ONLY.** These reports are not in general available, but the subject is typically covered in a more current fashion by available reports. Persons requesting these should contact the Project Science Office first.

IP **IN PREPARATION.**

LC **LIMITED COPIES** available. These reports are of a specialized or preliminary nature and should not be requested without first consulting with the Project Science Office.

***RV** **REVISED VERSION.**

NTA **NEVER TO APPEAR.** The author has lost interest in the subject or the subject matter has been superseded by more recent information before the report was completed.

/AP **ALSO PUBLISHED.**

*** Reports and Notes numbered less than 140 are historically referred to as UC Ten Meter Telescope Reports and Notes.**

W. M. Keck Observatory Reports

1977

HO 1. Design Considerations for a Large Telescope.
Jerry Nelson (July 1977)

HO 2. Proposal For Preliminary Design Study of a 10-Meter Telescope.
Robert P. Kraft (October 1977)

HO 3. Mirror Segmentation of the 10 Meter Telescope, Design Considerations.
Jerry Nelson (November 1977)

AV /AP 4. The Proposed University of California 10 Meter Telescope.
Jerry Nelson (December 1977)
Optical Telescopes of the Future. Conference proceedings. Dec. 1977. Geneva 23:ESO c/o CERN 1978.

1978

AV 5. Protostellar Condensation Studies with a 10-meter Telescope at an Exceptional Site.
David Cudaback (February 1978)

HO 6. Telescope Progress Reports: Majority and Minority Views.
Harland Epps, Sandra Faber, Joseph Wampler, Jerry Nelson (May 1978)

LC 7. An f/1.5 Wide Field Camera Design.
D. Schulte (May 1978)

HO 8. Study of Segmented Primary Mirrors.
Optical Sciences Center of U.of A. (June 1978)

HO 9. Summary and Proceedings of the The l0-meter Telescope Conference (Santa Cruz, Dec 15-18,1978).
(Last appendix of TMT Report #17)
edited by E.J. Wampler (Dec 1978)

1979

HO 10. Slumping a Thin Monolithic Mirror/ Stresses in a Monolith.
(Appendix C in TMT Report #24)
S.T. Gulati (January 1979)/ Jerry Nelson (April 1979)

LC 11. Prime Focus Corrector for the Ten Meter Telescope.
C.J. Kim and R.R. Shannon (January 1979)

AV /AP 12. Segmented Mirror Design for a 10-Meter Telescope.
Jerry Nelson (January 1979)
S.P.I.E., Vol. 172, p.31, Instrumentation in Astronomy III (1979).

AV /AP 13. Position Sensors and Actuators For Figure Control of a Segmented Mirror Telescope.
George Gabor (January 1979)
S.P.I.E., Vol. 172, p.39, Instrumentation in Astronomy III (1979).

AV 14. Possible Effects of Wind on the Operation of the Proposed 10-m Telescope.
W. J. Welch (February 1979)

HO 15. Figure Control For a Segmented Telescope Mirror.
Terry Mast and Jerry Nelson (March 1979)

HO 16. The U. of C. 400-inch Telescope from an Optical Point of View.
Harland Epps (March 1979)

HO 17. Progress Report of the Technical Design Committee.
(March 1979)

HO 18. U. of C. 10-m Telescope - Monolith Option MM-1,M-2.
A. B. Meinel (April 1979)

LC 19. Primary Mirror Fabrication Scenario.
("Scenario" section of TMT Report #25)
Jerry Nelson (October 1979)

HO 20. The Finite Element Analysis of a 10-meter Monolithic Telescope Mirror.
(Appendix D of TMT Report #24)
Ed Wilson (Engineering/Analysis Corp) (November 1979)

AV /AP 21. Stressed Mirror Polishing: A Technique for Producing Non-axisymmetric Mirrors.
Jacob Lubliner and Jerry Nelson (November 1979)
Applied Optics, Vol. 19, p. 2332, July 15, 1980.

AV /AP 22. Stressed Mirror Polishing: Fabrication of an Off-Axis Section of a Paraboloid.
Jerry Nelson, George Gabor, Leslie Hunt, Jacob Lubliner, and Terry Mast (November 1979)
Applied Optics, Vol. 19, p. 2341, July 15, 1980.

AV 23. Optical Tests For Mirror Segments.
Jerry Nelson and Terry Mast (November 1979)

HO 24. The Choice of Primary Mirror for the UC 10-Meter Telescope.
Harland Epps, Dave Rank, Joseph Wampler (November 1979)

HO 25. Proposal for a Segmented Primary Mirror For the U.C. Ten Meter Telescope.
Jerry Nelson, George Gabor, Jacob Lubliner, Terry Mast, and William J. Welch (November 1979)

AV 26. Support Dynamics for a Large Primary Mirror.
William J. Welch (November 1979)

HO 27. Cutting Hexagonal Mirror Segments.
Jerry Nelson (November 1979)

HO 28. Tolerances for the Ten Meter Telescope.
Harland Epps and Roger Ulrich (December 1979)

1980

AV 29. Use of the Ten Meter Telescope as an Element of an Interferometer.
Dave Cudaback (January 1980)

HO 30. Design Studies for the U.C. 10-Meter Segmented Mirror Telescope.
Aden and Marjorie Meinel (January 1980)

HO 31. Concept Integration Study for the 10-meter Segmented Mirror Telescope.
Aden and Marjorie Meinel (January 1980)

IP *RV 32. Fabrication and Alignment Tolerances for Mirror Segments and Sensors.
Jerry Nelson (February 1980, Rev. Feb. 1983, Rev. March 1985)

LC 33. Progress Report of Technical Design Committee. (April 1980)

AV 34. Focus, Collimation, and Pointing Control of the Ten Meter Telescope.
William J. Welch (June 1980)

HO 35. Conceptual Design and Specifications of the TMT Building and Dome.
(Appendix D of TMT Report #39)
John Wells (June 1980)

AV 36. Displacement Sensors and Actuators Needed to Control a Segmented Primary Mirror.
George Gabor (June 1980)

AV 37. Seeing Control in the TMT Dome.
(Appendix E of TMT Report #39)
Holland Ford (July 1980)

HO 38. Interim Report on Conceptual Structural Design.
(Appendix I of TMT Report #39)
Stefan Medwadowski (July 1980)

LC 39. Progress Report of the Technical Design Committee. (July 1980).

AV 40. Tests on a Graphite-Vinyl-Ester Rod as a Length Standard.
Donald Terndrup (July 1980)

AV 41. The Size and Number of Primary Segments.
(Appendix C of TMT Report #39)
Jerry Nelson (July 1980)

AV 42. Tests on the Hygroscopic Characteristics of Graphite-Vinyl-Ester Rods.
Peter Holland and Donald Terndrup (August 1980)

AV 43. The University of California Ten Meter Telescope: An Interim Report to the President.
Telescope Design Team (October 1980)

AV 44. A Precision Measurement of the Radius of Curvature of a Spherical Mirror.
Peter Holland and Donald Terndrup (December 1980)

LC 45. Operation of the Ten Meter Telescope and Auxiliary Instruments from a Remote Site.
Holland Ford (December 1980)

1981

IP 46. The Use of the Ten Meter Telescope At Infrared Wavelengths.
Keith Matthews (January 1981)

AV 47. The Effects of Wind Loads on the Ten Meter Telescope.
Jerry Nelson (January 1981)

AV 48. Mirror Segment Motions from Gravitational Deformations of the Cell.
Jerry Nelson and Terry Mast

AV 49. Geometrical Relations for an Altitude Azimuth Telescope.
Jerry Nelson (January 1981)

AV 50. Preliminary Design of the Tube for the TMT.
Jacob Lubliner (January 1981)

AV 5l. Effects of Altitude on Performance and Health: Stress and 4 km High
/AP Telescopes.
David Cudaback (January 1981)
PASP, Vol. 96, p. 463, June 1984.

AV 52. Setting Acceptable Limits for the Thermal Coefficient of Segments.
*RV Jerry Nelson (February 1981, Rev. 1984)

AV 53. UC TMT Pier Rotation due to Wind Action on the Observatory Dome.
*RV Steve Medwadowski (February 1981, Rev. July 1984)

HO 54. Project Summary for Executive Management Committee Meeting.
Telescope Design Team (11 February 1981)

AV 55. Formulae Relevant to the Optical Performance of Telescopes.
*RV Sandra Faber (April 1981, Rev. Aug. 1983)

AV 56. The Contribution of Focus Errors to the Optical Error Budget.
Sandra Faber (April 1981)

AV 57. Estimated Diameters of Infrared Images.
*RV Sandra Faber and Jerry Nelson (April 1981, Rev. Oct. 1982)

LC 58. Milestones for a Prototype Mirror.
Andy Dubois (April 1981)

LC 59. Conceptual Design of Structure of the U.C. Ten Meter Telescope: Final Report, Phase II.
Stefan Medwadowski (May 1981)

HO 60. Funding Proposal for the Technical Demonstration and Preliminary Design of the UC TMT.
Coordinator, Andy Dubois (June 1981)

AV 61. The Optimum Match between Image Size and the Size of Detector Pixels: The Choice of Angular Scale.
Sandra Faber (June 1981)

AV 62. Matching Representative Instruments and Detectors to the Ten Meter Telescope: Specific Examples.
Sandra Faber (June 1981)

LC 63. Science for the Ten Meter Telescope.
Sandra Faber (June 1981)

AV 64. Figure Control For a Fully Segmented Primary Mirror.
Terry Mast and Jerry Nelson (December 1981)

LC 65. Technical Demonstration Progress Report (December 1981).

AV 66. A Summary of Nine Years of Weather Data From Mauna Kea Observatory.
James Kaufman and Maurizio Vecchione (August 1981)

AV 67. Coherent Large Telescopes.
/AP Jerry Nelson (March 1981)
Proceedings of the ESO Conference on "Scientific Importance of High Angular Resolution at Infrared and Optical Wavelengths" Garching, 24-27 March 1981.

1982

AV 68. The Effects of Primary Mirror Segmentation on Image Quality.
/AP Terry Mast, Jerry Nelson, and William Welch (Jan 1982) S.P.I.E., Vol. 332, p. 123, Advanced Technology Optical Telescopes (1982).

LC 69. Technical Demonstration Progress Report (January 1982).

AV 70. An Investigation of the UC TMT Mirror Cell Structure.
Stefan Medwadowski (April 1982)

AV 71. An Investigation of the UC TMT Yoke Structure.
Stefan Medwadowski (February 1982)

AV 72. An Alternate Geometry for the UC TMT Yoke Structure.
Stefan Medwadowski (February 1982)

LC 73. Technical Demonstration Progress Report (February 1982).

AV 74. Telescope Mirror Supports: Plate Deflections on Point Supports.
/AP Jerry Nelson, Jacob Lubliner, and Terry Mast (March 1982)
S.P.I.E., Vol. 332, p. 212, Advanced Technology Optical Telescopes (1982).

AV 75. The University of California Ten Meter Telescope Project.
/AP Jerry Nelson (March 1982)
S.P.I.E., Vol. 332, p. 109, Advanced Technology Optical Telescopes (1982).

LC 76. Technical Demonstration Progress Report (March 1982).

LC 77. The Mirror Control System for the UC Technical Demonstration Prototype.
/AP George Gabor (March 1982)
S.P.I.E., Vol. 332, p. 382, Advanced Technology Optical Telescopes (1982).

LC 78. The Infrared Performance of the University of California Ten Meter Telescope.
/AP Barbara Jones, and Keith Matthews (March 1982)
S.P.I.E., Vol. 332, p. 117, Advanced Technology Optical Telescopes (1982).

AV 79. Remote Operation of Telescopes: Long-Distance Observing.
/AP Holland Ford (February 1982)
S.P.I.E., Vol. 332, p. 243, Advanced Technology Optical Telescopes (1982).

AV 80. Figure Control for a Segmented Mirror.
Terry Mast and Jerry Nelson (April 1982)

LC 81. Technical Demonstration Progress Report (April 1982).

AV 82. Wind Loading of Large Astronomical Telescopes.
/AP Fred Forbes and George Gabor (May 1982)
S.P.I.E., Vol. 332, p. 198, Advanced Technology Optical Telescopes (1982).

LC 83. Technical Demonstration Progress Report (May 1982).

LC 84. Technical Demonstration Progress Report (June 1982).

AV 85. Building and Dome Schematic Design.
Richard Rose and Robert Hoggan (Nov. 1981)

LC 85A. Building and Dome Schematic Drawings.
Richard Rose and Robert Hoggan (Nov. 1981)

LC 86. Technical Demonstration Progress Report (July 1982).

AV 87. Stressed Mirror Polishing of Polygonal Plates.
Jacob Lubliner (July 1982)

LC 88. Technical Demonstration Progress Report (Aug. 1982).

LC 89. Analysis of the Ritchey-Common Test for Optical Flats.
Terry Mast (Sept. 1982)

IP 90. The Design of the Keck Observatory and Telescope (Ten Meter Telescope).
Jerry Nelson, Terry Mast, and Sandy Faber, editors (Jan. 1985)

AV 91. Off-axis Expansions of Conics.
Jerry Nelson and Marc Temple-Raston (Oct. 1982)

LC 92. Ten Meter Telescope Progress Report (Sept. 1982).

IP 93. Ten Meter Telescope Drives and Bearings.
Jack Osborne

LC 94. Ten Meter Telescope Progress Report (Oct. 1982).

LC 95. Ten Meter Telescope Progress Report (Nov. 1982).

1983

LC 96. Ten Meter Telescope Progress Report (Dec. '82-Jan. '83).

LC 97. The University of California Ten Meter Telescope Project.
/AP Jerry Nelson (Dec. 1982)
The Annals of the New York Academy of Sciences, Vol. 422, p. 140, Eleventh Texas Symposium on Relativistic Astrophysics (Pub. 1984).

AV 98. Selecting the Sphere Radius for Stressed Mirror Polishing.
Jerry Nelson (Feb. 1983)

LC 99. Ten Meter Telescope Progress Report (Feb. 1983).

LC 100. Ten Meter Telescope Progress Report (Mar. 1983).

AV 101. A High Resolution Optical Spectrometer for the Ten Meter Telescope.
I. Design Study
Steven S. Vogt (Apr. 1983)

AV 102. Initial Phasing of the TMT Mirror Segments.
B. M. Oliver (Apr. 1983)

LC 103. Ten Meter Telescope Progress Report (Apr. 1983).

LC 104. Ten Meter Telescope Progress Report (May 1983).
LC 105. Ten Meter Telescope Progress Report (June 1983).
LC 106. Ten Meter Telescope Progress Report (July 1983).
AV /AP 107. Edge Sensors for a Segmented Mirror.
Terry Mast, George Gabor, Jerry Nelson (Sept. 1983)
S.P.I.E., Vol. 444, p. 297, Advanced Technology Optical Telescopes II (1983).
AV 108. The Segmented Mirror Control System Prototype for the TMT: Status Report.
Jerry Nelson, Michael Budiansky, George Gabor, Terry Mast (Sept. 1983)
S.P.I.E., Vol. 444, p. 274, Advanced Technology Optical Telescopes II (1983).
AV /AP 109. Analysis of Mirror Supports for the U.C. Ten Meter Telescope.
Michael Budiansky, Jerry Nelson (Nov. 1983)
S.P.I.E., Vol. 450, p. 59, Structural Mechanics of Optical Systems (1983).
LC 110. Ten Meter Telescope Progress Report (Aug./Sept. 1983).
AV /AP 111. Actuators for a Segmented Mirror Control System.
George Gabor (Sept. 1983)
S.P.I.E., Vol. 444, p. 287, Advanced Technology Optical Telescopes II (1983).
LC 112. Ten Meter Telescope Progress Report (Oct. 1983).
AV 113. The University of California Ten Meter Telescope Instrumentation Conference, 24-25 January 1983, Santa Cruz, CA.
IP 114. Analysis of McFarlane's Wide Field Camera Design.
Dan Schroeder
AV /AP 115. Figure Adjustment of Hexagonal Mirrors by Applied Moments.
Michael Budiansky (15 Oct. 1984)
Applied Optics, Vol. 23, No. 20, page 3684, Oct. 15, 1984.
LC 116. Ten Meter Telescope Progress Report (Nov. 1983).
LC 117. Ten Meter Telescope Progress Report (Dec. 1983).

1984

LC 118. Ten Meter Telescope Progress Report (Jan. 1984).
LC 119. Ten Meter Telescope Progress Report (Feb. 1984).
LC 120. Ten Meter Telescope Progress Report (Mar. 1984).
LC 121. Ten Meter Telescope Progress Report (Apr. 1984).
LC 122. University of California Ten Meter Telescope (a brief elementary introduction).
Jerry Nelson (17 May 1984)
AV /AP 123. A Comparison of Observing Conditions on the Summit Cones and Shield of Mauna Kea.
Merle F. Walker
Lick Observatory Bulletin, No. 973, PASP 95: 903-918, Nov. 1983.
AV /AP 124. Re-analysis of the British NHO Site Survey Observations at the NW Cone and 88-Inch Ridge Sites on Mauna Kea.
Merle F. Walker
PASP 96: 829-835, Oct. 1984.
AV /AP 125. The University of California Ten Meter Telescope Project: Recent Developments.
Jerry Nelson (April 1984)
Proceedings of IAU Colloquium No. 79,
"Very Large Telescopes, their Instrumentation and Programs,"
Garching, April 9-12, 1984.
LC 126. Ten Meter Telescope Progress Report (May 1984).

AV 127. High Quality Astronomical Sites Around the World.
Merle F. Walker (June 1984)

AV /AP 128. Large Optical Telescopes: New Views into Space and Time.
S. M. Faber (Dec. 1982)
The Annals of the New York Academy of Sciences Vol. 422, p. 171, Eleventh Texas Symposium on Relativistic Astrophysics (Pub. 1984)

AV 129. Schematic Phase Design Report.
MBT Associates (Sept. 1984)

1985

IP 130. TMT Site Wind Characteristics.
M. Budiansky, J. Nelson

IP 131. Acoustic Sounder Measurements of Low Level Turbulence at the TMT Site.
D. Cudaback

IP 132. Site Evaluation.
R. Kraft

IP 133. Analysis of Weather Data from CFHT.

IP 134. Thermal Modeling of the Dome.
B. Carroll, C. Conners

IP 135. Support of Concave Miniscus Lenses.
B. Iraninijad and J. Nelson

IP 136. Absolute Setting for the Ten Meter Telescope.
D. Cudaback

AV 137. Optimized Mirror Cell for the Ten Meter Telescope.
S. Medwadowski (April 1985)

AV /AP 138. Fabrication of the Keck Ten Meter Telescope Primary Mirror.
Terry Mast and Jerry Nelson (March 1985)
S.P.I.E., Vol. 542, Optical Fabrication and Testing Workshop (1985).

NTA 139.

IP 140. Keck Observatory Performance Specifications.
Jerry Nelson (June 1985)

IP 141. Geometry of the Segmented Primary Mirror.
Jerry Nelson (September 1985)

AV /AP 142. The Status of the W. M. Keck Observatory and Ten Meter Telescope.
Terry Mast and Jerry Nelson (September 1985)
S.P.I.E., Optical and Electro-Optical Engneering

W. M. Keck Observatory Technical Notes

1978

LC 1. Support Precision and Minimum Thickness of a Monolithic Mirror.
Jerry Nelson (April 1978)

LC 2. Chromatic Aberration with a Spherical Primary and Thin Correcting Plate.
Jerry Nelson (April 1978)

HO 3. Paraboloidal Surfaces.
Jerry Nelson (May 1978)

LC 4. The Support of Thin Monolithic Mirrors.
Jerry Nelson (November 1978)

1979

LC 5. Optical Characteristics of an f/3.5 All Reflective Focus.
Harland Epps (April 1979)

HO 6. Comments on the All Reflective Focus.
Jerry Nelson (July 1979)

AV 7. Finding the Conic of Revolution That Best Fits a Given Mirror Surface.
*RV Jerry Nelson (October 1979, Rev. January 1984)

1980

LC 8. Report on Grating Spectrometers and Interferometers For The 10 M Telescope.
Dave Rank (March 1980)

LC 9. Loss of Limiting Magnitude on Hypersensitized IIIa-J Plates.
Holland Ford (March 1980)

AV 10. Conceptual Design of Telescope Structure.
(Appendix H of TMT Report #39)
Jacob Lubliner (July 1980)

IP 11. Further Elaboration of the Wind Specification on the Ten Meter Telescope.
Jerry Nelson(October 1980)

AV 12. Mirror Segment Motions from Gravitational Deformations of the Cell.
Jerry Nelson and Terry Mast (October 1980)

1981

AV 13. The Integral of $x^n y^m$ Over a Hexagon.
Terry Mast (April 1981)

IP 14. Sensor Geometry and Deflections.
Jerry Nelson (April 1981)

AV 15. Radius of Curvature Tolerances.
Jerry Nelson (May 1981)

IP 16. Hindle Sphere Tests of Secondary Mirrors (and Revisions).
Jerry Nelson (May 1981)

AV 17. Zernike Series Expansion of Circular Mirror Deflections on an 18 point Support.
Jerry Nelson and Jim Patterson (May 1981)

AV 18. Zernike Series Expansion of the KPNO 82-inch Flat Deflections.
Jerry Nelson and Jim Patterson (June 1981)

AV 19. Preliminary Specifications.
Jerry Nelson (October 1981)

AV 20. Deflections of Semi-Infinite Plates Supported on Many Support Points.
*RV Jerry Nelson (October 1981, Rev. November 1981)
AV 21. Estimate of Segment Deflections Caused by Sensor Weight.
Jerry Nelson (November 1981)
AV 22. Droop Mode Sensing.
Barney Oliver (December 1981)
AV 23. Hartmann Testing of the KPNO 2-meter Mirror.
Terry Mast, Jerry Nelson, and Jim Patterson (December 1981)
AV 24. Comments on IR Chopping Secondaries.
Jerry Nelson (August 1981)
AV 25. Deflections of a Circular Plate on a Ring of Point Supports.
Jacob Lubliner (February 1982)
LC 26. TMT Technical Demonstration Structure: Conceptual Design.
Jerry Nelson (July 1981)

1982

AV 27. Deflections of a Simply Supported, Variable Thickness Plate.
Jacob Lubliner (February 1982)
AV 28. Thermally Compensated Ring Mirror Supports.
Jerry Nelson (February 1982)
LC 29. SAP4 Analysis of the Technical Demonstration Yoke.
Michael Budiansky (February 1982)
AV 30. Bimetallic Effects in the Displacement Sensors.
Jerry Nelson (February 1982)
IP 31. Acceptance Test for Thermal Expansion of Low Expansion Blanks.
David Cudaback (February 1982)
AV 32. A Computer Program to Determine Zernike Coefficients by Analytic Integration.
Michael Budiansky (March 1982)
AV 33. Deflections of a Hexagonal Mirror Segment due to Error in Position of Radial-Support Post.
Michael Budiansky (March 1982)
AV 34. An Atlas of Zernike Functions.
Michael Budiansky (March 1982)
LC 35. Deflections of the Tinsley 105 cm Flat and Comparison of Methods of Calculation.
Michael Budiansky (January/March 1982)
AV 36. Support Pads for Polishing Segments
Jerry Nelson (April 1982)
AV 37. Goal for TMT Image Quality.
Jerry Nelson (May 1982)
AV 38. The Use of Spherometers to Measure Radius of Curvature.
Jerry Nelson (May 1982)
AV 39. Specifications for a 15-Meter Segmented Mirror Telescope.
Jerry Nelson, Terry Mast, George Gabor (June 1982)
AV 40. Simulated Interferograms of Various Aberrations.
Michael Budiansky (June 1982)
AV 41. Effects of Masking on Zernike Coefficients.
Jerry Nelson (June 1982)
AV 42. Optical Tests for the Fabrication of a Large Spherical Mirror with a Precisely
*RV Defined Radius of Curvature.
Terry Mast and Jerry Nelson (May 1982, Rev. Dec. 1982)
AV 43. Comments on the Significance of Internal Stress in Glass and its Effect on Warping Due to Cutting.
Jerry Nelson (July 1982)

LC 44. Dimensional Parameters of Cell and Subcell.
Michael Budiansky (July 1982)

AV 45. Partially Coherent Diffraction.
Barney Oliver (July 1982)

AV 46. Figure Control for a Segmented Mirror: Curvature Control Without Tilt Sensors.
Terry Mast (May 1982)

AV 47. Deflections of a Curved Beam: An Approximate Model for Radial Support Deflections.
Jacob Lubliner (July 1982)

AV 48. The Warping of Mirrors Due to Cutting After Polishing: Elementary Theory.
Jacob Lubliner (July 1982)

AV 49. Thermal Deflections of Circular Plates.
Jacob Lubliner (July 1982)

LC 50. Effects of Loads on the Edge of the Technical Demonstration Mirror.
Michael Budiansky and Jerry Nelson (Aug. 1982)

AV 51. Focus and Spherical Aberration Introduced by the Deflection of Plates.
Jerry Nelson (Sept. 1982)

LC 52. Location of Axial Support Points for Hexagonal Mirror.
Michael Budiansky (Sept. 1982)

1983

AV 53. OMNI: A Program to Calculate Shear Forces and Moments for Stressed Mirror Polishing.
Leslie K. Hunt (Jan. 1983)

LC 54. FEAP Analysis of Axial Support of the Mirror Blank for the Technical
*RV Demonstration.
Michael Budiansky (Jan. 1983, Rev. 14 Feb. 1983)

AV 55. The Apparent Radius of Curvature in Optical Tests Made in Air with a Thermal Gradient.
Terry Mast (Jan. 1983)

NTA 56.

AV 57. Specifications of the UC Ten Meter Telescope.
Jerry Nelson, Terry Mast, George Gabor, Sandy Faber (Jan. 1983)

AV 58. Telescope Pier Rotation From Wind Loads on Building and Dome.
Jerry Nelson (Feb. 1983)

LC 59. Dimensional Parameters of TD Telescope Tube.
Michael Budiansky (Feb. 1983).

AV 60. Control Algorithm for the Technical Demonstration Control System Prototype.
Terry Mast (Feb. 1983)

AV 61. Temperature Measurement System for the TMT TD.
Michael Breen (Feb. 1983)

LC 62. Tests of a Position Actuator for the Ten Meter Telescope Segments.
/AP Lloyd Robinson (June 1982)
Lick 0bservatory Technical Reports No. 29.

AV 63. FORTRAN Subroutines for Geometric Manipulations in 3 Dimensions.
Michael Budiansky (Feb. 1983)

LC 64. Calculations of Center-of-Gravity of Hexagonal Mirror Segment for the Technical Demonstration.
Michael Budiansky (Apr. 1983)

IP 65. Deflection of a Self-loaded Circular Plate with a Concentric Hole on a Ring Support.
J. Lubliner

AV 66. The Control System Prototype Mirror: Final Fabrication Procedures.
ed. T. Mast (Apr. 1983)

AV 67. Handling, Installation, and Removal of Prime Focus Instruments.
Robert Weitzmann (May 1983)

LC 68. Evaluation of Recent KPNO Polish of Sphere.
Jerry Nelson (May 1983)

AV 69. Deflections of a Circular Plate on 3 and 6 Points.
Jerry Nelson (May 1983)

LC 70. Finite-Element Analysis of Support for Reference Mirror.
Michael Budiansky (May 1983)

AV 71. Results of the Technical Demonstration Polishing.
Jerry Nelson, Terry Mast, Michael Budiansky (July 1983)

LC 72. Deflections of the Circular Mirror When Supported by the Whiffletrees for the Hexagonal Mirror Segments.
Michael Budiansky (July 1983)

LC 73. Sensitivity of Hexagonal Mirror to Moments Introduced at Support Points.
Michael Budiansky (August 1983)

LC 74. Support of Hexagonal Mirror Segment When Pointed at the Horizon.
Michael Budiansky (Aug. 1983)

AV 75. Analysis of Bending of Flexrods in Mirror Support Assemblies.
Michael Budiansky (Sept. 1983)

AV *RV 76. Axial Mirror Support: Sensitivity Analysis (Circular Mirror Blank on Whiffletrees for Hexagon).
Michael Budiansky (Oct. 1983, Rev. Apr. 1984)

AV 77. Measuring the Radius of Curvature with a Reference Sphere.
Joseph Magner and Jerry Nelson (Oct. 1983)

AV 78. Zernike Coefficients of Off-Axis Segments.
Jerry Nelson (November 1983)

AV 79. U. C. Ten Meter Telescope Enclosure Requirements.
(March 1984)

LC 80. Further Analysis of Axial Support for Reference Mirror.
Michael Budiansky (Nov. 1983)

AV 81. Analysis of Axial Support of the Tertiary Mirror.
Michael Budiansky and Jerry Nelson (Nov. 1983)

LC *RV 82. Analysis of Distortions Introduced by Displacement of Actuator Posts.
Michael Budiansky (Dec. 1983, Rev. Apr. 1984)

AV 83. Decomposition of Wavefront Errors in Optical Testing.
Michael Budiansky, Terry Mast, Jerry Nelson

AV 84. Computer Method for R.M.S. Calculations of Function Described by Zernike Polynomials and Defined over Hexagonal Region.
Michael Budiansky (Dec. 1983)

IP 85. Axial Supporters for Reference Mirror.
Jack Osborne (Dec. 1983)

AV *RV 86. Definition of Coordinate Systems and Conventions for Labelling the Components of the TMT Primary Mirror.
Barbara Schaefer, Terry Mast

AV 87. Lifting Ring for the Hexagonal Mirrors for the Technical Demonstration.
Jerry Nelson, George Gabor, Terry Mast (Mar. 1983)

1984

AV *RV 88. Mirror Blank Specifications for the TMT.
Terry Mast, Jerry Nelson, Joseph Magner (Feb. 1984, Rev. April 1985)

AV *RV 89. TMT Specifications for Generating the Primary Mirror Segments.
Terry Mast, Jerry Nelson, Joseph Magner (Feb. 1984, Rev. April 1985)

AV 90. TMT Segment Specifications.
*RV Terry Mast (Feb. 1984, Rev. April 1985)
NTA 91.
LC 92. Summary of Test Results on Control Prototype Mirror.
Terry Mast
IP 93. Control System Response to Thermal Expansion of the Mirror Cell.
Terry Mast (Feb. 1984)
AV 94. Test of Figure Adjustment of a Segment Using Forces Applied to the Whiffletree Pads.
Terry Mast, Michael Budiansky, Jerry Nelson (Apr. 1984)
AV 95. Theory of Figure Adjustment of a Mirror Segment Using Forces Applied to the Whiffletree Pads.
Michael Budiansky
AV 96. Diffraction Limited Imaging and Spectroscopy with the NNTT: A Comparison of SMT and MMT Sensitivities.
Terry Mast and Jerry Nelson (April. 1984)
IP 97. Goals for the Technical Demonstration.
Terry Mast, Jerry Nelson, George Gabor (May 1984)
AV 98. A Pinhole Tester for the TMT Technical Demonstration Sphere.
J.A. Hudson (May 1984)
AV 99. Rediscussion of TMT Optical Design Parameters.
Jerry Nelson (June 1984)
LC 100. Request for Proposal (RFP) for Manufacture of TMT Primary Mirror Segments.
*RV Joseph Magner, Gerry M. Smith, Jerry E. Nelson (June 1984, Rev. April 1985)
AV 101. A Computer Program to Calculate the Geometry of a Segmented Array.
David Nelson (June 1984)
AV 102. Definite Integrals over a Hexagonal Region of Products of Zernike Polynomials.
Michael Budiansky (June 1984)
AV 103. A Technical Memoir of Finite-Element Programming for the TMT.
Michael Budiansky (June 1984)
AV 104. KPNO Stressed Mirror Polishing History.
Joseph Magner (June 1984)
AV 105. Technical Demonstration Task at Berkeley.
Joseph Magner (July 1984)
AV 106. On the Use of the Same Warping Whiffletrees for Different Types of TMT Mirror Segments.
Michael Budiansky (July 1984)
IP 107. Proposed "Inverted Crown" Yoke and "Turret" Pier System.
Fred Hendy
IP 108. IR Observing Time.
Jerry Nelson (Sept. 1984)
AV 109. Mirror Cell Structure for the 15-Meter NNTT Segmented Mirror.
Stefan Medwadowski (Aug. 1984)
AV 110. Preliminary Geotechnical Services.
Harding Lawson Associates (Aug. 1984)
IP 111. Deformations in a Flat from Grinding.
Jerry Nelson and Barbara Schaefer (October 1984)
AV 112. Infrared Characteristics of the Segmented Primary Mirror.
Terry Mast (Nov. 1984)

1985

IP 113. Primary Mirror Error Budget.
Jerry Nelson and Terry Mast

IP 114. Radial Support System for the Ten Meter Telescope.
Bob Weitzmann

AV 115. Warping of a Hexagonal Mirror Segment by Forces and Moments Applied at Edges.
Michael Budiansky (Jan. 1985)

AV 116. GENHEX: Program for Automatic Generation of Full Hexagonal Meshes for FEAP Input.
Michael Budiansky (Jan. 1985)

AV 117. An Alternative TMT ActuatorSystem Using a Lever-Fulcrum.
*RV Terry Mast and Jerry Nelson (Feb. 85, Rev. April 85)

AV 118. Modification of the Active Control Performance Requirements.
Terry Mast

AV 119. Bendix Flex Pivot Radial Stiffness.
*RV Terry Mast

AV 120. Modification to Sensor Design.
Terry Mast, George Gabor, Bob Minor, and Jerry Nelson

AV 121. Subcell Structure for the Ten Meter Telescope.
Stefan Medwadowski

IP 122. Segment Fabrication Test.
Terry Mast, Joseph Magner, and Jerry Nelson

AV 123. Ten Meter Telescopes Used as an Interferometer.
Cliff Stoll

IP 124. Ten Meter Telescope Whiffletree Specifications.
Terry Mast

AV 125. Actuator Performance Requirements.
Terry Mast

AV 126. A Spring Warping Harness: Test Results.
Terry Mast and Jerry Nelson (April 1985)

AV 127. Segment Handler Specifications.
Terry Mast

IP 128. Functions Requiring Computing.
Cliff Stoll

IP 129. Phase Support Specifications.
Terry Mast

IP 130. Northwest Cone Wind Data.
Kathy Poliakoff and Jerry Nelson

IP 131. CFHT Wind Data.
Kathy Poliakoff and Jerry Nelson

AV 132. Alternate Sensors.
Cliff Stoll

AV 133. Global Electronics.
Cliff Stoll

AV 134. An Alternative Actuator Design - Use a Differential Roller Screw.
Cliff Stoll and Jerry Nelson (May 1985)

IP 135. Mirror Segment Installation and Removal Procedures for the TMT Primary Mirror.
Robert Weitzmann, Terry Mast and Jerry Nelson

IP 136. Ten Meter Telescope Hydrostatic Bearing System:
Conceptual Design Study.
W. L. Pope (May 1985)

AV 137. Actuator Travel Range and Mechanical Sensor Range.
Andrew Dubois, Terry Mast, and Jerry Nelson (May 1985)

AV 138. Ten Meter Telescope Hydraulic Actuator.
Jack Franck (23 Feb. 1985)

AV 139. Fringe Field Effects in the Capacitive Displacement Sensors.
*RV Terry Mast (June 1985)

AV 140. Critical Telescope Dimensions.
Jerry Nelson (May 1985)

IP 141. Report on Fatigue Testing of the Ten Meter Telescope Radial Support Post.
Robert Weitzmann (May 1985)

IP 142. Stress-Strain Relationship for a Diaphragm Clamped at the Inner and Outer Edges, and Subjected to Axial Displacements.
Robert Weitzmann (May 1985)

AV 143. Segment Mass and Center of Gravity.
Jerry Nelson (June 1985)

AV 144. An Investigation into the Feasibility and Costs of Installation of Digital Data and Video Microwave Transmission Paths for the Ten Meter Telescope at Mauna Kea, Hawaii.
Aubrey Harris (December 1984)

AV 145. Location of the Actuator Nodes.
Terry Mast (July 1985)

AV 146. Satellite Communications from Hawaii to California.
Cliff Stoll (August 1985)

AV 147. Loads on the Primary Mirror Segments.
Terry Mast (August 1985)

IP 148. Optimum Location for a 6 Point Ring Supporting a Regular Hexagon.
Bijan Iraninejad (August 1985)

References

Allen, C. W., *Astrophysical Quantities,* Athlone Press, 1973.

Alvarez, L. W., private communication, 1978.

Angel, J. R. P., and Hill, J. M., *Advanced Technology Optical Telescopes II, Proceedings of SPIE,* **444,** 184, "Steps Toward 8m Honeycomb Mirror Blanks--III 1.8m Honeycomb Sandwich Blanks Cast From Borosilicate Glass" 1983a.

Angel, J. R. P., Woolf, N. J., Hill, J. M., and Goble, N., *Advanced Technology Optical Telescopes II, Proceedings of SPIE,* **444,** 194, "Steps Toward 8m Honeycomb Mirror Blanks--IV Some Aspects of Design and Fabrication" 1983b.

Aaronson, M., *Astrophysical Journal Letters,* **221,** L103, 1978.

Bahcall, J. N. and Soneira, R. M., *Astrophysical Journal Supplement,* **47,** 337, 1981.

Barakat, R., and Nisenson, P., *Journal of the Optical Society of America,* **71,** 1390, 1981.

Barr, L. D., Gillett, P. E., and Shu, K. L., *SPIE Proceedings,* **444,** 1983.

Barr, L. D., Richardson, J. H., and Shu, K-L, *SPIE Proceedings,* **540,** "Bend and Polish Fabrication Techniques" 1985

Beckers, J. M., *MMTO Technical Report No. 10,* Tucson: Multiple Mirror Telescope Observatory, 1981.

Beckers, J. M., Hege, E. K., and Murphy, H. P., *Instrumentation in Astronomy V, Proceedings of SPIE,* **445,** 63, "The Differential Speckle Interferometer" 1983.

Beckers, J. M., *et al., Telescopes for the 1980s,* Annual Reviews Monograph, ed. G. Burbidge and A. Hewitt, "The Multiple Mirror Telescope" 1981.

Beckmann, P. and Spizzichino, A., *The Scattering of Electromagnetic Waves From Rough Surfaces,* Macmillan, 1963.

Boesgaard, H., private communication, 1984.

Born, M., and Wolf, E. *Principles of Optics,* 6th edition, Pergamon Press, 1980.

Boyd, R. W., *J.O.S.A.,* **68,** 877, 1978.

Crane, R., *Optical Telescope Technology Workshop, NASA Report SP-233,* 297, "Figure Sensing Techniques" 1969.

Dainty, J. C., "Telescope Requirements for Speckle Interferometry" ESO Conference: Optical Telescopes of the Future, ed. Pacini, et al., Geneva, 1977.

de Vaucouleurs, G., de Vaucouleurs, A., and Corwin, H., *Second Reference Catalogue of Bright Galaxies,* University of Texas Press, 1976.

Epps, H. W., private communication (1985)

Epps, H. W., Angel, J. R. P., and Anderson, E., *I.A.U. Colloquium,* No. 79, in press, 1984.

Epps, H. W., preprint, "Optical Designs for the UC Ten-Meter Telescope" in preparation, 1984b.

Everhart, E., *Applied Optics,* **5,** 713, 1966.

Fienup, J. R., *Applied Optics,* **21,** 2758, 1982.

Firmani, *et al.,* Reviews of Scientific Instruments, **53,** 570, 1982.

Forster, P. J. G., *P.A.S.P.,* **96,** 478, 1984.

Fried, *J.O.S.A.,* **56,** 1372, 1966.

Gehrz, R., editor, *Report of the National New Technology Telescope Scientific Advisory Commitee,* Kitt Peak National Observatory, 1984.

Gillard, C. W., Buholz, N. E., and Ridder, D. W., *Proceedings of the International Society for Optical Engineering, SPIE,* **228,** 70-77, "Absolute Distance Interferometry" 1980.

Gillard, C. W., and Buholz, *Optical Engineering,* **22,** 348, "Progress in Absolute Distance Interferometry" 1983a.

Gillard, C. W., *Proceedings of the International Society for Optical Engineering, SPIE,* **444,** 310, "Segmented Mirror Edge Alignment Sensor" 1983b.

Gillingham, P., *AAT Dome Seeing,* Epping: Anglo Australian Observatory, 1978.

Golden, L., Gillett, P., Radau, R., Richardson, J., and Poczulp, G., *SPIE Proceedings,* **332,** 1982.

Griffiths, R., private communication, 1984.

Hall, D. N., editor, *The Space Telescope Observatory,* Space Telescope Science Institute, 1982.

Harrington, J. A., *Optics News,* September/October, page 23, 1984.

Hill, J. M., Angel, J. R. P., and Richardson, E. H., *Instrumentation in Astronomy V, Proceedings of SPIE,* **445,** 85, "Optical Matching for Fiber Optic Spectroscopy" September 1983.

Howell, R. R., remarks at the UC TMT Instrumentation Conference, Santa Cruz, January 24-25, 1983.

Hufnagel, R. E., *The Infrared Handbook,* ed. W. L. Wolfe, and G. J. Zissis, Chap. 6 Washington, DC: US Government Printing Office, 1978.

Jacobs, S. F., Johnston, S. C., and Hansen, G. A. *Applied Optics,* **23,** 3014, 1984.

Johnson, H. L., *Annual Review of Astronomy and Astrophysics,* **4,** 193, 1966.

King, I. R., *P.A.S.P,* **95,** 163, 1983.

Knox, K. T., and Thompson B. J., *Astrophysical Journal Letters,* **193,** L45, 1974.

LeMaitre, G. *Nouv. Rev. Optique,* 6, 361, 1974.

Leonard, A. S., Proceedings 69, Joint Convention of Western Amateur Astronomers and Association of Lunar and Planetary Observers, 1969.

McKay, C. D., *Instrumentation in Astronomy IV, Proceedings of SPIE,* **331,** 146, 1982.

McInnes, *Q.J.R. Astron. Soc.,* 266, 1981.

Merrill, K. M., and Forbes, F. F., *NNTT Site Evaluation Project Prompt Report No. 1,* 1984.

Merrill, K. M., and Forbes, F. F., *NNTT Site Evaluation Project Prompt Report No. 2,* 1984.

Merrill, K. M., private communication.

Mischung, K. N., *Proceedings of the IAU Colloquium No. 79: Very Large Telescopes, their Instrumentation and Programs,* Garching, April 9-12, 1984.

Morrison, *et al., P.A.S.P.,* **85,** 255, 1973.

Murdin, P. G., and Bingham, G., *Observatory,* **95,** 180, 1975.

Noethe, L., Franza, F., Giordano, P., Wilson, R., *Proceedings of the IAU Colloquium No. 79: Very Large Telescopes, their Instrumentation and Programs,* Garching, April 9-12, 1984.

Noxon, J., private communication, 1984.

Oke, J. B., Bertola, F., and Capaccioli, M., *Astrophysical Journal,* **243,** 453, 1981.

Oke, J. B., and Gunn, *P.A.S.P.,* **94,** 586, 1982.

Phillipps, S., *Astronomy and Astrophysics,* **136,** 371, 1984.

Pipher, J. L., Willner, S. P., and Fazio, G. G., in *Proceedings of the Twenty-Fifth Plenary Meeting of COSPAR, Advances in Space Research,* 1984.

Porter, S. C., *Geologic Society of America Bulletin, Part II,* **90,** 7, 1979a.

Porter, S. C., *Geologic Society of America Map and Chart Series, MC-30,* 1979b.

Powell, J. R. *Advanced Technology Optical Telescopes II, Proceedings of SPIE,* **444,** "Application of Optical Fibers to Astronomical Instrumentation" 1983.

Racine, R., *"Very Large Telescopes, Their Instrumentation and Programs"* IAU Coll. No. 79, Garching, 1984.

Radau, S., *KPNO Report, The Tripod Method--Sensitivity Factors,* 1981.

Rank, D., Capps, F., and Low, F., private communications, 1984.

Reed, M. A., *Smithsonian Astrophysical Observatory Report,* **385,** 65-77, "The Multiple Mirror Telescope Active Optics" 1979.

Roddier, F., in *Workshop on ESO's Very Large Telescope,* ed., J. P. Swings, and K. Kjar, ESO Conference and Workshop Proceedings No. 17, 155, 1983.

Sanger, G. M., Haffman, T. E., and Reed, M. A., *Proceedings of the Society of Photo-Optical Instrumentation Engineers, SPIE,* **28,** "Some Design Aspects of a Multi-Mirror Telescope" 1972.

Shack, *NGT Report No. 3: A Concept for a 25m Telescope--The Steerable Dish,* Kitt Peak National Observatory, 1977.

Shaffer, J. J., and Bennett, H. E., *Applied Optics,* **23,** 2852, 1984.

SIRTF Interim Report, SIRTF Working Group, 1978.

Hall, D. N., editor, *The Space Telescope Observatory,* Special Session of IAU Commission 44, Patras, Greece. 1982.

Stair, A. T., *et al.,* **in** *The Radiating Atmosphere,* ed. B. M. McCormac, Reidel Pub. Co., 185, 1971.

Strittmatter, P., editor, *The Scientific Case for a Very Large Aperture Ground-Based Telescope,* Kitt Peak National Observatory NGT Scientific Advisory Commitee, 1980.

Swanson, P., Breckinridge, J., Gulkis, S., and Kuiper, T. B. H., *Proceedings of the International Society for Optical Engineering, SPIE,* **332,** 357, "Plans for a Large Deployable Reflector for Submillimeter and Infrared Astronomy from Space" 1982. See also NASA Conference Publication #2275 (1982) and NASA Contractor Reports 152402 (1980) and 166493 (1983).

Swings, J. P., and Kjar, K., editors, *Workshop on ESO's Very Large Telescope,* ESO Conference and Workshop Proceedings No. 17, 1983.

Terndrup, D., private communication, 1984.

Thompson, L. A., and Ryerson, H. R., *Instrumentation in Astronomy V, Proceedings of SPIE,* **445,** 560, "An Active Mirror Image Stabilizing Instrument System (ISIS) for Use on Mauna Kea" 1983.

Turnrose, B. E., *P.A.S.P,* **86,** 545, 1974.

Walker, M., *P.A.S.P.,* **70,** 672, 1970.

Westphal, J. A., in *The Space Telescope Observatory,* ed. D. N. B. Hall, Space Telescope Science Institute, 28, 1982.

Westphal, *Preliminary Report of the 10 Micron Infrared Sky Noise Survey,* 1972.

Woolf, N. J., and Angel, J. R. P., *Optical and Infrared Telescopes for the 1990's,* ed. Hewitt, A., Tucson: Kitt Peak National Observatory, 1980. (Note an error in this paper corrected by Woolf, 1982, p. 377).

Woolf, N. J., *Ann. Rev. Astron. Astrophys.,* **20,** 367-98, "High Resolution Imaging From the Ground" 1982.

Woolf, N. J., *P. A. S. P.,* **91,** 542, "Dome Seeing" 1979

Woolf, N. J., private communication, 1985